

Atmospheric Dispersion of Radioactive Gaseous Discharges in the Near Field of Buildings

by

David John Gallacher



Submitted for the Degree of Doctor of Philosophy

Department of Mechanical Engineering Sciences
Faculty of Engineering and Physical Sciences
University of Surrey

Supervisors:

Professor Alan Robins
Dr Matteo Carpentieri
Professor Paul Marsden

©David John Gallacher 2021

Acknowledgements

With much thanks and warmest regards to my principal PhD supervisor, Professor Alan Robins, for his kind encouragement and support throughout the project. My thanks and best regards go to my co-supervisor Dr Matteo Carpentieri, and to collaborative supervisor Professor Paul Marsden from King's College London, for their support throughout the project.

My thanks also go to Dr Paul Hayward, of the EnFlo fluid dynamics laboratory at the University of Surrey.

Declaration

This thesis and the work to which it refers are the results of my own efforts. Any ideas, data, images or text resulting from the work of others (whether published or unpublished) are fully identified as such within the work and attributed to their originator in the text, bibliography or in footnotes. This thesis has not been submitted in whole or in part for any other academic degree or professional qualification. I agree that the University has the right to submit my work to the plagiarism detection service TurnitinUK for originality checks. Whether or not drafts have been so-assessed, the University reserves the right to require an electronic version of the final document (as submitted) for assessment as above.



Signature:

Date: 24th August 2021

ATMOSPHERIC DISPERSION OF RADIOACTIVE GASEOUS DISCHARGES IN THE NEAR FIELD OF BUILDINGS



Positron gaseous emission stack and anemometer at the St Thomas' Hospital site, London

Thesis submitted for the degree of PhD

Supervisor: Professor Alan Robins, University of Surrey

Co-Supervisor: Dr Matteo Carpentieri, University of Surrey

Collaborative Supervisor: Professor Paul Marsden, King's College London

Research Student: David J Gallacher BSc (Hons) MPhil CPhys CSci MInstP MIPeM

23rd August 2021

Summary

This work treats very short-range atmospheric dispersion of radioactive gases emitted from stacks just above the roof level of buildings and develops a methodology that provides realistic radiation dose estimates for that zone. Fluid flow in the rooftop region is complex, and the concentration field resulting from an emission into that flow also exhibits high levels of complexity, beyond the capability of existing operational dispersion models. Extensive Laser Doppler anemometry measurements were made in a meteorological wind tunnel to characterise the flow field in this region. Concentration fields were mapped with fast flame ionisation detectors and related to the associated flow characteristics. Parameters investigated were release position, release height, angle of approach flow and building geometry, the latter to contrast behaviour at a real site with that above a standard cuboid building (as would be used in operational dispersion models); sensitivity to surrounding buildings was also investigated. Methods were developed using Monte Carlo techniques to convert the complex spatial distribution of radioactive pollutant in the roof zone into accurate estimates of radiation doses received by persons in that zone. Effective dose estimates accounted for inhalation, immersion and external gamma-rays from the mixed positron/gamma-ray field – including doses within the radioactive plume at roof level. Short duration releases were covered as well as continuous releases. Novel methods are presented to specify the statistical confidence interval from different duration releases in terms of readily generalisable results. Full-scale measurements of gamma ray dose, wind speed and direction were made for one of the building cases and the results used to support the findings obtained by wind tunnel measurements and Monte Carlo calculations. Results are presented in generalisable form, for example as dimensionless concentrations, so that the methods and results can be applied to other similar types of pollutant release.



St Thomas' Hospital East Wing Cladding Project: Image by ARUP/Hopkins and ISG PLC

[0.1] Contents summary	Page
[0] Title pages and summary	1
[0.1] Contents summary	5
[0.2] Tables of contents and sub-chapter headings	8
[0.3] Table of figures and tables	17
[1] Introduction and research questions	28
[1.1] Introduction	28
[1.2] Research questions and methods	31
[1.3] Discussion	36
[1.4] Thesis structure	37
[2] Literature review	38
[2.1] Introduction: literature review	38
[2.2] Flows around buildings: dispersion of pollutants	39
[2.3] Models of pollutant dispersion: radiation dose modelling	47
[2.4] Chapter 4: citations from included published papers	57
[2.5] Further literature review: 2021	57
[2.6] Discussion: literature review	63
[3] Wind tunnel experimental methods	65
[3.1] Introduction	65
[3.2] Methods – Part 1: the wind tunnel	66
[3.3] Methods – Part 2: the experimental runs	70
[3.4] Discussion	91
[4] Plume radiation modelling approaches	93
[4.1] Introduction (related to published papers 1 and 2 in appendices)	93
[4.2] Publication 1: Gallacher, DJ <i>et al</i> , 2016a	93
[4.3] Publication 2: Gallacher, DJ <i>et al</i> , 2016b	93
[4.4] Discussion and Conclusions	94
[5] Flow field analysis	96
[5.1] Introduction	96
[5.2] Approach flow	98
[5.3] Cube at 0°	102
[5.4] Cube at -45°	110
[5.5] Cube at -22.5°	115
[5.6] EW Clad Full Building Model (FBM) at -22.5°	123
[5.7] EW Clad/FBM angle sensitivity analysis and EW isolated building	127
[5.8] Discussion	130
[5.9] Conclusions	133
[6] The Concentration field: Gaussian fitted plume spread parameters in the near-field of buildings	136
[6.1] Introduction	136
[6.2] Methods	137
[6.3] Results	152
[6.4] Discussion	193

[6.5] Conclusions	202
[7] Intermittent short releases in the flow field	205
[7.1] Introduction	205
[7.2] Methods	205
[7.3] Results	209
[7.4] Discussion	224
[7.5] Conclusions	226
[8] Monte Carlo computational methods	227
[8.1] Introduction	227
[8.2] Methods	227
[8.3] Results	239
[8.4] Discussion	240
[8.5] Conclusions	240
[9] Monte Carlo results	241
[9.1] Introduction	241
[9.2] Methods	243
[9.3] Results	244
[9.4] Discussion	273
[9.5] Conclusions	274
[10] Full scale rooftop gamma ray dose measurements	276
[10.1] Introduction	276
[10.2] Methods	276
[10.3] Results	286
[10.4] Discussion	293
[10.5] Conclusions	294
[11] Sensitivity analysis for building cases	296
[11.1] Introduction	296
[11.2] Methods	296
[11.3] Results	299
[11.4] Discussion	305
[11.5] Conclusions	307
[12] Practical application of methodology	308
[12.1] Introduction	308
[12.2] Methods	309
[12.3] Discussion	312
[12.4] Conclusions	312
[13] Conclusions and further developments	314
[13.1] Conclusions	314
[13.2] Further developments	320
[14] References and bibliography	322
[14.1] References	322
[14.2] Bibliography	330

[15] Appendices	332
[15.1] Appendix 15.1: Wind tunnel methods – indicative data sampling positions	332
[15.2] Appendix 15.2: Flow field further results	337
[15.3] Appendix 15.3: Concentration field supplementary results	342
[15.4] Appendix 15.4: Intermittent short release further results	353
[15.5] Appendix 15.5: Scientific Paper 1 Dispersion of positron emitting radioactive gases in a complex urban building array: a comparison of dose modelling approaches, <i>Journal of Radiological Protection</i> (JRP, 2016a)	366
[15.6] Appendix 15.6: Scientific Paper 2 Conversion of simulated radioactive pollutant gas concentrations for a complex building array into radiation dose, <i>Journal of Radiological Protection</i> (JRP, 2016b)	410

[0.2] Tables of contents

Chapter 1: Introduction and research questions

Section	Content	Pages
1	Introduction and research questions	28
1.1	Introduction	28
1.2	Research questions and methods	31
1.2.1	Research preliminaries	31
1.2.1.1	Applicability of existing models	32
1.2.1.2	Review of research literature of pollutant gases in near-field of buildings	32
1.2.2	Initial specific case investigations	32
1.2.2.1	Comparison of ranges of radiation dose from available models	32
1.2.2.2	Develop initial methods for converting wind tunnel concentrations into radiation dose	33
1.2.2.3	Compile initial wind tunnel dimensionless concentrations from different wind directions and convert these to expected dose	33
1.2.2.4	Analyse the results of a simulation from ADMS	33
1.2.2.5	Compare and contrast the initial dose results from wind tunnel and ADMS	33
1.2.2.6	Analyse the effect of rooftop structures (RTS)	33
1.2.3	Flow field investigation	33
1.2.3.1	Investigation of the flow field in the near field zone to buildings	33
1.2.3.2	Relate features of the flow field to the concentration field	33
1.2.4	Concentration field investigations	34
1.2.4.1	Analyse the plume dispersion and the radiation dose in the near-field region and in the roof zone of the building	34
1.2.4.2	Wind tunnel measurement for the EW building to determine plume spread parameters	34
1.2.4.3	Wind tunnel measurement for the cube building to determine plume spread parameters	34
1.2.4.4	Establish best parameter fitted plume spread parameters in the near-field region	34
1.2.4.5	Investigate corrections to be applied for simple Gaussian plume models using more sophisticated methods	34
1.2.4.6	Investigate the differences in radiation dose to a person in the vicinity of a radioactive plume in the near-field region for the plume geometry cases	35
1.2.5	Intermittent short duration releases	35
1.2.5.1	Analyse short release puff release concentrations using wind tunnel experiments	35
1.2.6	Monte Carlo methods and results	35
1.2.6.1	Write Monte Carlo code for the project to calculate radiation doses to persons that uses the plume spread parameters from the wind tunnel measurements	35
1.2.6.2	Carry out Monte Carlo gamma-ray cloud shine simulations also adding in dose terms from inhalation and immersion in a positron cloud	35
1.2.6.3	Investigate the differences in the radiation dose to persons in the vicinity of a radioactive plume in the near-field region to the release position	35
1.2.7	Full-scale site-specific measurements of wind and gamma-ray dose rate	35
1.2.7.1	Install two gamma-ray detectors on the EW roof for continuous monitoring and logging of the sky-shine dose rate from radioactive emissions	35

1.2.7.2	Install an anemometer and wind-logger system for continuous monitoring of wind speed and direction on the EW building roof	36
1.2.7.3	Develop methods to compare full-scale results to Monte Carlo calculation results knowing the time-logged spike releases of radioactive gas and comparing these to the gamma-ray dose rate time trace data	36
1.2.8	Sensitivity analysis for the different measurement cases	36
1.2.8.1	Investigate the variation of dose with different building configurations	36
1.2.8.2	Investigate the variations of results from small changes of the measurement conditions from small variations in the direction of approach flow	36
1.2.9	Practical application of the methodology	36
1.2.9.1	Develop a methodology to use the data sets and provide estimates of the concentration field values in the roof zone and main recirculation zone of the buildings to enable dose calculations to be performed for a wider set of problems	36
1.3	Discussion	36
1.4	Thesis structure	37

Chapter 2: Literature Review

Section	Content	Pages
2.1	Introduction: literature review	38
2.2	Flows around buildings: dispersion of pollutants	39
2.2.1	ASHRAE models section	42
2.2.2	ADMS plume dispersion basic model	43
2.2.3	Dispersion modelling studies	44
2.3	Models of pollutant dispersion: radiation dose modelling	47
2.3.1	NRPB Reports: R-91/R-101/R-157/W-63/R322-Annexe B	47
2.3.2	ADMS Radiation dose modelling of radioactive plumes	51
2.3.3	Other Radiation Dose models	52
2.4	Chapter 4: citations from published papers	57
2.5	Further Literature review: 2021	57
2.6	Discussion: Literature Review	63

Chapter 3: Wind Tunnel Experimental Methods

Section	Content	Pages
3.1	Introduction	65
3.2	Methods – Part 1: the wind tunnel	66
3.3	Methods – Part 2: the experimental runs	70
3.3.1	Measurement series #1	71
3.3.2	Measurement series #2	72
3.3.2.1	Part 1: EW clad/unclad: passive horizontal continuous releases of concentration	73
3.3.2.1.1	EW clad: measurement with existing stack position; passive release	73
3.3.2.1.2	EW unclad: measurement with existing stack position; passive release	76
3.3.2.2	Part 2: confirm plume trajectory and (Y, Z) profile with Active Vertical (AV) releases	76
3.3.2.2.1	EW clad building: steady, Active Vertical release with matched stack velocity	76
3.3.2.2.2	EW unclad building: steady, Active Vertical release with matched stack velocity	76

3.3.2.3	Part 3: Short duration releases clad/unclad cases, Active Vertical release	76
3.3.2.3.1	EW clad: fixed release height, AV, concentration vs puff ΔT	76
3.3.2.3.2	EW unclad: fixed release height, AV, concentration vs puff ΔT	76
3.3.2.4	Part 4: Short duration horizontal passive releases with EW clad/unclad	76
3.3.2.4.1	EW clad: fixed release height, Passive (P), concentration vs puff ΔT	77
3.3.2.4.2	EW unclad: fixed release height, Passive (P), concentration vs puff ΔT	77
3.3.2.5	Part 5: Short duration passive releases, EW unclad isolated building	77
3.3.2.5.1	EW clad: position offset sequence	77
3.3.2.5.2	EW unclad: position offset sequence	77
3.3.2.6	Flux Balance	77
3.3.2.6.1	No building: AV continuous release	77
3.3.2.7	Stack Velocity Ratio (SVR) and tracer flow rate calculations for AV releases	77
3.3.2.8	Tracer flow rate calculations for passive horizontal releases in experiment series #2	79
3.3.2.9	Release duration for puff release experiments	79
3.3.2.10	Experiment Series #2: Summary: 3.3.2.10.1 - 3.3.2.10.5	80
3.3.3	Experiment Series #3	80
3.3.3.1.1-3	Measure passive release concentration profiles 3.3.3.1.1A/B, 3.3.3.1.2A/B, 3.3.3.1.3A/B	81
3.3.3.2	Measure active vertical release concentration profiles with cube: 3.3.3.2.1A/B, 3.3.3.2.2A/B, 3.3.3.2.3A/B	84
3.3.3.3	Short duration active vertical puff releases with cube: 3.3.3.3.1A, 3.3.3.3.2A, 3.3.3.3.3A	84
3.3.3.4	Repeated EW clad model, no surrounding buildings, with different wind directions: 3.3.3.4.1, 3.3.3.4.2, 3.3.3.4.3	85
3.3.4	Experiment Series #4	85
3.3.4.1	Cube measurements	85
3.3.4.2	EW clad: isolated building	86
3.3.5	Experiment Series #5	86
3.3.5.1	Collect cases of $(v' w')$ for downstream positions to potentially correlate v'^2 with σ_y	87
3.3.5.2	Measure upstream velocity profiles and $(v' w')$ at cube centre line (A position)	88
3.3.5.3	Collect cases of (v') at low heights to building to also enable correlation of v'^2 with σ_y	88
3.3.5.4	Repeat cases with $(u' w')$ and complete fuller data set and correlate w'^2 with σ_z	88
3.3.5.5	Extend velocity profiles measurements for cases already measured	89
3.3.5.6	Re-measure shear stress and turbulence intensity where required	89
3.3.5.7	Test sensitivity for lead edge vortex ± 5 degrees for flow field and concentration field	89
3.3.5.8	Obtain FFID data on $u' C'$ using LDA and FFID simultaneous data	89
3.3.5.9	Perform sensitivity test with surrounding buildings: EW \pm NW \pm ECH \pm EWlow	89
3.3.5.10	Archbishop's Palace – downstream cross wind profiles: 10.1, 10.2, 10.3	89
3.3.6	Experimental Errors	89
3.3.6.1	Errors in the measured concentration field	89
3.3.6.2	Errors in the measured flow field quantities	90

3.4	Discussion	91
-----	------------	----

Chapter 4: Plume Radiation Modelling Approaches

Section	Content	Pages
4.1	Introduction	93
4.2	Publication 1: Refers to Appendix 15.5	93
4.3	Publication 2: Refers to Appendix 15.6	93
4.4	Discussion and conclusions	94

Chapter 5: Flow field analysis

Section	Content	Pages
5.1	Introduction	96
5.2	Approach flow	98
5.3	Cube: 0° flow direction	102
5.4	Cube: -45° flow direction	110
5.5	Cube: -22.5° flow direction	115
5.6	EW clad: -22.5° flow direction	123
5.7	EW clad/FBM angle sensitivity analysis and EW clad isolated building at -22.5°	127
5.8	Discussion	130
5.8.1	Wind tunnel advection velocities and turbulence intensities: cube	130
5.8.2	Wind tunnel advection velocities and turbulence intensities: EW building models	131
5.9	Conclusions	133

Chapter 6: Concentration Field

Section	Content	Pages
6.1	Introduction	136
6.2	Methods	137
6.2.1	Overview/Experimental Wind Tunnel Methods	137
6.2.2	Passive Releases: concentration profiles	138
6.2.2.1	Cube – Passive Releases	138
6.2.2.2	East Wing Clad – Passive Releases	140
6.2.2.3	East Wing Unclad – Passive Releases	141
6.2.3	Active Vertical Releases: concentration profiles	141
6.2.3.1	Cube – Active Releases	142
6.2.3.2	EW Clad – Active Vertical Releases	142
6.2.3.3	EW Unclad – Active Vertical Releases	143
6.2.4	Data Modelling Methods	143
6.2.4.1	Concentration Profile Models	144
6.2.4.2	Concentration weighted plume spread parameters: SGP formulation	146
6.2.4.3	Concentration weighted plume spread parameters: DGP formulation	147
6.2.4.4	Plume Concentration Maximum (PCM) variation with downstream distance X	148
6.2.4.5	Plume Concentration Maximum deflection in (Y, Z) with downstream distance	149
6.2.4.6	Plume height and normalisation to building scale	150
6.2.4.7	Roof Zone Maximum Measured Concentrations	150
6.2.4.8	Main Building RCZ Measured Concentrations	151

6.2.4.9	Mean value plume spread parameters with distance from source	151
6.2.4.10	Caveat	152
6.3	Results	152
6.3.1	Concentration Profiles: Horizontal and Vertical	152
6.3.1.1	Cube: Passive Cases – Roof Zone	152
6.3.1.1.1	Cube: normal incidence of flow (0°)	152
6.3.1.1.2	Cube: -22.5° incidence of flow	156
6.3.1.1.3	Cube: -45° incidence of flow	158
6.3.1.2	Cube: Active Vertical Release Cases – Roof Zone	159
6.3.1.3	EW Clad and Unclad buildings: Passive Release Cases	160
6.3.1.4	EW Clad and Unclad: Active Vertical Release Cases	161
6.3.2	Cube: Main Recirculation Zone	162
6.3.3	Plume Concentration Maximum variation with downstream distance	166
6.3.3.1	Cube: 0°/-22.5°, ‘A’ Position: SGP/DGP results	166
6.3.3.2	EW Clad: -22.5°, ‘Vertex’ Position: SGP/DGP results	167
6.3.3.3	Cube: -22.5°, ‘B’ Position: SGP/DGP results	167
6.3.4	Roof Zone Maximum Measured Concentrations: Cube/EW Clad/Unclad	168
6.3.4.1	Cube position ‘A’: SGP/DGP/Rooftop RCZ	168
6.3.4.2	EW Clad/Unclad, position ‘Vertex’: SGP/DGP/Rooftop RCZ	171
6.3.4.3	Cube position ‘B’: SGP/DGP/Rooftop RCZ	173
6.3.5	Main building RCZ concentrations: cube	176
6.3.6	Concentration Weighted Dispersion Parameters	178
6.3.6.1	Cube position ‘A’ spread parameters	178
6.3.6.2	EW Clad spread parameters	182
6.3.6.3	Cube position ‘B’ spread parameters	183
6.3.7	Concentration Weighted Dispersion Parameters: Mean Values over distance from the source X	184
6.3.7.1	Cube position ‘A’: Mean Values of dispersion parameters over distance X	185
6.3.7.2	EW Clad: Mean Values of dispersion parameters over distance X	186
6.3.7.3	Cube position ‘B’: Mean Values of dispersion parameters over distance X	186
6.3.8	Plume Concentration Maximum (PCM) horizontal deflections with normalised release height Z_{norm}	187
6.3.9	PCM normalised vertical deflection vs normalised release height Z_{norm}	189
6.3.10	Concentration Weighted Dispersion Parameters: Summary over cube ‘A’ and EW release cases: SGP/DGP/IGP formulations with normalised release height Z_{norm}	190
6.3.11	Summary values of roof zone Maximum Measured Concentrations with release height: Cube and EW clad and unclad cases	191
6.4	Discussion	193
6.4.1	Concentration Profiles in the Roof Zone	194
6.4.2	Concentration Profiles in the Main Recirculation Zone (RCZ) downwind of the cube	195
6.4.3	Concentration Weighted Dispersion Parameters: Variation with Distance from Source	196
6.4.4	Plume Deflection: Horizontal and Vertical	198
6.4.5	Variation of Plume Concentration Maximum (PCM) with downstream distance	199
6.4.6	Rooftop Maximum Concentrations	200

6.4.7	Downstream Main RCZ concentrations	201
6.5	Conclusions	202

Chapter 7: Intermittent Short Releases in the Flow Field

Section	Content	Pages
7.1	Introduction	205
7.2	Methods	205
7.2.1	Release durations for puff release experiment and dimensionless factors	205
7.2.2	Short duration active puff vertical releases with cube	207
7.2.3	Short duration active puff vertical releases with EW clad and unclad buildings	207
7.2.4	Short duration passive puff vertical releases with EW clad and unclad buildings	208
7.2.5	Convergence analysis of sampled data series	208
7.3	Results	209
7.3.1	Cube: 0° flow incidence, 'A', Active Vertical release (AV)	209
7.3.2	Cube: -22.5° flow incidence, 'A', AV	211
7.3.3	Cube: -45° flow incidence, 'A', AV	212
7.3.4	EW clad: -22.5° flow incidence, 'Vertex', AV	213
7.3.5	EW unclad: -22.5° flow incidence, 'Vertex', AV	214
7.3.6	EW clad: -22.5° flow incidence, 'Vertex', Passive release (P)	214
7.3.7	EW unclad: -22.5° flow incidence, 'Vertex', Passive release (P)	215
7.3.8	Cube: coefficient of variation (CV) and 95 th percentile of χ vs (Puff Length Scale)/H	215
7.3.9	EW clad/unclad: coefficient of variation (CV) of χ at different crosswind positions (Y/H)	220
7.3.10	EW clad/unclad: coefficient of variation (CV) of χ at different vertical positions: $(Z_s - Z_{RH})/H$	221
7.3.11	Overall Summary: Cube and EW clad/unclad: Normalised statistical parameters	222
7.4	Discussion	224
7.5	Conclusions	226

Chapter 8: Monte Carlo Computational Methods

Section	Content	Pages
8.1	Introduction	227
8.2	Methods	227
8.2.1	Gamma plume-shine integral formulation	227
8.2.2	Sampled receptor point grid	230
8.2.3	Co-ordinate sampling in the world-space	230
8.2.4	Main recirculation zone (RCZ) region	232
8.2.5	Plume parameterisation and evaluation of the main plume concentration	233
8.2.6	Roof Recirculation Zone (RCZ)	236
8.2.7	Receptor point size and the Dose Point Kernel (DPK) method	237
8.2.8	Calculation of the dose rate levels from different zones	238
8.2.9	Practical considerations with respect to the MC code and runs	239
8.3	Results	239

8.3.1	Combined dose rate from all routes (inhalation, positron immersion, gamma-rays)	239
8.3.2	Combined dose rate from gamma-ray dose rate sources	240
8.4	Discussion	240
8.5	Conclusion	240

Chapter 9: Monte Carlo Results

Section	Content	Pages
9.1	Introduction	241
9.2	Methods	243
9.3	Results	244
9.3.1	Variation of radiation dose rate with release height and angle	244
9.3.1.1	Cube: release position 'A', Passive release (P)	244
9.3.1.2	Cube: release position 'A', Passive release (P)	251
9.3.1.3	EW clad and unclad: Passive release (P)	257
9.3.1.4	Active vertical releases: all cases	260
9.3.1.5	Positional co-ordinates of effective dose rate and gamma-ray dose rates	261
9.3.2	Spatial variation of effective dose and gamma-ray dose from Monte Carlo calculations	269
9.4	Discussion	273
9.5	Conclusion	274

Chapter 10: Full Scale Rooftop Gamma-Ray Dose Measurements

Section	Content	Pages
10.1	Introduction	276
10.2	Methods	276
10.2.1	EW building layout and detector placements	276
10.2.2	Gamma-Ray detectors	278
10.2.3	Ultrasonic anemometer	279
10.2.4	Source release term	280
10.2.5	Gamma-ray peak analysis	280
10.2.6	Wind speed analysis	281
10.2.7	Wind direction analysis	281
10.2.8	Comparison of measured dose values against Monte Carlo computations	281
10.3	Results	286
10.3.1	Anomalous results	286
10.3.2	Mean gamma dose rate from MC compared against wind tunnel derived results	287
10.3.3	Probability density function (pdf) for the measured full-scale results	287
10.3.4	Measured gamma-ray dose rate corrected to standard release rate of pollutant	288
10.3.5	Variability in wind direction over the sample period	290
10.3.6	Variability in the velocity field: downstream and crosswind directions	291
10.3.7	Turbulence intensity results	292
10.4	Discussion	293
10.5	Conclusion	294

Chapter 11: Sensitivity analysis for building cases

Section	Content	Pages
11.1	Introduction	296
11.2	Methods	296
11.2.1	Building layout investigated	296
11.2.2	Particular combinations in the building complex (STH) investigated in the wind tunnel	299
11.2.3	Measurements made in the wind tunnel	299
11.3	Results	299
11.3.1	Concentration field maxima (across cases 1-8)	299
11.3.2	Velocity profiles in (U , W) for the EW cases: sensitivity to wind direction	300
11.3.3	Vertical component of turbulence intensity	302
11.3.4	Shear stress ($-u'w'/U_{ref}^2$): sensitivity to angle of approach flow	304
11.3.5	Sensitivity of Plume Concentration Maximum (PCM) to angle of approach wind	304
11.4	Discussion	305
11.5	Conclusion	307

Chapter 12: Practical application of the methodology

Section	Content	Pages
12.1	Introduction	308
12.2	Methods	309
12.2.1	Example case: cube building	309
12.2.2	The intermittent short release method	311
12.3	Discussion	312
12.4	Conclusion	312

Chapter 13: Conclusions and further developments

Section	Content	Pages
13.1	Conclusions	314
13.2	Further developments	320

Appendix 15.1: Wind tunnel experimental methods – indicative data sampling positions

Section	Content	Pages
15.1.1	EW clad and unclad experimental measurement positions: Table 3.3 refers	332
15.1.2	Cube experimental measurement positions (with additional EW data): Table 3.4 refers	335

Appendix 15.2: Further flow field results

Section	Content	Pages
15.2.1	Cube: 0° flow direction	337
15.2.2	Cube: -45° flow direction	338
15.2.3	Cube: -22.5° flow direction	339
15.2.4	EW clad: -22.5° flow direction	341

Appendix 15.3: Supplementary Results on Concentration Field

Section	Content	Pages
15.3	Appendix 15.3: Supplementary Results on Concentration Field	342
15.3.1	Concentration Profiles: Supplementary Results	342

15.3.1.1	Cube: Concentration Profiles – Passive Releases	342
15.3.1.2	Cube: Concentration Profiles – Active Vertical Releases	343
15.3.1.3	EW Clad/Unclad: Concentration Profiles – Passive Releases	344
15.3.2	Plume Concentration Maximum (PCM) variation with downstream distance: Supplementary Results	344
15.3.2.1	Cube: ‘A’: SGP/DGP	344
15.3.2.2	EW Unclad: ‘Vertex’: SGP/DGP	345
15.3.2.3	Cube: ‘B’: SGP/DGP	345
15.3.3	Concentration Weighted Dispersion Parameters: variation with distance from the source – SGP and DGP/IGP formulations with release height	346
15.3.3.1	EW Unclad: concentration weighted dispersion parameters	346
15.3.3.2	Cube: ‘B’: concentration weighted dispersion parameters	347
15.3.4	Concentration Weighted Dispersion Parameters: Mean values over distance from source of SGP and DGP/IGP formulations: Supplementary Results	349
15.3.4.1	Cube: ‘A’: Mean dispersion parameters over distance from source	349
15.3.4.2	EW Unclad: Mean dispersion parameters over distance from the source	350
15.3.4.3	Cube: ‘B’: Mean dispersion parameters over distance from source	350
15.3.5	Concentration Weighted Dispersion Parameters: Summary Data over ‘B’ release positions	351
15.3.5.1	Concentration Weighted Dispersion Parameters: Summary Data over ‘B’ release positions: SGP formulation with normalised release height	351
15.3.5.2	Concentration Weighted Dispersion Parameters: Summary Data over ‘B’ release positions: DGP/IGP formulation with normalised release height	352

Appendix 15.4: Supplementary results for intermittent short releases

Section	Content	Pages
15.4.1	Cube: 0° flow incidence, ‘A’, Active Vertical release (AV), sampling co-ordinates	353
15.4.2	Cube: -22.5° flow incidence, ‘A’, AV, sampling co-ordinates	353
15.4.3	Cube: -45° flow incidence, ‘A’, AV, sampling co-ordinates	353
15.4.4	EW clad: -22.5° flow incidence, ‘Vertex’, AV, sampling co-ordinates	353
15.4.5	EW unclad: -22.5° flow incidence, ‘Vertex’, AV, sampling co-ordinates and number of puffs for different ΔT runs	353
15.4.6	EW clad: -22.5° flow incidence, ‘Vertex’, Passive release (P), sampling co-ordinates and number of puffs for different ΔT runs	354
15.4.7	EW unclad: -22.5° flow incidence, ‘Vertex’, Passive release (P), sampling co-ordinates and number of puffs for different ΔT runs	354
15.4.8	Cube: statistical parameters for various angles of incidence, AV releases and at different source distances	356
15.4.9	EW clad/unclad: coefficient of variation (CV) of χ at different crosswind positions (Y/H)	357
15.4.10	EW clad/unclad: CV of χ results at different vertical positions: $(Z_s - Z_{RH})/H$	358
15.4.11	Overall Results Summary: Cube and EW clad/unclad cases: statistical parameters	359

[0.3] Table of Figures/Tables (all entries refer to figures unless stated as tables)

Chapter 2: Literature Review

Heading	Content	Pages
2.1	Flow field features for a rectangular building at normal incidence to flow	40
2.2	Flow field features for a cube at 45° to flow	41

Chapter 3: Wind Tunnel Experimental Methods

Heading	Content	Pages
3.1	Diagram showing the main features of the wind tunnel	67
3.2	Interior of the wind tunnel looking upstream with the cube model in place	67
3.3	Schematic layout of the wind tunnel (plan view)	68
3.4	Schematic layout of the wind tunnel (elevation view)	68
3.5	Fast Response Flame Ionisation Detector (FFID)	68
3.6	LDA mode of operation in one plane	69
Table 3.1	Experimental Timelines and Overview	70
Table 3.2	Experimental Run Details: various release heights and angles of flow	71
Table 3.3	Experimental Timeline Series 2: EW building: experimental log	72
3.7	Measurement planes shown on plan view of EW clad building	74
3.8	Stack location on EW North stair tower and new proposed stack	74
3.9	EW cladding project proposed work	78
Table 3.4	Experiment Timeline Series #3	81
3.10	Cube measurement planes (normal incidence, 0°)	82
3.11	Cube measurement planes (oblique incidence, -45°)	83
Table 3.5	Experiment Timeline Series #4	85
Table 3.6	Cube LDA measurements	85
Table 3.7	EW clad: LDA measurements	86
Table 3.8	Experiment Timeline Series #5	86
Table 3.9	Methods: outline measurements summary for Experiment Series #5	87
Table 3.10	Error quantities measured at plume concentration maximum	90
Table 3.11	Error quantities in the normalised flow velocities near the PCM	91
Table 3.12	Error quantities in the turbulence intensity close to the PCM	91

Chapter 5: Flow field analysis

Heading	Content	Pages
5.1	Flow field for a rectangular building at normal incidence	97
Table 5.1	Wind tunnel LDA experiments	97
5.2	Co-ordinate system for the flow field measurements	98
5.3	Downstream flow velocity upwind of the cube at $X/H=-5/4$	98
5.4	Logarithmic plot of flow velocity upwind of the cube at $X/H=-5/4$	100
5.5(a)	Turbulence intensity plots against height Z/H for $X/H=-5/4$ (July 2017)	101
5.5(b)	Turbulence intensity normalised to u^* and plotted against Z/H_{bl} for $X/H=-5/4$	101
5.6	Turbulence intensity plots against height Z/H for $X/H=-2$ (June 2019)	102
5.7(a/b)	Cube: 'A': 0°; (a) co-ordinate system/arrangement; (b) U/U_{ref} , $X/H=0.65$	103
5.8(a/b)	Cube: 'A': 0°; U/U_{ref} : (a) $X/H=0.98$; (b) $X/H=1.65$	104
5.9(a/b/c)	Cube: 'A': 0°; W/U_{ref} : (a) $X/H=0.65$; (b) $X/H=0.98$; (c) $X/H=1.65$	104
5.10	Cube: 'A'; 0°; $X/H=0.65$: $W(z)/ U(z) $	105

5.11	LES simulations for the cube case for (v, w) from Lim HC <i>et al</i> (2009)	106
5.12	Expanded view of Figure 5.11 with annotations by this thesis author showing the lateral sampling planes used	107
5.13	LES simulations of the vorticity in the (Y, Z) plane from Lim HC <i>et al</i> (2009)	108
5.14(a/b)	Cube; 'A'; 0° ; $X/H=0.65$: (a) u'^2/U_{ref}^2 ; (b) w'^2/U_{ref}^2	109
5.15(a/b)	Cube; 'A'; 0° : (a) $X/H=0.98$, u'^2/U_{ref}^2 ; (b) $X/H=1.65$, w'^2/U_{ref}^2	109
5.16	Development of flow features with angulation of the cube away from normal incidence of flow	110
5.17	Flow features for the cube at -45° to approach flow from Hosker (1984)	110
5.18(a/b)	Cube; 'A'; -45° ; $X/H=0.65$: (a) arrangement and co-ordinate system; (b) U/U_{ref}	111
5.19(a/b)	Cube; 'A'; -45° ; U/U_{ref} : (a) $X/H=0.98$; (b) $X/H=1.65$	111
5.20(a/b/c)	Cube; 'A'; -45° ; W/U_{ref} : (a) $X/H=0.65$; (b) $X/H=0.98$; (c) $X/H=1.65$	112
5.21	Cube; 'A'; -45° ; $X/H=0.98$: $W(z)/ U(z) $	113
5.22(a/b)	Cube; 'A'; -45° ; $X/H=0.65$: (a) u'^2/U_{ref}^2 ; (b) w'^2/U_{ref}^2	113
5.23(a/b)	Cube; 'A'; -45° : (a) u'^2/U_{ref}^2 ; $X/H=0.98$; (b) u'^2/U_{ref}^2 ; $X/H=1.65$	114
5.24(a/b)	Cube; 'A'; -22.5° : (a) co-ordinate system/arrangement; (b) U/U_{ref} , $X/H=0.65$	115
5.25(a/b)	Cube; 'A'; -22.5° ; U/U_{ref} : (a) $X/H = 0.98$; (b) $X/H=1.65$	115
5.26(a/b/c)	Cube; 'A'; -22.5° ; W/U_{ref} : (a) $X/H = 0.65$; (b) $X/H=1$; (c) $X/H=1.65$	116
5.27	Cube; 'A'; -22.5° ; $X/H=0.98$: $W(z)/ U(z) $	117
5.28(a/b)	Cube; 'A'; -22.5° ; $X/H=0.67$: (a) u'^2/U_{ref}^2 ; (b) w'^2/U_{ref}^2	117
5.29(a/b)	Cube; 'A'; -22.5° : (a) u'^2/U_{ref}^2 ; $X/H=0.98$; (b) u'^2/U_{ref}^2 ; $X/H=1.65$	118
5.30(a/b/c/d)	Cube; 'A'; -22.5° ; VW vector plots: (a) $X/H=1/3$; (b) $X/H=2/3$; (c) $X/H=1$; (d)	119
5.31(a/b)	EW clad; Full Building Model (FBM): 'Vertex': -22.5° ; (a) co-ordinate system/arrangement; (b) U/U_{ref} , $X/H=0.65$	123
5.32(a/b)	EW clad/FBM: 'Vertex'; -22.5° ; U/U_{ref} : (a) $X/H = 0.98$; (b) $X/H=1.65$	123
5.33(a/b/c)	EW clad/FBM: 'Vertex'; -22.5° ; W/U_{ref} : (a) $X/H = 0.65$; (b) $X/H=0.98$; (c) $X/H=1.65$	124
5.34	EW clad/FBM: 'Vertex'; -22.5° ; $X/H=0.65$: $W(z)/ U(z) $	125
5.35(a/b)	EW clad/FBM: 'Vertex'; -22.5° ; $X/H=0.65$: (a) u'^2/U_{ref}^2 ; (b) w'^2/U_{ref}^2	125
5.36(a/b)	EW clad/FBM; 'Vertex'; -22.5° ; u'^2/U_{ref}^2 : (a) $X/H=0.98$; (b) $X/H=1.65$	126
5.37(a/b)	EW clad/FBM: 'Vertex'; $X/H = 0.65$; U/U_{ref} : (a) -27.5° ; (b) -17.5°	127
5.38	EW isolated building; 'Vertex'; $X/H = 0.65$: U/U_{ref}	127
5.39(a/b)	EW clad/FBM: 'Vertex'; $X/H = 0.65$; W/U_{ref} : (a) -27.5° ; (b) -17.5°	128
5.40(a/b)	EW clad isolated building; 'Vertex'; -22.5° ; $X/H=0.65$: (a) W/U_{ref} ; (b) $W(z)/U(z)$	128
5.41(a/b)	EW clad/FBM: 'Vertex'; $X/H = 0.65$; u'^2/U_{ref}^2 : (a) -27.5° ; (b) -17.5°	129
5.42	EW clad isolated building; 'Vertex'; $X/H = 0.65$: u'^2/U_{ref}^2 :	129
Table 5.2	EW Full Building Model (FBM): $W(z)/U(z)$ sensitivity analysis for $-22.5^\circ \pm 5^\circ$ at $Z=265\text{mm}$	133

Chapter 6: Concentration Field

Heading	Content	Pages
6.1	Cube Measurement Planes (Normal Incidence, 0°)	139
6.2	Cube Measurement Planes (Oblique, -45°)	140

6.3	EW Clad Building (-22.5°)	141
6.4	EW Stack Dimensions and Efflux Velocity Profile	142
6.5	Measurement Planes and Leading-Edge Offset Distance	143
6.6(a/b/c/d)	Cube: normal incidence flow: 'A'	152
6.7(a/b/c)	Cube: normal incidence flow: 'B'	154
6.8(a/b/c)	Cube: normal incidence flow: 'B'	155
6.9	Cube: -22.5° incidence flow: 'A'	156
6.10	Cube: -22.5° incidence flow: 'A'	156
6.11(a/b)	Cube: -22.5° incidence flow: 'B'	157
6.12	Cube: -45° incidence flow: 'A'	158
6.13	Cube: -45° incidence flow: 'B'	158
6.14(a/b)	Cube: -22.5°/-45° incidence flows: 'A'/Active Vertical	159
6.15(a/b)	Cube: 0°/-22.5° incidence flows: 'B'/AV	159
6.16(a/b)	EW Clad: -22.5° incidence flow: 'Vertex'/Passive	160
6.17	EW Unclad: -22.5° incidence flow: 'Vertex'/Passive	161
6.18(a/b)	EW Clad: -22.5° incidence flow: 'Vertex'/AV	161
6.19(a/b)	Cube: 0° flow: 'A', Main RCZ: $X/H=5/3$, $Z_{rh}=245\text{mm}$	162
6.20(a/b)	Cube: 0° flow: 'A', Main RCZ: $X/H=5/3$, $Z_{rh}=255\text{mm}$	163
6.21(a/b)	Cube: 0° flow: 'B', Main RCZ: $X/H=5/3$, $Z_{rh}=245\text{mm}$	163
6.22(a/b)	Cube: -22.5° flow: 'A', Main RCZ: $X/H=5/3$, $Z_{rh}=245\text{mm}$	164
6.23(a/b)	Cube: -45° flow: 'A', Main RCZ: $X/H=5/3$, $Z_{rh}=245\text{mm}$	165
6.24(a/b)	Cube: normal incidence flow: 'A': SGP/DGP	166
6.25(a/b)	Cube: -22.5° flow: 'A': SGP/DGP	166
6.26(a/b)	EW Clad: -22.5° flow: 'Vertex': SGP/DGP	167
6.27(a/b)	Cube: -22.5° flow: 'B': SGP/DGP	167
6.28(a/b/c)	Cube: 0°, 'A': SGP/DGP/Rooftop RCZ	168
6.29(a/b/c)	Cube: -22.5°, 'A': SGP/DGP/Rooftop RCZ	169
6.30(a/b/c)	Cube: -45°, 'A': SGP/DGP/Rooftop RCZ	170
6.31(a/b/c)	EW Clad: -22.5°, 'Vertex': SGP/DGP/Rooftop RCZ	171
6.32(a/b/c)	EW Unclad: -22.5°, 'Vertex': SGP/DGP/Rooftop RCZ	172
6.33(a/b/c)	Cube: 0°, 'B': SGP/DGP/Rooftop RCZ	173
6.34(a/b/c)	Cube: -22.5°, 'B': SGP/DGP/Rooftop RCZ	174
6.35(a/b/c)	Cube: -45°, 'B': SGP/DGP/Rooftop RCZ	175
6.36(a/b/c)	Cube: 0°/-22.5°/-45°, 'A': Main RCZ concentrations	176
6.37(a/b/c)	Cube: 0°/-22.5°/-45°, 'B': Main RCZ concentrations	177
6.38(a/b)	Cube: 0°, 'A': SGP: lateral and vertical spread parameters	178
6.39(a/b)	Cube: 0°, 'A': DGP/IGP: lateral and vertical spread parameters	179
6.40(a/b)	Cube: -22.5°, 'A': SGP: lateral and vertical spread parameters	180
6.41(a/b)	Cube: -22.5°, 'A': DGP/IGP: lateral/vertical spread parameters	180
6.42(a/b)	Cube: -45°, 'A': SGP: lateral and vertical spread parameters	181
6.43(a/b)	Cube: -45°, 'A': DGP/IGP: lateral/vertical spread parameters	182
6.44(a/b)	EW Clad: -22.5°, 'Vertex': SGP: lateral/vertical spread parameters	182
6.45(a/b)	EW Clad: -22.5°, 'Vertex': DGP/IGP: lateral/vertical spreads	183
6.46(a/b)	Cube: 0°, 'B': SGP: lateral and vertical spread parameters	183
6.47(a/b)	Cube: 0°, 'B': DGP/IGP: lateral and vertical spread parameters	184
6.48(a/b)	Cube: 0°, 'A': Mean value lateral/vertical spread parameters over X	185

6.49(a/b)	Cube: -22.5°, 'A': Mean value lateral/vertical spread parameters	185
6.50(a/b)	EW Clad: -22.5°, 'Mean value lateral/vertical spreads	186
6.51(a/b)	Cube: 0°, 'B': Mean value lateral/vertical spread parameters over X	186
6.52(a/b)	Cube/EW-clad/unclad: SGP: PCM horizontal deflection with Z_{norm}	187
6.53(a/b)	Cube/EW-clad/unclad: DGP: PCM horizontal deflection with Z_{norm}	188
6.54(a/b)	Cube/EW-clad/unclad: RCZ maximum horizontal deflection	188
Table 6.1	Downstream distance X_{max}/H of the rooftop RCZ maximum	189
6.55(a/b)	Cube/EW-clad/unclad: SGP: PCM normalised vertical deflection Z_{PCM} vs normalised release height Z_{norm}	189
6.56(a/b)	Cube/EW-clad/unclad: DGP: PCM normalised vertical deflection Z_{PCM} vs normalised release height Z_{norm}	189
6.57(a/b)	Summary: Cube/EW-clad/unclad: SGP mean spread parameters	190
6.58(a/b)	Summary: Cube/EW-clad/unclad: DGP/IGP mean spread parameters	190
6.59(a/b)	Summary: Cube 'A' /EW-clad/unclad: SGP: Maximum Measured Concentrations with normalised release height	191
6.60(a/b)	Summary: Cube 'A' /EW-clad/unclad: DGP: Maximum Measured Concentrations with normalised release height Z_{norm}	192
6.61(a/b)	Summary: Cube 'A' /EW-clad/unclad: DGP: Rooftop RCZ maximum concentrations with normalised release height Z_{norm}	193
Table 6.2	Summary of plume concentration profile findings with passive releases	195
Table 6.3	Normalised Plume Spread Parameters: General Patterns in the Roof Zone	196
Table 6.4	Mean Normalised Plume Spread Parameters over Distance from Source	197
Table 6.5	Empirical Variation of PCM: $\ln(\chi)$ vs $\ln(x)$ for $Z_{rh}=49m$ (full-scale)	199
Table 6.6	Roof Top Maximum Concentrations	200
6.62	Cube Recirculation Zones: Main and Roof Zone	201
Table 6.7	Downstream Main RCZ Concentration in the Well-Mixed Zone	202

Chapter 7: Intermittent Short Releases in the Flow Field

Heading	Content	Pages
7.1	EW clad building: (-22.5°) main direction studied	208
7.2(a/b)	PDF of dimensionless concentration for the cube: 0°; 'A'; AV; $X/H=1/3$, $Z_{RH}=255mm$: (a) $\Delta T=0.1s$; (b) $\Delta T=1.0s$	209
7.3(a/b)	PDF of dimensionless concentration for the cube: 0°; 'A'; AV; $X/H=2/3$, $Z_{RH}=255mm$: (a) $\Delta T=0.1s$; (b) $\Delta T=1.0s$	209
7.4(a/b)	PDF of dimensionless concentration for the cube: 0°; 'A'; AV; $X/H=1$, $Z_{RH}=255mm$: (a) $\Delta T=0.1s$; (b) $\Delta T=1.0s$	210
7.5(a/b)	PDF of dimensionless concentration for the cube: 0°; 'A'; AV; $X/H=5/3$, $Z_{RH}=255mm$: (a) $\Delta T=0.1s$; (b) $\Delta T=1.0s$	210
7.6(a/b/c)	PDF of dimensionless concentration for the cube: -22.5°; 'A'; AV; $X/H=2/3$, $Z_{RH}=255mm$: (a) $\Delta T=0.1s$; (b) $\Delta T=0.5s$; (c) $\Delta T=1.0s$	211
7.7(a/b/c)	PDF of dimensionless concentration for the cube: -45°; 'A'; AV; $X/H=2/3$, $Z_{RH}=255mm$: (a) $\Delta T=0.1s$; (b) $\Delta T=0.5s$; (c) $\Delta T=1.0s$	212
7.8(a/b/c)	PDF of dimensionless concentration for EW clad: -22.5°; 'A'; AV; $X/H=2/3$, $Z_{RH}=255mm$: (a) $\Delta T=0.1s$; (b) $\Delta T=0.5s$; (c) $\Delta T=1.0s$	213
7.9(a/b/c)	PDF of dimensionless concentration for EW clad: -22.5°; 'A'; Passive release (P); $X/H=2/3$, $Z_{RH}=245mm$: (a) $\Delta T=0.1s$; (b) $\Delta T=0.5s$; (c) $\Delta T=1.0s$	214

7.10(a/b/c)	Cube: coefficient of variation (CV) vs (PLS/H); 'A'; AV; $Z_{RH}=255\text{mm}$: (a) 0° ; (b) -22.5° ; (c) -45° ;	215
7.11(a/b/c)	Cube: Normalised CV vs (PLS/H); 'A'; AV; $Z_{RH}=255\text{mm}$: (a) 0° ; (b) -22.5° ; (c) -45° ; form-factor F_x	216
7.12(a/b/c)	Cube: 5 th percentile (χ_{5th}/χ_{mean}) vs (PLS/H); 'A'; AV; $Z_{RH}=255\text{mm}$: (a) 0° ; (b) -22.5° ; (c) -45°	217
7.13(a/b/c)	Cube: 95 th percentile (χ_{95th}/χ_{mean}) vs (PLS/H); 'A'; AV; $Z_{RH}=255\text{mm}$: (a) 0° ; (b) -22.5° ; (c) -45°	218
7.14(a/b/c)	Cube: Normalised 95 th percentile (χ_{95th}/χ_{mean}) vs (PLS/H); 'A'; AV; $Z_{RH}=255\text{mm}$: (a) 0° ; (b) -22.5° ; (c) -45° ; form-factor F_x	219
7.15(a/b/c)	Cube: variation of form-factors F_x vs (X/H); 'A'; AV; $Z_{RH}=255\text{mm}$: (a) $F_{x,CV}$; (b) $F_{x,5th}$; (c) $F_{x,95th}$	220
7.16(a/b)	EW clad: coefficient of variation (CV) of χ vs PLS/H for each ensemble of various crosswind positions (Y/H): (a) non-normalised CV; (b) normalised CV (with form-factor, F_y)	220
7.17(a/b)	EW clad: coefficient of variation (CV) of χ vs PLS/H for each ensemble of vertical measurement positions: (a) non-normalised CV; (b) normalised CV (with form-factor, F_z)	221
7.18(a/b)	EW unclad: coefficient of variation (CV) of χ vs PLS/H for each ensemble of vertical measurement positions: (a) non-normalised CV; (b) normalised CV (with form-factor, F_z)	221
7.19(a/b)	Summary of statistical parameters vs PLS/H : (a) CV; (b) 95 th percentile	222
7.20(a/b)	Convergence of statistical parameters with puff sequence: cube; 'A'; -22.5° , AV; $X/H=2/3$; $\Delta T=0.1\text{s}$: (a) mean; (b) CV	223
7.21	Convergence of FFID signal mean measurement with sample number: no upstream building; $\Delta T=30\text{s}$; $Z_{RH}=320\text{mm}$	224

Chapter 8: Monte Carlo Computational Methods

Heading	Content	Pages
8.1	MC calculation co-ordinate axes and plume geometry	231
8.2	Line-of-sight geometry for the sampled point in the main RCZ	232
8.3	Offset distance resulting in the plume extent matching source size at $X=0$	234
8.4(a)	Roof recirculation zone (RCZ) co-ordinate and geometry	236
8.4(b)	RCZ lateral deconvolved concentration profiles at (X_{max} , Y_{max} , Z_{max})	236
Table 8.1	MC code parameter input page	239
8.5	Cube, 'A', 0° flow incidence, $Z_{norm}=(Z_{RH} - H)/H=0.021$: combined effective dose rate from all routes	239
8.6	Cube, 'A', 0° flow incidence, $Z_{norm}=(Z_{RH} - H)/H=0.021$: combined dose rate from gamma-ray dose rate sources	240

Chapter 9: Monte Carlo Results

Heading	Content	Pages
Table 9.1	Monte Carlo cases analysed	241
9.1(a/b)	Cube: total effective dose rate; release position 'A': (a) 0° ; (b) -22.5°	244
9.2(a/b)	Cube: total effective dose rate; release position 'A': -45° : (a) DGP; (b) SGP	245
9.3(a/b)	Cube: mean effective dose rate sampled on a grid around a receptor point; release position 'A': -45° : (a) DGP; (b) SGP	246

9.4(a/b)	Cube: gamma-ray maxima dose rates vs passive release height; release position 'A': (a) 0°; (b) -22.5°	247
9.5(a/b)	Cube: gamma-ray maxima dose rates vs passive release height; release position 'A', -45°: (a) DGP; (b) SGP	248
9.6(a/b)	Cube: gamma-ray mean dose rates sampled around the maxima vs passive release height; release position 'A', -45°: (a) DGP; (b) SGP	248
9.7(a/b)	Cube: 'A'; effective dose rate vs angle of approach flow; Z_{rh} =245mm (1m above roof at full-scale); (a) DGP; (b) SGP	249
9.8(a/b)	Cube: 'A'; effective dose rate vs angle of approach flow; Z_{rh} =255mm (3m above roof at full-scale); (a) DGP; (b) SGP	249
9.9(a/b)	Cube: 'A'; effective dose rate vs angle of approach flow; Z_{rh} =265mm (3m above roof at full-scale); (a) DGP; (b) SGP	250
9.10(a/b)	Cube: 'A'; effective dose rate vs angle of approach flow; Z_{rh} =275mm (3m above roof at full-scale); (a) DGP; (b) SGP	251
9.11(a/b)	Cube: effective dose rate vs release height; 'B'; Passive release (P); DGP: (a) 0°; (b) -22.5°	251
9.12(a/b)	Cube: effective dose rate vs release height; 'B'; -45°; Passive release (P); (a) DGP; (b) SGP	252
9.13(a/b)	Cube: mean effective dose rate sampled around local maxima vs release height; 'B'; -45°; Passive release (P); (a) DGP; (b) SGP	252
9.14(a/b)	Cube: gamma-ray maxima dose rate vs release height; 'B'; Passive release (P); DGP: (a) 0°; (b) -22.5°	253
9.15(a/b)	Cube: gamma-ray dose rate at local maxima vs release height; 'B'; -45°; Passive release (P); (a) DGP; (b) SGP	254
9.16(a/b)	Cube: gamma-ray dose rate sampled around local maxima vs release height; 'B'; -45°; Passive release (P); (a) DGP; (b) SGP	254
9.17(a/b)	Cube: 'B'; effective dose rate vs angle of approach flow; Z_{rh} =245mm (1m above roof at full-scale); (a) DGP; (b) SGP	255
9.18(a/b)	Cube: 'B'; effective dose rate vs angle of approach flow; Z_{rh} =255mm (3m above roof at full-scale); (a) DGP; (b) SGP	255
9.19(a/b)	Cube: 'B'; effective dose rate vs angle of approach flow; Z_{rh} =265mm (3m above roof at full-scale); (a) DGP; (b) SGP	256
9.20(a/b)	Cube: 'B'; effective dose rate vs angle of approach flow; Z_{rh} =275mm (3m above roof at full-scale); (a) DGP; (b) SGP	256
9.21(a/b)	EW clad/unclad: effective dose rate at maxima vs Z_{rh} ; DGP: (a) EW clad; (b) EW unclad	257
9.22(a/b)	EW clad/unclad: effective dose rate at maxima vs Z_{rh} ; SGP: (a) EW clad; (b) EW unclad	257
9.23(a/b)	EW clad/unclad: mean effective dose rate around maxima position vs Z_{rh} ; DGP: (a) EW clad; (b) EW unclad	258
9.24(a/b)	EW clad/unclad: gamma-ray dose rate maxima vs Z_{rh} ; DGP: (a) EW clad; (b) EW unclad	258
9.25(a/b)	EW clad/unclad: gamma-ray dose rate maxima vs Z_{rh} ; SGP: (a) EW clad; (b) EW unclad	259
9.26(a/b)	EW clad/unclad: mean gamma-ray dose rate around maxima positions vs Z_{rh} ; DGP: (a) EW clad; (b) EW unclad	259
9.27(a/b)	Mean dose rate for all cases; Active Vertical (AV) release; Z_{rh} =255mm; -22.5°; DGP: (a) effective dose; (b) gamma-ray dose	260

9.28(a/b)	Cube: AV; effective dose rate vs angle of approach flow; $Z_{rh}=255\text{mm}$; DGP: (a) 'A'; (b) 'B'	260
9.29(a/b)	Cube: AV; mean effective gamma-ray dose rate around maxima vs angle of approach flow; $Z_{rh}=255\text{mm}$; DGP: (a) 'A'; (b) 'B'	261
9.30(a/b)	Cube: downstream maxima positions $X(\text{m})$ vs release height $Z_{rh}(\text{mm})$: 'A'; P; 0° approach flow: (a) DGP; (b) SGP	261
9.31(a/b)	Cube: downstream maxima positions $X(\text{m})$ vs release height $Z_{rh}(\text{mm})$: 'A'; P; -22.5° approach flow: (a) DGP; (b) SGP	262
9.32(a/b)	Cube: downstream maxima positions $X(\text{m})$ vs release height $Z_{rh}(\text{mm})$: 'A'; P; -45° approach flow: (a) DGP; (b) SGP	263
9.33(a/b)	Cube: downstream maxima positions $X(\text{m})$ vs release height $Z_{rh}(\text{mm})$: 'B'; P; 0° approach flow: (a) DGP; (b) SGP	263
9.34(a/b)	Cube: downstream maxima positions $X(\text{m})$ vs release height $Z_{rh}(\text{mm})$: 'B'; P; -22.5° approach flow: (a) DGP; (b) SGP	264
9.35(a/b)	Cube: downstream maxima positions $X(\text{m})$ vs release height $Z_{rh}(\text{mm})$: 'B'; P; -45° approach flow: (a) DGP; (b) SGP	265
9.36(a/b)	Mean downstream maxima dose rate for all cases vs $X(\text{m})$; Active Vertical (AV) release; $Z_{rh}=255\text{mm}$; -22.5° : (a) DGP; (b) SGP	265
9.37(a/b)	Cube: lateral deflection of maxima positions ΔY vs Z_{rh} ; 'A'; P; 0° flow direction: (a) DGP; (b) SGP	266
9.38(a/b)	Cube: lateral deflection of maxima positions ΔY vs Z_{rh} ; 'A'; P; -22.5° flow direction: (a) DGP; (b) SGP	266
9.39(a/b)	Cube: lateral deflection of maxima positions ΔY vs Z_{rh} ; 'A'; P; -45° flow direction: (a) DGP; (b) SGP	267
9.40(a/b)	Cube: lateral deflection of maxima positions ΔY vs Z_{rh} ; 'B'; P; 0° flow direction: (a) DGP; (b) SGP	267
9.41(a/b)	Cube: lateral deflection of maxima positions ΔY vs Z_{rh} ; 'B'; P; -22.5° flow direction: (a) DGP; (b) SGP	268
9.42(a/b)	Cube: lateral deflection of maxima positions ΔY vs Z_{rh} ; 'B'; P; -45° flow direction: (a) DGP; (b) SGP	268
9.43(a/b)	All cases: AV release; lateral deflection of maxima positions ΔY ; -22.5° flow direction: (a) DGP; (b) SGP	269
9.44(a/b)	Cube: dose rate vs (X, Y) 3D plot: 'A'; 0° ; DGP; Passive; $Z_{rh}=245\text{mm}$; $Z=50\text{m}$ (full-scale): (a) effective dose rate; (b) gamma-ray dose rate	269
9.45(a/b)	Cube: dose rate vs (X, Y) 3D plot: 'A'; -22.5° ; DGP; Passive; $Z_{rh}=245\text{mm}$; $Z=50\text{m}$ (full-scale): (a) effective dose rate; (b) gamma-ray dose rate	270
9.46(a/b)	Cube: dose rate vs (X, Y) 3D plot: 'A'; -45° ; DGP; Passive; $Z_{rh}=255\text{mm}$; $Z=49\text{m}$ (full-scale): (a) effective dose rate; (b) gamma-ray dose rate	270
9.47(a/b)	Cube: dose rate vs (X, Y) 3D plot: 'A'; -45° ; DGP; Passive; $Z_{rh}=255\text{mm}$; $Z=49.5\text{m}$ (full-scale): (a) effective dose rate; (b) gamma-ray dose rate	271
9.48(a/b)	Cube: dose rate vs (X, Y) 3D plot: 'B'; 0° ; DGP; Passive; $Z_{rh}=255\text{mm}$; $Z=49.5\text{m}$ (full-scale): (a) effective dose rate; (b) gamma-ray dose rate	271
9.49(a/b)	EW clad: dose rate vs (X, Y) 3D plot: 'Vertex'; -22.5° ; DGP; AV; $Z_{rh}=255\text{mm}$; $Z=49.5\text{m}$ (full-scale): (a) effective dose rate; (b) gamma-ray dose rate	272
9.50(a/b)	Cube: dose rate vs (X, Y) 3D plot: 'A'; -22.5° ; DGP; AV; $Z_{rh}=255\text{mm}$; $Z=49.5\text{m}$ (full-scale): (a) effective dose rate; (b) gamma-ray dose rate	272

Chapter 10: Full Scale Rooftop Gamma-Ray Dose Measurements

Heading	Content	Pages
10.1	Gamma-ray (γ_1 , γ_2) and Wind (W) detectors in relation to the EW roof	276
10.2(a/b)	Gamma-ray detector 1 (γ_1) facing: (a) West; (b) North	277
10.3(a/b)	Detectors: (a) Gamma-ray detector 2 (γ_2) facing SE; (b) Wind detector facing West	278
10.4(a/b)	Gamma-ray detector: (a) LB6360-H10 compensated Geiger Gamma-ray detector; (b) Photon energy response	278
Table 10.1	Twenty-minute time-traces of detector γ_1 and γ_2 dose rates and wind speed/direction	282
Table 10.2	Wind speed values and velocity correction factor V_{cf}	283
Table 10.3	Release quantities corrected to Monte Carlo calculated steady release values	284
Table 10.4	Rotation of the co-ordinate system, to apply the MC calculated dose rate values	285
Table 10.5	Monte Carlo dose rates at the detectors under co-ordinate transform to wind direction	286
Figure 10.5	Monte Carlo gamma-ray dose rate for the EW clad DGP method	286
10.6	PDF of calculated/measured (C/M) values for gamma-ray (γ_1 , γ_2) detectors	287
10.7	Measured gamma-ray dose rate corrected to standard release rate of pollutant	288
10.8	Angular polar plot of measured gamma-ray dose rate vs wind direction	289
10.9	Measured gamma-ray dose rate vs wind direction averaged in 30° sectors	289
10.10	Angular polar plot of gamma-ray dose rate averaged in 30° sectors vs wind direction	290
10.11	Standard deviation in peak dose rate angle (over four one-minute samples) vs wind direction	291
10.12	Variation in the velocity field components (σ_U/U) and (σ_V/U) averaged in 30° sectors vs wind direction	292
10.13	Estimates of turbulence intensity (σ_U^2/U_{ref}^2) and (σ_V^2/U_{ref}^2) based on the full-scale sampled values	293
Table 10.6	Statistical parameters from the full-scale data set	294

Chapter 11: Sensitivity analysis for building cases

Heading	Content	Pages
11.1	Wind tunnel model coverage	296
11.2	General site layout	297
11.3	Constructed model for wind tunnel experiments	298
Table 11.1	Building heights of the models used in the experiments	298
Table 11.2	Building combinations measured in the wind tunnel	299
Table 11.3	Maximum concentration field values: $X=160\text{mm}$ (32m); -22.5° ; $Z_{rh}=265\text{mm}$ (53m)	299
Table 11.4	Maximum concentration field values vs X ; -22.5° ; $Z_{rh}=265\text{mm}$	300
11.4(a/b/c)	Lateral profile of mean streamwise velocity at three heights for the EW/Full Building Model (FBM) case: (a) -27.5° ; (b) -22.5° ; (c) -17.5°	300
11.5	EW clad building showing point co-ordinates: $X=160\text{mm}$; -22.5°	301
11.6(a/b/c)	Lateral profile of mean vertical velocity at three heights for the EW/Full Building Model (FBM) case: (a) -27.5° ; (b) -22.5° ; (c) -17.5°	302

Table 11.5	Dispersion, mean flow and vertical turbulence intensity data at the positions of maximum concentration: $X=160\text{mm}$ (32m); -22.5° ; $Z_{rh}=265\text{mm}$ (53m)	302
Table 11.6	Turbulence intensity w'^2/U_{ref}^2 vs angle of approach flow at the position of maximum concentration: $X=156\text{mm}$; $Z_{rh}=265\text{mm}$; $-27.5^\circ/-22.5^\circ/-17.5^\circ$	303
11.7	East Wing Clad (FBM) lateral profile of the vertical component of turbulence intensity w'^2/U_{ref}^2 : $X=156\text{mm}$; -22.5°	303
Table 11.7	PCM shear stress $-u'w'/U_{ref}^2$: $X=156\text{mm}$; $Z_{rh}=265\text{mm}$; $-27.5^\circ/-22.5^\circ/-17.5^\circ$	304
Table 11.8	Concentration maxima: χ_{max} ; $X=160\text{mm}$ (32m); $-17.5^\circ/-22.5^\circ/-27.5^\circ$; $Z_{rh}=265\text{mm}$	304
Table 11.9	Concentration maxima: χ_{max} ; $X=800\text{mm}$ (160m); $-17.5^\circ/-22.5^\circ/-27.5^\circ$; $Z_{rh}=265\text{mm}$; $Z=30\text{mm}$	304
Table 11.10	Concentration maxima: χ_{max} ; $X=1200\text{mm}$ (240m); $-17.5^\circ/-22.5^\circ/-27.5^\circ$; $Z_{rh}=265\text{mm}$; $Z=30\text{mm}$	305
Table 11.11	Cube/A; χ_{max} ; $-45^\circ/-27.5^\circ/-22.5^\circ/-17.5^\circ/0^\circ$; $Z_{rh}=265\text{mm}$	305

Chapter 12: Practical application of the methodology

Heading	Content	Pages
Table 12.1	Case input data	309

Chapter 13: Conclusions and further developments

Heading	Content	Pages
Table 13.1	Chapter 4 estimates of the total radiation dose at 5m above the roof from the ^{18}F release	315
Table 13.2	Best estimates of the EW model total radiation dose at 1.5m from the roof level from the ^{18}F releases	316
Table 13.3	Best estimates of the total cube model radiation dose at 1.5m from the roof level from the ^{18}F releases	317

Appendix 15.2: Flow field further results

Heading	Content	Pages
15.2.1(a/b)	Cube; 'A'; 0° ; $X/H=0.98$: (a) w'^2/U_{ref}^2 ; (b) co-ordinate schematic layout	337
15.2.2(a/b)	Cube; 'A'; 0° ; $X/H=1.65$: (a) u'^2/U_{ref}^2 ; (b) co-ordinate schematic	337
15.2.3	Cube; 'A'; 0° ; $X/H=1.65$: (a) w'^2/U_{ref}^2	338
15.2.4(a/b)	Cube; 'A'; -45° ; $X/H=0.98$: (a) w'^2/U_{ref}^2 ; (b) co-ordinate schematic	338
15.2.5(a/b)	Cube; 'A'; -45° ; $X/H=1.65$: (a) w'^2/U_{ref}^2 ; (b) co-ordinate schematic	339
15.2.6(a/b)	Cube; 'A'; -22.5° ; $X/H=0.32$: (a) W/U_{ref} ; (b) co-ordinate schematic	339
15.2.7(a/b)	Cube; 'A'; -22.5° ; $X/H=0.98$: (a) w'^2/U_{ref}^2 ; (b) co-ordinate schematic	340
15.2.8(a/b)	Cube; 'A'; -22.5° ; $X/H=1.65$: (a) w'^2/U_{ref}^2 ; (b) co-ordinate schematic	340
15.2.9(a/b)	EW clad/FBM; -22.5° ; $X/H=0.98$: (a) W/U_{ref} ; (b) co-ordinate schematic	341
15.2.10(a/b)	EW clad/FBM; -22.5° ; $X/H=1.65$: (a) W/U_{ref} ; (b) co-ordinate schematic	341

Appendix 15.3: Supplementary Results on Concentration Field

Heading	Content	Pages
15.3.1	Cube; 'A'; -22.5° flow: concentration profile/passive: $X/H=2/3$	342
15.3.2	Cube; 'A'; -22.5° flow: concentration profile/passive: $X/H=1$	342

15.3.3	Cube: ‘A’: -45° flow: concentration profile/passive: $X/H=2/3$	342
15.3.4	Cube: ‘B’: -45° flow: concentration profile/passive: $X/H=2/3$	343
15.3.5	Cube: ‘B’: -45° flow: concentration profile/AV: $X/H=2/3$	343
15.3.6	EW unclad: -22.5° flow: concentration profile/passive: $X/H=1$	344
15.3.7	Cube: ‘A’: -45° incidence flow: passive: PCM variation with downstream distance	344
15.3.8	EW unclad: -22.5° incidence flow: passive: PCM variation with downstream distance	345
15.3.9	Cube: ‘B’: 0° incidence flow: passive: PCM variation with downstream distance	345
15.3.10	Cube: ‘B’: -45° incidence flow: passive: PCM variation with downstream distance	346
15.3.11	EW unclad: -22.5° incidence flow: SGP: spread parameters vs X/H	346
15.3.12	EW unclad: -22.5° incidence flow: DGP/IGP: spread parameters vs X/H	347
15.3.13	Cube: ‘B’: -22.5° incidence flow: SGP: spread parameters vs X/H	347
15.3.14	Cube: ‘B’: -22.5° incidence flow: DGP/IGP: spread parameters vs X/H	348
15.3.15	Cube: ‘B’: -45° incidence flow: SGP: spread parameters vs X/H	348
15.3.16	Cube: ‘B’: -45° incidence flow: DGP/IGP: spread parameters vs X/H	349
15.3.17	Cube: ‘A’: -45° incidence flow: SGP/DGP/IGP: mean spread parameters over distance from source vs normalised release height Z_{norm}	349
15.3.18	EW unclad: -22.5° incidence flow: SGP/DGP/IGP: mean spread parameters over distance from source vs normalised release height Z_{norm}	350
15.3.19	Cube: ‘B’: -22.5° incidence flow: SGP/DGP/IGP: mean spread parameters over distance from source vs normalised release height Z_{norm}	350
15.3.20	Cube: ‘B’: -45° incidence flow: SGP/DGP/IGP: mean spread parameters over distance from source vs normalised release height Z_{norm}	350
15.3.21	Cube/EW-clad/unclad: ‘B’: 0°/-22.5°/-45° incidence flow: SGP: Summary of mean spread parameters over distance from source vs normalised release height Z_{norm}	351
15.3.22	Cube/EW-clad/unclad: ‘B’: 0°/-22.5°/-45° incidence flow: DGP/IGP: Summary of mean spread parameters over distance from source vs normalised release height Z_{norm}	352

Appendix 15.4: Supplementary results for intermittent short releases

Heading	Content	Pages
15.4.1(a/b/c)	PDF of dimensionless concentration χ for the EW unclad: -22.5°; ‘Vertex’; AV; $X/H=2/3$, $Z_{RH}=255\text{mm}$: (a) $\Delta T=0.025\text{s}$; (b) $\Delta T=0.1\text{s}$; $\Delta T=1.0\text{s}$	353
15.4.2(a/b/c)	PDF of dimensionless concentration for EW unclad: -22.5°; ‘Vertex’; Passive (P); $X/H=2/3$, $Z_{RH}=245\text{mm}$: (a) $\Delta T=0.025\text{s}$; (b) $\Delta T=0.1\text{s}$; (c) $\Delta T=1.0\text{s}$	354
15.4.3(a/b/c)	PDF of dimensionless concentration for EW unclad: -22.5°; ‘Vertex’; Passive (P); $X/H=2/3$, $Z_{RH}=245\text{mm}$: (a) $\Delta T=0.025\text{s}$; (b) $\Delta T=0.1\text{s}$; (c) $\Delta T=1.0\text{s}$: sampled off-plume axis vertically ($\Delta Z/H=+1/6$)	355
15.4.4(a/b/c)	Cube: 5 th percentile ($\chi_{5\text{th}}/\chi_{\text{mean}}$) vs (PLS/H); ‘A’; AV; $Z_{RH}=255\text{mm}$: (a) 0°; (b) -22.5°; (c) -45°	356

15.4.5(a/b)	EW unclad: coefficient of variation (CV) of χ vs PLS/H for each ensemble of various crosswind positions (Y/H): AV; $Z_{RH}=255\text{mm}$; (a) measured values with Y/H ; (b) normalised CV (with form-factor, F_y)	357
15.4.6(a/b)	EW unclad: coefficient of variation (CV) of χ vs PLS/H for each ensemble of various crosswind positions (Y/H): Passive (P); $Z_{RH}=245\text{mm}$; (a) measured values with Y/H ; (b) normalised CV (with form-factor, F_y)	358
15.4.7(a/b)	EW clad: CV of χ vs PLS/H for each ensemble of vertical measurement positions: (a) non-normalised CV; (b) normalised CV (with form-factor, F_z)	358
15.4.8(a/b)	EW clad: CV of χ vs PLS/H for each ensemble of vertical measurement positions: (a) non-normalised CV; (b) normalised CV (with form-factor, F_z)	358
15.4.9	Cube and EW clad/unclad cases: summary of 5 th percentile (χ_{5th}/χ_{mean}) vs PLS/H	359
15.4.10(a/b/c)	EW clad/unclad cases: P/AV; summary statistical parameters vs PLS/H : (a) CV; (b) 5 th percentile (χ_{5th}/χ_{mean}); (c) 95 th percentile (χ_{95th}/χ_{mean})	360
15.4.11(a/b/c)	EW clad/unclad cases: P/AV; mean values of statistical parameters over all crosswind positions vs PLS/H : (a) CV; (b) 5 th percentile (χ_{5th}/χ_{mean}); (c) 95 th percentile (χ_{95th}/χ_{mean})	360
15.4.12(a/b/c)	EW cases: P/AV; crosswind form-factor F_y vs Y/H offset from plume centreline: (a) $F_{y,CV}$; (b) $F_{y,5th}$; (c) $F_{y,95th}$	361
15.4.13(a/b/c)	EW clad/unclad cases: P/AV; mean values of statistical parameters over all vertical sampled positions vs PLS/H : (a) CV; (b) 5 th percentile (χ_{5th}/χ_{mean}); (c) 95 th percentile (χ_{95th}/χ_{mean})	362
15.4.14(a/b/c)	EW cases: P/AV; vertical form-factor F_z vs $(Z_s-Z_{RH})/H$ offset from plume centreline: (a) $F_{z,CV}$; (b) $F_{z,5th}$; (c) $F_{z,95th}$	363
15.4.15(a/b)	Convergence of statistical parameters with puff sequence: cube; 'A'; - 22.5°, AV; $X/H=2/3$; $\Delta T=0.25\text{s}$: (a) mean; (b) CV	364
15.4.16(a/b)	Convergence of statistical parameters with puff sequence: cube; 'A'; - 22.5°, AV; $X/H=2/3$; $\Delta T=0.5\text{s}$: (a) mean; (b) CV	364
15.4.17(a/b)	Convergence of statistical parameters with puff sequence: cube; 'A'; - 22.5°, AV; $X/H=2/3$; $\Delta T=1.0\text{s}$: (a) mean; (b) CV	365

CHAPTER 1: INTRODUCTION AND RESEARCH QUESTIONS

1.1 Introduction

There is little available data on the near-field dispersion of plumes of pollutant material in the roof zone immediately above buildings, yet this is the zone where these releases frequently occur due to activities carried out within the building. In many cases the harmful effects of the pollutant are related to the spatial concentration of the plume at the position where it is inhaled, where the dose received will be proportional to the integral of the plume concentration over time. For radioactive releases the situation is more complex still: radiation dose is received not only from inhalation of the radioactivity, but from external irradiation of the subject in the radiation field from particulate radiations and gamma ray photons from the plume of radioactive material. The spatial distribution of the concentration field of radioactive material is therefore key to being able to evaluate the radiation dose to persons being exposed in or close to the plume of radioactive material. The spatial distribution in turn depends upon the characteristics of the release such as the height of the release in relation to the roof of the building, the emission conditions, the angle of approach flow, and the wind velocity. Other factors such as the shape of the building come into play as well, as the spatial position of the point at which the radiation dose is to be evaluated. Coupled with these factors is the usual presence of other buildings surrounding the building under investigation and the effects of these surrounding buildings on the flow field and dispersion of pollutant material. This work aims to explore and present evidence to fill gaps in this knowledge: a range of standard geometry (cube) cases was investigated with a range of pollutant release heights and angles of approach flow, along with site-specific investigations of real-world buildings, together with sensitivity analyses for wind direction uncertainty and the presence of surrounding buildings.

Furthermore, the main aim of the project is to investigate and improve the evaluation of radiation dose received by persons in the near field of a radioactive plume of gas released close to buildings. The initial driver for the research was in the context of the St.Thomas' Hospital (STH) site in central London, where the radioactive plume was generated from ventilation of a cyclotron radiochemistry facility and the emitting stack was mounted on the East Wing (EW) site building.

Radiation dose is expressed in terms of the effective dose (ICRP, 2007) which accounts for the radiation dose contributions to different organs and may be related to the level of radiation risk in terms of causing cancers. The linear-no-threshold model adopted by scientific consensus in the ICRP holds that the radiation risk of cancers is a stochastic, or probabilistic, effect and that there is not a lower threshold dose below which the risk reduces to zero. At high levels of radiation dose deterministic effects caused by acute radiation injury may be seen above certain threshold levels of radiation dose. The approach taken to limit the risk from radiation is firstly to set upper dose limits in regulation, which must not be exceeded, and which avoid the deterministic dose thresholds. Secondly, since there is thought to be no completely safe level of radiation exposure, the dose to individuals must be limited to 'as low as reasonably practicable' in regulation. In UK law (IRR, 2017) the dose limit to a member of the public must be limited to an effective dose of 1000 μ Sv (or 1mSv) per year. This limit is further reduced by application of a dose constraint of 300 μ Sv per year from any given activity, for example a polluter releasing radioactive material to the environment which would give rise to radiation doses to the local population (EA, 2010). A dose of 1mSv gives rise to a risk of cancer of approximately 1 in 20,000 per individual in the population. Doses for radiation workers are permitted to exceed 1000 μ Sv per year, but if the effective dose is likely to exceed 6000 μ Sv in

a given calendar year the worker must be made into a classified radiation worker and undergo closer monitoring of radiation dose and medical surveillance for possible risks to health. Ordinary non-radiation workers have the same dose limits applied as a member of the public (EA, 2012) – and in the context of this work personnel working in the roof zone, and inside the buildings considered (where there are building air intake systems on the roof) would have the 300 μ Sv per year dose constraint applied as their permissible level of occupational exposure. Potential radiation doses from the pollutant releases considered in this work could easily exceed the 300 μ Sv per year level, given unfavourable meteorological conditions, and this is the reason that careful evaluation of the radiation doses was necessary.

The STH site has produced radioactive materials using a proton cyclotron for many years, producing positron emitting radionuclides (^{18}F , ^{11}C , ^{15}O , ^{13}N) for chemical synthesis into radioactive tracers for patient diagnostic Positron Emission Tomography (PET) studies. Recent developments on site have meant that a new, second cyclotron of higher bombardment energy (16 MeV) was installed to supplement the production of the existing machine.

Radioactive discharges, arising from the radiochemistry laboratory that produces radioactive tracers for patient use, have been discharged for many years from a flue stack at the top of the East Wing (EW) building at the STH site. The EW building underwent the installation of a glass canopy cladding layer (2014-15) in the form of a glass envelope: changing the existing ‘T’ shape plan view into a triangular cross section (Fig1). A 1:200 scale wind tunnel model was built by the Medical Physics Department at Guy’s and St.Thomas’ NHS Foundation Trust (GSTFT, 2021) of the EW building and surrounding buildings on the STH site, in order to carry out wind tunnel investigations of dispersion from the EW stack. Different model buildings were constructed for the pre-clad and post-clad EW buildings to investigate the effects on flow and dispersion for the two cases.

Preliminary work carried out at STH Medical Physics, in conjunction with studies in the EnFlo wind tunnel facility at the University of Surrey (EnFlo, 2021), enabled an analysis of the most critical wind direction for the plume releases and allowed the required height of the proposed new stack on the EW building to be determined. However, further work was required to analyse the extra data for different wind directions to generate a more comprehensive radiological assessment of radiation doses to critical groups of persons: not only workers on the EW building during the cladding works, but persons inside the EW building, other persons on the STH site and persons in the surrounding area. A radiological assessment was required to provide the regulating authority for radioactive releases, the Environment Agency, the necessary assurance that radioactive discharges were being minimised to ‘as low as reasonably practicable’ in accordance with Best Achievable Technology (BAT) requirements (EA/SEPA/HPA, 2012). The initial results from wind tunnel measurements, and the consequent safety case assessment, were documented in two published scientific papers which are discussed in this work in Chapter 4 (and reproduced in Appendices 15.5 and 15.6 according to the publication rules of the publishing journal in the accepted manuscript format).

The experiments in the EnFlo wind tunnel provided the means for detailed investigation of flow and dispersion behaviour of pollutant material in close proximity to the building cases investigated. However, coupled with the experimental cases investigated in the wind tunnel, real-world measurements of the gamma ray external dose rate from actual radioactive releases from the STH EW building were also conducted. These measurements on the EW building roof recorded the gamma ray dose rate from emitted radioactive gas plumes at two detectors of known location and this was coupled with simultaneous wind velocity magnitude and direction

measurements to determine plume direction and advection velocity during radioactive gas release events from the radiochemistry facility. The results of these experimental investigations are also presented in this research. Flow around buildings has been recognised as a complex problem arising from the turbulent nature of the flow around obstacles (Gayev and Hunt, 2007) and the behaviour of plume discharges near to obstacles in a wind flow (Robins and Macdonald, 2001). Not only did this provide a means of evaluating the wind tunnel simulations, but the combined use of wind tunnel and field measured data afforded a robust test of the methodologies developed for dose evaluation in this work and also validated the wind tunnel methods employed in the analysis.

As well as investigation of the ‘real world’ scenario the research also aims to address more generalised topics such as dispersion in close proximity to more standard geometrical building conditions i.e. an isolated cuboid building at incidence to the oncoming flow: a case which has been considered as a standard case in the literature (Robins and Castro, 1977a, 1977b) for wind tunnel investigational measurements. The aims for this work also encompass an assessment of the velocity flow field in highly proximal regions to the building and to relate these flow field features to the local micro-scale concentration field from the release of pollutant material. The sensitivity to local flow and geometrical conditions, such as the angulation of the building with respect to the approaching wind flow and the height of the pollutant release in relation to the building height were investigated in this work. An investigation of the sensitivity of the measurements to different configurations of buildings adjacent to the primary building under study was also conducted in this research.

Detailed wind tunnel measurements of the concentration field for all experimental configurations were made and these enabled a parameterisation of the plume spread for highly proximal cases to the building. These results are presented in the chapter covering concentration field measurements and involve the fitting of the experimental data to the Gaussian Plume Model (GPM).

A further series of measurements was made to investigate the dose arising from intermittent short ‘puff’ releases and the statistical properties of these releases in order to determine the 95th percentile dose arising from a release to be received by a maximally exposed individual. These results are presented in chapter 8 of this work.

To evaluate the doses received from radiation to human subjects in the complex near field geometry a dose point kernel Monte Carlo code was written to evaluate doses from gamma ray disintegrations occurring inside the plume. Special consideration was made to the fact that the measurements positions were inside the actual plume: a situation where simplified methods treating the plume as a line source, or other simplified geometry, were not applicable. The program developed also evaluated inhalation and beta particle immersion doses based on the parameterised values of the plume geometry over the range of experimental cases investigated. Chapters providing information on the development of the Monte Carlo model, and the subsequent results from application of that model are presented in this work.

As has been stated, results relating to the sensitivity of the measurement cases to surrounding building configurations are also presented. This information enables the results to be interpreted in a wider context and gives an indication of the range and sensitivity of results that may be expected given real-world scenarios of varying complexity.

A summary has been made of the methodological approaches developed in this work in the best methodologies chapter – a summary of the methods by which to apply the results of this work to evaluation of radiation dose to persons in the vicinity of buildings from radioactive plumes. A summary of the research findings, considered in the context of the initial research questions has been presented. The appendix contains further information accumulated and recorded in the development of this work.

The following activities and research questions cover a mixture of the site-specific and generic. For the purposes of this research, it was proposed that emphasis would be placed on the more generic tasks, whilst also completing sufficient work to treat the important site-specific issues. Publication of two peer reviewed scientific journal papers was completed during the thesis submission period and these are discussed in Chapter 4 and presented in Appendices 15.5 and 15.6. The research objectives have been re-ordered to match the final configuration layout of chapters to present the research themes in the order that they are presented in this work.

1.2 Research questions and methods

From a review of the literature and the problems of characterisation of very near-field releases of pollutant in the region of buildings, and in particular in the roof zone, the following research questions emerged. These are listed below in various categories: research preliminaries, in which the initial scoping exercise was conducted. Secondly, the initial site-specific investigations which were made using available methods for determining radiation dose in the very near-field of buildings: these results are discussed in chapter 4 and in the two published scientific papers in Appendices 15.5 and 15.6. Thirdly, flow field investigations to characterise the flow field, in particular for the intermediate angle case (-22.5°) between the conventional analysis of normal incident and -45° of approach flows, and these results have been used to explain the physical processes underlying the findings with respect to variations in the concentration field – a major determinant in the radiation dose contribution. Fourthly, extensive measurements of the concentration field were proposed to map the variation in concentration field over the very near-field zones and to parameterise the pollution spread so that this could be utilised by the Monte Carlo computational methods. To deal with the effects of very short duration releases puff release experiments were conducted. To convert the concentration field into radiation dose estimates a Monte Carlo code was written, for this work by the author, to evaluate inhalation, positron immersion and gamma-ray shine doses using the concentration field parameterised mappings. To validate and support the simulations in wind tunnel and with Monte Carlo methods, full-scale measurements at the investigation site were conducted and compared to the MC simulated dose rate values. Further experiments were carried out to investigate the sensitivity of surrounding building configurations in affecting the roof top measured concentrations. A chapter is presented showing examples of the developed methodology from this work. Finally, conclusions and findings are given, with recommendations for future work.

1.2.1 Research preliminaries

A review using database engines (Web of Science) was made of the scientific literature for Gaussian plume dispersion models, radioactive gas dispersion dose models and plume dispersion in building arrays. The review also included literature for radiation dose estimation from environmental releases to atmosphere.

[1.2.1.1] Various models for calculating the radiation dose to persons exposed to a radioactive gaseous release were applied to the specific St Thomas' Hospital (STH) site. The process involved analysing and refining models used for gamma dose build-up factor for gaseous gamma emitters in air: these were applied in the static hemisphere model and drifting hemisphere model (Chapter 4). Various simple 'small user' analytic models were also applied to the problem (MacDonnell, 2004) such as the Gaussian Plume Model (GPM) originally from NRPB R-91 (Clarke *et al*, 1979) under different assumptions, such as fixed wind direction for a downwind dose receptor and uniform wind rose. More sophisticated techniques originally developed for isolated buildings were applied as detailed in NRPB R-157 (Jones, 1983). The range of dose results for the critical groups varied over several orders of magnitude and showed that there was a wide disparity of dose figures received over the course of one year, and that the simple models did not have sufficient rigour to satisfy the scrutiny of any regulation of the environmental and occupational exposure of persons to the plume release from the site under consideration.

Results for concentration field values obtained from an ADMS simulation (CERC, 2012a) were used to obtain another estimate of the radiation dose to the critical groups of the STH East Wing (EW) workers and others on site. The inhalation and immersion (positron doses to the skin) doses were converted from concentration field values. The gamma doses at roof level, and intermediate positions above the ground, were estimated from the ADMS values at an elevated ground plane and ground level following a method devised for the task (Chapter 4). The ADMS doses took account of five years of meteorological data, the same data set used in the Wind Tunnel (WT) analysis.

A wind tunnel (WT) data set from EnFlo (2012a) was analysed to calculate radioactive plume shine, inhalation and positron (beta immersion) doses to EW roof workers. This was supplemented by data obtained in an initial experiment series. The WT concentration field values (Bq.m^{-3}) were converted into inhalation and immersion doses using the same meteorological data set as was used for ADMS to enable comparison of approaches and the results are presented in Chapter 4 of this work. For the initial WT series of data limitations of running time and sample mesh co-ordinates required that WT concentration was measured at approximately head level for a roof worker on the EW building. Using data from the initial experiment series the vertical dispersion parameters for the plume above the building were used in a method devised to correct for single horizontal plane sampling of pollutant concentration in the EnFlo (2012) data. In this way the plume gamma shine component of dose was evaluated and is presented in Chapter 4, along with the other evaluated dose contributions.

[1.2.1.2] A review of the research literature of the dispersion of pollutant gases in the near field of buildings. Investigate literature covering dispersion in the near field of buildings including publications on block spacing and urban models. Also, a review of methods of calculation of radiation dose to persons from radioactive gaseous emissions, whether from inhalation, immersion or dose from plume gamma-ray shine.

1.2.2 Initial specific case investigations

[1.2.2.1] Compare and contrast the ranges of radiation dose to critical groups (roof workers and persons in surrounding area including the source building) for given source release terms. In particular, carry out a sensitivity study of modelling assumptions for a range of models ranging from the simple fixed hemisphere uniform distribution, a moving hemisphere dispersion model, and a simple Gaussian plume release using fixed wind direction appropriate for a short-

term release, and also established building wake models (MacDonnell, 2004). The results of this analysis are presented in Chapter 4 and associated Appendices 15.5 and 15.6.

[1.2.2.2] Develop a method for converting dimensionless concentration of radioactive pollutant, as measured in a wind tunnel experiment, to radiation dose received by a person in the concentration field e.g. a roof worker. The devised method will take into account contributions from inhaled radioactive materials using accepted dose coefficients (ICRP, 72), dose from local beta (positron) irradiation of skin and dose from gamma shine component from the cloud source of radioactive pollutant (Smith and Simmonds, 2009). Derivation of the appropriate conversion factors to effective dose from measurable field quantities: e.g. $H^*(10)$ dose index were detailed, as well as the effect of build-up factors for secondary scatter of photons in the radiation field from the pollutant radioactive gas. The results of this analysis are presented in Chapter 4 and associated Appendices 15.5 and 15.6.

[1.2.2.3] Compile wind tunnel measured dimensionless concentrations from several wind directions over the St.Thomas' Hospital site measured in the wind tunnel experiment in simulated neutral atmospheric stability conditions (Burt, Robins and Hayden, 2012) and convert these, using wind rose data (wind direction and velocity) for five years of meteorological conditions, to expected radiation doses to critical groups within and outside the perimeter of the hospital site. The results of this analysis are presented in Chapter 4.

[1.2.2.4] Analyse the results of a simulation of the site carried out using a computational method, ADMS (CERC, 2012b) that takes account of building wake effects for a single rectangular building, simulating the source building from which the stack release was occurring. To then compare the results of the ADMS simulation (run over same 5 years of meteorological data) to the wind direction weighted radionuclide (pollutant) concentration obtained from the wind tunnel experiment, comparing the results for an assumed constant steady state release for both cases. The results of this analysis are presented in Chapter 4.

[1.2.2.5] Further from point [1.2.2.4], to then compare and contrast the differences between the radiation dose estimates from the ADMS model to that obtained from the wind tunnel modelling. This given the limitation that ADMS can calculate only at the ground plane, or an elevated ground plane release. The simulations were modelled in ADMS. The developed 'gamma grid' method from the papers presented in Chapter 4 enabled calculation of radiation doses in any field co-ordinate over the roof zone.

[1.2.2.6] Analysis of the effect of Roof Top Structures (RTS) on the recirculation zones in the building roof zone and the investigation of the correction of standard building wake models (Robins and MacDonald, 2001). A new methodology for analysing recirculation zones was presented in Chapter 4, in the published papers.

1.2.3 Flow field investigation

[1.2.3.1] Investigate the flow field in the near-field zone immediately above the building and in the near field adjacent region. This investigation to be carried out for the cube buildings and the EW building configurations. To present information on the advection velocities and the turbulent intensity terms and how these vary with position with respect to the building.

[1.2.3.2] Relate features of the flow field to the concentration field later in terms of advection of pollution to receptor position regions and dose terms near to the roof level of the building.

1.2.4 Concentration field investigations

[1.2.4.1] Analyse the plume dispersion and the radiation dose in the nearfield region (<100m from release point) where plume dimensions as described by the dispersion parameters are smaller than the buildings themselves ($\sigma_y < W/4$, $\sigma_z < H/3$) (Robins and MacDonald, 2001). In particular, the objective was to analyse the spatial distribution of the concentration field of pollutant at roof level and the immediate surrounding area downwind of the building from which the release occurred. The objective was then to use the dimensionless concentration field measurements in the wind tunnel to use this developed method to estimate the radiation doses to persons in the vicinity of the building roof, and compare these estimates to established simple Gaussian dispersion e.g. semi-infinite plume models and compare to conventional building wake models (MacDonnell, 2004).

[1.2.4.2] Carry out a series of measurements in the WT for the EW building sets to measure plume dispersion at different release heights close to the building roof, and at different downstream measurement planes. To characterise these releases in terms of determined spread parameters with release height and angle of approach flow. Investigation of a cuboid building of similar size to the site-specific building models at different orientations to the direction of flow for passive releases matching the approach flow velocity at the building height. To carry out a series of measurements to determine plume spread parameters with release height above the building and at different downstream distances.

[1.2.4.3] Investigate a cube-shaped building of similar size to the site-specific building models at different orientations to the direction of flow for passive releases matching the approach flow velocity at the building height. To carry out a series of measurements to determine plume spread parameters with release height above the building and at different downstream distances.

[1.2.4.4] Establish best parameter fitted values for the near field region (<100m) of plume dispersion parameters σ_y and σ_z for the EW cases (clad and unclad) and the standard cuboid building case at different orientations to the flow and release heights. Investigate corrections to be applied to the Gaussian model for near field effects for roof zone.

[1.2.4.5] Investigate corrections to be applied to the Gaussian model for near field effects for roof top releases in terms of the gamma shine component. The W-63 method (MacDonnell, 2004), derived from R-91 (Clarke *et al*, 1979) makes assumptions about a semi-infinite uniform dispersion above a ground plane in order to calculate cloud gamma shine doses which are significantly in error when used to describe the radiation dose from a near field exposure to a radioactive plume (Gallacher *et al*, 2012).

Establish best parameter fitted values for the near field region (<100m) of plume dispersion parameters σ_y and σ_z for the EW cases (clad and unclad) and the standard cuboid building case at different orientations to the flow and release heights. Investigate corrections to be applied to the Gaussian model for near field effects for roof top releases in terms of the gamma shine component. The W-63 method (MacDonnell, 2004), derived from R-91 (Clarke *et al*, 1979) makes assumptions about a semi-infinite uniform dispersion above a ground plane in order to calculate cloud gamma shine doses which are significantly in error when used to describe the radiation dose from a near field exposure to a radioactive plume (Gallacher *et al*, 2012).

[1.2.4.6] Investigate the differences to the radiation dose to a person in the vicinity of a radioactive plume in the near field region from the plume geometry for the cases investigated.

1.2.5 Intermittent short duration releases

[1.2.5.1] Analyse short release puff release concentrations in wind tunnel experiment. Due to large eddy effects on concentration in the near field turbulent building wake this will require statistical analysis of fluctuations. This may be used to estimate, statistically, the most probable radiation dose from plume inhalation and beta immersion based on expected concentrations of pollutant. Gamma shine is likely to be less sensitive to smaller scale eddies because the dose rate at a point from gamma emitters is related to the volume integral of distribution around the point at interest over a scale greater than small eddies. Larger eddies may be expected to have a larger effect, but this may require further investigation.

1.2.6 Monte Carlo methods and results

[1.2.6.1] Monte Carlo gamma ray cloud shine dose simulations, from computer code written for this project, from the plume spread for the different building cases calculated for the EW (clad and unclad) cases and the cube in different orientations, and for different release heights and wind velocities. The model developed also accounted for the dose terms arising from inhalation and beta particle immersion in the concentration field.

[1.2.6.2] Monte Carlo gamma ray cloud shine dose simulations from the plume spread for the different building cases calculated for EW (clad and unclad) and cuboid in different orientations, and for different release heights and wind velocities. The variations of radiation dose based on these variations was determined.

[1.2.6.3] Investigate the differences to the radiation dose to a person in the vicinity of a radioactive plume in the near field region from the plume geometry for the cases investigated. Using various plume geometry assumptions e.g. line source, cone source, Gaussian distribution source, calculate the dependence of radiation plume gamma shine dose with plume direction, concentration and velocity and expected doses from inhalation and beta skin dose from plume immersion. The dose 'kernel' equation may be expressed corrected to unit release rate, plume height above the building, and as a directional function with different wind directions. A sensitivity to building shape may be carried out to investigate variations in the building conditions. Note: detailed dose calculations are presented for the cases investigated, including those for inside the plume.

1.2.7 Full-scale site-specific measurements of wind and gamma ray dose rate

[1.2.7.1] Two gamma detectors were installed proximal to the EW building air intake at the STH site downwind in the most significant plume direction for radiation doses to persons on EW roof and inside the EW building. These were sensitive proportional gamma counter detectors for environmental measurements (range down to 30nSv h^{-1} ; i.e. background levels) suitable for detection of the gamma ray emissions from positron annihilation gammas (511 keV). They are connected to a time logging monitoring program (MEVIS, Berthold, UK) which enables a display, at one-minute intervals, of all releases during the day and these are recorded in a csv database file that can be analysed. This data was coupled with the stack release data showing the activity released during the day at intervals of one minute. In this way the measured gamma dose at detector #1 and #2 locations were as recorded during the installation

of the glass cladding layer and canopy. To analyse this data and compare to the expected gamma ray dose from the other measurement methods.

[1.2.7.2] In conjunction with [1.2.7.1], a wind logger was installed on top of the EW top stair tower near the current stack release point. Data obtained at the wind tunnel was used to calculate a wind speed during radiation dose measurements. The data was used to determine the wind direction and short-term fluctuation during each ‘spike’ release event. This provided data to enable the directional dose factor from measured dose rate data which was compared to the calculated values.

[1.2.7.3] Results of the wind logger data, coupled with the gamma dose data from detectors #1 and #2, and given a known release of radionuclide will enable some dynamic characterisation of the plume based on the integral averaged dose rate from the positions of both detectors. The mathematics to extract this information will be developed in which different plume geometry models will be investigated. For example, the plume activity advection velocity can be estimated using wind direction coupled with time difference of peak concentration at the two detectors, and this compared to the wind logger wind velocity. It was proposed that in some cases it may be possible to obtain information about the plume dispersion coefficients σ from the ratio and difference of the integrated detector #1 and #2 signals under each radioactive release ‘peak’ where steady wind direction conditions apply during the spike release event. However, the actual data indicated short term fluctuations in direction that did not permit this analysis. Note: an analysis of the plume catching events will be presented and compared to Monte Carlo calculated values for the mean advection velocity.

1.2.8 Sensitivity analysis for different measurement cases

[1.2.8.1] Investigate the variation of dose with different building configurations: in particular, the variation between isolated single buildings and variations of the full building set, by selectively adding sets of buildings.

[1.2.8.2] Investigate the variations of results resulting from small changes in the measurement conditions i.e. small variations in directions of approach flow.

1.2.9 Practical Application of Methodology

[1.2.9.1] Develop a methodology to use the data set and results provide estimates of concentration field values in the roof zone and main recirculation zone of the buildings to enable dose calculations to be performed for a wider set of problems.

1.3 Discussion

Near surface, near-field continuous release tracer concentration measurements using low height passive stack emissions, were performed in several measurement planes to investigate near-field effects on plumes close to the release building. Active vertical cases were measured in some instances.

The proposed work is based on the results of experimental wind tunnel modelling, with analysis of relevant theory in order to refine and develop models relating radiation exposure of persons exposed by radioactive plume releases. Gamma detector measurements supplement this experimental data and allow comparison, adaptation and validation of the wind tunnel studies.

An improvement of the simple Gaussian model for most probable estimates in the near field region of less than 100m from the plume release point is postulated, as well as a better characterisation of errors in the models used to produce the radiation dose estimates. The results of the work and the methodology adopted should prove valuable for situations where estimates of radiation dose were required in a near field region to a plume release, such as a roof of a building or to persons via inhalation via an air intake into a building.

1.4 Thesis structure

A review of relevant literature is given in Chapter 2, covering both building affected flow and dispersion and radiation dose evaluation. Experimental methods are described in Chapter 3 and approaches to plume radiation modelling in Chapter 4 and associated published papers reproduced in Appendices 15.5 and 15.6. Chapter 5 describes velocity field measurements taken to characterize the flow conditions affecting the dispersing plumes. The observations are related back to the description of flow fields around buildings in Chapter 2. Chapter 6 presents the concentration field measurements and their description in terms of Gaussian plume models. Empirical models are developed that will be subsequently used to evaluate radiation dose. The data presented is substantial, reflecting the number of parameters that play a role in whole process. Chapter 6 treats continuous emissions, whilst Chapter 7 treats short-duration emissions. Chapters 8 and 9 present the Monte Carlo methods developed for dose modelling (Chapter 8) and its application (Chapter 9). Extensive output is presented, reflecting the range of data presented in Chapter 6, and allowing interpolation to cases not presented here. Field measurements of gamma ray dose on the roof of the East Wing at St Thomas' Hospital are analysed in Chapter 10. Chapter 11 describes a sensitivity analysis. Recommended methods for practical applications are set out in Chapter 12, followed by conclusions of the whole body of work in Chapter 13 and ideas for further work and developments.

CHAPTER 2: LITERATURE REVIEW

2.1 Introduction: literature review

The following review of the literature indicates that there is a considerable gap in knowledge related to near-field concentration dispersion in the vicinity of buildings and the radiation dose to persons from the release of radioactive pollutants in this very near-field region. This thesis tackles modelling of plumes in the near-field region above buildings, close to the source of pollutant, using Gaussian plume models and uses the results obtained from dispersion modelling to evaluate the radiation dose to persons in the very near-field of radioactive pollutant releases.

A review of the available literature is presented in this chapter to show the state of knowledge with respect to the research questions posed in chapter 1. The literature available with respect to dispersion around buildings has been reviewed and shown in section 2.2 and associated sub-sections. Section 2.3 of this chapter covers available knowledge on radiation dose modelling from radioactive plumes, and methods used to evaluate radiation dose from exposure to radioactive gases. Very little of this available information relates to the topic of radiation doses to persons in the near-field from plumes emitted from a building. Citations are given in section 2.4 to the two papers reproduced in Appendices 15.5 and 15.6 of this thesis which address some of the initial research questions set out in chapter 1 of this thesis. A further literature review was carried out in 2021, to assess progression of related literature to the research questions and is shown in section 2.5, where further discussion is given.

The topic of the dispersion of radioactive materials by gaseous emissions has undergone considerable development in the scientific literature since the advent of nuclear reactor technology. The consequences of a nuclear accident were experienced first in the UK with the Windscale fire of October 1957 (Crick and Linsley, 1982, 1983) where a significant amount of ^{131}I was released over the UK and Northern Europe, giving rise to a population radiation dose. The population dose as a result of this incident was reduced by countermeasures that included the restriction of consumption of milk contaminated by surface deposition of radioactive material. A more detailed reappraisal of the releases was provided in Garland and Wakeford (2007), who showed that reviews using modern meteorological methods to estimate plume dispersal, compared to available environmental data from the time, enabled the releases of radionuclides in the accident to be estimated to within a factor of two.

The current regulatory scheme for radioactive releases in the UK requires radiological assessments to be performed appropriate to the dose likely to be received by the public (EA, 2012). In particular, where the dose is likely to exceed the level of no regulatory concern ($10\mu\text{Sv}$ per year) the assessment should be ‘more realistic’. A public dose level potentially greater than $20\mu\text{Sv}$ per year exceeds the threshold of ‘optimisation’ and requires an even more detailed and accurate assessment. In the current work the dose levels were indeed above this level and therefore a detailed assessment was required for regulatory purposes.

The radioactive gases under consideration in this study consisted of positron emitting radionuclides in various chemical forms. The radiochemistry production facility involved the production of these radionuclides with a cyclotron using proton or deuteron bombardment of generally light elements to produce proton-rich nuclei likely to undergo positron emission. Target radionuclide atoms then underwent a radiochemical labelling process to produce tracers for use in Positron Emission Tomography (PET) scanning of patients. One of the most commonly used PET radioactive tracers is ^{18}F -Fluorodeoxyglucose (FDG) produced by proton

bombardment in the reaction $^{18}\text{O}(\text{p},\text{n})^{18}\text{F}$. Releases from the production of this radiotracer have been documented by Kleck *et al* (1991) who monitored gaseous emissions over 40 production runs at a facility in California and correlated the release peaks in the stack monitor with eight different parts of the radiochemical production process. Two peaks were commonly encountered, the first during the glucose precursor phase part 3 and then during part 4, the addition of ethyl and column evaporation of reaction products. Other phases showed an increasing signal due to plating out of the effluent onto the stack detector. Gaseous releases of 2.7% of produced tracer were reported. Given the relatively short half-life of ^{18}F (109 minutes) significant levels of production are necessary to ensure that enough material is produced to enable sequential scanning of patients through the working day at a clinical centre. In this way unabated emissions of the order of a few GBq daily were possible at a busy production facility. Dilution factors were established by Kleck *et al* (1991) to assess compliance to the regulatory standards in the US, which showed the breathing of the effluent gases, where even for four modest production runs per week of yield 15.9GBq, would lead to what would currently be considered significant occupational exposure in the UK (2.3mSv per annum). Dilution factors were required in order to achieve US regulatory standards on the site perimeter for members of the public and an effluent release stack connected to the radiochemistry facility fume hood was required to obtain the necessary dilution at this location.

A further assessment of radiological discharges from a PET facility, and abatement measures to reduce discharges to the environment was presented by Calandrino *et al* (2007) for a site in Italy. A simple conical shape model was employed to calculate the gamma dose rate and inhalation dose to a member of the public at 150m from the discharge point of the facility. Monthly releases of ^{11}C (8.3GBq) and ^{18}F (2.8GBq) resulted in doses of 41.2 and 9.4 μSv per year respectively from the emissions. The assessment indicated that abatement measures were required in order to reduce emissions and hence public doses from those emissions.

The short half-lives of the radioactive tracers implies that environmental effects are concentrated close to emission points, typically on-site and in the near environment. In turn, this implies that dispersion is dominated by conditions in the flow around and close to buildings. This makes the prediction of doses particularly complex and results highly site-specific.

2.2 Flows around buildings: dispersion of pollutants

Atmospheric dispersion results from the interaction of the flow field and emission conditions and for low level emissions, as of interest here, is particularly sensitive to atmospheric stability and the characteristics of the underlying surface. In broad terms, the mean flow transports and turbulence disperses plume material in the atmospheric boundary layer, processes that are modified by plume rise and related source term effects. Both the intensity and scale of turbulence are important - the former determines the rate of spread and the latter the decrease in spread rate with travel distance (or time). Concentration fluctuations are also governed by flow and emission conditions, particularly important being the ratio of the source size to the turbulence length scales. The flow around buildings includes regions of reversed flow (recirculation regions), mean flow deflections and enhanced turbulence intensities, all of which affect dispersion behaviour near and downstream from buildings. The classical dispersion picture is thus broken and replaced by something that is much more complex and difficult to predict.

The basic formulation of the dispersion of pollutants problem is detailed by Pasquill (1974) who derives the concentration from a point source for ground level and elevated sources and

describes the features of the standard Gaussian Plume Model (GPM). The A-F formulation of atmospheric stability is presented, along with procedures allowing determination of the stability class (or stability parameter, P), adjustment to the actual stability class of the vertical dispersion coefficient, and a modifier for ground roughness.

Flow and turbulent diffusion around buildings has been discussed in Meroney (1982) who noted that in the vicinity of buildings the flow field is complex, and that buildings disperse effluent in a complicated manner related to source configuration and building geometry. In that work the areas discussed included isolated and collections of buildings, transport pollution in urban street canyons and cases of dense or cold gas plumes. Cases where a cube is inclined at 0° and 45° to oncoming flow were considered for the isolated building case and are shown in Figures 2.1 and 2.2 respectively. This thesis adds to this by covering the intermediate angle case of 22.5° which was an important wind direction for the building cases considered in this thesis. From Figure 2.1 separation zones are seen with reattachment on the on the roof and sides. A strong horseshoe vortex will be expected around the cube case, with reverse flow back into the recirculation zone shown as the cavity zone in the figure.

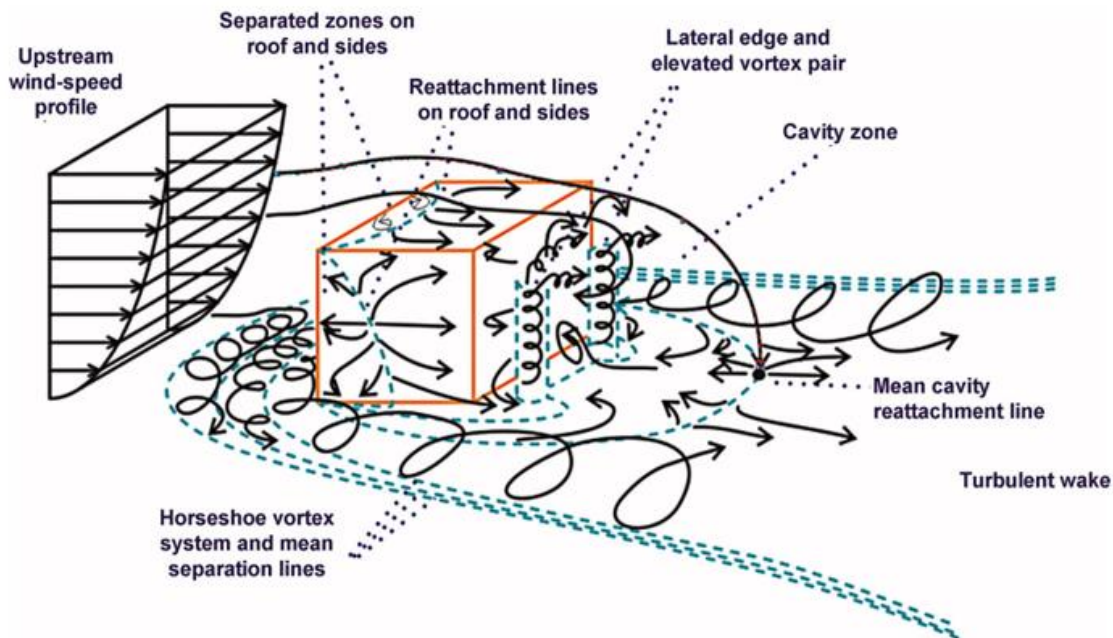


Figure 2.1 Flow field for a rectangular building at normal incidence. From Hosker (1984) and modified by Blocken et al (2011)

From Figure 5.2 the cube angulated case at 45° is shown from Hosker (1984). Strong rooftop vortices can be seen forming over the roof into a roof vortex system, and a strong horseshoe wider vortex can be seen propagating from the sides of the cube. Recirculation into the main recirculation zone can be seen from the sides and the top. Further information is given in Figure 5.4 and this thesis provides an investigation into the intermediate 22.5° angle case between 0° and 45° for the cube. Information is also provided in this thesis on the flow field for the specific East Wing building cases which were also investigated, which were at an angle to flow equivalent to 22.5° , and these may be compared to the 22.5° results for the cube.

From Meroney (1982) very approximate estimates of dimensionless concentration were presented for the isolated building case and an isolated group of buildings in otherwise level terrain. The discussion on urban flows concluded that pollutant concentration values in the street of the traffic were highest when the wind direction was perpendicular to the line of traffic.

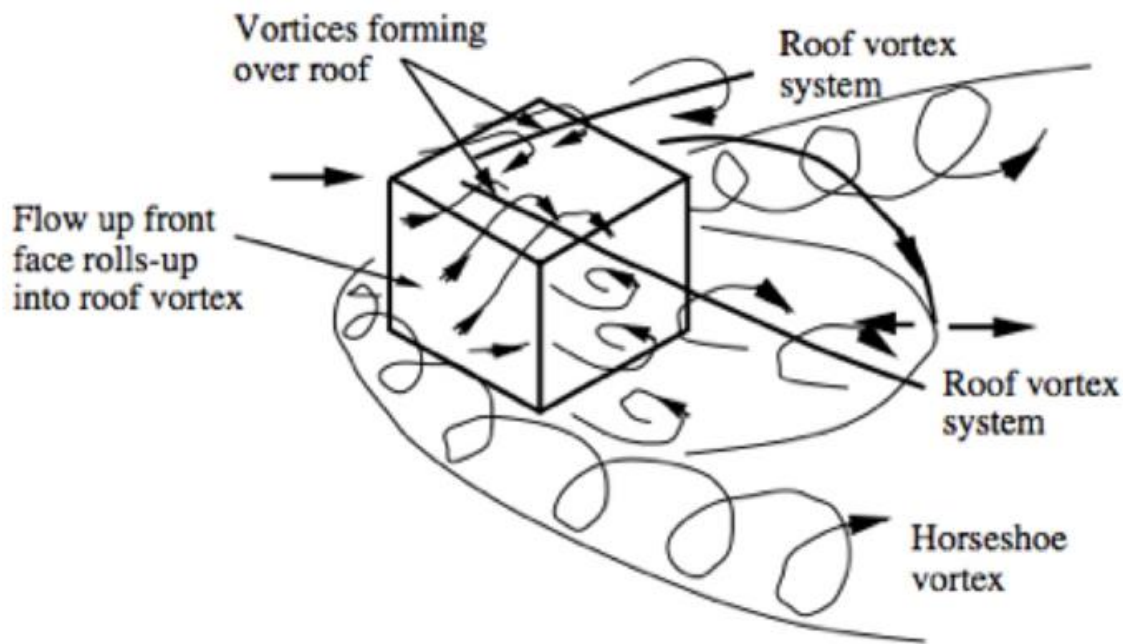


Figure 5.2 Flow features for cube at 45° to approach flow from Hosker (1984)

In a review of flow and dispersion of pollutants in urban areas, Britter and Hanna (2003) considered four scales: regional, city, neighbourhood and street. It was noted that large buildings affecting fluid motion, and heating in the city scale, has the effect of increasing the mixing layer depth for pollutants. Dispersion of pollutants was enhanced in cities by the two factors of heat emissions, causing increased thermal turbulence, and mechanical turbulence increased by large obstacles. Turbulent velocity components in the urban canopy were found to be approximately constant when expressed as a ratio to the friction velocity, which was itself greater due to the friction caused by large buildings, thus showing that enhanced turbulent velocities were expected in urban areas. The effect of reduced pollutant concentrations, due to the greater dissipation from enhanced turbulence, was set against the effect of increased concentrations due to a reduced advection velocity within the urban canopy. The interactions between these effects was noted to be complex, with the ground level concentrations initially reducing with increasing roughness length to a minimum value, but again increasing with increasing ground roughness to possibly greater values than encountered in the unobstructed flow situation.

Fackrell and Robins (1982), investigated ground level (GL) and elevated sources (ES) in a series of wind tunnel experiments looking at the fluctuation of concentration values. A passive, non-buoyant release into the flow was used in order to reduce the complicating effects of plume upward buoyancy and momentum. Measurements were carried out with a flame ionisation detector to sample the tracer gas used. The variance, intermittency (probability of plume material being present), peak values, and probability density function of the concentration measurements were investigated. The characteristics of the background flow were also fully determined. At full scale, experimental times investigated were equivalent to some tens of minutes to an hour. Results showed that vertical dispersion was greater from an ES than from a GL source. Concentration fluctuations were generally greater from the ES, and increased markedly with a reduction in source diameter, reducing with distance from source. In other words, the fluctuations increased rapidly with fetch from the source (where they were zero), reach a maximum that depended on source size (and elevation) and thereafter decayed, though

the effect of source size persisted for some distance downwind. The pdf generally followed an exponential form, with a delta function at zero concentration that reflected plume intermittency. For receptors close to the ground a greater proportion of sampled concentration values are closer to the mean, and a Gaussian form was observed. The overall findings of the paper were that there were differences in concentration fluctuation characteristics dependent on whether the source was elevated or at ground level, and that close to the release point the source dimensions relative to the turbulence scales affect the fluctuations to a large extent.

Robins and MacDonald reviewed flow and dispersion near buildings in NRPB R-322(2001). Different models were compared such as that from R-91(Clarke *et al*, 1979) which employs a virtual source further from the building to simulate the plume broadening effects of a building. ADMS modelling is also described and is described more fully in section 2.2.2 below.

Hort and Robins (2002) showed that the dispersion of pollutants in the vicinity of cylindrical and cuboid buildings was affected by the wind orientation and building shape to a significant extent. The cube at 45° to flow is believed to generate roof top vortices which entrain more material into the building wake. A similar effect was apparent with the cylindrical structures.

2.2.1 ASHRAE models section

ASHRAE have produced models for stack height design (2007,2011) that can be used to calculate plume concentrations based on different building sizes and stack heights. In the earlier of the publications (2007) there are two general approaches presented to determining the minimum required stack height for a pollutant release on a building. The first is a geometrical method where the plume broadens on a 1:5 gradient to the horizontal. The size and length of the building recirculation zone is determined by some empirical equations related to the building effective cross-sectional size. Three regions are described: Z_1 the roof top recirculation zone; Z_2 the zone on top of the building where there is a high degree of building turbulence, and Z_3 the extent of the boundary to the flow above Z_2 . The gradient of Z_2 is taken as 1:10 to the horizontal. The stack height is taken as the line of projection at gradient 1:5 which just avoids the recirculation zones present. The final adjustment to stack height allows for plume rise and downwash affects, although buoyancy is treated as a safety margin. The second method presented by ASHRAE(2007) is based on a Gaussian plume dispersion model, which gives worst-case roof level dispersion. The dilution is dependent on wind speed to a large extent: (a) for low wind speeds plume upward momentum will tend to reduce roof level concentrations, and (b) at high wind speeds the concentration is reduced by spreading of the pollutant along the direction of travel. There is an intermediate critical wind velocity where the roof top concentration is a maximum, which corresponds to the smallest level of dilution in the model. Equations are given for the dispersion parameters in terms of the initial plume size at the efflux point and in terms of downstream co-ordinate. A short time plume meander factor is incorporated in the model for the horizontal dispersion, which enables lateral dispersion to be calculated for release times down to two minutes. Determination of a stack height is made by a trial-and-error procedure, evaluation of the plume rise and downwash for U_H set at the meteorological 99th percentile wind speed, at which value the plume dispersion parameters and dilution factors are calculated. The dilution is then evaluated at a range of wind speeds to determine the critical speed at which it takes the lowest value. If the critical dilution is too low, the stack height is increased, or conversely if it is too high the stack height is decreased. The stack height required is then obtained by iteration. The Gaussian plume method is stated to apply only when the plume avoids all recirculation zones and roof top structures on its way to the point of interest, such as an intake vent. In cases where the emission is directly entrained

into a recirculation region, a simplified model for intake at the exhaust is presented which would apply for a flush vent.

ASHRAE (2011) updated the methods presented in their previous publication (2007). Plume rise is calculated not only from the ratio of efflux velocity to wind speed, but also takes account of the friction velocity, the surface roughness length and the associated wind velocity height profile. The method also includes an allowance for distance from the receptor point. Plume spread parameters are calculated from turbulence intensities in the x, y and z directions. The turbulence intensities are related to height above rooftop and are incorporated into a term which accounts for the source size. The dilution is calculated according to a Gaussian dispersion model, with the default averaging time set at 15 minutes. This can be modified using a power law formula to assess different averaging times. Dilution is calculated according to the height of the plume above the recirculation zone with an exponent term to allow for the fall of concentration away from the plume centreline. A comparison in the literature between ADMS, ASHRAE and CFD methods is presented in section [2.2.3] in this report.

2.2.2 ADMS plume dispersion basic model

The ADMS computer code for modelling air dispersion has been developed to simulate the spread of pollution in the atmospheric boundary layer of the earth (Carruthers *et al*, 1994). The basic model involves modules to calculate the profiles of wind speed and turbulence in the in the boundary layer, plume rise due to emission momentum and buoyancy, plume spread and concentration levels. The boundary layer structure is based on Monin-Obukhov similarity theory, with the Monin-Obukhov length scale calculated from the friction velocity, u_* , and the heat flux to or from the ground. Further modules treat loss processes (wet and dry deposition), radioactive decay, terrain (hills and coastlines) and buildings effects. Separate dispersion coefficients are applied to model the vertical Gaussian plume above and below the plume centreline. Variations of concentration fluctuations, for short term releases of less than one hour, are accounted for in the model by a function that depends on travel time from the source and turbulence velocities. The ratio of standard deviation of the concentration values to the mean concentration falls with increasing distance and travel time from the source. For time periods of release in excess of one hour, hourly averages are calculated and compared statistically. Gamma dose from the plume is modelled from the mean concentration field and evaluated only at the ground plane.

The ADMS building effects module, BUILD, is described in some detail in Robins *et al* (1997). BUILD divides the flow field in the region of a single building into a number of zones. The recirculation zone in the near-wake is described by an ellipsoidal upper boundary with sides parallel to the oncoming flow. A flux balance relation based on a well-mixed approximation in the near wake and an entrainment velocity on the boundary is used to derive the dimensionless wake time and length scales, leading to a prediction for the mean concentration in the near-wake. Downwind, a dual plume model is used to represent dispersion in the main wake of the building. A ground level, upwind source is used to model the entrained fraction from the wake, and the remaining, un-entrained component is accounted for by a source at the release stack, but with plume adjusted as the motion proceeds downwind. The combined concentration field from the two sources models the downstream concentration. The presence of the plume centreline in one of four zones in the wake cross-section is used to determine the appropriate Gaussian dispersion coefficients. Main building wake and external regions of flow are also described. The dimensions of the near wake are determined using empirical functions derived from extensive wind tunnel studies. The building to be modelled is replaced with a cuboid at

the appropriate angle to the oncoming flow. Plume dispersion parameters for the main wake region are adjusted to account for the velocity deficit and turbulence excesses experienced there, both of which decay with fetch downwind. Conventional boundary layer dispersion is recovered in the far-field.

In the same paper, Robins *et al* (1997) validated the ADMS code against wind tunnel and field experiments. Data from a series of experiments with a cube showed that ADMS presented concentration values within a factor of two, except for stack height close to building height for the 45° flow orientation, where the agreement was somewhat worse. In another experiment an L-shaped low-lying building was modelled, showing agreement in concentration field values of a factor of two to three. In the last series of measurements the Hinkley point reactor site was modelled with ADMS against combined wind tunnel and field study data. Dimensionless concentration normalised for release rate from ADMS were somewhat lower in this case by a factor of two further from the source and higher by the same margin at closer distances.

The development of the ADMS building effects module is covered in greater detail by Robins and McHugh (2001). In this paper it is assessed against a number of other studies in terms of ground level plume centreline concentrations for seven experiments in the literature. Near-wake and main-wake results are compared separately. There is a tendency to over-predict near-wake concentrations and under-predict main wake concentrations. Conclusions were that the sensitivity to the mixing of the concentration field in the near wake could be explored with the use of a group of buildings, or a building of complex shape. The presence of buildings could be explored with an alternative building shape. The separation of the plume axis to the boundary of the recirculation zone is an important parameter, as is also the orientation with respect to the wind direction which affects building induced downwash. ADMS assumes a well-mixed region and it was noted that data on the detailed structure of the near-wake recirculation zone was limited, especially for field studies that tended to measure averaged quantities. ADMS uses a mean streamline deflection algorithm to model the flows around a cuboid and it was recommended that further examination of the near-wake streamline deflections for buildings of different shapes and orientations was required. In conclusion, a factor of three accuracy would be expected for concentration levels around a single isolated large building, with precision downgraded for more complex arrangements.

2.2.3 Dispersion modelling studies

Hajra *et al* (2010) considered pollutant dispersion from rooftop stacks and compared ASHRAE, ADMS and wind tunnel simulations of pollutant concentrations. The pollutants considered were not necessarily radioactive. Four different cases were considered with low-rise and high rise buildings considered, stack heights of 1 to 7m, and exhaust momentum ratios ranging from 1 to 5. The wind direction was considered at 0 and 45° (i.e. normal and diagonal directions) with a neutral stability approach flow. The ASHRAE 2007 scheme was considered in the analysis: this employs a Gaussian dilution term when the effective release height lies above the top of the roof recirculation zone, and dilution for a flush vent model where the plume is entrained into the recirculation zone. Dispersion parameters for the Gaussian plume of σ_y and σ_z were presented in terms of an initial spread, dependent on the stack velocity ratio (SVR) or momentum ratio (M) to the oncoming flow, and a turbulent spread proportional to the downstream distance.

The different dispersion models assessed by Hajra *et al* (2010) showed a significant spread of dilution values. For the high rise building the dilution estimated from wind tunnel and ADMS

was 100 times greater than the ASHRAE 2003 and 2007 models. For the low-rise case and a short stack (1m) the wind tunnel dilution was 10 times greater than ASHRAE for $M=3$. ADMS dilution was greater than wind tunnel by a factor of 2-3. For higher values such as $M=5$, ASHRAE 2003 agreed well with ADMS and wind tunnel whilst by comparison ASHRAE 2007 gave a dilution factor of 10 times higher.

For the low rise building at 45° to flow, ADMS compared well to wind tunnel for downwind distances of greater than 15m for stack height 1m and $M=3$, but well for all distances for $M=5$. This may indicate that ADMS models conditions better when the plume is further away from the roof, but is less able to model building generated turbulence, and edge vortices that would affect a lower efflux velocity release with consequently lower plume rise.

For the low-rise buildings there was a greater spread between all of the models used, with factors of 10 times dilution discrepancies being apparent at $M=3$ and $M=5$, for a 1m tall stack. Similar discrepancies were apparent for the tall building at $M=1$ between all models. In summary considerable differences exist between the models for concentration values in the near field of the release: the paper recommended a reassessment of the formulation of the ASHRAE models used in these conditions. For radioactive releases the concentration field values would have a significant effect on the immersion dose from inhalation, beta skin dose and would also affect the gamma shine dose from the plume. All of the conditions studied related to a steady-state release of pollutant.

In a follow up paper by the same group Chavez *et al* (2011) investigated Computational Fluid Dynamics (CFD) models versus wind tunnel measurements, paying particular attention to the role of the turbulent flow Schmidt number (Sc_t). This is defined as the ratio of the eddy viscosity to the eddy diffusivity - the ratio of the turbulent momentum transfer and turbulent eddy diffusion coefficients.

ASHRAE 2007 was also included in the analysis for comparison purposes. CFD has been widely employed for isolated buildings but in this study upwind and downwind buildings were also considered. Sc_t is affected by height within the atmospheric boundary layer but has little dependence on atmospheric stability; values of 0.1, 0.3 and 0.7 were considered, 0.7 being conventional. Results for the low-rise isolated building wind tunnel (WT) $M=1$ agreed well with CFD when $Sc_t=0.3$ was selected. For the conventional value of 0.7, CFD gave a dilution of the order of 10 times less than WT. ASHRAE 2007 gave a dilution factor of ten times less than the latter figure. For $M=3$ and the same building set-up CFD agreed well with WT for $Sc_t=0.1$. Higher values of this parameter yielded dilutions of the order of 10 – 100 times less, as did ASHRAE 2007. Reformulation of ASHRAE 2007 was again recommended in this study. It was clear from this study that CFD results were sensitive to the selection of the turbulent Schmidt parameter and that variation of the order of a factor of ten was apparent, which could be a significant margin for the design of a building stack or of compliance to a regulatory standard.

For the building upwind of the source, differences between WT and CFD were less apparent with variation in Sc_t , being generally of the order of a factor of ten spread for $M=1$. ASHRAE 2007 gave a dilution lower by a factor of approximately 100, again questioning its suitability.

With the buildings both upwind and downwind, and the source building in the middle, the value of Sc_t was again of less importance, and WT and CFD agreed within a factor of ten dilution

over a range of distances. The spread of results between CFD and WT was reduced somewhat for the higher $M=3$. The pattern for ASHRAE was unchanged from the previous case.

In a follow up paper to the Hajra (2010) and Chavez (2011) studies Hajra *et al* (2012) presented a work on WT simulations of the effect of downstream buildings on the near-field pollutant dispersion from rooftop stacks. The ASHRAE 2011 formulation was considered in addition to the earlier 2007 formulation. In all cases the emitter building was a long low-rise building. The downstream building was a selection of low and high buildings, all of them being taller than the emitter building. In summary, a spread between the experimental results of a dilution factor of up to 100 was encountered. Generally, a taller downstream building significantly increases pollutant concentration i.e. results in reduced dilution. A taller stack and greater M value appears to be less effective at reducing downstream concentrations with the presence of a taller downstream building, thus emphasising the need to account for adjacent buildings in order to obtain an accurate determination of pollutant concentration.

Further work by Hajra *et al* (2013) investigated WT dispersion from roof top emissions with adjacent buildings in the near-field. Upwind and downwind buildings were considered. The spread of results was similar to that reported in the previous studies. For taller upstream and downstream buildings compared to the middle (emitter) building, elevated pollutant levels were experienced on the leeward wall of the upper building, roof of emitter building and windward wall of the downstream building. For an upstream building of similar height only the roof of the emitter building and windward wall of the downstream building experienced higher pollutant concentrations compared to the taller upwind building case.

The ASHRAE models were again considered in Hajra *et al* (2014). It was found that ASHRAE were generally conservative i.e. lower dilution compared to WT, though the results of the latter 2011 formulation were in better agreement with the WT results. The inability of ASHRAE to model upstream building effects was demonstrated. It was also found that, although improved, it was found that ASHRAE 2011 did not model greater M releases well.

It is hard to draw any firm conclusions from this work as the dispersion data used was too sparse, and not supported by detailed flow measurements, to enable a detailed investigation. Furthermore, no functional dependence of Sc_t on flow or geometrical parameters was discussed or proposed. It could well be argued that the Schmidt number was being used to rectify other errors in the CFD predictions, such as the location of the plume centreline. The data used was too sparse to answer such questions.

In summary, from the series of papers from Hajra *et al* (2010, 2012, 2013) and Chavez *et al* (2011) showed that dispersion is significantly affected by the presence of surrounding buildings, which leads to extreme difficulties in short range modelling of atmospheric pollutants.

Xie and Castro (2009) considered the problem of Large Eddy Simulation (LES) techniques in urban streets at the DAPPLE (<http://www.DAPPLE.org.uk>) study site in central London. Resolution values were down to 1m and 1s in the domain tested, of dimensions 1.2, 0.8 and 0.2km in the streamwise, lateral and height directions respectively. It was found that there was reasonable agreement with the experimental data for the location, and the resolution at full scale yielded accurate prediction of the mean dispersion and flow characteristics. A reasonable prediction of concentration fluctuations was found. However, it was also found that mean

concentration, and concentration fluctuations in the near field, were highly dependent on the local geometry and source location; whereas in the far field (>100m) they were not.

A further series of papers by Nakayama *et al* (2009, 2011, 2013, 2014) cover development of a local scale high resolution atmospheric dispersion model using LES CFD techniques. In Part 1(2009) a detailed comparison was made against the experimental wind tunnel experiments of Fackrell and Robins(1982). It was found that LES/CFD computations showed good agreement with the experimental results in terms of the vertical velocity profile, turbulence intensities (in all three directions) and the Reynold's shear stress. Measured values of the downstream concentration normalised for release rate also agreed well with the experiment. The data from wind tunnel was the natural standard with which to compare the computational results.

In Part 2, Nakayama *et al* (2011) investigated plume dispersion around a cubical building. The addition of extra roughness elements into the flow was used, meaning that a direct comparison against Fackrell and Robins (1982) was not possible. The authors claimed that the model captured the basic flow and dispersion well with respect to the wind tunnel, but it could be argued that the sample grid for computation was not capturing the local high concentration values that were measured in the wind tunnel. The presence of building generated turbulence near the cube was shown, and the concentration fluctuation measurements were characterised by different probability density functions for different regions.

In Part 3, Nakayama *et al* (2013) investigated building arrays with LES computation. Three cube block spacing regimens were investigated. For the smallest spacing, in which interference effects were most evident, the root mean square (RMS) concentration fluctuations were less with LES than for wind tunnel (WT). This might well have been a result of the limitation of spacing on the grid mesh size, a limitation imposed by the computational effort required for even finer spacing. For wider building spacing the agreement between LES and WT was better. The LES model showed lower concentrations than WT in the street canyons, but the concentration fluctuations appeared well matched.

In Part 4, Nakayama *et al* (2014) investigated an actual urban area: the Central Business District in Oklahoma City. The agreement on basic flow patterns between WT and LES was good but LES underestimated wind speed and turbulence intensities. This could be due to the coarse grid mesh spacing on the computational grid not adequately modelling local effects, such as high local concentrations. The authors nevertheless claim that accurate concentrations were obtained, even given the relatively coarse grid network. They propose to extend the LES model to include real meteorological conditions in further work.

2.3 Models of pollutant dispersion: radiation dose modelling

2.3.1 National Radiological Protection Board (NRPB) Reports and other literature

The following NRPB reports are relevant to the problem of calculation of the radiation dose from radioactivity in air and the methods they use are described further in this chapter: Report R-91 (Clarke et al, 1979), R-101 (Jones, 1980), R-157 (Jones, 1983), W-63 (MacDonnell, 2004), (Robins AR, MacDonald, R, 1998).

During normal operation of nuclear plants there are releases to environment of radioactive effluent gases, so that an assessment of radiation doses to persons from those releases is necessary to ensure that regulatory levels are not exceeded. Imai and Iijima (1970) looked at

calculated external gamma ray exposure from a Gaussian radioactive plume released from a point source. Such a point source would be considered to approximate an effluent stack from which radioactive emissions were occurring from normal operations. The gamma dose rate from a time-varying concentration field $C(\underline{r}, t)$ can be written as follows.

$$\dot{D}_\gamma(t) = K Y E_\gamma \left(\frac{\mu_a}{\rho} \right) \iiint C(\underline{r}, t) B(\mu |\underline{r} - \underline{r}_p|) \frac{e^{-\mu |\underline{r} - \underline{r}_p|}}{4\pi |\underline{r} - \underline{r}_p|^2} dv$$

K is a constant that converts absorbed energy to radiation dose and can be expressed as $1.6 \times 10^{-13} \text{ Gy kg MeV}^{-1}$. Y is the photon yield per nuclear disintegration, numerically close to two due to the pair of gamma photons produced in a positron annihilation event. E_γ is the photon energy in MeV (0.511 MeV in this case), and $\frac{\mu_a}{\rho}$ is the mass energy absorption coefficient for air ($\text{m}^2 \text{ kg}^{-1}$). A further correction is applied to convert the air kerma given by the expression above into effective dose (Appendix 15.6). B is a dimensionless build-up factor in air further described in Appendix 15.6. The vectors \underline{r} and \underline{r}_p are respectively to the cloud point source and to the dose receptor point, respectively. The linear attenuation coefficient in air is denoted by μ (m^{-1}). The triple integral covers integration of the source term over all space. The distance from the source element to the receptor point p can be expressed as follows.

$$|\underline{r} - \underline{r}_p|^2 = (x - x_p)^2 + (y - y_p)^2 + (z - z_p)^2$$

The dispersion was an idealised Gaussian Plume Model (GPM) with no building effects. The GPM basic time averaged equation for a constant release rate that describes dispersion at a downwind co-ordinate was defined in terms of the wind speed, release rate, and dispersion parameters in the vertical and cross wind directions, z and y , respectively.

$$C(\underline{r}) = \frac{Q}{2\pi U_H \sigma_y \sigma_z} e^{-\frac{1}{2} \left\{ \frac{(y - y_0)^2}{\sigma_y^2} + \frac{(z - z_{RH})^2}{\sigma_z^2} \right\}}$$

The dispersion parameters of the Gaussian cloud σ_y and σ_z were varied according to atmospheric stability (Pasquill categories A-F), with dose calculations actually carried out for A (extremely unstable), D (neutral) and F (moderately stable). In the above equation the wind speed at the building height is denoted by U_H , Q is the release rate and C is the concentration at position vector \underline{r} . Results showed that the downwind external gamma-ray exposure on axis of flow increased gradually towards a maximum downwind of the release point, the maximum moving downstream as the source became more elevated. The maximum gamma dose rate was in all cases at a point upstream of the maximum concentration point. Doses from inhalation and ingestion of the radionuclide were not considered, and the photon energy chosen was 1 MeV. Crosswind axis results showed that the dose fall off (with y , the crosswind co-ordinate) was more gradual than concentration, and this was more evidently the case when atmospheric conditions were unstable or with a more elevated release, due to the effect of gamma ray dose at a distance. The analysis showed that the maximum ground level dose rate point varied as $H^{1.2}$, where H was the release height, under any conditions of stability. The corresponding maximum ground level concentration varied between $H^{-1.8}$ (stability class A) and $H^{-2.3}$ (stable, class F). A complete 'submersion' model was considered based on the ground level concentration. The submersion model was found to overestimate the external dose at low release heights close to the release, but underestimate that for high level releases.

A major development in the topic of radiological assessments from gaseous emissions came with NRPB Report R-91 (Clarke *et al*, 1979). The calculations assume a free release into an undisturbed flow: i.e. with the absence of buildings. In NRPB R-91 only air concentrations were considered, there being no attempt to convert these into a radiation dose metric, such as effective dose.

In this model the basic formulation of the Gaussian Plume Model is extended to cover an additional series of reflections inside the mixing layer for different heights of the atmospheric boundary layer. The reflections from ground were considered to have equal vertical dispersion coefficients to that of the source plume, thus becoming a virtual source below ground level. Allowance is made in the scheme for reflections from temperature inversions in the lower levels in the atmosphere, an inversion being an increase in temperature against the normal temperature lapse rate with altitude. The top of the mixing height would be in this case the inversion layer height. Plume reflections become virtual sources above the mixing layer height. Multiple reflections from ground and aloft were considered in the scheme, the summation of the Gaussian plume concentrations taken to approximate the real-world conditions. Where σ_z became greater than the depth of the boundary layer, uniform mixing with height was assumed up to that level. Horizontal wind speed was calculated using a power law with an exponent related to ground roughness length, z_0 . The ground roughness length for different conditions such as open parkland, cities etc. was chosen as appropriate to the conditions. Sector averaging of concentrations over an angle of 30° was considered, based on available Met Office data. Longer term average doses were based on a probability weighted function of atmospheric conditions within a given sector.

The Pasquill atmospheric stability definitions were replaced by a more sophisticated scheme, taking into account upward heat flux from the ground based on incoming solar radiation with month and time of day, and cloud amounts. Given the incoming heat flux and wind speed, the atmospheric stability parameter is determined by a nomogram in terms of a parameter, P, which can be related to the conventional A-F, extended to G, Pasquill categories. The boundary layer depth is given by another nomogram, which given the local time, approximate date, cloud amount and wind speed, enables an estimate of boundary layer depth to be made. The vertical dispersion parameter, σ_z , is first estimated based upon neutral stability and then ground roughness length of $z_0=0.1\text{m}$, and then adjusted for atmospheric stability and ground roughness length by a series of multiplying factors. The horizontal dispersion parameter, σ_y , was expressed in terms of a '3 minute' short-term diffusion term plus a term that takes into account wind direction variations, expressed in terms of the wind velocity, release time and downwind distance, x.

From NRPB R-91 (Clarke *et al*, 1979) the temporal variation of signal levels of pollutant compared to ensemble averages showed a variation of between 0-3 times the mean, with the majority of signal being detected at null concentration. Interestingly, for conditions determined by mechanical turbulence e.g. elevated plume close to a building in the flow, or at ground level, the dispersion of results about the ensemble mean were shown to be much more central i.e. with a reduced peak-mean ratio and smaller number of null signal readings. This aspect was proposed to be subject to further investigation. Time integrated air concentration values per unit release are presented for different stability categories and release heights.

The period over which the release occurs is a significant factor in the lateral or crosswind dispersion parameter σ_y . For short releases, of less than one hour, the '3 minute' or microscale turbulence term σ_{yt} becomes significant and is itself a function of atmospheric stability as

detailed in Moore (1975). The value of the lateral dispersion depends on plume meander and was determined from empirical measurements in the South East of the UK (Moore,1975). The microscale turbulence is affected by the turbulence produced by thermal convection but also by mechanical stirring as the air passes over the earth's surface. The overall effect is offset by the effect wind shear at greater height with plume progression: the net effect is to lead to a realistic model where the combined effects lead to a linear increase of crosswind dispersion parameter with distance (Moore,1975).

Short term releases were considered to be of 30 minutes duration in NRPB Report R-91 (Clarke *et al*, 1979). Correction factors were applied for longer duration releases to allow for the greater temporal spread of wind directions over a longer release. In the present study continuous and very short releases over the timescale of a few minutes (relative to the full scale case) will be considered. Experimental data indicates that the cross wind dispersion coefficient is only weakly dependent upon the wind velocity so that the plume dispersion can be modelled at different scales and with different flow velocities in a wind tunnel (WT) experiment without undue error.

A whole series of reports were generated by the Atmospheric Dispersion Modelling Working Group (ADMWG), a subsequent report being the NRPB ESCLOUD model (Jones, 1980) - a computer program to estimate doses from gaseous releases, and dry and wet deposition of radionuclides onto surfaces. The formulation used a standard point dose kernel formulation, the same as Imai and Iijima (1970). The external gamma dose rate build-up factor, taking account of dose rate from secondary scattered photons reaching the receptor point as well as primary photons from the source, was the more sophisticated one originally formulated by Berger (Raza and Avila, 2005). The GPM was essentially the same that in R-91 (Clarke *et al*, 1979) with different options available for the dispersion scheme chosen. The formulation made no allowance for the presence of buildings and essentially enabled the models presented in R-91 to be used to calculate external dose rates from gaseous plumes and ground deposition of radionuclides.

Following the previous developments the ADMWG produced report R-157 (Jones, 1983). The report extended the approach of R-91 to cover coastal sites, plume rise and the dispersion in the presence of buildings, as well as guidance on the values to be used for deposition velocity and wash-out coefficients for plume material. In the analysis various scenarios were considered in terms of the source in relation to a building. Two main methods were presented. The first was for sources on or just above the roof or in the near wake recirculation region. This presented a normalised dimensionless concentration value proportional to a dimensionless residence time divided by a dimensionless wake length scale. Both of these last two quantities were expressed in terms of the actual wake residence time, building height, wind speed and actual wake length. Empirical equations gave the dimensionless time and wake length quantities. From the dimensionless concentration the actual concentration in the wake could be calculated. Robins and MacDonald (2001) noted that for point sources inside the near-wake the uniform mixing assumption was a poor one, and in these cases more sophisticated modelling e.g. wind tunnel simulation would be more appropriate.

The second model presented in R-157(Jones, 1983) used a back projected virtual source. The y and z dispersion parameters were set to be a third of the building width and height respectively. The dispersion coefficients were then taken to follow the plume broadening profiles for an undisturbed flow i.e. were projected back towards a virtual source point, that was different for the y and z plume axes. Given the virtual source positions the standard GPM

was then applied to determine the concentration values with (x,y,z) co-ordinates. The effective release height was taken to be a third of the height of the building. The limitations of the model were that only the concentrations in the main wake region are given. The two models may be interpolated in the downstream wake region between the edge of the near-wake and 3-5 building heights downstream where the main wake model would apply.

Both of the models presented in NRPB R-157(Jones, 1983) for use near buildings only apply where the entrainment fraction from the source is large. It was reported that the entrainment fraction in the wake reduced as the stack height was increased. Conversely, the near wake model was very pessimistic if only a small part of the material was entrained (Robins and MacDonald, 2001). In this case a more accurate model may be warranted. The report did not consider sources close to a building to be accurately modelled by either of these methods. The ADMS building model essentially uses the formulation developed from R-157 as detailed in Robins and MacDonald (2001).

The effect of building turbulence on the concentrations of pollutant dispersed was noted to be significant in R-157. Further details were given in Robins and MacDonald (2001) covering dispersion near groups of buildings. It was shown that trailing roof-edge vortices were noted to persist at long distance downwind: for a cube at significant incidence to the oncoming flow elevated ground level concentrations were measured at twenty building heights downstream, for release heights up to twice the building height. It was reported that for continuous short term releases (of less than one hour) close to the building, the effects of source location, wind direction and building geometry dominate over effects of atmospheric stability as far as concentrations close to the building are concerned.

One of the primary references for ‘small users’ carrying out radiological assessments is NRPB Report W63 (MacDonnell, 2004). Methods were presented for basic assessments using the techniques presented in R-91, R-157 and R-322 and other NRPB publications. Fixed wind direction concentration-distance curves per unit release rate are given for atmospheric stability classes A-F in accordance with methods given in report R-91(Clarke *et al*, 1979). Aspects of the radiological dispersions are presented covering the source release term, modelling of dispersion and evaluation of dose to the individual. Dose constraint values for members of the public were stated as 300 μ Sv per year, along with the guidance that above 20 μ Sv per year a more refined assessment was required. Simplified methods for dose from inhalation and beta cloud immersion were given. A semi-infinite cloud model was used to estimate the gamma dose from exposure to the radioactive plume. The near-wake building concentration model from R-157(Jones, 1983) was also presented.

2.3.2 ADMS Radiation dose modelling of radioactive plumes

The method ADMS uses to calculate the gamma dose rate is detailed in CERC(2012a). Radiation doses from inhaled radioactive materials and from surface deposited materials are calculated separately. For the calculation a point dose kernel with a Berger build-up factor (Raza and Avila, 2005) was used to estimate the photon flux, which was then converted into dose in tissue, and this latter figure corrected into effective dose by an energy dependent conversion factor. Gauss-Legendre (GL) integration was used to estimate the gamma dose rate at each receptor point selected in the ground plane. The cumulative dose was obtained by summation over the running time of the model selected. The calculation makes some concessions to computational time required to run the model. For a narrow elevated plume a line source approximation is employed. The semi-infinite cloud approximation applies when

the cloud is large enough compared to the mean free path of the gamma rays and the lateral coordinate is sufficiently small that the receptor is not situated towards the lateral extent of the plume. In other cases GL integration is performed with $N=15$ points. A question arises as to the applicability of the model where the receptor is at an elevated position in relation to the ground plane, and the line source approximation may not be satisfied. Also for conditions in the near field of the plume the sampling grid ($N=15$) may not adequately sample the concentration field in order to achieve a sufficiently accurate estimate of the gamma dose rate to persons in close proximity, or inside the active plume. This area warrants some investigation. The validity of the point kernel inverse square calculation for positron emitters, where the positrons have a given range in air before undergoing an annihilation event, would also warrant investigation.

ADMS was used to calculate occupational radiation doses to workers (CERC, 2012b) as part of a radiological assessment for radiation doses to workers in the vicinity of a plume at a site discharging positron emitting gases from a PET radiochemistry facility. Receptor dose points were chosen on top of and around the building from which the emission was occurring. The model was run over 5 years of meteorological data (2007-2011) every day between 07:00-15:00, during the usual period of emissions. The gamma dose rates at rooftop level were calculated by running the model with an elevated ground plane, as well as at the full plume height. Errors inherent in this approximation required further investigation. The maximum annual mean figures for radionuclide concentrations, assuming a uniform release rate term, were calculated and presented. These would be used to compare to the wind tunnel measured figures for the concentration field. The papers discussed in Chapter 4, and associated Appendices 15.5 and 15.6 and cover the results of the analysis to compare WT and ADMS, where it was found that these methods generally agreed to within a factor of three.

2.3.3 Other Radiation Dose models

In terms of protection from radioactive gases emitted during nuclear medicine procedures a paper by Pilkingsrud and Gels (1982) showed the effects of different hemispherical cloud radii of ^{133}Xe in a standard slab phantom. A test 'phantom' typically being a slab or sphere of tissue equivalent material that scatters and absorbs radiation in a similar way to the human body, but with a defined reproducible geometry (ICRU, 1992). ^{133}Xe has beta particle and other relatively low energy X and gamma-ray emissions. The relative importance of X and gamma-ray radiation was compared to the effects of beta radiation in terms of the dose to the skin, which is conventionally assessed at a depth of 0.07mm. The dose from the radiations at 0.07mm depth was measured and compared to the calculated dose at 10mm depth, the latter figure taken as the depth appropriate for whole body dosimetry (ICRU, 1992). The ratio of the equivalent dose to skin against the ambient whole body dose equivalent for different hemispherical radii was thereby determined. For small radii the beta and low energy photon radiation contribution to the skin dose is significant, and the ratio of skin dose at 0.07mm to 10mm depth is 85.6 for radius 1m. As the cloud increases in radius contributions from greater distances and the more energetic photons become significant and the dose ratio tends to an asymptotic value of 1.58 corresponding to a semi-infinite plane source. The significance of the skin dose for the larger cloud radii is much reduced in importance due to the weighting factor for skin of 0.01 (1%) in terms of its contribution to effective dose (ICRP, 2007). Nevertheless, the importance of limited extent concentrations e.g. inside a laboratory, in terms of the contribution to the skin dose limit were clear. The findings of the paper were that measurement of external whole body ambient dose equivalent or whole body dose may be insufficient to show acceptable protection in terms of permissible skin dose levels.

Models for metabolic uptake of other PET gases administered by gaseous inhalation were considered in a paper by Kearfott (1983). The gases considered were inert gases ^{19}Ne and ^{77}Kr for the measurement of *in vivo* cerebral blood flow. A bio-kinetic uptake model was developed based on transfer from the lung compartment into the bloodstream based on the solubility of the gases. The linear first order equations made some assumptions about uniform mixing in the lung compartment, and took account of physical radioactive decay processes, which were not insignificant for the short half-life of one of the gases, ^{19}Ne (17.4s). The longer half-life of ^{77}Kr made it more suitable for single bolus inhalation. It was reported that a significant proportion of the dose received by the subjects was via irradiation of the lung by the positron emitting gases. Subject dosimetry was considered for intravenous (IV) administration and showed significantly lower lung doses, but the practicality of achieving this route of administration to the subjects was considered to be problematic.

The radiological exposure from the simplified hemisphere model was extended by Pilkingsrud and Gels (1985) for PET radionuclides: specifically ^{18}F , ^{15}O , ^{13}N , ^{11}C and also for comparison with the previous study ^{133}Xe . The study extended work carried out by Pilkingsrud and Gels (1982) where only ^{133}Xe was considered. This paper considered in detail the immersion doses from these positron emitting radionuclides and the skin doses in relation to other dose metrics such as eye lens dose at depth 3mm, as well as the 10mm depth for ambient dose equivalent (ICRU, 1992). The method was to calculate dose equivalent as a function of hemisphere radius for the radionuclides considered at 0.07mm (skin), 3mm (eye) and 10mm (whole body dose). The cloud radii generally exceeded the positron range in air. The dose integrals for gamma-ray dose were made by integration of the finite volumes by computer. For a 1m cloud radius, dose ratios for skin dose to 10mm depth were respectively 86, 180, and 55 for radionuclides ^{11}C , ^{15}O and ^{18}F respectively. These ratios fell asymptotically to 1.4, 1.8, and 1.3 in the limit of large radius which approaches the semi-infinite uniform cloud model. There exists a finite radius at which the skin dose rate becomes the limiting factor in terms of compliance with regulatory limits of exposure to skin and the effective dose. It was established that for laboratories of limited size the skin dose equivalent would be the limiting factor in radiation exposure for persons working under those conditions, and consequently air concentration monitoring could be indicated, even if external gamma-ray doses were within prescribed levels. The paper did not consider the exposure arising from inhalation of the radioactive gases, and the consequent contribution to overall effective dose.

The dose metrics for ionising radiation from external photon and electron radiations are defined in ICRU Report 47(1992). The operational dose quantities used to assess human exposure to external radiation fields are detailed in terms of conversion factors from basic measurable quantities. Ambient dose equivalent is specified with the conversion factors to the ICRU sphere or slab geometries from the scalar field quantity of air kerma for a range of photon energies. The shallow dose metric for beta particles $H'(0.07)$ is also detailed. Instrumentation for measurement of radiation fields is also covered in Report 47: a discussion of the operation of proportion counters and their much lower detector dead time than Geiger-Muller detectors make them a versatile detector for measuring dose rates. A proportional counter detector was used for plume shine measurements from the full scale measurement site in the present study.

Recent publications by the ICRP provide estimates of radiation risk based on exposure to ionising radiation. ICRP Report 72 (1996) provides the basic conversion factors that enable radiation exposure to be determined from an intake of radionuclides. Ingestion and inhalation coefficients of dose per unit intake (Sv.Bq^{-1}) are presented for a range of ages. The inhalation

coefficients are of main interest for the present work. These are presented in terms of lung class: fast/medium/slow (F/M/S), the class being dependent on the chemical formulation and bio-kinetics of the radioactive material. Inspection of the values indicates that the effective dose from inhaled positron emitters tends to be greater from S class formulations, not an unexpected result given that the tissue weighting factor for lung is appreciable and positrons would tend to deliver higher local doses to lung surfaces. ICRP72 also gives volume breathing rates: for the present study the figure of $1.2\text{m}^3\text{h}^{-1}$ corresponding to light work was selected for occupational exposure of plume releases.

ICRP Report 103(2007) provides the latest tissue weighting factors that express risk from the irradiation of organs within the human body to radiation dose. Radiation weighting factors for gamma rays and beta particles, which include positrons, were unchanged from the previous reports from the Commission.

Another significant development came with the publication of a method of assessing gamma-ray exposures due to finite plumes from Lahti *et al* (1981) who reported an extensive series of calculations to enable rapid assessment of ground-level, plume centreline doses. Two release heights (0, 100m), seven stability classes (A-G) and thirteen noble gas nuclides were considered, with downwind ranges of 400-16,090m. The model required wind direction, speed and stability class and nuclide information to estimate dose rates. The linear form of the secondary scatter gamma-ray photon build-up factor was used. A dose kernel was calculated for each radionuclide as a function of downwind distance, release height and atmospheric stability. Doses were calculated for a straight line downwind model and a meandering plume model.

Further development of the GPM was made by Overcamp (1983), who determined an exact solution to the problem of determining the external gamma-ray dose rate for ground level releases. A comparison is made against the standard semi-infinite cloud model. The inverse square point source dose kernel method was similar to that used by Imai and Iijima (1970) except that the linear form of the scatter build-up factor was used. The linear form, although simpler in formulation, was recognised to overestimate the dose from build-up (collided scatter photons) but to underestimate the contribution to doses further from the source point. The integration of the Gaussian plume equation was achieved by simplifying the horizontal component into a uniform cross wind concentration, but retaining the traditional Gaussian form for the vertical distribution with height. The primary (i.e. un-collided) flux dose integral I_1 (which integrated the dose rate from the cloud from primary, or un-collided photons reaching the receptor point) was evaluated analytically at ground level by expanding and integrating the series terms of a special function, E_1 . The integral shows slow convergence for large values of $\mu\sigma_z$; i.e. 26 series terms were required for $\mu\sigma_z \sim 3$ to attain 1% accuracy. Integral I_2 was the collided scatter flux integral dose from the cloud at the receptor point and was expressed in terms of the complementary error function $\text{erfc}()$. Given the linear attenuation coefficient in air was μ , the photon mean free path before collision would be $1/\mu$. It could be seen that for small vertical dispersion the cloud size is small compared to the mean free path (MFP) and the dose estimate is significantly reduced compared to the uniform semi-infinite cloud model. A similar order of magnitude dose contribution from each of the integrals for the collided (I_2) and un-collided (I_1) photon flux was estimated. The plume spread and dosimetry did not take into account the presence of obstacles or obstructions in this ground release model.

Further development of the Gaussian plume model, for unobstructed flow, was made by Overcamp(1987) who presented a paper showing a simple approximation for estimating

centreline gamma-ray external dose rates due to a continuous plume. Following earlier work, the linear build up factor was selected and a standard inverse square point dose kernel used. An angular sector of $\pi/8$ was selected (22.5°) according to the standard analysis. In this analysis, the release term is specified as being above ground level, and is thus an elevated release. The I_1 and I_2 integrals for primary and collided flux respectively follow the convention of the earlier paper (Overcamp, 1983). As before, the crosswind spread is neglected and treated as uniform with lateral co-ordinate in one analysis, and the more accurate Gaussian spread model also calculated: the dose is evaluated at ground level. As before, decay and deposition were neglected. Atmospheric stability A-F was considered for the calculations. The paper presents the dose rate results for the uniform semi-infinite cloud, the uniform lateral spread cloud with vertical Gaussian distribution and the Gaussian plume. In all cases, the models converge for each stability class with increasing distance from the release point, with the semi-infinite cloud showing the highest doses in the downwind asymptotic limit. The short-range characteristics are of more interest: a factor of ten exists between the semi-infinite cloud and the Gaussian plume model for stability class A. For class F the ratio is somewhat greater. The uniform distribution cross wind calculation shows a better match to the full Gaussian plume calculation. For 1MeV photons and a ground level source the estimates based on the uniform cross wind distribution and the full GPM were within a factor of two for A stability class at a range of up to 100m, and at a distance of 300m for F stability.

Gamma absorbed doses from overhead plumes were considered further in Overcamp(1991) who considered specifically the problem of meandering plumes. The case considered was a very stable atmospheric condition in which low wind speed and large eddies result in dose estimates that may differ from the conventional GPM. The findings were that the dose rate is high whilst the narrow plume lay directly overhead of the detector (receptor point) and lower, as expected, when it meanders further away. An average dose rate was calculated from plume meander and the overall effect was that the dose was approximately one third of the conventional model with standard class G dispersion parameter. The differences reduce closer to the source where plume meander has less effect, and far downstream where plume broadening starts to have a greater effect.

Tarasov (1993) investigated the GPM by factorization of terms in the integrand in terms of integral special functions. In this way energy and space terms were expressed as separate terms in the integrand. This enabled a simpler formulation where the concentrations were expressed as separable independent functions. For the standard GPM model an analytic formulation was possible for the space terms, which simplified for cases where a ground level source and receptor were considered. The computation of the energy factor with the space integrand still represents a challenge, and is dependent on the form of the build-up factor chosen. In some simplified cases the factorized form represents a useful formulation that can be solved analytically in special cases.

Absorbed dose from traversing a spherically symmetric Gaussian cloud was presented in Thompson (1999). This treats external gamma-ray doses received from flying through a cloud. The analysis was carried out for 700keV photons, taken to be representative of nuclear reactor fission products. Results were presented for a cloud holding a fixed quantity of radionuclide against an infinite cloud, for an assumed airspeed of 75ms^{-1} . Doses were presented against lateral fly-through distance from the cloud centre against flying directly through the cloud centre. Dose for a given air path scales with cloud activity and airspeed. The dose rate at different distances may be used to calculate the cloud dispersion parameter, σ . The analysis shows that for the geometry of a spherical Gaussian cloud the more distant the fly-by from the

centre the lower the dose compared to the route taken through the cloud centre. For the cloud centre route the dose compared to an infinite cloud approximation was lower for all cloud radii, but as expected approached asymptotically the infinite cloud case in the limit of large cloud radius.

The gamma dose rate from plumes of radioactive material was considered by Raza and Avila (2001) using a 3D Lagrangian (i.e. moving with the flow) formulation and compared to a standard GPM model. A computer program was written to evaluate the dose rate from a ground level source in atmospheric class D conditions. Wind shear and eddy time was based on a geostrophic model, so the model was suited to longer range conditions. One hundred radioactive particles were emitted per 'puff' release. A simple linear build-up factor was assumed for the modelling. Results showed that the Lagrangian model matched the GPM accurately up to 20km, after which the GPM gave doses which were too high due to the neglect of the broadening effect on lateral dispersion of wind shear. Conclusions were that wind shear must be taken into account for distances in excess of 20km from the point of release. The Lagrangian model was also useful for modelling the radioactive decay of the plume with distance travelled. The Lagrangian model employed Monte Carlo sampling from turbulent velocity fluctuations vertically and laterally to determine new velocity vectors after the duration of each eddy lifetime.

Following on previous work Overcamp (2007) developed analytical solutions for some of the GPM gamma dose rate integrals. A solution for I_1 , the primary gamma un-collided flux was presented for a ground level source in terms of special functions. For an elevated source an expression of the collided flux integral I_2 was also determined. No special functional form was found for I_1 for an elevated release. A problem of slow series convergence in the series expressions for these integrals generally was noted, so that computational accuracy may be an issue. A drawback for the use of these formulations for gamma dose determination is that the vertical distribution is assumed to hold downstream of the source, which would only be appropriate without the presence of buildings. An integration by Monte Carlo (MC) techniques of random sampling may be used to investigate the accuracy of convergence of the integrals.

In a study using CFD Large Eddy Simulation (LES) Vervecken *et al* (2015) investigated the gamma dose rate from a continuous source at different ground level receptor positions. It was found that significant peaks and troughs of instantaneous dose rate were recorded due to the inverse square nature of the gamma ray source term: when the receptor was immersed in plume material the dose rate peaked, when the plume moved away a trough occurred. The height of the peaks and troughs reduced with increasing averaging time, and this was demonstrated in the probability density function, which took a log-normal characteristic. The 99th and 1st percentile dose rates showed maximum range of variation at a position downstream of the source point which was reflected by plume meander and the dispersion of the cloud with increasing distance downwind.

Following on from their 2001 paper, Raza and Avila (2005) presented an analysis of radiation dose estimates from external gamma-ray exposure to a Gaussian plume. Their paper refers to immersion doses: exposure from beta, or positron, radiations is not considered, nor are doses from inhalation of radioactive gases. The paper presents a generalised method using Gauss-Legendre integration of the point dose kernel over the plume space. Three different build-up factor regimes were considered: Linear, Berger and Geometric Progression (GP). The Gaussian plume equation used did not consider reflections from the top of a mixing layer, however a ground reflection term was incorporated. Noble gases Kr and Xe were considered as the

nuclides released from a nuclear reactor to atmosphere. Consideration of the build-up factors for an appropriate energy indicated a similar response out to 4.5 mean free photon paths, or 500m. Further from the source the Linear build-up model under-predicts the build-up factor compared to the Berger and GP forms, which were similar. Beyond 4km the Berger form predicts the largest build-up factor, so can be considered conservative for secondary photons from this distance and beyond. However, this would correspond to 18 or more mean free paths, and the contribution from primary photons at this distance is very much reduced: Raza (2005) does not mention this point in their subsequent selection of the GP model for the build-up factor. For the results presented for the radionuclides in question a crosswind dose profile is presented at a downstream distance of 400m from the release point. Based on the concentration at crosswind distances considered, the semi-infinite cloud approximation significantly under-predicts the gamma dose rate compared to the Gaussian plume method considered for neutral stability (Pasquill D). These results support those of Lahti *et al* (1981). At greater downwind distances the greater plume broadening leads to an increase of off axis concentration values, meaning that the uniform cloud model dose rate prediction improves compared to the Gaussian plume calculation method, the agreement being best at 16,000m downwind of the release point of the four distances presented.

Plume centreline doses at an elevated position were presented: the height of release was not stated, but assumed to be 0m in accordance with one of the cases considered by Lahti *et al* (1981). At all four downwind distances considered the dose rate at ground level for the semi-infinite cloud is greater than that predicted from the Gaussian plume. Away from the plume centreline in a vertical direction the dose rate from the semi-infinite model (based on concentration values at the receptor point) falls away rapidly with increasing height. As before both models converge for the largest downwind distance considered. Convergence is faster for the crosswind co-ordinate due the greater value of σ_y compared to σ_z .

2.4 Chapter 4: citations from published papers

The citation list is presented in Chapter 14 for the pair of papers from the author which were published in the Journal of Radiological Protection in December 2016 (Gallacher *et al*, 2016a, 2016b). These represented citation lists applicable at that time relevant to the research questions in this thesis, and applicable to those published papers. The context of these references, and the full list of citations for each of the references listed below is also discussed in Chapter 4, along with exposition in the text and the content of these references is not considered further in this literature review chapter.

2.5 Further Literature review: 2021

The following mesh terms were used in the Web of Science search engine in February 2021 and were used to refresh and review published literature potentially relevant to the research question. In total a total of 583 papers were identified as potentially related to the research question from this analysis of the literature. From this total a total of 23 papers were judged, by review of title and abstract, to be relevant for citation and a description and citation are given as follows.

MESH Terms#1: Gaussian \cap Plume \cap Radiation

MESH Terms#2: Dispersion \cap Pollutant \cap Buildings

Total papers from search = 583

Total paper considered after rejection from abstract contents = 23

All papers from the reduced list were considered appropriate for citation, although none approached the research objectives of this work – they were nevertheless considered as supplementary information that give extra contextual background to the research questions considered, and limitations in the field of evidence related to the research questions pursued in this work. A review of the references is given in date order of publication.

A release of radionuclides into a stable planetary boundary layer was considered in Basit (2006) using a Lagrangian model for radioactive particles released into the flow. Ground level concentrations and radiation dose are calculated using the model. Distance scales involved are up to 200km downstream, and up to ± 70 km crosswind, and there was no allowance for the presence of buildings. This was an interesting application of the use of Monte Carlo methods for long scale calculation of ground concentration and radiation dose but of limited relevance to the very near-scale distances in a turbulent concentration field highly proximal to buildings considered in this thesis.

Further work by Basit et al (2008) covered the simulation of atmospheric dispersion of radionuclides using a Eulerian-Lagrangian modelling system. A hypothetical accidental release of radionuclides was considered from a nuclear power plant. A Lagrangian stochastic model was used for the radionuclide aspects coupled with a Eulerian regional atmospheric modelling scheme. Surface heat flux was considered along with mean wind velocities affected by the regional tomography were considered in the model. The dose point kernel (DPK) method was used to calculate radiation dose rates. A 12-hour ground release was considered over an area of terrain of 400km². It was found that the simple Gaussian Plume Model (GPM) was considered not sufficient to model the dose in regions of complex terrain. This paper does not apply in the ultra-near scale considered for this research thesis work with high levels of building generated turbulence in the very-near scale of the radioactive pollutant release but the paper cited here is nevertheless part of the background information considered relevant to the research questions considered relevant to this thesis.

Srinivas *et al* (2009) considered the effect of different turbulent diffusion models on relatively short-range pollutant dispersion. Hypothetical releases from a planned fast-breeder reactor were considered. A mesh area of 50km x 50km was considered with a resolution of 1km. Site boundary doses at 1.5km were different depending upon which of the turbulent diffusion models was considered i.e. (A) velocity deformation; (B) short range isotropic similarity and (C) turbulent kinetic energy (TKE). Results at the site boundary distance were broadly similar. In this thesis concentration field and radiation dose levels are considered at much shorter range and with the effect of buildings at a scale of less than 100m. The results of this cited paper, although interesting for longer scale dispersion studies, are nevertheless not particularly relevant to the research questions considered in this thesis.

Another Lagrangian analysis using particle trajectories was presented by Andronopoulos and Bartzis (2010) based on a Gaussian Plume Model (GPM) technique for the evaluation of real-time emergency response systems. Comparison with three days of experimental running from a nuclear reactor was made with what appears to be order of magnitude variations between computed radiation fluence rate and calculated values at 1.5km downstream of the release position from a 60m tall stack. This distance is of the order of ten times or more compared to the very near-scale distances considered in this thesis, and consequently the cited paper does not account for near-scale building effects relevant to the work in this thesis. Nevertheless, the

overall discrepancy between computational models and measured values is nevertheless of some interest.

The SIRANE model for atmospheric dispersion (Soulhac, L *et al*, 2011) was seen to consider concentration field values using simplified methods to deal with complex urban topography. Simplified parametric transfer methods were used to describe the transfer of pollutants in complex environments, covering advection in street canyons, differences at street level with overlying flow and exchanges at street intersections. Local building details were noted as significant although simplified in model inputs with the building canopy being modelled as a simple overall frictional surface. In terms of the research question considered in this thesis the analysis in the cited paper is not particularly relevant as this thesis considers near-field dispersion in relation to a limited field of buildings, although comparisons may be inferred from some of the later experiments in the cited paper looking into the sensitivity analysis when extending the very near-field results with isolated buildings in the real-world modelled case to the full building model. In this thesis most of the results relate to a single cube model with very near-field dispersion in respect of concentration field values at or near roof level at location of persons or of building ventilation intakes.

In situ tracer release experiments were considered in Jeong, H *et al* (2014) and these were compared to a GPM. It was found that the GPM generally overestimates concentrations compared to actual measured concentrations. This indicates that GPM is suitably conservative when applied in a safety case analysis. However, it was noted that the ‘wake phenomena’ from reactor buildings explained, at least to some extent, the reduced downstream concentrations – in which meteorological conditions played at least some part. Downstream doses were assessed at distances >1.5km from the release point. In summary, this paper provides evidence that an assessment of near-field effects, such as was carried out in this thesis, that accounts for buildings is necessary in order to modify the GPM model to account for actual concentrations: a central aim of the work presented in this thesis.

Fawaz, A and Waller, E (2014) presented a computational fluid dynamics (CFD) assessment of resuspension of radioactive particles from a flat plate in a wind tunnel simulation. The calculated distribution was then used to compute expected radiation doses from a Monte Carlo computational code. These authors noted that the current computational fluid dynamics codes were unable to calculate radiation doses arising from resuspension of particulates. The study showed results for calculated radiation doses for a simple isolated single building case at normal incidence to flow, and calculated radiation dose at only two distances from the building (at 0.5m and 1.5m, compared to a building height of 0.32m). The radionuclide chosen for the computational assessment was ¹⁴⁰La. These results were not particularly applicable to the research questions considered in this thesis for three main reasons: (a) releases from simulated resuspension of particles from a flat ground plane in front of the building studied were presented, (b) only the limited geometry of a single building at normal incidence was considered; (c) limited results at only two spatial positions downstream of the building were presented; (d) very limited information is given on the flow field and how it may have influenced to the dose with variations in sample position. In contrast this thesis covers releases close to the building roof, experimental data from multiple angulations of an isolated building – and experimental wind tunnel results on other building cases in a truly complex urban flow field, also showing in detail how the flow field and radiation dose fields vary over a range of spatial positions in the micro-scale close to the building.

A different model of distribution of pollutant material was investigated in Hawkley (2014) where it was noted that the Gaussian Plume Model (GPM) needs to be modified for near-field effects. In this paper the results of air monitoring stations distal to the point of pollutant release were considered and the Lorentzian distribution was employed to model the concentration field. A simple well-mixed approximation was used with an ellipsoid model for the main recirculation zone and only ground level doses were considered. It was noted the GPM was accepted as the standard model and the need to allow for building effects was recognised. It was recorded that the heavier tails of the concentration field in terms of the lateral spread of the plume were better recognised by the Lorentzian distribution. In this thesis the distribution has been in the context of a GPM, but with modified methods to allow dual Gaussian fitting to concentration field values, whereby the concentration field can be described by a superposition of main plume and recirculation zones. The dual Gaussian approach described in this thesis applies a standard methodology but allows for effects distal to the plume centreline to model concentration field values in the very-near range to buildings. Furthermore, in this thesis the wind tunnel simulations have enabled the spread and structure of the plume to be accurately characterised at different levels and in particular very near to the roof level for highly proximal buildings and under various experimental conditions, something that this cited paper does not address.

Pecha, P and Pechova, E (2014) described a model for evaluation of the external radiation dose from a radioactive cloud via a fast algorithm. The situation modelled was for an emergency release scenario with one hour time segments accounting for variations in meteorological conditions. The broadening plume modelled with a near-Gaussian plume approximation was split into circular disks as an approximation and the ground level dose calculated from each disk according to a derived algorithm which simplified the calculations and reduced computing time. Convergence to the semi-infinite plume approximation was confirmed. The method was applied to calculating ground level doses at relatively large distances of at least several kilometres from the release position. By contrast, in this thesis the more computationally expensive Monte Carlo method was necessary because of the very near scale in relation to the plume source position being considered i.e. doses within the plume on the roof of the emitting building are calculated in this thesis – a scenario where the convergence of simplified reduced integral solutions, such as employed in this cited paper, are not satisfactory.

Optimisation of the calculation grid for atmospheric dispersion modelling was considered in the publication from Van Thielen *et al* (2015) where the optimal grid sizes for emergency planning calculations and measurements were considered. A Gaussian Plume Model (GPM) was used as the dispersion model used in the study. Various grid configurations were investigated, termed telescopic, polar and irregular - and it was found that the optimised polar grid gave the best results with the minimum number of sample points: however, it should be noted that the distances under consideration were generally much greater than considered in this work. In some cases very fine grid cells (1m dimension cells) were used for validation purposes for the comparison with exact solutions. For this thesis work the Monte Carlo calculations were made on a rectangular grid with 0.5m which is comparatively ultra-fine spacing and was appropriate for the very near field conditions being investigated: there was not the constraint of computational time and it was possible to compute the doses from the very near field regions to the release position and roof i.e. doses above roof level were computed at heights of 1.0, 1.5 and 2.0m which encompassed the height range of human subjects exposed to the concentration field of pollutants.

Vickers, L (2015) investigated doses to the Maximally Exposed Offsite Individual (MEOI) according to applicable US safety standards. A spreadsheet model was used to calculate doses to persons in a region 1.6km downstream of radioactive plume releases. Wind speed data over one year, in 22.5° sector sizes, was used in 15-minute intervals with information included on atmospheric stability class to determine plume broadening according to canonical models. The 5th and 95th percentile doses were computed given the conditions applied. The GPM model was considered to be a fast and accurate tool to evaluate radiation doses for the safety assessments considered. In this thesis work doses from plumes have been evaluated at very close range, much closer to the release point than considered in this study, but the methodology of taking into account the 95th percentile dose from the puff (intermittent short duration) releases has been used in this thesis in order to estimate an upper range estimate figure for doses arising from radioactive releases.

Evidence of ingestion in human subjects of radioactive ¹³¹I released in the form of a plume from the Fukushima accident was presented in Uchiyama et al (2015). Some of the subjects had stable iodine blocking to reduce the uptake of radioactive iodine ingested from inhalation of the plume. The paper was an example of a general increase of interest and research activity in the field of radioactive plume dispersion arising from the Fukushima accident but not of particular relevance to the work presented in this thesis.

Rishel, JP *et al* (2016) published a publication on using atmospheric dispersion theory to inform the design of short-lived radioactive particle release experiments. The GPM model was used to design a release experiment to model venting from an underground nuclear explosion. Distance ranges applicable were a few kilometres from the venting release sites. Methods using the deposition velocity of airborne pollutant were employed to determine settling out of released ¹⁴⁰La and ¹⁹⁸Au tracers onto ground level. It was found that larger particles deposited closer to the release position and were employed for greater release heights to enable sufficient ground deposition within the experimental test site (range of 2km). The work enabled the design of the release experiment to enable sufficient ground deposition for detection and analysis of data. The applicability of this cited paper to the research questions considered in this thesis was limited, but it should be noted that Chapter 4, and associated Appendices 15.5 and 15.6, include publications as part of this work where the effects of surface deposition were to some extent considered.

Gamma-ray dose from an overhead plume was considered in McNaughton *et al* (2017a). This work compared the dose from external radiation between those derived from local ground level concentration and those calculated from an overhead plume. Monte Carlo (MC) codes were used to calculate ground level doses using standard GPM plume models. It was found that at long distances and unstable atmospheric conditions the MC code agreed with the standard GPM models. At shorter distances and for elevated releases it was noted that the semi-infinite model underestimates the external gamma-ray dose because local ground level concentrations are effectively zero, although the plume was overhead and giving rise to gamma-ray shine dose. The MC models used in this thesis by contrast to this cited paper incorporate fully gamma-ray dose from the concentration field distribution, and moreover they account for dose in the very near-field effectively inside the plume at very close distances from the release position – also including immersion doses from the positrons for the radionuclide pollutants considered.

A companion paper from McNaughton et al (2017b) considered more practical matters in terms of the calculation of gamma-ray cloud shine doses. A comparison was made against ground level doses using the semi-infinite cloud approximation. Further evidence was presented for

the underestimate of gamma-ray dose from elevated plumes using local ground level concentrations with the semi-infinite approximation. Distances considered were 800-3000mm, for release heights of 0-50m. Sector averaging was completed over 22.5° angular sectors. At greater distances of 3km the semi-infinite method was more accurate. From the work in this thesis models have been developed which account accurately, based on the measured concentration field in the wind tunnel, for dose from the mapped concentration field at very close distances to the release position. In this thesis this includes inhalation dose, directly from the concentration field, and for gamma-ray dose highly proximal and even inside the plume. This thesis work must therefore be considered to extend the knowledge of near-field plume behavior with respect to the radiation doses received.

A standard application of the standard canonical GPM was presented in Calais, PJ (2017) applicable for crematoria releases of ^{131}I arising from deceased nuclear medicine therapy patients. Atmospheric stability was estimated and used to estimate plume spread from a buoyant plume over open terrain for a 10m release height. It was found that the applied atmospheric stability had a large effect on the maximum downstream concentrations. Very narrow plumes from stable atmospheric conditions were also estimated to confer high local concentration values from limited dispersion and the consequent narrow plume. Although background information on the application of the GPM model this cited paper was not considered particularly applicable to the research questions considered in this thesis, which consider very near-field releases very close to, or on top of, buildings and the consequent radiation doses received at these very close distances e.g. at roof top level.

In a review paper Leelosy, A *et al* (2018) considered numerical models used to predict the atmospheric dispersion of radionuclides. Findings were that the best modelling tool depended on the distance scale of the dispersion. Local scale was defined at 1-10km, and regional scale at 100-1000km. At the latter scale meteorological and temporal changes were of considerable importance. The value of computational fluid dynamics (CFD) in the micro-scale of <1km was noted, particularly in an urban environment. It was noted that the GPM model could provide a fast and easy to compute response over the local scale. The paper was of limited relevance to the topics presented in this thesis, other than to note that CFD would be applicable to micro-scale evaluations such as considered in this work.

Oura, M *et al* (2018) carried out a validation study of atmospheric dispersion using effective source heights determined from wind tunnel experiments. The field of application was nuclear safety analysis, where it was noted that the GPM model was applied for nuclear safety analysis in Japan and the UK for fifty years. In the work effective source heights determined from wind tunnel experiments were considered and their effects on the safety cases and determined outputs at the site boundary of nuclear plants, taken at 1km for this paper. Effective source height was considered with and without terrain for the wind tunnel methods. A main finding was that the effective release height was lower than the actual release height (92m vs 102m) when accounting for concentration levels at the site boundary location. It was also noted that the effective release height may need to be reduced for atmospheric stability levels E-F, although it was noted stability classes A-D compared well. In this thesis work it should be noted that plume rise and effective release height were accurately determined from mapped downstream concentration profiles, and that the stability class applicable for the wind tunnel experiments was class D, applicable for neutral stability.

Dey, R *et al* (2019) presented evidence on the effective dose arising from exposure to an overhead plume of radioactive material using a Monte Carlo (MC) code using an adult

reference phantom. Only ground level doses were considered downwind of the elevated release. It was found that the coefficient used to convert to effective dose was consistent with that applied in this thesis, so this publication was useful further evidence to support the computational methods employed in this thesis.

Becerra, VM *et al* (2020) looked into the inverse problem of the estimation of source term estimation from downwind measurements of radioactive releases, using sophisticated statistical techniques i.e. Kalman filtering algorithms. A GPM model was applied in the analysis and applying wind speed changes during the release to better define the release values. Release height was estimated using adaptive filtering of results. Wind direction was assumed to be constant throughout the simulation. Reasonable estimates of the source term were obtained from the downstream measurement results and application of the algorithm. In terms of applicability to this thesis work it should be stated that the GPM model is still widely applied, with good effect, and sometimes in combination with sophisticated modelling techniques such as employed in this paper.

Another application of Kalman filtering techniques was evident in Di Ronco, A *et al* (2020) where the source term for an accidental release was estimated using statistical techniques. Distances in the range of 1-2km were considered in the analysis. A GPM was used in the analysis. Good accuracy was reported for over 30 iterations of the algorithm. It was noted with reference to this thesis work that the GPM model still appears, in the latest publications in the literature, to be the basic method of choice for analysis of plume dispersion, even when applied with sophisticated algorithms for estimation of releases.

Matthews, JC *et al* (2020) report results from a chemical tracer release experiment into an urban boundary layer over a 2km distance from release scale. It was noted from results of the experiments, in many cases measured inside of buildings selected for the measurements, that the GPM underestimates peak concentration values, and this was posited due to complex building effects. Overall, the cited paper validated that GPM was still an established method but indicated that complex flow effects due to buildings need to be taken into account: this is a central aim of this thesis work.

Satoh, D *et al* (2021) showed result from a local scale atmospheric model coupled with a simulation code for estimating external gamma-ray doses from a radioactive plume and contaminated ground. A local scale model was employed. Lattice dose response functions were used coupled with an MC code. Various source heights were used ranging from 1-1000m, however there was no allowance for flow around buildings. It was determined that the results were applicable from the cited paper to dose evaluation at longer range dispersion than the micro-scale. Results were also given at ground level and hence not applicable to the very near-scale cases considered highly proximal to buildings and the radioactive release position considered in this thesis work.

2.6 Discussion: Literature Review

The review of the literature indicated a significant gap of knowledge around modelling of dispersion plumes in the very near-field of buildings. Furthermore, there is a need for radiation doses to be assessed for near-field dispersion in the presence of buildings - as the current models generally only calculate radiation dose from external gamma-ray doses from a Gaussian dispersion model with undisturbed flow without taking into account very near-scale distances. In the case of ADMS, radionuclide concentration values are calculated using an isolated

building main wake recirculation zone using an entrainment fraction. ADMS has the limitation that gamma-ray doses cannot be calculated at an elevated roof plane from the concentration distribution, but only at the ground plane. This is a major source of error when doses at or near the top of elevated levels are required. ADMS considers only an isolated building so that effects from nearby buildings are not modelled. This is another limitation against which wind tunnel (WT) modelling can be considered superior. The determination of roof level concentrations is important as this is where roof terraces and in many cases air intakes are located.

This review shows that receptor concentration values differ between WT and ADMS by a factor of the order of three. The main research proposal was to investigate the dispersion parameters of plumes in proximity to a number of different building cases and to determine the dose contributions from all sources of radiation exposure: inhalation, beta immersion dose and gamma-ray external dose. The evaluation of the errors in the formulation of the rooftop models in terms of radiation dose was carried out in a sensitivity analysis in this thesis to experimental conditions. The formulation of a more accurate near-field radiation dose determination method was investigated in this thesis, and information on the likely spread of pollutant concentration values with different conditions: wind direction in the approach to the building, effective release height and information on the sensitivity of the concentration field results to the presence of surrounding buildings.

In the context of the wider review of the available literature there was identified a significant lack of information available for the case of very near-field building scale dispersion evaluation of the concentration field of pollutant and consequent radiation doses arising from the concentration field. Furthermore, the available methods in no way enabled evaluation of radiation dose rate for receptors positions situation highly proximal or within the plume of radioactive material. This thesis has addressed these research questions and produced methods by which these research questions can be answered.

CHAPTER 3: WIND TUNNEL EXPERIMENTAL METHODS

3.1 Introduction

A series of experiments were planned for the EnFlo (EnFlo, 2021) boundary layer wind tunnel facility at the Department of Mechanical Engineering Sciences (MES) at the University of Surrey, UK. The broad outline of the experiments was to evaluate different pollutant release scenarios in the near field of a release point, with a particular focus on the roof top zone of the buildings investigated proximal to the release position. Measurements were made of two ‘real world’ building configurations: namely the St Thomas’ Hospital (STH) East Wing (EW) building with a set of scale building models encompassing the site and significant tall upstream buildings. The EW building was the site of a roof top stack releasing positron emitting gases arising from radiochemical production of tracers used in Positron Emission Tomography (PET) scanning of patients in the hospital. Measurement of the concentration field enabled estimates of the roof top concentrations of radioactive gases to be made, with consequent estimation of the doses received by persons working in the roof zone and elsewhere on the STH site. These measurements of the East Wing building were required on two grounds: firstly, the EW building was due to undergo the addition of a glazed cladding layer significantly changing the building shape to wind flows for which the regulator of radioactive emissions, the Environment Agency (EA, 2020), had required an updated radiological assessment (EA, 2012) of the site, in particular concerning changes to intake into buildings proximal to the release site. Secondly, an assessment of the occupational radiation doses from the radioactive gas emissions to construction operatives was required for the lengthy construction process of the addition of the glass cladding to the EW building, extending just over one year.

The case of an isolated cubical building was investigated in order provide generality to the scope of the measurement cases investigated, a standard configuration for which the flow field characteristics been investigated (Robins and Castro, 1977a, 1977b). In this way the specific EW building cases measurements could be placed in comparison to an idealised building shape.

Conventional continuous release rates of pollutant were first investigated in order to assess the concentration field with the different building configurations tested under stable conditions of wind direction and pollutant release rate. However, from STH release trace logging data it was known that the actual release rates were in the form of short intermittent ‘spike’ releases, characteristic of radiochemical production of PET radiopharmaceuticals (Kleck *et al*, 1991). In order to simulate the dose arising from these short releases of pollutant ‘puff’ releases were simulated in the wind tunnel experiments for a range of cases covering different release conditions for the EW ‘clad’ and ‘unclad’ cases and the cube model. A range of different release durations of the puff releases in order to investigate the temporal variation of the expected dose from the pollutant material.

To better understand the dispersion pattern of pollutants in the concentration field investigations of the flow field were made with a Laser Doppler Anemometer (LDA). In these experiments simultaneous measurements of the velocity were possible in two orthogonal directions for any given experimental run. In some cases these were coupled with simultaneous measurements of the concentration field with a Fast Flame Ionisation Detector (FFID). The LDA measurements not only were used to derive flow mean advection velocity at a range of measurement positions, but due to the relatively high sampling frequency of the LDA system, the unsteady components of the flow were measured to determine the turbulence intensity in the right-angled orthogonal co-ordinate system used for the measurements i.e. the downstream,

crosswind and vertical components respectively. Furthermore, Reynolds vertical shear stress was also able to be determined from these measurements, giving further information on the nature of the flow field.

All measurements were made in Pasquill-Gifford (Pasquill, F, 1974) neutral stability (class D) conditions i.e. with no radiative heating of the ground causing convective processes (classes A-C). These conditions corresponding to class D correspond approximately to windy and overcast daytime meteorological conditions. Stable classes (E-G) would correspond to night-time conditions with little wind and a reduced plume spread but a generally enhanced plume meander (Jones, HA, 1983).

Additional parameters investigated during the measurements were the effect of release position on maximum roof top concentrations and the effect of angle of approach flow to the building scenarios tested. A key parameter is the actual nature of the release: a passive continuous release (CR) with the release nozzle aligned to the direction of flow with the emitted tracer gas released at the same wind velocity as the surrounding flow at the release point, or an active vertical (AV) release from a stack simulating the release conditions at the EW site. Active vertical releases were simulated at an appropriate Stack Velocity Ratio (SVR) with the release velocity of the trace, mixed with carrier, gas matched to the velocity of approach flow at the release position. In other words:

$$\left(\frac{W_0}{U_{ref}}\right)_{WindTunnel} = \left(\frac{W_0}{U_{ref}}\right)_{FullScale} \quad [1]$$

Where W_0 is the emission speed in equation [1]. This, combined with geometrical similarity, ensures that plume rise due to emission momentum is correctly modelled. Using the passive releases a range of release heights in relation to the buildings the concentration field maxima, in terms of value and spatial position, were investigated for each release condition at a range of downstream sample planes. AV releases were conducted at a fixed release height and SVR, matching those of typical conditions experienced with the EW building.

The overall aim of the experiments conducted was to investigate the effect of varying the parameters on the concentration field maximum values experienced and to better understand the effect of the flow field on those maxima in terms of the parameters varied during the course of the measurements.

3.2 Methods - Part 1: the wind tunnel

The wind tunnel facility at the University of Surrey has been described in detail by, for example, Contini *et al* (2008). It is an atmospheric boundary layer simulation wind tunnel which models the planetary boundary layer at distances in the lower atmosphere and enables experiments under controlled conditions of flow and dispersion. As such, it was ideally suited to these measurements which simulate flows in an urban environment with a range of buildings and experimental conditions.

The wind tunnel has a working section of 20m length, 3.5m wide and 1.5m tall. The design is of an open-circuit wind tunnel where the external circulation is in the larger laboratory area, although the flow is reconditioned by honey-combe and screens at the inlet before being passed through the tunnel again. Figure 3.1 shows diagrammatically the main features. The free stream reference velocity, at the top of the generated boundary layer, was at 1m height from the floor of the tunnel. The downstream wind velocity was maintained by virtue of a software-controlled

feedback system utilising a two-dimensional Solent Wind Observer 1172T ultrasonic anemometer (Gill Instruments, 2021). To create the boundary layer there were five Irwin (1981) spires of height 1.2m (as shown in Figure 3.2) which were situated at 1m from the inlet of the tunnel. The whole floor of the tunnel was covered with roughness elements of height 20mm and 80mm wide with lateral spacing of 240mm, which can be also seen in Figure 3.1: each strip of elements running crosswind across the tunnel was placed such that the protruding elements formed an alternating pattern with adjacent strips. Shorter roughness element strips were used around the tunnel turntable, enabling rotation to the different wind directions studied.

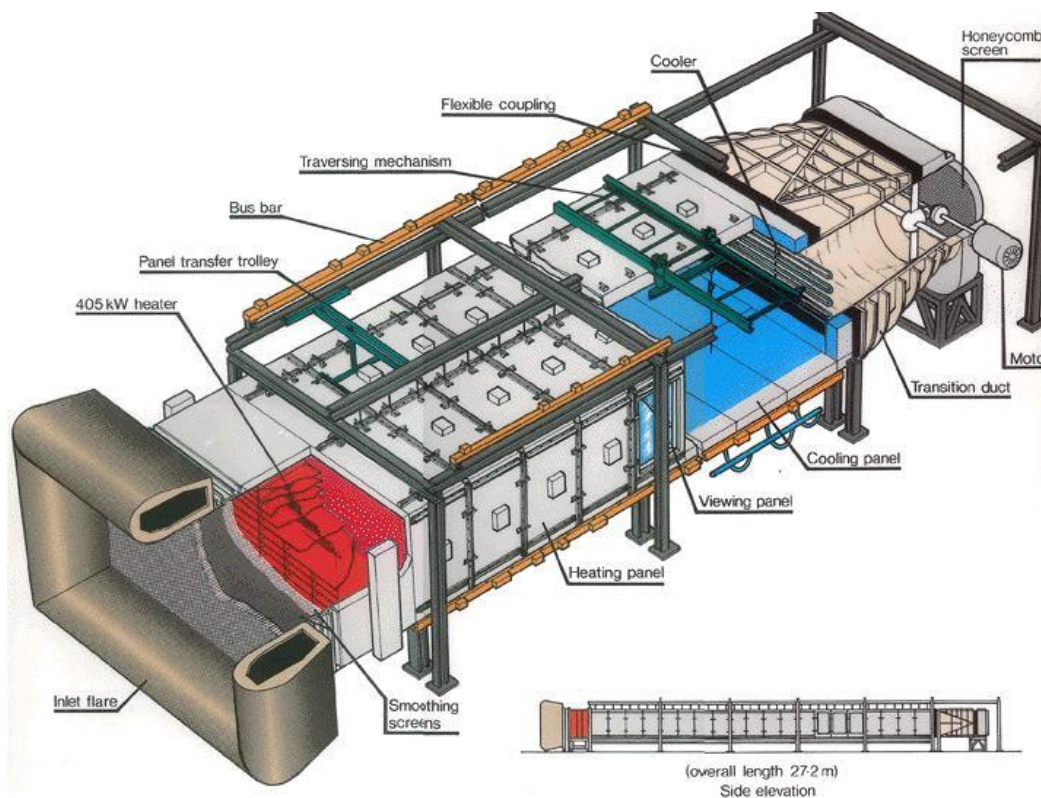


Image courtesy of EnFlo at the University of Surrey

Figure 3.1: Diagram showing the main features of the wind tunnel



Figure 3.2: Interior of the wind tunnel looking upstream with the cube model in place

Figures 3.3 and 3.4 show the wind tunnel as schematic diagrams in plan and elevation view respectively. The wind tunnel turntable is shown at 6 metres from the end of the tunnel, with the turbulence generating spires near the inlet. The orientations of the right-angled co-ordinate system are also shown, with (X, Y, Z) axes shown pointing downwind, crosswind and vertically respectively.

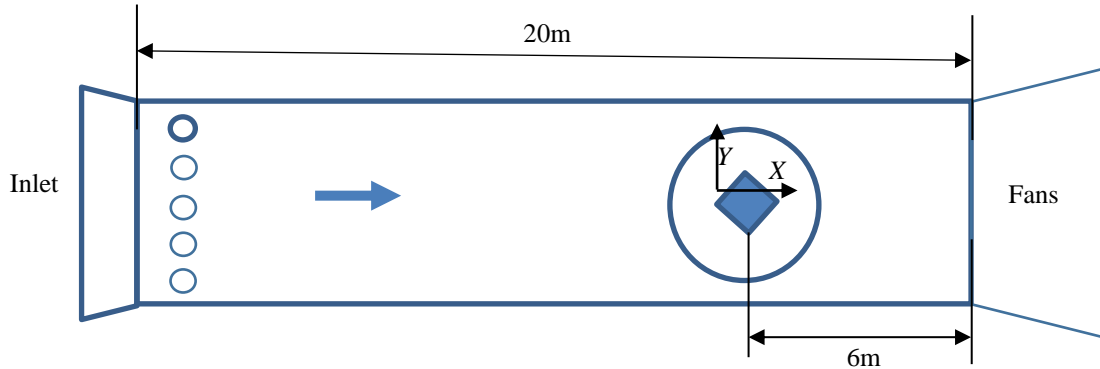


Figure 3.3 Schematic layout of the wind tunnel (plan view)

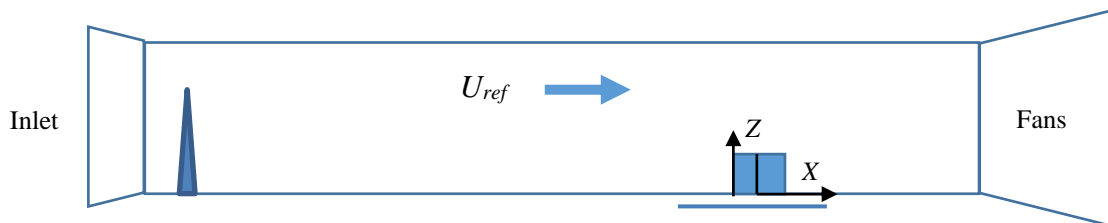


Figure 3.4 Schematic layout of the wind tunnel (elevation view)

The concentration measurements were made with an HRF400 Fast Flame Ionisation Detector (Cambustion, 2021) operating at a frequency of 400Hz and mounted on a robotically driven traverse arm to achieve measurements at different spatial sampling points. Due to the Nyquist sampling criterion expected instrument temporal frequency response for measurements was therefore below 200Hz. Figure 3.5 shows a schematic of the FFID. Sample gas is fed in through the capillary tube into the hydrogen flame inside the flame chamber. Hydrocarbons produce ions when burnt which are collected at the ion collector biased with a high DC voltage. The current at the detector is proportional to the ion production rate, which itself is proportional to the hydrocarbon concentration in the sample gas. The sampling system can give millisecond response times.

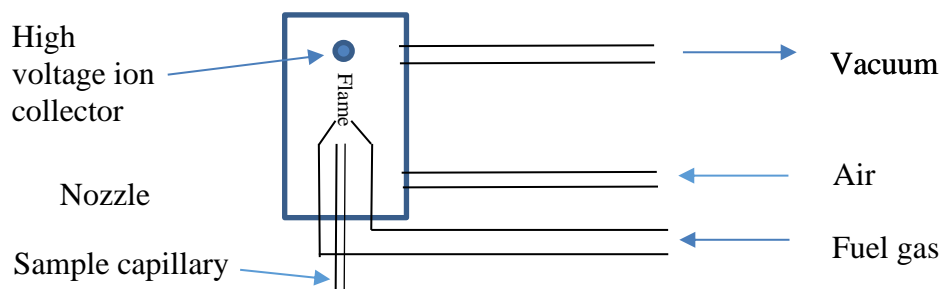


Figure 3.5 Cambustion Fast Response Flame Ionisation Detector (FFID)

The LDA operates accordance with the way shown in Figure 3.6: further exposition regarding LDA theory of operation is available in Buchave, P and George, WK (1976). A laser beam is split into two components, and one of the beams is frequency shifted with a Bragg cell (Dantec Dynamics, 2021). The two laser beams (shown in green in Figure 3.6) are of equal intensity and are coherent laser beams and focused onto the detector sampling region where they intersect: the sampling volume is typically a few millimetres long and less than a millimetre in diameter. The laser beams set up a fringe pattern due to interference in the plane of the two lasers.

Micron sized seeding particles are present in the flow and these particles reflect the laser beam fringes, and the reflection is detected in the receptor (shown in orange in Figure 3.6). The seeding particles, because of their velocity in the flow cause a Doppler shift in the reflected light which is detected in the LDA system (orange disk in Figure 3.6). The Doppler shift is measured in the system and calibrated against the speed of light - which is a universal constant, giving an accurate indication of the flow velocity and independent of local temperature. Different LDA probes, aligned in different orientations, are simultaneously used to measure different spatial components of the velocity field.

The slightly different frequencies of the lasers, caused by the frequency shift applied with the Bragg cell to one of the beams, causes the interference pattern to move in the direction of the sampled velocity direction shown in Figure 3.6 to enable the LDA system to determine the component of velocity of the seeded particles measured in the flow in the sampled direction. Therefore, seeded particles with zero or negative flow velocities can be distinguished from those with positive velocity. This is one of the strengths of the LDA method.

The LDA measurements were made with twin lasers aligned to measure orthogonal components of flow i.e. (U, W) or (V, W) where (U, V, W) were the instantaneous flow velocities in the (X, Y, Z) directions respectively. The system used was a DANTEC BSA F60 (Dantec Dynamics, 2021) burst analyser.

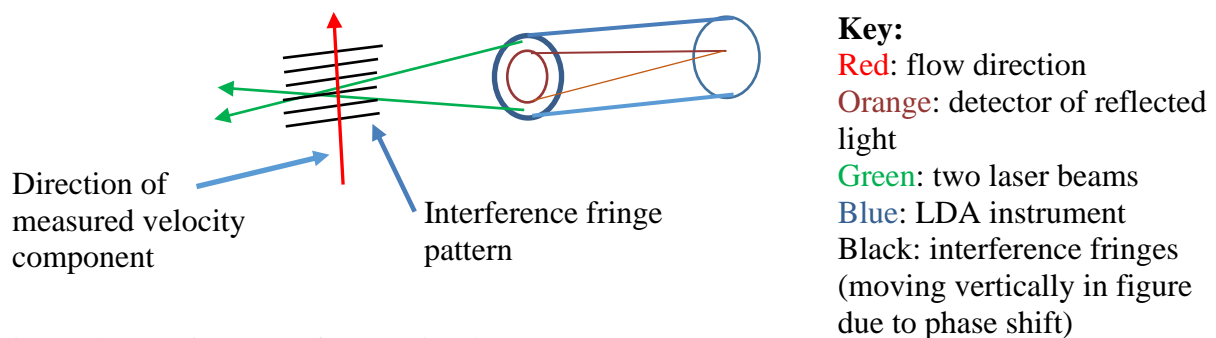


Figure 3.6 LDA mode of operation in one plane

Sugar solution in water was evaporated in a commercial haze generator placed just outside the tunnel inlet to provide the particulate velocity counting upon which the LDA system operated. Previous characterisation of the tunnel (Contini *et al*, 2008) has shown that the seeding generated in the experimental set up for this tunnel was acceptably uniform. The LDA operated at a frequency of approximately 100Hz, which reflects the seeding particle density entering the sampling region of the LDA.

Calibration of the detectors was achieved, in the initial experimental series, using a propane tracer in air with two standard calibration strengths. The response against these known

calibration concentrations was used to determine the response characteristic of the FFID against different known concentrations. Later experiments used a range of known concentration mixes to determine the linearity of response of the FFID to input concentration of the tracer gas. All experiments used gases of neutral buoyancy but with somewhat varying concentrations of trace gas dependent on the experimental series being investigated e.g. where measuring distal points from the release position an increased concentration of trace gas was appropriate to maintain sufficient signal level at the FFID detectors. Results in this work have been presented in the form of dimensionless concentration, which normalised the concentration measurements to take account of variations in the tracer gas concentration. Hence the results presented for dimensionless concentration were independent of propane trace gas concentration.

Puff release experiments were conducted Bronkhorst Hi-Tec F201C-FAC-22V flow controllers (Bronkhorst, 2021) placed inside the tunnel and close to the source release point – this enabled the acquisition of puff releases with near square wave profiles for the ensemble averages, though with any individual puff release intermittency in the signal was seen at the FFID due to temporal fluctuations in the concentration time profile of any given puff. Puff release experiments were therefore conducted with many individual puff releases being generated to ensemble average puff which conformed to the expected near square wave like profile. Statistical analysis of the integral doses of the puffs measured in the ensemble was carried out in further analysis.

3.3 Methods – Part 2: the experimental runs

An outline of the measurements conducted with a brief description is presented in Table 1. The St Thomas' Hospital East Wing building (EW) is referred to in two configurations, namely East Wing post-cladding installation (EWC) and unclad (EWUC) prior to introduction of a cladding layer that changed the sample from a plan view 'T' section through to a triangular cross section. The EW building configurations will be detailed in Chapter 4 and later chapters.

Table 3.1 Experimental Timelines and Overview

Series	Dates	Description
#1	2012/2013	EW clad and unclad concentration field measured in downstream planes from passive releases. Some distal points to release also measured. Measurement details and results presented in Chapter 4.
#2	August 2014	EW clad and unclad models tested with various configurations of passive releases at a range of heights, and one active vertical (AV) release height, for continuous tracer releases. Puff releases for the EWC and EWU cases at the AV release height and also for horizontal puff releases at a fixed height.
#3	September 2016	Cube cases for puff and continuous release at a range of angles of approach flow. Measurements were made with an active vertical (AV) release geometry and passive horizontal releases.
#4	October 2016	Limited cases for the flow field studied with the LDA wind (U , W) wind directions measured. Cube and EW isolated building cases were investigated.
#5	July 2017	Full series of flow field measurements for the cube at release position A near the vertex. Flow cases studied were (V , W) with the LDA only, and simultaneous measurements of (U , W) with the FFID. Flow field measurements with LDA and FFID were extended to cover a full range of

		building models from the EWC full building model (FBM) through to the isolated building being tested.
--	--	---

More specific details of the experiments conducted are presented in Table 3.2, with further details of the types of releases, release conditions and whether concentration field (via FFID) and/or flow field (LDA) measurements were made.

Table 3.2 Experimental Run Details: various release heights and angles of flow

Series	Building	Position	Angle	Release (CR/puff)	Passive/AV	FFID	LDA
#1	EW Clad/ EW Unclad	Vertex	Various	CR	Passive	√	X
#2	EWC/EWU	Vertex	-22.5°	CR/puff	P/AV	√	X
#3	Cube	A/B	-45°, -22.5°, 0°	CR/Puff	P/AV	√	X
#4	Cube/EW isolated	A/ Vertex	-45°, -22.5°, 0°	N/A	N/A	X	√
#5	Cube/EW	A/Vertex	-45°, -27.5°, - 22.5°, -17.5°, 0°	CR	P	√	√

3.3.1 Measurement Series 1

The first experiment (Series#1) as summarised in Tables 3.1 and 3.2 covered the EW clad and unclad buildings configurations, with the full building model as fully detailed later in Chapter 4 and Appendices 15.5 and 15.6. These measurements were solely of the concentration field, but with a range of directions of the approaching wind which enabled the full contribution to the total radiation dose term in the building roof zone to be established from a wide range of wind directions. The maximum dose rate was obtained where the plume was blowing directly over the building, corresponding to the main wind direction studied: a feature that was carried through to subsequent measurements.

Various passive release heights were investigated in Series#1. A further series of measurements were made during 2013 to investigate the plume (Y, Z) profiles for the clad building and a proposed taller (58m above datum ground level) stack at a series of downstream (X) co-ordinates. For these measurements, a vertical stack release was simulated at the proposed new stack position. The stack velocity ratio was matched to the mean wind speed for the primary wind direction of interest. These measurements showed that the dimensionless concentration was reduced to very low values near roof-level from the proposed taller stack; i.e. the proposed stack would be effective at reducing pollutant ingress into the EW building by reducing concentration near the EW air intakes, and in the roof area generally. Results are presented in the two reproduced published scientific papers presented in Chapter 4 and Appendices 15.5 and 15.6 of this thesis. The remainder of the measurements with the EW clad (EWC) and EW unclad (EWUC) buildings focused on the concentration fields related to a release at the existing stack position on the EW building on the North stair tower (referred to as the ‘vertex’ position in Tables 3.1 and 3.2). Flow fields in terms of velocity, and other measures from the velocity field, were also investigated in later experiment series. Limited LDA flow velocity measurements were carried out to determine the ‘speed up factor’ for releases from the existing stack in the main wind direction studied, in order that the stack velocity ratio (SVR) could be determined for the active vertical releases.

3.3.2 Measurement Series #2

Experiment Series 2 involved the EW building in EW clad (EWC) and EW unclad (EWC) versions of the main East Wing building models. The measurements provide a detailed investigation of plume dispersion in the near-field region of different configurations of a building with a full set of surrounding buildings. The timeline for the experiments was selected in order to carry out the detailed measurements of the concentration field for both cases at a series of downstream plans in the roof region and repeat these for an AV release at a fixed release height.

This series of measurements was designed to investigate the more challenging cases where there was greater plume entrainment into the building rooftop re-circulation region from the existing stack. These were expected to show the effects of enhanced plume entrainment on the model and investigate cases where the release point was even closer to the roof level than the existing stack i.e. for a lower stack release height.

The measurements were designed to assess the plume rise from the active vertical release with matched stack velocity ratio against the passive release cases. Measurements were made in the (Y, Z) plane at a range of three downstream (X) co-ordinates for a continuous release. In this way the plume centreline trajectory was mapped and the effective plume rise compared to the passive horizontal release profiles. The maximum concentration positions in the (Y, Z) plane were therefore determined.

The later sequences covered ‘puff’ releases for the AV configuration and also for a horizontal passive release at a fixed height close to the building roof. In this way the plume concentration maximum (PCM) position was determined for each configuration, enabling the puff release sequences to be measured at the PCM. The intermittency and statistical properties of the puff releases were investigated by using multiple puff releases in a given release position and sample position in the flow. Key quantities under investigation were the integrated dose per puff release established from the mean value of the ensemble sequence, but also the dose per puff histogram over the ensemble and statistical measures such as the coefficient of variation.

Table 3.3 shows a listing of the experiment dates and associated summary notes. The experiments presented a range of technical challenges which were overcome, and in each case the latter repeated data sets were carried forward to further analysis.

Table 3.3 Experiment Timeline Series 2: EW building; experimental log of events

Date	Experiment	Clad/ Unclad	Passive /AV	CR/ Puff	Notes
05/08/2014	Set-up	Clad	--	--	Setting up models
06/08/2014	2.2.1.1	Clad	Passive	CR	Vary release height Z_{RH}
07/08/2014	2.2.1.1	Clad	Passive	CR	Repeat 2.2.1.1 for 36 overflow points
07/08/2014	2.2.1.2	Unclad	Passive	CR	Vary release height Z_{RH}
08/08/2014	2.2.2.2	Unclad	AV	CR	Fixed Z_{RH}
11/08/2014	2.2.3.2	Unclad	AV	Puff	Fixed Z_{RH} . Diverter found to create mixing in the pipe – emission pulse therefore not sharp. Carry out calibration sequence.
12/08/2014	2.2.2.2	Unclad	AV	CR	Fixed Z_{RH} . Sample higher Z-axis points not covered in previous run.

12/08/2014	2.2.3.2	Unclad	AV	Puff	Fixed Z_{RH} . Square pulse release profile - no pipe mixing. Carry out calibration sequence to show no leaking. Collected inverse data set compared to previous 2.2.3.2 on 11/08/2014. This latter data set was used in analysis.
13/08/2014	n/a	Unclad	AV	Puff	Calibration sequence: calibrate Hi-Tec flow regulator against FFID so data file reads correct flow rate.
13/08/2014	2.2.2.1	Clad	AV	CR	Fixed Z_{RH} . Quick run check setup.
13/08/2014	2.2.3.1	Clad	AV	Puff	Fixed Z_{RH} . Square pulse release - no mixing in pipe.
13/08/2014	2.2.2.1	Clad	AV	CR	Fixed Z_{RH} . Full run tacked on to puff release sequence.
14/08/2014	2.2.4.2	Unclad	Passive	Puff	Fixed Z_{RH} . Measurement made with pulse switched flow.
15/08/2014	2.2.5.2	Unclad	Passive	Puff	Run puff release ΔT sequence with downstream measurement position X varied.
15/08/2014	2.2.4.1	Clad	Passive	Puff	Fixed Z_{RH} . FFID collision occurred on some data points causing high calibration drift which was corrected.
15/08/2014	2.2.1.1	Clad	Passive	CR	Vary Z_{RH} . Repeat full data set with nozzle adjustment. Look at data set differences.
18/08/2014	2.2.6.1	n/a	AV	CR	Flux balance: continuous release, fixed release height, sample (Y,Z) in plane downstream

3.3.2.1 Passive horizontal continuous releases with EW clad/unclad cases to get (Y,Z) concentration profiles at a range of downstream co-ordinate planes

3.3.2.1.1 Measurement with existing stack position (passive release): EW clad building

Measurements of the (Y,Z) concentrations with a continuous release (CR) were carried out at $X=16, 32$ and 48m in full scale downwind of the existing stack release position (see Figure 3.7). Given that the EW (North) stair tower was of height 240mm at wind tunnel scale (corresponds to 50m full scale with 2m datum offset) the following co-ordinates were measured. They intercepted the plume and showed the effects of plume interaction with the building roof out to the plume ‘tails’ both vertically and horizontally. The model was rotated by -15° to geographical North using tunnel co-ordinates centred on the emission stack. This represented wind coming from a bearing of 345° ; i.e. from NNW direction. Given that the West face of the building was oriented at a bearing of 7.5° to geographical North, this meant that the main wind direction tested was actually aligned at -22.5° to the West face of the building i.e. wind direction would impinge at 67.5° to the normal to the West face of the building as shown in Figure 3.7. Figure 3.8 shows the new stack, which is covered in Chapter 4 relating to the published papers reproduced in Appendices 15.5 and 15.6. However, the focus of this work will concentrate on result related to the former or existing stack.

The tunnel co-ordinate system was centred upon the stack position in the horizontal $X-Y$ plane with $Z=0$ at the floor of the tunnel (see Figures 3.3/3.4). The right-handed co-ordinate system

was chosen so that X pointed directly stream wise, Y was crosswise to the flow and Z was positive in a vertical direction. Positions of the two roof gamma-ray shine detectors (γ_1 , γ_2) are given in cylindrical polar co-ordinates in relation to the release position at the stack.

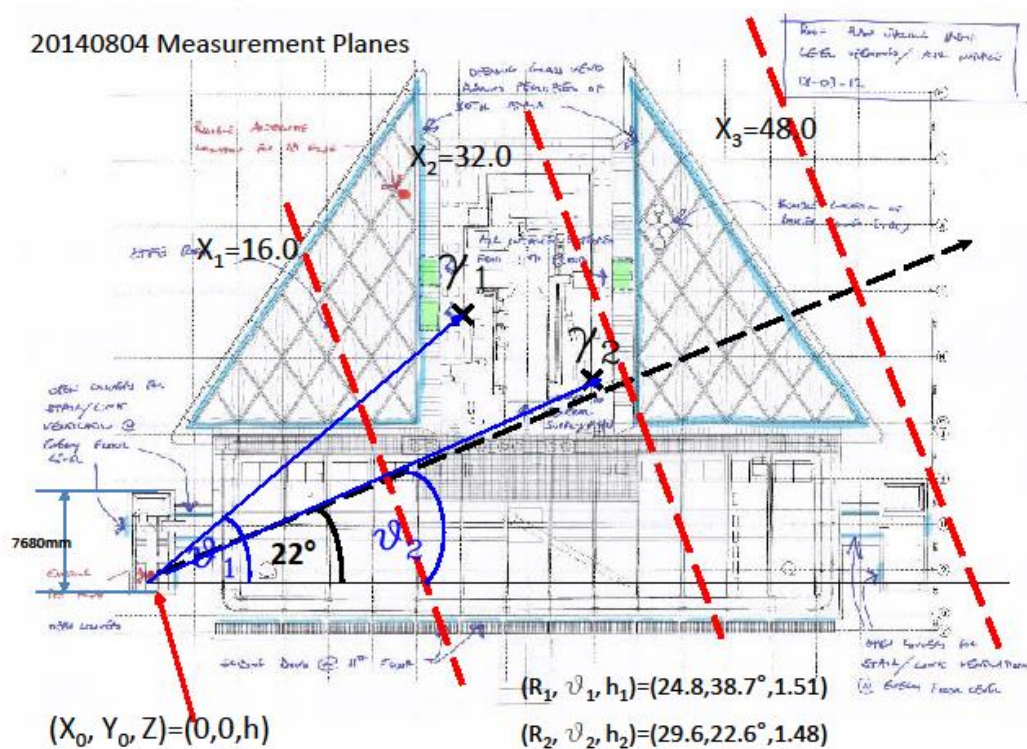
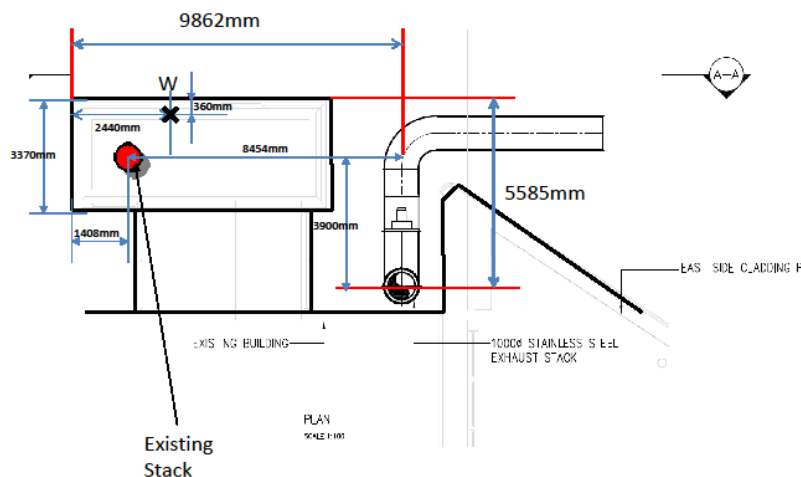


Image by ARUP/Hopkins and ISG PLC, with annotations by the author

Figure 3.7. Measurement planes shown on plan view of EW clad building

Figure 2. 2040730: STH EW (North) Stair Tower: Stack and Anemometer Co-ordinates



X is anemometer location (near W)

Image by Scitech Engineering Ltd, with annotations by the author

Figure 3.8. Stack location on EW North stair tower and new proposed stack

Figure 3.8 shows the EW North stair tower release position and the proposed new stack, with an expanded detail that can be related to Figure 3.7. The anemometer referred to in later experiments, marked with a 'W', is also shown.

Passive, steady releases were carried out and two Fast Flame Ionisation Detectors (FFIDs) working in parallel (offset at 20mm along the Y -axis co-ordinate) were used to obtain concentration sample data in two positions simultaneously. A one-minute sample at each traverse location was obtained. The FFID sampling Y co-ordinates were specified for the dominant FFID position Y_1 resulting in a simultaneous acquisition at Y_2 , where $Y_2=Y_1-20\text{mm}$. The release height Z_{RH} was varied between 5 to 50mm (1-10m full scale) above the building roof at the North stair tower platform stack position. The stair tower platform was the same height as the roof of the unclad building. The height of the existing stack was 3m (or 15mm in model space) above the stair tower roof, which therefore lay within the release height range investigated. In model scale Z_{RH} took the values of 245, 255, 265, 275, and 290mm, with a roof level of 240mm.

This experiment run corresponded to approximately $3 \times 7 \times 10 \times 5 = 1050$ measurement positions in the plane. At 1.1 minutes duration per point this was approximately 1155 minutes, and for the five release heights the total running time was approximately 20 hours. The run was carried out at 0.3 litres/min source flow rate that was the minimum selectable with 1.0% tracer concentration. The signal over-range count was evaluated post-run and it was found that 36 points were identified with signal over-range; approaching 1% of samples. This effect had been controlled by reduced by reducing the trace gas concentration to 1% from 1.5%, but not to a sufficient degree. The remaining 36 data points were re-acquired in a subsequent tracer release experiment.

In order for signal over-range effects to be eliminated the FFID gain was reduced to 40% of its previous value (one notch down on the amplifier), thereby reducing the signal level to 40% of its previous value. The tracer gas concentration was kept at 1% however, as the trace gas controller was near the bottom of its calibrated range. For the passive release, the flow rate was set at the minimum possible value of $0.31 \text{ l} \cdot \text{min}^{-1}$ in order to match the adjacent flow velocity as closely as possible. The internal diameter of the stack pipe for the passive release was 1.6mm and the outside diameter was 1.9mm. For this experiment the tunnel velocity was set at a standard figure of 2.0 ms^{-1} . The detector was recalibrated with 'zero air', and two calibration mixes 148 and 764ppm (tracer) for the new FFID voltage gain setting. Upon successful recalibration the 36 over-range points were re-measured to make a complete data set. Brief inspection of the plume measurement profiles indicated no systematic differences between the re-measured points and the original data set, which would indicate that there was no systematic under estimation of the plume centreline values (which being highest concentration would be expected to show the greatest number of over-range high signal measurement points). The reduced FFID gain setting was carried forward into the next passive release experiment with the EW unclad building.

At the end of the whole series of experiments the whole run was repeated with the passive release nozzle alignment undergoing a slight adjustment into the flow to test the sensitivity of the results to the alignment. The adjusted alignment was approximately 3° to the previous setting. A constant 1.0% tracer gas concentration was chosen to match the initial sequence [2.2.1.1]. The tracer flow rate was left on $0.31 \text{ l} \cdot \text{min}^{-1}$ to match experiment [2.2.1.2] in order to prevent any potential problem with the carrier flow rate. The consistency was found to be good between both experimental runs.

3.3.2.1.2 Measurement of existing stack: EW unclad building; passive release

The measurements were repeated as per [3.3.2.1.1] with the EW unclad building with 24 hours running time. The FFID gain was again set to 40% of standard setting with a trace gas concentration of 1.0%-2.0%. Trace gas concentration was set higher for more distal positions from the release to compensate for the reduction of FFID signal with distance. The sample time was 1 minute at each sample point. The sample space co-ordinates were set to reduce the run time by elimination of uninteresting measurement co-ordinates (i.e. those that return little or no mean concentration): this was achieved by reduction of the size of the sampled region. The building shape file (i.e. the computer stored co-ordinate file that defined the volume occupied by the building) was also different in accordance with the different building shape, and the 'jump bad points' option was selected in order to achieve as full a sample grid as possible. In model scale Z_{RH} took the values of 245, 255, 265, 275, and 290mm, with a roof level of 240mm. Indicative sample co-ordinates for this and subsequent runs are presented in Appendix 15.1.

The flow rate for the 2.0% trace gas experiment at $X=240\text{mm}$ needed to be increased to $0.311.\text{min}^{-1}$ as the increase of propane concentration reduced the carrier flow rate below the minimum operating level. Increasing the flow demand rate to $0.311.\text{min}^{-1}$ restored the normal operation.

3.3.2.2 Part 2: Confirm plume trajectory and (Y, Z) profile with active vertical releases

3.3.2.2.1 EW Clad building, steady, active vertical release with matched stack velocity

Same as [2.2.2] measurements described later with EW clad building shape. Run time was approximately 20 hours. The release height was fixed at $Z_{RH} = 255\text{mm}$. Four minute samples were used at each point.

3.3.2.2.2 EW Unclad building, steady, active vertical release, with matched stack velocity

The wind tunnel was run at selected 1ms^{-1} wind velocity with matched stack velocity ratio. $Z_{RH} = 255\text{ mm}$. Four minute samples were used at each point.

3.3.2.3 Part 3: Short duration releases with clad and unclad cases – active vertical release

A series of calibration releases was carried out to investigate the detected puff release profile to calibrate the actual puff dose against release duration. For this series of experiments the flow controller was located underneath the wind tunnel directly underneath the release stack projecting from the floor of the tunnel at the centre of the turntable. The source gas was released vertically from a stack of height 255mm from the tunnel floor.

3.3.2.3.1 EW Clad case: select fixed release height and measure downstream concentration variation with release times.

The release height was $Z_{RH} = 255\text{ mm}$ with release times of $\Delta T = 0.025, 0.05, 0.10, 0.25, 0.5, 1, 2,$ and 4 seconds.

3.3.2.3.2 EW Unclad case: select low release height and measure downstream concentration variation with release times.

The release height was $Z_{RH} = 255\text{ mm}$ with release times of $\Delta T = 0.025, 0.05, 0.10, 0.25, 0.5, 1, 2,$ and 4 seconds.

3.3.2.4 Part 4: Short duration horizontal passive releases with clad and unclad cases

3.3.2.4.1 EW Clad case: select low release height and measure downstream concentration variation with release times; passive release; puff release

These experiments were conducted with the release gas from the source directed horizontally and aligned with the direction of the downstream flow. The release stack was connected to a motorised arm with adjustable vertical movement. The lowest stack height was selected in order to maximise building effects i.e. 245mm height. Tracer gas was released at 1.0% at flow rate of $0.311\text{ l}\cdot\text{min}^{-1}$. The release height was $Z_{RH} = 245\text{ mm}$ and runs for $\Delta T = 0.025, 0.05, 0.10, 0.25, 0.5, 1, 2, \text{ and } 4$ seconds.

3.3.2.4.2 EW Unclad case: select same release height as [2.4.1] and measure downstream concentration variation with release times; passive release; puff release

Any differences between the two sequences could be attributed to the different building shapes between EW clad and EW unclad cases. The same release height was selected as for the previous experimental run. The release height was $Z_{RH} = 245\text{ mm}$ and runs for $\Delta T = 0.025, 0.05, 0.10, 0.25, 0.5, 1, 2, \text{ and } 4$ seconds.

3.3.2.5 Part 5: Short duration horizontal passive releases one building case

The unclad building was used for these observations. The position of the dominant FFID was adjusted to match exactly (but 1mm downstream) of the release nozzle. This was the measurement at the source location. Tracer gas at 1.0% was used with flow rate of $0.311\text{ l}\cdot\text{min}^{-1}$. The tunnel velocity was $1.0\text{ m}\cdot\text{s}^{-1}$. Measurements were then made at the same ΔT but with increasing downstream sample distances.

3.3.2.5.1 EW Clad: position offset sequence

Due to a limitation on experimental running time measurements with the EW clad were not carried out.

3.3.2.5.2 EW unclad: position offset sequence.

The distance downstream from the release nozzle was increased out to the measurement plane.

3.3.2.6 Flux Balance

3.3.2.6.1 No building: AV continuous release

As an overall measure of tracer flow conservation i.e. a flux balance was performed in order to validate the technique, with no building model present, which established the flow continuity of tracer by integration of concentration and flow advection velocity over a plane normal to flow velocity. By summation of the product of flow velocity and concentration values over the measurement plane an estimate of the tracer release rate was made and compared to the known release rate value. Vertical flow velocity profile according to the standard power-law fitted model was taken into account in these calculations.

A continuous vertical active release was carried out with buildings removed. Tunnel velocity was set to $1.0\text{ m}\cdot\text{s}^{-1}$ with vertical release at flow rate of $Q=0.64\text{ l}\cdot\text{min}^{-1}$. Tracer concentration was set at 0.5% and the plume (Y, Z) concentration mapped at $X=160\text{ mm}$.

3.3.2.7 Stack Velocity Ratio and tracer flow rate calculations for Active Vertical releases

The flow rate required for the stack velocity calculation estimated as follows. Assuming a 53m stack and 53m tall building corresponding to 255mm in model space. The weighted mean velocity at Heathrow Airport (Gallacher *et al*, 2016a) HTW was $2.745\text{ m}\cdot\text{s}^{-1}$ from direction 345° measured at 10m from ground level. Using a ground roughness length of 0.2m from R-

91(Clarke *et al*, 1979) suitable for that site the correction to 53m, the new clad building height from the power law, requires multiplication by a velocity factor of 1.477.

The measured wind tunnel speed-up factor for the 345° (from Series#1) wind bearing direction was:

$$S_{UF} = 1.75\text{ms}^{-1}/1.96\text{ms}^{-1} = 0.893$$

The tunnel undisturbed upstream wind velocity was selected to be 1ms^{-1} rather than the more commonly used value of 2ms^{-1} . At this speed selection the flow velocity was 0.75ms^{-1} at building height in the tunnel, in that case 250mm from floor level. This was the flow velocity at the building height but upstream where the buildings were not appreciably affecting the flow.

Therefore the effective wind speed at full scale was calculated as follows;

$$U_{eff} = 2.745 \times 1.477 \times S_{UF} = 3.62 \text{ ms}^{-1}$$

Stack Velocity Ratio (S_{VR}) given that the efflux velocity of 15.03 m/s:

$$S_{VR} = 15.03/3.62 = 4.15$$

Therefore: at model scale, with the tunnel running at 1.0ms^{-1} , the emission speed required V_o is: $V_o = 4.15 \times (1.50/2) = 3.113 \text{ ms}^{-1}$

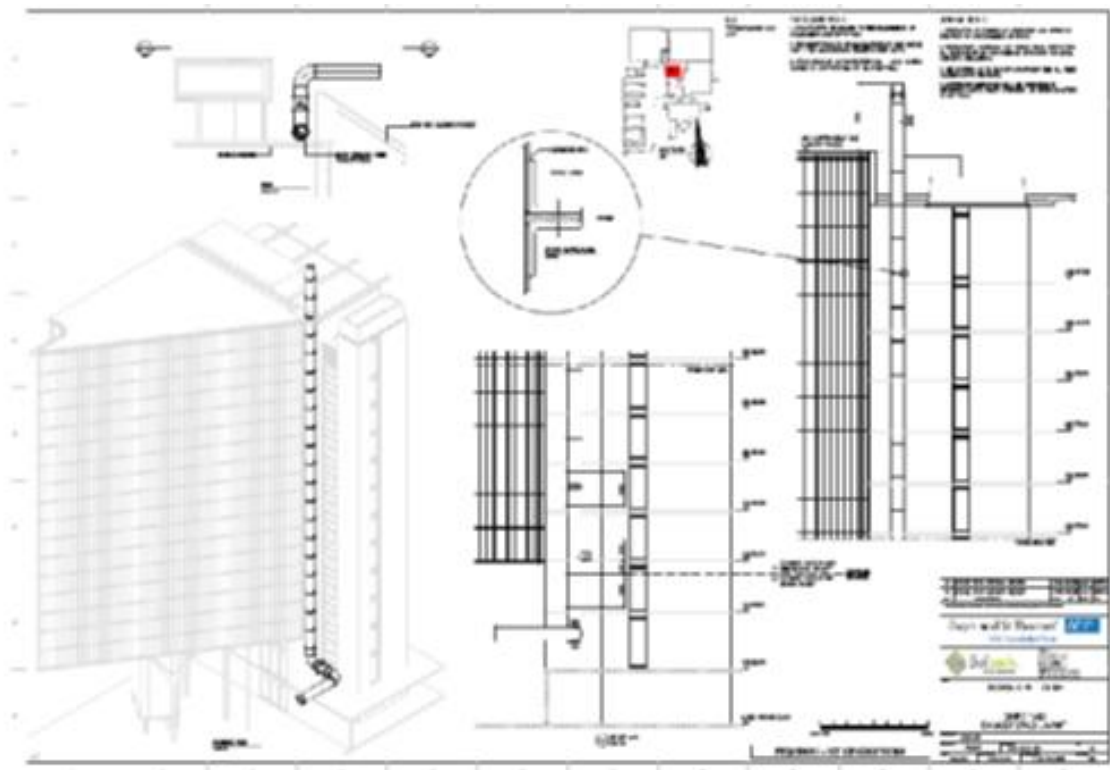


Image by Scitech Engineering Ltd.

Figure 3.9 EW Cladding project proposed work: proposed new stack is also shown

In Figure 3.9, the new proposed stack is shown in relation to the EW clad building (see also Figure 3.7). It was shown as 5m taller than the existing stack on the North stair tower of the EW. This work focuses on the emissions from the former EW stack, however information

regarding the doses received in the radiological assessment for the proposed stack is presented in Chapter 4 and associated Appendices 15.5 and 15.6 of this work.

For a stack of exit diameter of 354mm a 1.77mm internal diameter tube would be appropriate. The closest match available was an inner diameter of 1.9 ± 0.2 mm, and this was used in the experiment. The flow rate is Q :

$$Q = V_o A = 3.113 \times \pi (0.0019)^2 / 4 = 8.826 \times 10^{-6} \text{ m}^3 \text{ s}^{-1} = 0.530 \text{ litres/min}$$

where A is the cross-sectional area and V_o is the efflux velocity. In practice the lowest selectable flow rate of active tracer and carrier at the concentrations selected was 0.639 litres/min, therefore the actual release velocity was greater by 20.6% than that required for a matched flow and was marginally super-kinetic. In practice this was of the same order as the estimated cross sectional area error of the stack pipe used in the experiment (+22%, -20%) and was the closest that could reasonably be experimentally achieved.

3.3.2.8 Tracer Flow Rate Calculations for Passive Horizontal releases

The inner diameter of tube used was 1.6mm with an outer diameter of 1.9mm for the passive horizontal and horizontal puff release sequences. At a stack release height of 255mm the flow velocity was 1.5 ms^{-1} at building height for a selected wind tunnel speed of 2 ms^{-1} . The required source flow rate was therefore as follows.

$$Q = V_o A = 1.50 \times \pi (0.0016)^2 / 4 = 3.016 \times 10^{-6} \text{ m}^3 \text{ s}^{-1} = 0.181 \text{ litres/min}$$

The minimum selectable flow rate on the system was 0.31 litres/min. This was mainly due to a lower range limitation in the valve controlling the amount of tracer into the carrier gas in the flow. As such for the passive releases the flow was super-kinetic compared to the surrounding flow velocity by a factor of 1.71. For the passive puff release sequences the wind tunnel was run at 1 ms^{-1} to match the flow velocity used for the vertical puff releases. At this velocity the release from the nozzle was super-kinetic by a factor of 3.42 compared to the surrounding flow. However, it should be noted that the flow rate of tracer was correctly stated.

3.3.2.9 Release Duration for puff release experiments

We have that the plane of interest corresponds to $X=32 \text{ m}$, 160 mm at model scale. We are seeking $U_{eff} \Delta T / X \sim 1$ (for puff dispersion), where U_{eff} is the roof-top wind speed. As an order of magnitude $U_{eff} \sim 1 \text{ ms}^{-1}$ and $\Delta T = 0.025 \text{ s}$, so we have $U_{eff} \Delta T / X \sim 0.16$: well under the target range of unity. That defines, in general terms, the wind tunnel conditions.

At full scale, $U_{eff} \Delta T / X = 1$ leads to $U_{eff} \Delta T = X = 32 \text{ m}$. For the wind speed determined above [2.2.7] of 3.62 m/s, this implies $\Delta T \sim 9 \text{ s}$. Alternatively, if, for sake of argument we take $\Delta T = 60 \text{ s}$ then $U_{eff} \sim 0.5 \text{ m/s}$, perhaps not that meaningful.

From similitude, where t is the release time in real space this corresponds to a time $t = X / V_{eff}$:

$$t = X / V_{eff} = 32 / 3.62 = 8.8 \text{ s, where:}$$

$H / (V_{eff} t) = (H / 200) / (V_{wt} \Delta T)$; where V_{wt} is the wind tunnel reference velocity, so that:

$$\Delta T = (V_{eff}/V_{wt})(t/200) = (3.62/1.75) \times (8.8/200) = 0.0914s$$

Suggested sample times would therefore be the minimum $\Delta T=0.025$, $2\Delta T=0.05$, $4\Delta T=0.10$, 0.25, 0.5, 1.0, 2.0 and 4 seconds to approach a steady state release. This range corresponds to the eight measurement release times investigated for the puff releases i.e. encompassing the full range of interest corresponding to the full scale case.

3.3.2.10 Experiment Series #2: Summary

3.3.2.10.1 Experiment investigated the most testing cases with expected significant plume entrainment over the building for emission with the shortest stack. The distorted plume profiles were investigated for a range of conditions for the two building shapes using a passive horizontal release at a range of release heights.

3.3.2.10.2 Using a continuous vertical stack release with matched stack velocity ratio to the flow the plume rise and plume profiles were investigated at a range of downstream measurement planes to investigate the distortion of the plume in the building near field region. The plume rise was confirmed for the active vertical release with matched stack velocity.

3.3.2.10.3 Effects for short duration releases was investigated for both building cases at durations short enough to be affected by building generated turbulent eddies. These were investigated with active vertical stack puff releases for a range of release times, ranging from very short releases equivalent to short length scales on the building to relatively long times approaching continuous release flow. The detected time traces were measured at a range of locations ranging from proximal to the building to the plume centreline downwind.

3.3.2.10.4 Sensitivity analysis was carried out by readjustment of the passive horizontal release nozzle into the flow and measurement of the tracer concentration downstream to compare to the differences between the two measurement runs to determine the repeatability of the measurements.

3.3.2.10.5 Flux balance with a vertical isolated stack release was carried out, without buildings, to determine the summed release for the flow in a vertical plane normal to the flow. From the measured concentration plots the total tracer flow was estimated and compared to the actual release rate. This served as an independent check on the measurement system. The vertical velocity profile was taken into account in determining the tracer flow rate past the sample plane.

3.3.3 Experiment Series #3

The measurements were planned to provide a detailed investigation of plume dispersion in the near-field zones of a cubical building. Previous measurements were with actual building models (STH EW pre-cladding and post-cladding) and some of those were repeated for consistency and to assess the repeatability against previous experimental data.

For experiment series#3 an idealised building shape was investigated at normal incidence (0°), 22.5° and 45° incidence to flow. Limited measurements for the EW Clad case were repeated for continuous release to get a measure of repeatability of the measurement series in terms of peak dimensionless concentration value and location, and plume rise effects. Some of the main sequences of experiment #2 were repeated with the cubical building.

Table 3.4 Experiment Timeline Series #3

Date	Experiment	Building	Release	Passive /AV	Angle	CR/Puff
09/09/2016	2.3.1.1A	Cube	A	Passive	0°	CR
10/09/2016	2.3.1.3A	Cube	A	Passive	-45°	CR
12/09/2016	2.3.1.2A	Cube	A	Passive	-22.5°	CR
13/09/2016	2.3.1.1B	Cube	B	Passive	0°	CR
13/09/2016	2.3.1.3B	Cube	B	Passive	-45°	CR
14/09/2016	2.3.1.2B	Cube	B	Passive	-22.5°	CR
15/09/2016	2.3.2.1A	Cube	A	AV	0°	CR
15/09/2016	2.3.2.2A	Cube	A	AV	-22.5°	CR
15/09/2016	2.3.2.3A	Cube	A	AV	-45°	CR
16/09/2016	2.3.2.1B	Cube	B	AV	0°	CR
16/09/2016	2.3.2.2B	Cube	B	AV	-22.5°	CR
16/09/2016	2.3.2.3B	Cube	B	AV	-45°	CR
19/09/2016	2.3.4.1	EW	Vertex	AV	0°	CR
19/09/2016	2.3.4.2	EW	Vertex	AV	-22.5°	CR
19/09/2016	2.3.4.3	EW	Vertex	AV	-45°	CR
20/09/2016	2.3.3.1A	Cube	A	AV	0°	Puff
20/09/2016	2.3.3.2A	Cube	A	AV	-22.5°	Puff
20/09/2016	2.3.3.3A	Cube	A	AV	45°	Puff

3.3.3.1 Measure passive release concentration profiles

3.3.3.1.1A Experiment #1/A. Cube model with wind direction 0°, no surrounding buildings, source position A

Measurements of the (Y, Z) concentrations were carried out at X=80, 160, 240 and 400mm at model scale downwind of the stack release position. Cube dimension was 240mm at wind tunnel scale (corresponds to 48m full scale EW building roof height). These planes were proposed to intercept the plume and show the effects of plume interaction with the building roof out to the plume ‘tails’ both vertically and horizontally. The model was rotated so the flow was incident normally on the upwind face i.e. 0° using tunnel co-ordinates centred on the emission stack. Two source positions were investigated A and B (see Figure 10).

Passive horizontal releases were carried out in steady release conditions. Two Fast Flame Ionisation Detectors (FFIDs) working in parallel at variable offset along the Y-axis co-ordinate were used to obtain concentration sample data in two positions simultaneously. A one minute sample at each traverse location was obtained. The FFID sampling Y co-ordinates were specified for the dominant FFID position Y_1 resulting in a simultaneous acquisition at Y_2 , where Y_2 varied so as to not collide with the first FFID. The release height Z_{RH} was varied between 5 to 50mm (1-10m full scale) above the building roof height.

The Z sample starting co-ordinate was selected to be close to the plume centreline corresponding to the downwind position measured. In this way a concentration value close to the peak was measured. Also, this enabled the measurement low concentration ‘cut-off’ to be established: this was set at 2.5% of the concentration measured maximum. The sample patterns used were vertical FFIDs, offset from one another in the Y-axis. They first sampled up from the plume centreline until the cut-off threshold was reached. They then sampled down to the

minimum Z co-ordinate. This pattern was repeated at manually selected Y -axis co-ordinate positions to give the necessary cross-wind coverage. Points below the cut-off threshold were not measured, reducing the run time. The 2.5% cut-off threshold was chosen to enable sufficient sampling of the Gaussian distribution tails, but limiting run times to achievable values.

At one minute duration per point this was approximately 1500 minutes and for the 5 release heights the total running time was approximately 24 hours. The run was carried out at 0.3litres/min tracer flow rate (the minimum selectable with 1.0% tracer concentration). This is the minimum selectable and gave a slightly super-kinetic release velocity into the flow.

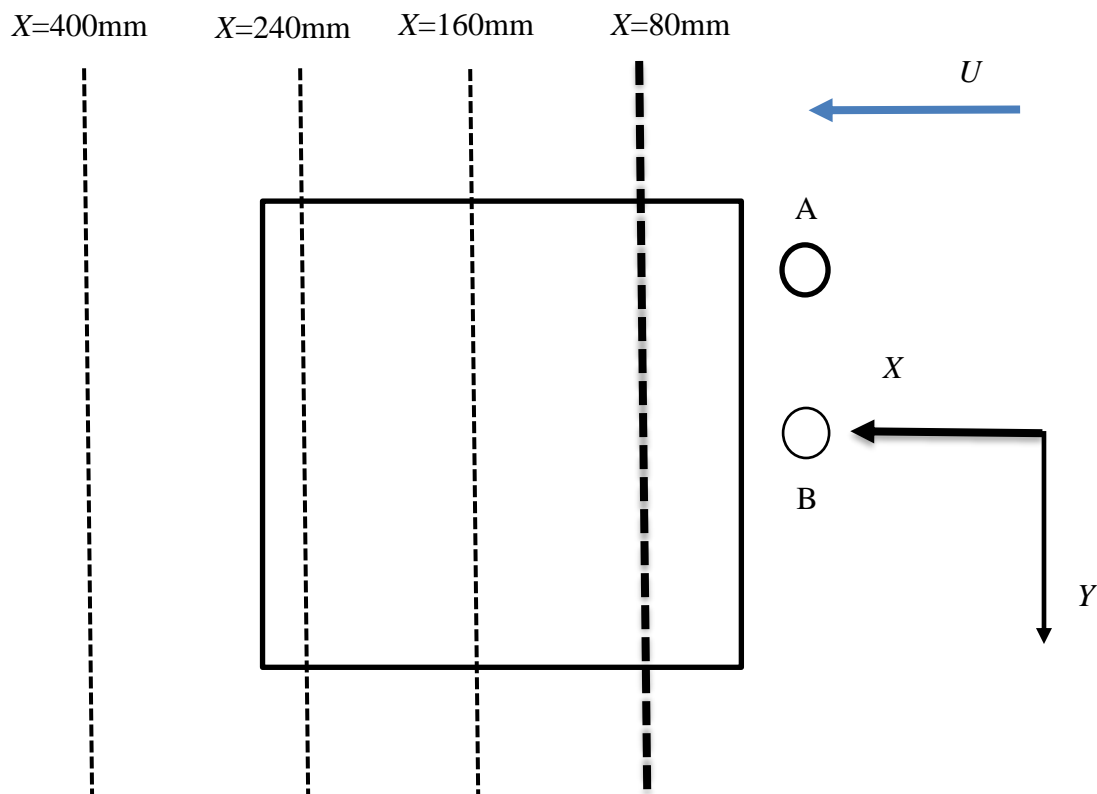


Figure 3.10 Cube Measurement Planes (Normal Incidence, 0°)

The tracer gas concentration was kept at 1% for the nearest measurement plane at $X=80\text{mm}$. For more distal sample planes the concentration was increased to the maximum practicable value of 1.8% to increase the detected signal on the FFIDs. For the passive release the flow rate was set at the minimum possible value of $0.3\text{l}\cdot\text{min}^{-1}$ in order to match the adjacent flow velocity as closely as possible. The internal diameter of the stack pipe for the passive release was 1.6mm and the outside diameter 1.9mm. The tunnel velocity was set at a standard figure of $2.0\text{m}\cdot\text{s}^{-1}$. The detector was recalibrated with 'zero air', and various calibration mixes chosen to represent the dynamic range of the experiment concentrations measured.

3.3.3.1.1B Experiment #1/B. Cube model with wind direction 0° , no surrounding buildings, source position B

The experiment was repeated with the source at position B, central to the upwind face of the cube. Sample co-ordinates were shifted along the positive Y -axis as shown i.e. co-ordinates were set in relation to the tunnel and not the building.

3.3.3.1.2A Experiment#1/A. Cube model with wind direction -22.5° , no surrounding buildings, source position A

The experiment was repeated with the source at position A, near the upwind vertex of the cube. Sample co-ordinates were the same as the previous experiment #1/A. The clockwise rotation of the tunnel turntable (as viewed from above) was achieved by selecting a -22.5° rotation command in the turntable traverse command file instruction (as this relates to wind direction impinging on the model).

3.3.3.1.2B Experiment#1/B. Cube model with wind direction 22.5° , no surrounding buildings, source position B

The experiment was repeated with the source at position B, central to the one face of the cube. Sample co-ordinates were the same as the #1/B position experiment.

3.3.3.1.3A Experiment#1/A. Cube model with wind direction -45° , no surrounding buildings, source position A

The experiment was repeated with the source at position A, near the upwind vertex of the cube. Sample co-ordinates were the same as the previous experiment #1/A.

3.3.3.1.3B Experiment#1/B. Cube model with wind direction -45° , no surrounding buildings, source position B

The experiment was repeated with the source at position B, central to the one face of the cube. Sample co-ordinates were the same as the #1/B position experiment.

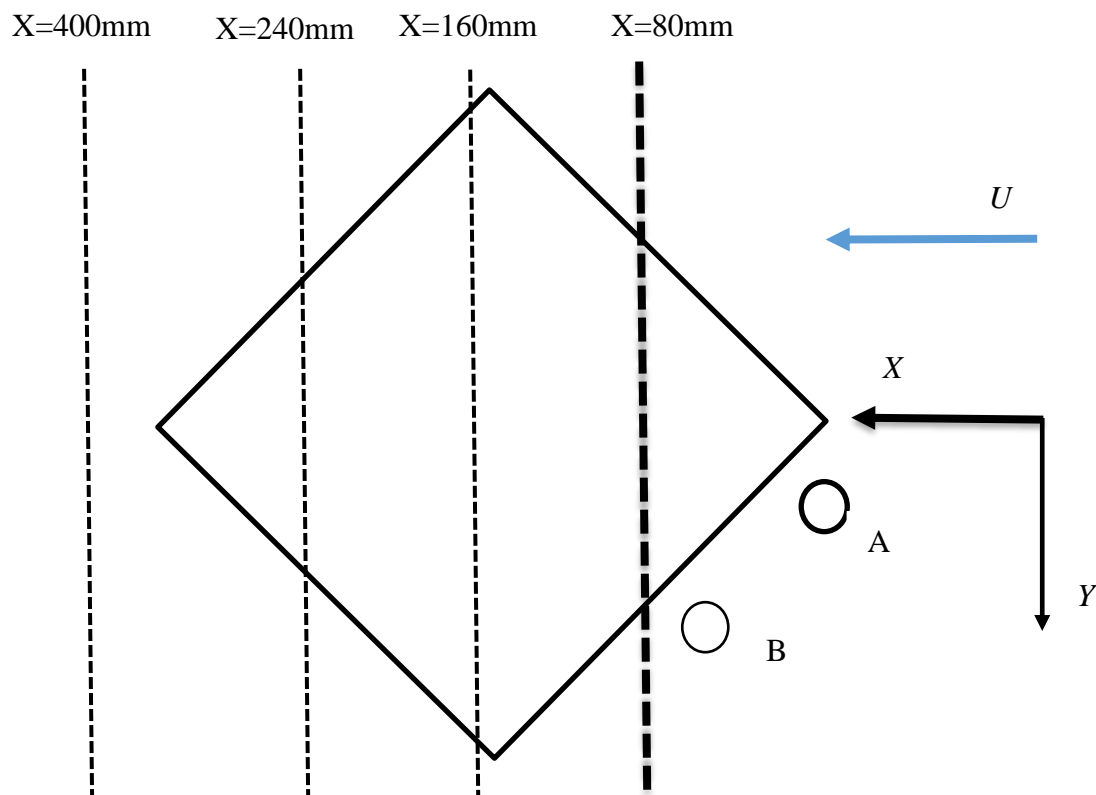


Figure 3.11 Cube Measurement Planes (Oblique, -45°)

3.3.3.2 Measure active vertical release concentration profiles with cube

3.3.3.2.1A Experiment#2/A. Cube building at normal incidence, steady active vertical release, with matched stack velocity.

Wind tunnel was run at selected 2.0ms^{-1} wind velocity. FFID gain setting was at 100% as previously. Flow rate of 1.06litres/min was set to match velocity profile and required stack velocity ratio. One minute samples were used throughout. Running time was less than approximately 9 hours.

3.3.3.2.1B Experiment #2/B. Cube model with wind direction 0° , no surrounding buildings, source position B

The experiment was repeated with the source at position B, central to the upwind face of the cube. Sample co-ordinates were the same as the #2/A position experiment.

3.3.3.2.2A Experiment#2/A. Cube model with wind direction -22.5° , no surrounding buildings, source position A

The experiment was repeated with the source at position A, near the upwind vertex of one face of the cube. Sample co-ordinates were the same as the #2/A position experiment.

3.3.3.2.2B Experiment#2/A. Cube model with wind direction -22.5° , no surrounding buildings, source position B

The experiment was repeated with the source at position B, near the upwind vertex of one face of the cube. Sample co-ordinates were the same as the #2/A position experiment.

3.3.3.2.3A Experiment#2/A. Cube model with wind direction -45° , no surrounding buildings, source position A

The experiment were repeated with the source at position A, near the upwind vertex of the cube. Sample co-ordinates were the same as experiment #2/A.

3.3.3.2.3B Experiment#2/B. Cube model with wind direction -45° , no surrounding buildings, source position B

The experiment were repeated with the source at position B, central to the one face of the cube. Sample co-ordinates were the same as the #2/A position experiment.

3.3.3.3 Short duration active puff vertical releases with cube

3.3.3.3.1A Experiment#3/A. Cube case at 0° incidence, stack position A near vertex: selected fixed release height and measured downstream concentration variation with release times for active releases.

The release height was $Z_{RH} = 255\text{ mm}$ and the release times $\Delta T = 0.10, 0.25, 0.5, 1.0\text{ second}$.

3.3.3.3.2A Experiment#3/A. Cube case at -22.5° incidence, stack position A near vertex: select fixed release height and measure downstream concentration variation with release times for active releases

Repeated as for #3/A.

3.3.3.3.3A Experiment#3/A. Cube case at -45° incidence, stack position A near vertex: select fixed release height and measure downstream concentration variation with release times for active releases

Repeated as for #3/A.

3.3.3.4.1-2-3 Experiment #4. Repeated EW Clad model (no surrounding buildings) with different wind directions

Measurements of the (Y,Z) concentrations were carried out at $X=16, 32, 48$ and 80m in full scale downwind of the existing stack release position (see Figure 7). The EW (North) stair tower was of height 240mm at wind tunnel scale (corresponds to 50m full scale with 2 metre datum offset). The model will was rotated by $0^\circ, -22.5^\circ$ and -45° to geographical North using tunnel co-ordinates centred on the emission stack from the EW face.

Active releases were carried out in steady release conditions. Two Fast Flame Ionisation Detectors (FFIDs) working in parallel offset at various distances along the Y -axis co-ordinate were used to obtain concentration sample data in two positions simultaneously. A one minute sample at each traverse location was obtained. The FFID sampling Y co-ordinates were specified for the dominant FFID position Y_1 resulting in a simultaneous acquisition at Y_2 . The release height Z_{RH} was fixed at 255mm . The height of the existing stack was 3m (or 15mm in model space) above the stair tower roof, which therefore lay within the release height range investigated.

The SVR was recalculated to match the experimental conditions. The release position 'A' in relation to the leading edge of the cube matched the EW building condition at -22.5° angle of flow incidence i.e. the release point distance to the edge of the roof was the same with this direction of flow as was the case for the EW building. Position 'B' was offset the same distance from the cube nearest face as position A i.e. 24mm or $H/10$, where H was the length dimension of the cube. The distances of A and B to the nearest face of the cube i.e. $H/10$, were retained for the experiments at $0^\circ, -22.5^\circ$ and -45° wind incidence angles.

3.3.4 Experiment Series #4

During this experimental series LDA measurements were made with the cube model.

Table 3.5 Experiment Timeline Series #4

Date	Experiment	Building	Release	Passive/ AV	Angle	CR/Puff
October 2016	2.4.1	Cube	N/A	N/A	$0^\circ, -22.5^\circ, -45^\circ$	N/A
October 2016	2.4.2	EW clad only	N/A	N/A	$0^\circ, -22.5^\circ, -45^\circ$	N/A

The flow field for the cube model was tested with the cube centre in the roof plane at the centre of the wind tunnel turntable. The flow field in the (U, W) directions i.e. downstream and vertical directions, was tested over a range of positional co-ordinates, but with very limited sampling, as summarised below.

3.3.4.1 Cube Measurements

Table 3.6 Cube LDA measurements (co-ordinates in relation to the centre of the cube)

Plane/Axis	Angle	$X(\text{mm})$	$Y(\text{mm})$	$Z(\text{mm})$
XZ	0	$-1000, -64, 16, 96, 256$	0	$70-1000$
Y	0	0	-200 to $+200$	265
XZ	-22.5°	-96 to 237	0	$260-390$
XZ	-45°	-1000 to $+200$	0	$70-1000$

3.3.4.2 EW clad – isolated building

The EW building was placed with the source at the origin of co-ordinates for the -22.5° angulation of flow.

Table 3.7. EWC: LDA measurements (co-ordinates centred at vertex release position)

Plane/Axis	Angle	X(mm)	Y(mm)	Z(mm)
Z	0°	160	0	280-390
Y	0°	160	-100 to +100	280
Z	-22.5°	160	0	280-390
Y	-22.5°	160	-100 to +100	280
Z	-45°	160	0	280-390
Y	-45°	160	-100 to +100	280

3.3.5 Experiment Series #5

For experiment series #5 the flow field for the idealised cube building shape was further investigated at normal, -22.5° and -45° incidence to the approach flow, with some limited other cases at $\pm 5^\circ$ to the main direction studied of -22.5° . For the initial measurements the components of (V, W) were measured using the LDA appropriately oriented in the tunnel. Later measurements were made with the LDA and FFID working simultaneously and acquiring flow field data in (U, W): it should be noted that the LDA measurement was 4mm upstream of the FFID e.g. if the LDA was at 156mm the FFID would be at a distance of 160mm from the source. Further measurements for the EW Clad and EW Unclad cases were made for the (U, W) components of flow simultaneously with the FFID concentration measurements. The experimental cases covered in series #5 are summarised in Table 3.8.

Table 3.8 Experiment Timeline: Series #5

Date	Experiment	Building	Angle	X(mm)
14-15/07/2017	(V, W) flow cases	Cube	$-45^\circ, -27.5^\circ, -22.5^\circ, -17.5^\circ, 0^\circ$	80, 160, 240, 400
17/07/2017	V at low heights on roof, LDA only	Cube	-22.5°	80, 160, 240
19-20/07/2017	(U, W) cases with extended range and FFID	Cube	$-45^\circ, -27.5^\circ, -22.5^\circ, -17.5^\circ, 0^\circ$	80, 160, 240, 400
24/07/2017	(U, W) flow case	EWUC	-22.5°	400
24/07/2017	(U, W) flow case	EWC	-22.5°	400
25-26/07/2017	(U, W) flow case with FFID	EWC*	-22.5°	160

*EWC combination of building configurations ranging from full building model (FBM) those without North Wing, ECH through to an isolated EW clad building.

The following areas in Table 3.9 were investigated in this series of experiments.

Table 3.9. Methods: outline measurements summary for Experiment Series #5

No.	Objective
1	Collect cases of $(v' w')$ for downstream positions to potentially correlate v'^2 with σ_y
2	Measure upstream velocity profiles and $(v' w')$ at cube centre line (A position)
3	Collect cases of (v') at low heights to building to also enable correlation of v'^2 with σ_y
4	Repeat cases with $(u' w')$ and complete fuller data set and correlate w'^2 with σ_z
5	Extend velocity profiles measurements for cases already measured
6	Re-measure shear stress and turbulence intensity where required
7	Test sensitivity for lead edge vortex ± 5 degrees for flow field and concentration field
8	Obtain FFID data on $u' C'$ using LDA and FFID simultaneous data
9	Perform sensitivity test with surrounding buildings: EW \pm NW \pm ECH \pm EWlow

Methods: experimental conditions for series #5

The turntable was set up for Cube/A release case. The surface plotter was used with the previous definition file for the full STH model set to mark out the building shapes. The turntable was aligned so that the 0 degree case for Cube/A aligned the West face of the EW model. In this was the angle of wind attack on the EW and Cube could be set at the same value for the run files (previously the EW was tested at -15degrees, on top of an existing -7 degree offset: the half degree discrepancy was neglected).

The LDA was aligned to the cube model back face and the laser focus point (160mm offset from front face) was aligned to the model. The LDA alignment was adjusted to be horizontal and parallel with the tunnel centre line and turntable centre. The Z-axis height was adjusted to the correct to the model. The passive release vertical stack was aligned to the turntable centre using the LDA laser, to an accuracy of approximately 0.5mm. To match the release conditions the stack was run at a release rate of $Q=0.3$ litres/min with the nozzle used in the previous experiments. It was noted previously that the release was marginally super-kinetic (at approximately 2.5ms^{-1}) compared to the selected wind tunnel reference flow velocity of 2ms^{-1} . However, a lower release rate would have been on the operational limit of the flow controlled of 0.25litres/min, and operation at this value was expected to cause problems in calibration, control and consistency. The previously used flow release value was therefore retained. Given the upstream pointed direction of the LDA probe the minimum height that could be measured at roof level was 260mm.

A trial run (..Res_1.xls) was carried out to test the system at $Z_s=265\text{mm}$. Analysis of the figures indicated w'^2 (vertical turbulence velocity component) out of the tolerance range of the LDA acquisition system, causing peak value losses. The range was doubled for subsequent runs where this measurement was repeated. The correlation quantity of $-v'w'/U_{ref}^2$ was added to the analysis to for the (V, W) measurements. For the (v', w') measurement only the LDA was used i.e. it was not possible for concentration field measurements were made with a FFID simultaneously with this combination.

3.3.5.1 Collect cases of (v', w') -> correlate v'^2 with σ_y

- (1.1) Cube_-22.5deg_Xc=-90 ($X_s=80/A$, $Y_c=-34/A$) -> measure (v', w') with $Z_s = 260, 265, 270, 280, 300\text{mm}$ (lead edge vortex). Sample $-250 < Y_c < +250\text{mm}$ at 25mm intervals (22 sample points, with extra points where $Y_s=0$).
- (1.2) Repeat (1.1) at -17.5deg_Xc=-86 ($X_s=80/A$, $Y_c=-48/A$) -> sample downstream plane relative to release position A
- (1.3) Repeat (1.1) at -27.5deg_Xc=-92 ($X_s=80/A$, $Y_c=-19/A$) -> sample downstream plane relative to release position A.

- (1.4) Cube_-22.5deg_Xc=-10 (Xs=160/A, Yc=-34/A) -> measure horizontal at Zs=260, 265, 280, 320mm. Sample -250 < Yc < +250mm at 25mm intervals (21 sample points).
- (1.5) Cube_-22.5deg_Xc=70 (Xs=240/A, Yc=-34/A) -> measure horizontal (v' , w') at Zs=260, 265, 280, 320mm. Sample -250 < Yc < +250mm at 25mm intervals (21 sample points).
- (1.6) Cube_-22.5deg_Xc=230 -> (Xs=400/A, Yc=-34/A) -> horizontal planes in recirculation zone at Zs=30, 60, 120, 265(repeat), 320mm. Sample at Ys=30mm intervals -300 < Yc < +300m (21 samples)

3.3.5.2 Measure upstream velocity profiles and (v' , w')

Measure upstream profile at cube centre location (Ys=+96mm) upstream of cube position with cube removed.

- (2.1) No model: measure (v' , w') at range of heights Zs=30 – 400mm.

3.3.5.3 Collect cases of v'^2 at low heights to building -> correlate v'^2 with σ_y

Angled probe to ensure no surface reflections but no (w') measurements.

- (3.1) Cube_-22.5deg_Xc=-90 (Xs=80/A, Yc=-34/A) -> measure v' only with Zs =245, 250, 255 (lead edge vortex). Sample -200 < Yc < +200mm at 25mm intervals (18 sample points, with extra points where Ys=0).
- (3.2) Cube_-22.5deg_Xc=-10 (Xs=160/A, Yc=-34/A) -> measure v' only horizontal at Zs=245, 250, 255mm. Sample -250 < Yc < +250mm at 25mm intervals (21 sample points).
- (3.3) Cube_-22.5deg_Xc=70 (Xs=240/A, Yc=-34/A) -> measure horizontal (v') only at Zs=245, 250, 255mm. Sample -250 < Yc < +250mm at 25mm intervals (21 sample points).

3.3.5.4 Repeat same cases plus others with (u' , w') -> correlate w'^2 with σ_z

Also measure ($u'C'$) and concentration field at downstream positions.

- (4.1) Cube_-22.5deg_Xc=-90 (Xs=80/A, Yc=-34/A) -> measure (u' , w') and ($u'C'$) with Zs =260, 265, 280, 300mm (lead edge vortex). Sample -200 < Yc < +200mm at 25mm intervals (19 sample points, with extra points around Ys=0).
- (4.2) Repeat (2.1) at -17.5deg_Xc=-86 (Xs=80/A, Yc=-48/A) -> sample downstream plane relative to release position A
- (4.3) Repeat (2.1) at -27.5deg_Xc=-92 (Xs=80/A, Yc=-19/A) -> sample downstream plane relative to release position A.
- (4.4) Cube_-22.5deg_Xc=-10 (Xs=160/A, Yc=-34/A) -> measure horizontal at Zs=260, 265, 280, 300, 320mm. Sample -225 < Yc < +250mm at 25mm intervals (20 sample points).
- (4.5) Cube_-17.5deg_Xc=-6 (Xs=160/A, Yc=-48/A) -> measure horizontal at Zs=260, 265, 280, 300, 320mm. Sample -225 < Yc < +250mm at 25mm intervals (20 sample points).
- (4.6) Cube_-27.5deg_Xc=-12 (Xs=160/A, Yc=-19/A) -> measure horizontal at Zs=260, 265, 280, 300, 320mm. Sample -250 < Yc < +250mm at 25mm intervals (21 sample points).
- (4.7) Cube_0deg_Xc=16 (Xs=160/A, Yc=-96/A) -> measure horizontal at Zs=260, 265, 280, 300, 320mm. Sample -250 < Yc < +250mm at 25mm intervals (21 sample points).
- (4.8) Cube_-45deg_Xc=+10 (Xs=160/A, Yc=+34/A) -> measure horizontal at Zs=260, 265, 280, 300, 320mm. Sample -250 < Yc < +250mm at 25mm intervals (21 sample points).
- (4.9) Cube_-22.5deg_Xc=70 (Xs=240/A, Yc=-34/A) -> measure horizontal (u' , w') and ($u'C'$) at Zs=260, 265, 280, 300, 320mm. Sample -250 < Yc < +250mm at 25mm intervals (21 sample points).
- (4.10) Cube_0deg_Xc=96 (Xs=240/A, Yc=-96/A) -> measure horizontal at Zs=260, 265, 280, 300, 320mm. Sample -250 < Yc < +250mm at 25mm intervals (21 sample points).

- (4.11) Cube_-45deg_Xc=+70 ($X_s=240/A$, $Y_c=+34/A$) -> measure horizontal at $Z_s=260, 265, 280, 300, 320\text{mm}$. Sample $-250 < Y_c < +250\text{mm}$ at 25mm intervals (21 sample points).
- (4.12) Cube_-22.5deg_Xc=230 -> ($X_s=400/A$, $Y_c=-34/A$) -> horizontal planes in recirculation zone at $Z_s=30, 60, 120, 265(\text{repeat}), 320$ Sample at $Y_s=30\text{mm}$ intervals $-300 < Y_s < +300\text{m}$ (21 samples)
- (4.13) Cube_0deg_Xc=256 -> ($X_s=400/A$, $Y_c=-96/A$) -> horizontal planes in recirculation zone at $Z_s=30, 60, 120, 265(\text{repeat}), 320$. Sample at $Y_s=30\text{mm}$ intervals $-300 < Y_s < +300\text{m}$ (21 samples)
- (4.14) Cube_-45deg_Xc=230 -> ($X_s=400/A$, $Y_c=+34/A$) -> horizontal planes in recirculation zone at $Z_s= 30, 60, 120, 265(\text{repeat}), 320$. Sample at $Y_s=30\text{mm}$ intervals $-300 < Y_s < +300\text{m}$ (21 samples)
- (4.15) Cube_-45deg_Xc=-113-> measure horizontal at $Z_s=260, 265, 280, 300\text{mm}$
- (4.16) EW/Unclad_-22.5deg_Xs=400 -> measure horizontal at $Z_s= 30, 60, 120, 265, 320\text{mm}$
- (4.17) EW/Clad_-22.5deg_Xs=400 -> measure horizontal at $Z_s=30, 60, 120, 265, 320\text{mm}$

3.3.5.5 Extend velocity profiles measurements for cases already measured

See results from [1], [2], [3] and [4].

3.3.5.6 Re-measure shear stress and turbulence intensity where required

As [1], [2], [3], and [4] above.

3.3.5.7 Test sensitivity for lead edge vortex +/- 5 degrees

As per [1] and [4] above.

3.3.5.8 Get FFID data on ($u'C'$) for same planes as velocity profiles

Measure concentration profiles plus (u', w') and ($u'C'$) shown for cases in [4].

3.3.5.9 Sensitivity test with surrounding buildings: EW +/- NW +/- ECH

- (9.1) EW/Clad_only_-22.5deg_Xs=160 -> $Z_{RH}=265\text{mm}$, measure horizontals at $Z_s= 260, 265, 280, 300\text{mm}$. Sample to $-200 < Y_s < +200$ on 25mm spacing (18 samples, including extra points around $Y_s=0$)
- (9.2) Case (9.1) + NW
- (9.3) Case (7.1) + NW + ECH
- (9.4) Case (7.2) - NW + ECH (limited run with $Z_s=265$ only).

3.3.5.10 Archbishop's Palace – downstream cross wind profiles

- (10.1) EW/Clad_full_model_-22.5deg_Xs=400 -> $Z_{RH}=265\text{mm}$, measure horizontals at $Z_s= 30, 60, 120, 265, 320\text{mm}$. Sample $-300 < Y_s < +300\text{mm}$ at 30mm intervals.
- (10.2) EW/Clad_full_model_-22.5deg_Xs=800 -> $Z_{RH}=265\text{mm}$, measure horizontals at $Z_s= 30, 60, 120, 265, 320\text{mm}$. Sample $-400 < Y_s < +400\text{mm}$ at 40mm intervals.
- (10.3) EW/Clad_full_model_-22.5deg_Xs=1600 -> $Z_{RH}=265\text{mm}$, measure horizontals at $Z_s= 30, 60, 120, 265, 320\text{mm}$. Sample $-500 < Y_s < +500\text{mm}$ at 50mm intervals.

3.3.6 Experimental Errors

3.3.6.1 Errors in the measured concentration field

The dimensionless concentration χ is defined in equation [1] where C is the concentration at a given point in the flow field, U_{ref} is the wind tunnel reference velocity downstream measured at 1000mm from the tunnel floor, H is the building height and Q is the release rate of the

pollutant. Further explanation is given in Chapter 4, published papers as part of this thesis shown in Appendices 15.5 and 15.6, and subsequent chapters in this work.

$$\chi = \frac{CU_{ref}H^2}{Q} \quad [1]$$

Table 3.10 shows some selected results for the cube model of χ and the standard error on χ : the standard error is also shown as percentage error normalised to the mean. The values in the table are given for the sampling position closest to the maximum concentration position in the plume at a given downstream position $X/H=0.67$. The standard error of the mean of U_{ref} for the wind tunnel reference velocity over the included runs below was 0.031%. Results are presented for a passive continuous release of tracer into the flow and all dimensions are given in model scale (mm).

Table 3.10: Error quantities measured at plume concentration maximum ($X/H=0.67^*$)

Building	Release position	θ°	Z_{rh} (mm)	Y_{max} (mm)	Z_s (mm)	χ	SE of χ	SE/ χ (%)
Cube	A	-22.5	245	13	245	92.0	2.5	2.7
Cube	A	-22.5	255	0	250	81.7	6.4	7.8
Cube	A	-22.5	265	0	265	92.0	7.0	7.6
Cube	A	0	255	-20	265	48.1	2.6	5.5
Cube	A	-45	255	-10	255	89.2	6.4	7.2
Cube	B	-22.5	245	-10	265	37.8	1.3	3.5
Cube	B	-22.5	255	-10	275	33.0	2.0	5.9
Cube	B	-22.5	265	-10	295	47.2	3.0	6.4
Cube	B	0	255	0	275	42.5	1.9	4.6
Cube	B	-45	255	-10	275	37.1	2.8	7.5
EW Clad	Vertex	-22.5	255	-10	261	46.9	2.0	4.2
EW Unclad	Vertex	-22.5	255	-20	252	57.9	3.6	6.2

*- where $H=240$ mm is the height of the building in model scale, or 48m at full scale

From Table 3.10 the standard error (SE) expressed as a percentage of the measured value of dimensionless concentration χ varies between 2.7% and 7.8% for the range of experimental cases presented, with a mean value of 5.8% and sampled standard deviation of 1.7% for this statistic. The standard error for continuous tracer release experiments is not normally distributed, and it is necessary to include the influence of higher order moments of the probability distribution to calculate the SE values presented according to the method of Cochran, WG (1963).

3.3.6.2 Errors in the measured flow field quantities

Table 3.11 presented results for the measured errors in the advection velocities in the X, Y and Z directions: U , V and W , normalised to U_{ref} at or close to the plume concentration maximum (PCM). Values for the flow field quantities are given for the corresponding positions from Table 3.10 in section [3.3.6.1] or given at the spatially nearest available measured data point available from the data set used from experiment series five. Data for a range of different release heights is presented for the ‘A release position with respect to the cube model and for separate cases of the EW clad and EW unclad models. In the case of the EW clad model the results from the full building model are given, but for the EW unclad case the results are given for the full building model minus two downstream buildings of lower height compared to the EW unclad building.

Table 3.11: Error quantities in the normalised flow velocities near the PCM ($X/H=0.67$)

Building/ Release position	θ°	Z_{rh} (mm)	Y_{max} (mm)	Z_s^{*1} (mm)	U/U_{ref} Mean \pm SE ^{*2}	V/U_{ref} Mean \pm SE	W/U_{ref} Mean \pm SE
Cube/A	-22.5	245	13	245	0.740 \pm 0.011	0.268 \pm 0.004	-0.036 \pm 0.001
Cube/A	-22.5	255	0	250	0.815 \pm 0.011	0.167 \pm 0.003	-0.052 \pm 0.002
Cube/A	-22.5	265	0	265	0.881 \pm 0.007	0.061 \pm 0.004	-0.096 \pm 0.004
Cube/A	0	255	-20	265	0.699 \pm 0.012	--	-0.123 \pm 0.003
Cube/A	-45	255	-10	255	0.479 \pm 0.010	--	-0.051 \pm 0.003
EW Clad/ Vertex	-22.5	255	-10	265 ^{*3}	0.559 \pm 0.008	--	0.002 \pm 0.002
EW Unclad/ Vertex	-22.5	255	-20	260 ^{*4}	0.614 \pm 0.007	--	-0.004 \pm 0.002
Root Mean Square (RMS) ratio: %SE/Mean					1.4%	1.9%	3.8%

*1: Z_s is the actual sampled height; *2: Standard Error (SE); *3: $Z_{max}=261\text{mm}$; *4: $Z_{max}=252\text{mm}$

The relative magnitude of the SE values can be described by taking the root mean square (RMS) of the SE values for U/U_{ref} , V/U_{ref} and W/U_{ref} and dividing this figure by the RMS value of the respective means and expressing these as percentages – a measure of the relative magnitude of the SE for those results are presented in the bottom row of Table 3.11 showing a range of values between 1.4 to 3.8%.

In Table 3.12 the percentage standard error (normalised to the mean value of each quantity) is given for the turbulence intensity terms for (u' , v' , w') normalised to U_{ref}^2 . In the last column the mean vertical shear stress and SE are given separately due to the small magnitudes of the quantities involved. The ratio of the RMS SE to the RMS mean for each column is presented in the last row of the table: the SE% to mean expressed in this way varied from 3.2% to 10.0%.

Table 3.12: Error quantities in turbulence intensity close to the PCM ($X/H=0.67^{*1}$)

Building/ Release position	θ°	Z_{rh} (mm)	u'^2/U_{ref}^2 SE/mean (%)	v'^2/U_{ref}^2 SE/mean (%)	w'^2/U_{ref}^2 SE/mean (%)	$-u'w'/U_{ref}^2$ Mean \pm SE
Cube/A	-22.5	245	10.6	3.9	2.9	-0.0012 \pm 0.0003
Cube/A	-22.5	255	15.0	3.8	4.3	-0.0001 \pm 0.0004
Cube/A	-22.5	265	13.1	6.4	10.0	0.0019 \pm 0.0003
Cube/A	0	255	7.2	--	3.0	0.0155 \pm 0.0014
Cube/A	-45	255	10.7	--	2.4	-0.0001 \pm 0.0004
EW Clad/ Vertex	-22.5	255	5.3	--	3.0	0.0026 \pm 0.0004
EW Unclad/ Vertex	-22.5	255	5.1	--	2.6	0.0050 \pm 0.0004
Root Mean Square (RMS) ratio: %SE/Mean			8.3%	4.4%	3.2%	10.0%

*1: Y_{max} and Z_s values as per Table 11 for each respective release case

3.4 Discussion

An extensive range of measurements was performed using the wind tunnel at the University of Surrey. Various buildings ranging from the idealised case of the cube building, to provide generality to the findings from the measurements, through to a range of 'real world' cases from the St Thomas' Hospital site of the EW clad and unclad buildings were investigated. In all

cases the source release position was close to the target building under consideration and concentration values were measured very close to the source in the roof zone of the building.

The EW buildings, with surrounding full building model, were investigated for a range of passive release heights to determine the concentration field in relation to the roof. Coupled with this an active vertical (AV) release configuration was tested with a stack with matched stack velocity ratio to real world cases, to estimate the concentration field for AV releases. An error analysis was presented for the passive continuous releases showing that the expected error in the concentration field measurements, as converted to dimensionless concentration χ , was in the range of 2.7% to 7.8% for a range of cases selected. As a typical range of percentage error for the concentration field this is acceptably small in comparison to the variations in concentration that were seen in the experimental results between the different building models, release positions, release heights and sampled positions.

The results of an analysis of the flow field measurements are presented in Chapter 5. Typical errors in the turbulence intensities and shear stresses have been presented in this chapter and these results showed that standard error in these quantities was in the region of 10%. This level of error was acceptably small in terms of the scope and aim of the experiments to distinguish and differentiate between the flow field quantities for the parameters varied in the experiment.

Short duration ‘puff’ releases were performed over a range of times, ranging down to very short times of 0.025 seconds in the wind tunnel, were performed to simulate the effects of ‘spike’ releases and the consequent doses from pollutant exposure these would cause in the full scale, or real world, scenario.

Further experiments accurately mapped the concentration field for the cube proximal to the roof zone, to enable a more accurate determine of pollutant doses from near-roof releases, for a range of experimental conditions for release height and angle of approach flow to the building. For the cube, an extensive range of puff release experiments were made to analyse the statistical nature of the dose received from pollutant in this type of release.

In order to relate concentration field values to flow field effects, detailed measurements were made of the flow field for the cube and EW cases. This involved combinations of the (U , W) components and (V , W) components, but given the experimental limitation that only two pairs of velocity components could be measured at a given time.

Further to this, the full building model for the STH site, which contained a range of other buildings, was investigated in a sensitivity analysis to the selective removal of nearby buildings and the effects on roof top concentrations at the target EW building. These experiments gave information on the likely ranges of pollutant and the relative influence of other building effects on roof top concentrations.

In summary, the measurements performed provided an extensive basis from which to assess the concentration and flow fields for a range of wind tunnel simulated conditions, and to provide a basis for understanding doses received for a range of conditions ranging from continuous release to relatively short intermittent puff releases.

CHAPTER 4: PLUME RADIATION MODELLING APPROACHES

4.1 Introduction

In this chapter the two scientific papers (Gallacher, DJ *et al* 2016a, 2016b) published in the peer-reviewed scientific *Journal of Radiological Protection* (JRP) in 2016 during the research work are presented: in accordance with the rules for publication from journals the final submitted manuscripts for publication are reproduced. These incorporate the changes arising from referee comments in the review process. In accordance with University of Surrey rules they are bound within the content of this thesis. It should be noted that the figures and tables are presented at the end of each reproduced paper as per the final submitted manuscripts. The papers are by the author of this thesis, and this is reflected in the lead author position – however, the author lists reflect the collaborative nature of the work in conducting the experiments, and the simulations, and also that the work was initially conducted to prepare a radiological site assessment for regulatory authorities. This work includes that included in the ADMS simulations (CERC, 2012a) for which recognition is also given in the co-author list.

4.2 Publication 1: Gallacher, DJ *et al*, 2016a

Publication 1 is entitled ‘Dispersion of positron emitting radioactive gases in a complex urban building array: a comparison of dose modelling approaches’ (Gallacher *et al*, 2016a) and is reproduced in Appendix 15.5 of this thesis. This paper presents results from the application of a range of methods for evaluating the radiation dose from release of radioactive material for the site under consideration. The aim was to establish the range of those dose estimates and to establish the suitability of the methods employed against the more sophisticated methods also investigated, the wind tunnel experimental methods and the ADMS model (CERC, 2012a). The paper was written by the first author during the period covered by PhD registration period, with comments and suggestions from the second author and main PhD supervisor, Professor Alan Robins. Most of the results for wind tunnel experiments in the initial experiment were obtained by Andrew Burt under the supervision of Dr Paul Hayden, a faculty member at University of Surrey. These wind tunnel results were provided to the author of this thesis for analysis of results, and to be converted into radiation dose estimates using methods developed by the author of this thesis in Publication 2 - but were also added to by a further series of experiments in which the author of this thesis carried out in conjunction with Dr Paul Hayden and were also used in this work. Susan Chadwick was primarily involved in the initial work for setting up the initial collaboration and collaboration with the author on the report prepared for the Environment Agency. Matthew Williams was employed by CERC and carried out the ADMS simulation, using sample points agreed with the author of this thesis. CERC provided their results to the author of this thesis and these concentration values were converted into effective dose to persons using methods developed by the author of this thesis and published in this paper. Overall, approximately 70% of the work for this paper is that of the author of this thesis, which includes writing the paper and submitting to peer review and through to publication: the remaining 30% is recognised as being from the other authors recognised in their citations as co-authors of the paper.

4.3 Publication 2: Gallacher, DJ *et al*, 2016b

Publication 2 is entitled ‘Conversion of simulated radioactive gas concentrations for a complex building array into radiation dose’ (Gallacher *et al*, 2016b). This paper deals with the complex process of converting a measured set of concentration values of a trace gas released into the wind tunnel, and sampled at a wide range of spatial positions, into a radiation dose estimate for persons in the roof zone of the ‘source’ building and in the wider surrounding area. The total

radiation dose, or effective dose, was comprised as that arising from inhalation of, immersion in and external gamma ray dose from the radioactive emissions. Methods to evaluate these dose terms are presented in some detail as applicable to a gaseous concentration field. The models described in the first paper are also included in the analysis and the associated methods to determine the radiation dose from these has been set out. The models were respectively the static hemisphere gas cloud, the moving hemisphere, the standard building wake model, a novel building wake model for roof top structures, ADMS and wind tunnel simulations.

Publication 2 is mostly the work of the author of this thesis, who developed the methods to convert concentration field in the wind tunnel into estimates of radiation dose to persons in the roof area and other areas of the site under consideration. However, particular acknowledgement is given to Professor Alan Robins, as second author, for the development of the novel building wake model for roof top structures (RTS) which is included as one of the methods presented within the paper. The third author, Dr Paul Hayden, was instrumental in assisting the main author in setting up wind tunnel experiments for this work. Both co-authors reviewed and commented on the manuscript before submission. The main first author wrote the manuscript and submitted the paper through the peer review process for the journal and dealt with all referee comments and enquiries. Overall, the paper is approximately 80% work from the author of this thesis.

For each of the papers reproduced, comments are made in a discussions and conclusions section [3] at the end of this chapter with particular emphasis on how far the papers answer the corresponding research questions posed in Chapter 1 covering the research questions set out for this work.

4.4 Discussion and Conclusions

Paper 1 covers the range of doses received in the site-specific building configuration. It was necessary, because of wind tunnel running time limitations, to develop a method of evaluating the gamma ray dose contributions in the roof plane from a single plane of measurements of the plume above the roof line. Mathematical methods were developed in Paper 2 to achieve this, also based on data from plume vertical spread in this zone. Paper 2 also covers the methods of converting wind tunnel measured concentration field values into radioactive gas concentrations, using wind rose data. The wind tunnel methods developed also enabled gamma ray dose contributions from a range of wind directions to be accounted for in the effective dose totals established for the various cases presented in Paper 1. ADMS effective dose results were also presented in Paper 1 and compared to the wind tunnel estimates.

The height of the release, the stack height, was also considered in detail in the first paper and the consequent effect on concentration field values and radiation dose to persons on the site. This was an important consideration in the specification of a new stack for the radiochemistry facility at the site under investigation. A new methodology for estimating concentration field values for roof top structures was also devised and presented in the second paper. Some limited dose results were available and are presented for regions just beyond the edge of the site under investigation. In low wind speed or calm conditions, the hemisphere models presented in the first paper, with dose evaluation methods detailed in the second paper, go some way towards investigating such conditions, albeit with rather crude assumptions. This is an area in which further work may be productive.

It may be seen that the papers address the initial research question topics identified in Chapter 1. Later chapters investigate and tackle research questions posed later in that chapter, covering different building and configuration cases: the velocity flow field, concentration field maps (fitted to modified Gaussian plume spread parameters) and the statistical nature of intermittent short duration releases and their effect on dose received by persons in the concentration field of the released plume.

Further work in later chapters refines the gamma ray dose evaluation using a Monte Carlo dose point kernel method using measured plume spread parameters and concentration field values, and these are compared against full-scale measured gamma ray dose rate values at the 'real world' site of investigation. Further work was done to investigate sensitivity of received dose on building configurations for the building model configurations investigated.

CHAPTER 5: FLOW FIELD ANALYSIS

5.1 Introduction

In the review Chapter 2, flow around obstacles and obstructions was discussed due to the fact that buildings disperse effluent in a complex manner due to the complex flow field encountered in the near field region of buildings. In particular, there are particular sensitivities to source configuration in relation to the building and source geometry with respect to the building (Meroney, 1982), where very limited cases for an isolated cube at normal and 45 degree incidence were considered. From work by Hort and Robins (2002) it was found that the cube at 45 degrees incidence to flow entrained more material into the building wake than other angulations, and a similar effect was seen with cylindrical structures. Robins *et al* (1997) showed wind tunnel results from a validation of ADMS simulations for the cube gave ADMS concentration values within approximately a factor of two for a range of tests, except for the 45 degree angulation with a stack height close to the building where the agreement was somewhat worse. It can therefore be seen that considerable uncertainties exist in the near field of buildings with respect to the flow field and the effects on advection and dispersion of pollutant, especially with regards to short stack releases i.e. releases close to the building height level.

To resolve or quantify these issues, flow field measurements were made in the EnFlo wind tunnel for a number of model configurations. These were not intended to be thorough investigations of flow around the the buildings of interest, but measurements sufficient to characterise the flow conditions experienced by the dispersing plumes described in Chapters 6 and 7. These measurements of the flow field were done essentially to get a feel for the flow field for the experiments. Since the reference velocity U_{ref} has been defined at 1 metre from the wind tunnel floor and this corresponds to 200 metres above ground level at full-scale, and is defined in this way throughout this thesis, all of the concentrations presented in dimensionless form are referenced only to a flow velocity measured in the approach flow and more than four times the height of the building models used in the wind tunnel. Local variations near the roof of the building will not affect the normalisation using U_{ref} , so flow field results are not used explicitly in any further analysis in this thesis.

The upwind approach flow is shown later in this chapter but the velocity at the building height $U(H)/U_{ref}$ was 0.78 with respect to the free-stream flow at 1 metre height in the tunnel. The magnitude of the root mean square Reynolds stress downstream flow component u' , normalised to the mean advection velocity $U(H)$, i.e. $u'/U(H)$, took the value of 0.135 in the approach flow. The characteristic building Reynolds number was computed as follows from equation [1]:

$$Re = \frac{U(H)H}{\nu} \quad [1]$$

where ν is the kinematic viscosity of air calculated at standard temerature and pressure. The calculated value of Re was 20,534, well in excess of the threshold value of Reynold's number of around 4,000 marking Reynolds number independence of fully turbulent flow around both cylindrical and square bluff-edged bodies (Hort and Robins, 2002).

Figure 1.1 illustrates the complexity of the flow field for a cube at normal incidence, showing the expected flow features. Key features include the horseshoe vortex, the downwind recirculation region (labelled cavity), and the flow patterns over the roof and side faces, driven by separation at the leading edge and subsequent re-attachment. Flow field measurements to be described later will be referenced against this sketch. The effect of orientation will then be treated, in particular the -45° case.

Full details of the experimental tests completed were given in Chapter 3, including those conducted with the Laser Doppler Anemometry (LDA), for the characterisation of the flow field. These are summarised in Table 5.1.

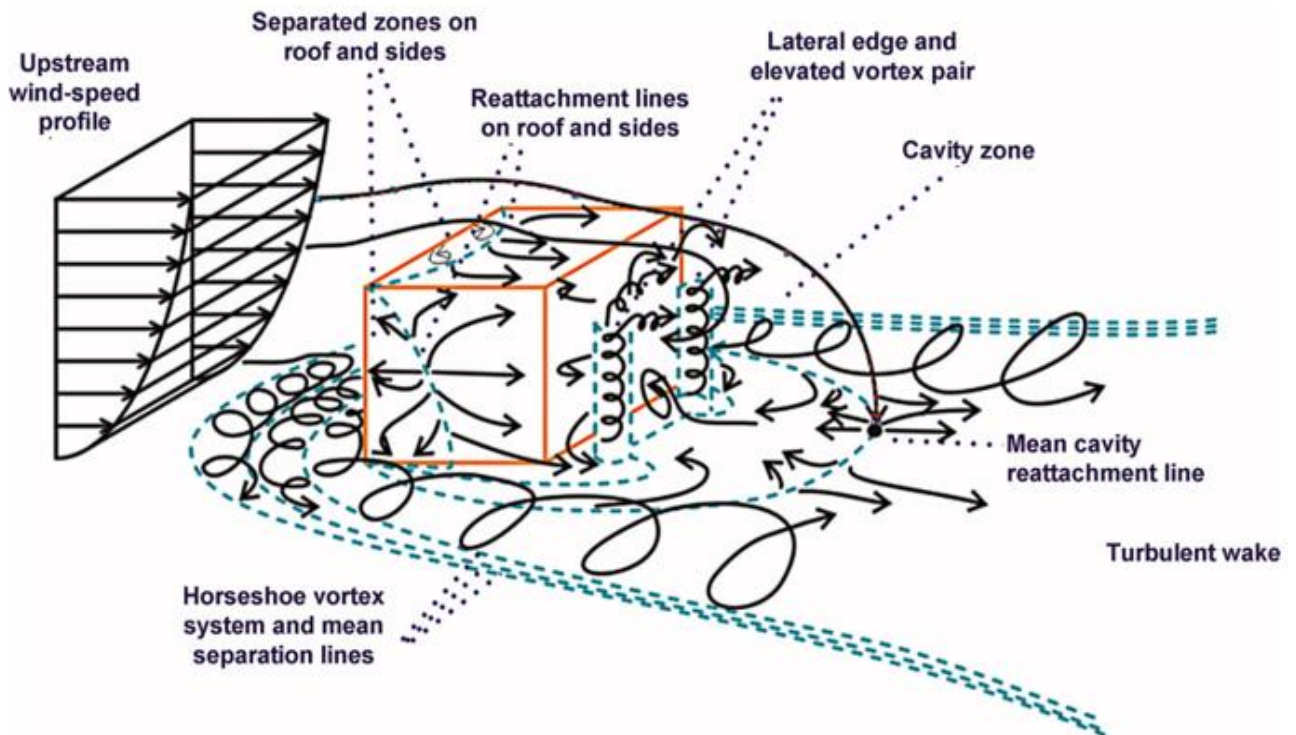


Figure 5.1 Flow field for a rectangular building at normal incidence. From Hosker (1984) and modified by Blocken et al (2011)

Table 5.1 Wind tunnel LDA experiments

Experiment	Building	Angle	X(mm)
(V, W) flow cases	Cube	-45°, -27.5°, -22.5°, -17.5°, 0°	80, 160, 240, 400
V at low heights on roof, LDA only	Cube	-22.5°	80, 160, 240
(U, W) cases with extended range and FFID	Cube	-45°, -27.5°, -22.5°, -17.5°, 0°	80, 160, 240, 400
(U, W) flow case	EWUC	-22.5°	400
(U, W) flow case	EWC	-22.5°	400
(U, W) flow case with FFID	EWC*	-22.5°	160

*EWC combination of building configurations ranging from full building model (FBM) those without North Wing, ECH through to an isolated EW clad building.

The co-ordinate system is a right-angled co-ordinate system, centred at release position 'A' as shown in Figure 5.2. The Z-axis is vertical with zero at ground level. For experiments with 'B' as the source the origin was relocated to 'B'.

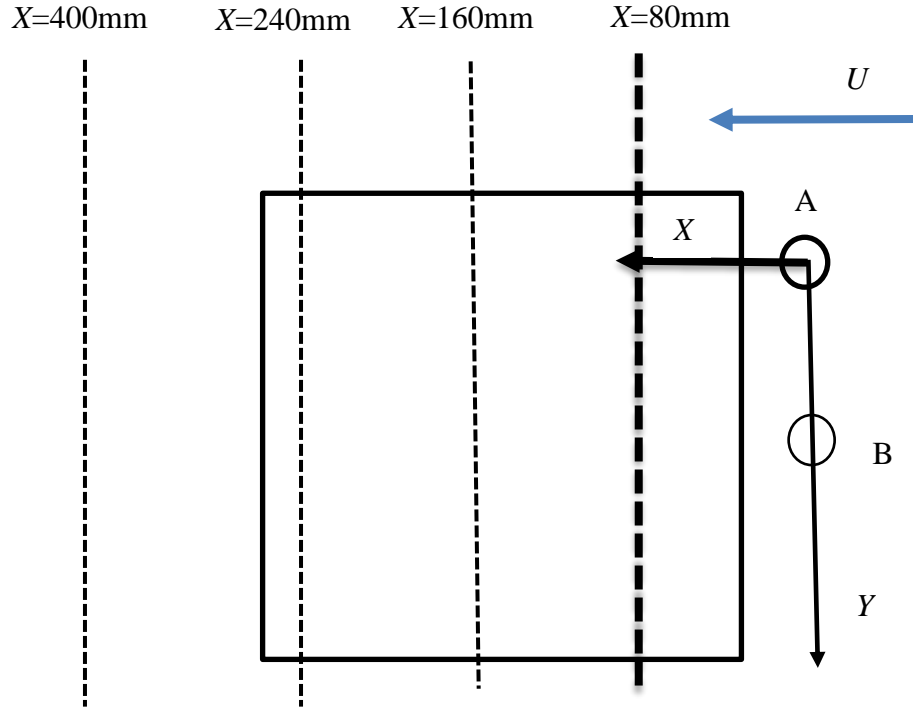


Figure 5.2 Plan view of co-ordinate system for the flow field measurements (Z-axis is vertical at 'A' in figure shown)

5.2 Approach flow

The upstream flow velocity variation with height is presented at the cube centreline position in Figure 3. The streamwise mean flow velocity is approximately 0.8 of the reference velocity at the building height, H .

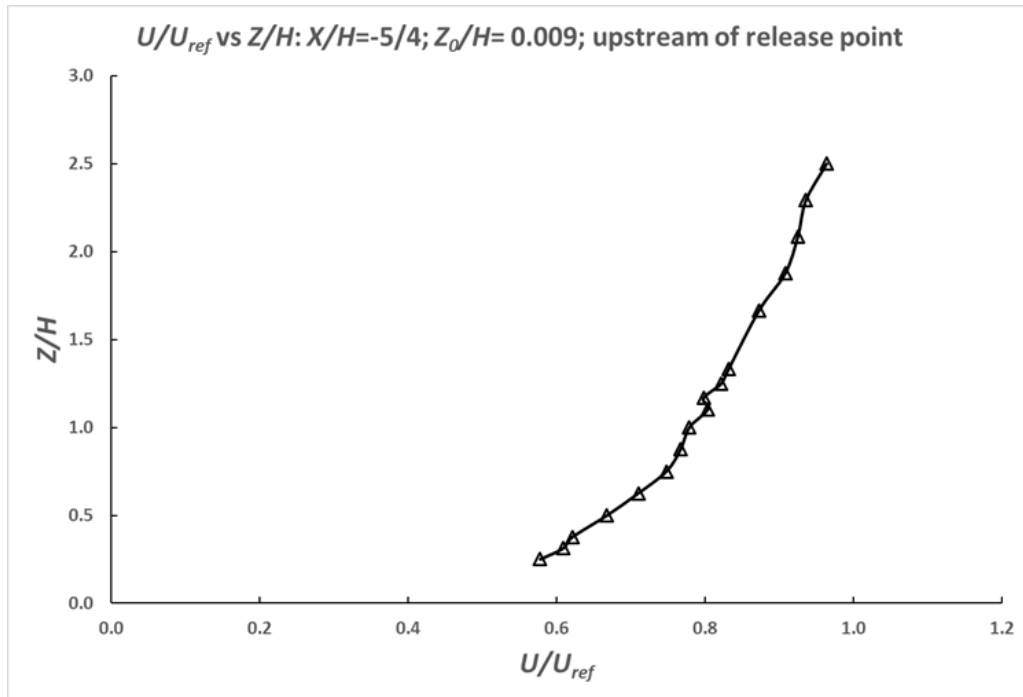


Figure 5.3 Downstream flow velocity upwind of the cube at $X/H=-5/4$ ($H=0.24m$)

A logarithmic law is expected to fit the lower portion of Figure 5.3. Figure 5.4 shows the streamwise normalised advection velocity plotted against the natural logarithm of the measurement height Z .

From R-91 (Clarke *et al*, 1979) the logarithmic velocity profile with height is given in equation [1].

$$u(z) = \frac{u_*}{k} \ln \left(\frac{z}{z_0} \right) \quad [1]$$

Applying equation [1], normalising to U_{ref} , and expanding log terms we obtain equation [2].

$$\frac{U(z)}{U_{ref}} = \left(\frac{u_*}{kU_{ref}} \right) \ln(z) - \left(\frac{u_*}{kU_{ref}} \right) \ln(z_0) \quad [2]$$

By comparison to the conventionally stated linear equation $y=mx+c$, where m is the gradient and c is the intercept, and by comparison with Figure 5.4 where the x-axis is plotted on a natural logarithmic scale so that $x=\ln(z)$ we have that the gradient and intercept are given in equations [3] and [4] and the ratio c/m is shown in equation [5].

$$m = \left(\frac{u_*}{kU_{ref}} \right) \quad [3]$$

$$c = - \left(\frac{u_*}{kU_{ref}} \right) \ln(z_0) \quad [4]$$

$$\frac{c}{m} = -\ln(z_0) \quad [5]$$

From where we obtain equations [6] and [7] for u_* and z_0 respectively, where k is von Karman's constant taken as 0.41.

$$u_* = mkU_{ref} \quad [6]$$

$$z_0 = \exp \left(-\frac{c}{m} \right) \quad [7]$$

From the gradient and intercept values given in Figure 5.4 and using equations [6] and [7], it was determined that the friction velocity for the experimental conditions in the wind tunnel was $u_*=0.137\pm0.23\text{ms}^{-1}$ with a standard error estimated from the linear regression driven by the uncertainty in extending the curve fitting towards ground level. Reference to the measured shear stress validates the central value of u_* . From NRPB Report R-91, Appendix A (Clarke, *et al*, 1979) the ratio of $u_*/u(10\text{m})$ where $u(10\text{m})$ is at 10m from ground level is in the range of 0.05 for a smooth open surface and up to 0.20 for a very rough surface, with a value of 0.1 over typical countryside: the corresponding value based on the mean of u_* given above was 0.13. The ground roughness length (given the scale of 1:200 for the model in the wind tunnel) was $Z_0=2.12\text{mm}$ (0.42m full-scale). For these experiments $U_{ref}=2.0\text{ms}^{-1}$. This leads to a Roughness Reynolds number, u_*Z_0/ν , of order 20 at model scale, confirming fully turbulent upwind conditions (see Snyder and Castro, 2002).

The boundary layer thickness H_{bl} is conventionally defined as the height from the surface at which the mean velocity reaches 99% of its free-stream velocity, or U_{99} . If it is assumed that

the log-law applies throughout the boundary layer then using the linear regression gradient and intercept values determined above and equations [2], [3] and [4] leads to equation [8] given below.

$$\ln(H_{bl}) = \frac{\left(\frac{U_{99}}{U_{ref}}\right) - c}{m} \quad [8]$$

Insertion of the values for intercept, c , and gradient, m , shown in Figure 5.4 leads to a value of $\ln(H_{bl}) = (0.99 + 0.1255)/0.1674 = 6.663$, so that $H_{bl} = 783\text{mm}$. However, the log-law does not generally apply throughout the boundary layer (typically it is confined to the lower 20%) so this estimate is likely to be too small. Previous work in the Enflo laboratory has established that this set-up provides a boundary layer depth of approximately 1 metre. Therefore, the reference velocity measured at the height of 1m did indeed measure the free-stream speed. Furthermore, it may be confirmed that since the maximum model building height was 240mm, the building models used were of the order of one quarter of the height of the boundary layer, H_{bl} .

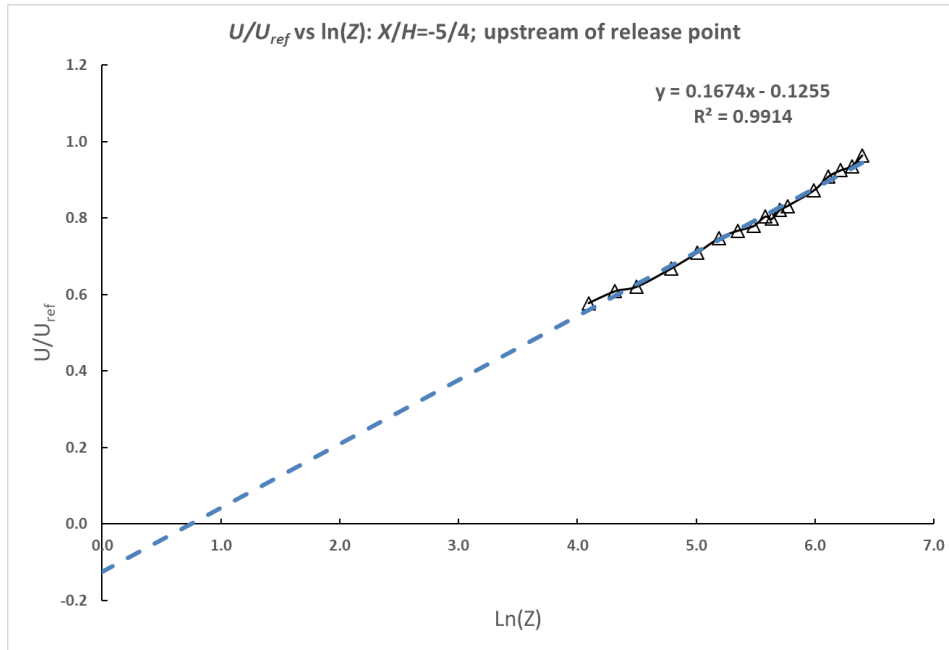


Figure 5.4. Logarithmic plot of flow velocity upwind of the cube at $X/H=-5/4$ ($H=0.24\text{m}$)

Figure 5.5(a) shows the turbulence intensity plots for the upstream flow from the measurements completed in July 2017 with an averaging time in the wind tunnel of 30 seconds. The height is normalised to the building height, H . It can be seen that the magnitude of the turbulence for the downstream (X axis) component u' is larger than the v' and w' components in the direction of the Y, Z axes respectively. Vertical and horizontal shear stresses are shown for completeness. The turbulence intensities peak near ground level. A continuous line is presented for u'^2/U_{ref}^2 which joins all experimental points but it should be noted that there is some experimental scatter which reflect the experimental tolerances on measurement of the unsteady components of velocity that are more evident at approximately one building height where $Z/H \sim 1$.

Figure 5.5(b) presents the data that produced Figure 5.5(a) but normalised to the friction velocity u_* and plotted height against boundary layer depth H_{bl} . The vertical component of turbulence intensity w'/u_* was reported from NRPB Report R-91 (Clarke, *et al*, 1979) for neutral stability to be approximately 1.3 within the first few tens of metres from ground level.

From Figure 5.5(b) w'/u_* peaks at a value just below 1.1 at a height of 24m at full-scale broadly consistent with this value. More recent values have been presented for the neutral stability case for the London area (Wood, CR, *et al*, 2010) for u'/u_* , v'/u_* and w'/u_* of 2.3, 1.85 and 1.35 and these may be compared to the respective peak values from Figure 5.5(b) of 1.81, 1.31 and 1.06. The latter figures follow the same trend but take values which are in the range of 70-80% of those given for the London area, nevertheless showing broad agreement given the differences between the two comparisons.

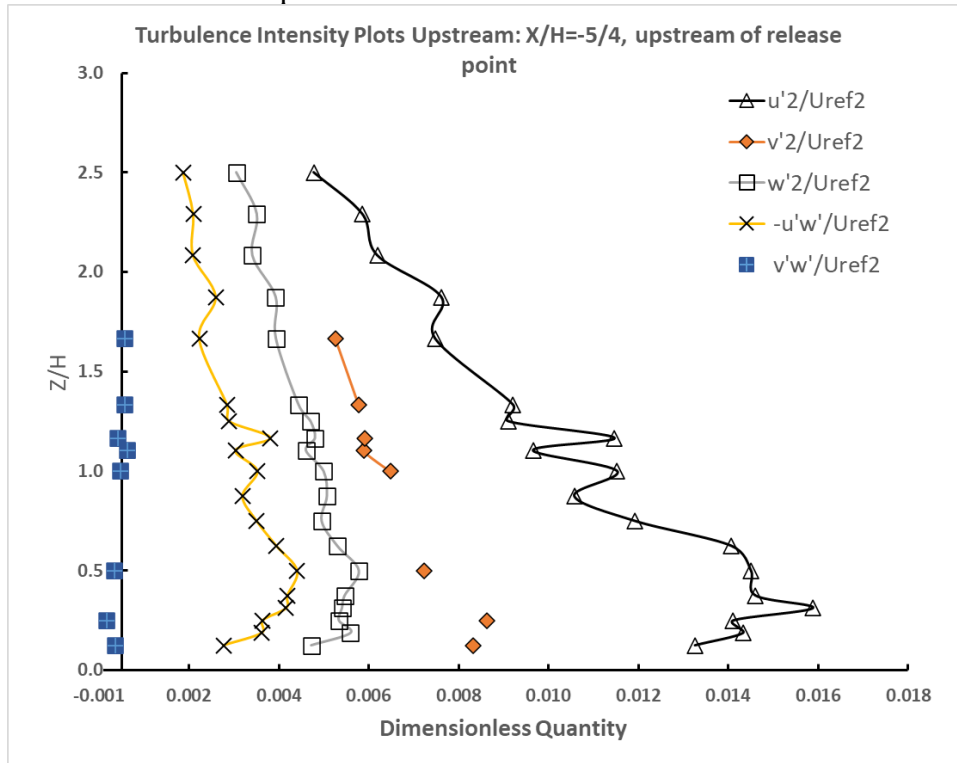


Figure 5.5(a) Turbulence intensity plots against height Z/H for $X/H=-5/4$ ($H=240\text{mm}$)

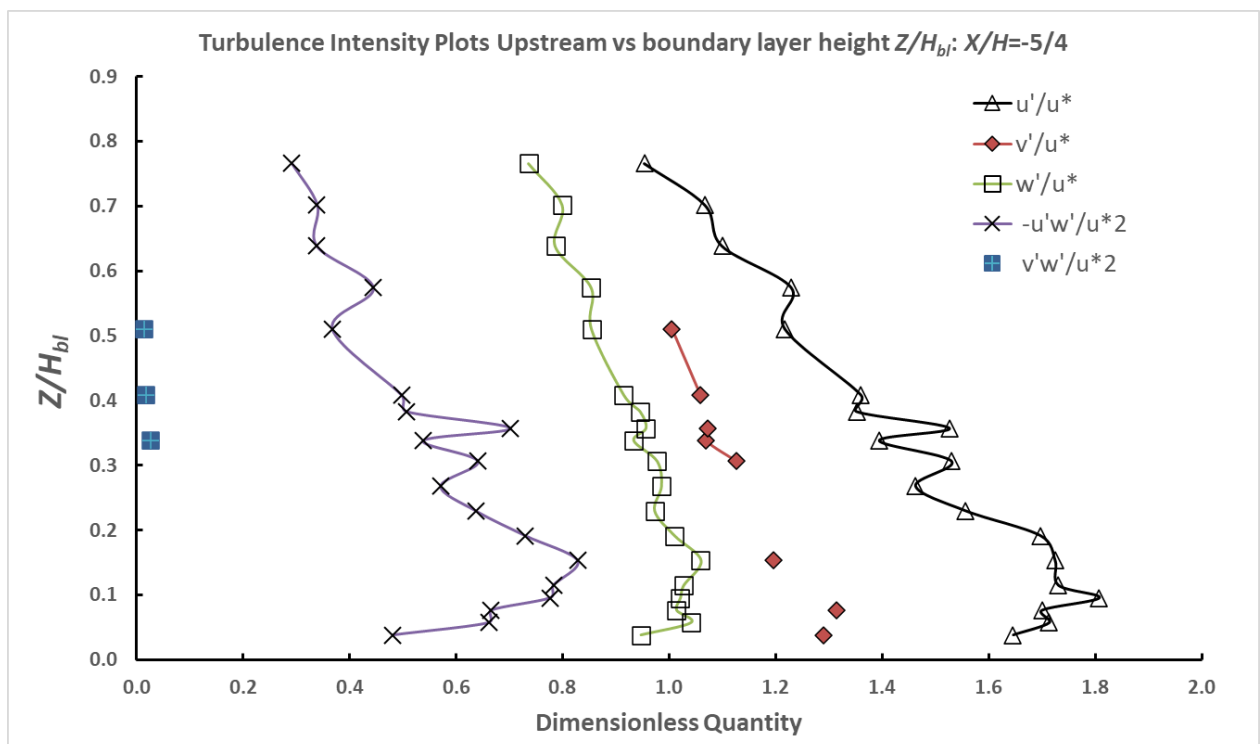


Figure 5.5(b) Turbulence intensity normalised to u^* plots against Z/H_{bl} for $X/H=-5/4$

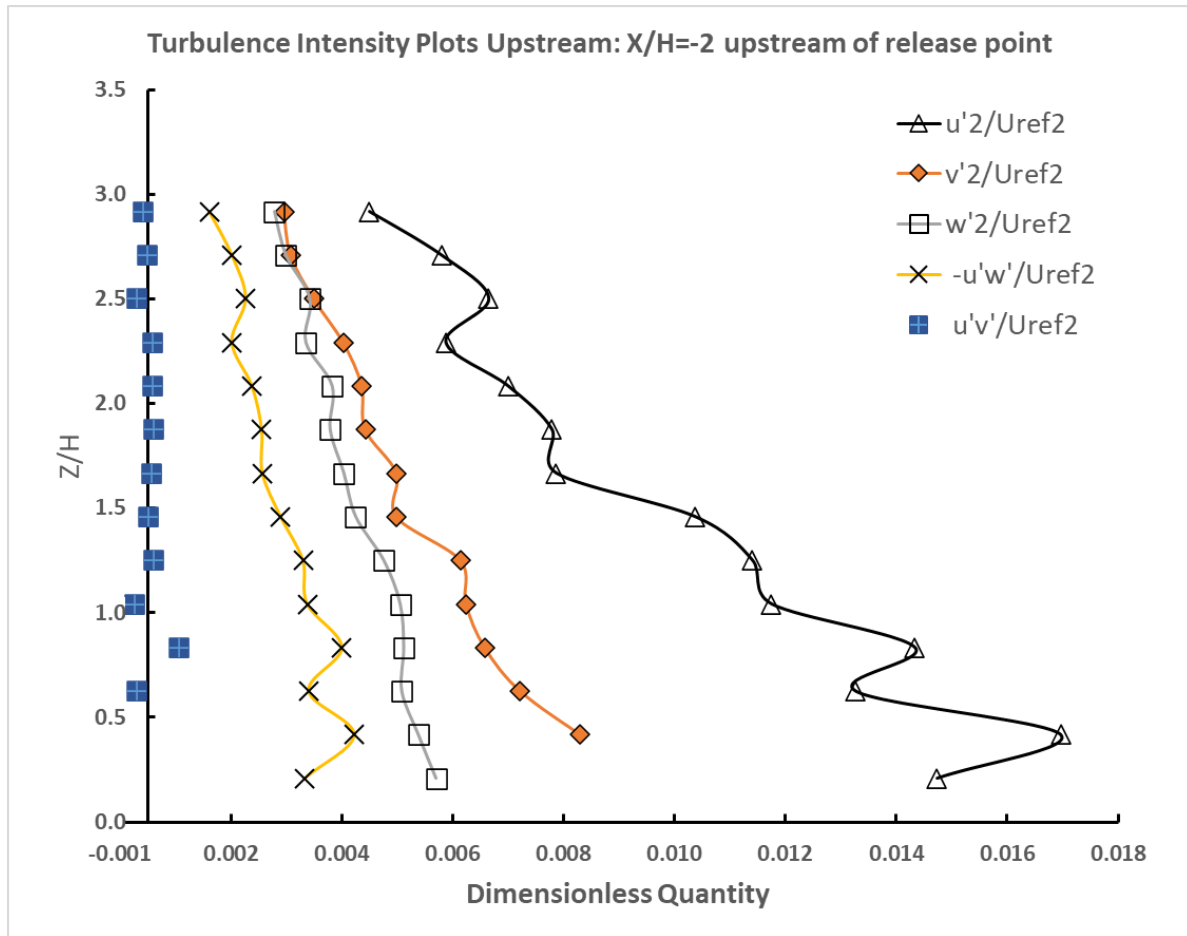


Figure 5.6 Further turbulence intensity plots against height Z/H for $X/H=-2$ ($H=240\text{mm}$)

Further results from a repeat experiment in June 2019 for the upstream flow, with no building downstream, are presented in Figure 5.6 showing the turbulence intensity. The results for the turbulence of v' are more complete in this case. The data shows that the measured values were very similar in both independent measurement cases, providing assurance as to the robustness of the results. As in figure 5.5(a) all measured points have been joined in the graph of streamwise normalised turbulence u'^2/U_{ref}^2 that shows a certain amount of experimental scatter in the measurements reflecting the tolerances on the measurement of these quantities. Note that the dimensionless shear stress near the ground is about 0.004, leading to $u^*/U_{ref} = 0.063$. With $U_{ref} = 2 \text{ ms}^{-1}$, this gives $u^* = 0.126 \text{ ms}^{-1}$, very close to the value determined above from the log-law plot – a quality check on the curve fitting process. It is because u^* from the log-law fit has been used in producing the dimensionless plots, Figure 5.5(b), that the maximum value of dimensionless shear stress is a little less than 1.0.

5.3. Cube at 0 degrees

Results from the flow field measurements have been presented further onwards in this chapter. Dimensions are given in mm for model-scale so that flow features identified as of particular interest can be directly compared to features of the model and sampled wind tunnel co-ordinates, which includes release heights specified in model scale. Since the models are 1:200 scale the cube building height H in model scale is 240mm and equates to a building height of

48m at full-scale. In many of the figures a ‘thumb-nail’ plan view of the model is presented to orientate the reader: the convention used is that the origin of co-ordinates in each case is centred on the source release position at ground level on the wind tunnel floor with the Z-axis going vertically - as was the convention described in chapter 3. For the cube cases that origin may be at release positions ‘A’ or ‘B’ or for the East Wing model (also of height 240mm in model scale) the North Wing stair tower stack position, in some cases in the text the latter referred to as the ‘Vertex’ release position because of its relative position to the building given the directions of approach flow studied. The choice of placing the co-ordinate system origin at the source in the X-Y plane for each set of measurements was a logical one because rotation of the building to different angles of approach flow was achieved in the wind tunnel by rotation of the turntable around the source position at the origin to achieve the measurements made and the measurement co-ordinates for each experiment were programmed in model-scale. In each ‘thumb-nail’ plan view the corner co-ordinates are given for the model as well as the location of the centre of the roof for the cube. The streamwise sampling plane is shown as a dotted line in each thumb-nail figure and the results for the adjacent figure relate to this downstream sampled plane: in each case the ‘thumb-nail’ will orientate the reader to where the sampled measurement plane is in relation to the source, the relative position on the roof, and the relative positions of the corners of the cube or building being: wind direction is shown as a blue arrow in each figure. For reasons of brevity some thumb-nail figures have been moved to Appendix 15.2 for the different building angulations to flow.

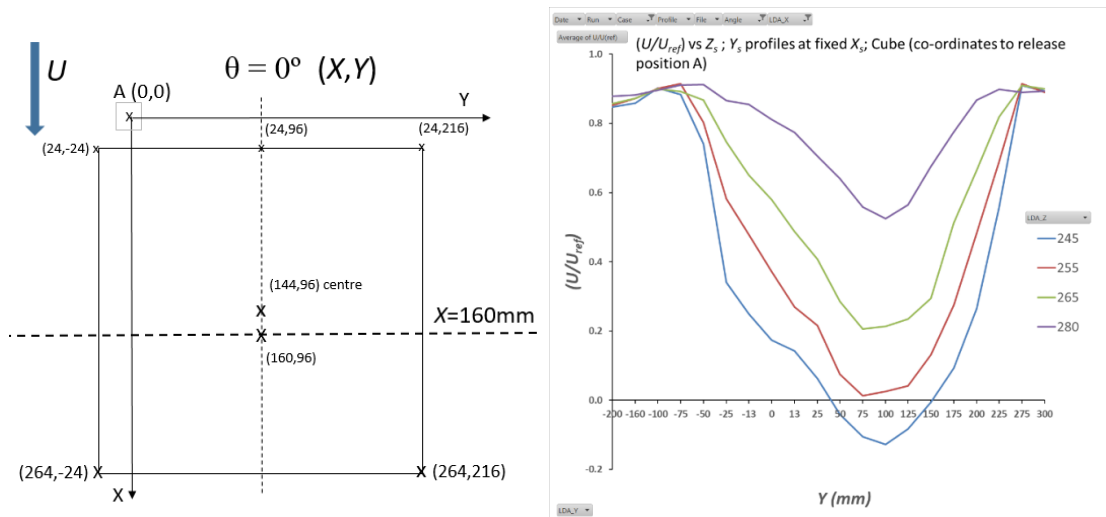


Figure 5.7(a/b). Cube/A; 0°; (a) Arrangement and coordinate system; (b) (U/U_{ref}) ; $X=156$ mm ($X/H=0.65$).

In Figure 5.7(a) the cube at normal incident (0°) is shown. The cube edges are at $Y = -24$ mm and 216 mm, with the centre at $Y = 96$ mm. The origin of the co-ordinate system was 24mm upwind of the cube ($X/H=0.1$). Later profiles of the mean velocity component, U/U_{ref} , are plotted in Figure 5.7(b), showing a small region of reversed flow at the lowest height sampled (245mm, 5mm above cube surface) between $Y = 50$ to 150 mm; i.e. within ± 54 mm from the cube centre. Comparing to Figure 5.1 the reattachment line is expected to be parabola-like. The central velocity deficit region was seen to extend upwards to $Z = 280$ mm ($Z/H=1.167$) and beyond.

Figure 5.8 shows U/U_{ref} for the cube at normal incidence at sampled planes (a) towards the back of, and (b) beyond, the cube roof. From (a) the mean flow can be seen to be in a positive downstream direction everywhere, although transient reversals of flow due to turbulence may still occur at levels closest to the roof surface. From Figure 8(b) two of the profiles are below

roof level at $Z=30\text{mm}$ and 120mm above the ground plane and these show mean reversed flow between $Y=25$ and 175mm (between -71mm and 79mm in relation to the centre of the cube): this relates to the flow picture of the near wake shown in Figure 1 where reverse flow is clearly evident. At the greatest height sampled of $Z=320\text{mm}$ ($Z/H=1.33$) the downstream flow is not affected as evidenced by the near-uniform lateral velocity profile.

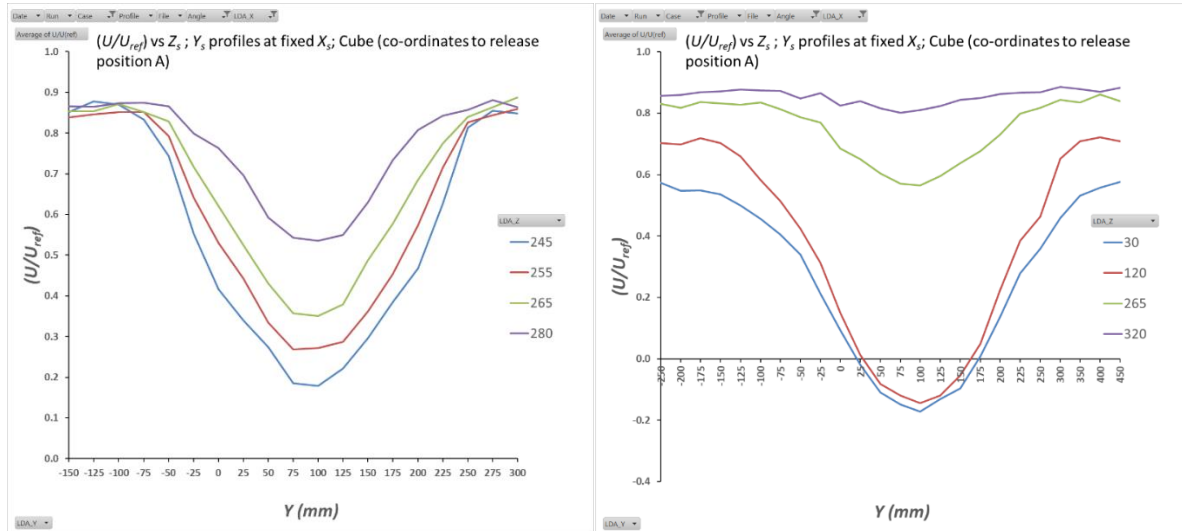


Figure 5.8(a/b). Cube/A, U/U_{ref} at 0° ; (a) $X=236\text{mm}$ ($X/H=0.98$); (b) $X=396\text{mm}$ ($X/H=1.65$)

The flow profiles for the vertical component of flow, W , were also sampled and results are presented in Figure 9(a/b/c) for the three downstream distances analysed in the above Figures at approximately $X/H=2/3$, 1 and $5/3$ from release point ‘A’ respectively, normalised to U_{ref} .

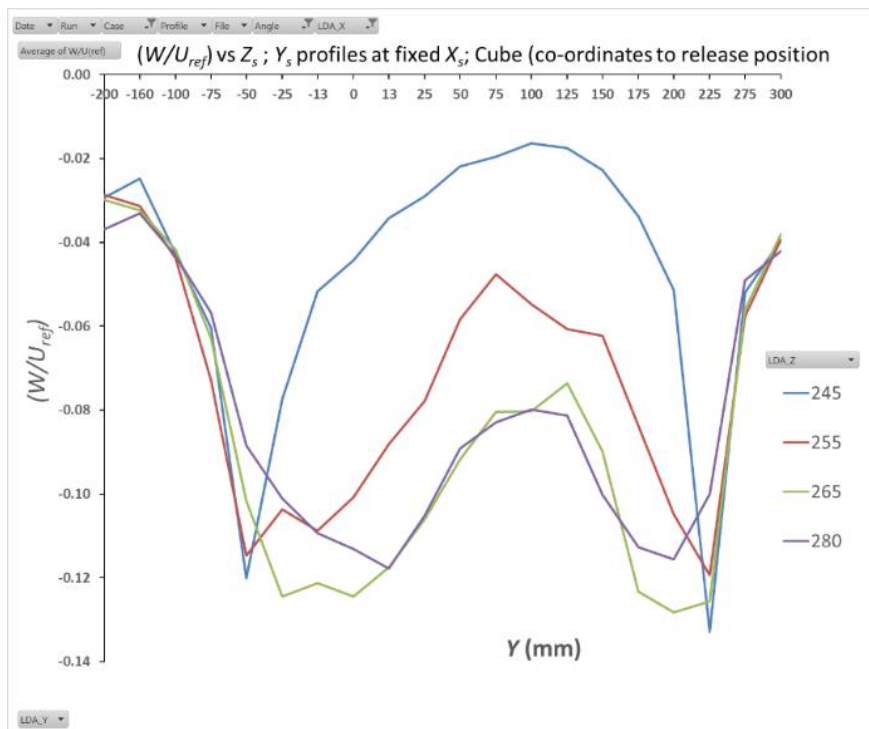


Figure 5.9(a). Cube/A; 0° ; $X=156\text{mm}$; (W/U_{ref})

From Figure 5.9(a) downwards flow is apparent at all positions and at all sampled heights in a Y - Z plane close to the roof centre. With negative maxima apparent at values of down to $W/U_{ref}=-$

0.13 when referenced against U_{ref} . It was noted that W/U_{ref} had minima at $Y=-50$ and 225 mm, or positions at -146 mm and $+129$ mm with respect to the centre of the cube ($-0.61H$, $+0.54H$). These strong downwards flows were apparent at either side of the roof of the cube.

From Figure 5.9(b) at a further downstream distance of $X=236$ mm the vertically downwards flow patterns seen in Figure 5.9(a) are continued. From Figure 5.9(c) upwards flow was seen for sampled heights below roof level in the middle region of the cube.

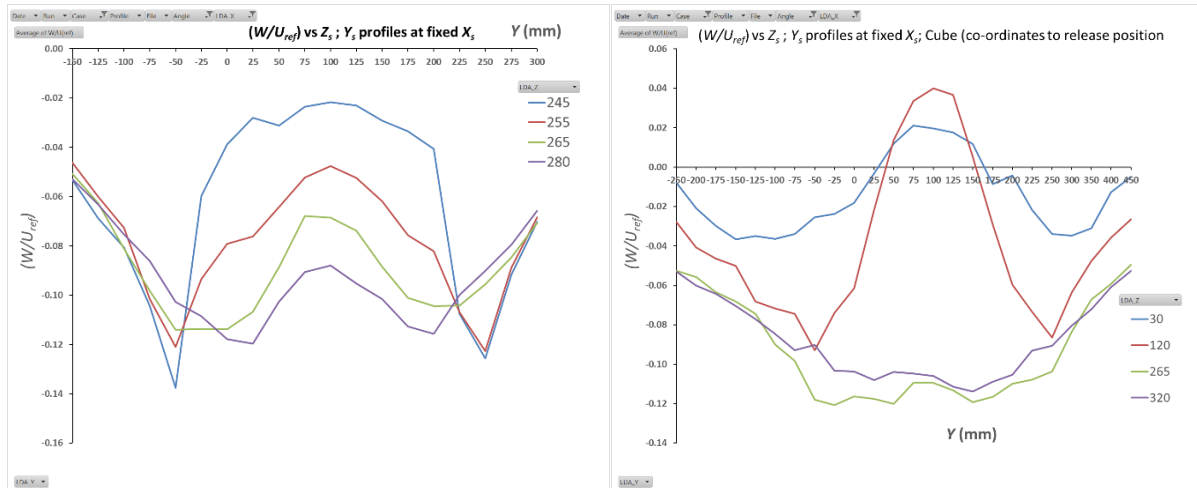


Figure 5.9(b/c). Cube/A; 0° ; (W/U_{ref}) ; (b) $X=236$ mm; (c) $X=396$ mm

Figure 5.10 shows plots of values of the flow inclination $W(z)/|U(z)|$ at $X=156$ mm – which reflects the local magnitude of downstream flow $|U(z)|$ at different positions in the flow. Large downward values of up to a magnitude of approximately four are seen showing a high extent of flow inclination at some positions. A negative region is seen at approximately $Y=150$ mm for the $Z=245$ mm sampled height: this is in the region where the flow reversal was seen in Figure 7(b) and corresponds to the negative downflow coupled with a small magnitude of streamwise flow leading to a negative gradient. For the $Z=255$ mm sampled height a similar effect was seen at $Y=75$ mm: this can be related to the edge of the reattachment region on the top of the cube shown in the flow features diagram in Figure 5.1.

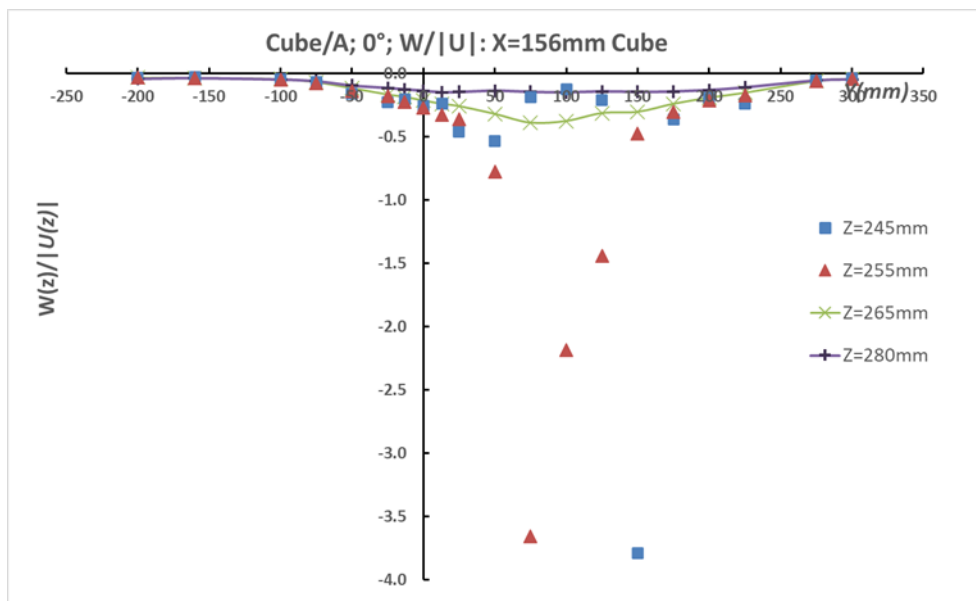


Figure 5.10. Cube/A; 0° ; $(W(z)/|U(z)|)$; $X=156$ mm

To understand what drives the downwards flow at either side of the cube we can compare the results to those arrived at by Large Eddy Simulation (LES) calculations provided by Lim HC *et al* (2009) shown in Figure 11. We can compare the results from Figure 9(a) at traverse sample heights of $Z=245, 255, 265$ and 280mm or $1.02, 1.06, 1.10$ and 1.17 against a unit dimension cube shown below.

From Figure 5.11 we see that just above roof level there is downflow at all locations, which switches to up and outflow at large magnitude values of $|Y|$ and also at large values of Z . There is downflow within and close to the roof recirculation region. The up and out flows result from displacement of the flow by the cube. The lateral turbulence in the approach flow implies short duration variations in wind direction, perhaps by up to $\pm 10^\circ$. These direction variations will then cause the secondary flows to transiently separate from one edge or the other. It should be noted that the results presented from the wind tunnel experiments here reflect mean values averaged over a time of half a minute, but that during that time transient flow features will present and then disappear.

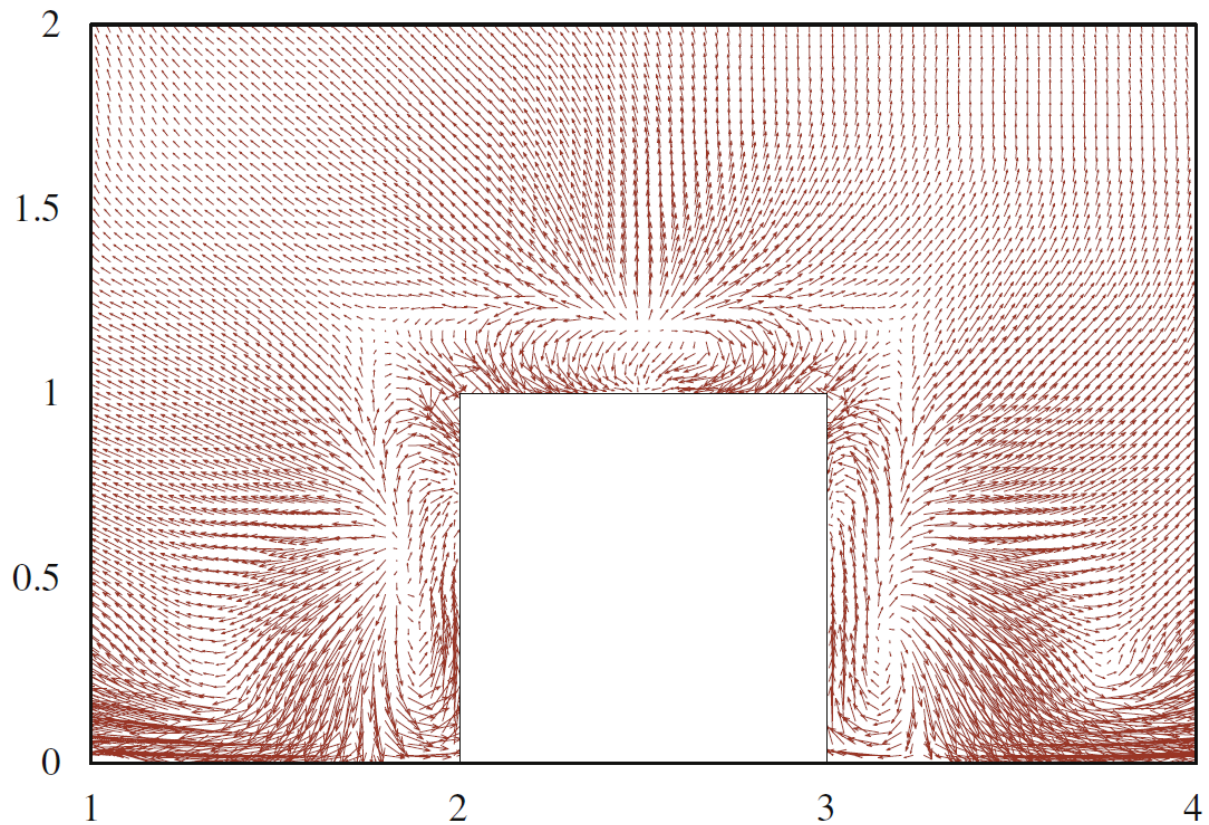


Figure 5.11. LES simulations for the cube case from Lim HC *et al* (2009): mean velocity vectors of (v, w) in the Y - Z plane through the cube

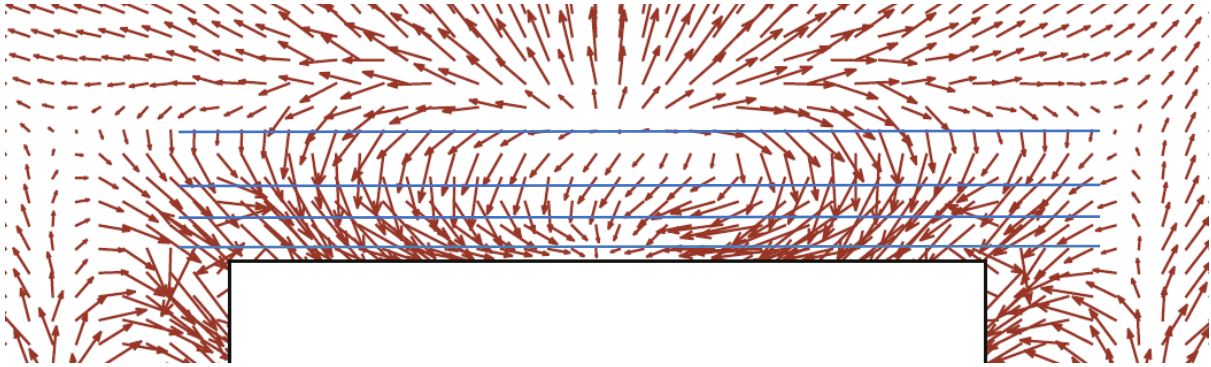


Figure 5.12. Expanded view of LES simulations for the cube case from Lim HC *et al* (2009): with annotations by the author showing lateral sampling heights used

Figure 5.12 from shows an expanded view of Figure 5.11 for the flow close to the roof region, adapted from Lim HC *et al* (2009), with superimposed lateral sample heights (as blue lines) used for the experiments in this work at 1.02, 1.06, 1.10 and 1.17 cube heights.

Looking upwind at a time when the secondary flow is from left to right, it can be seen:

- Separation at the right-hand roof edge producing a vortex below roof level, that emanates from the right upwind corner. This rotates clockwise.
- Separation at the left-hand edge of the flow up the left-hand face producing a vortex above roof level, that emanates from the left upwind corner. This also rotates clockwise.
- Note that one vortex is above roof level, the other below, the left-hand vortex lies above and inboard of the edge, the right-hand below and outboard of the edge.
- With the secondary flow in the opposite direction, the situation is reversed. The left-hand vortex is now below roof level and rotates anti-clockwise; the right-hand above roof level and it too rotates anticlockwise.
- This overall effect means that these small vortices do not cancel-out on averaging over the measurement time for the experiment at any given position but the mean flow is presented over that time.
- Along the superimposed lines in Figure 12 showing the sample heights from Figure 9 it can be seen that there is general downflow, greatest where the vortices above roof level are intercepted

Figure 5.13 below also from Lim HC *et al* (2009) and shows vorticity (s^{-1}) in the same plane as above.

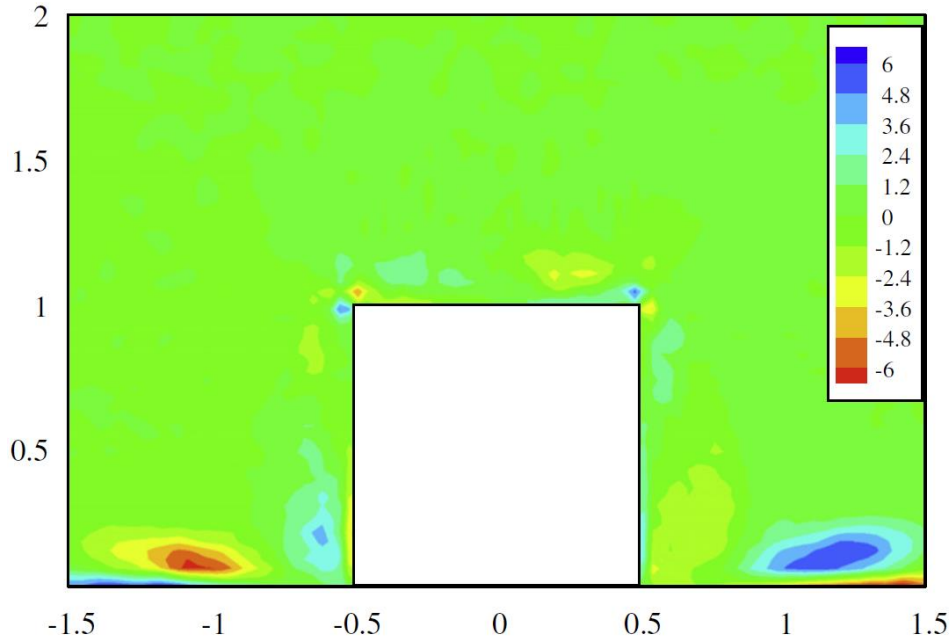


Figure 5.13. Contours of mean vorticity ω_x in the Y-Z plane through a cube from Lim HC *et al* (2009)

Figure 5.13 shows the mean vorticity for the cube. The vortex pairs can be seen just above roof level: the blue pair are the clockwise vortices looking upwind and the orange pair are anti-clockwise when looking into the downstream flow.

At a greater distance downwind of $X=236\text{mm}$ as shown in Figure 5.9(b) the downwards flow, especially just beyond the lateral edges of the cube, can be seen in a similar way to the case at $X=156\text{mm}$. The greater downstream velocity as shown in Figure 5.8(a) means that the inclination will be reduced compared to the $X=156\text{mm}$ case.

Beyond the back edge of the roof at $X=396\text{mm}$ as shown in Figure 5.9(c) two sampled heights extend downwards to nearer ground level, being at $Z=30$ and 120mm or $Z=H/8$ and $H/2$. Two levels are also shown above roof level at $Z=265$ and 320mm . From Figure 5.9(c) the upwards flow regions at $Z=H/8$ and $Z=H/2$ extend from approximately $Y=40$ to 160mm : in relation to the central line of the cube from -56mm to 64mm ; $-0.23 < Y/H < 0.27$. Elsewhere, the flow was downwards. At the greatest height sampled of $Z=4H/3$ the downwards component of the flow was still strong with $W/U_{ref}=-0.12$ around the central line of symmetry: a feature than can be seen in the flow schematic presented in Figure 5.1 where flow over the cube will feed the cavity zone.

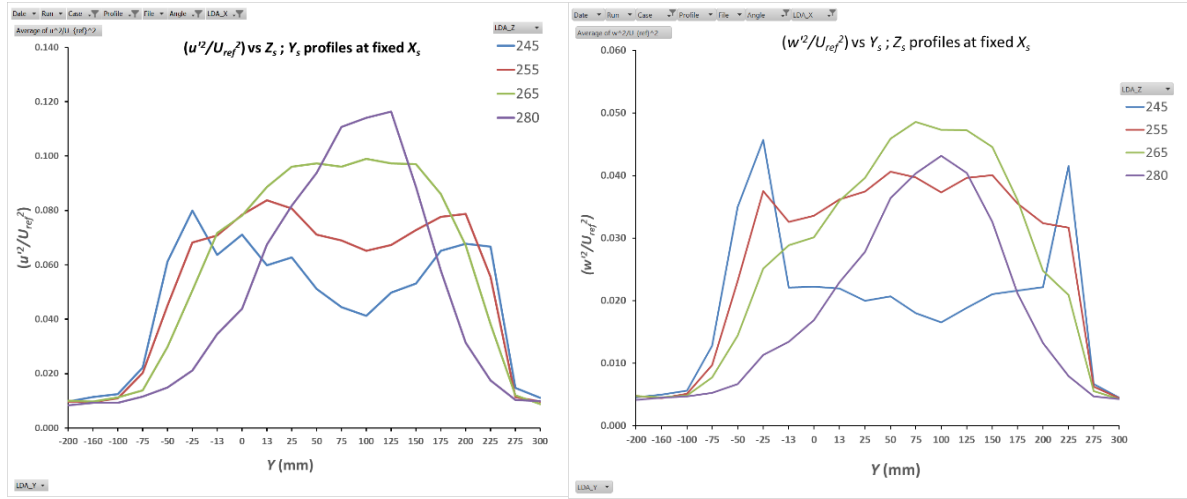


Figure 5.14(a/b). Cube/A; 0°; $X=156\text{mm}$; (a) (u'^2/U_{ref}^2) ; (b). (w'^2/U_{ref}^2)

Figure 5.14 shows the turbulence intensities for the downstream and vertical flow, (a) for u'^2/U_{ref}^2 and (b) for w'^2/U_{ref}^2 normalised to the reference downstream velocity, U_{ref} . It can be seen from (a) that the turbulence ranges from approximately 0.05 at $Z/H=1.02$ close to the roof surface up to a peak of 0.12 for $Z/H=1.17$. These may be compared to the approach flow in Figure 6 where at the same height the turbulence intensity of the downstream component was just 0.012. The higher values in Figure 5.14(a) are building generated turbulence. In Figure 5.14(b) the vertical component of turbulence intensity w'^2/U_{ref}^2 shows values in the central region of the cube of 0.02 for the lowest height sampled and 0.05 for the greatest sample height. These figures can be compared to the approach flow values in Figure 5.6 of 0.005, showing again building generated turbulence in the flow.

Taking $u'^2/U_{ref}^2 = 0.05$ for the height of $Z=245\text{mm}$ indicates that $|u'|/U_{ref} = 0.22$. Given a value of $U/U_{ref} \approx \pm 0.1 - 0.2$, from Figure 5.7(b), where negative values indicate reversed flow, we have that $|u'|/U \approx \pm 0.5 - 1.0$. The variations of the non-steady fluctuation component u' are of similar magnitude to the mean downstream component close to the roof surface: this indicates there will be frequent periods with substantial reversed flow. It should be noted that $u'(z)/U(z)$ is a first order variation.

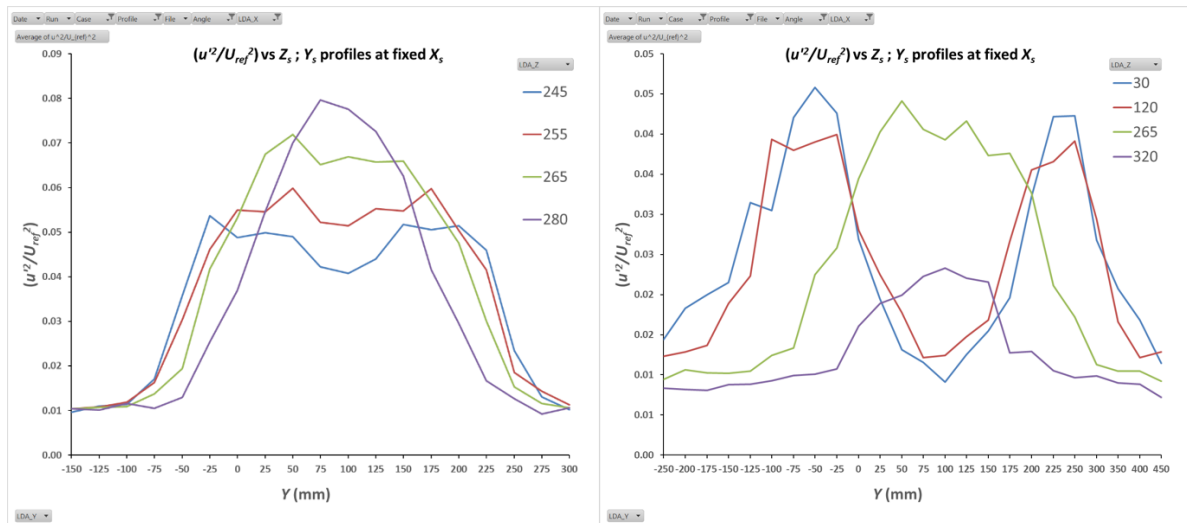


Figure 5.15(a/b). (a) $X=236\text{mm}$; (u'^2/U_{ref}^2) ; (b) $X = 396 \text{ mm}$; (u'^2/U_{ref}^2)

Figure 5.15(a) shows results for u'^2/U_{ref}^2 for $X=236\text{mm}$ towards the back edge of the cube roof. For $Z=245\text{mm}$ the value of u'^2/U_{ref}^2 was approximately 0.05 in the central region and $U_{ref} \approx 0.2-0.3$ from Figure 5.8(a). A similar calculation to above yields $|u'|/U \approx 0.9$ indicating once again frequent periods of reverse flow at this downstream distance.

Figure 5.15(b) shows results for u'^2/U_{ref}^2 for $X=396\text{mm}$ past the back edge of the cube roof. In the central region for $Z=30$ and 120mm u'^2/U_{ref}^2 was approximately 0.015, and $U/U_{ref} \approx -0.1$. These figures yield an estimate of $|u'|/|U| \approx 1.2$, so that even for this central reverse flow region there will be significant temporal fluctuation in the local velocity U .

5.4. Cube at -45°

As the angle of the cube is changed from normal incidence to some small angle, α , off-normal the cross flow becomes biased in one direction. Once the angle α is increased so that the left-hand side face in Figure 5.16 is clearly exposed to the oncoming flow we see the formation of a tight vortex on the left side, with the large recirculation region (now vortex-like) remaining from the other forward-facing cube face.

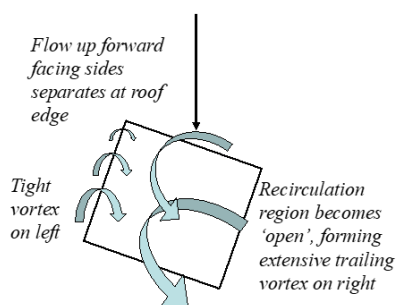


Figure 5.16.
Development of flow features with angulation of the cube away from normal incidence of flow

Wake, viewed from behind: tight trailing vortex on left, broad trailing vortex on right (developing from what was the recirculation region), in addition to the recirculation region behind the block and the wake downstream.

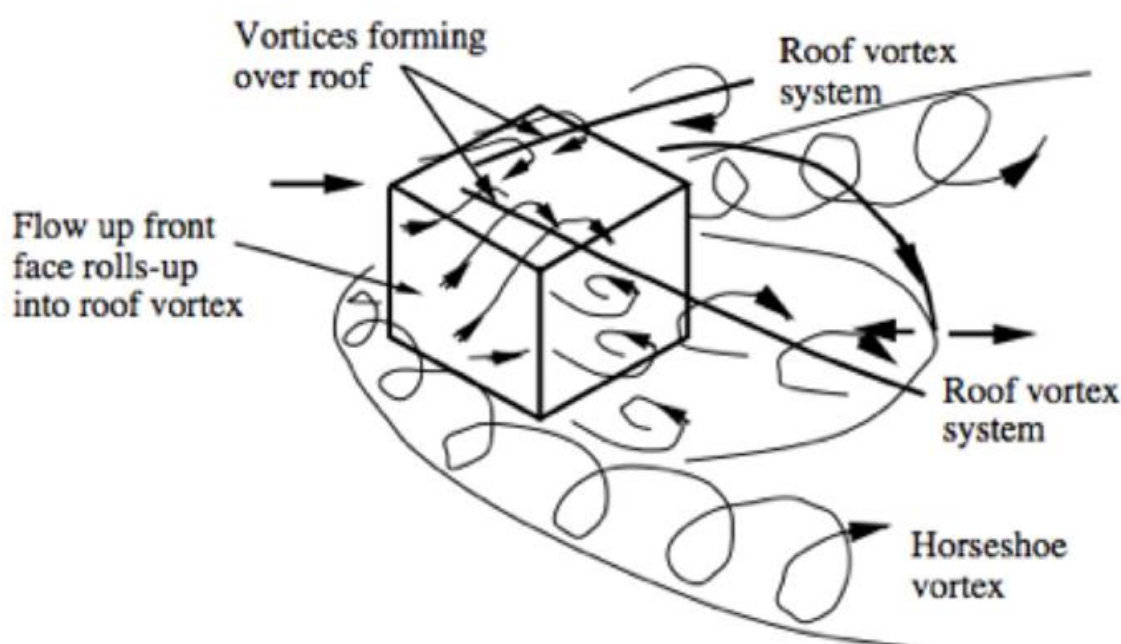


Figure 5.17. Flow features for cube at -45° to approach flow from Hosker (1984)

The process develops with increasing angles until we reach the situation shown in Figure 5.17 from Hosker (1984) where the vortices generated from the two leading edges have equal strength. It can also be seen that the pair of roof vortices generated from flow separation at the leading edges generate strong downwash over the central region in the roof, the rooftop recirculation zone, and into the main recirculation zone in the near-wake. A wider horseshoe-type vortex around the sides of the building is also apparent, this effect peaking in magnitude for this symmetrical orientation.

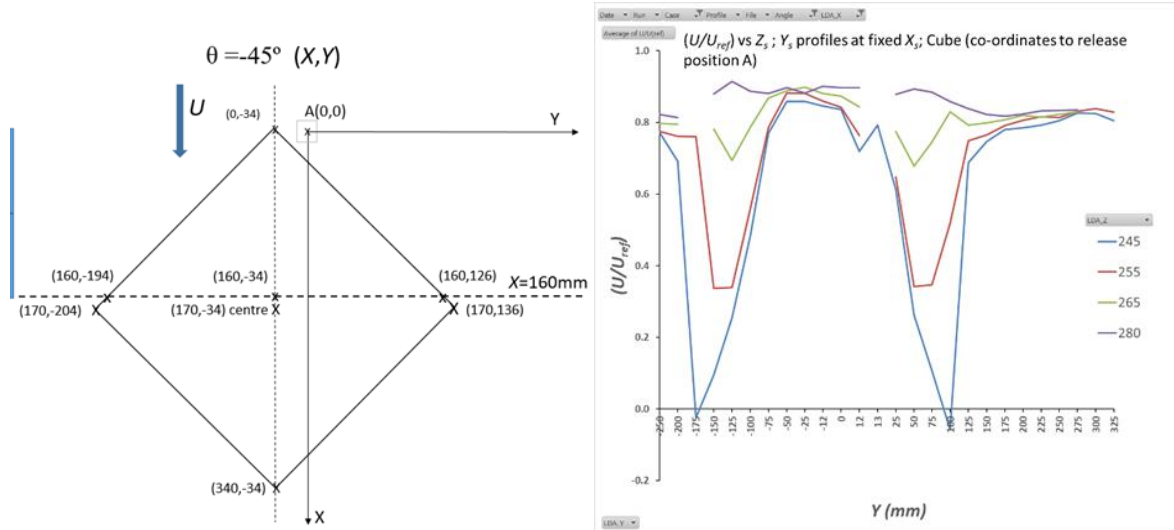


Figure 5.18(a/b). Cube/A; -45° ; (a) arrangement and coordinate system; (b) (U/U_{ref}) ; $X=156\text{mm}$ ($X/H=0.65$).

In Figure 5.18(a) the co-ordinates of the sampled plane in relation to the cube are given: note that the blue indicator line in the left margin indicates a dimension of 160mm to aid with visualisation of the scales in the figure. Not all positions in Figure 5.18(b) were able to be sampled so the curves are not continuous in some cases. It may be noted from Figure 5.18(b) that there are significant velocity deficits in the downstream direction for the lowest height studied of $Z=245\text{mm}$ at $X \approx 160\text{mm}$ at $Y = -175\text{mm}$ and $Y = 100\text{mm}$ (-140mm and $+134\text{mm}$ in relation to the cube centre, or $-0.58H$ and $0.56H$). However, the downstream flow is maintained in the central region of the cube, even for the lowest height sampled of $Z=245\text{mm}$.

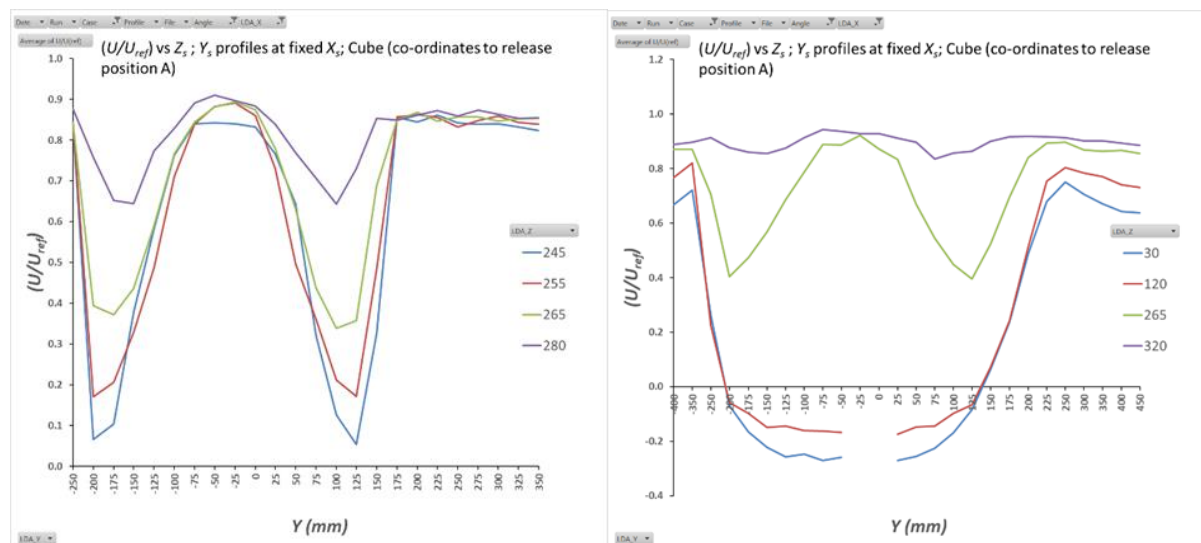


Figure 5.19(a/b). Cube/A, U/U_{ref} at -45° ; (a) $X=236\text{mm}$ ($X/H=0.98$); (b) $X=396\text{mm}$ ($X/H=1.65$)

Figure 5.19(a) shows some significant velocity deficits near to, but downstream, of the lateral edges of the cube at the lateral corner vertices. These are more pronounced the closer to the roof level of $Z=240\text{mm}$ at $Y=-200\text{mm}$ and $Y=125\text{mm}$ (-166mm and 159mm in relation to the cube centre, or $-0.69H$ and $0.66H$). Flow downstream in the middle of the cube was relatively unaffected with the normalised minima being approximately 0.85 for the lowest sample height tested of $Z=245\text{mm}$ above the roof surface at $Z=240\text{mm}$.

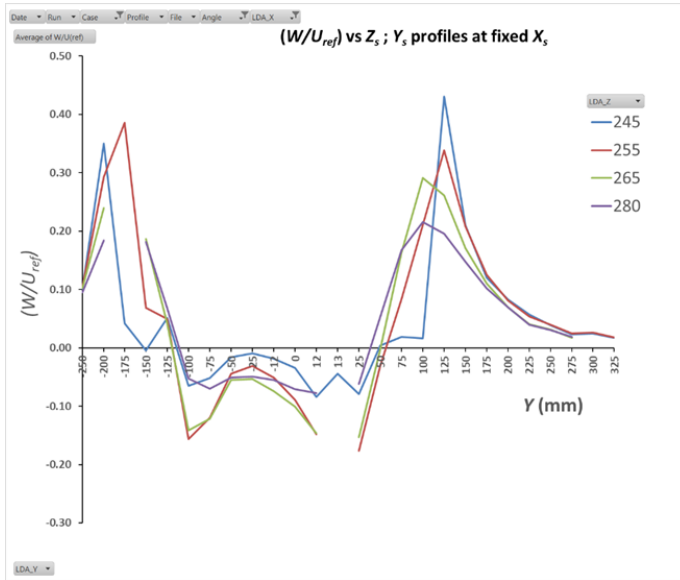


Figure 5.20(a). Cube/A; -45° ; $X=156\text{mm}$; (W/U_{ref})

Figure 20(a) indicates a pronounced downwards flow for the intermediate heights ($Z=255\text{mm}$ and $Z=265\text{mm}$) in the central region of the roof and a countervailing strong upwards flow near to the lateral edges of the cube. This indicates the presence of vortices which would cause advection of pollutant in the flow towards levels near the roof height – this feature can be seen in the flow schematic given in Figure 17.

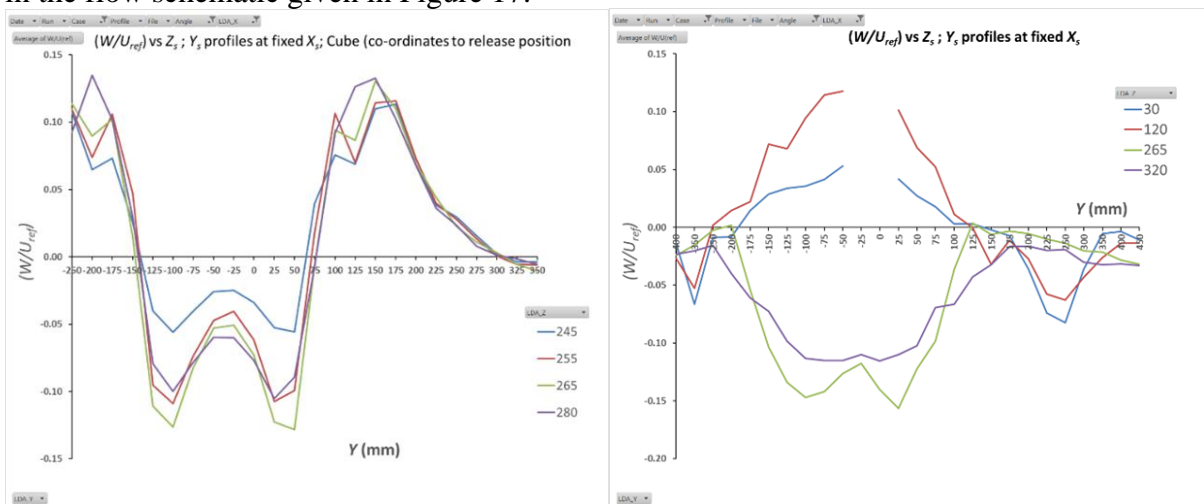


Figure 5.20(b/c). Cube/A; -45° ; (W/U_{ref}) ; (b) $X=236\text{mm}$; (c) $X=396\text{mm}$

From Figure 5.20(b) we see significant upwards flow near the cube corner vertices, corresponding to the positions of reduced downstream flow velocity in Figure 5.19(a). There is a countervailing double peaked downwards directed flow pattern nearer the centreline of the cube at $Y \approx -100\text{mm}$ and $Y \approx 40\text{mm}$, most evident for ranges of height $Z=255\text{--}280\text{mm}$. The downwards flow is suggestive of roof top generated vortices, and it would follow that these

would be responsible for the advection of pollutant releases closer to the heights nearer the roof top.

In Figure 5.20(c) the flow downstream of the cube was sampled at heights lower than the roof plane of the building at $Z=240\text{mm}$ at heights $Z=30\text{mm}$ and $Z=120\text{mm}$ ($H/8$ and $H/2$ respectively). There is clear evidence of the recirculation zone downwind of the building with the reverse flow seen at the lower sampled heights. Velocity deficits corresponding to the lateral positions of the edge vertices of the cube were seen in the plot above roof level at $Z=265\text{mm}$. The side lobes at $Y=-350\text{mm}$ and $Y=250\text{mm}$ (-316mm and $+284\text{mm}$ in relation to the cube centre at $Y=-34\text{mm}$, or $-1.32H$ and $+1.18H$ respectively) indicate downwards flow for the lowest sample heights sampled outside and downstream of the lateral edge vertices of the cube – the positions can be seen in Figure 5.18(a).

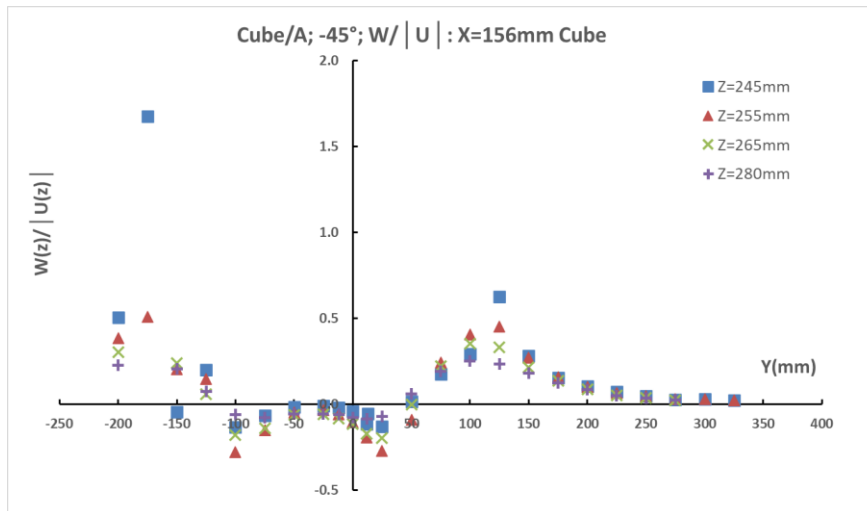


Figure 5.21. Cube/A; -45°; $(W(z)/|U(z)|)$; $X=156\text{mm}$

Figure 5.21 indicates the local values of $W(z)/|U(z)|$ or the flow inclination. Positions $Y=-175\text{mm}$ and $Y=125\text{mm}$ correspond to low streamwise flow velocities as shown in Figure 5.18(b), but W is positive at these positions from Figure 5.20(a): the net result locally is a flow with high local gradient. For sampled heights of $Z=255\text{mm}$ and above the magnitude of the gradient was within a maximum value of approximately 0.5.

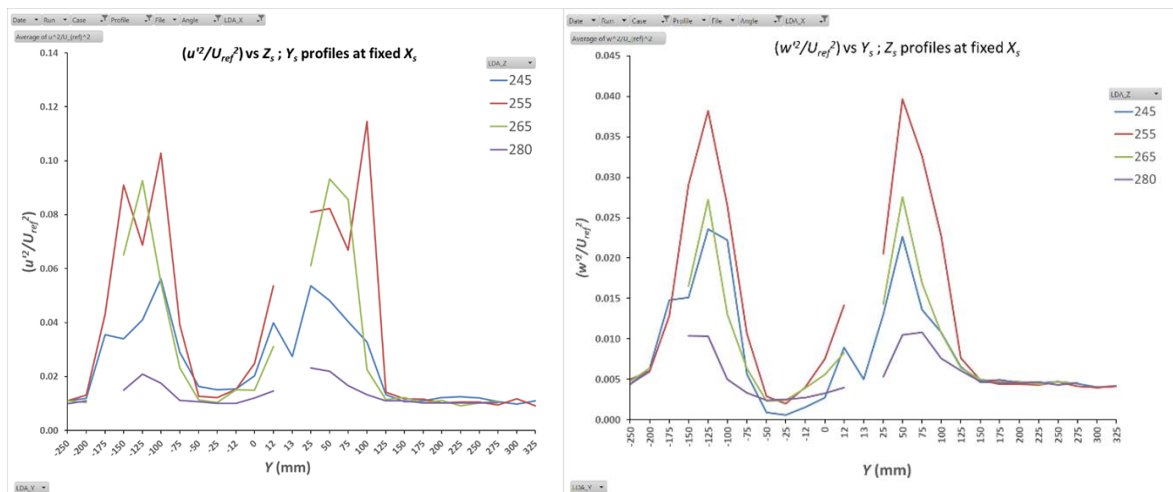


Figure 5.22(a/b). Cube/A; -45°; $X=156\text{mm}$; (a) (u^2/U_{ref}^2) ; (b) (w^2/U_{ref}^2)

From Figure 5.22(a) and 5.22(b) a general pattern of high turbulence intensity for the downstream and vertical components is seen close to the lateral cube edges, this was particularly pronounced for the heights of $Z=255\text{mm}$ and $Z=265\text{mm}$. Levels of downstream component turbulence are low for the greatest height sample of $Z=280\text{mm}$, and for all heights close to the centre of the cube $Y=-34\text{mm}$ for this angulation.

Taking $u'^2/U_{ref}^2 = 0.10$ for the height of $Z=255\text{mm}$ indicates that $|u'|/U_{ref} = 0.32$. Given a value of $U/U_{ref} \approx 0.35$, from Figure 5.18(b) for that sample height at the flow deficit, we have that $|u'|/U \approx 1.0$. The variations of the non-steady fluctuation component u' are of similar magnitude to the mean downstream component close to the roof surface: this indicates there will be frequent periods with substantial reversed flow even at this height: closer to the roof at $Z=245\text{mm}$ there is mean flow reversal.

The vertical component of turbulence intensity in Figure 5.22(b) was relatively small for all heights close to the central regions of the cube, with a particularly low value of w'^2/U_{ref}^2 constrained by the boundary of the roof plane at $Z=240\text{mm}$ for the lowest sampled height of $Z=245\text{mm}$.

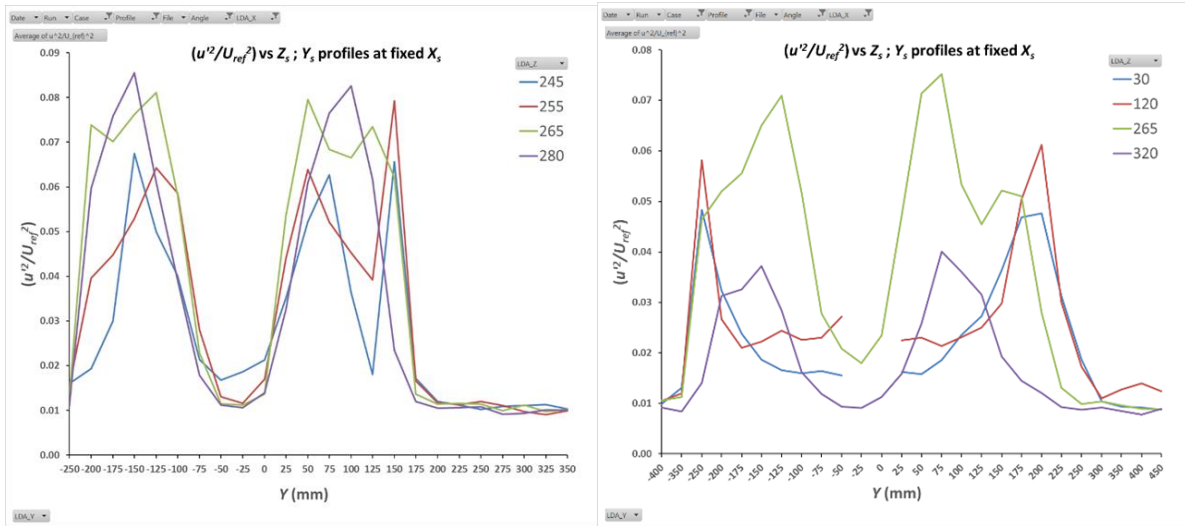


Figure 5.23(a/b) Cube/A; -45°: (a) $X=236\text{mm}$; (u'^2/U_{ref}^2) ; (b) $X= 396 \text{ mm}$; (u'^2/U_{ref}^2)

From Figure 5.23(a) we can see that the downstream component of turbulence intensity peaks at approximately the same lateral positions as the upwards deflection features in Figure 5.20(a) and the velocity deficit features in Figure 5.18(a). Low values of turbulence close to the cube centreline at $Y=-34\text{mm}$ were also apparent.

For Figure 5.23(b) the downstream component of turbulence intensity values at $Z=265\text{mm}$ are greatest and correspond to positions approximately halfway along the trailing edges of the cube. The lowest sampled heights show peaks downstream of and just outside the lateral position of the edge vertices of the cube at this angulation.

5.5. Cube at -22.5°

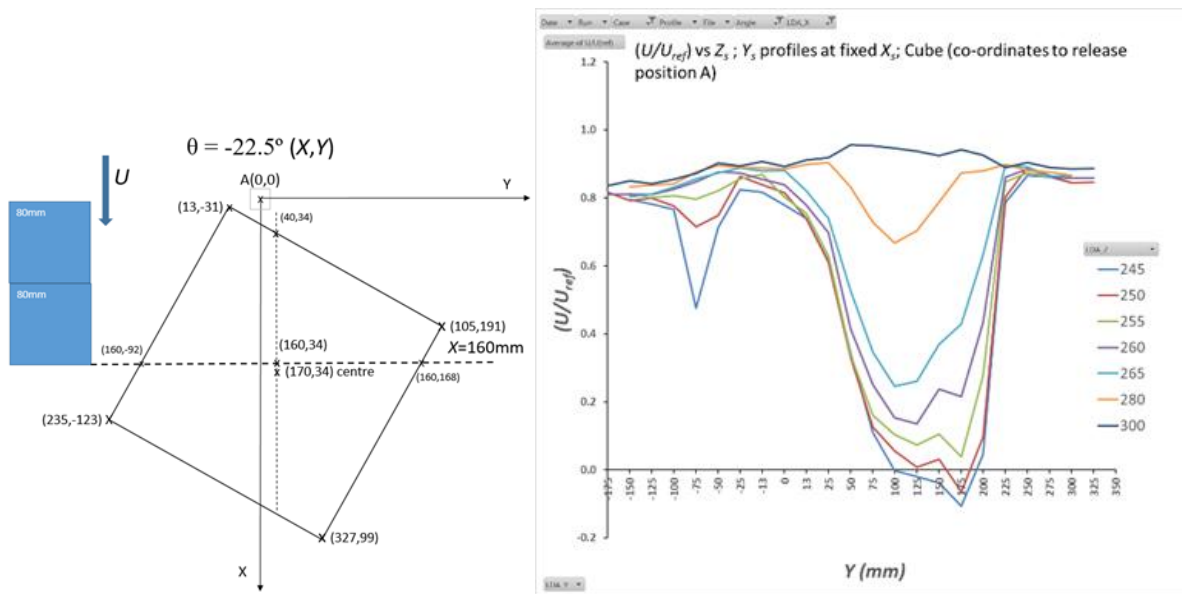


Figure 5.24(a/b). Cube/A; -22.5° ; (a) Arrangement and coordinate system; (b) (U/U_{ref}) ; $X=156\text{mm}$ ($X/H=0.65$)

Note that in the left margin of Figure 5.24(a) a stepped scale is displayed, with features of length 80mm , to aid visualisation of the scales in the figure. Similar step or block scales are presented in the left margin in other co-ordinate plots in this work – it should be noted that these are presented to aid visualisation and do not correspond to adjacent building features. In this figure showing angulation of the cube at -22.5° the cube centre is at $Y=34\text{mm}$.

At the intermediate angle of approach flow of -22.5° , halfway between the previous cases presented of 0° and -45° , there is a deep velocity deficit with mean sampled reverse flow at the lowest sample heights of $Z=245$ and 250mm and this is in the region of $Y=140\text{mm}$ ($Y=106\text{mm}$ in relation to the cube centreline, or $0.44H$). A smaller velocity deficit at $Z=245\text{mm}$ can also be seen at $Y=-75\text{mm}$ ($Y=-109\text{mm}$ in relation to the cube centre, or $-0.45H$).

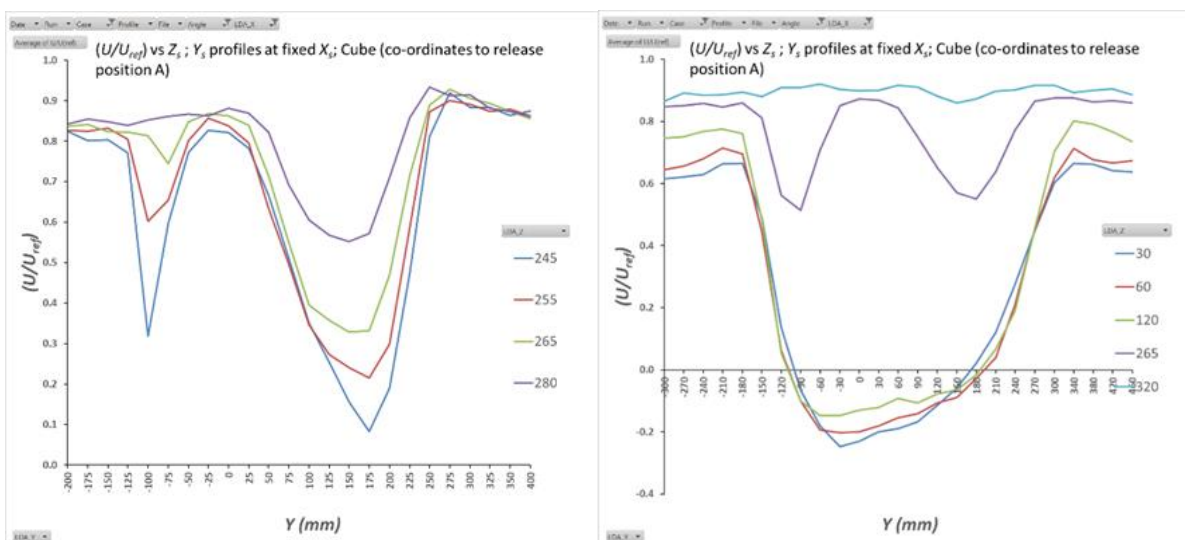


Figure 5.25(a/b). Cube/A; -22.5° ; U/U_{ref} : (a) $X=236\text{mm}$ ($X/H = 0.98$); (b) $X=396\text{mm}$ ($X/H=1.65$)

Figure 5.25(a) shows the main velocity deficit now extending beyond the trailing edge of the cube at $Y=175\text{mm}$. There was no mean reverse flow in any profile. A second velocity deficit near the trailing edge contact point with the sample plane at $Y=-111\text{mm}$ was seen to be prominent for the lowest sample height of $Z=245\text{mm}$.

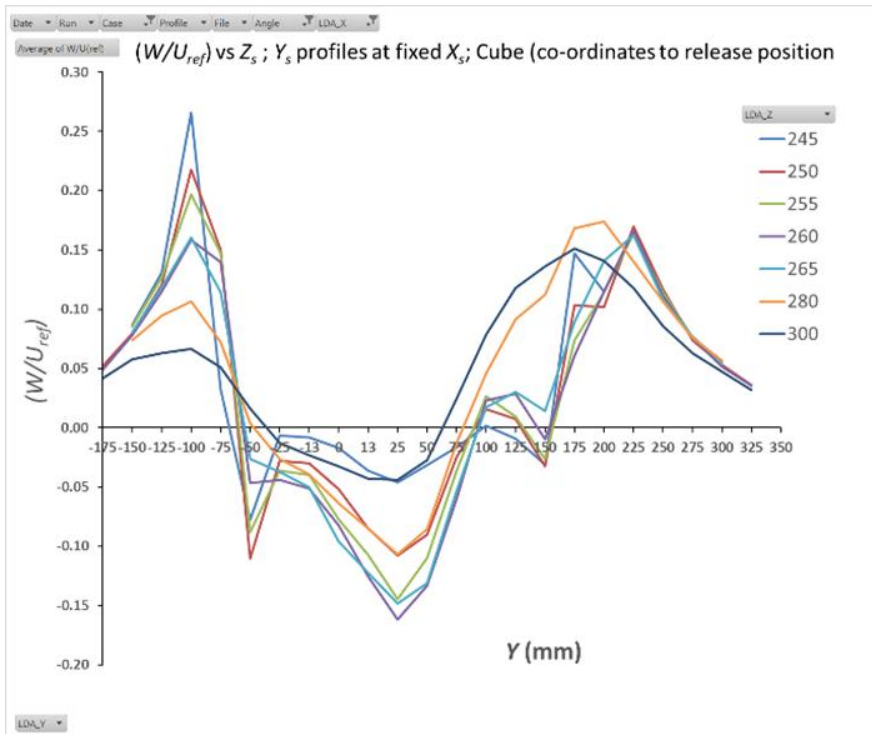


Figure 5.26(a). Cube/A; -22.5° ; $X=156\text{mm}$; (W/U_{ref})

Figure 5.26(a) shows a downwards vertical flow component over the central region of the cube, with corresponding strong upwards flow at the lateral edges. This is the large over roof vortex as shown in the schematic Figure 5.17 appropriate for an angulation between the symmetrical cases of normal incidence and -45° incidence.

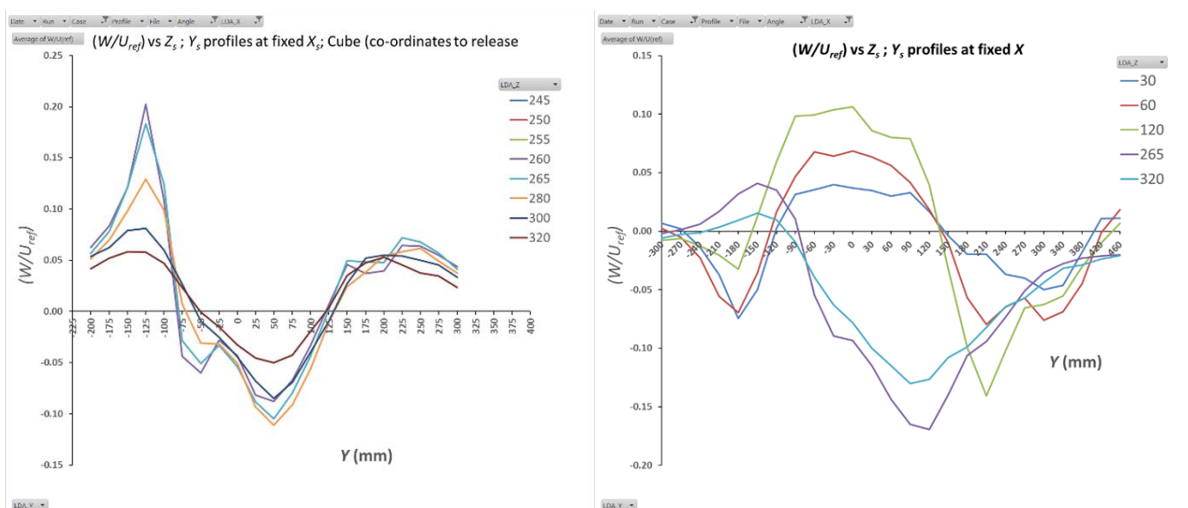


Figure 5.26(b/c). Cube/A; -22.5° ; (W/U_{ref}) ; (b) $X=240\text{mm}$; (c) $X=396\text{mm}$

Figure 5.26(b) for $X/H=1$ shows vertical upwards flow at $Y=-125\text{mm}$ corresponding to the projection of the lateral vertex of the cube upstream. The flow switches to vertically downwards

over the central region and then shifts upwards past $Y=125\text{mm}$. Further downstream at $X/H=1.65$ shown in Figure 5.26(c) two flow schemes are apparent: for sampled heights below the roof level of $Z=30, 60$ and 120mm there is downflow beyond the lateral edges and upwards flow in the central region; for $Z=265$ and 320mm above the roof level this pattern reverses. The downwards flow above roof level will be important in the downwards advection of pollutant released above roof level into the flow.

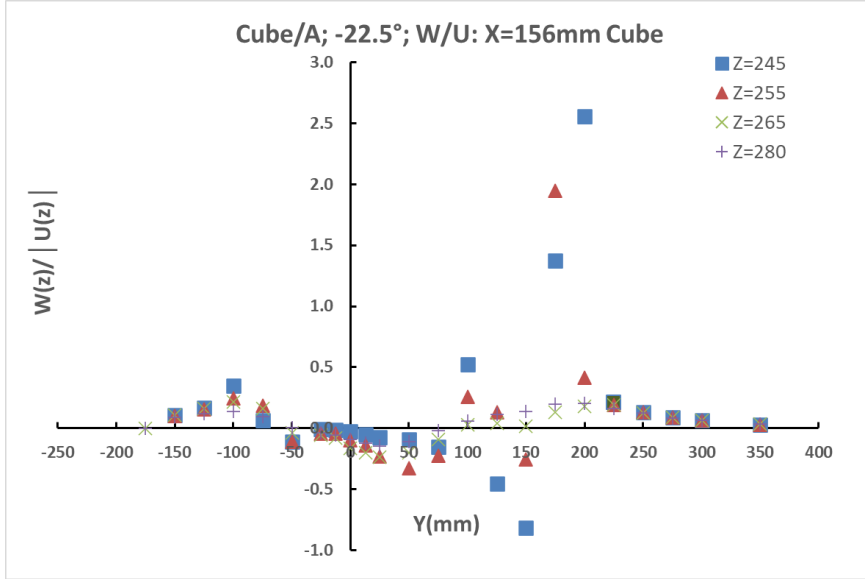


Figure 5.27 Cube/A; -22.5°; $(W(z)/U(z))$; $X=156\text{mm}$

Figure 5.27 shows the local gradient or inclination of flow $W(z)/|U(z)|$ and a complex pattern of behaviour is evident between $Y=100$ and $Y=225\text{mm}$, which may be related to Figures 5.25(a) and 5.26(a). In this region there is mean reversed downstream flow at some positions and mean upwards and downwards flow at some positions. The figure indicates the complex nature of the flow field in this region, with a magnitude of gradient reaching values of 2.5 in some localised positions.

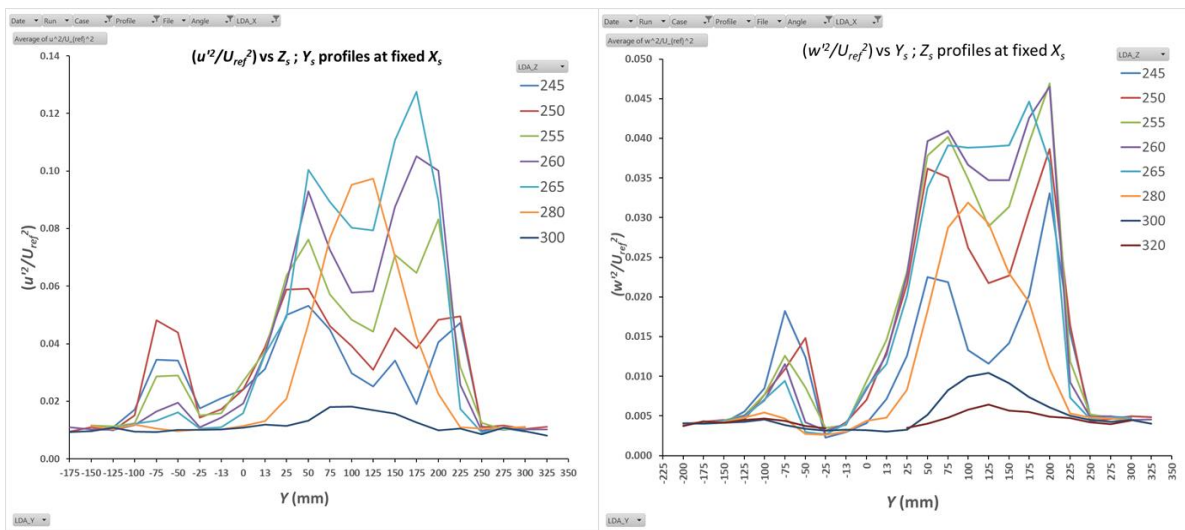


Figure 5.28(a/b). Cube/A; -22.5°; $X=160\text{mm}$; (a) (u'^2/U_{ref}^2) ; (b) (w'^2/U_{ref}^2)

Figure 5.28(a) at $X/H=2/3$ indicates increasing levels of turbulence over the region between $Y=50$ and $Y=200\text{mm}$ as one moves in height from $Z=245$ up to 280mm . Thereafter with

increasing height the turbulence reduces reaching low levels at $Z=300\text{mm}$. A similar pattern is evident in Figure 5.28(b) for the vertical component of turbulence intensity.

Taking $u'^2/U_{ref}^2 = 0.04$ for the height of $Z=255\text{mm}$ and $Y=100\text{mm}$ within the boundary of the roof indicates that $|u'|/U_{ref}=0.2$. Given a value of $U/U_{ref} \approx 0.1$, from Figure 5.24(b) for that sample height at the flow deficit, we have that $|u'|/U \approx 2$. The variations of the non-steady fluctuation component u' are of larger magnitude than the mean downstream component close to the roof surface: this indicates there will be frequent periods with substantial reversed flow even at this height: closer to the roof at $Z=245\text{mm}$ there was mean flow reversal.

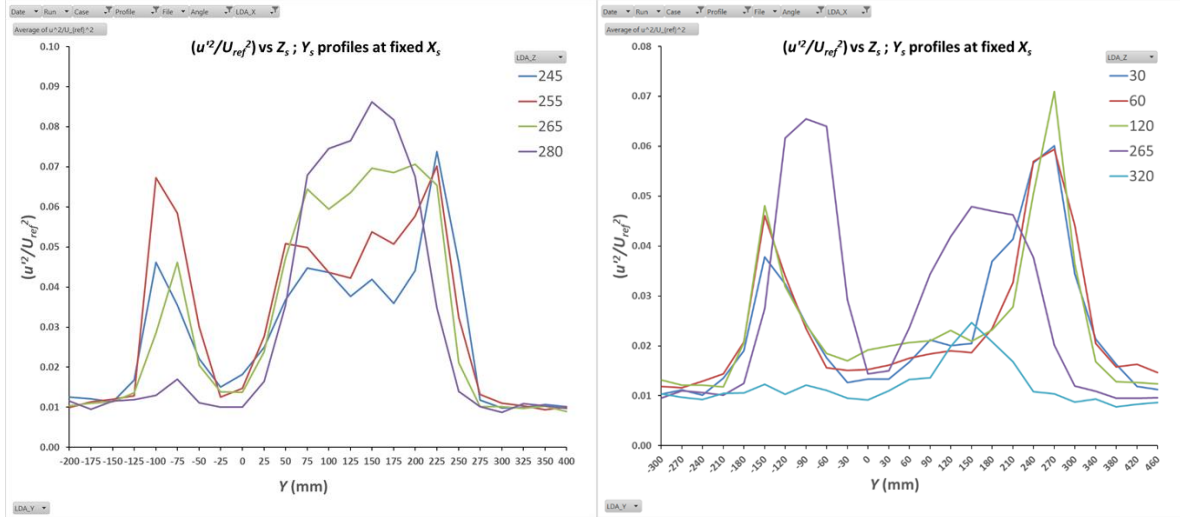
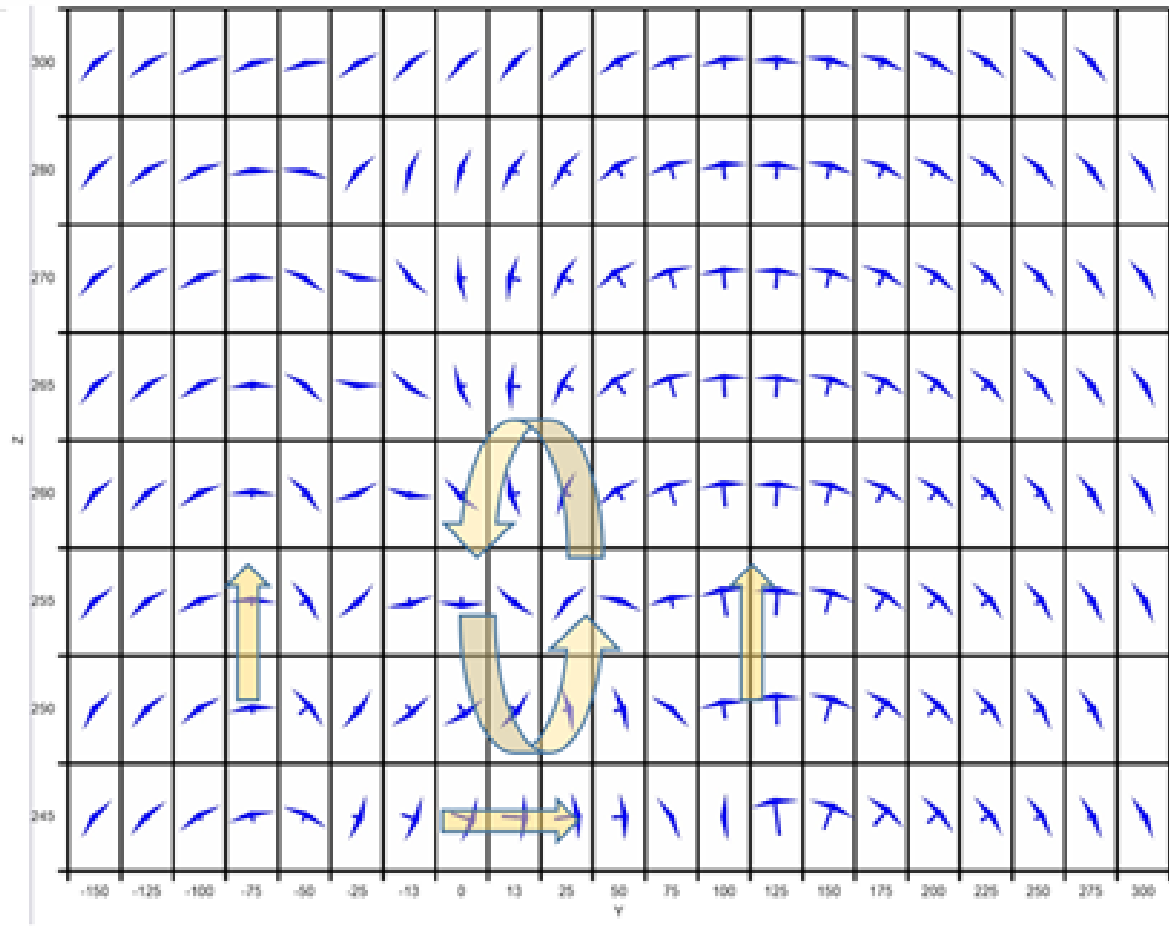


Figure 5.29(a/b). Cube/A; -22.5° ; (a) $X=236\text{mm}$; (u'^2/U_{ref}^2) ; (b) $X=396\text{mm}$; (u'^2/U_{ref}^2)

Figure 5.29(a) indicates lower levels of peak turbulence compared to Figure 5.28(a) but with a similar pattern of increasing turbulence with height up to $Z=280\text{mm}$. The side lobe at $Y=-100\text{mm}$ is also more prominent. Figure 5.29(b) at $X/H=1.65$ shows an overall slight reduction in the level of turbulence compared with the case at $X/H=1$ in Figure 5.28(a).

Figures 5.30(a-d) show vector plots in downstream $Y-Z$ planes of (V, W) with the magnitude of the velocity vector indicated by the length for the intermediate angulation case of -22.5° . Direction of flow is shown by the orientation of the arrowhead. The orientation is that of looking into the approaching downstream flow. The downstream planes are presented at $X=80, 160, 240$ and 400mm for Figures 5.30(a) through to 5.30(d): these distances correspond to $X/H=1/3, 2/3, 1$ and $5/3$ respectively, where H is the building height. Note that the vertical axis scale is stretched to aid visualisation compared to the horizontal axis.

Analysis of plots in Figures 5.30(a-d) indicate a complex intermediate case between the flow schematics given in Figure 5.1 for normal incidence at 0° and Figure 5.17 showing the other symmetrical case of -45° . Figure 5.16 gives some indication of how tighter vortices may be generated on the left-hand edge of the cube in that figure, and how extensive trailing vortices may be generated over the main roof zone from the front leading edge of the cube to the right of the figure. Note that left and right edge Y co-ordinates are given where sampling plane intersects the edges of the cube, and (X, Y) co-ordinates are given for the upstream, left, right and trailing cube vertex positions in Figures 5.30(a-d).





VW: Cube; A; -22.5°; $X=80\text{mm}$; V component aligned to positive Y direction, W component vertically. Arrow:  indicates flow direction in the co-ordinate system. Swirl symbol:  indicates rotation as viewed looking into the direction of approaching flow.

Figure 5.30(a). Cube/A; -22.5°; VW vector plot; $X=80\text{mm}$; left edge at $Y=-59\text{mm}$; leading vertex at $(X, Y) = (13\text{mm}, -31\text{mm})$; right edge at $Y=131\text{mm}$

From Figure 5.24(a) it may be seen that the leading apex of the cube is at $Y=-31\text{mm}$ and the cube centre at $Y=34\text{mm}$ in the co-ordinate system used for Figures 5.30(a-d). At this distance of $X/H=1/3$ for Figure 5.30(a) a single anti-clockwise vortex can be seen extending from $Z=245$ up to approximately 270mm . Cross flow in the positive Y direction is seen close to the roof at $Z=245\text{mm}$. Upwards flow is evident to either side of the vortex pattern laterally.

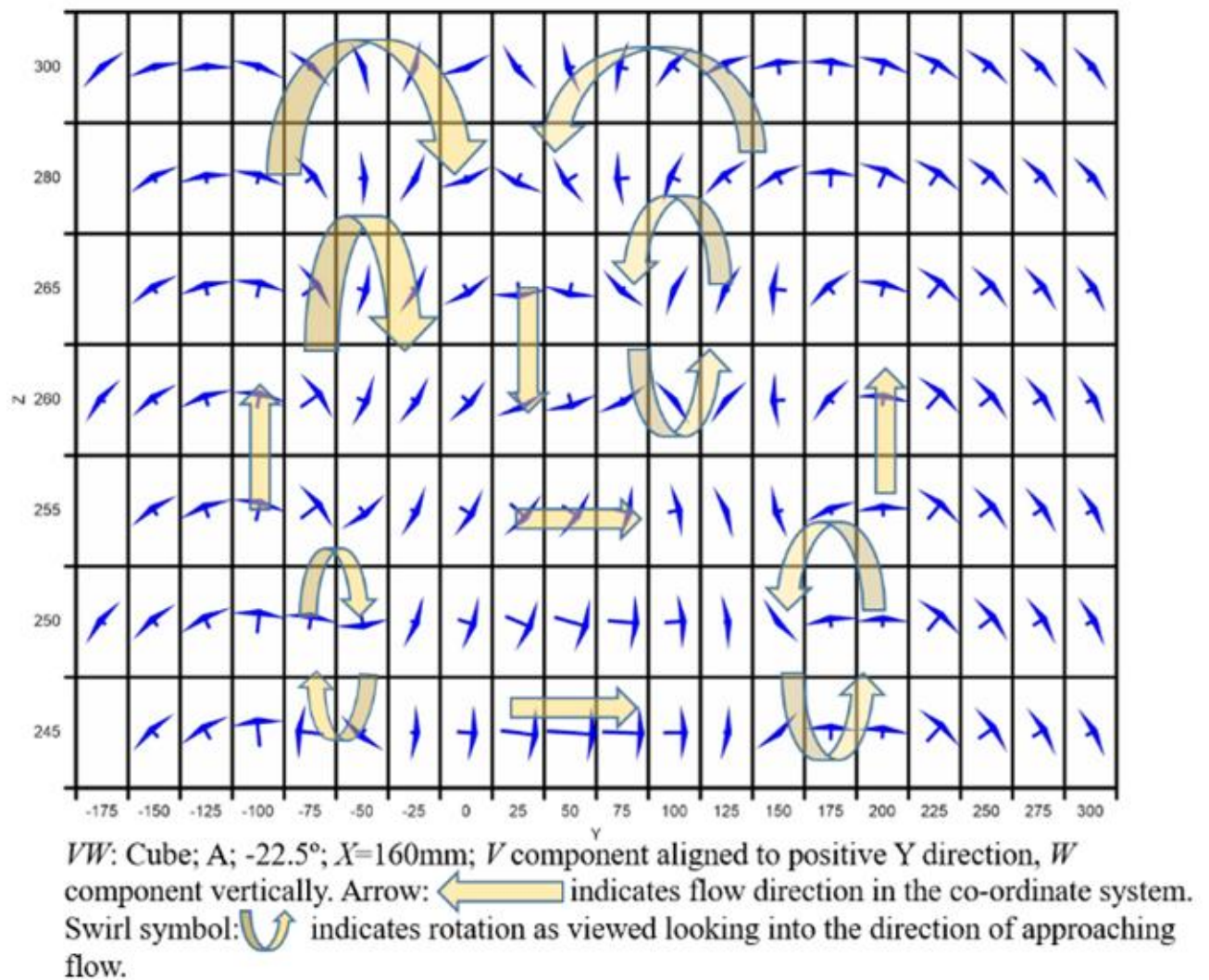


Figure 5.30(b). Cube/A; -22.5°; *VW* vector plot; X=160mm; left edge at Y=-92mm; leading vertex at Y=-31mm; right edge at Y=168mm; right vertex (X, Y) = (105, 191)

The (*V*, *W*) vector plot in Figure 5.30(b) shows a very complex pattern of flow and a number of vortices. Looking into the flow two larger vortex features, generated further upstream on the building edge, can be seen extending upwards to Z=300mm rotating as shown in the figure. To the left of the apex at Y=-31mm these rotate clockwise and will act to move pollutant material from aloft downwards nearer the roof. To the right of the apex at Y=-31mm the vortices are anti-clockwise in direction and will also act to move material from aloft down towards the roof plane. Lateral cross wind flow in the positive *Y* direction is evident in the central region of the roof up to a height of Z=255mm. Pollutant releases from position 'A' at the origin of co-ordinates at Y=0 may be advected into the down flow region at Y=25mm (approximately in line with the cube centre) which can be seen to also feed crosswind flow nearer the roof in the positive *Y* direction at heights Z=245-255mm. This feature, given that it was located close to the release position 'A', may be important in the advection of material downwards towards the roof and into the roof recirculation zone. Smaller vortices were apparent at Y≈-60mm and Y≈175mm which are expected to have been generated at closer downstream positions to this measurement plane from the building edges.

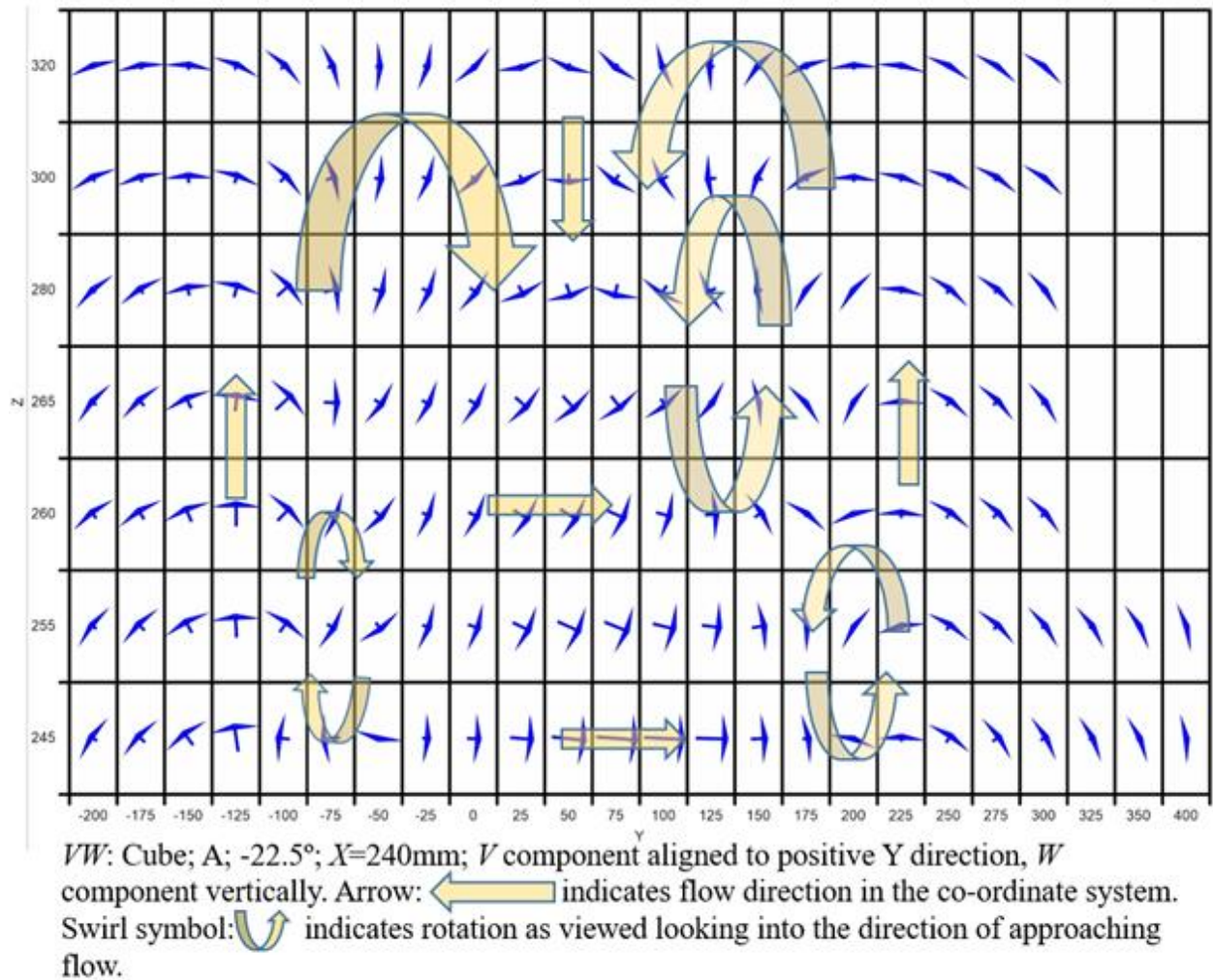
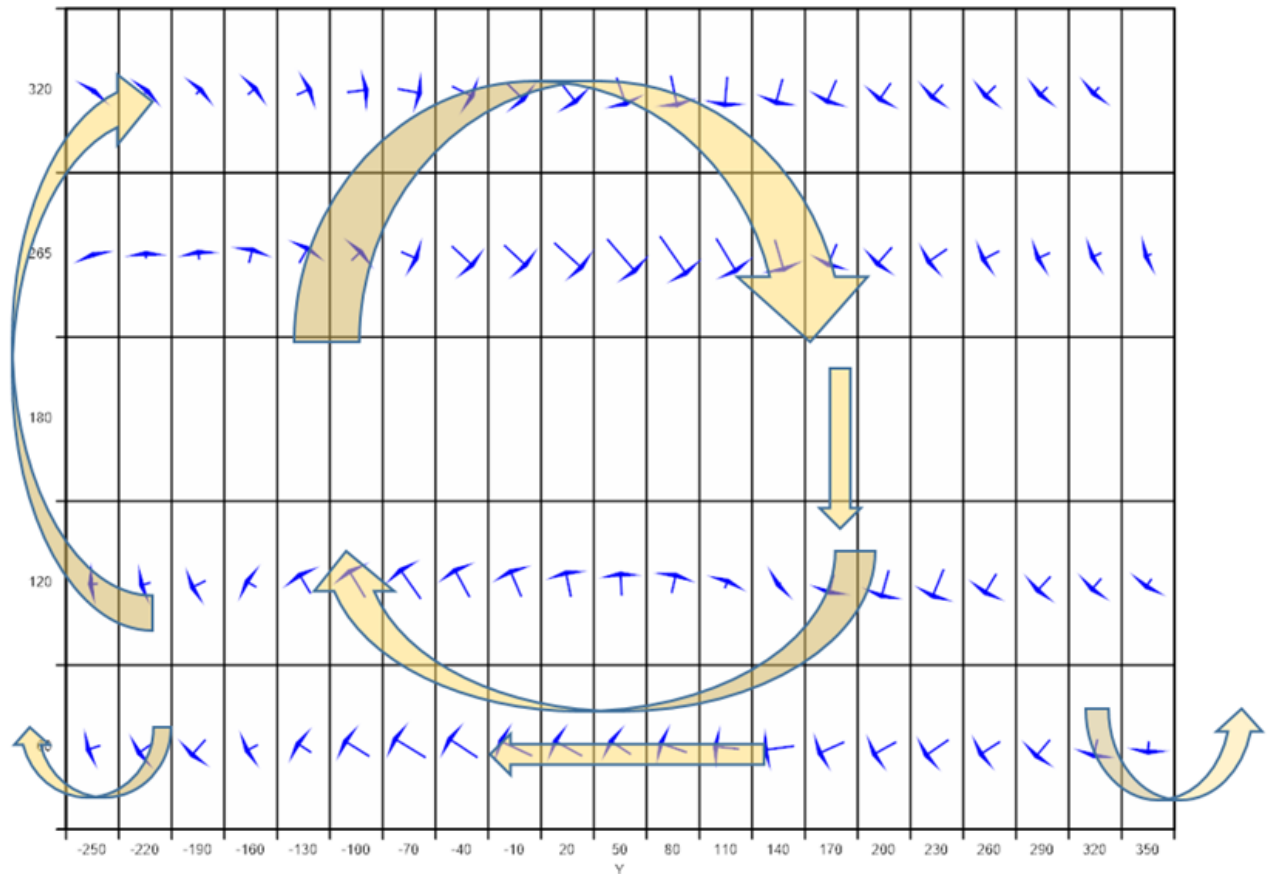


Figure 5.30(c). Cube/A; -22.5°; VW vector plot; $X=240\text{mm}$; left edge at $Y = -111\text{mm}$; leading vertex at $Y=-31\text{mm}$; right edge at $Y=135\text{mm}$; left vertex $(X, Y) = (235, -123)$; right vertex $(X, Y) = (105, 191)$

The flow vector plot in Figure 5.30(c) shows a developing pattern of vortices propagating from the planes shown upstream. Two larger vortices are apparent in the region of $Z=260\text{mm}$ to $Z=320\text{mm}$, with a middle downwards flow section at $Y=50\text{mm}$. Smaller vortices are apparent at $Y=-75\text{mm}$ and $Y=200\text{mm}$. The downward portion of the vortices feed into the middle region $Y \approx -25\text{mm}$ to 150mm where the flow is in the positive Y direction and extends now up to a height of $Z=260\text{mm}$. Maximum vector magnitude for the (V, W) plot in 31(c) is 0.339 at $(75, 245)$.





VW: Cube; A; -22.5° ; $X=400\text{mm}$; V component aligned to positive Y direction, W component vertically. Arrow:  indicates flow direction in the co-ordinate system. Swirl symbol:  indicates rotation as viewed looking into the direction of approaching flow.

Figure 5.30(d). Cube/A; -22.5° ; VW vector plot; $X=400\text{mm}$; left vertex $(X, Y) = (235, -123)$; leading vertex $(X, Y) = (13, -31)$; trailing vertex $(X, Y) = (327, 99)$; right vertex $(X, Y) = (105, 191)$

Figure 5.30(d) shows the (V, W) flow downstream of the back edge of the cube at -22.5° , with measurements at heights of $Z/H = 0.25, 0.5, 1.10$ and 1.33 . The lowest heights were below the roof of the cube at this downstream position. The magnitude of the maximum vector velocity in the displayed (V, W) flow field was just 0.117 at $(-10, 265)$ which indicates reduced velocities in the vortex flow. A large vortex is seen according to the range of sampled heights shown, though it should be noted that there is a gap in sampled data between $Z=120\text{mm}$ and $Z=265\text{mm}$. Reverse flow in the negative Y direction was seen at height $Z=30\text{mm}$. There is some evidence here that the vortices have formed the general pattern of a larger clockwise vortex downstream, noting that the -22.5° angulation case is not symmetrical in the flow stream.

5.6. EW Clad Full Building Model at -22.5°

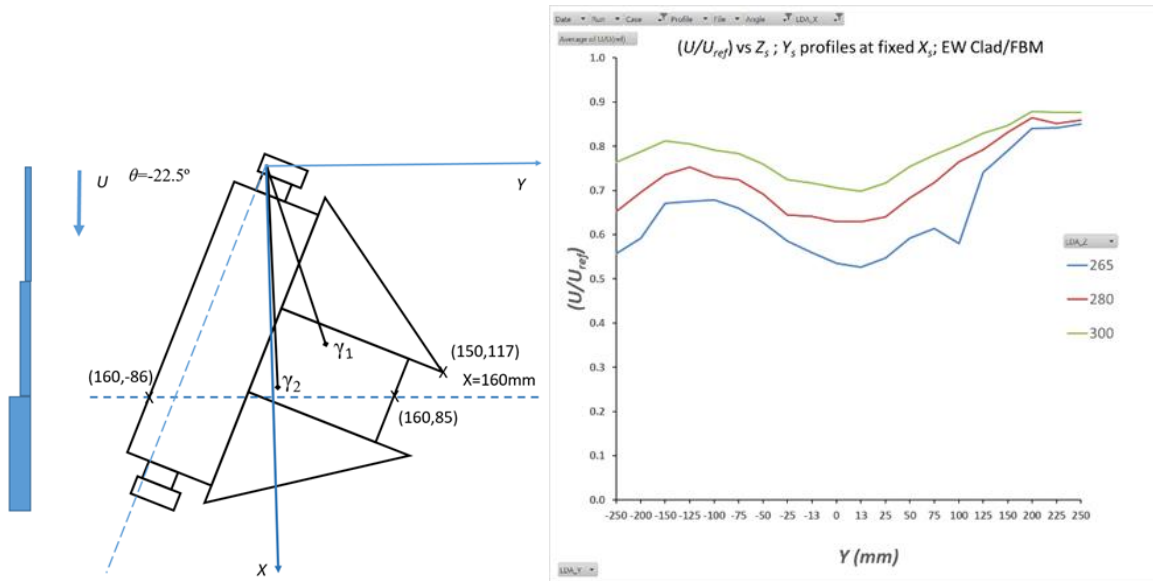


Figure 5.31(a/b). EW Clad/FBM; -22.5°; (a) arrangement and coordinate system; (b) (U/U_{ref}) ; $X=156\text{mm}$ ($X/H=0.65$)

Notes: Full Building Model (FBM) includes all buildings in the set; for (a) scale block markers of length $X=H/3$ are shown down the left margin (drawing is accurate to scale).

Figure 5.31(a) shows the EW clad building oriented to -22.5° into the flow: this is a scale drawing with scale marker blocks down the left margin corresponding to a dimension of 80mm (or $H/3$). Figure 5.31(b) shows the downstream velocity at the three sampled heights in a sampled plane overlying the level section of roof between the two elevated glass triangular sections seen in Figure 5.12(b). A small perturbation in U/U_{ref} was seen in the region of $Y \approx 75$ -100mm for the lowest sampled height of $Z=265\text{mm}$.

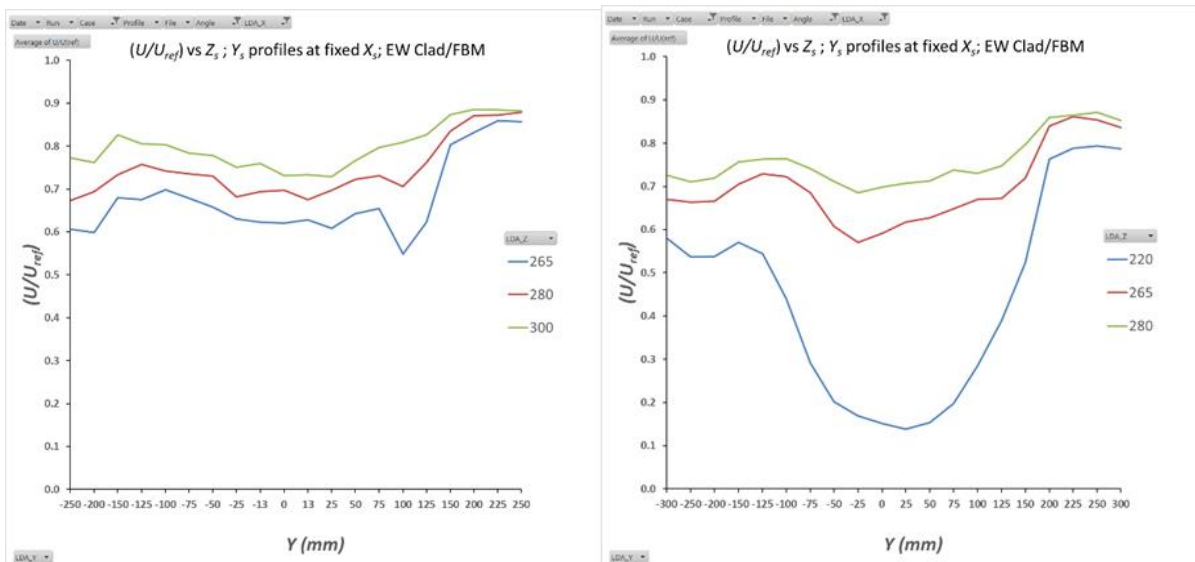


Figure 5.32(a/b). EW Clad/FBM, U/U_{ref} at -22.5° ; (a) $X=236\text{mm}$ ($X/H = 0.98$); (b) $X=396\text{mm}$ ($X/H=1.65$)

From Figure 5.32(a) the perturbation of velocity seen in Figure 5.31(b) has been propagated to the further downstream distance shown in the figure. Figure 5.32(b) shows the significant

downstream velocity deficit in the wake of the EW building. The lowest height sampled of 220mm below the roof plane at height 240mm shows a minimum value of U/U_{ref} in the region of 0.15. Sampled heights above the roof plane were similar to the upstream planes shown previously.

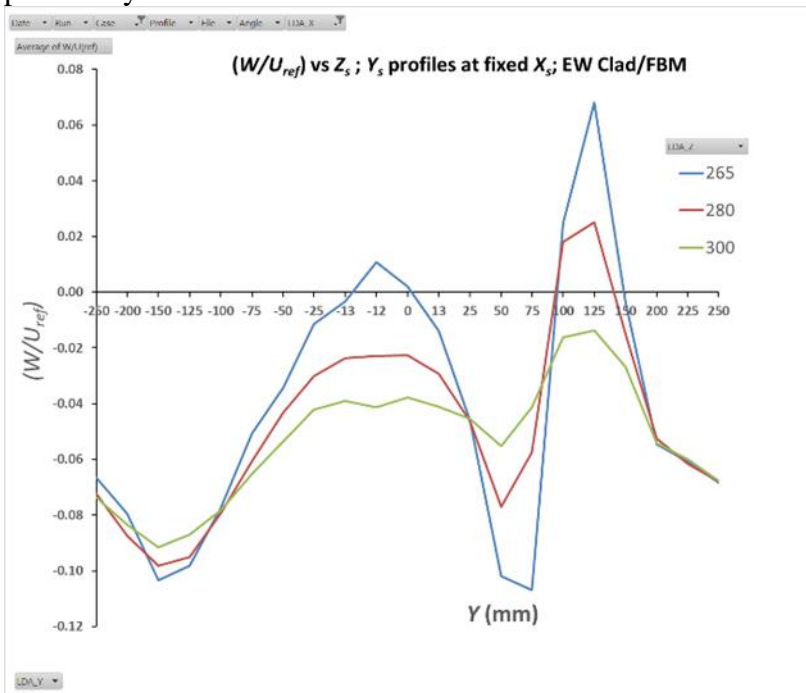


Figure 5.33(a). EW Clad/FBM; -22.5°; $X=156\text{mm}$; (W/U_{ref})

From Figure 5.33(a) can be seen a more complex pattern to the vertical component of flow W/U_{ref} . At sampled height $Z=265\text{mm}$ there is down flow at $Y\approx 50\text{mm}$ (corresponding to the recess between the triangular glass elevated sections) and upwards flow at $Y\approx 125\text{mm}$ (corresponding to the lateral extent of the building from Figure 5.31(a)). At the greater sampled heights of 280mm and 300mm there is the same flow pattern, though the vertical component of velocity is correspondingly reduced with increasing height above the building. Over the middle region of the roof zone in the range $Y=-25$ to 13mm there is a modest downwards flow deflection, and a relatively stronger downwards flow component in the region of $Y<-100\text{mm}$.

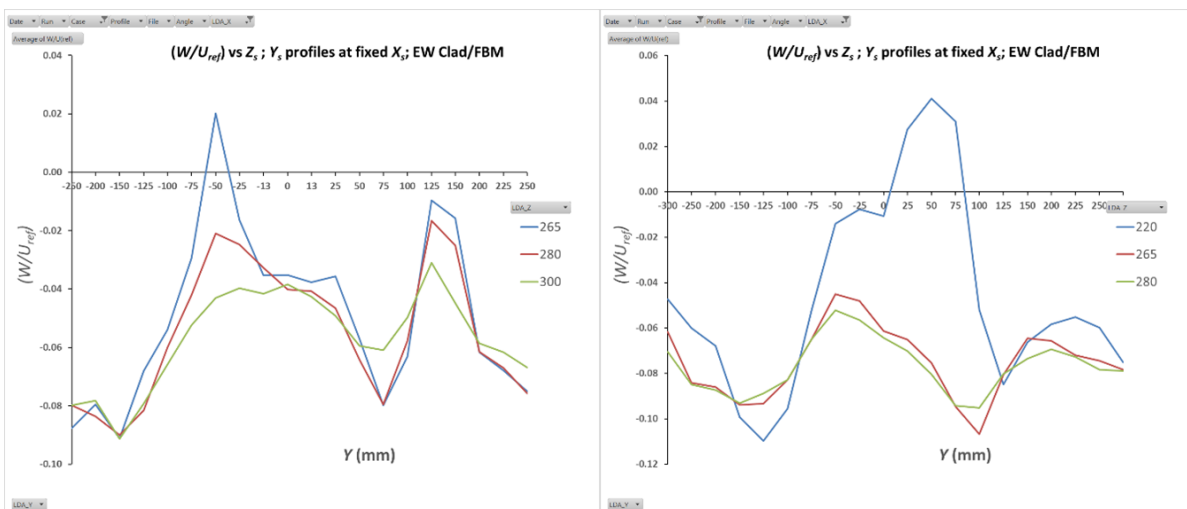


Figure 5.33(b/c). EW Clad/FBM; -22.5°; (W/U_{ref}) ; (b) $X=236\text{mm}$; (c) $X=396\text{mm}$

Figure 5.33(b) at downstream distance $X=236\text{mm}$ shows an overall pattern of flow velocity similar to Figure 5.33(a) for the downstream case at $X=156\text{mm}$, but with an overall downwards

shift into the negative Z direction i.e. most of the flow is directed downwards, with the exception of an isolated peak at $Y=-50\text{mm}$ for the $Z=265\text{mm}$ sampled height. This figure may be taken to indicate the overall effect of downwash for any pollutant material in the flow.

Figure 5.33(c) for the distance of $X=396\text{mm}$ shows two regions of flow with a downwards directed component at $Y\sim-125\text{mm}$ and $Y\sim90\text{mm}$, that are close to the lateral edges of the building projected onto the downstream sampling plane as can be seen from Figure 32(a). Upwards directed flow was seen that the lowest sampled height of 220mm , which lay just below the roof level at 240mm , in a central position with respect to the building at $Y=50\text{mm}$.

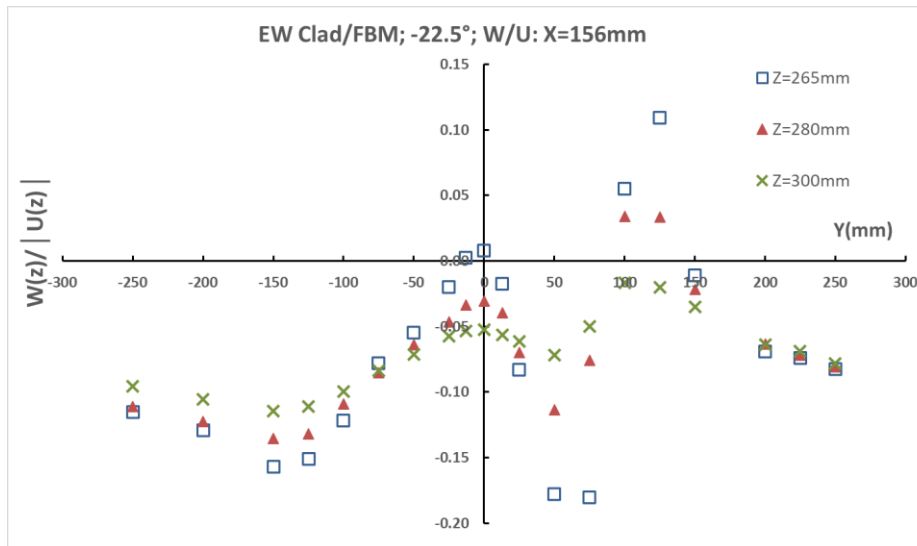


Figure 5.34. EW Clad/FBM; -22.5°; $(W(z)/U(z))$; $X=156\text{mm}$

Figure 5.34 shows the gradients for the EW clad FBM case. It was noted that the magnitude of fluctuations was relatively modest at a maximum of just under 0.2, although the lowest sample height was 265mm ($Z/H=1.1$) relatively far from the roof compared to previous cases shown and with no regions where the magnitude of the streamwise flow took low values – a contributory factor in reducing the variations in $W(z)/|U(z)|$.

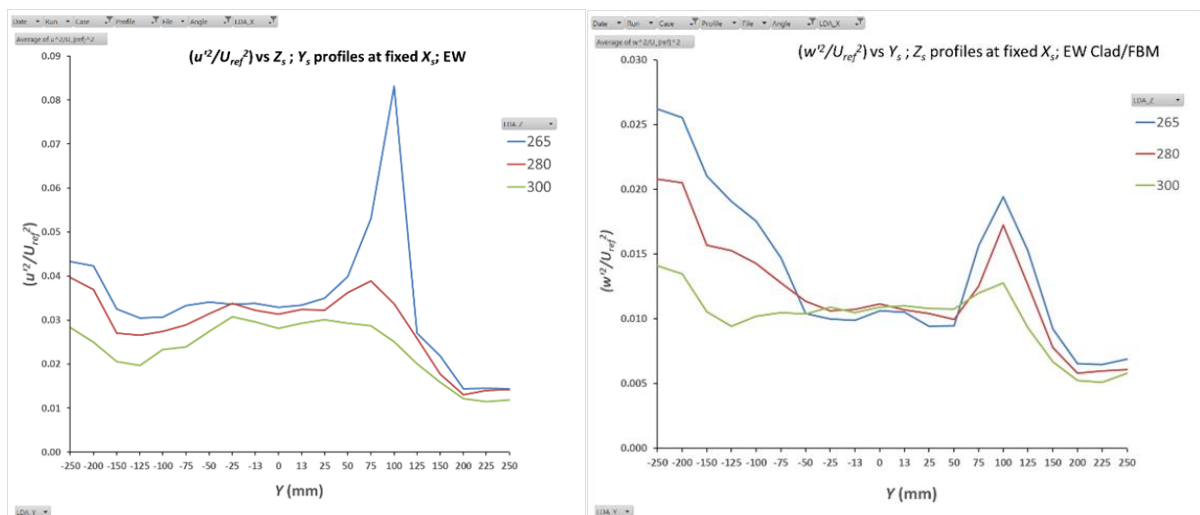


Figure 5.35(a/b). EW Clad/FBM; -22.5°; $X=156\text{mm}$; (a) (u'^2/U_{ref}^2) ; (b) (w'^2/U_{ref}^2)

The downstream component of turbulence intensity showed a marked increase in the region of $Y=100\text{mm}$, as shown in Figure 5.35(a), approaching a value of 0.09 – this was also the position

of the identified flow perturbation in Figure 5.33(a). Elsewhere over the roof region at this sampled plane the normalised turbulence intensity value was of the order of 0.03.

Figure 5.35(b) shows the vertical component of the turbulence intensity over the roof middle section at $X=156\text{mm}$. There is a localised peak at $Y=100\text{mm}$, which corresponds from Figure 5.31(a) to a position just downwind, and inwards towards the centre of the building, of the edge of the elevated triangular glass section. The effect of this perturbation to the flow was seen to reduce with height at the greater sampled heights of $Z=280\text{mm}$ and $Z=300\text{mm}$. At the other lateral edge of the building, and beyond, in the region of $Y<-50\text{mm}$ to -250mm there was seen to be increased values of turbulence intensity at the lowest height sampled of $Z=265\text{mm}$: for the wind approach angle studied with the EW full building model there was a large building upwind in this direction, namely the North Wing, and the presence of such a large building would be expected to give rise to these increased level of turbulence intensity.

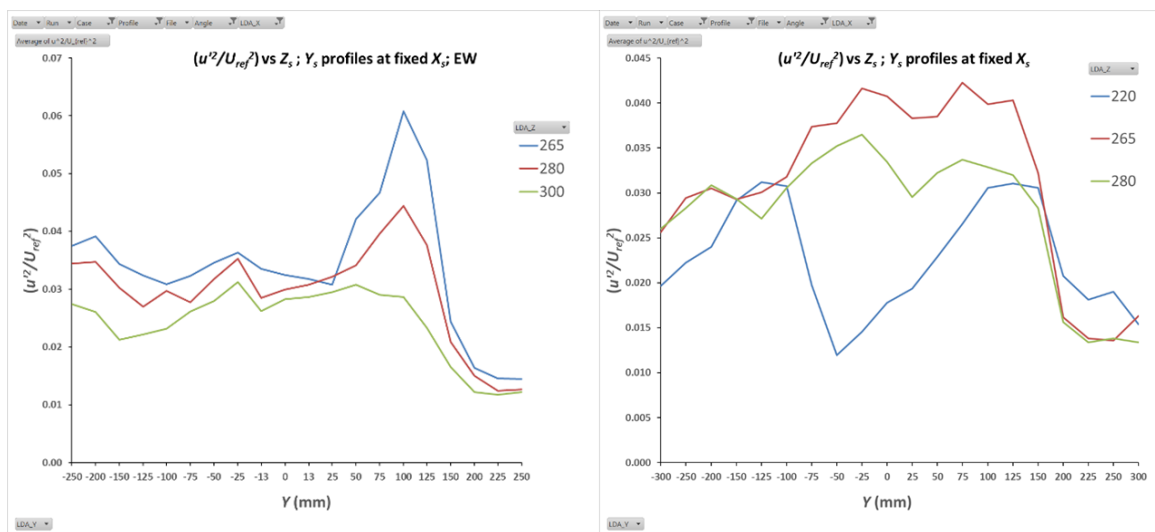


Figure 5.36(a/b). EW Clad/FBM; -22.5° ; (a) $X=236\text{mm}$; (u'^2/U_{ref}^2) ; (b) $X = 396\text{ mm}$; (u'^2/U_{ref}^2)

Figure 5.36(a) for the downstream component of turbulence intensity at $X=236\text{mm}$ may be compared to the upstream plane at $X=156\text{mm}$. The overall levels of turbulence are similar, and it may be noted that the peak in turbulence for the sampled height of 265mm occurs at $Y=100\text{mm}$ contrasted with the peak in Figure 5.35(a) at $Y=75\text{mm}$: evidence of lateral deflection over the roof zone for this flow feature.

The overall level of the downstream component of turbulence intensity can be seen in overall magnitude, from Figure 5.36(b) for the downstream plane sampled at $X=396\text{mm}$, to be similar to Figure 5.36(a). There was one different flow feature seen as a dip in value corresponding to the lowest sampled height of 220mm and a position of $Y=-50\text{mm}$.

5.7. EW Clad/FBM angle sensitivity analysis and EW clad isolated building at -22.5°

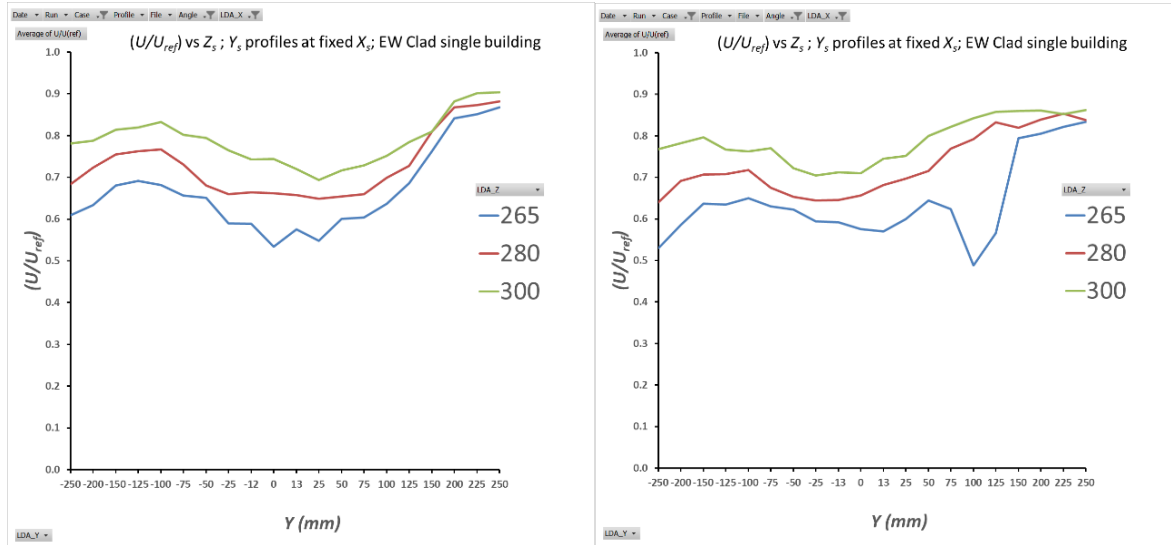


Figure 5.37(a/b) EW Clad/FBM; (a) -27.5°; (b) -17.5° (U/U_{ref}); $X=156\text{mm}$ ($X/H=0.65$)

From Figure 5.37(a) at -27.5° there is little evidence of the flow perturbations seen in Figure 33(b). However, from Figure 5.37(b) at -17.5° angulation we can evidence of this flow perturbation at $Y=100\text{mm}$ reducing normalised flow velocity at this point to approximately 0.5. Positions of the contact points of the sampled plane with the building with these different angulations are shown in Appendix 15.2.

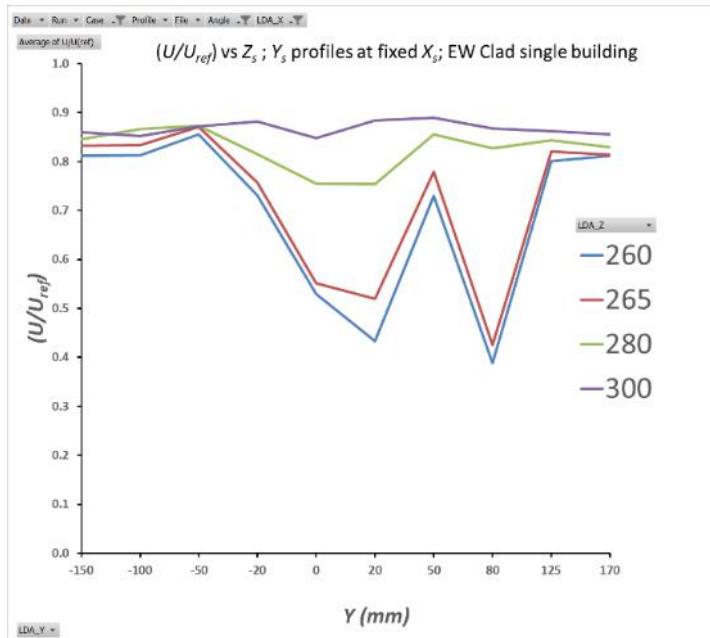


Figure 5.38 EW Clad isolated building; -22.5°; (U/U_{ref}); $X=156\text{mm}$ ($X/H=0.65$)

Figure 5.38 shows the flow field for the isolated EW clad building. For the lowest heights sampled of $Z=260$ and 265mm a pair of distinct flow deficits can be seen at $Y=20$ and 80mm and the mean flow in this region is around 0.6: similar to that seen with the Full Building Model (FBM) in Figure 5.37(b). The presence of the upstream, and to some extent downstream,

buildings in the full model set can be seen to ‘smooth out’ local variations more apparent with the isolated building.

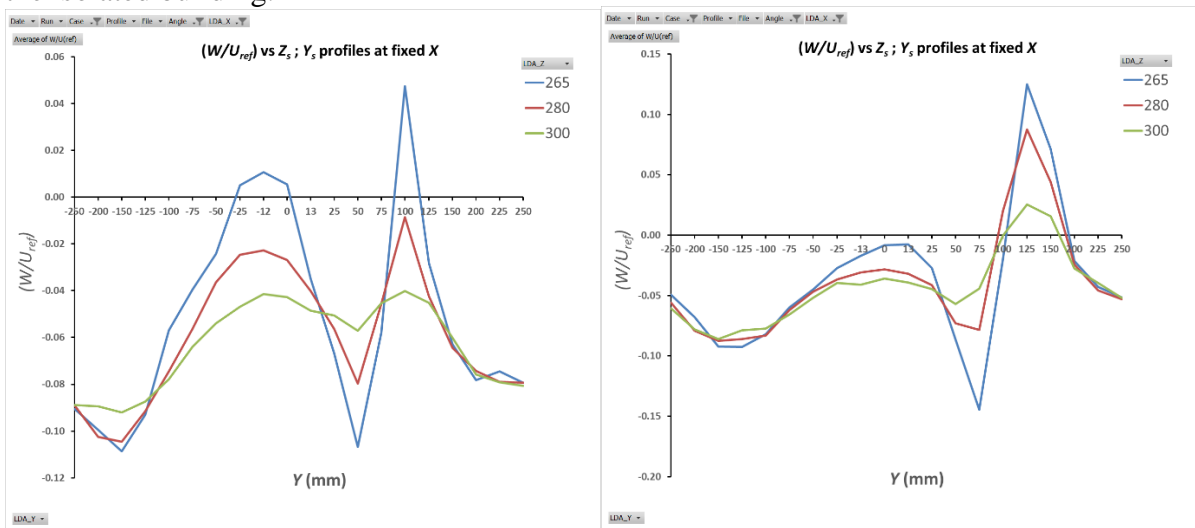


Figure 5.39(a/b). EW Clad/FBM; (a) -27.5°; (b) -17.5° (W/U_{ref}); $X=156$ mm ($X/H=0.65$)

Figure 5.39(a) for the -27.5° angulation may be compared directly to Figure 5.33(b) for the -22.5° case, and the same pattern is evident across both velocity profiles, but with the peak positive upwards flow being at $Y=100$ mm compared to $Y=125$ mm for the same feature in Figure 5.33(b), a change which may be associated with the lateral edge of the building changing position with the rotation compared to the approach flow.

From Figure 5.39(b) the same overall pattern is shown as Figure 5.33(b) for the -22.5° case. However, the amplitude of the peak at $Y=125$ mm for -17.5° angulation is approximately double that for the -22.5° case. Similarly, the down flow peak is slightly shifted to $Y=75$ mm and takes a negative peak value of $W/U_{ref} = -0.15$, compared to $Y=50$ mm and approximately -0.10 for the -22.5° graph in Figure 5.33(b).

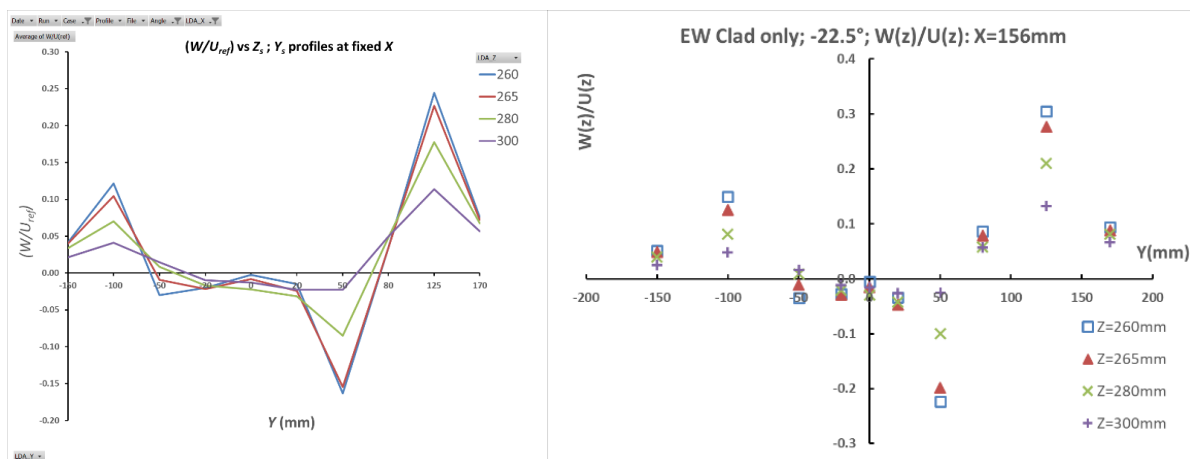


Figure 5.40(a/b). EW Clad isolated; -22.5°; $X/H=0.65$; (a) (W/U_{ref}); (b) $W(z)/U(z)$

Figure 5.40(a) showing the isolated EW clad building shows greater magnitude downflow ($Y=50$ mm) and upwards flow ($Y=125$ mm) than are seen in Figure 5.33(a) for the same approach angle but with the FBM. The maximum gradient of the flow inclination shown in Figure 5.40(b) was a maximum of 0.3 at $Y=125$ mm, the modest value being reflected by the minimum sampling height being $Z=265$ mm or relatively far from the roof, reducing the flow perturbations generated by the building on the flow.

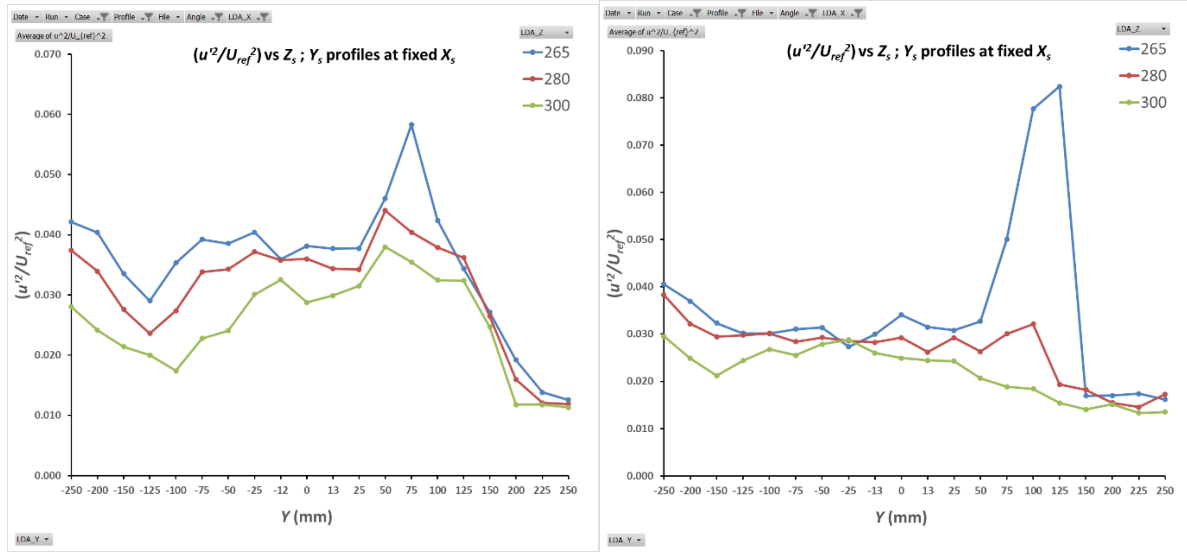


Figure 5.41(a/b). EW Clad/FBM; $X=156\text{mm}$; (u'^2/U_{ref}^2) (a) -27.5° ; (b) -17.5°

The overall downstream turbulence intensity level component shown in Figure 5.41(a) was similar to the -22.5° case shown in Figure 5.35(a), although the peak at $Y=75\text{mm}$ is lower at 0.06 compared to the value of 0.08 in the former case. Figure 5.41(b) for the -17.5° angulation retains a peak value of 0.08, positioned at $Y=100\text{mm}$ reflecting the position of the building features at this angulation to the flow.

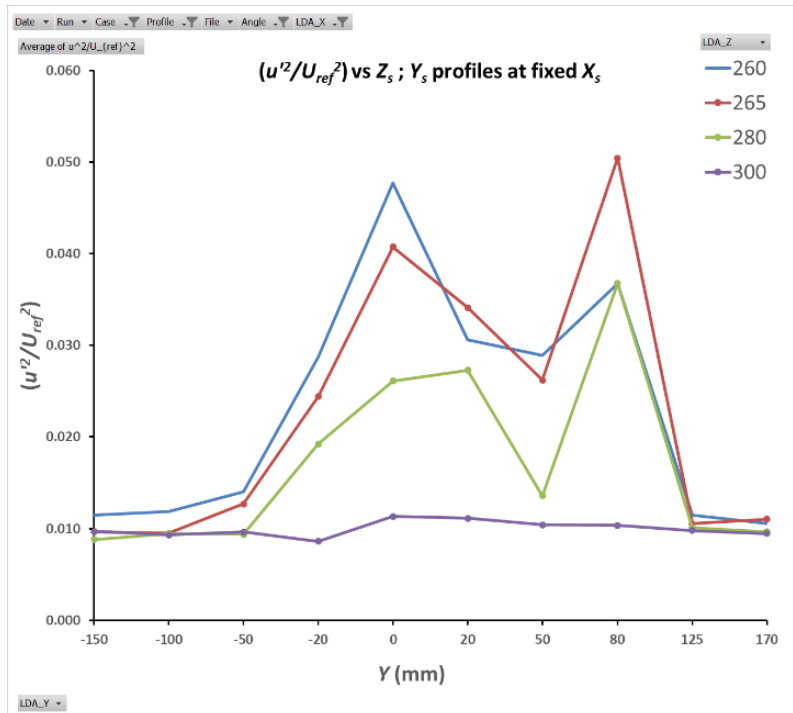


Figure 5.42. EW Clad isolated building; -22.5° ; $X=156\text{mm}$; (u'^2/U_{ref}^2)

The turbulence intensity for the isolated EW clad building in Figure 5.42 shows an overall level of downstream component turbulence in the region of 0.03-0.05 for $Z=265\text{mm}$, compared to a value of around 0.03 in Figure 5.35(a) - but the latter figure showing a peak of 0.08. What is notable is the spatial variation in the values between $Y=-20$ and 125mm and also that in this case the turbulence level at $Z=300\text{mm}$ has reduced to low levels compared to the earlier figure.

5.8. Discussion

5.8.1 Wind tunnel advection velocities and turbulence intensities: cube

For normal incidence with the cube building a significant reduction of U/U_{ref} was seen over the roof zone, with some reverse flow at the lowest sampled height in Figure 5.7(b) at the plane close to the centre of the cube. A little upwind of the back edge of the cube in Figure 5.8(a) there was no mean flow reversal, indicating the boundary of the roof top recirculation zone was close to the cube roof centre. Further downstream in Figure 5.8(b) beyond the back edge of the cube strong reverse flow was seen at sample heights mid-height and close to the ground. Both the recirculation zones: the roof recirculation zone (RCZ) and the main building recirculation zone extending to ground level are regions in which pollutant, or tracer material, may be recirculated giving rise rapid mixing within the zones and increased levels of pollutant or tracer at locations that otherwise would not be affected.

For the normal incidence case of the cube strong downwards advection was seen at the lateral cube sides as seen in Figures 5.9(a) and 5.9(b). For the sample plane beyond the back edge of the cube shown in Figure 5.9(c) strong downwash was evident for sample heights above roof level: sampling below roof height indicated there was positive flow directed upwards in the cavity zone. This flow feature indicates that pollutant may undergo advection downwards from above the roof plane with the presence of reverse flow backwards with an upward component at lower heights feeding the main building recirculation region. High local inclination of flow was seen in Figure 5.10 in regions with slow downstream mean velocity.

The flows for the normal incidence on the cube gave rise to a high extent of turbulence, with the value of u'^2/U_{ref}^2 reaching a maximum of approximately 0.12 in Figure 5.14(a) for the sample position near the centre of the cube (compared to a value of about 0.01 outside of the wake). The vertical component of normal stress w'^2/U_{ref}^2 reached a maximum value of approximately 0.045 in Figure 5.14(b) at the same position (compared to a value of about 0.005 outside of the wake). In the downstream position past the end of the cube u'^2/U_{ref}^2 showed a maximum of 0.05 in Figure 5.15(b), but with peaks corresponding to positions outside the lateral edges of the cube: much lower values of this quantity were seen in the cube midline position at levels nearer the ground.

The next flow situation considered was the cube at -45° incident to the flow. Two deep velocity deficits in the downstream flow were apparent from Figure 5.18(b) extending down to have small regions of reverse flow at the lowest sample height tested, 5mm from the cube roof level. The downstream velocity deficits corresponded to strong regions of upwards flow in Figure 20(a) with moderate downwards flow over the central region of the cube also evident. The value of u'^2/U_{ref}^2 reached a maximum of approximately 0.10 in Figure 5.22(a) for the sampled downstream position near the centre of the cube at lateral positions. The vertical component of shear stress w'^2/U_{ref}^2 reached a maximum value of approximately 0.037 in Figure 5.22(b) at the same lateral positions. These maxima were attained at the sampled height of $Z=255\text{mm}$ - not the sampled plane closest to the roof at height 245mm. For passive releases entering the flow at height 255mm these turbulence and advection processes may be important factors in the dispersion of pollution.

The dual deficit flow features in the downstream velocity were also seen in Figure 5.19(a) for the downstream plane at $X=240\text{mm}$ towards the back edge of the angled cube. Strong upwards flow was seen in Figure 5.20(b) at the lateral edges of the cube and downwards peaks inboard on the roof revealing the presence of the roof vortices. The value of u'^2/U_{ref}^2 reached a

maximum of approximately 0.085 in Figure 5.23(a) for the sampled downstream position near the back cube at lateral positions.

For the cube at -45° the downstream component of velocity at the $X=400\text{mm}$ plane showed strong recirculation reverse flow at half cube height and closer to the ground plane: this feature can be seen in the flow schematic in Figure 5.17 where reverse and upwards flow can be seen at the back of the cube. From Figure 5.20(c) a strong upwards component of flow was seen at the lowest heights with W/U_{ref} of up to 0.12 indicating that flow was recirculating backwards and upwards in the main wake of the building. Turbulence intensities for the downstream component of flow for this position reached a maximum value of 0.07 from the data obtained.

After considering the symmetrical flow fields associated with the 0° and -45° cases the intermediate -22.5° case was considered from the results obtained. From Figure 5.24(b) a single, but skewed towards the midline of the cube, U/U_{ref} velocity profile was seen. For this series of results data from LDA measurements of the crosswind flow velocity were also available and these are presented in Appendix 15.2. As can be seen in Figure 5.26(a) at $X/H=2/3$ a strong downflow can be seen above the cube roof of magnitude of $W/U_{ref} \approx -0.1$ to -0.15 extending up to a height of $Z/H=1.17$. Strong upwards flow of up to $W/U_{ref} \approx 0.25$ was seen in Figure 5.26(a) towards the lateral edges of the cube. A complex pattern of vertical flow gradients was seen over the roof zone in Figure 5.27.

The value of u'^2/U_{ref}^2 reached a maximum of approximately 0.13 in Figure 5.28(a) for the sampled downstream plane near the middle of the cube at $X/H=2/3$ at a height of $Z/H=1.1$ (compared to values at the edge of the building work of approximately 0.01). The vertical component of shear stress w'^2/U_{ref}^2 reached a maximum value of approximately 0.045 in Figure 5.28(b) near the cube centreline position at the same height (compared to a value at the edge of the building wake of 0.005). High values of turbulence persisted down to heights close to the cube roof surface at this angulation of building to the approaching flow.

The overall (V , W) flow patterns in Figures 5.30(a-d) can be seen to be important in the entrainment of material in the central vortex for passive release heights up to $Z/H=1.17$ with advection down to lower levels near the roof surface at $Z/H=1.02$. There was also evidence of crosswind advection of flow into the recirculation zone centrally on the roof. In Appendix 15.2 additional information is available on the lateral cross wind velocity measurements of V/U_{ref} .

5.8.2 Wind tunnel advection velocities and turbulence intensities: EW building models

The EW building model cases presented were mostly of the full site model, with some limited results for the isolated EW clad building model presented to enable comparison of the flow fields downstream comparing the full building and isolated EW clad model. The focus was on a simulated 'real world' scenario and presentation of flow features particular to that experimental configuration. Limitations of the experimental results were evident, in that the lowest sample height achievable being 265mm, as seen in Figure 5.31(b), some 25mm above the flat portions of the EW building roof at $H=240\text{mm}$: it should be noted that the results presented previously in this chapter relate to a cube of the same height $H=240\text{mm}$. The EW building model had projecting features above the 240mm roof plane; notably the triangular profiles seen in Figure 5.31(a) which were 10mm above the 240mm roof plane. Also, experiments with the EW building focused on the main wind direction for previous experiments of -22.5° : a direction of flow that resulted in tracer material concentrations of significant interest in the roof zone.

Figure 5.31(b) shows a velocity deficit with a dip extending down to $U/U_{ref} \approx 0.6$ for the lowest height sampled of 265mm at $X=156$ mm. Heights above this at 280mm and 300mm showed less flow velocity reduction in a consistent pattern. A downflow pattern, which was proposed to be due to local building features, were seen in Figure 5.33(a) at $Y=75$ mm for the W/U_{ref} plot at $X=156$ mm. A complex variation of vertical flow inclination $W(z)/U(z)$ was shown in Figure 5.34, but the magnitude of the gradient was limited to below 0.2, due to the relatively greater minimum sampling height of $Z=265$ mm for these experiments set by experimental limitations of getting close to the model surface caused by projecting features on the model roof.

The cube flow pattern, at the same incidence of approach flow of -22.5° gave rise to a strong downwards flow in the sampled height range of 250-265mm in the region of $Y=0$ mm to 50mm i.e. close to the release point position 'A'; a minima of $W/U_{ref} = -0.15$. By contrast, the EW full building case showed minimal downwards flow for the lowest sampled height of 265mm (an experimental limitation in not being able to sample closer to the roof plane because of the shape features of the EW building, where it would be expected that features of the flow such as the effect on streamwise velocity would be more pronounced) in the region $Y=-25$ mm to 25mm. Stronger downwards flow was seen in the region of $Y=50$ mm, but countervailing upwards flow was seen at $Y=125$ mm. The finding here was that local flow features for a given case could have significant implications for flow advection from a given release position in relation to a building. Turbulence intensities maxima for this downstream distance for the u'^2/U_{ref}^2 and w'^2/U_{ref}^2 components were 0.08 for the local feature at $Y=75$ mm, and approximately 0.035 elsewhere, and 0.020 for the vertical component, each showing a peaked feature at $Y=100$ mm. However, it is also true that the EW building presents at least one face, and usually two, that are at incidence to the oncoming flow and therefore generate roof vortices and flow recirculation. Although the EW building features have more local spatial significance compared to the cube building nevertheless both models are subject to roof vortices and flow recirculation regions which are important in both cases for the significant plume dispersion behaviour in the two cases.

The sensitivity to angulation of flow for the EW full building model was investigated for the approach angles $-22.5^\circ \pm 5^\circ$. Figure 5.37(b) for the -17.5° case showed an enhanced velocity deficit at $Y=100$ mm compared to the same feature in the -22.5° case shown in Figure 5.31(b). The isolated EW clad building showed larger location variations in downstream velocity in Figure 39 compared to the FBM set, but the flow inclination maxima were still relatively modest being up to a maximum of 0.3 as shown in Figure 5.40(b).

The magnitude of the upwards flow maximum for W/U_{ref} at $Y=125$ mm was found to be much greater in Figure 5.39(b) for the -17.5° angulation compared to the corresponding feature in the -22.5° angulation. The corresponding figures for the EW clad isolated case were greater still as shown in Figure 5.40(a).

Turbulence intensities maxima for this downstream distance of $X=156$ mm for the u'^2/U_{ref}^2 and w'^2/U_{ref}^2 components were 0.06 for the local feature at $Y=75$ mm in Figure 5.41(a) and 0.08 for the corresponding feature in Figure 5.41(b) for the -17.5° case.

For all three angles of approach flow at -17.5° , -22.5° and -27.5° there was generally downwards flow over the middle region of the building corresponding to around crosswind position $Y=0$ mm, the release point in experiments presented elsewhere in this work, but a significant downwards flow was adjacent to this in the region of $Y \approx 50$ mm as can be seen from Figures

5.39(b), 5.33(a) and 5.39(a) respectively for the angles stated above. To establish what the likely effects may be on downwards advection of pollutant material, and the sensitivity to release position, the sampled height of $Z=265\text{mm}$ was considered and the local maxima and minima of W/U_{ref} in the region described presented in Table 5.2.

Table 5.2 EW full building model: $W(z)/U(z)$ sensitivity analysis for $-22.5^\circ \pm 5^\circ$ at $Z=265\text{mm}$

Angle	$(W(z)/U(z))_{\max}$	$Y_{\max} \text{ (mm)}^*$	$(W(z)/U(z))_{\min}$	$Y_{\min} \text{ (mm)}$
-17.5°	-0.014	0	-0.232	75
-22.5°	0.008	0	-0.180	75
-27.5°	0.018	-12	-0.178	50

*-positions of the local maxima and minima are referred to as Y_{\max} and Y_{\min} .

From Table 5.2 the region from $Y=-12 - 0\text{mm}$ through to $Y=75\text{mm}$ marks a rapid transition from a small vertical component of velocity to a strong downwards flow. A different release position of pollutant in relation to the building would therefore be sensitive to this steep velocity gradient: more consistent downwards advection to roof level would be expected from a release in the co-ordinate range $Y=50-75\text{mm}$ compared to a release at position $Y=0\text{mm}$. By contrast, the sensitivity to variation of $W(z)/U(z)$ across the range of angles in Table 2 was relatively modest at the maxima and minima positions.

For the EW clad FBM measurements were made in a plane downstream at $X=396\text{mm}$, and the downstream velocity was shown in Figure 5.32(b) with a strong velocity dip in the central region measured at $Z=220\text{mm}$ height just below roof level. Figure 5.33(c) showed W/U_{ref} as positive in the region of $Y=25-75\text{mm}$ for the same sampled height – however, strong downward flow features were evident at the lateral extent of the building in this plane and these may be the means that roof released material can undergo advection into the main building recirculation zone. The maxima for u'^2/U_{ref}^2 was 0.04 for this sampled plane. Further information on the flow field for the EW clad FBM case downstream of this position has been given in Appendix 15.2.

5.9. Conclusions

The complexity of flows in the near field around obstacles has been discussed. In these experiments with the cube two conventional orientations, namely normal incidence and -45° were investigated and measured flow fields compared to previous published work. Added to this the intermediate angle case at -22.5° halfway between the established cases was investigated and an extensive set of results presented characterising this flow field, which was of relevance to the conditions investigated elsewhere in this work. The upstream approach flow was characterised to establish the amount of building generated turbulence added in the experimental cases investigated. An examination of the flow conditions established that the flow was fully turbulent with a Reynold's number well above the transition to fully turbulent flow conditions so the results were independent of Reynold's number, thus providing greater generality.

The flow field results for the cube have been presented showing a complex pattern of variation of flow velocity with spatial position. Flow features such as streamwise velocity deficits in the roof zone and downwind of the building have been shown, as well as evidence of roof generated vortices and the mechanisms by which they may cause advection of pollutant material close to the roof surface. A significant recirculation zone on the roof is evident with significant periods of reverse flow, caused by the turbulence levels seen, even for locations where there is a net

positive mean streamwise advection velocity. Pollutant is expected to be spread from aloft downwards by the vortex systems and by crosswind flows into the rooftop recirculation zone. Examples were seen of near rooftop flows in the positive Y -direction for the angles of approach flow studied and of downwards flow onto the roof. This fact can be used to explain the greater crosswind spread, to a large extent, for releases close to the roof level presented elsewhere in this work.

The cube cases showed symmetry for the 0° and -45° cases, which would be as expected. In both cases there were regions of relatively strong deflection downwards towards the roof level, bringing pollutant to near the roof zone. Turbulence intensities were high in relation to the undisturbed approach flow (without buildings in place).

There were some interesting features associated with the intermediate angle case of -22.5° studied where results from simultaneous measurements were presented in a series of (V, W) plots. These showed the development of a single rotating vortex at the first downstream plane, developing at the next plane into dual pairs of vortices either side of the leading corner to the approaching flow, with downwards advection in the region $Y \approx 0$ and strong crosswind advection in the positive Y direction for the lowest sampled heights over the roof region. The downstream component of flow velocity developed dual dip profiles with propagation downwind, an intermediate case between the normal incidence at 0° and -45° - this can be seen schematically in Figure 5.16 where vortices develop asymmetrically but propagate streamwise from both edges of the cube meeting the downstream flow: smaller, tighter vortices (and a smaller dip profile for downwind velocity) at the edge sharply angled to the flow and broader deeper vortices resulting from the bluff edge to the flow resulting in a deeper flow deficit over the main section of the roof. These dual features were regions of enhanced turbulence intensity in all of the velocity component directions.

For planes sampled beyond the downstream edge of the building there was clear evidence of downwash and reverse flow: important features for the entrainment of material into the main recirculation zone.

For the EW building, evidence of downwards flow was apparent from the sampled planes studied, but there was significant evidence of local features of the building affecting the flow field downstream, with some flow features propagating downstream and recognisable as related to building features upstream: this included local maxima in turbulence intensity. At the mid-roof sampled plane the sensitivity of the flow field with a five-degree variation of angle was assessed: in terms of the downwards flow velocity the differences were modest – but it could be seen that by far the most significant factor was the position of any release in relation to the building. Some positions would experience high mean downwards flow, and advection of material to near roof level, whereas others would only encounter moderate downwash: these variations would be lessened to some extent by fluctuations in flow direction due to building generated turbulence and changes in wind direction.

Local differences in vertical velocity W/U_{ref} were seen between the EW clad full building model and the EW clad isolated building. The absence of the full building model acted to amplify local features seen in the flow for the isolated building case.

In summary advection processes are significant in transferring pollutant out of the plume and giving rise to plume broadening near the roof surface. The direction of flow in the vortices seen would feed material down and across the roof and feed into the roof recirculation zone.

Turbulence also plays its part in spreading the concentration field and significant building generated turbulence is evident on the sampled planes with distance from the source. In order of magnitude the components of turbulence for the cube, normalised to U_{ref}^2 , show overall peak values in the region of 0.13 for (u'^2/U_{ref}^2) , 0.06 for (v'^2/U_{ref}^2) (refer to Appendix 15.2 for details) and 0.045 for (w'^2/U_{ref}^2) which may be compared to values of 0.012, 0.007 and 0.005 which would be obtained if the buildings were absent. Much more rapid plume dilution is therefore expected.

CHAPTER 6: THE CONCENTRATION FIELD: GAUSSIAN FITTED PLUME SPREAD PARAMETERS IN THE NEAR-FIELD OF BUILDINGS

6.1 Introduction

A detailed investigation was made of plume dispersion in the near-field region of three building configurations. The experiments significantly expanded the extant data for the previous specific real-world building cases and introduced the standard geometry of the cube in order to enable comparison with an established general building case. The concentration field was measured for steady state continuous releases of a tracer at a range of sampled planes downstream of the release point. A range of release conditions was investigated: angle of approach flow to the building, release position in relation to the building upwind edges and release height in relation to the roof plane. The cube model used matched the other building cases in terms of height to enable a more ready comparison.

Concentration profiles, measured in planes normal to the direction of flow in the wind tunnel, were then analysed to determine important parameters related to the release conditions: plume vertical and lateral deflection in the flow field, plume concentration maximum variation (plume centre line maximum concentration value) with downstream distance, and dispersion parameters corresponding to the horizontal (crosswind) and vertical spread of concentration with distance from the release point. The results obtained for the fitted Gaussian plume have been used later in this thesis to determine the maximum concentration in the roof zone of the buildings cases investigated and the location of these maximum values for the different cases investigated in terms of release height, angle of approach flow and release position with respect to the building. Furthermore, the novel methods developed for fitting the concentration profiles presented in this chapter have enabled the rooftop recirculation maximum and its spatial location to be determined for different release heights, angles of approach flow and release position. The spread of the plume, both crosswind and vertically, has been expressed in terms of distance-normalised parameters which enable the plume spread to be determined in the near field region in the roof zone streamwise from the source. Results for deflection of the peak concentration maximum both vertically and crosswind have been presented so that the location of peak concentration can be determined for the range of conditions studied. A method has also been formulated to express the variation of downstream concentration with distance from the source. The above parameters describing spread of the plume and downstream concentration with distance were then directly used in a Monte Carlo code written as part of this thesis work to compute radiation doses that is covered in later chapters.

Three building cases were investigated – an isolated cube, at different angles of approach flow - and those described as East Wing (EW) Clad or Unclad, including the surrounding buildings corresponding to the real site in question. The East Wing is a building on the site of St Thomas' Hospital site in central London from which there are releases of positron emitting radioactive waste gases arising from the production of radiopharmaceuticals: the release stack position corresponded to the existing stack on the EW North stair tower. The clad/unclad status referred to the difference in shape of the EW building after and prior to the addition of glass cladding that significantly changed the building shape from a 'T' plan cross section to a triangular shape after the addition of large glass atriums. These experiments followed on from measurements made of the roof top concentrations for the EW clad/unclad buildings, surrounded by buildings corresponding to those surrounding the EW buildings, reported from the first series of measurements (Gallacher *et al*, 2016a/2016b, Ibid Chapter 4): in those measurements a passive release (horizontally directed, and velocity-matched streamwise to the ambient flow field at the

point of release into the flow) was made at different release heights at the position of the existing release stack.

In this series of experiments the dispersion of tracer around the cube was measured for three angles of approach flow, up to five heights of release for the passive case, and two release positions in relation to the building. The five release heights were chosen to be close to the roof surface of the cube to investigate changes in the plume concentration and spread with varying height in the roof zone and immediate downstream wake of the building. For the EW clad and unclad measurements the same range of release heights were investigated as the cube, with a release position corresponding to the existing North stair tower release position on the EW building. One of the cube release positions (A, Figure 1) in these experiments matches the EW release position in terms of distance from the leading edge of the building upwind in the direction of flow.

The lowest release heights chosen investigated the expected more challenging cases where there was greater plume entrainment into the building rooftop re-circulation region from the existing stack. Release heights closer to the roof level than the existing stack were included in the measurement series.

In addition to the passive release cases active vertical releases were studied: these involved a release at a fixed height close the roof planes for the models studied. The main feature of the active vertical release is that the upward velocity of the release in the wind tunnel is chosen so that the velocity ratio against the upstream approach value corresponds to a value matching a case of interest: in this case, the mean wind velocity derived from meteorological data for the approach flow direction in the real-world case.

For the cube case studied the release height was equal to that studied for the EW cases, and the release position corresponded to the same relative position to the upwind vertex of the EW model. The aim was to find an equivalent case in terms of release height, distance to the building vertex, and distances from the leading-edge vertex. For the cube and two EW cases the flow was directly over the roof zone for the main direction studied (-22.5°) in terms of the positive wind bearing. In addition, the cube was also measured for approach flows normal to the leading edge (0°) and one quarter turn (-45°). From all of these measurements the behaviour of the plume in terms of plume rise, horizontal deflection and decay of plume concentration maximum with distance was established. The plume centreline trajectory was established for all of the concentration profiles studied enabling the effective plume rise to be compared between the passive horizontal and active vertical release profiles. The maximum concentration positions in the downstream profiles were determined as part of this process.

6.2 Methods

6.2.1 Overview/Experimental Wind Tunnel Methods

The measurements were made at the EnFlo (2021) boundary layer simulator wind tunnel (WT) facility at the University of Surrey. The release point for the passive release was positioned directly above the centre of the wind tunnel turntable so that experimental runs could be made that involved different wind directions approaching the building: all co-ordinates downstream were specified in relation to the fixed release point. The wind direction was specified as the direction in terms of a positive clockwise bearing with 0° at normal incident to the upwind face. The other two wind directions studied were -22.5° and -45° . The model used in the experiment was 1:200 full scale, and the convention used in this analysis will be that all dimensions in mm

refer to the wind tunnel model and those in metres refer to the full scale case respectively. A right-handed orthogonal co-ordinate system was used with the X -axis pointing in the direction of flow in the wind tunnel, Y -axis crosswind and Z -axis vertical. The model cube was of side $H=240\text{mm}$ (48m full scale). For the cube experiments the downstream (Y, Z) planes, measured from the release point were at $X=80, 160, 240$ and 400mm (corresponding to 16, 32, 48 and 80m respectively full scale). The two cube release positions selected were 'A', near the leading-edge vertex, and 'B' central to the windward face of the cube.

For the EW building measurements of the (Y, Z) concentrations were carried out at $X=16, 32$ and 48m in full scale downwind of the existing stack release position (see Figure 1). Given that the EW (North) stair tower was of height $H=48\text{mm}$ at wind tunnel scale the downstream sampled plane co-ordinates corresponded to $X/H=1/3, 2/3$ and 1 . The (Y, Z) co-ordinates were chosen to intercept the plume and show the effects of plume interaction with the building roof out to the plume 'tails' both vertically and horizontally. The model was rotated by -15° from geographical North, using tunnel co-ordinates centred on the emission stack at $(0, 0)$ in the (X, Y) plane: this represented wind coming from a bearing of 345° i.e. from NNW direction. Given that the West face of the building was oriented at a bearing of 7.5° to geographical North, this would mean that the main wind bearing in relation to the building was aligned at angle of -22.5° to the West face of the building: the wind direction would impinge at 67.5° to the normal from the West face of the building as shown in Figure 1.

6.2.2 Passive Releases

The release heights for the continuous passive release were: 245, 255, 265, 275 and 290mm above ground plane in the wind tunnel; 49, 51, 53, 55 and 58 metres in full scale, corresponding to heights of release above roof horizontal plane of 1, 3, 5, 7 and 10 metres. The furthest of the four measurement planes was at $X=400\text{mm}$, or $X/H=5/3$, beyond the leeward trailing edge of the cube, which enabled measurements to be made at vertical Z co-ordinates closer to the ground plane and in the main building recirculation zone at this downstream position. The two cube source positions investigated were A, near the leading-edge vertex, and B midline (Figure 1).

6.2.2.1 Cube – Passive Releases

The (Y, Z) planes were sampled over ranges of co-ordinates to intercept the plume and show the effects of plume interaction with the building roof out to the plume 'tails' both vertically and horizontally. Two Fast Flame Ionisation Detectors (FFIDs) working in parallel at variable offset along the Y -axis co-ordinate were used to obtain concentration sampled data in two positions simultaneously. A one-minute sample at each traverse location was obtained. The FFID sampling Y co-ordinates were specified for the dominant FFID position Y_1 resulting in a simultaneous acquisition at Y_2 , where Y_2 varied so as not to collide with the first FFID. The release height Z_{RH} was varied between 5 to 50mm (1-10m full scale) above the building roof height.

The Z sample starting co-ordinate was selected to be close to the plume centreline corresponding to the downwind position so that a sample position close to the peak was measured first. This enabled the measurement low concentration 'cut-off' to be established for the 'intelligent' sensing algorithm applied: the cut off threshold was set at 2.5% of the concentration measured maximum. This sample pattern used was for vertical slice profiles using the FFID pair, offset from one another in the Y -axis by 20mm. Initially, sampling was from the plume centreline upwards vertically until the cut-off threshold was reached, followed by sampling downwards to the minimum Z co-ordinate below the plume centreline. This pattern was repeated at manually selected Y -axis co-ordinate positions to give the necessary crosswind

coverage. Points below the cut-off threshold were not measured, reducing the run time for each profile. The 2.5% cut-off threshold was chosen to enable sufficient sampling of the Gaussian distribution tails but limiting overall wind tunnel run times to achievable values.

The wind tunnel experiment was repeated with the source at position B, central to the upwind face of the cube (Figures 1 and 2). All sample co-ordinates in the experiments were set in relation to the wind tunnel source and not the building. The intermediate wind direction case (-22.5°) was carried out with the source at position A, near the upwind vertex of the cube. The clockwise rotation of the tunnel turntable (as viewed from above in Figures 1 and 2) was achieved by selecting a -22.5° rotation command in the turntable traverse command file instruction (as this relates to wind direction bearing impinging on the model).

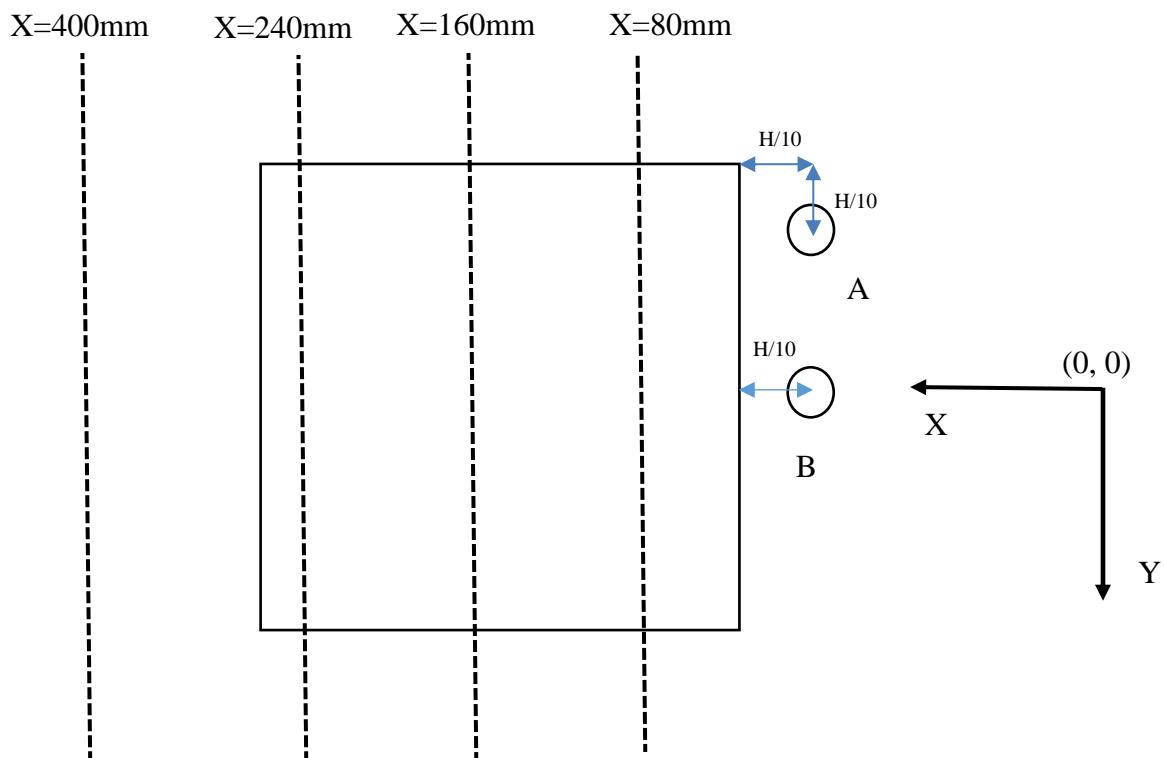


Figure 6.1. Cube Measurement Planes (Normal Incidence, 0°)

Likewise, the B midline release position was also measured at the intermediate wind direction of -22.5° for the cube model with rotation around the source position 'B' in Figure 6.1.

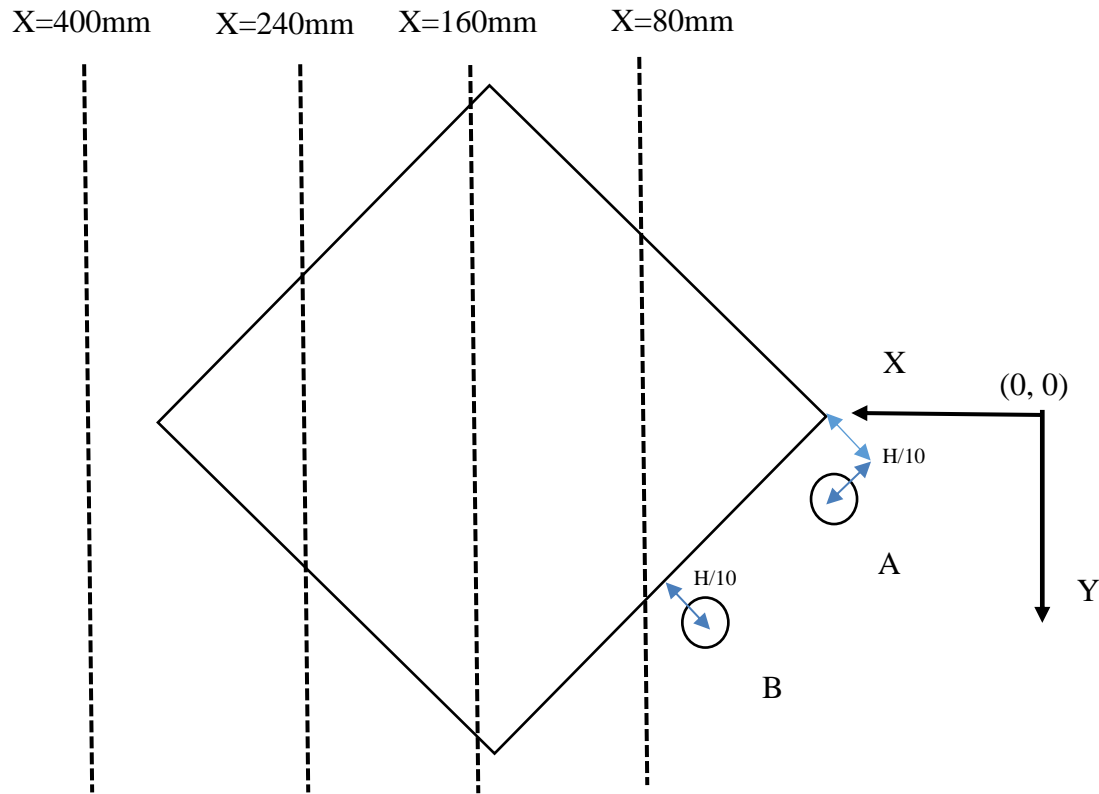


Figure 6.2. Cube Measurement Planes (Oblique, -45°)

6.2.2.2 EW Clad – Passive Releases

Passive releases were carried out in steady release conditions with two FFIDs working in parallel offset at 20mm along the Y-axis co-ordinate to obtain concentration sample data in two positions simultaneously. Each position was sampled at for one minute sample at each traverse location studied. The FFID sampling Y co-ordinates were specified for the dominant FFID position Y_1 resulting in a simultaneous acquisition at Y_2 , where $Y_2 = Y_1 - 20$. The release height Z_{RH} was varied between 5 to 50mm (1-10m full scale) above the building height at the North stair tower platform stack position (Figure 3). The stair tower platform was the same height as the unclad building. The height of the existing stack was 3m (or 15mm in model space) above the stair tower roof, which lay within the release height range investigated. The sample co-ordinates for the passive release case are presented in Appendix 15.1.

As with the cube passive measurements of (Y, Z) concentrations were carried out at X=16, 32 and 48m in corresponding full scale downwind of the existing stack release position (Figure 3). The EW (North) stair tower was of height 240mm at wind tunnel scale equal to that of the cube model dimension.

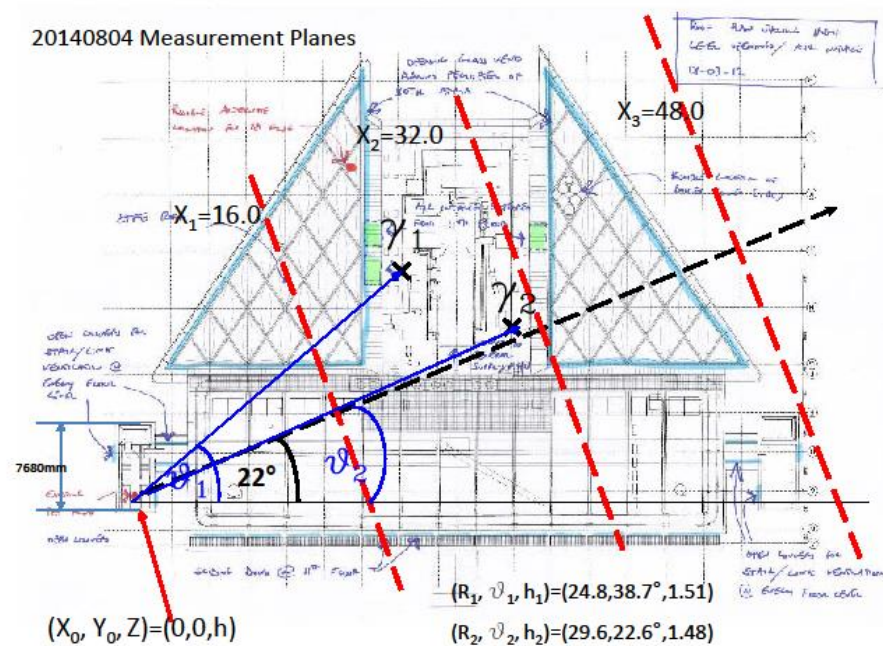


Figure 6.3. EW Clad Building (-22.5°)

Image by ARUP/Hopkins and ISG PLC, with annotations by the author

6.2.2.3 EW Unclad – Passive Releases

Each experimental run was carried out over approximately 24 hours running time with a one-minute sample time per position matching the cube measurements. FFID gain was 40% of the standard setting with a trace gas concentration range of 1.0-2.0% to reduce the incidence of detector sampling overflow points. Sample space co-ordinates were set to reduce the overall run time by elimination of measurement co-ordinates yielding low signal levels i.e. corresponding to sampled values of low concentration. In this experiment a building ‘shape file’ was used in the measurement controller software to avoid collision of the sample FFIDs with the building and the ‘jump bad points’ algorithm was selected in order to achieve as full a sample grid as possible at the downstream positions measured over the building model roof – bad points in this context being those which the FFID could not reach without a building collision. At increasing downstream distances the signal level reduced due to concentration reduction in the plume, and the tracer concentration percentage was increased to compensate. Flow rate of the tracer was maintained at the specified value for all of the downstream measurement planes investigated.

6.2.3 Active Vertical Releases

Further tests were carried out to confirm the plume rise from the active vertical (AV) release with matched stack velocity ratio (SVR) against the passive release case for the cube model and the EW clad and unclad cases. Measurements were made in the (Y, Z) plane at a range of three downstream (X) co-ordinates for a continuous release. In this way the plume centreline trajectory was mapped including the effective plume rise, which involved the upward velocity component of the release and the upward deflection as the plume approached and moved over the roof. The maximum concentration positions in the (Y, Z) were therefore determined from these measurements.

The stack velocity ratio was determined to match the EW full-scale cases. For a stack of exit venturi nozzle diameter of 354mm a 1.77mm internal diameter tube would be appropriate at 1:200 scale. The closest match available was an inner diameter of 1.9 ± 0.2 mm, and this was used in the experiment, and it was also noted the outer tube diameter of 3.0mm was well matched to the full-scale outer diameter of 613mm (Figure 4).

Three vertical velocity profiles were calculated using the power law formulation of the velocity profile (Clarke, 1979) corresponding to the Heathrow wind data ($n=0.234$), wind tunnel profile ($n=0.201$) and the environment at STH ($n=0.386$) all normalised to the same velocity at the reference height in the wind tunnel (200m full scale). A minimum flow rate of 0.64 l min^{-1} was selected on the pump valve controller, and with the internal diameter of the model stack pipe of 1.9mm this corresponded to a model efflux velocity of 3.755 ms^{-1} .

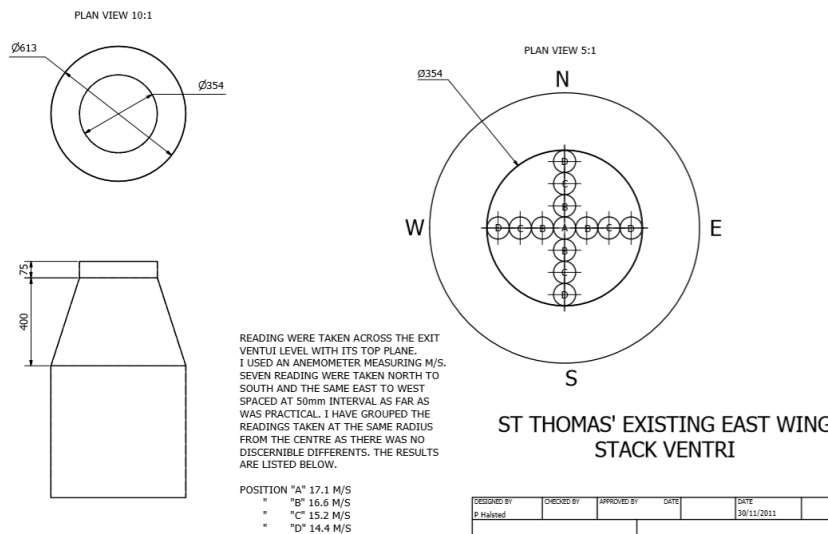


Figure 6.4. EW Stack Dimensions and Efflux Velocity Profile (full-scale)

For a 1 ms^{-1} wind tunnel velocity (at the reference height of 1000mm from the floor of the tunnel) the WT profile indicated a flow velocity of 0.76 ms^{-1} , giving $\text{SVR} = 3.755/0.76 = 4.94$. For an EW mean efflux velocity at full scale of 15.03 ms^{-1} this SVR corresponds to a wind velocity of 3.04 ms^{-1} at the 51m stack height at full-scale, which corresponded to the 255mm stack height used in the wind tunnel. Using the velocity profile matching a power of $n=0.386$ for a rough urban canopy flow at STH (Gallacher, DJ *et al*, 2016a) this velocity corresponded to a wind velocity of 2.08 ms^{-1} measured at the standard 10m height at Heathrow.

6.2.3.1 Cube – Active Releases

The cube measurements were carried out with a wind tunnel velocity U_{ref} of 2 ms^{-1} , and the flow rate was therefore doubled to 1.28 l min^{-1} to preserve the same SVR between cube and EW measurements. Dispersion of tracer in this configuration enabled a FFID gain setting at 100%. One-minute samples were used throughout.

6.2.3.2 EW Clad – Active Vertical Releases

The EW stack release position is shown in Figure 5, with dimensions of the building. The main wind direction studied, for the clad and unclad cases, was the -22.5° direction as shown and this corresponds to the previous cases for this building investigated (Chapter 4, Ibid). For this direction the centre of stack to leading building edge was 4.99m, and as a ratio of the building width (48.5m) to approach flow this was approximately 0.10. This offset distance was adopted for the cube measurements i.e. $H/10$ as shown in Figures 1 and 2, so that the interaction of the

[illegible]

Image by ARUP/Hopkins and ISG PLC, with annotations by the author

6.2.3.3 EW Unclad – Active Vertical Releases

6.2.4 Data Modelling Methods

$$\chi = \frac{cU_{ref}H^2}{O} \quad [1]$$

143

$$C(\underline{r}) = \frac{Q}{2\pi U_H \sigma_y \sigma_z} e^{-\frac{1}{2} \left\{ \frac{(y-y_0)^2}{\sigma_y^2} + \frac{(z-z_{RH})^2}{\sigma_z^2} \right\}} \quad [2]$$

It should also be noted that the Gaussian formulation indicates tracer (or more generally pollutant) release conservation with downstream distance. This can be shown as follows in equation [3] by integration of the downstream wind velocity U and the concentration, C from equation [2], over a (Y, Z) plane at downstream distance X using the normalisation properties of the Gaussian integral. The equation holds, despite the effect of the boundary condition at the ground plane, if there is a reflection term and no surface permeation or losses.

$$\iint_{-\infty}^{+\infty} UC(x, y, z) dy dz = Q \quad [3]$$

6.2.4.1 Concentration Profile Models

To improve the applicability of the GPM model to the situation where there is the interaction of a pollutant (or tracer) release into a complex flow field, arising from the interaction of an approaching wind stream with a building or group of buildings, modifications were made to equation [2]. In particular, the modifications had to enable realistic modelling of the plume in the very near field of the release position i.e. in the roof zone of the building immediately downstream of the release position.

Two modelling approaches were taken, which have been termed the Single Gaussian Plume (SGP) and Dual Gaussian Plume (DGP) models. A roof reflection term was added to account for reflection of the low plume from the roof surface, analogous to the ground reflection term in R-91 (Clarke, 1979). However, no reflection term from the mixing layer aloft was required, given the very short-range measurements in relation to the release position in this study. In full scale the mixing layer for Pasquill-D neutral stability would be some hundreds of metres above ground level (Pasquill, 1974), several times the height of the buildings under consideration.

The SGP formulation is derived from equation [4]. The vector from the origin $\underline{r}(x, y, z)$ defines the point at which the concentration is determined, subject to the boundary conditions i.e. zero concentration below the level of the roof, H . The crosswind plume centre line deflection variable y_0 is itself a function of downstream distance x and height above the roof z , but also factors specific to the building case under consideration: angle of building leading edge to the approach flow, release position in relation to the building leading vertex and leading edge (for the cube and other building cases under consideration), and height of the release above the roof. Also, in these experiments there were two classes of releases studied: (i) the passive release of tracer horizontally into the approach flow with a matched wind velocity at the release point, and (ii) for other cases studied an ‘active vertical’ (AV) release where the vertical release velocity divided by the approach flow velocity at the stack/flue height i.e. the Stack Velocity Ratio (SVR) that simulated the real world case for the building being studied. The effect of an AV release with matched SVR yielded a pronounced extra plume rise compared to the passive cases studied.

$$C(\underline{r}) = \frac{Q}{2\pi U_H \sigma_y \sigma_z} e^{-\frac{1}{2} \left\{ \frac{(y-y_0)^2}{\sigma_y^2} \right\}} \left\{ e^{-\frac{1}{2} \left\{ \frac{(z-z_{RH})^2}{\sigma_z^2} \right\}} + e^{-\frac{1}{2} \left\{ \frac{(z+z_{RH}-2H)^2}{\sigma_z^2} \right\}} \right\} \quad [4]$$

The wind speed in the main wind direction U_H is given at the building height and represents the advection velocity carrying the plume over the building. Furthermore, the plume dispersion parameters σ_y and σ_z are themselves complex varying functions which depend upon the wind angle to building, release height and position in relation to the building. In the wind tunnel experiments neutral stability conditions (Clarke, 1979) apply i.e. Pasquill-D so the effect of surface heat flux and atmospheric stability on σ_y and σ_z are not considered further in this analysis.

For the SGP model the plume crosswind spread and amplitude were determined by fitting measured values of CU_{ref}/Q from the wind tunnel data to the following equation [5]. Parameters for amplitude N , plume spread σ_y and y co-ordinate of plume concentration maximum y_{pcm} were obtained by using the solver function in Excel 2013 and minimising the least squares residual difference between the measured and fitted curve.

$$\frac{C_y(x,y,z)U_{ref}}{Q} = \frac{N}{\sqrt{2\pi}\sigma_y} e^{-\frac{1}{2}\left(\frac{(y-y_{pcm})^2}{\sigma_y^2}\right)} \quad [5]$$

The vertical plume spread profiles were analysed independently for each vertical section corresponding to a given sampled co-ordinate along the Y -axis. The SGP formulation was given by fitting experimental data to equation [6] with minimisation of least squares difference using the solver function: a single Gaussian with a roof-reflection term centred about a plume concentration maximum at height z_p and a vertical dispersion parameter σ_z .

$$\frac{C_z(x,y,z)U_{ref}}{Q} = \frac{N_z}{\sqrt{2\pi}\sigma_z} \left\{ e^{-\frac{1}{2}\left(\frac{(z-z_p)^2}{\sigma_z^2}\right)} + e^{-\frac{1}{2}\left(\frac{(z+z_p-2H)^2}{\sigma_z^2}\right)} \right\} \quad [6]$$

The SGP maximum z_p was found to differ from the release height z_{RH} – experimental data reported here showed that there is clear evidence of upwards deflection of the plume due to the approach flow towards the building and a countervailing effect of plume downwash with increasing distance along the roof and into the downwind side of the building. From the wind tunnel experimental series, there were some measurements carried out in planes beyond the end of the building. For analysis of those downwind measurements the value of H in equation [6] was set to zero, to allow for the fact that the plume lay above the ground which became the new source of the reflection term downwind of the building.

On the basis of inspection of results for concentration profiles obtained in these experiments a Dual Gaussian Plume (DGP) model was formulated, by the author as part of this work, which involved the linear superposition of two best-fitted Gaussian peaks for the crosswind analysed concentration profiles. Each peak has (a) different crosswind (y_{pcm1} and y_{pcm2}) centre values with suffices 1 and 2 being allocated to the respective peaks; (b) different amplitudes (N_1 and N_2); and (c) crosswind plume spread parameters (σ_{y1} and σ_{y2}) fitted to each crosswind concentration profile at a given sample height (Z). When sampling at a given downstream distance (X) in the (Y, Z) plane each horizontal row of concentration field data had different values for the two Gaussian distributions of: (a) deflection (Y/X) from the approach flow wind direction; (b) Gaussian peak amplitude scaling; and (c) lateral plume dispersion parameter (σ_y). The two Gaussian peaks, when evident in the crosswind concentration profiles, were considered to correspond to the main plume and a secondary peak: the latter either corresponded to a roof Recirculation Zone (RCZ) or otherwise appeared to be a bifurcated plume caused by the

interaction with roof generated vortices in the flow field. The formulation of the crosswind fitting function for the DGP method is given as follows in equation [7].

$$\frac{C_y(x,y,z)U_{ref}}{Q} = \frac{N_1}{\sqrt{2\pi}\sigma_{y1}} e^{-\frac{1}{2}\left(\frac{(y-y_{pcm1})^2}{\sigma_{y1}^2}\right)} + \frac{N_2}{\sqrt{2\pi}\sigma_{y2}} e^{-\frac{1}{2}\left(\frac{(y-y_{pcm2})^2}{\sigma_{y2}^2}\right)} \quad [7]$$

Where σ_{y1} and σ_{y2} are the plume spread parameters for the main and the secondary (or RCZ) components respectively: N_1 and N_2 are normalising coefficients that reflect the relative amplitude of the two concentration peaks and are implicitly also a function of U_H . The left-hand side can be converted into dimensionless concentration by multiplication with H^2 . The values of y_{pcm1} and y_{pcm2} are the peak centreline co-ordinates, which could potentially be co-incident, but with the two peaks corresponding to the main plume and secondary peak (RCZ or bifurcated plume) and having different plume spread parameters σ_y with suffices 1 and 2.

Another method of analysis of the data was also devised as part of this work by the author to attempt to de-convolve the effects of a roof top RCZ from, in principle, a narrower isolated peak at height z_p . This method has been termed the Isolated Gaussian Plume (IGP) method: because the equations describing the method are different to the DGP method. In the IGP method the vertical concentration profile is assumed to be the linear superposition of a constant RCZ, of well-mixed uniform concentration C_{RCZ} that extends up to a truncation height of Z_{RCZmax} , with an isolated Gaussian plume above the roof level. The equation describing the IGP method is given in equation [8].

$$\frac{C_{igp}(x,y,z)U_{ref}}{Q} = \frac{N_{igp}}{\sqrt{2\pi}\sigma_{zi}} \left\{ e^{-\frac{1}{2}\left(\frac{(z-z_p)^2}{\sigma_{zi}^2}\right)} + e^{-\frac{1}{2}\left(\frac{(z+z_p-2H)^2}{\sigma_{zi}^2}\right)} \right\} + \frac{C_{RCZ}U_{ref}}{Q} \vartheta(z - Z_{RCZmax}) \quad [8]$$

Where the step function: $\vartheta(z - Z_{RCZmax}) = 1$, if $H \leq z \leq Z_{RCZmax}$; 0 otherwise.

Least squared function fitting was carried out by including N_{igp} , σ_{zi} , z_p , C_{RCZ} and Z_{RCZmax} in the list of parameters to be adjusted in the solver function to minimise the least squares residual.

6.2.4.2 Concentration weighted plume spread parameters: SGP formulation

The SGP formulation of fitting the Gaussian plume was shown from the experimental data in this work to give rise to different values of crosswind dispersion parameter σ_y with vertical sampled height above the roof of the building model. Furthermore, the dispersion parameter was found to be increasing with downstream distance as would be found for an elevated plume above ground level (Jones, 1983). To remove a large component of the variation in the near field above the roof zone, and immediately downwind of the building, the dispersion parameter was normalised to the downstream distance i.e. expressed as σ_y/X and this quantity was taken forward in the analysis: it also had the advantage of converting the dispersion parameter into a generalizable dimensionless quantity.

For the measured horizontal profiles the crosswind dispersion parameter was found to be a function of height (z) and can be expressed as $\sigma_y(z)$. In order to take into account the magnitude of the concentration field, and to not over-represent horizontal profiles with low concentration values away from the plume centreline, the weighted mean dispersion parameter $\sigma_{y,cw}$ was calculated according to equation [9] at a given distance from source of X. Summation is over

vertical n co-ordinates z_i , with the weighting function given by the value $(CU_{ref}/Q)_{max,i}$ corresponding to the maximum concentration value in a given horizontal profile. Measured maximum concentration values were used and not the best-fitted curve values.

$$\frac{\sigma_{y,cw}}{X} = \frac{\sum_{i=1}^n \left(\frac{CU_{ref}}{Q} \right)_{max,i} \frac{\sigma_y(z_i)}{X}}{\sum_{i=1}^n \left(\frac{CU_{ref}}{Q} \right)_{max,i}} \quad [9]$$

Similarly to the horizontal profiles, the vertical measured profile dispersion parameter was found to be a function of crosswind co-ordinate (y) and can be expressed as $\sigma_z(y)$. In this case the best-fitted SGP curve was used to obtain values for the maximum concentration $(CU_{ref}/Q)_{max,j}$ in each vertical profile because of goodness of fit considerations close to the sharp discontinuity posed by the roof. Summing over sampled co-ordinates y_j over m profiles we obtain the concentration-weighted value for vertical dispersion coefficient normalised for a particular downstream distance from the source X as shown in equation [10].

$$\frac{\sigma_{z,cw}}{X} = \frac{\sum_{j=1}^m \left(\frac{CU_{ref}}{Q} \right)_{max,j} \frac{\sigma_z(y_j)}{X}}{\sum_{j=1}^m \left(\frac{CU_{ref}}{Q} \right)_{max,j}} \quad [10]$$

6.2.4.3 Concentration weighted plume spread parameters: DGP formulation

The least squares solver algorithm could potentially provide results for the dual peaks where it was necessary to ascribe one peak as the isolated or de-convolved Gaussian plume and the other as the recirculation zone (RCZ). In order to make the distinction the following set of selection rules were used when processing and reviewing the data. The curve fitting was carried out by use of a programmed Excel 2013 macro function, and in all cases the SGP fitting was also carried out and the results plotted together, to inform the comparison. In some cases it was necessary to reverse the initial parameter value estimates (on the y -axis) and run the macro again, so that the peaks would be labelled correctly for further processing.

For the crosswind profiles:

- (a) Where the peaks were nearly co-incident along the y -axis the broader peak position was compared to the roof zone position, and denoted the RCZ;
- (b) Where the parameter fitting resulted in a negative normalisation parameter (either N_1 or N_2) the negative parameter was forced to zero and the fitting reverted to a single Gaussian plume. In this case the SGP parameters for plume spread and lateral peak position were applied to both the Gaussian plumes. The values allocated to the secondary peak (RCZ peak) would not carry forward into the production of weighted values σ_y , because of the zero normalisation applied;
- (c) Where the fitting algorithm gave rise to an unrealistically small value of dispersion parameter when compared to the SGP, and by inspection this could be attributed to scatter in the experimental results e.g. a small sharp peak superimposed on a broader peak, the parameters were reverted to the SGP default values.
- (d) For limited sampled profiles for the EW clad building, where because of the shape of the building and the inability to sample fully across the lowest profiles closest to the roof because of roof top structures on the model, limited cases e.g. $Z=245, 253\text{mm}$ adopted the plume centre line position, and apportioned the split of the normalisation values between N_1 and N_2 according to the nearest fully sampled profile above at $Z=263\text{mm}$.

- (e) Where the deconvolution of the DGP and RCZ roof zones gave rise to a narrow spread fitted Gaussian for the RCZ, where the fitted centreline was away from the measured concentration field points, and the expected value of the fitted peak to that Gaussian was physically unrealistic and unsupported by measurement points in the near vicinity the values used for the RCZ component were taken from the nearest adjacent horizontal profile.

For the vertical profiles:

- (a) Select an initial seeding value of the height of the RCZ zone to be within the range H to $5H/4$. Run the analysis macro and analyse the graph for goodness of fit.
- (b) Where the recirculation zone concentration C_{RCZ} takes a negative value force that value to zero and take the same parameters as for the SGP model.
- (c) Where C_{RCZ} is positive iterate the height of recirculation zone to investigate goodness of fit and the minimisation of the least squared residual (root mean square difference value)
- (d) Where the Gaussian peak value is below H the roof height, take the maximum value at the roof height.

The horizontal profile for the DGP main plume $\sigma_{y,dgp}$, and the secondary plume/RCZ region, were concentration weighted in the same manner as was given in equation [9]. In terms of the normalisation, the main plume was normalised with distance from source X to the sample plane. Since the size of the RCZ for a given building is a function of building size, the dispersion parameter for the secondary plume/RCZ was normalised with the building height i.e. $\sigma_{y,RCZ}/H$. The Isolated Gaussian Plume (IGP) for determination of the vertical spread, when decoupled from the RCZ, was determined not to be suitable for a concentration weighted treatment: this was due to the relatively crude step function truncation method used. In this case the sample mean over the vertical profiles was taken as a more robust measure of this quantity and less likely to introduce bias into the result.

6.2.4.4 Plume Concentration Maximum (PCM) variation with downstream distance (X)

The dispersion coefficients are functions of downstream distance, X , but it has been found from these experiments are strongly varying functions of the release height of the plume, the position of the release in relation to the building and the angle of approach flow to the building. Experiments were carried out also for two ‘real world’ building cases referred to as East Wing (EW) ‘Clad’ and ‘Unclad’ which tested the effects of a different building shape on the measured concentration field.

From the experimental data, which was obtained at different downstream planes at distances x from the source, the Plume Concentration Maximum (PCM) was obtained from the cross-sectional concentration field in the (Y, Z) plane. By substitution of the y value corresponding to the concentration peak value, the z_p value corresponding to the height of the plume centre and also using equation [1], equation [4] reduces to equation [11].

$$\chi(x) = \frac{C(x)U_{ref}H^2}{Q} = \frac{U_{ref}}{2\pi U_H \sigma_y \sigma_z} \left\{ 1 + e^{-\left(\frac{(z_p + z_{RH} - 2H)^2}{2\sigma_z^2}\right)} \right\} \quad [11]$$

It can be seen from equation [11] that the only terms which are functions of x are σ_y , σ_z and z_p . The formulation described below was devised by the author as part of this thesis work, to reduce

the equation and thereby express the plume centreline concentration with distance from the source in terms of general parameters. Iwai and Ijima (1970) presented logarithmic plots of concentration at ground level with downstream distance and analysis of their plots indicated a value of power law value of $\alpha=1.6$ for a ground level release. They also present a quadratic form of the power-law showing variation of the spread parameters with downstream distance from the source, from which a value of $\alpha=1.85$ would be the equivalent to the formulation given here for an elevated release at neutral stability with no buildings. The ground-level release case is closer to the relatively small release heights above the roof of the building considered in this thesis. Further information is available from NRPB Report R-91 (Clarke *et al*, 1979) where the value of α is approximately 1.8 for neutral conditions.

Treating the plume height as approximately constant over the roof zone in question, we neglect the differences between release height plus plume deflection - which may be averaged over the roof zone - and replace z_p with a constant z_{RH} . The plume spread parameters are then written as linear functions proportional to x over the near scale range i.e. $\sigma_y = \sigma_{y0} x$ and $\sigma_z = \sigma_{z0} x$, where σ_{y0} and σ_{z0} are defined at unit distance of 1 metre in the full scale co-ordinate system. Likewise, χ_1 can be defined as the dimensionless concentration of the plume at unit distance i.e. 1 metre from the source. From this analysis an empirical function of the form in equation [12] can be postulated, where α is a power decay coefficient with distance from the source.

$$\chi(x) = \chi_1 x^{-\alpha} = \frac{C(x)U_{ref}H^2}{Q} = \frac{U_{ref}}{2\pi U_H \sigma_y \sigma_z} \left\{ 1 + e^{-\frac{(z_p + z_{RH} - 2H)^2}{2\sigma_z^2}} \right\} \quad [12]$$

Where χ_1 can be defined in equation [13].

$$\chi_1 = \frac{U_{ref} x^{\alpha-2}}{2\pi U_H \sigma_{y0} \sigma_{z0}} \left\{ 1 + e^{-\frac{2(z_{RH}-H)^2}{\sigma_z^2}} \right\} \quad [13]$$

For the simple Gaussian case given in equation [2], we can see that α would take the value of 2 and χ_1 would take the value of a constant. For empirical values of χ_1 where α is close to the value of two we can see that χ_1 is a weakly varying function with distance x and may be treated as a constant. To determine the value of α from experimental data we take logarithms of equation [9] and obtain values of χ_1 and α from best-fitted linear regression. Using the values thus obtained the value of the Plume Concentration Maximum (PCM) can be readily obtained as a function of distance from the source.

$$\ln \chi(x) = \ln \chi_1 - \alpha \ln x \quad [14]$$

The use of the best-fitted linear regression line obtained by plotting natural logarithms of the dimensionless concentration values for the downstream planes χ against $\ln(x)$ yields the exponential decay constant α , and from the intercept $\ln(\chi_1)$ from which χ_1 is easily obtained. From this empirical data a simple analytic function which models the PCM effectively with distance can be used in subsequent calculations.

6.2.4.5 Plume Concentration Maximum deflection in (Y,Z) with downstream distance

The co-ordinates of the plume centre line for the SGP model, or the DGP and IGP models were important parameters for the characterisation of plume direction and deflection with distance in terms of the interaction with the building model. For each profile, described by the building,

angle of approach flow, release height and release position there was a sampled grid in the (Y , Z) plane of the (CU_{ref}/Q) values. The method for selection of the appropriate plume maxima is described as follows.

For the SGP the horizontal samples, at a given sample height Z , were analysed independently for the SGP best fitting, however the maximum concentration value was selected for each horizontal profile from the actual measured data to not introduce any potential bias or distortion from using the SGP fitting method. This was possible because there was only one fitted peak from using this method. However, for the DGP method, applied to the horizontal profiles, it was necessary to apply the best-fitted Gaussian formula, using the fitted parameters for y_{pcm1} , plume spread and amplitude normalisation to obtain the plume maximum amplitude for further analysis. Similarly, y_{pcm2} was obtained from the secondary or RCZ resolved component of the dual plume but at the same sample height as the first peak, and the corresponding concentration amplitude calculated at that spatial position in the (Y , Z) plane. In general, the maximum value of the concentration in the RCZ or secondary plume would not necessarily correspond to this sample height, and in many cases the amplitude of the RCZ would be greater at a height closer to the roof. An approach for dealing with this difference was devised and is presented later.

For each downstream plane a series of vertical profiles of the SGP were analysed to give the plumes cross sectional profiles across the concentration field. The maximum value of concentration amplitude was determined across the full range of profiles, and that Y co-ordinate deflection taken according to the profile containing the maximum value of concentration. The Z co-ordinate of the maximum was taken from the best-fitted SGP curve at that horizontal co-ordinate.

The deflection of the DGP isolated primary plume was assessed for each downstream plane: the horizontal deflection in Y was taken from the horizontal profile with the maximum fitted value of concentration amplitude. The vertical height was taken from the horizontal profiles analysed for dual plumes. Another parameter was also determined in the data analysis: the maximum height at which the RCZ values were considered non-zero, taking into account fluctuations in the fitted values. This parameter, $Z_{RCZ,max}$, was obtained from the horizontal profiles and used to determine the effective height of the RCZ in subsequent analysis.

6.2.4.6 Plume height and normalisation to building scale

The plume height at each downstream plane and measurement condition was normalised to the building height: a dimensionless quantity was derived which took into account the plume height difference from the release height, but scaled to the dimension of the building i.e.

$Z_{norm} = (z_p - z_{RH})/H$. This quantity varied with downstream distance, for the same set of release conditions, showing the PCM spatial variation according to building effects and flow field conditions. Taking the mean value of Z_{norm} over the roof surface sampled planes gives an idea of the net deflection of PCM with downstream distance: this analysis was carried out for SGP and SGP formulations of the data, but only over the measurement planes directly over the roof at $X = 80, 160$ and 240mm in model scale.

6.2.4.7 Roof Zone Maximum Measured Concentrations

A significant quantity in terms of exposure of persons to the pollutant in the plume is the concentration field value at close to the roof height. Measurement values were obtained as close as $Z=245\text{mm}$ in model scale, corresponding to 1m from roof plane at full scale. In other cases, due to the intelligent sampling algorithm run in the wind tunnel measurements which omitted points showing small values of concentration in relation to peak concentration, the minimum

sampled value was at 250mm or 255mm model scale, or greater for elevated plumes aloft of the building. It was necessary to determine a value of sampled height at which a person could be exposed to concentrations of pollutant: the value selected was 1.5m above the roof plane at full scale, or a height of 247.5mm in model scale. This value was selected for two reasons: firstly, the height approximated to the nasal/mouth height of a human subject of approximately average height, and secondly this value was considered more robust in terms of near-field effects close to the roof: in the data collected an interpolated concentration value between sampled heights of $Z=245$ and 250mm was often obtainable. In cases where the minimum sampled height was 250mm or greater, the concentration value at 247.5mm was obtained by extrapolation, but usually in these cases the concentration values thus obtained were small. The concentration field value, at the specified height above the roof, was obtained for the SGP at a single Y co-ordinate and for the DGP at two positions, namely the primary and secondary (RCZ) components of the concentration field. For the DGP model the concentration at the same height as the main primary plume was averaged with the concentration at roof level at any given source distance to provide a 'well-mixed' value. These well-mixed values over distance were further averaged over the roof zone to provide a global roof zone mean RCZ concentration for feeding into further analysis. The value of $Z_{RCZ,max}$ was likewise averaged over the roof zone to characterise the mean value of the height of the roof top RCZ over the roof zone.

The downstream distance from the source, normalised to the fraction of building height X/H , at which the maximum concentration near roof level (1.5m height above roof) occurred for the SGP method was therefore obtained, from the above analysis, as well as the Y crosswind co-ordinate for this maximum. Likewise, Y position for the primary and secondary maxima values were obtained for the DGP/IGP method, with in the latter case the co-ordinate of the roof RCZ maximum also obtained for subsequent analysis.

6.2.4.8 Main Building RCZ Measured Concentrations

For the cube cases an extra measurement was made at $X=400$ mm (80m full-scale), which extended beyond the end of the model, for all angles of approach flow including -45° : in which case the trailing edge model vertex was 61mm upstream of the downstream measurement plane, approximately $H/4$, in building scale. For this downstream case measurement of the main building RCZ extending to the ground plane was possible: the roof measurements had given data on the rooftop RCZ, this further downstream position gave information on the concentration field immediately beyond the building in the direction of flow. For this measurement configuration the minimum sampled height was constrained by the available vertical movement of the FFID detector: in most cases sampling to a height of 85-95mm above the WT ground plane level was possible, corresponding to almost $H/3$ from ground level in terms of the building scale. Furthermore, the vertical profiles showed clear evidence of a building RCZ of approximately constant concentration up to a height close to the roof level, above which the influence of a main plume undergoing downwash deflection was apparent. It was therefore possible to specify a mean concentration in the well-mixed main building RCZ zone, and this is presented for the different release conditions in this analysis.

6.2.4.9 Mean value plume spread parameters with distance from source

The normalised plume spread $\sigma_{y,cw}/X$ was determined for a range of downstream measurement planes for the SGP method. These values were also obtained for the primary DGP plume, and a selection of results will be presented for both of these cases. A further modification was devised as part of this work to reduce these quantities to an idealised conical Gaussian plume with constant rate of spread with distance: this parameter was obtained by taking the mean value of the normalised dispersion quantity with distance from the source.

In a similar way the vertical plume spread was obtained for the SGP method applied to the vertical spread of the plume $\sigma_{z,cw}/X$ to characterise a conical spread rate with distance from the source. As before, a set of values for the IGP method of vertical spread was also obtained: in this case the values were not concentration weighted but an arithmetical average over the available concentration profile at each downstream position.

For both of these plume spreading directions the mean values of normalised spreading parameter could be presented as a single generalizable parameter, dependent upon the release conditions specified previously: invariant with distance from source, but with dependence upon wind direction of approach to building, release height, building shape and surrounding buildings (where applicable i.e. for the EW cases) and release position.

6.2.4.10 Caveat

At this point, it should be emphasised that the topic of very short range (in atmospheric dispersion terms) dispersion over a building roof is expected to yield behaviour that is not easily parameterised. The aim of the empirical models described below is therefore simplicity, whilst maintaining a reasonable depiction of the observations. The roof-top geometry of the EW building is complex and this will inevitably affect plume behaviour in ways that simple models cannot match.

6.3. Results

6.3.1 Concentration Profiles: Horizontal and Vertical

6.3.1.1 Cube: Passive Cases – Roof Zone

6.3.1.1.1 Cube: normal incidence flow (0°)

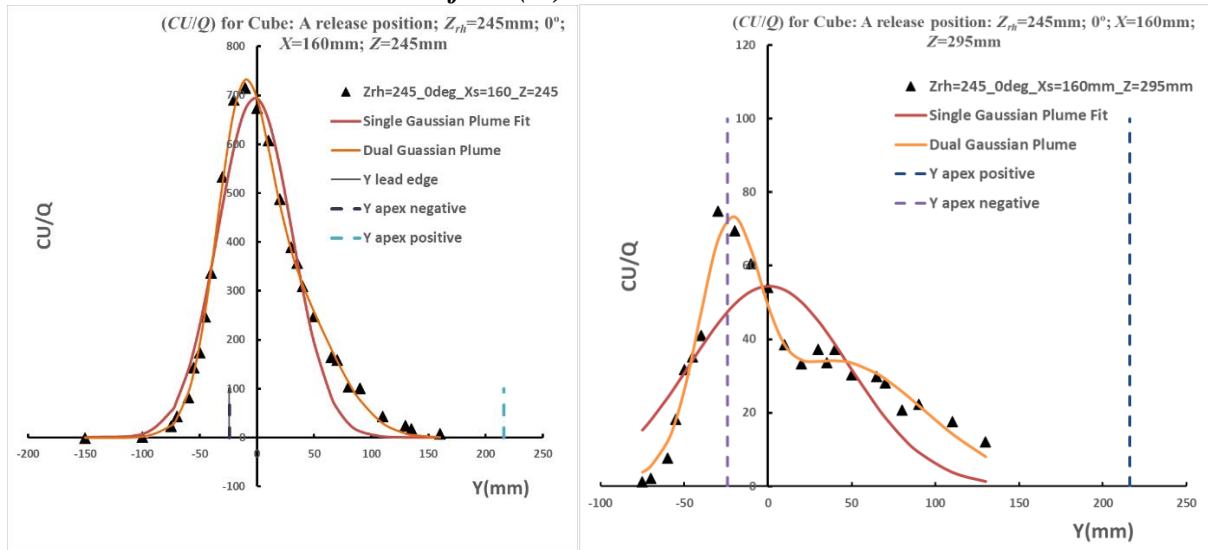


Figure 6.6(a/b): (CU/Q) variation with crosswind co-ordinate Y ; release height $Z_{rh}=245\text{mm}$ (5mm above model roof plane), near vertex position A; normal incidence (0°) to cube face; sampled (a) $Z=245\text{mm}$ and (b) 295mm respectively, cube vertex edges are shown as vertical dashed lines. All dimensions specified in mm are in model co-ordinates.

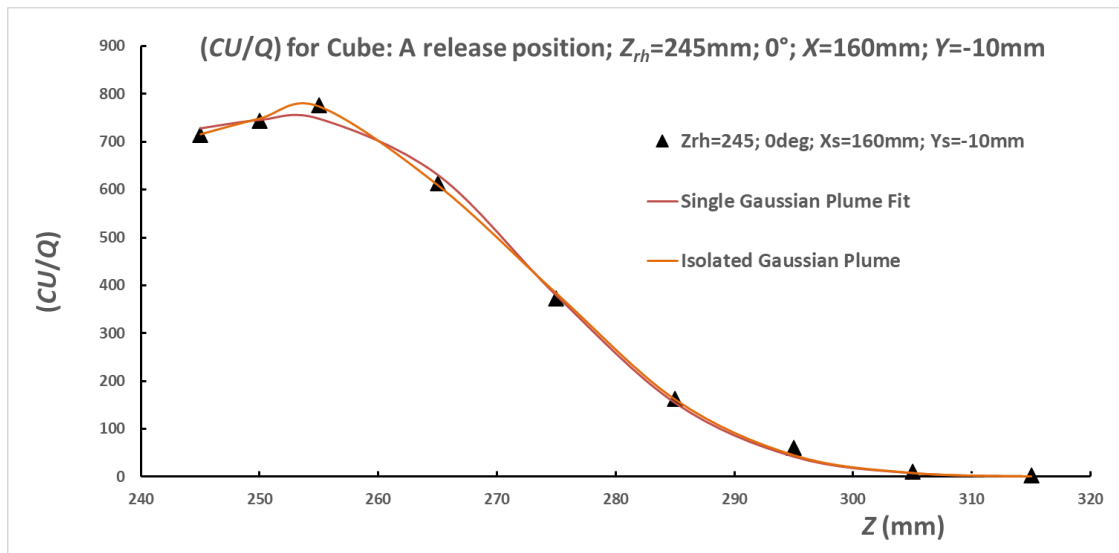


Figure 6.6(c): CU/Q variation with Z with $H=240\text{mm}$; release height $Z_{rh}=245\text{mm}$, release position ‘A’; normal incidence (0°) to cube face; $X=160\text{mm}$; sampled $Y=-10\text{mm}$ corresponded to the plume concentration maximum in this (Y, Z) plane

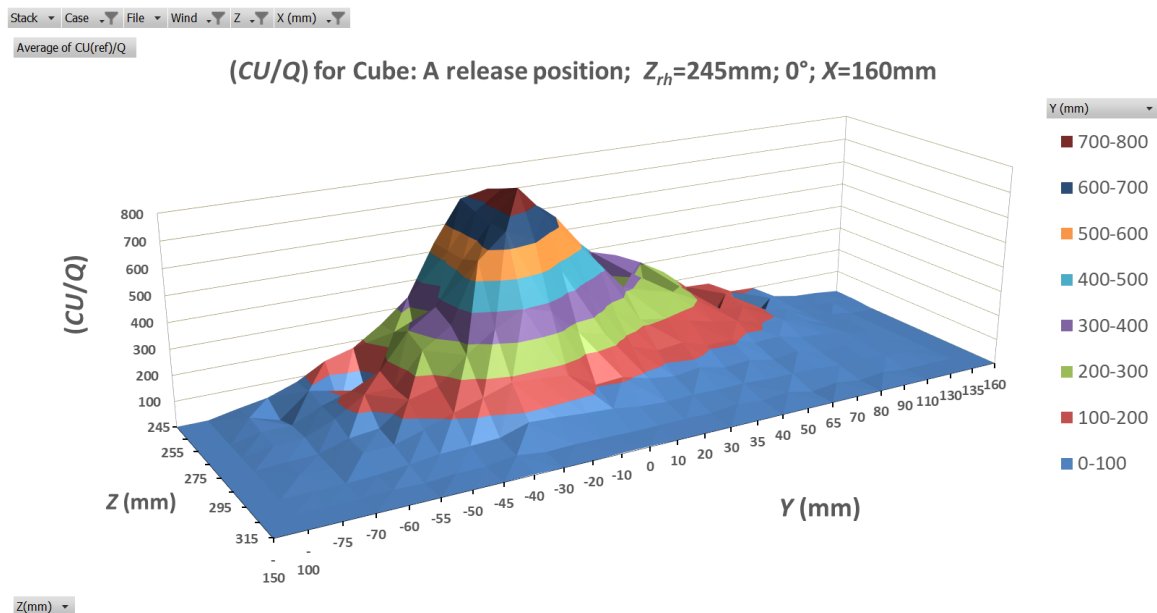


Figure 6.6(d): (CU/Q) for Cube: variation with (Y, Z) at sample plane $X=160\text{mm}$; release height $Z_{rh}=245\text{mm}$; normal incidence (0°) to cube face

From Figure 6.6(a/b) a near-roof release from position ‘A’ at normal incidence to the cube is shown for two sample heights at the downstream position close to the cube centre at $X=160\text{mm}$. The superiority of the DGP formulation was evident in terms of goodness of fit in (a) to a broadened peak over the cube, corresponding to two superimposed Gaussians which were evaluated via the DGP fitting algorithm. The second peak, sampled at greater height in (b), corresponded to the position expected for the RCZ, and was more evident where the main peak was reduced in amplitude because of distance from the plume centreline. Figure 6.6(c) shows the IGP method against the SGP along a vertical profile close to the plume concentration maximum – in this example both fitting methods yielded similar results in terms of vertical plume dispersion parameter. In Figure 6.6(d) a three-dimensional plot shows the overall Gaussian shape in the Y and Z directions, but the plume broadening is evident along the positive Y -axis extending over the building roof.

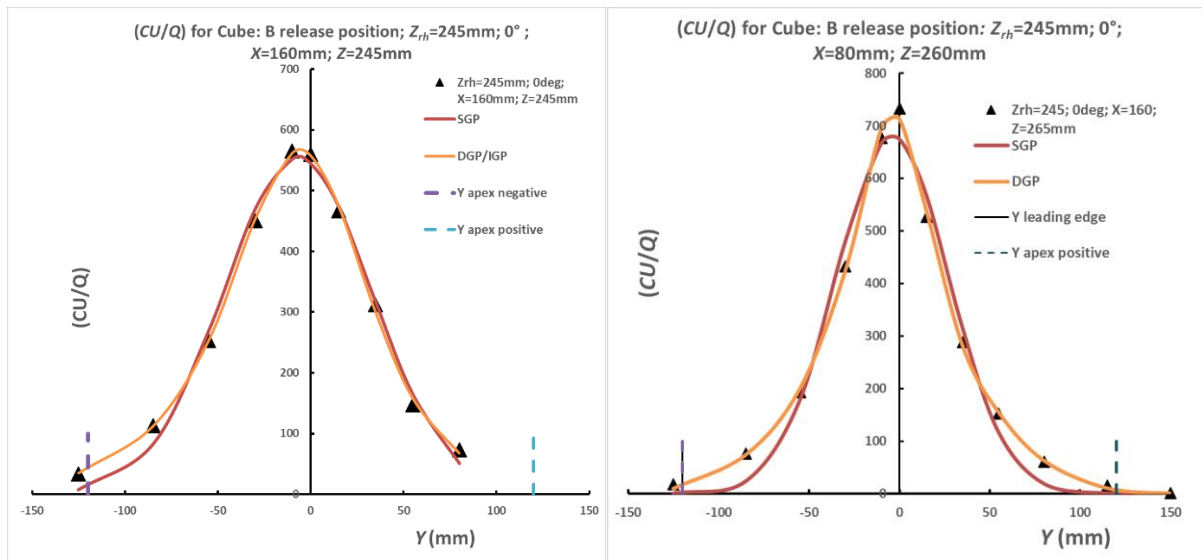


Figure 6.7(a/b): (CU/Q) variation with crosswind co-ordinate Y ; release height $Z_{rh}=245\text{mm}$ (5mm above model roof plane), release position 'B'; normal incidence (0°) to cube face; sampled (a) $Z=245\text{mm}$ and (b) 265mm respectively, cube vertex edges are shown as vertical dashed lines

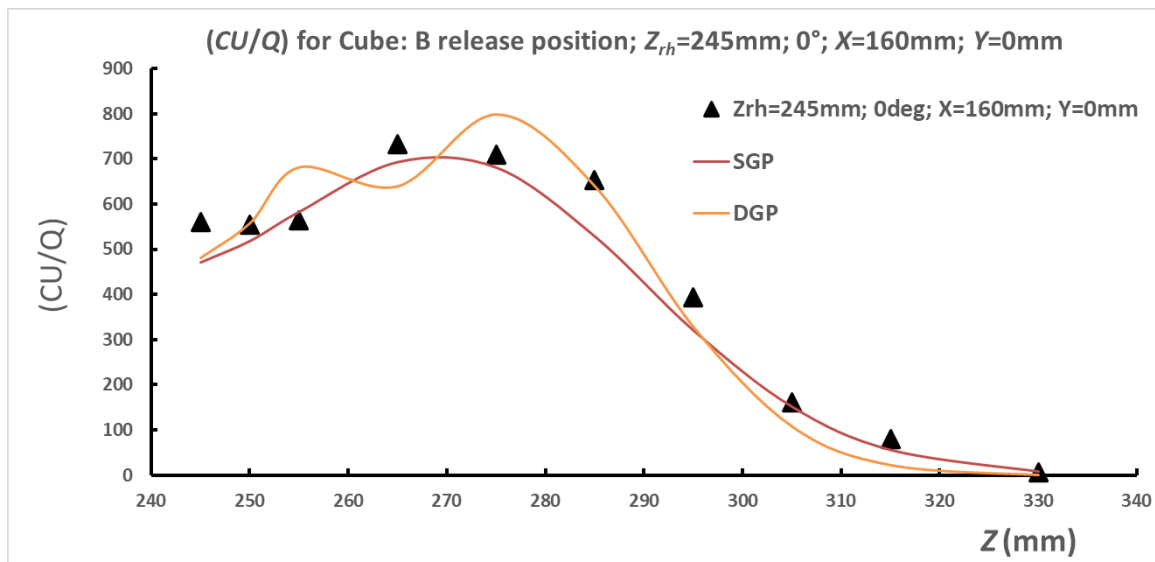


Figure 6.7(c): (CU/Q) variation with sampled vertical height Z ; roof height at $H=240\text{mm}$; release height $Z_{rh}=245\text{mm}$, midline centre release position 'B'; normal incidence (0°) to cube face; $X=160\text{mm}$; sampled $Y=0\text{mm}$ at plume concentration maximum in (Y, Z) plane. Figure 6.7(c) shows the effect of release position (B) on a near roof release at normal incidence to the cube: the downstream position considered was closest to the middle of the cube, with sampling at two heights. It can be seen from (a) that the enhanced tails of the DGP fitted the measured concentration field data better than the SGP: in this case the second plume was a Gaussian with larger crosswind dispersion (corresponding in effect to the RCZ) superimposed on the primary narrower peak, but both centred near to the central axis of the cube and release position. A similar pattern is evident in (b) at a greater sample height. In Figure 6.7(c) the SGP and IGP were sampled over a vertical profile aligned with the source, and cube centre at $Y=0$: it can be seen that the SGP fitted the concentration profile reasonably well, but the IGP with a fixed RCZ concentration zone and truncation at a given height shows evidence of the discontinuous change applied at the truncation height. In this example it may be argued that the measured concentration values are marginally better fitted than the SGP.

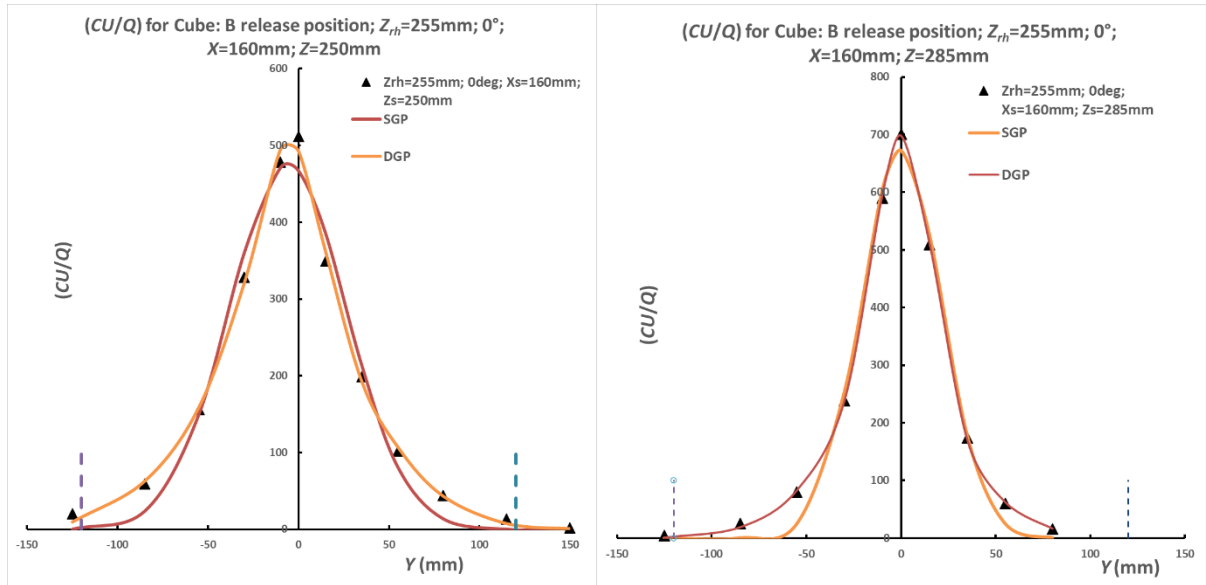


Figure 6.8(a/b): (CU/Q) variation with crosswind co-ordinate Y ; release height $Z_{rh}=255$ mm (15 mm above model roof plane), release location at 'B'; normal incidence (0°) to cube face; sampled (a) $Z=250$ mm and (b) 285 mm respectively, cube edges shown as vertical dashed lines of fixed magnitude (100)

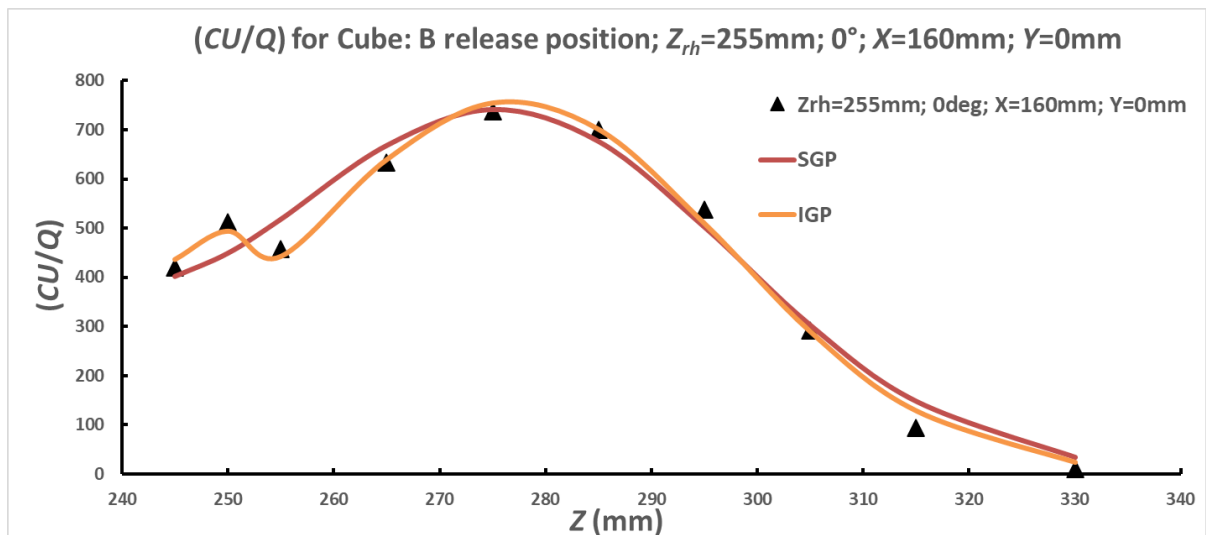


Figure 6.8(c): (CU/Q) variation with sampled vertical height Z ; roof at $H=240$ mm; release height $Z_{rh}=255$ mm; release position 'B'; normal incidence (0°) to cube face; $X=160$ mm; sampled $Y=0$ mm corresponded to the plume concentration maximum in (Y, Z) plane

From Figure 6.8 we have further evidence of the plume dispersion but with a greater release height ($Z_{rh}=255$ mm) for normal incidence on the cube at central release position B. In (a) the enhanced tails of the fitted DGP are evident at both the sampled heights. From 6.8(c) we see a vertical profile showing a Gaussian plume but with greater plume height, corresponding to the greater release height, compared to Figure 6.7. The IGP peak was narrower in terms of vertical dispersion parameter than the SGP and more elevated, showing some deconvolution.

6.3.1.1.2 Cube: -22.5° incidence of flow

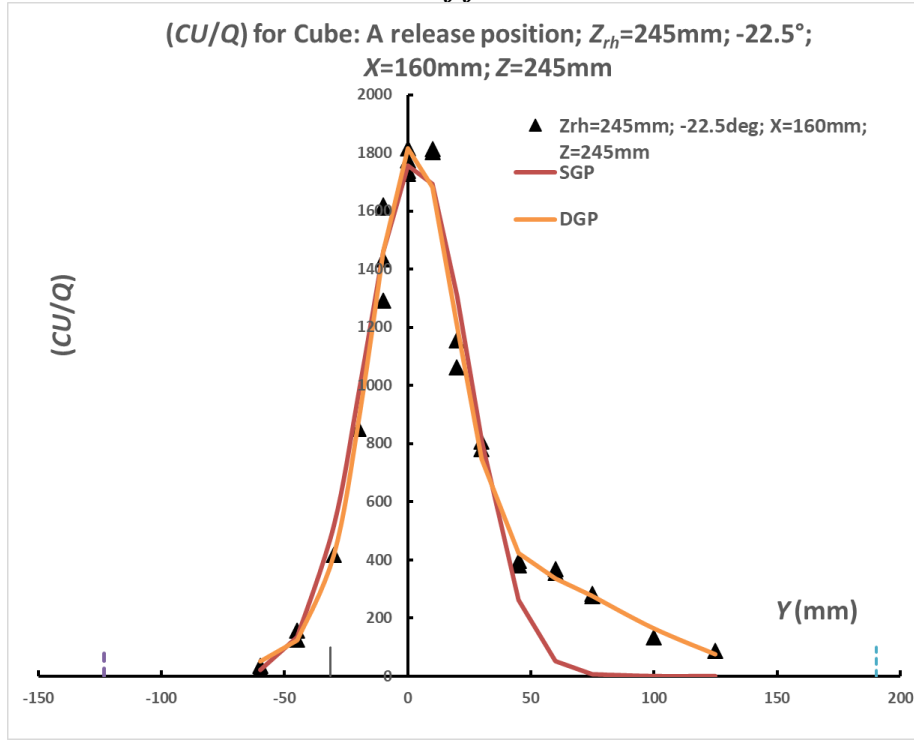


Figure 6.9:
(CU/Q) variation with crosswind coordinate Y; release height $Z_{rh}=245\text{mm}$; release position 'A' (near cube vertex); angle -22.5° to cube face; Y range sampled at height $Z=245\text{m}$: cube vertex edges are shown as vertical dashed lines

Figure 6.9 shows the cube with -22.5° angle of approach flow in relation to the building, with tracer release near the vertex at position A: release height was the closest to the building from the experiments ($Z_{rh}=245\text{mm}$), and the profiles were taken at $X=160\text{mm}$. The secondary peak (RCZ) was evident, which showed the advantage of the DGP fitted method.

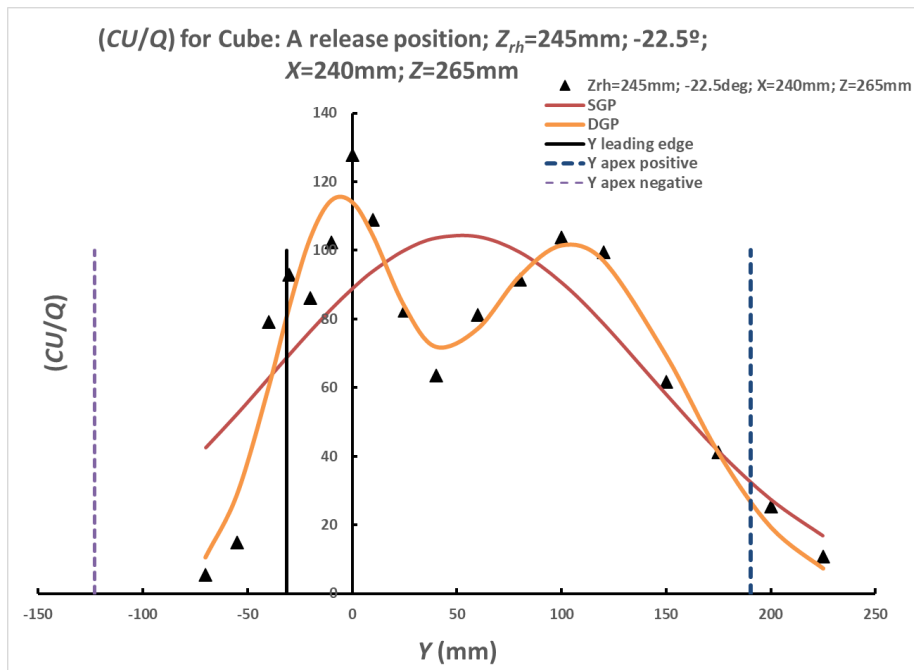


Figure 6.10
(CU/Q) at $X=240\text{mm}$ with crosswind coordinate Y; release height $Z_{rh}=245\text{mm}$ (5mm above model roof plane), release position 'A'; -22.5° to cube face; Y range sampled at height $Z=265\text{mm}$: cube vertex edges are shown as vertical dashed lines

In Figure 6.10, evidence of propagation of the plume further downstream near the back of the cube at $X=240\text{mm}$ is shown, with low release height, release position 'A' and angle -22.5° to flow: sampling is marginally greater height compared to Figure 6.9. In this case the primary peak - identified on the left of the figure and closest to the release position is similar in magnitude to the secondary (RCZ) peak, which is in positive Y direction over the building roof.

The SGP fitted formulation can at best estimate the overall magnitude of the concentration field in this downstream profile.

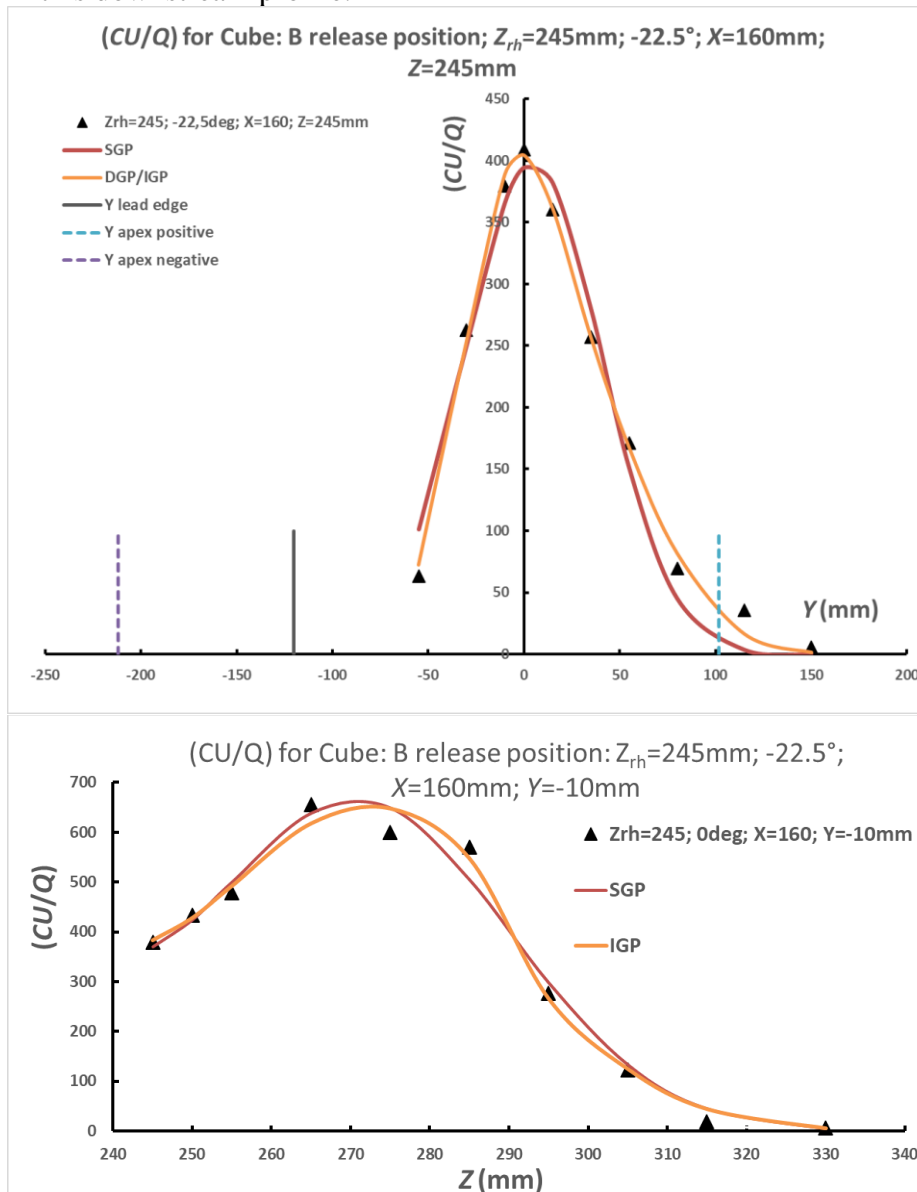


Figure 6.11(a, top)/(b, bottom):

(CU/Q) variation, at $X=160mm$:

(a) with crosswind coordinate Y ; release height $Z_{rh}=245mm$ (roof plane height 240mm), at midline position 'B'; angle -22.5° to cube face; Y range sampled at $Z=250m$;

(b) Z range sampled at $Y=-10mm$ corresponding to the roof RCZ; in (a) cube vertex edges are shown as vertical dashed lines

In Figure 6.11 the cube 'B' release position is considered at $X=160mm$, angle -22.5° and release height $Z_{rh}=245mm$. As before, the enhanced Gaussian plume tails can be seen and the fitted main plume is differentiated from the SGP fitted profile with a negative Y -shift. The vertical profile was taken through the plume centreline and showed an elevated peak with marginal differences between the SGP and IGP fitted algorithms.

6.3.1.1.3 Cube: -45° incidence of flow

It can be seen in Figure 6.12 for an angle of approach flow of -45° to the building, cube release position 'A', that there is evidence of a small RCZ, or secondary, peak.

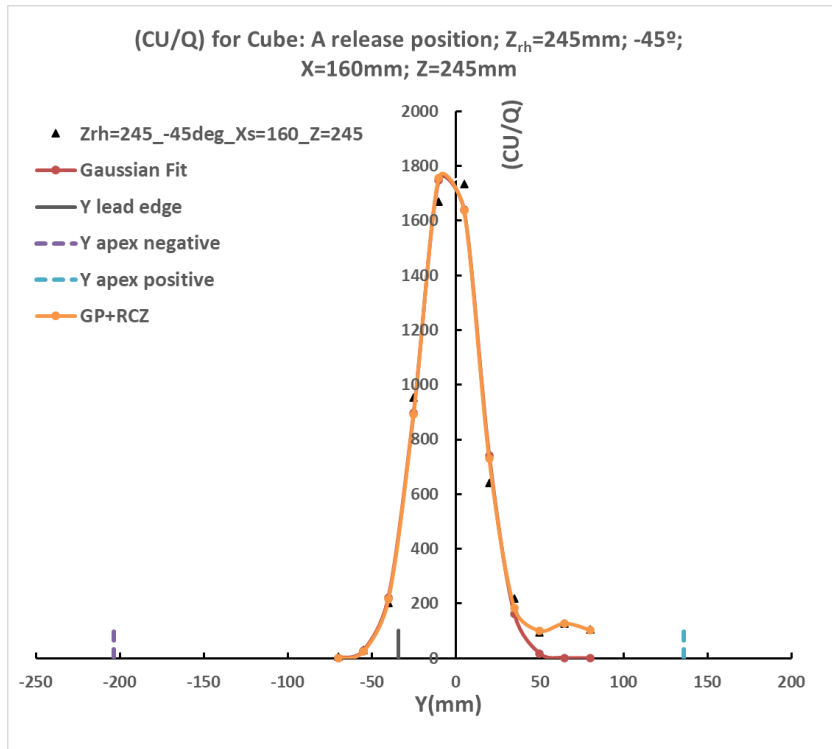


Figure 6.12
(CU/Q) variation, at $X=160\text{mm}$, with crosswind co-ordinate Y ; release height $Z_{rh}=245\text{mm}$ (5mm above model roof plane), at position 'A'; -45° to cube face; Y range sampled at $Z=250\text{m}$: cube vertex edges are shown as vertical dashed lines

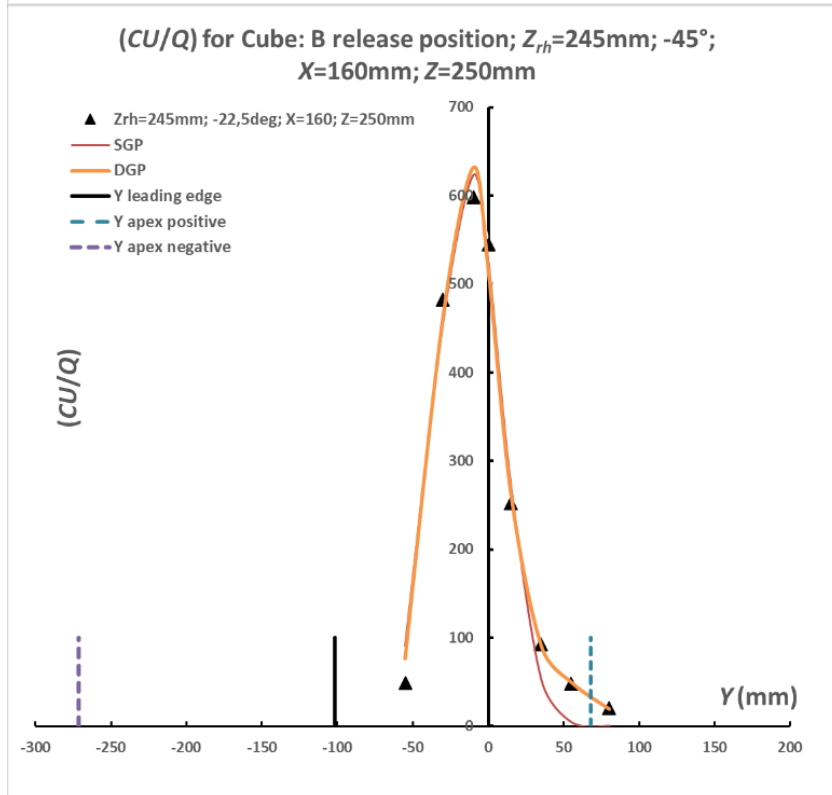


Figure 6.13
(CU/Q) at $X=160\text{mm}$; $Z_{rh}=245\text{mm}$; midline position 'B'; -45° to cube face: variation with Y sampled at $Z=250\text{mm}$

From Figure 6.13, with similar conditions to Figure 6.12, but with a marginally greater sample height ($Z=250\text{mm}$) and the 'B' release position in relation to the cube at -45° to flow the enhanced tail of the DGP fitted profile was evident. As with the 'B' release position in Figure 6.11, graph (b) shows a distinct elevated peak above the roof plane, with no difference between SGP and IGP fitted curves.

6.3.1.2 Cube: Active Vertical Release Cases – Roof Zone

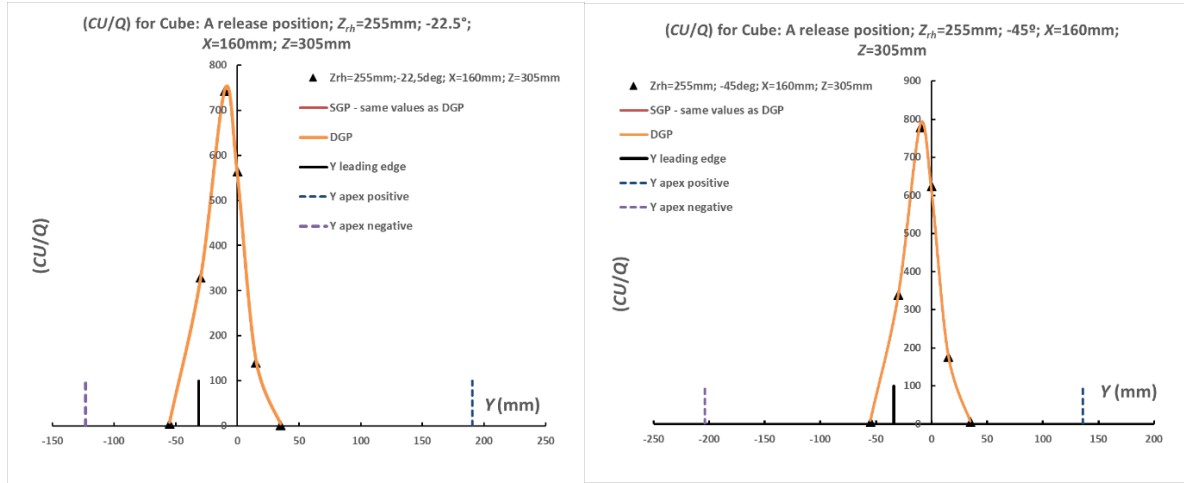


Figure 6.14(a/b): (CU/Q) variation for PCM profiles at $X=160\text{mm}$; $Z_{rh}=255\text{mm}$ with active vertical release at near vertex position 'A'; Y sampled at $Z=305\text{mm}$; vertical Z sampled at $Y=-10\text{mm}$; (a) -22.5° incidence to cube face; (b) -45° incidence to cube face.

From Figure 6.14 we see active vertical releases with the cube at position 'A' for (a) -22.5° and (b) -45° . The release height was 255mm, but with upward plume velocity matched to approach flow velocity to match the EW clad and unclad cases, covered later. The profiles were taken at plume maximum concentration: both show an elevated plume where the magnitude of concentration was similar, and an accurate SGP fitting, to which the DGP converged.

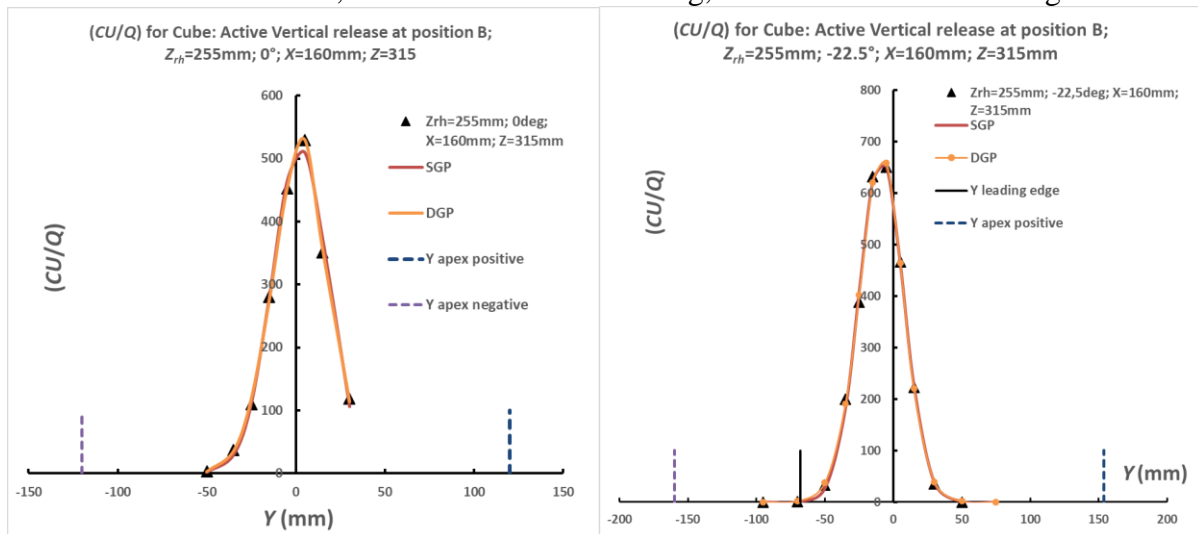


Figure 6.15(a/b):

(CU/Q) variation for plume concentration maximum profiles at $X=160\text{mm}$; release height $Z_{rh}=255\text{mm}$; active vertical release at position 'B' (midline of cube); crosswind co-ordinate Y sampled at $Z=315\text{mm}$:

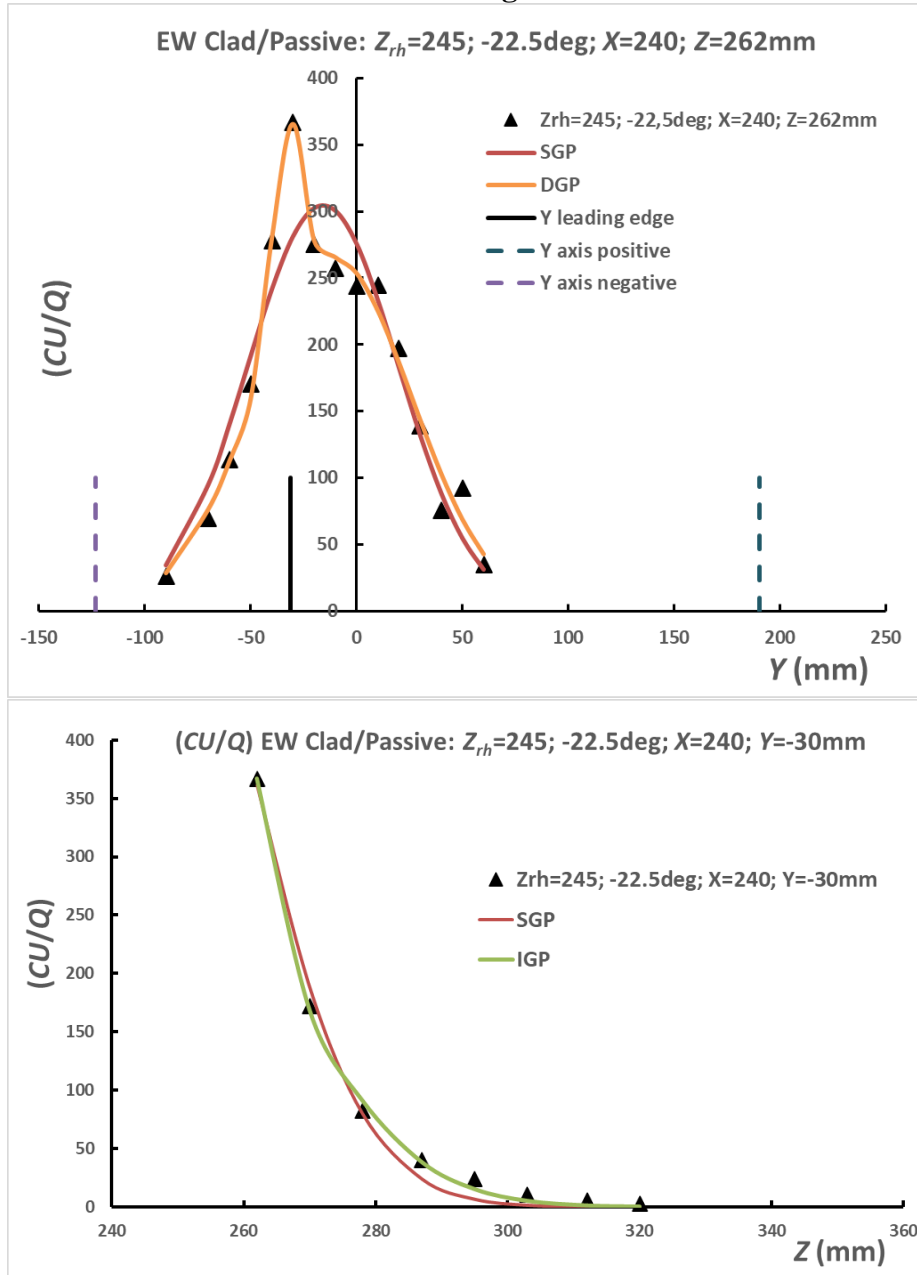
(a, left) 0° incidence to cube-face

(b, right) -22.5° incidence to cube-face

From Figure 6.15 active vertical releases are presented with the cube at release position 'B' for (a) 0° , (b) -22.5° . Release height was 255mm. The profiles were taken at plume maximum concentration, at a greater sampled height than Figure 6.14, showing evidence of greater upward deflection of the plume concentration maximum. Elevated plumes are shown where the SGP

and DGP fitted methods are convergent because of the height of the plumes above the level of the roof plane.

6.3.1.3 EW Clad and Unclad buildings: Passive Release Cases



The EW clad case is shown in Figure 6.16, once again for a passive release height close to the roof of $Z_{rh}=245$ mm. The angle of approach flow was -22.5° , and the release was at the North stair tower position, approximately corresponding to release case A for the cube in terms of distance to the roof leading edge: this would be the natural case with which to compare the EW building cases. Profiles are presented at $X=240$ mm near the downstream back edge of the building. As with the corresponding cube case ('A', -22.5°) the vertical profile near the plume centreline does not have an elevated peak but reaches a maximum close to the building roof.

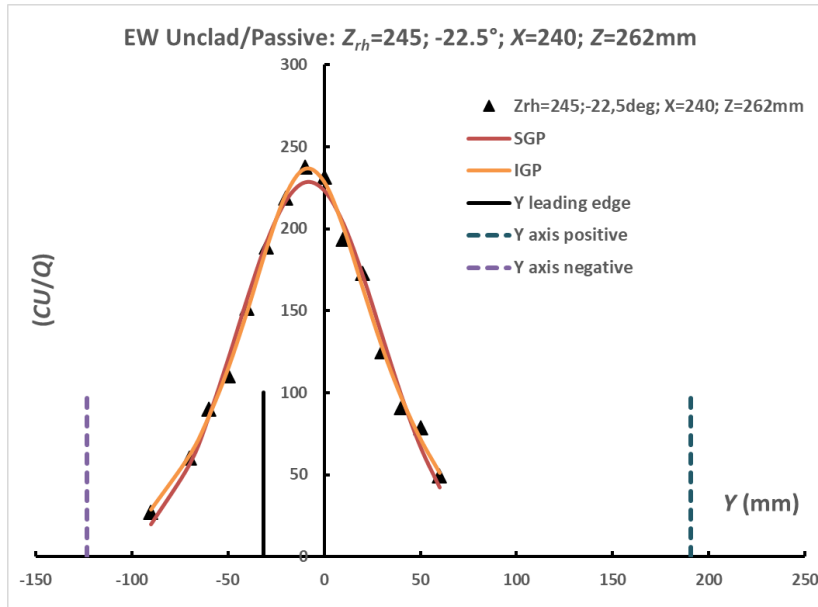


Figure 6.17

EW Unclad (CU/Q) variation for plume concentration maximum profiles at $X=240$ mm with passive release height $Z_{rh}=245$ mm: sampled height at $Z=262$ mm

For comparison, the leading edge and corners of the cube are superimposed for the same angle of approach flow

The EW unclad case is shown in Figure 6.17, for similar release conditions and sample height. The concentration magnitude was noted as being smaller than the EW clad case, at the same sample height (262mm).

6.3.1.4 EW Clad and Unclad: Active Vertical Release Cases

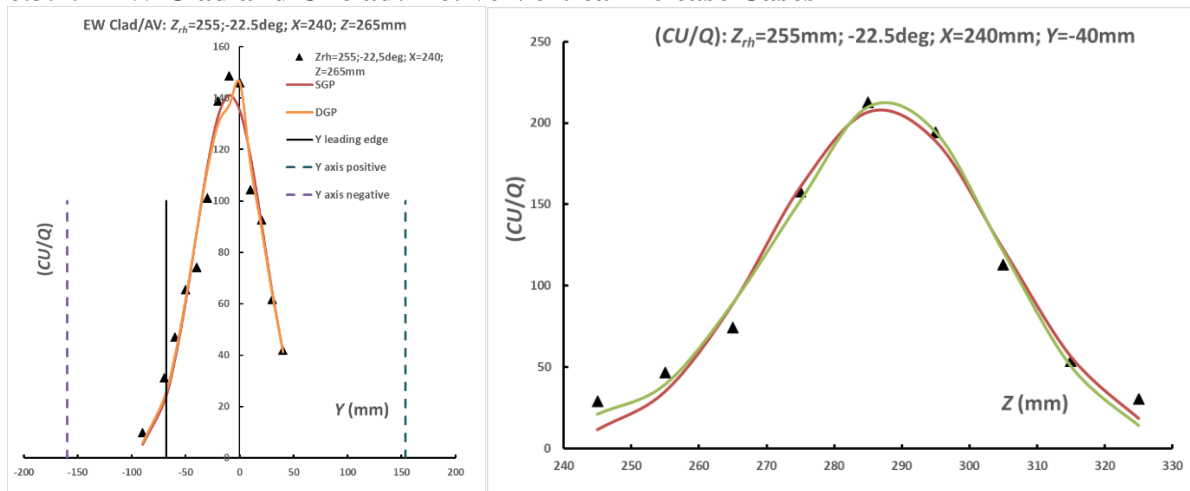


Figure 6.18(a/b):

EW Clad (CU/Q) for PCM; $X=240$ mm; AV release; $Z_{rh}=255$ mm: (a) sampled height $Z=265$ mm; (b) sampled at $Y = -40$ mm

From Figure 6.18 the active vertical case is presented for the EW clad case at a downstream position of 240mm. An elevated plume is evident, with little distinction possible between the DGP and SGP fitted algorithms in the crosswind or vertical directions.

6.3.2 Cube: Main Recirculation Zone

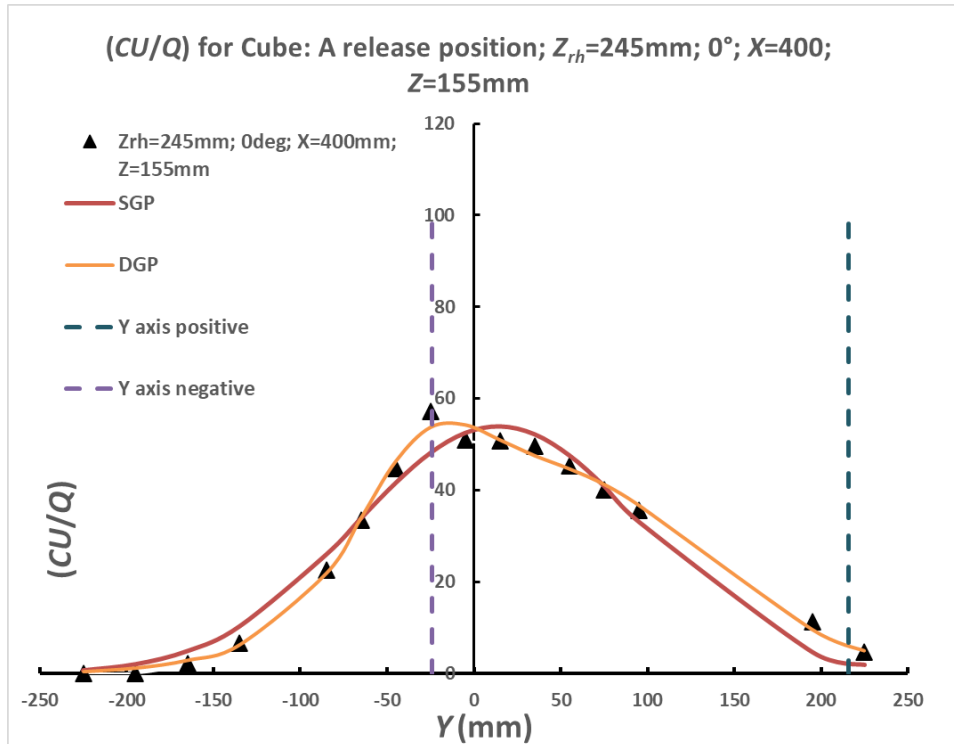
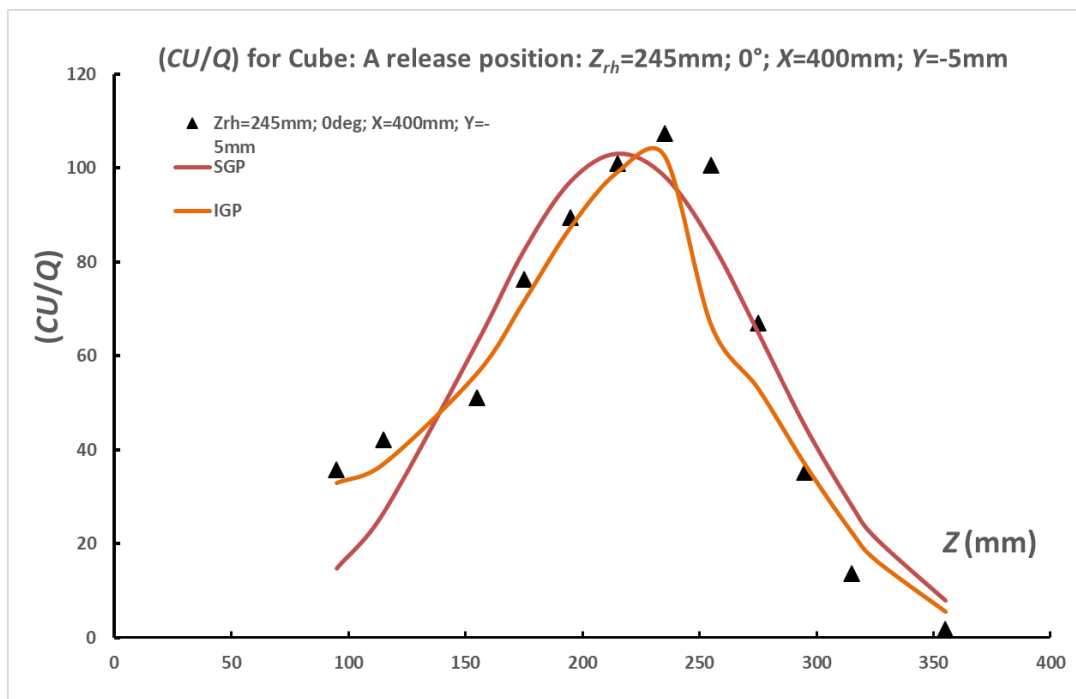


Figure 6.19(a, top/b, below):
(CU/Q) variation with crosswind co-ordinates Y/Z; release height $Z_{rh}=245\text{mm}$; incidence 0° to cube face:

- (a) Y range sampled horizontally at $Z=155\text{mm}$ ($Z/H=0.65$)
- (b) Z range sampled vertically at $Y=-5\text{mm}$



The downstream plane past the building at $X=400\text{mm}$ was investigated for the cube cases. In Figure 6.19 results for the closest release height to roof plane ($Z_{rh}=245\text{mm}$) are shown at normal incidence of flow for release position A. The sample height for the crosswind profile (a) was 155mm or 65% of the building height, H , and the vertical profile (b) was close to the release position. It can be seen from (b) that there is a significant amount of entrainment in the main RCZ of the building, extending down to the minimum sampled height of 85mm , with the superimposed profile of the main plume. The crosswind profile in (a) shows concentration in the main RCZ, with some overspill around the cube in the negative Y co-ordinates.

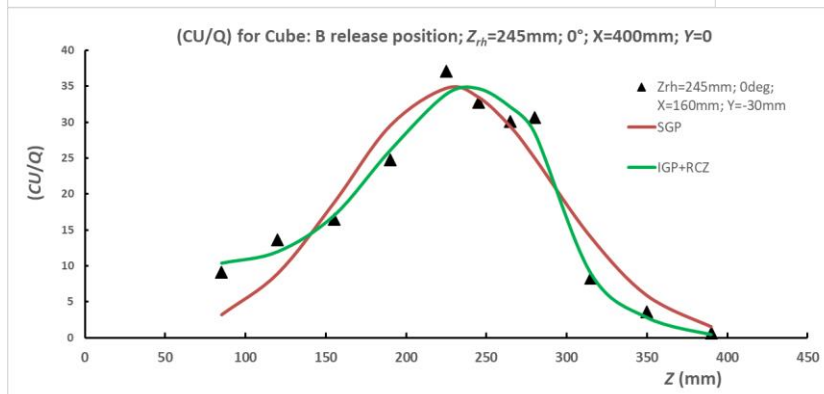
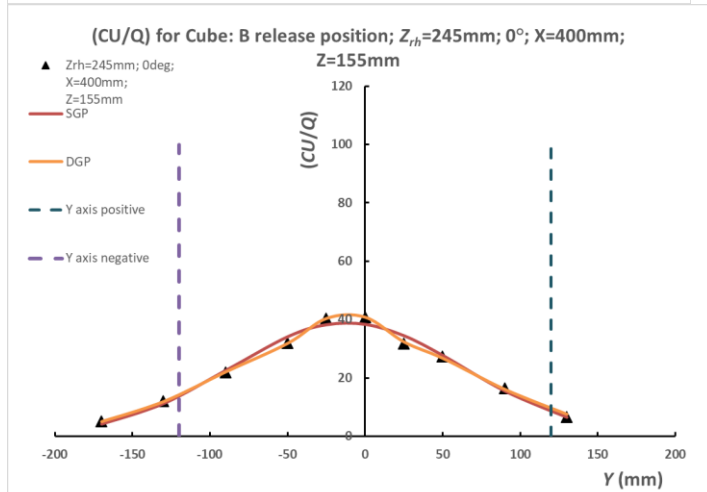
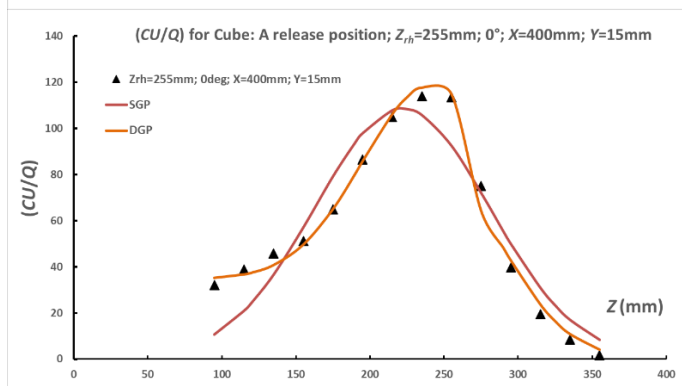
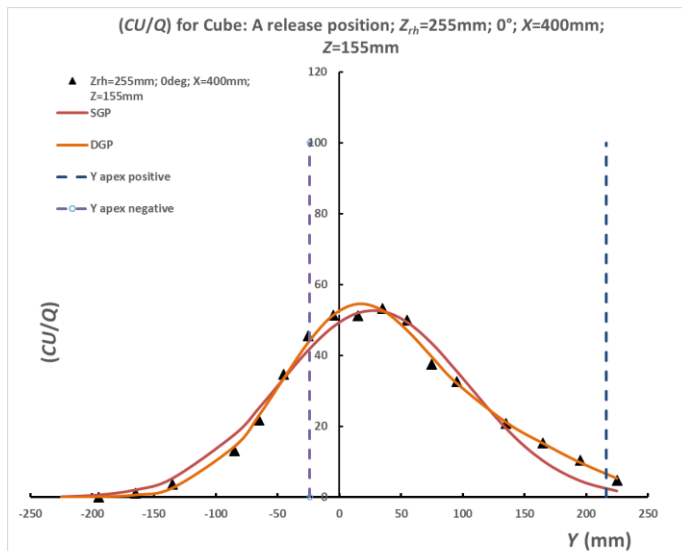


Figure 6.20(a, top/b, below):
CU/Q variation with crosswind co-ordinate Y and vertical height Z;
X=400mm; release height
Z_{rh}=255mm (15mm above model
roof plane), near vertex release
position ‘A’; normal incidence (0°)
to cube face;
(a) Y; range sampled at Z=155mm;
(b) Z; range sampled at Y=15mm

Figure 6.20 shows the effect of a more elevated passive release at Z_{rh}=255mm for the cube at release position ‘A’ at normal incidence. The entrainment is of a similar magnitude, but it can be seen from (b) that the main plume is more elevated and the main RCZ is marginally more distinct and appears to tend to a more uniform concentration at the lowest sampled heights.

Figure 6.21(a, top/b, below):
(CU/Q) variation with crosswind
co-ordinate Y and vertical height
Z; X=400mm; release height
Z_{rh}=245mm (15mm above model
roof plane), centreline release
position ‘B’; normal incidence
(0°) to cube face;
(a) Y range sampled at
Z=155mm;
(b) Z range sampled at Y=0mm

From Figure 6.21 at $Z_{rh}=245\text{mm}$ normal incidence of flow for release position 'B' is shown. Sampled height for the crosswind profile (a) was 155mm as per Figures 6.19/6.20 and vertical profile (b) was close to the release position. From (a) the main building RCZ is well fitted from the DGP and DGP Gaussian formulations and the concentration field is broadly symmetric. The vertical profile in (b) shows a lower level of concentration near the lowest sampled height of 85mm compared to the case in Figures 6.19/6.20 with the superimposed profile of the main plume shown aloft: the expected effect here would be the upwards deflection of plume with wind from this direction and a consequent reduction in entrainment into the main RCZ.

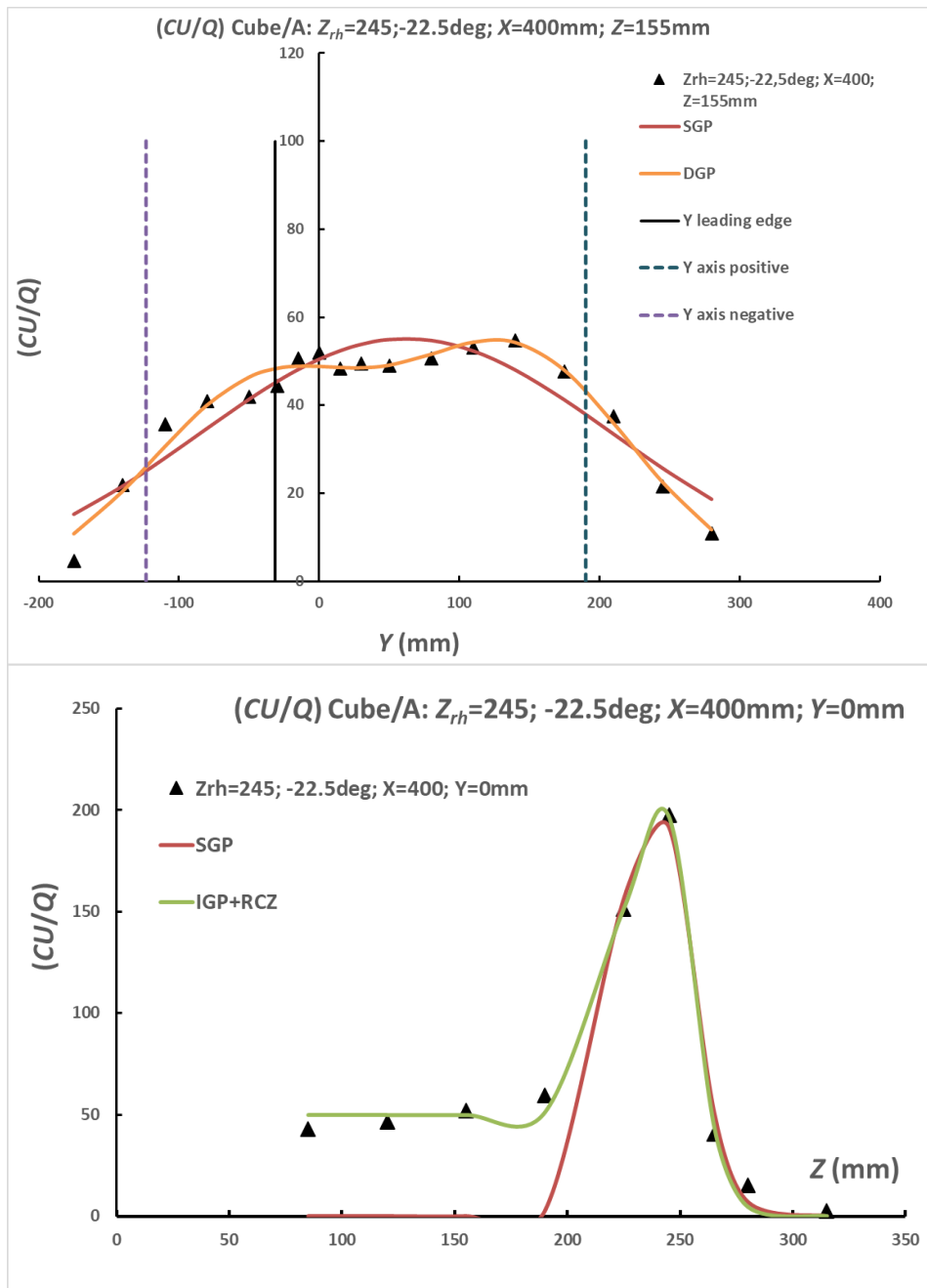


Figure 6.22(a/b):

(CU/Q) variation with crosswind co-ordinate Y and vertical height Z ; release height $Z_{rh}=245\text{mm}$ (15mm above model roof plane), vertex release position 'A'; incidence -22.5° to cube face:

(a) Y ; range sampled at $Z=155\text{mm}$;

(b) Z ; range sampled at $Y=0\text{mm}$

From Figure 6.22 the effect of rotation of building to the approach flow can be seen (-22.5°) for release position A with the profile of maximum in (a) distal from the plume centre line at $Y=0$. The vertical profile (b) shows a uniform well-mixed main RCZ concentration in below the main peak close to the crosswind release position.

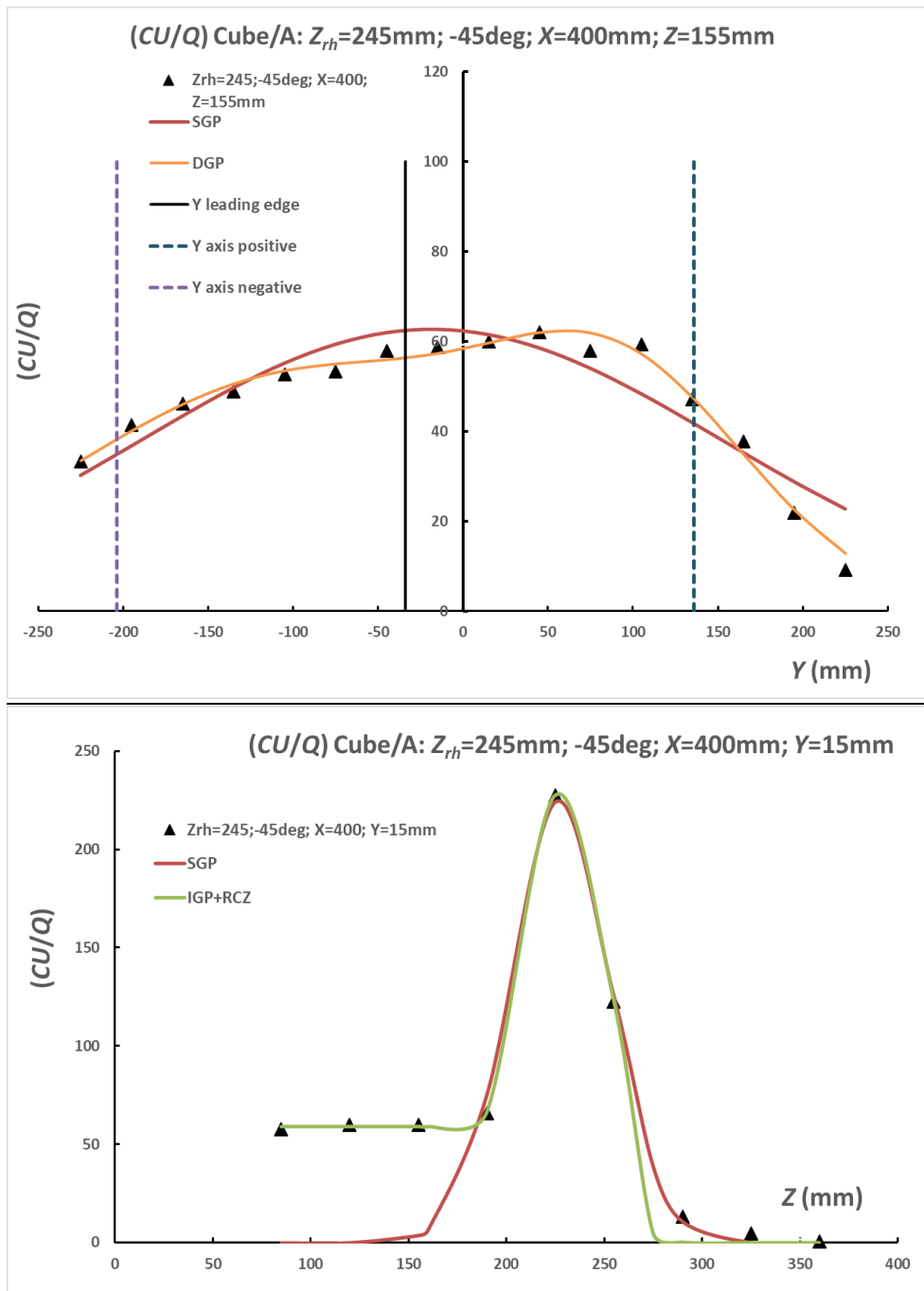


Figure 6.23(a/b): (CU/Q) variation with crosswind co-ordinate Y/Z ; release height $Z_{rh}=245\text{mm}$ (15mm above model roof plane), vertex position 'A'; incidence -45° to cube face; (a) Y range sampled at $Z=155\text{mm}$; (b) Z range sampled at $Y=0\text{mm}$

From Figure 6.23 the effect of further rotation of building to the approach flow can be seen (-45°) for release position A with the profile maximum on the same side of the release position at $Y=0$. The vertical profile close to the crosswind release position in (b) once again shows a uniform well-mixed main RCZ concentration below the main peak.

6.3.3 Plume Concentration Maximum variation with downstream distance

6.3.3.1 Cube Vertex 'A' position

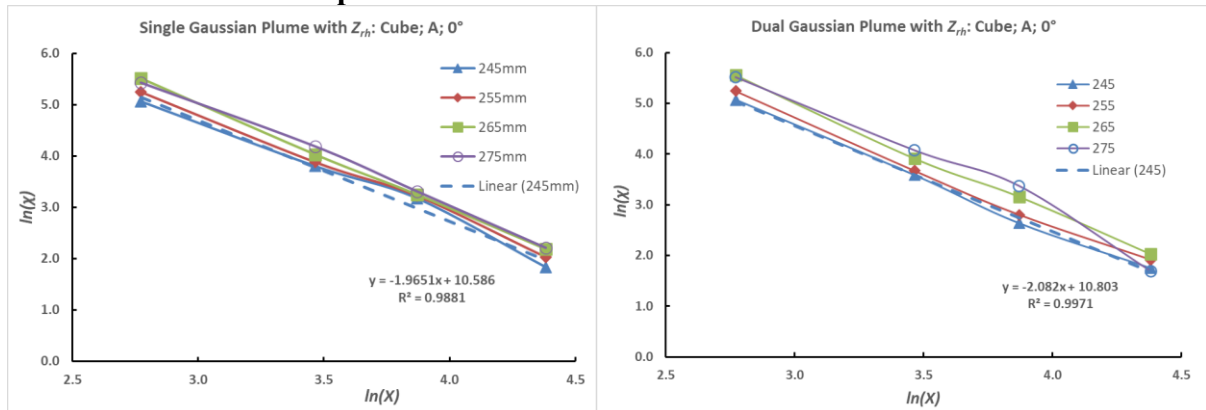


Figure 6.24(a/b): $\ln(\chi)$ variation with $\ln(X)$ for different release heights Z_{rh} for the PCM with downstream distance; vertex position 'A'; incidence 0° to cube face; (a) SGP; (b) DGP. Regression trend line is presented for $Z_{rh}=245\text{mm}$, lowest release height case

Figure 6.24 shows the plume concentration maximum (PCM) fitted using logarithmic scales for passive releases with the cube at normal incidence of flow. The sample trend-line for $Z_{rh}=245\text{mm}$ and fitted linear parameters are shown as an example. The SGP fitted data in (a) shows a clear linear characteristic for all of the passive release data considered with correlation coefficient R^2 close to unity. In (b) the DGP fitted data is shown: the convergence of the data with release height is not as strong, but this may be considered to be related to the de-convolution split of the main and secondary profiles and the consequent introduction of a greater element of uncertainty i.e. the SGP may be the more robust model in this consideration.

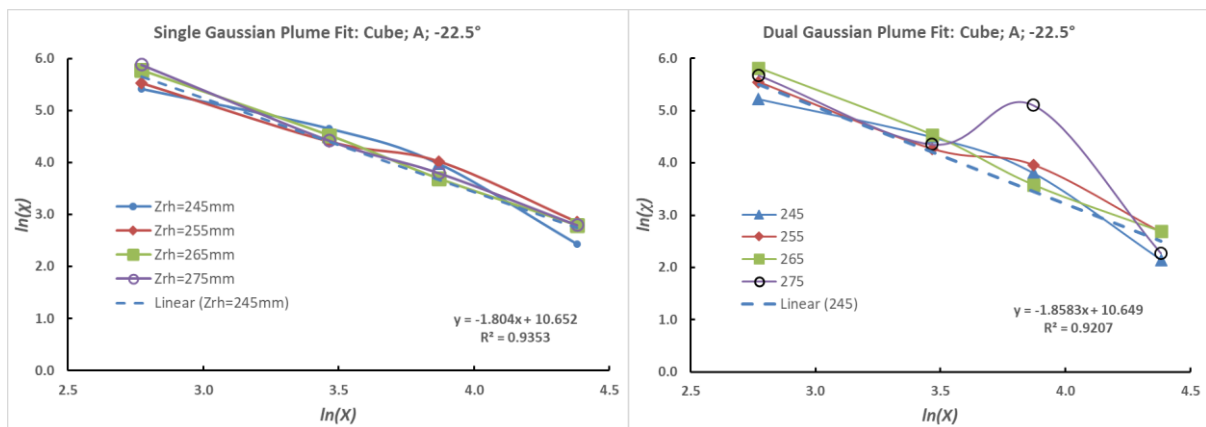


Figure 6.25(a/b): $\ln(\chi)$ variation with $\ln(X)$ for different release heights Z_{rh} for the PCM with downstream distance; vertex position 'A'; incidence -22.5° to cube face; (a) SGP; (b) DGP. Regression trend line is presented for $Z_{rh}=245\text{mm}$, lowest release height case

From Figure 6.25 the cube at A, with incidence -22.5° is shown. The SGP (a) shows a robust linear characteristic with high correlation coefficient, but the DGP (b) shows a generally poorer correlation with the linear fit model and with a greater gradient. Results for -45° are presented in Appendix 15.3.

6.3.3.2 EW Clad releases

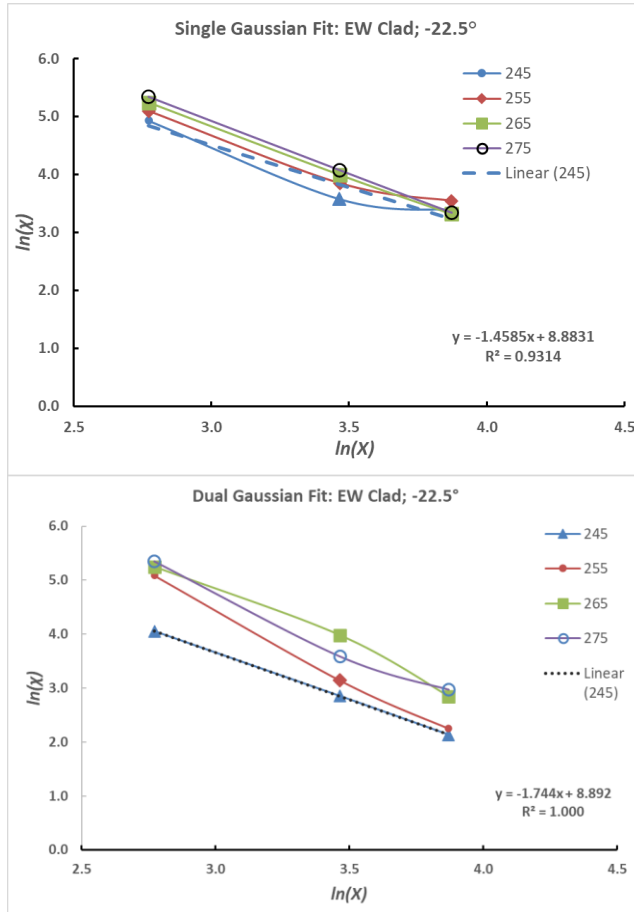


Figure 6.26(a, top/b, below):

$\ln(\chi)$ variation with $\ln(X)$ for different release heights Z_{rh} for the PCM with downstream distance; vertex position 'A'; incidence -22.5° to EW Clad face:

(a) SGP

(b) DGP

Regression trend line is presented for $Z_{rh}=245\text{mm}$, lowest release height case. Figure 6.26 for the EW clad building for (a) SGP and (b) DGP show a lower gradient than the respective cube cases for this same -22.5° angle of approach flow

6.3.3.3 Cube centreline 'B' position

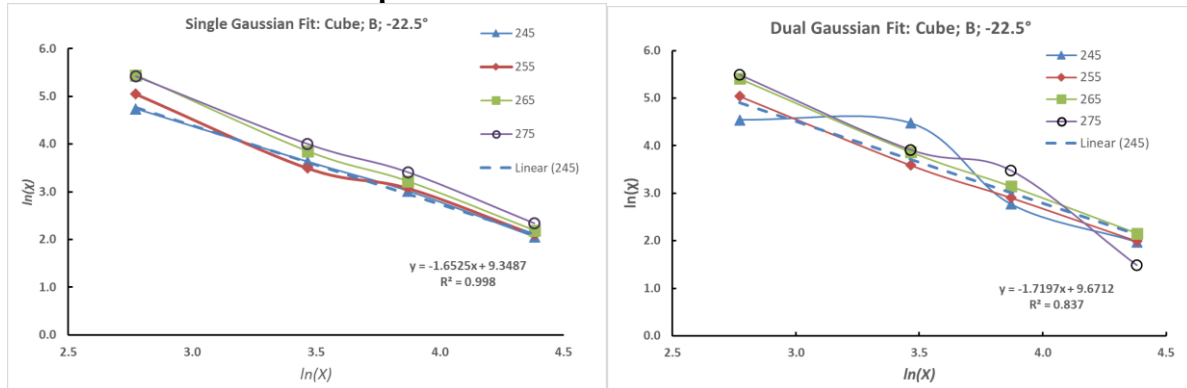


Figure 6.27(a/b): $\ln(\chi)$ variation with $\ln(X)$ for different release heights Z_{rh} for the PCM with X ; position 'B'; -22.5° ; (a) SGP; (b) DGP. Regression trend line for $Z_{rh}=245\text{mm}$

The results for release position 'B' shows regression lines where the gradient is lower than the 'A' case at the same angle of -22.5° for the approach flow. This can be contrasted to the normal incidence 0° flow direction where the gradients for the 'A' and 'B' release positions are similar, and these results are shown in Appendix 15.3.

6.3.4 Roof Zone Maximum Measured Concentrations: Cube and EW Clad and Unclad

6.3.4.1 Cube vertex position A

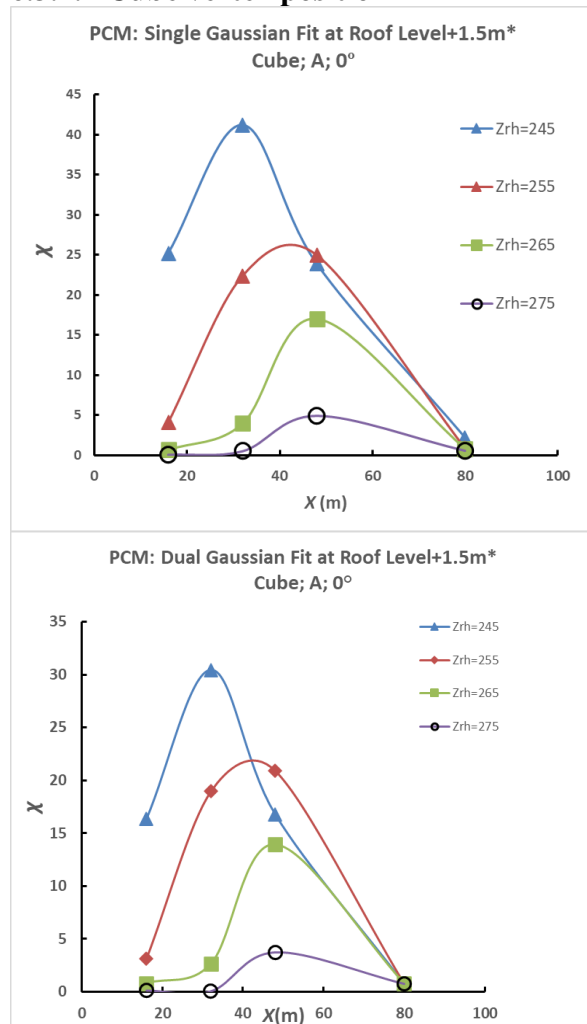


Figure 6.28(a,b,c; top/left/right): maximum dimensionless concentration χ variation in the cube roof zone, and RCZ maximum, with X for different release heights Z_{rh} ; position 'A'; incidence 0° to cube face: *values presented are for those closest to a sample height on 1.5m full scale above the roof plane ($Z=247.5\text{mm}$ model scale):

(a) SGP
(b) DGP
(c) Roof Zone RCZ.

Figure 6.28 shows roof zone maximum concentrations for different passive release heights with normal incidence of flow. It is evident that the greatest concentrations peak at approximately 40 for the SGP, and the de-convoluted DGP shows a reduced figure of 30, for the lowest release height of 245mm model scale. Maximum concentration reduced with release height and the downstream distance of the maximum concentration point also increases with release height. The roof top RCZ shows a similar pattern, with a maximum value of approximately 18 for the lowest release height tested.

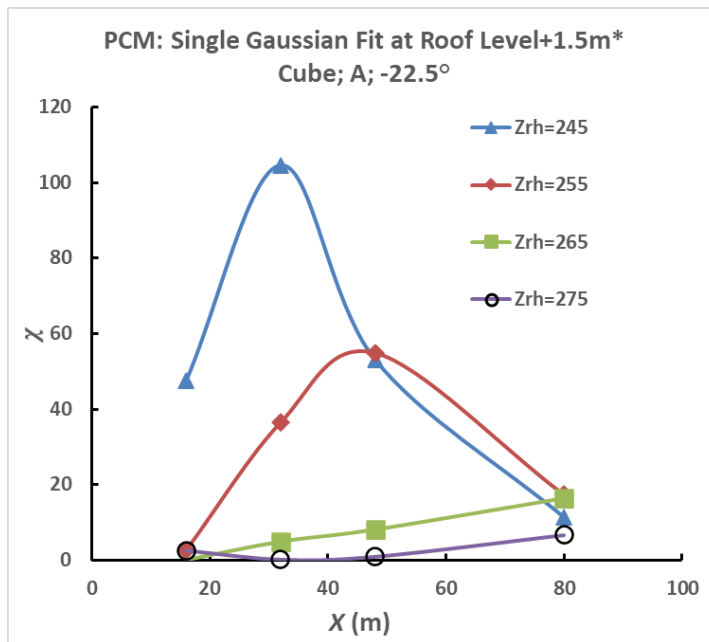
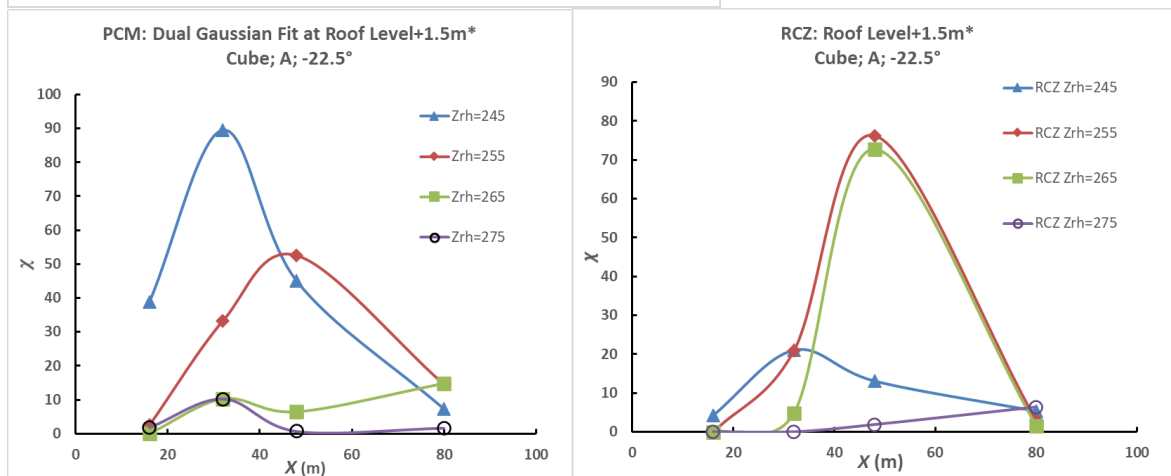


Figure 6.29(a,b,c; top to bottom): maximum dimensionless concentration χ variation in the cube roof zone, and RCZ maximum, with X for different release heights Z_{rh} ; position 'A'; incidence -22.5° to cube face; values presented are for those closest to a sample height on 1.5m full scale above the roof plane ($Z=247.5$ mm model scale):
(a) SGP
(b) DGP
(c) Roof Zone RCZ. For cases where 245mm and 250mm sample height data was available, the maximum value was taken.



In Figure 6.29 the maximum concentrations for the A release position at incidence of -22.5° were greater than the values for the normal incidence case for the two lowest release heights. However, for the greater release heights this pattern reversed and the corresponding concentrations were measured to be lower for both the SGP and DGP methods in the roof top zone. The roof top RCZ showed low values for the lowest release height of 245mm, and greater values for the intermediate release heights tested (255 and 265mm) the latter magnitudes being comparable to the main plume (in either SGP or DGP methods). It is expected that these effects are related to the effect of roof top vortices and the corresponding advection of material from the plume.

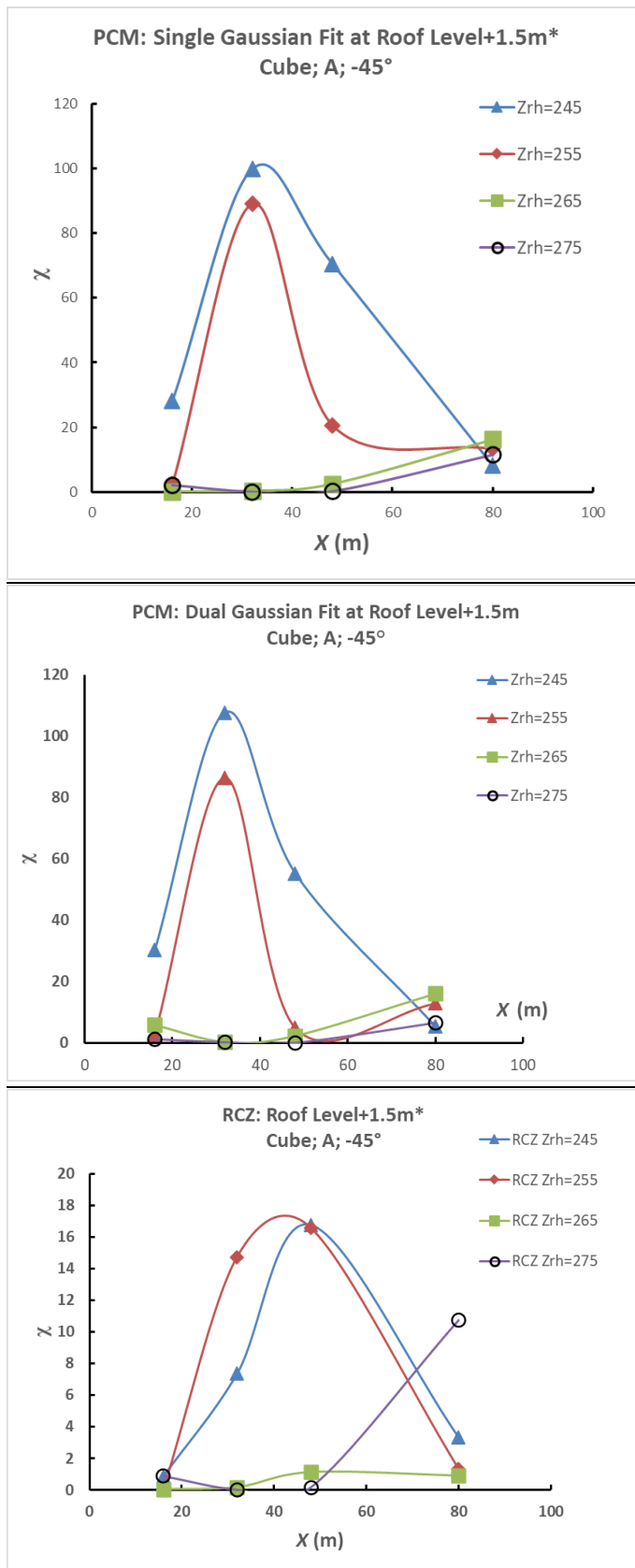


Figure 6.30(a,b,c; top to bottom):
Maximum dimensionless concentration χ variation in the cube roof zone, and RCZ maximum, with X for different release heights Z_{rh} ; position ‘A’; incidence -45° to cube face; values presented are for those closest to a sample height on 1.5m full scale above the roof plane ($Z=247.5$ mm model scale):
 (a) SGP
 (b) DGP
 (c) Roof Zone RCZ.
 For cases where 245mm and 250mm sample height data was available, the maximum value was taken.

Figure 6.30 shows the A release case at -45° approach flow, where the concentration peaks in magnitude for the lowest (245mm) release height: of note is also that the 255mm release height is nearly the same magnitude as the 245mm release compared to Figure 28 where it was approximately half. The maximum roof top concentrations for the lowest release height of 245mm was similar in magnitude to the -22.5° case. For the next highest release height of 255mm the maximum concentration increases from 0° through to -44.5°. For the 265 and 275mm release heights the maximum concentrations in the roof zone ($X < 70$ m, full scale) decrease from 0° through to -45°. The roof top RCZ dimensionless concentration is similar for release height 245mm across all three angles of approach flow with a magnitude in the region of 15–20. For the normal incidence case the reduction of concentration with increasing release height follows a clear monotonic reduction pattern: but for the -22.5° case the 255 and 265mm release heights show significant peaks in the region of a value of 70. The greatest release height tested shows a relatively low concentration peaking in the region of 4 for normal incidence: the increased value at $X=80$ m, full scale and past the roof zone, may be caused by only partial deconvolution of the main peak in the algorithm and in any case does not correspond to a value on the roof surface.

6.3.4.2 EW Clad and Unclad releases

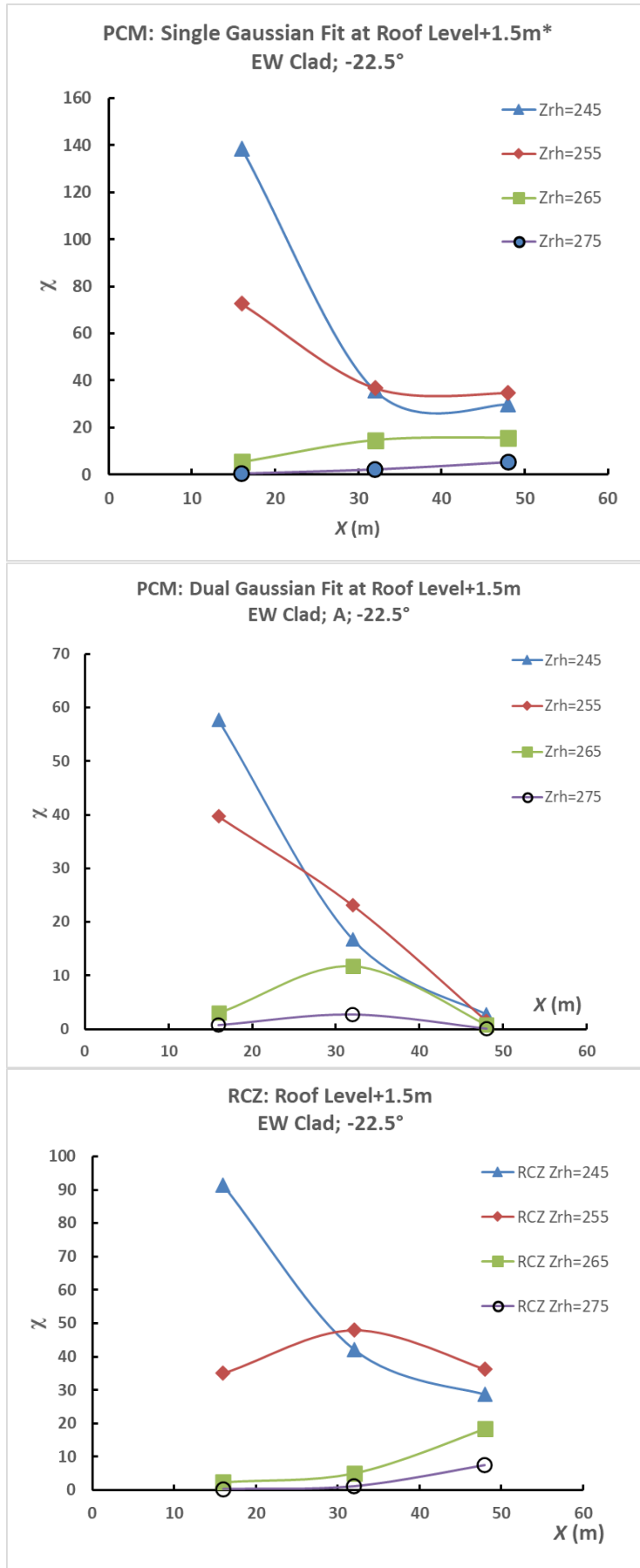


Figure 6.31(a,b,c; top to bottom):
maximum dimensionless
concentration χ variation in the EW
Clad roof zone, and RCZ maximum,
with X for different release heights
 Z_{rh} ; values presented are for those
closest to a sample height on 1.5m
full scale above the roof plane
($Z=247.5$ mm model scale):
(a) SGP
(b) DGP
(c) Roof Zone RCZ

Results are presented for the EW clad case at -22.5° in Figure 6.31 and comparison will be made against the cube case with release position A at the same angle of approach flow. The maximum concentrations for the lowest release height of 245m are greater by approximately 40% for the SGP formulation but lower by approximately 30% for the DGP method: these maxima occur at the closest distance from the source sampled. The corresponding values for the 255mm release are approximately 40% and 20% respectively for the SGP and DGP methods. For the rooftop RCZ the maximum is approximately 90/50 for the EW clad for the 245/255mm release heights respectively, but for the cube at -22.5 the peak values are 20/75. This indicates a greater degree of comparative plume entrainment for the EW building case which may be related to local features closer to the release position.

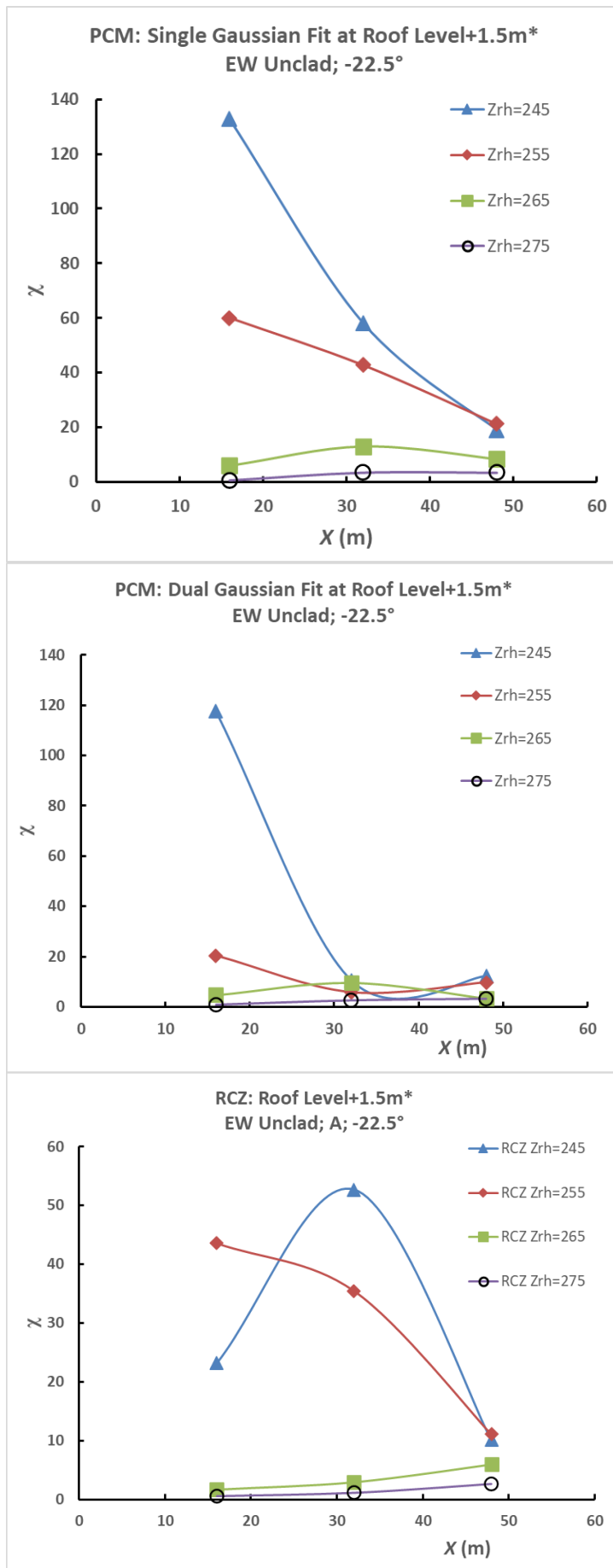


Figure 6.32(a,b,c; top to bottom):
maximum dimensionless
concentration χ variation in the EW
Unclad roof zone, and RCZ
maximum, with X for different
release heights Z_{rh} ; incidence -22.5°:
values presented are for those closest
to a sample height on 1.5m full scale
above the roof plane ($Z=247.5\text{mm}$
model scale):
(a) SGP
(b) DGP
(c) Roof Zone RCZ

Figure 6.32 shows the EW unclad case: compared to the EW clad case the EW unclad SGP model gives similar values of maximum dimensionless concentration.

For the DGP case the pattern is less clear: the EW unclad case results indicate double the concentration maximum for the 245mm release height. For 255mm release height the unclad case is a factor of two lower.

Rooftop RCZ values are comparable for 255mm but lower in the EW unclad case by approximately a factor of two. For the greater release heights of 265mm and 275mm the results indicate generally higher concentrations for the clad case compared to the unclad case.

6.3.4.3 Cube centreline release position 'B'

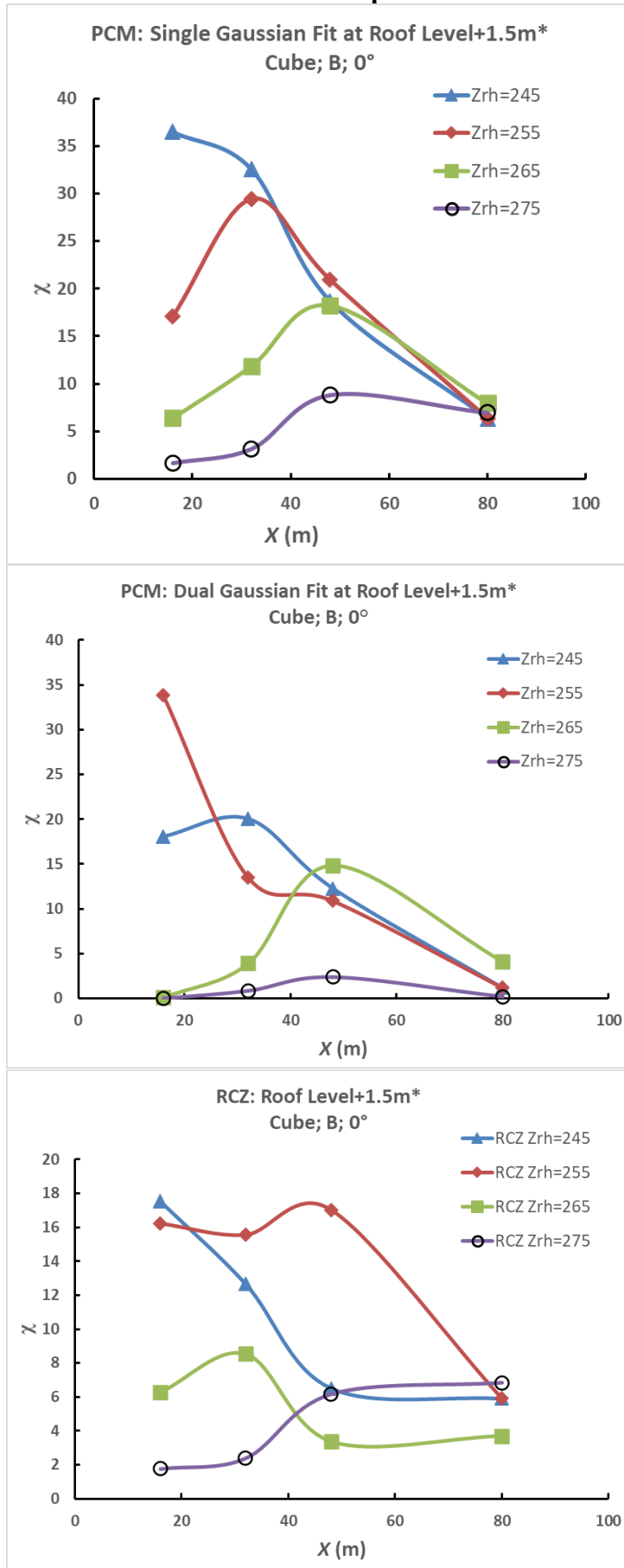


Figure 6.33(a,b,c; top to bottom):
 maximum dimensionless concentration χ variation in the cube roof zone, and RCZ maximum, with X for different release heights Z_{rh} ; position 'B'; incidence 0° to cube face: *values presented are for those closest to a sample height on 1.5m full scale above the roof plane (at $Z=247.5$ mm model scale):

- (a) SGP
- (b) DGP
- (c) Roof Zone RCZ

From Figure 6.33 the SGP concentrations for the centreline release position 'B' for the cube follow a monotonic reducing pattern with increasing release height Z_{rh} , with values generally slightly lower than the 'A' release position.

For the DGP main plume the maximum value of dimensionless concentration was approximately $\chi=35$ at $Z_{rh}=255$ mm and was matched by a value of just over $\chi=20$ for the corresponding 'A' release case.

RCZ rooftop maximum concentrations reduce from maxima of approximately 18 to 6, compared to a similar range of approximately 18 to 4, for release heights increasing from 245mm to 275mm in model scale.

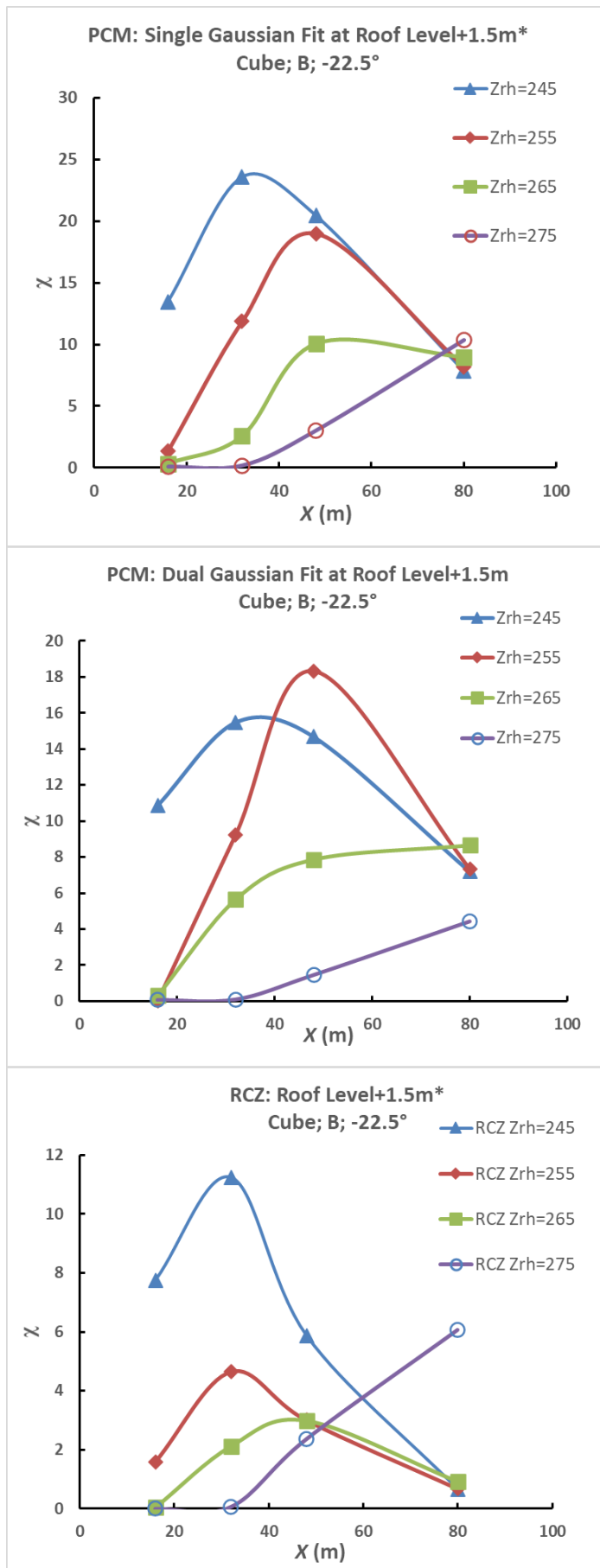


Figure 6.34(a,b,c; top to bottom):
maximum dimensionless
concentration χ variation in the
cube roof zone, and RCZ
maximum, with X for different
release heights Z_{rh} ; position 'B';
incidence -22.5° to cube face:
***values presented are for those**
closest to a sample height on 1.5m
full scale above the roof plane
($Z=247.5\text{mm}$ model scale):
(a) SGP
(b) DGP
(c) Roof Zone RCZ

For the -22.5° approach flow in Figure 6.34 for the cube at B release position the concentrations are considerably lower than the corresponding angle cases for the A release position. They are also somewhat lower than the normal incidence case for the cube at release position B.

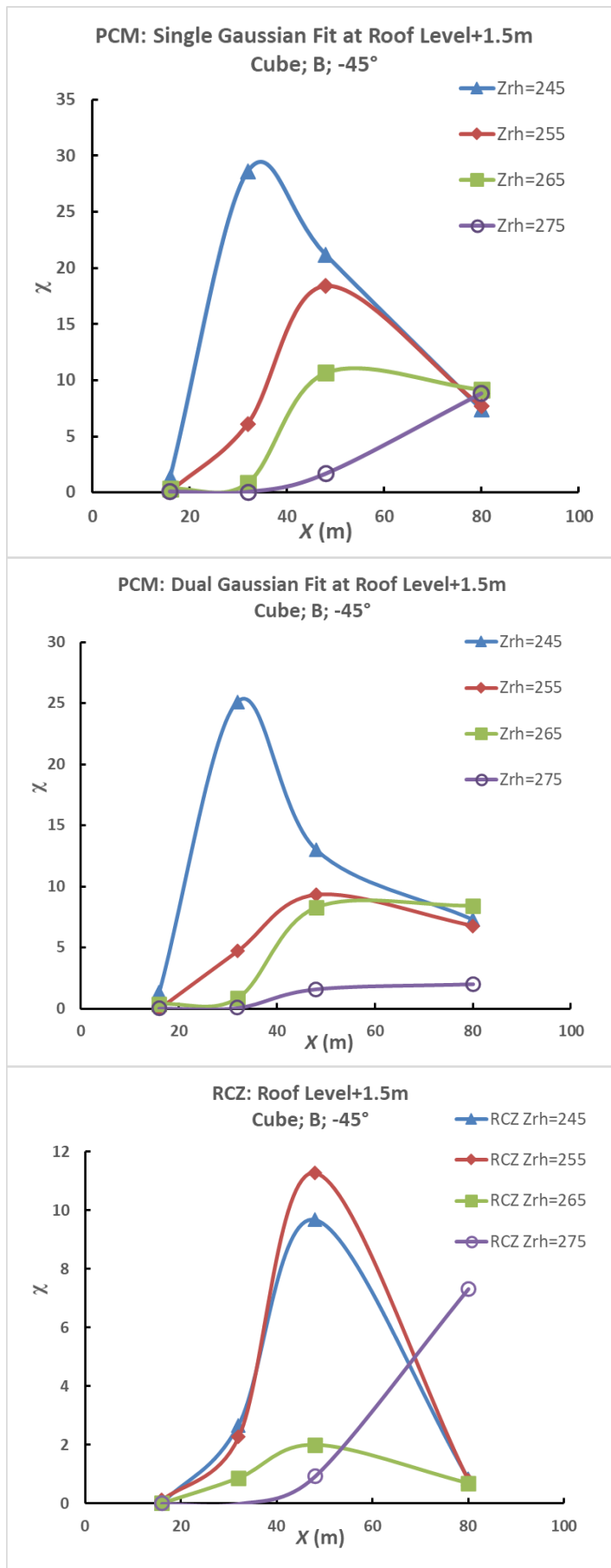


Figure 6.35(a,b,c; top to bottom):
maximum dimensionless concentration χ variation in the cube roof zone, and RCZ maximum, with X for different release heights Z_{rh} ; position 'B'; incidence -45° to cube face: *values presented are for those closest to a sample height on 1.5m full scale above the roof plane ($Z=247.5\text{mm}$ model scale):

(a) SGP

(b) DGP

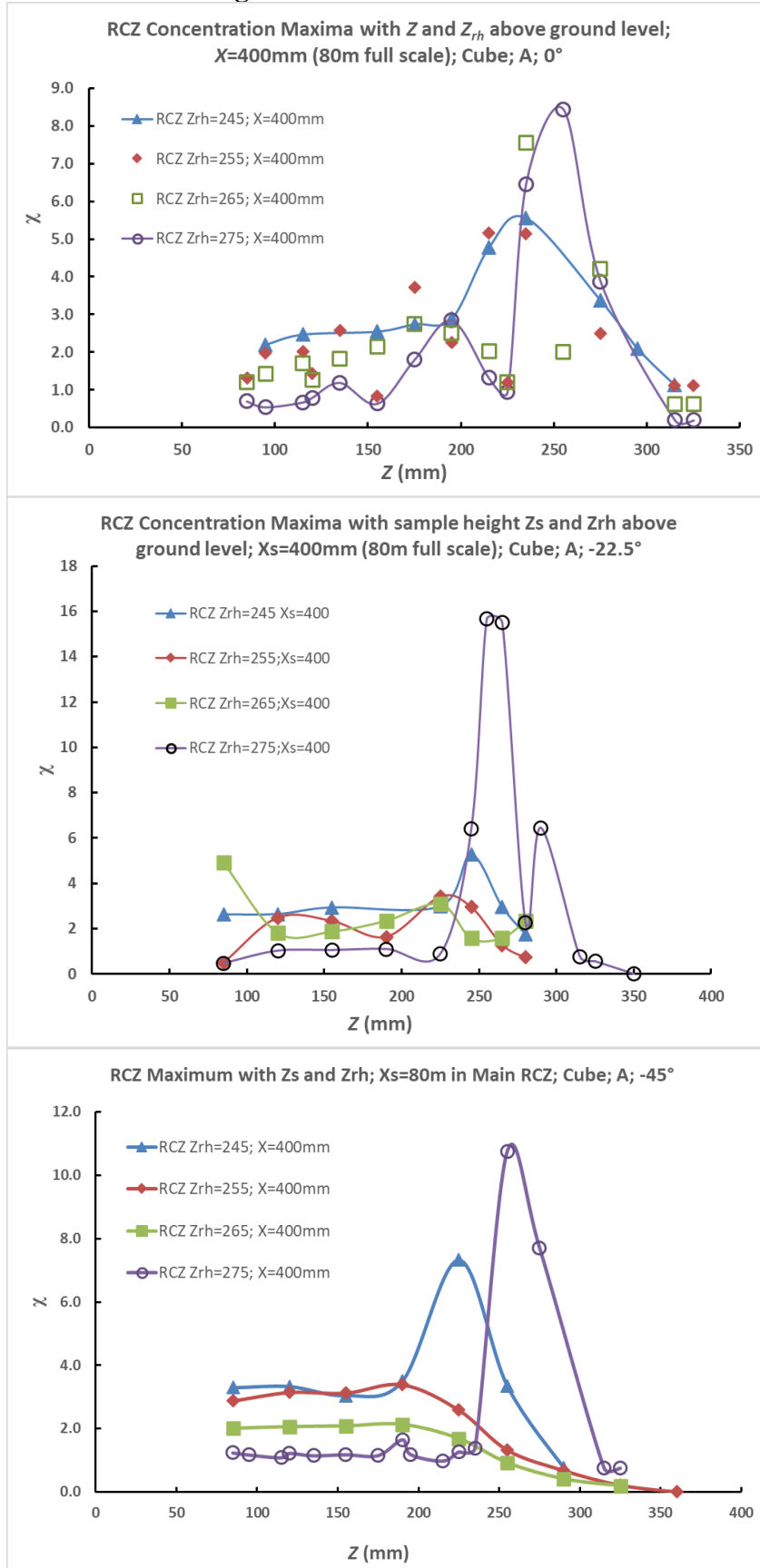
(c) Roof Zone RCZ

For the -45° approach flow in Figure 6.35 for the cube at 'B' release position the concentrations are considerably lower than the corresponding angle cases for the 'A' release position, as was also the case for the -22.5° approach flow direction.

The rooftop RCZ maximum values are slightly lower than the corresponding release position 'A' case.

From the results presented the flow field, and consequent advection of the plume, lead to higher values of the concentration at roof level for angled approach flow, and these are much more evident for the 'A' position release cases compared to the 'B' release position. These differences should be related to flow field patterns by further investigation of the flows over the building for different angles of approach flow. It should be postulated that the greater entrainment, and higher consequent concentrations, of the angled approach flows develop as a result of the roof top vortices generated close to the leading vertex of the building to the approach flow. Lower relative concentrations at angled directions of flow to the cube, for the 'B' release case, could be postulated to be because of the greater distance of B from the leading-edge vortices on the cube flow field.

6.3.5 Main building RCZ concentrations: cube



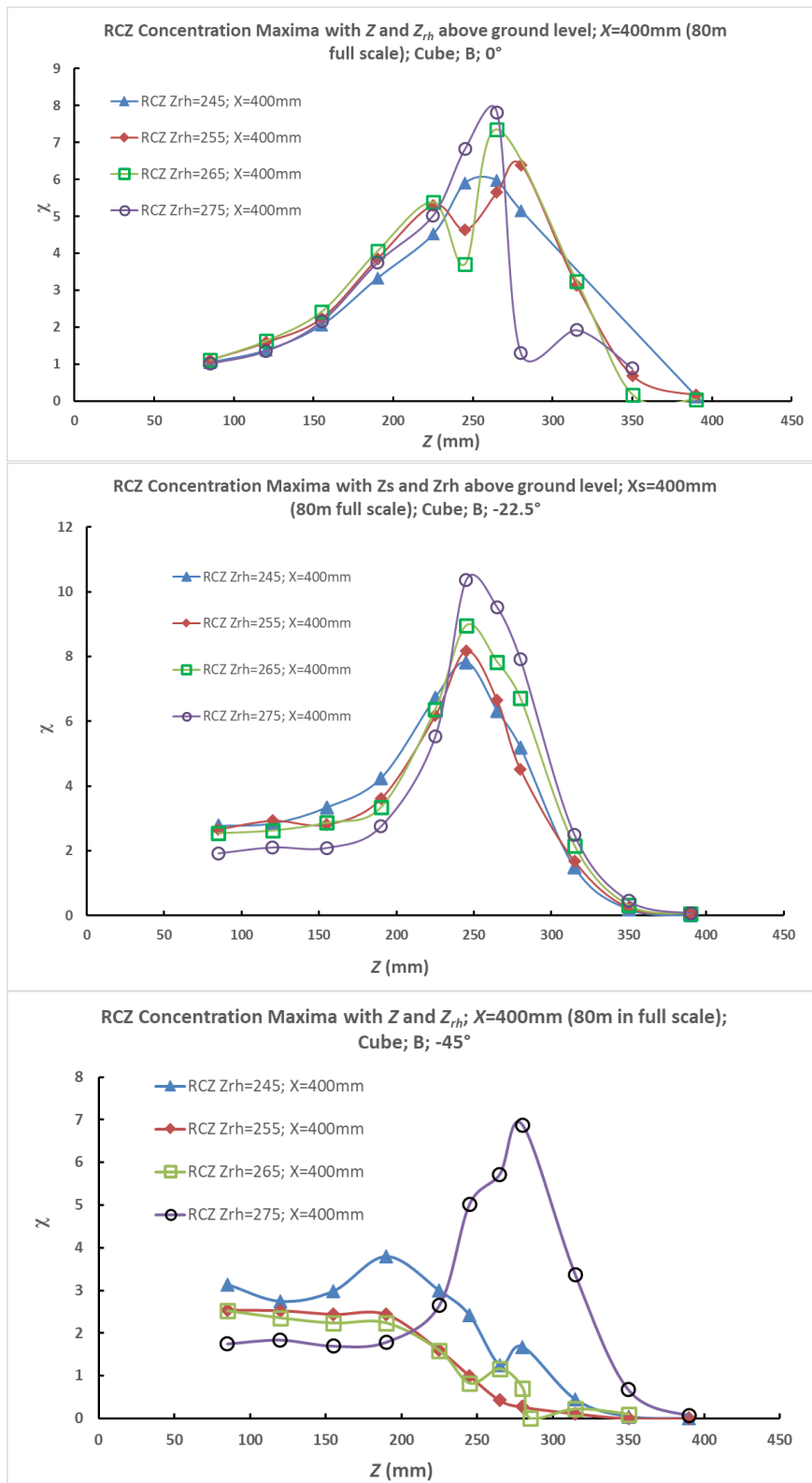


Figure 6.37(a,b,c, top to bottom):
 χ variation of the main building RCZ above ground level just downwind of the building with sampled Z for different release heights Z_{rh} ; maxima for each value of Z were taken; centreline release position 'B'; Incidence:
 (a) 0°
 (b) -22.5°
 (c) -45°

Figure 6.37 shows the main RCZ downstream of the cube at the three tested angles of approach flow, for the release position 'B' aligned to the central face of the cube. The same pattern (as with the 'A' release position) of a greater degree of plume entrainment with reduction in release height is seen for the non-normal incidence angled cases. These show dimensionless concentrations in the region of 2-3.5, a greater minimum value than the release close to the cube lead vertex position 'A'.

The normal incidence case shows a narrow spread of values reducing to a common lowest value of approximately $\chi=1$. This indicates a lower extent of mixing in the profiles downstream of the cube – a potential consequence of the absence of strong roof top vortices which are generated by an oblique angle of incidence to the roof leading edges into the approach flow. For the 'B' cases that the overall magnitude of the maximum peaks is broadly similar to the 'A' release cases (a range of 7 – 16).

6.3.6 Concentration Weighted Dispersion Parameters: variation with distance from the source SGP and DGP/ICP formulations with release height

6.3.6.1 Cube vertex position 'A' spread parameters

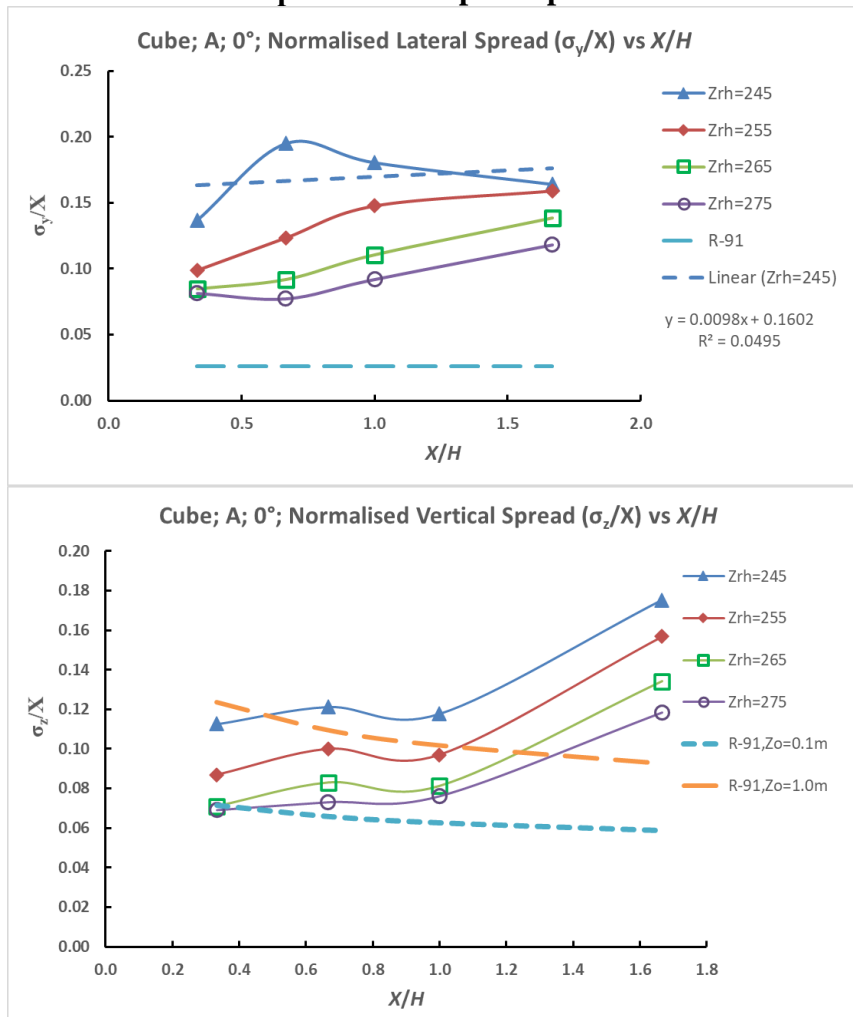


Figure 6.38(a, top/b, below) cube release; position 'A'; 0°; variations with normalised distance from release X/H for the SGP model:

(a) σ_y/X

(b) σ_z/X

Error bars are given as the sampled standard deviation of the values over range of downstream distance

Figure 6.38 shows the lateral and vertical dispersion parameters, from the SGP case, normalised against downstream distance for the cube case, plotted against downstream distance normalised to building height, for normal incidence.

The spread of an isolated plume against the R-91(Clarke, 1979) model is presented, in the vertical dispersion case shown in Figure 6.38(b), for two ground roughness lengths (0.1m and 1.0m full scale). One of the points is relatively far downstream of the roof zone ($X/H=1.67$).

From (a) the lateral normalised dispersion coefficient can be seen to be a strongly varying function of release height – the strong influence of buildings effects, in causing plume lateral broadening, can be seen the closer the release height to the roof at 240mm model scale, and the overall magnitude of these effects can be compared to the R-91 no building case curve. From (b) the vertical normalised dispersion coefficient can be seen to also show building generated effects, which cause plume broadening, and diminish with increasing release height above the building roof level. The two curves from R-91 show dispersion at two ground roughness lengths: it should be noted that the wind tunnel experiment was carried out with an undisturbed velocity profile corresponding to $z_o=0.1m$. All measured cases show vertical dispersion spread above this level, and the building effects lead to normalised dispersion coefficients which exceed those of the $z_o=1.0m$ level for the lowest release height ($Z_{rh}=245mm$). The building effects can be seen to increase the plume spread significantly above that which would be expected from an isolated plume within the approach flow within the boundary layer for releases close to the roof plane.

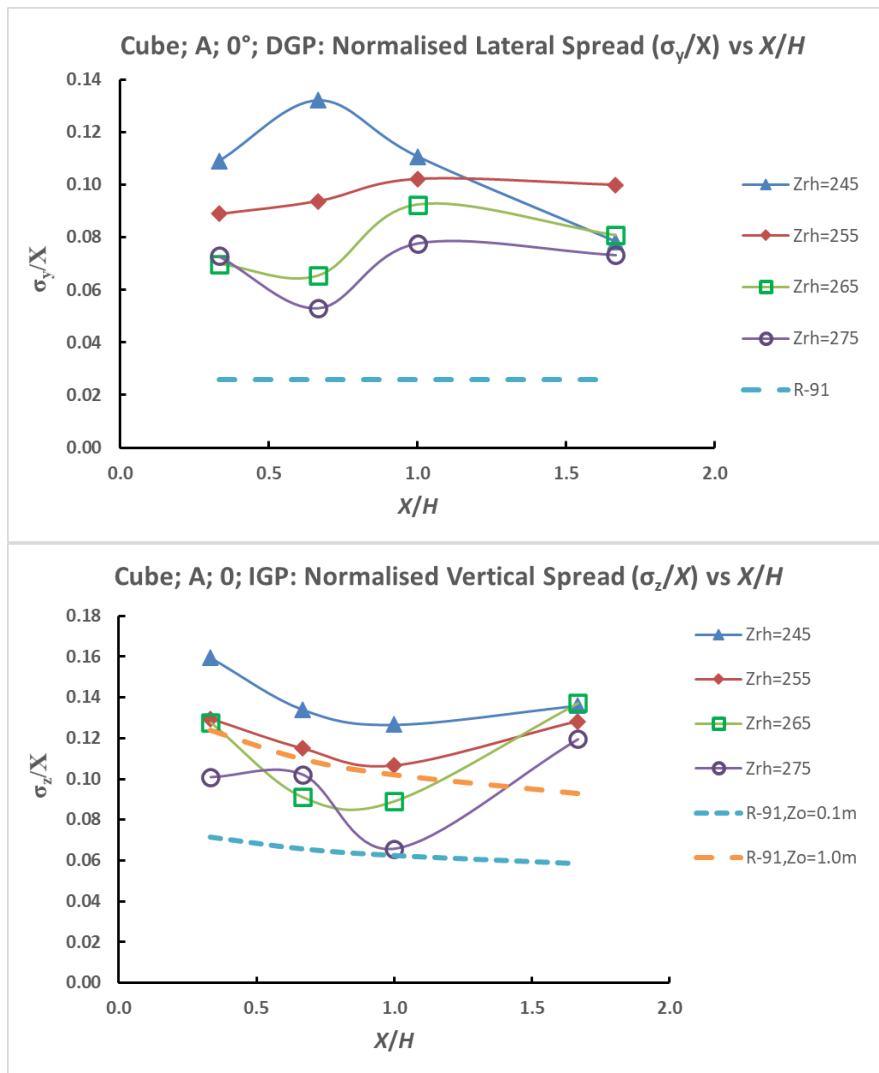


Figure 6.39 (a, top/b, below): cube release; position ‘A’; 0°; σ_y/X and σ_z/X variations with normalised distance from release X/H for the DGP/IGP models. Error bars are given as the sampled standard deviation of the value over range of downstream distance

Figure 6.39 shows the normal incidence case with the DGP/IGP models. A similar pattern can be seen compared to the DGP model but the lateral spread of the de-convolved peak can be seen to be significantly smaller in magnitude. In both Figure 6.39(a) and (b) downstream effects of plume broadening caused by interaction with the main building wake have been largely removed leading to a broadly generally constant coefficient value with downstream distance. For the normalised vertical dispersion coefficient downstream effects of plume broadening over the roof zone are more significant than the SGP case: this is at least partly because the IGP method did not permit the use of a concentration weighted estimate of the vertical plume spread, hence a larger value may result due to greater influence of vertical profiles of lower concentration away from the plume centreline.

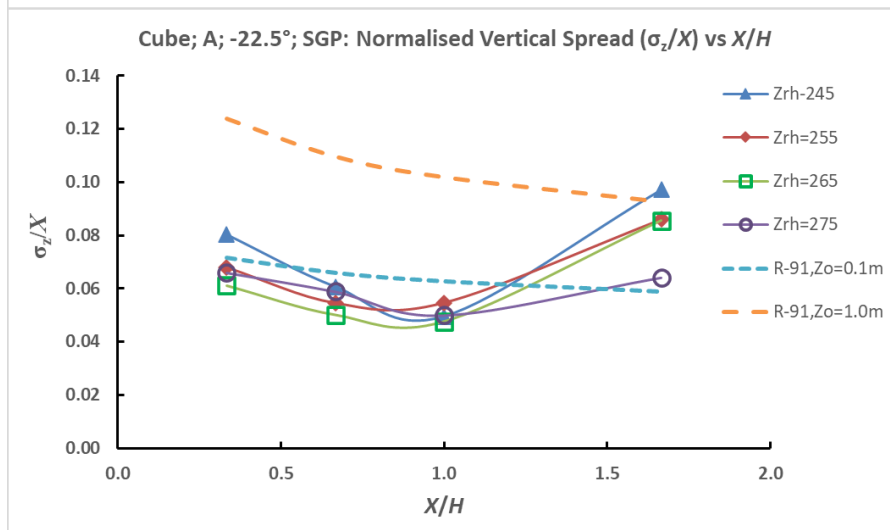
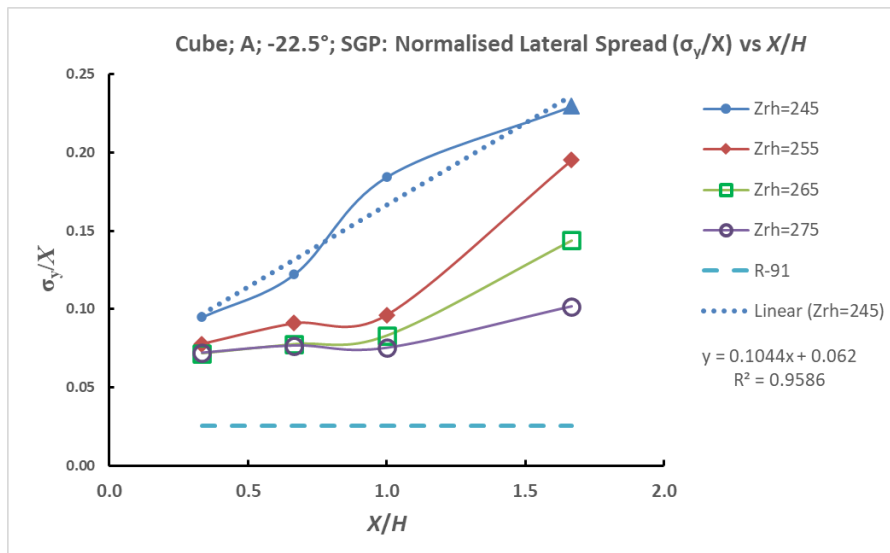


Figure 6.40(a, top)/(b, bottom): cube release; position ‘A’; -22.5°; σ_y/X and σ_z/X variations with normalised distance from release X/H for the SGP model. Error bars are given as the sampled standard deviation of the value over range of downstream distance

From Figure 6.40(a) at an approach flow angle of -22.5° the lateral dispersion coefficient shows a similar level of spread over the roof as the normal case, and in (b) the vertical spreads are significantly lower than the normal incidence case.

Figure 6.41 for the DGP/IGP models shows generally lower values of spread than the SGP analysis, and for the vertical spread only the 245mm release height shows significant plume broadening above the R-91 level at $z_0=0.1m$. This may be an indication the roof vortices may contribute to lateral advection but contribute less to vertical spread.

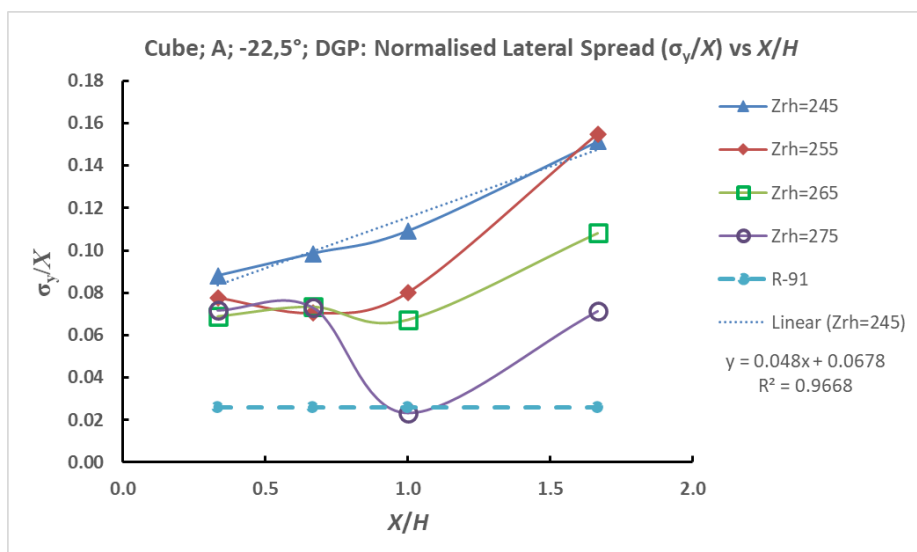


Figure 6.41(a, top)/(b, lower): cube release; position ‘A’; -22.5°; σ_y/X and σ_z/X variations with normalised distance from release X/H for the DGP/IGP model. Error bars are given as the sampled standard deviation of the value over range of downstream distance

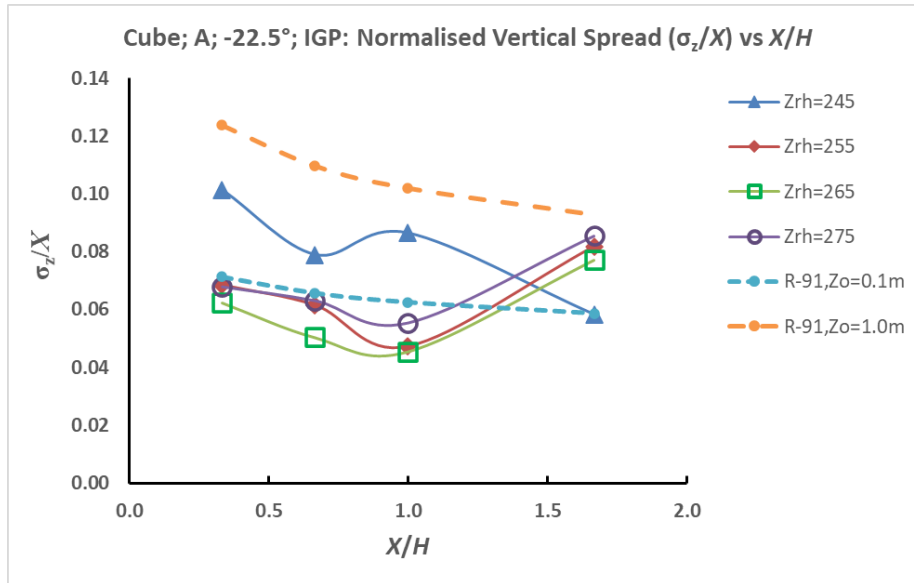


Figure 6.41(b): cube release; position 'A'; DGP/IGP model; -22.5°; σ_z/X

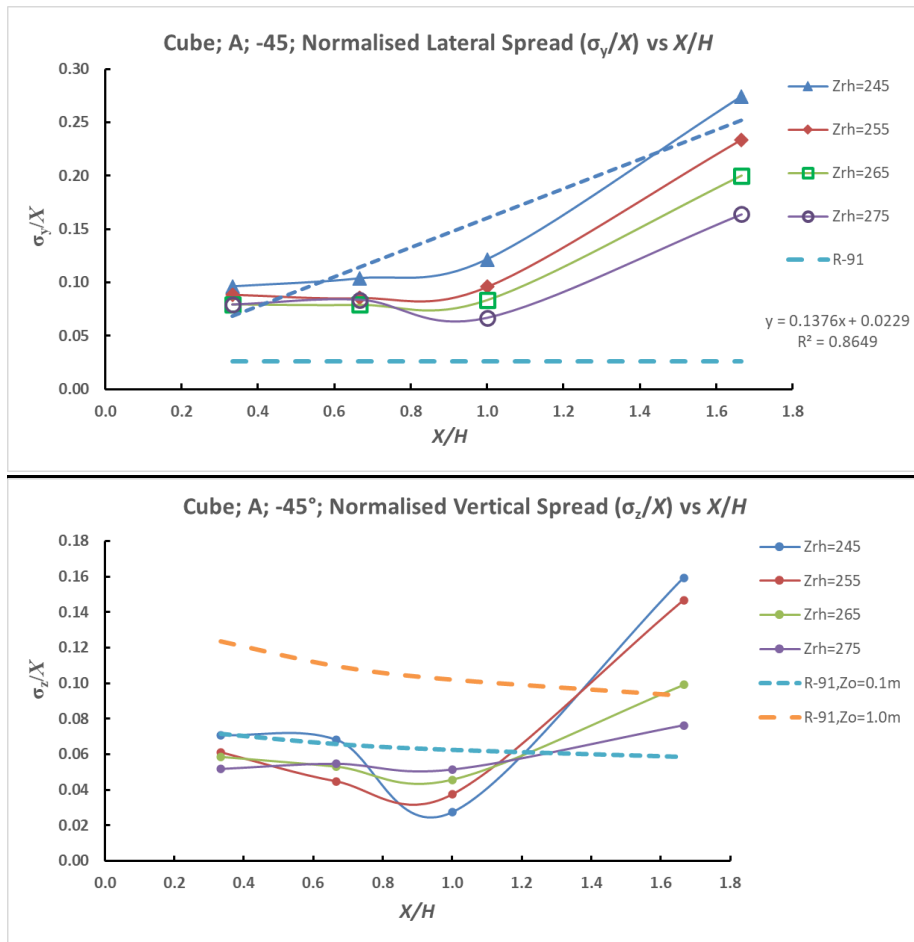


Figure 6.42(a, top)/(b, bottom): cube release, position A, -45°; $\sigma_{y,cw}/X$ and $\sigma_{z,cw}/X$ variations with normalised distance from release X/H for the SGP model. Error bars are given as the sampled standard deviation of the value over range of downstream distance

From Figure 6.42 significant lateral spread with the SGP model can be seen at the most distal point downstream from the release. Considering only the effects in the roof zone a similar level of dispersion can be seen compared to the other angles of approach flow. In terms of vertical

dispersion, the vertical dispersion can be seen to be generally below the $z_0=0.1\text{m}$ value from R-91.

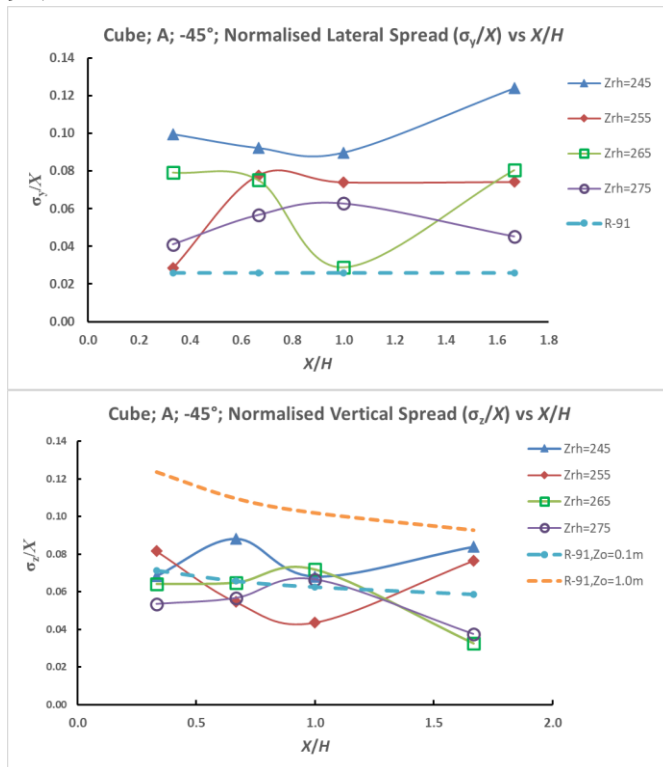


Figure 6.43(a, top)/(b, below): cube release; position 'A'; -45°; $\sigma_{y,cw}/X$ and σ_z/X variations with normalised distance from release X/H for the DGP/IGP model.

Error bars are given as the sampled standard deviation of the value over range of downstream distance

From the DGP/IGP analysis in Figure 6.43 the monotonic relationship between the spread and release height generally holds but individual points from the de-convolution process show a greater degree of scatter: the overall magnitude of the dispersion at the lowest release heights is the same as other angles of flow: but in this case the greater release heights do show lower plume spread.

The largest dispersion values correspond with the lowest release heights. Vertical dispersion is approximately in the range of $z_0=0.1\text{m}$ for all cases of release height. Overall, the presence of roof top generated vortices, can be seen to lead to advection of flow, but not necessarily an increase of the plume spread.

6.3.6.2 EW Clad spread parameters

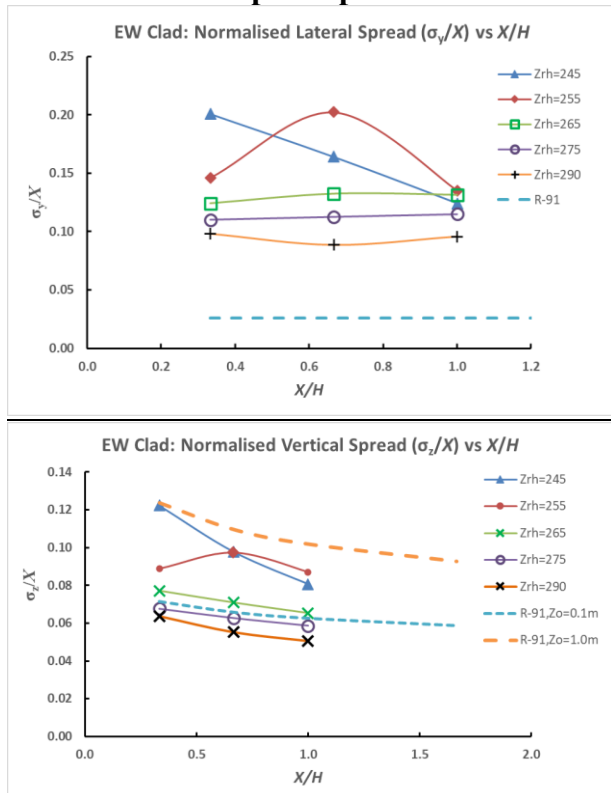
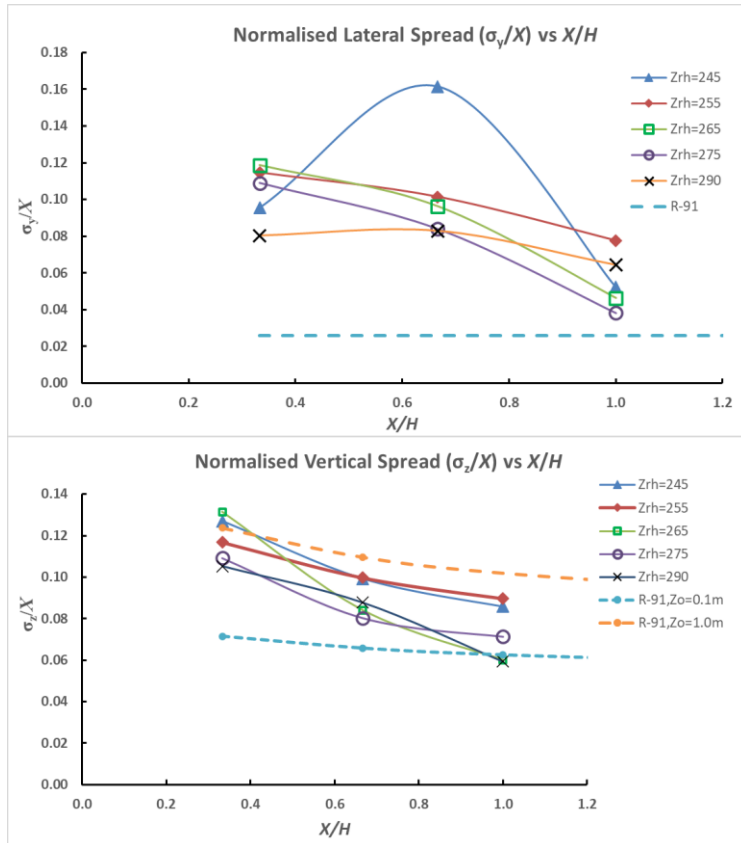


Figure 6.44(a, top)/(b, below): EW clad release, -22.5°; $\sigma_{y,cw}/X$ and $\sigma_{z,cw}/X$ variations with normalised distance from release X/H for the SGP model

It can be seen from Figure 6.44 that the 'real world' building case, at angle of approach flow -22.5°, gives rise to normalised lateral dispersion coefficients which are greater than the cube case at the same angle of approach flow; particularly significant are the lowest release heights. Similarly, only the lowest release heights (245/255mm), show significant broadening above the $z_0=0.1\text{m}$ characteristic curves. In these cases the additional 290mm greater release height shows the reduction of building effects on plume spread with increased height very clearly.



EW unclad case results are presented in Appendix 15.3.

6.3.6.3 Cube centreline position B spread parameters

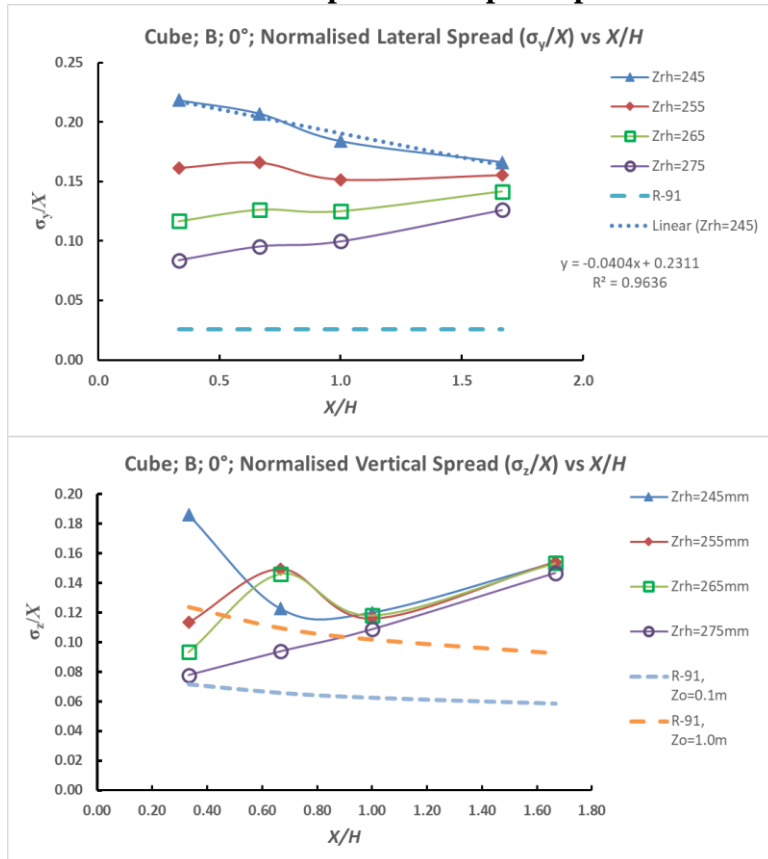


Figure 6.45(a, top)/(b, below):
EW clad release, -22.5° ;
 $\sigma_{y,cw}/X$ and σ_z/X variations
with normalised distance
from release X/H for
DGP/IGP models.
Error bars are given as the
sampled standard deviation
of the value over range of
downstream distance

Figure 6.45 shows the reduced plume spread evident from the plume DGP/IGP de-convolution process and the monotonic relationship is less pronounced with release height for the lateral spread.

Conversely, the DGP/IGP method shows enhanced values of vertical spread for this angle of approach flow.

Figure 6.46(a, top)/41(b, bottom):
cube release; position 'B'; 0° ;
 $\sigma_{y,cw}/X$ and $\sigma_{z,cw}/X$ variations with
normalised distance from release
 X/H for the SGP model.

The 'B' position in Figure 6.46 shows an enhanced level of lateral plume spread compared to the 'A' release position for the SGP model. This is also shown for the vertical spread.

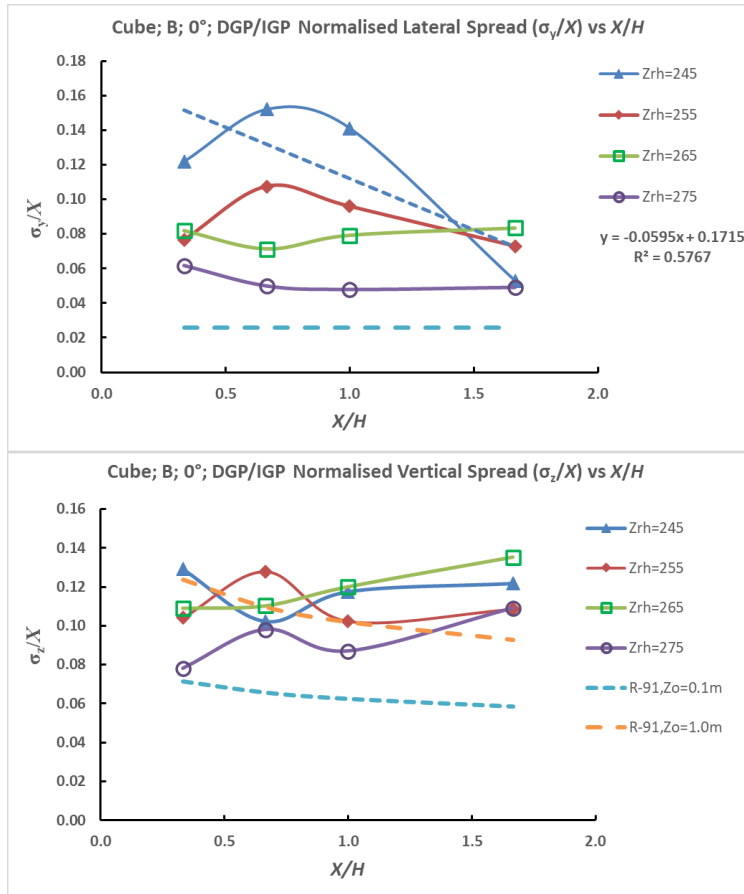


Figure 6.47(a, top)/42(b, below):
 cube release; position ‘B’; 0°;
 σ_y/X and σ_z/X variations with
 normalised distance from
 release X/H for the DGP/IGP
 models.

The plume spread parameters shown in Figure 6.47 for the ‘B’ case are similar to the ‘A’ case for lateral spread at normal incidence. However, significant enhancement is shown with the DGP/IGP models for the vertical plume spread normalised parameters.

Release position ‘B’ results for angles -22.5° and -45° are presented in Appendix 3.

From this section, and the additional results presented in Appendix 15.3, we have seen the variation of fitted plume spread parameters, for concentration weighted profiles sampled in the lateral and vertical directions, shown with downstream distance: however, each downstream point was subject to the fitting of the Gaussian profile. For the SGP algorithm the fitting gave relatively robust results, but for the DGP/IGP methods significant variation was seen with distance, and some of this additional variation may be considered to have been generated from incomplete deconvolution of the main plume from the secondary (or RCZ) peak profile.

6.3.7 Concentration Weighted Dispersion Parameters: Mean values over distance from the source of SGP and DGP/ICP formulations with release height

In the following analysis the variation with downstream distance is reduced from the data set by taking the mean value of the lateral and vertical normalised dispersion coefficients. The coefficients having been already normalised with distance, this operation determines a dimensionless mean coefficient reflecting the mean plume spread normalised for distance from the source. The mean plume spread coefficients are plotted against the normalised release height $Z_{norm} = (Z_{rh} - H)/H$. Error bars are the sampled standard deviation of the plume spread parameter over the downstream distances over a maximum of four downstream planes.

6.3.7.1 Cube position A: Mean Values of dispersion parameters over distance from source

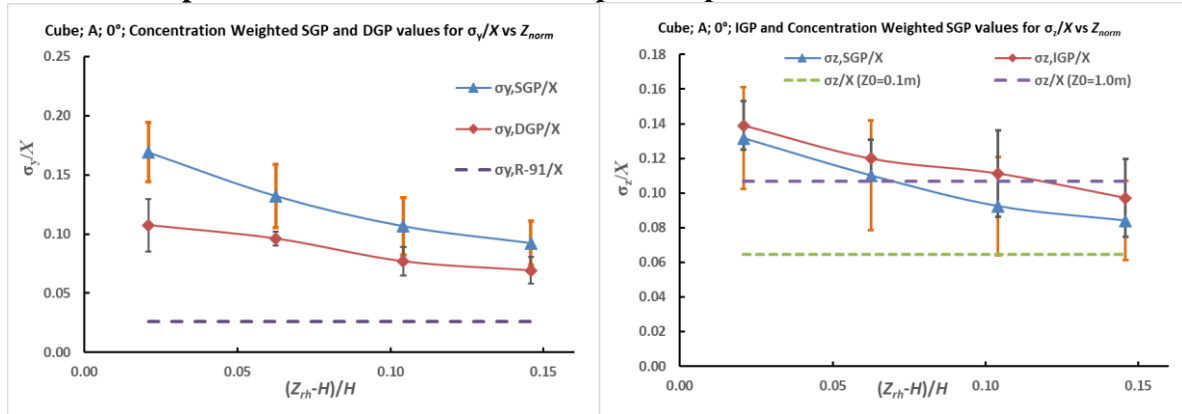


Figure 6.48(a,left)/(b,right): cube release, position A, 0°; $\sigma_{y,cw}/X$ and $\sigma_{z,cw}/X$ variations with normalised passive plume release height $Z_{norm}=(Z_{rh}-H)/H$ for both the SGP and DGP/IGP models. Error bars are given as the sampled standard deviation of the value over range of downstream distance

From Figure 6.48 the mean normalised plume spread is shown with release height: the deconvolution of the lateral plume has resulted in a significantly lower plume spread: both greater than the R-91 reference values. For the vertical direction there is a paradoxical result, with the SGP lower than the IGP values, a pattern which is not repeated for the other angles of approach flow. This effect is explained by the especially well-developed rooftop RCZ for the normal approach flow meaning the deconvolution of the vertical plume, using the IGP method where a constant RCZ concentration is fitted up to a truncation height, is incomplete and an effective plume broadening is seen vertically. The SGP model when used for a vertical profile, fits only a simple Gaussian, which inspection of the concentration profile indicates is affected little by RCZ concentration.

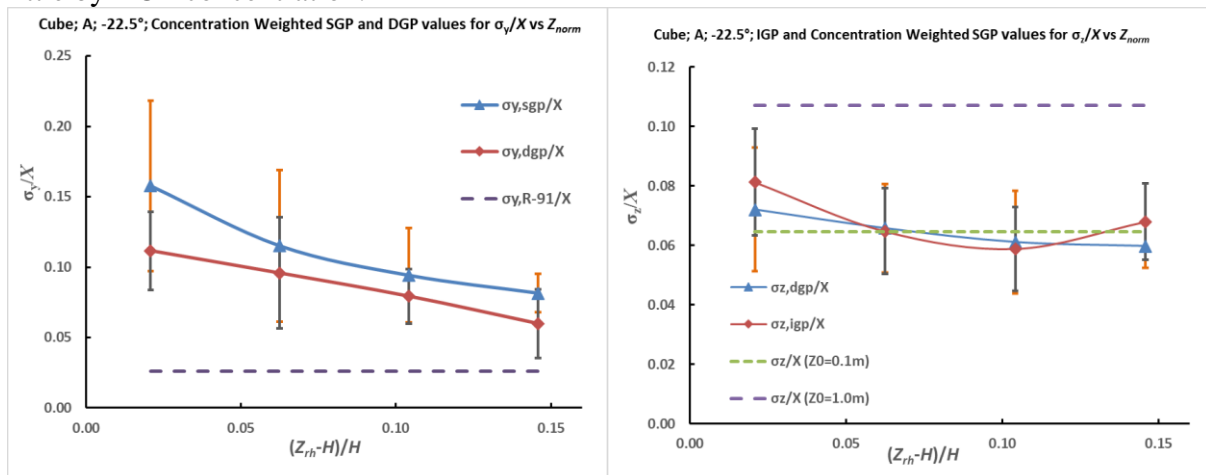


Figure 6.49(a,left)/(b,right): cube release, position A, -22.5°; σ_y/X and σ_z/X variations with normalised passive plume release height $Z_{norm}=(Z_{rh}-H)/H$ for both the SGP and DGP/IGP models. Error bars are given as the sampled standard deviation of the value over range of downstream distance

For the ‘A’ release position and -22.5° incidence of flow in Figure 6.49 similar values of the lateral spread are evident compared to the normal incidence case. However, the vertical spread is markedly different: both SGP and IGP methods show much smaller values than the normal spread for the normal incidence case.

Results are given for the ‘A’ release position and -45° incidence of flow in Appendix 15.3, where similar values of the lateral spread are evident compared to the normal incidence case. However, the vertical spread is similar to the -22.5° case: both SGP and IGP methods show much smaller values than the spread for the normal incidence case.

6.3.7.2 EW Clad: Mean Value of spread parameters over distance from source

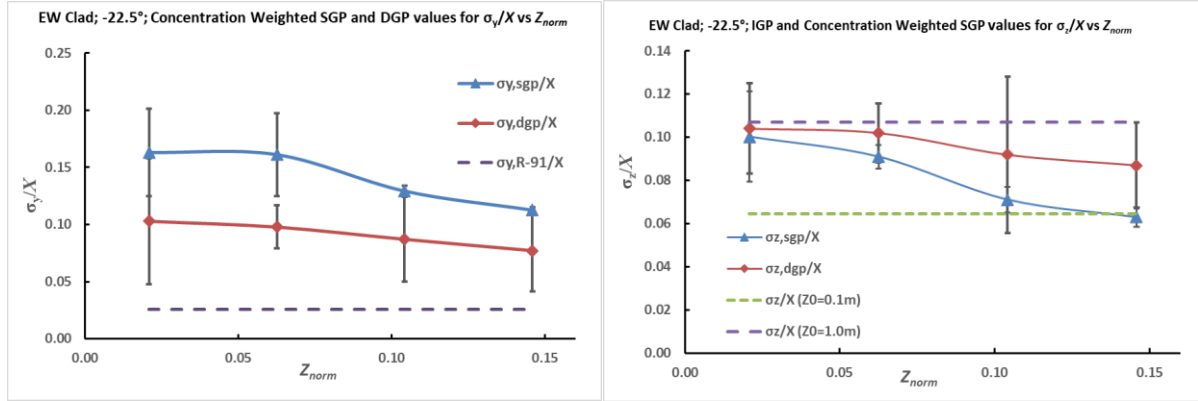


Figure 6.50(a,left)/(b,right): EW Clad release, position NW stair tower, -22.5° ; σ_y/X and σ_z/X variations with normalised passive plume release height $(Z_{rh}-H)/H$ for both the SGP and DGP/IGP models. Error bars are given as the sampled standard deviation of the value over range of downstream distances

For the EW clad building and -22.5° incidence of flow in Figure 6.50, similar values of the lateral spread are evident compared to the cube cases at all angles of incidence of flow tested. However, the vertical spread is significantly greater for the lowest release heights, and for the DGP/IGP method.

Results are given for the EW unclad building in Appendix 15.3: where significant differences are apparent with the EW unclad building in terms of the lateral plume spread which is significantly greater than the EW clad building for both the SGP and DGP methods. The vertical plume spread is however similar to the EW case for the IGP model. The SGP model indicates smaller vertical spread for the EW unclad than the EW clad model.

6.3.7.3 Cube centreline position B: Mean Value of spread parameters over distance

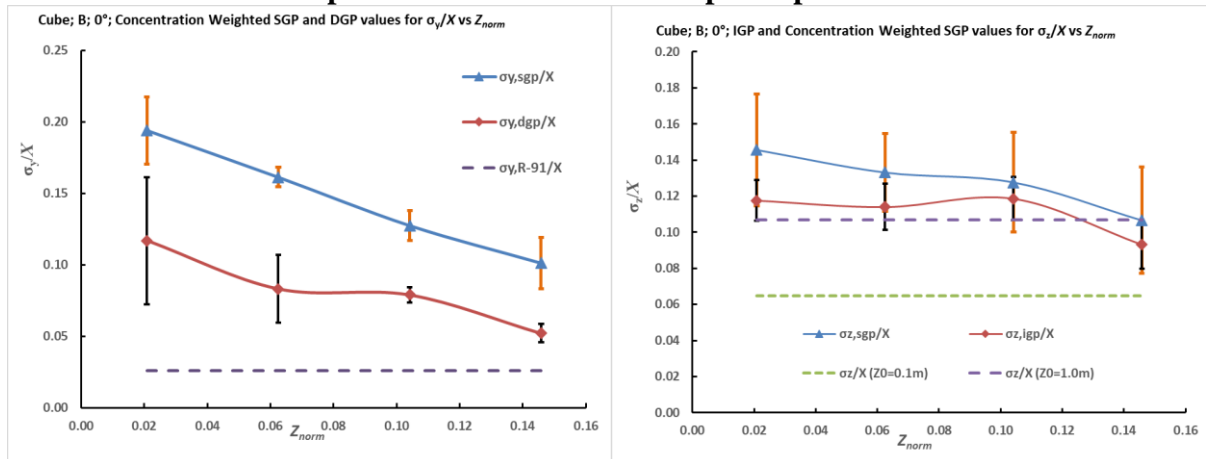


Figure 6.51(a,left)/(b,right): cube release, position B, 0° ; σ_y/X and σ_z/X variations with normalised passive plume release height $Z_{norm}=(Z_{rh}-H)/H$ for both the SGP and DGP/IGP

models. Error bars are given as the sampled standard deviation of the value over range of downstream distances

Compared to the ‘A’ case for normal incidence the cube ‘B’ release position in Figures 6.51 shows similar values of lateral dispersion for the DGP model, and the SGP method gives generally larger values. This is expected to be the plume broadening seen with the influence of the roof top RCZ. The vertical spread appears generally larger than the ‘A’ case for the IGP, and more so for the SGP model.

Results are given for the ‘B’ release case at flow incidence of -22.5° in Appendix 15.3: where compared to the ‘A’ case for normal incidence the cube ‘B’ release position shows similar values of lateral dispersion for the DGP model, and the SGP method gives generally larger values. This is expected to be the plume broadening seen with the influence of the roof top RCZ. Also, the vertical spread is significantly larger for the ‘B’ case for the compared to the ‘A’ release position.

Results are given for the cube ‘B’ release position at -45° in Appendix 15.3: this shows similar values of lateral dispersion for the DGP model to the ‘A’ release case for this angle of flow, and the SGP method gives generally larger values. The vertical spread is significantly larger for the ‘B’ case for the compared to the ‘A’ release position.

6.3.8 Plume Concentration Maximum horizontal deflection with normalised release height over the roof zone

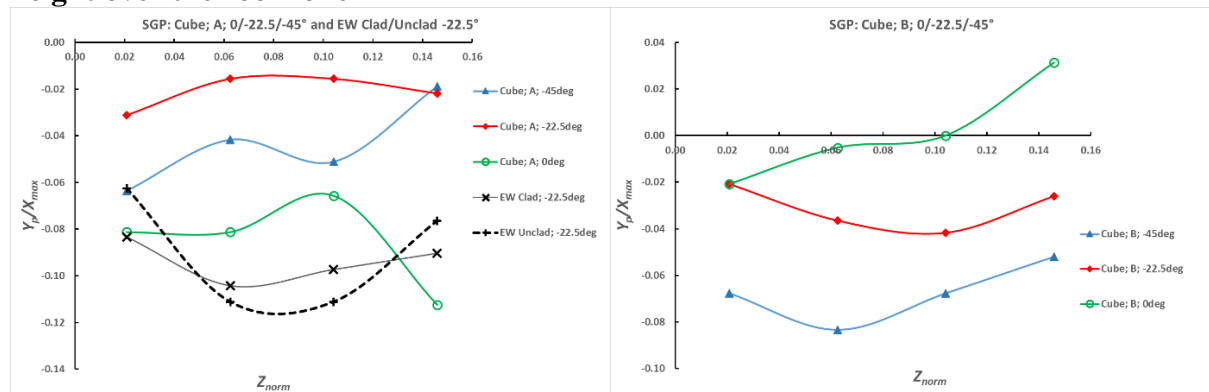


Figure 6.52(a, left)/(b, right): cube and EW clad and unclad releases, 0° , -22.5° , -45° ; mean value of normalised deflection Y_p/X_s with downstream distance over the roof zone is presented versus normalised passive plume release height $Z_{norm} = (Z_{rh} - H)/H$ for the SGP model: (a) release position ‘A’ for cube and NW stair tower for EW cases; (b) release position ‘B’ for cube

Figure 6.52(a) shows the plume centreline deflection plotted as normalised lateral co-ordinate against the downstream distance for the near vertex ‘A’ position: a strong deflection to the positive Y direction - left, in the direction of the approach flow, is apparent for the -22.5° – -45° cases. For the normal incidence the deflection is greater still – attributed to edge effects at the cube. For the EW clad and unclad cases the deflection is still further in the negative Y direction. This may be attributed to the (i) the greater angle of the side of the EW building to the flow, and (ii) the flow conditions in the stem of the ‘T’ shape of the EW unclad building. The maximum deflection is seen at intermediate release heights, where the roof vortices are able to move material outwards in the negative Y direction by advection. Figure 6.52(b) shows the ‘B’ release case the normal case deflection is minimal, which accords with the symmetry of the

measurement conditions. Greater deflections to the negative Y direction are seen with increasing angle of obliquity from -22.5° through to -45° .

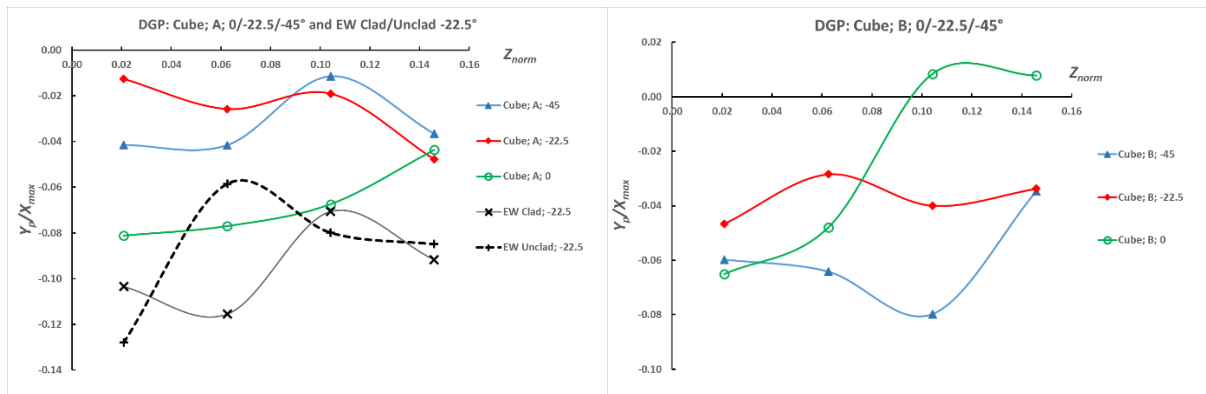


Figure 6.53(a,left)/(b,right): cube and EW clad and unclad releases, 0° , -22.5° , -45° ; mean value of normalised deflection Y_p/X_s with downstream distance over the roof zone is presented versus normalised passive plume release height $Z_{norm}=(Z_{rh}-H)/H$ for the DGP model: (a) release position A for cube and NW stair tower for EW cases; (b) release position B for cube

Figure 6.53(a), for the DGP method, shows broadly similar negative deflections for the oblique cube 'A' release cases, and a greater still negative Y -deflection for the normal incidence case. The EW clad and unclad cases show a large extent of negative Y -deflection, as was seen in the SGP analysis. From 6.53(b) a negative Y -deflection is apparent from the lowest release heights for normal incidence, with an overall pattern of increasing negative Y -deflection with increasing angle of obliquity.

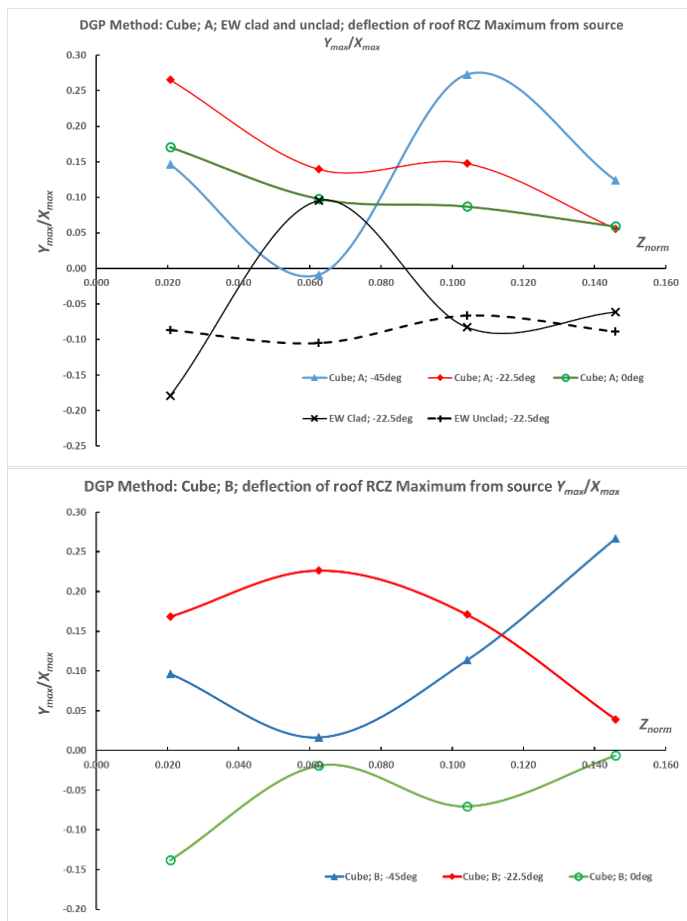


Figure 6.54(a, top)/(b, below): RCZ maxima for the cube and EW clad and unclad releases; 0° , -22.5° , -45° ; deflection gradient of the rooftop recirculation zone (RCZ) maximum concentration position Y_{max}/X_{max} versus normalised passive release height $Z_{norm}=(Z_{rh}-H)/H$ for the DGP model:

(a) release position 'A' for cube and NW stair tower for EW cases
(b) release position 'B' for cube

Figures 6.54(a/b) show the relative position of the rooftop recirculation zone (RCZ) maxima in terms of a ratio of Y_{max}/X_{max} where X_{max} and Y_{max} are the maximum concentration co-ordinate values at a sample height of 1.5m above the roof plane.

Figure 6.54(a) shows RCZ local concentration maxima for the cube with ‘A’ release position and the EW clad and unclad cases at -22.5° of approach flow. Figure 6.54(b) shows the same for the cube with the ‘B’ release position at the range of angles of approach flow studied. Table 6.1 presents the value of X_{max} for the rooftop RCZ normalised to the building height, H . These deflection parameters are required in the later Monte Carlo calculations of dose arising from the radioactive plume so to enable this are presented in a complete form.

Table 6.1: Downstream X_{max}/H of rooftop recirculation zone (RCZ) maximum

Z_{norm}	0.021	0.063	0.104	0.146
A/ -45°	1.000	1.000	1.000	1.000
A/ -22.5°	0.667	1.000	1.000	1.000
A/ 0°	0.667	1.000	1.000	1.000
B/ -45°	1.000	1.000	1.000	1.000
B/ -22.5°	0.667	0.667	1.000	1.000
B/ 0°	0.333	1.000	0.667	1.000
EW clad/ -22.5°	0.333	0.667	1.000	1.000
EW unclad/ -22.5°	0.667	0.333	1.000	1.000

6.3.9 Plume Concentration Maximum (PCM) normalised vertical deflection vs Z_{norm}

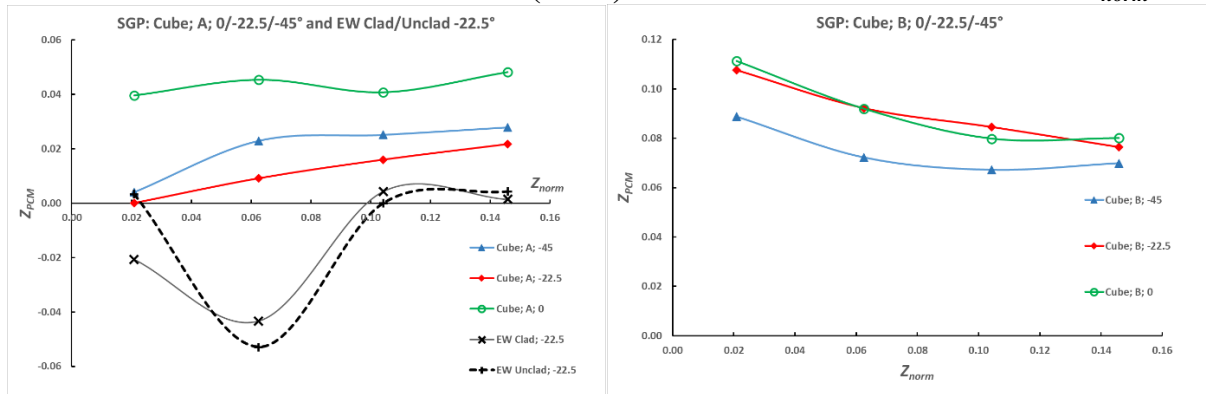


Figure 6.55(a,left)/(b,right): cube and EW clad and unclad passive releases, 0° , -22.5° , -45° ; mean value over the roof zone of normalised vertical plume deflection $Z_{PCM}=(Z_{pcm}-Z_{rh})/H$ versus normalised release height $Z_{norm}=(Z_{rh}-H)/H$ for the SGP model: (a) release position ‘A’ for cube and NW stair tower for EW cases; (b) release position ‘B’ for cube

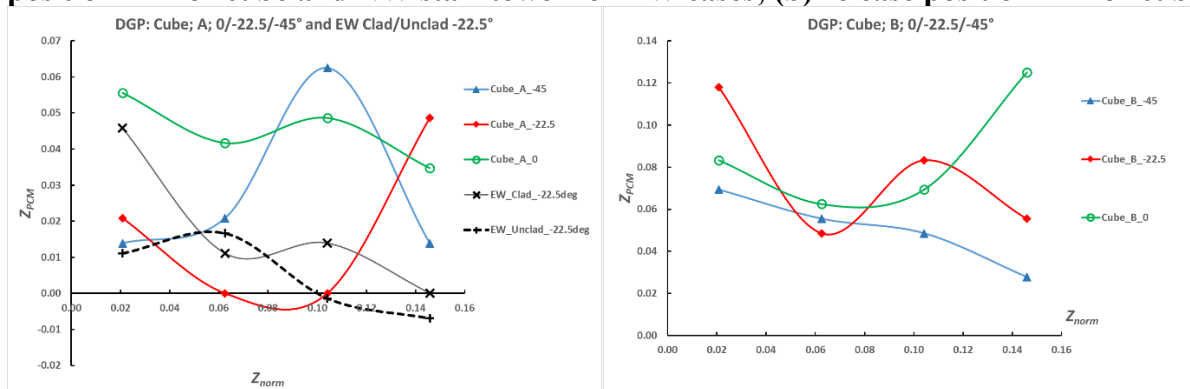


Figure 6.56(a,left)/(b,right): cube and EW clad and unclad releases, 0° , -22.5° , -45° ; mean value over the roof zone of normalised vertical plume deflection $Z_{PCM}=(Z_{pcm}-Z_{rh})/H$ versus normalised release height $Z_{norm}=(Z_{rh}-H)/H$ for the DGP model: (a) release position ‘A’ for cube and NW stair tower for EW cases; (b) release position ‘B’ for cube

6.3.10 Concentration Weighted Dispersion Parameters: Summary data over cube 'A' release position cases and EW: SGP and DGP/IGP formulations with normalised release height

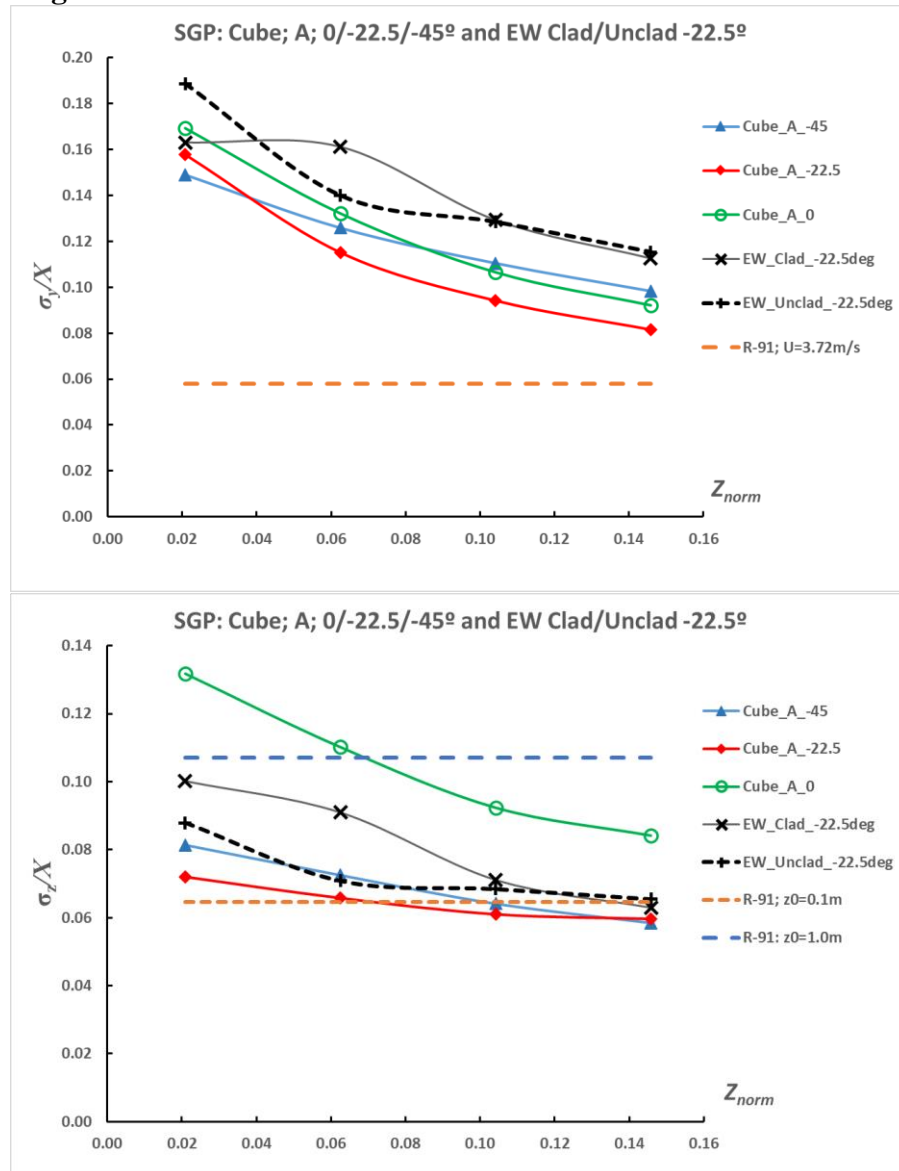


Figure 6.57(a, top)/(b, below):

cube release; position 'A', 0°/-22.5°/-45° and -22.5° EW clad and unclad cases:

(a) σ_y/X

(b) σ_z/X

Variations with normalised passive plume release height $Z_{norm}=(Z_{rh}-H)/H$ for the SGP model. Mean values over X values over the roof zone and immediate vicinity of the roof. EW results are also presented to enable direct comparison

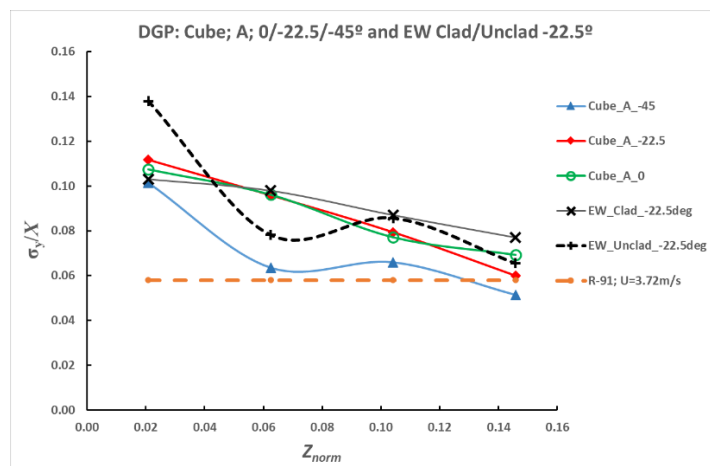


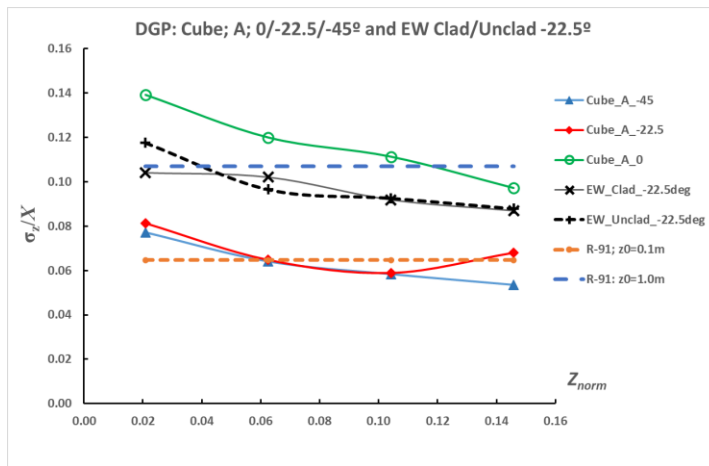
Figure 6.58(a, top)/(b, below): cube release; position 'A'; 0°/-22.5°/-45° and -22.5° EW clad and unclad cases:

(a) σ_y/X

(b) σ_z/X

Variations with normalised passive plume release height $Z_{norm}=(Z_{rh}-H)/H$ for the DGP model.

Data represents mean values with distance X over the roof zone and immediate vicinity of the roof. EW results are presented to enable direct comparison



6.3.11 Summary values of roof zone Maximum Measured Concentrations with release height: Cube and EW Clad and Unclad cases

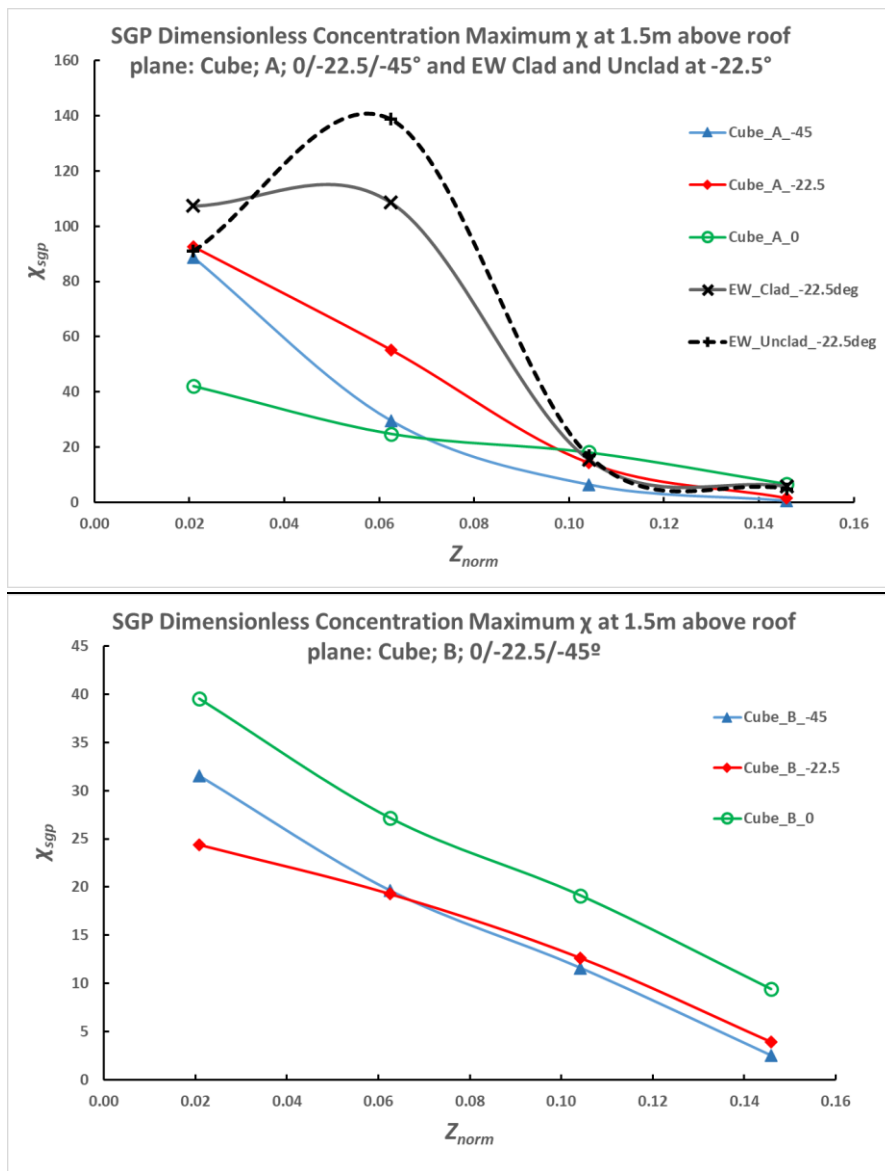


Figure 6.59(a,b; top/bottom): maximum SGP model fitted dimensionless concentration χ variation in the cube and EW roof zones with normalised release height Z_{norm} : (a) position 'A'; incidence 0/-22.5/-45° to cube face and EW clad and unclad at -22.5°, and: (b) position 'B' incidence 0/-22.5/-45° to cube face: Values presented are for those closest to a sample height on 1.5m full scale above the roof plane ($Z=247.5\text{mm}$ model scale)

From Figure 6.59(a) results from the SGP analysis are given for dimensionless concentrations just above the roof surface. The EW clad and unclad cases give rise to the greatest concentrations, and that these peak for the release height of 255mm ($Z_{rh}=51\text{m}$ at full scale). The cube 'A' release position concentrations reduce from a maximum measured for the lowest release height tested. From Figure 6.59(b) the 'B' release positions results indicate a peak roof concentration comparable for the normal release angle to the 'A' normal case, but below this value for the angled cases and reducing steadily with increasing building height.

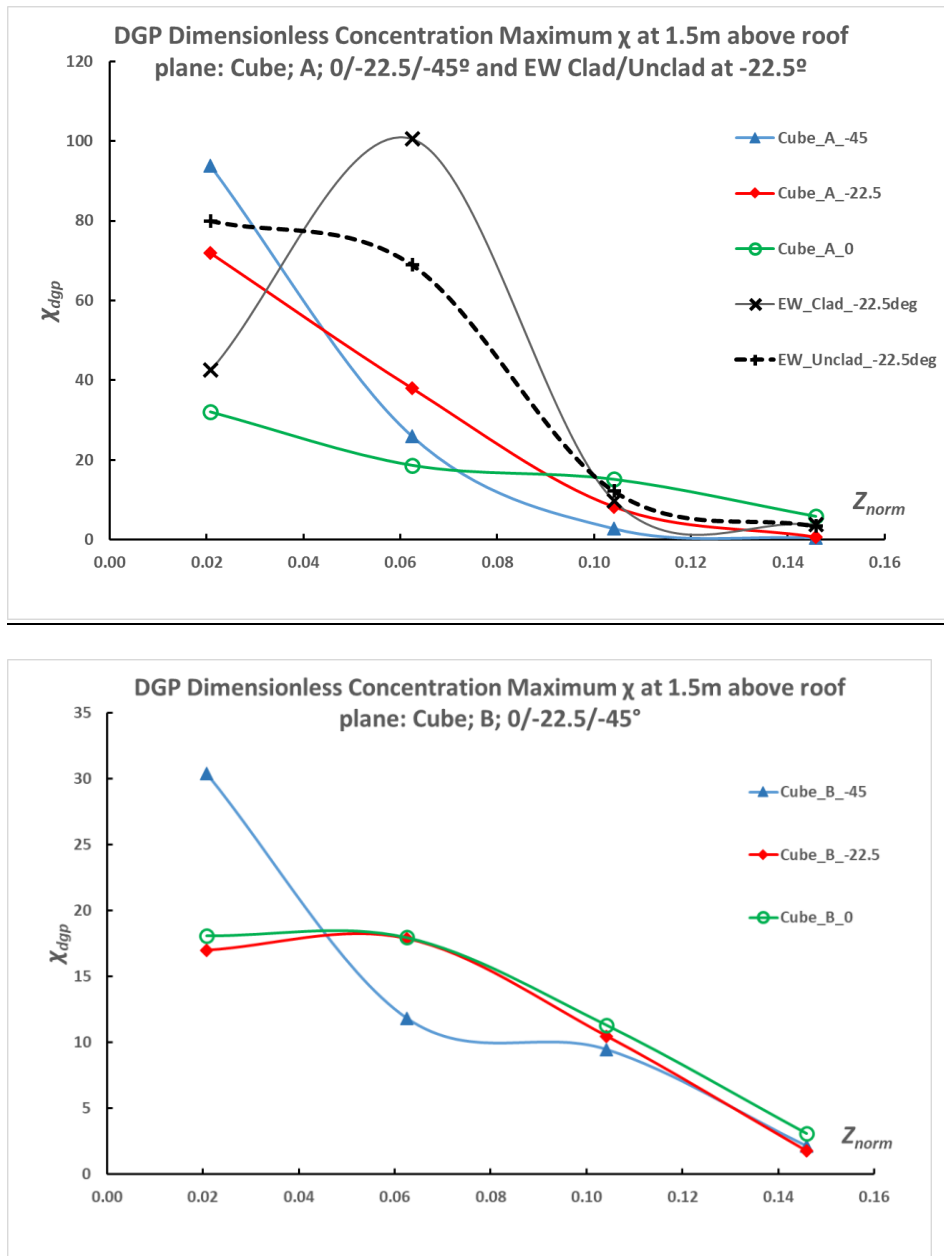


Figure 6.60(a,b; top/bottom): maximum DGP model fitted dimensionless concentration χ variation in the cube and EW roof zones with normalised release heights: (a) position 'A'; incidence $0^\circ/-22.5^\circ/-45^\circ$ to cube face and EW clad and unclad at -22.5° , and: (b) position 'B' incidence $0^\circ/-22.5^\circ/-45^\circ$ to cube face. Values presented are for those closest to a sample height on 1.5m full scale above the roof plane ($Z=247.5\text{mm}$ model scale)

It can be seen from Figure 6.60(a) using the DGP method of analysis of the results that the EW clad and unclad building cases give rise to relatively high values of dimensionless concentration at just above roof level, however in this case the 'A' release position for the cube also gives a comparable maximum value. Maximum values for -22.5° and normal incidence are below this value. From Figure 6.60(b) the cube at -45° case is likewise the greatest maxima, with the normal and -22.5° angles giving rise to similar concentration values with release height.

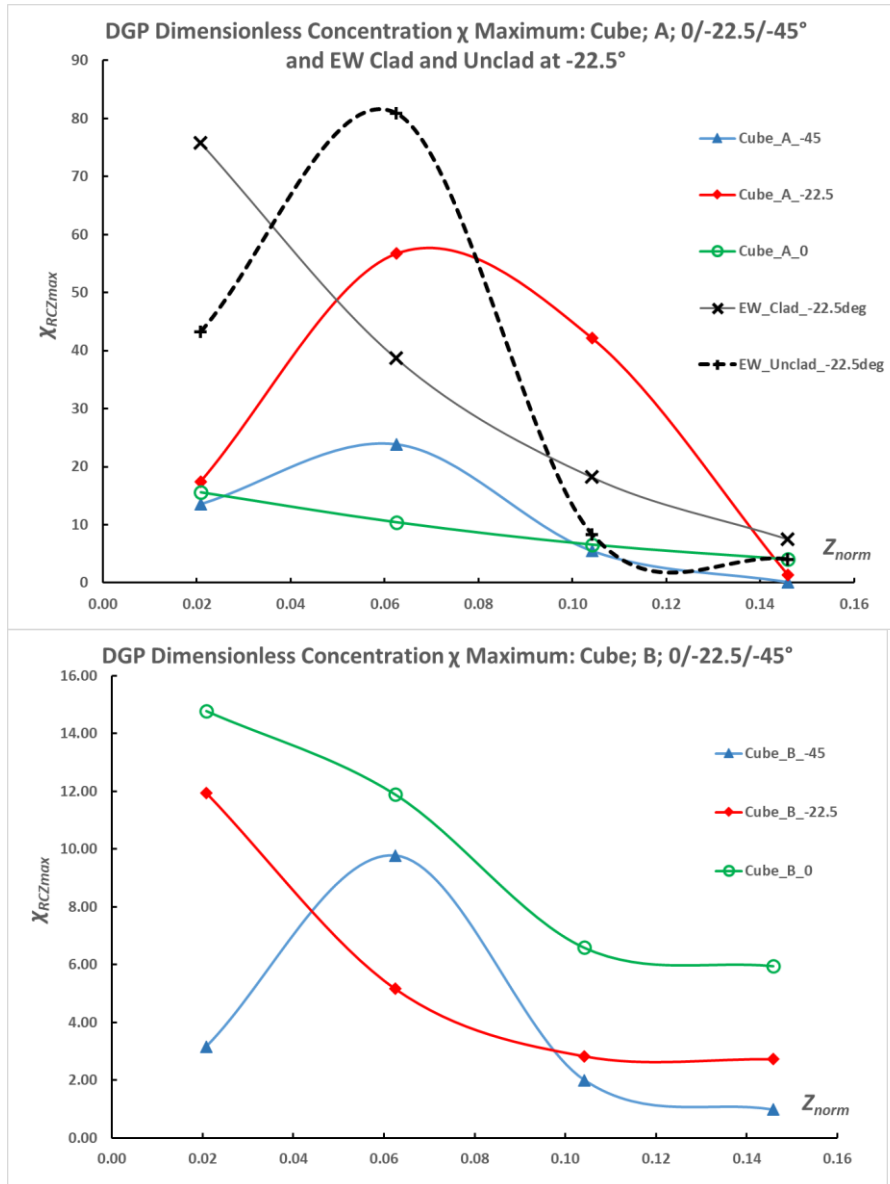


Figure 6.61(a,b; top/bottom): RCZ maximum DGP model fitted dimensionless concentration χ variation in the cube and EW roof zones with normalised release heights: (a) position ‘A’; incidence 0/-22.5/-45° to cube face and EW clad at -22.5°, and (b) position ‘B’ incidence 0/-22.5/-45° to cube face: Values presented are for those closest to a sample height on 1.5m full scale above the roof plane ($Z=247.5\text{mm}$ model scale)

From Figure 6.61(a) we see that the EW clad cases give rise to the greatest values of the RCZ (or secondary) peak just above roof level. These are then followed by the cube at -22.5°, -45° and normal incidence in order of reducing size. From Figure 6.61(b) for the cube ‘B’ release position we see similar values of concentration compared to the ‘A’ case for the normal incidence. For the angled ‘B’ cases the concentration values lay below the corresponding ‘A’ case figures.

6.4. Discussion

The concentration field in the roof zone of the cube and two ‘real world’ building cases; i.e. the EW clad and unclad were investigated with a range of angles of approach flow to the cube, release positions in relation to the cube, and passive release heights. Also, active vertical releases were investigated for a limited range of cases. Downstream planes, normal to the flow direction, from the release point were measured using FFID detectors to measure concentration field values and obtain values of generalizable dimensionless concentrations.

6.4.1 Concentration Profiles in the Roof Zone

To analyse the measured behaviour of the plume in the roof zone of the building a novel Dual Gaussian Plume (DGP) method was formulated to allow for plume bifurcation or rooftop recirculation zones in order to model plume dispersion behaviour more accurately at very short ranges from the release point: the DGP method was applied only to the lateral crosswind spread of the plume in this work. A standard Gaussian plume model was also used to fit the measured concentration field data, termed the SGP in this analysis. Plume spread parameters, based on the Gaussian plume modelling for lateral and vertical spread, were obtained for each downstream profile at a range of vertical and horizontal positions. These were used to calculate concentration weighted values of plume spread for each profile. For the vertical profiles, a novel method termed the Isolated Gaussian Plume (IGP) was proposed in this work, using a vertically truncated RCZ combined with a de-convolved best-fitted Gaussian plume to obtain RCZ concentration values close to the roof surface and vertical plume spread parameters. Results were presented for a typical selection of data from all these approaches.

Plume spread parameters, for both SGP and DGP data fitting methods have been presented, and also results from the IGP analysis of vertical profiles. Selection rules have been proposed in order to carry out the DGP/IGP de-convolution process and the results from applying these methods have been presented compared to the simpler SGP model.

The greater accuracy of the DGP method for the determination of the lateral crosswind concentration for the cube was determined by evidence from plots of the concentration profile over the roof zone: in particular, the enhanced tails of the distribution were well modelled by the dual Gaussian approach. The value of the IGP method, with the fixed truncation height above a well-mixed roof top RCZ, was not established in terms of superiority over a SGP method applied to the vertical profile, but for more elevated release profiles showed some evidence of a narrower more elevated peak. The ‘real world’ cases of the EW clad and unclad cases were well fitted to the SGP and showed little difference between the SGP and IGP methods.

From Table 6.2 we can see a pattern emerging as to how well the SGP fitting method matches the DGP/IGP methods. Inspection of the table indicates that for the ‘A’ and vertex release positions, only the normal incidence case shows an elevated distinct plume in the vertical profile. For the ‘B’ case, over all three angles tested, an elevated peak is evident from all the vertical profiles. This finding is expected to be due to the greater effect of roof top vortices, generated from the portion of the building edges upstream close to the release point, and their consequent effect in ‘mixing down’ (by advection) the plume to be closer to the roof surface: the ‘B’ release position was halfway along the roof leading edge and not subject to the same extent of mixing by roof top vortices, preserving an elevated plume in the vertical profiles.

In the experimental cases considered for the active vertical releases the plume was considerably aloft of the building roof and markedly narrower than for the passive releases close to the roof surface. For the active-vertical (AV) releases the SGP and DGP/IGP methods gave very similar results for the cube and EW cases. It may be considered that with sufficient effective plume release height, according to the parameters determined from these experiments, that the SGP method will be sufficient to characterise the plume rise and spread. In these experiments the effective plume height from the active vertical releases was generally in the range of approximately $Z=290-325\text{mm}$, or a range of Z_{norm} of 0.15 to 0.29.

Table 6.2: Summary of plume concentration profile findings with passive releases

Building Case	Angle	Release Position (A/B/Vertex*)	SGP findings	DGP/IGP findings
Cube	0°	A	Very approximate when away from PCM	DGP superior fitting to plume; IGP similar to SGP – distinct elevated plume
Cube	-22.5°	A	SGP does not model very evident roof top RCZ zone, compared to DGP	DGP much superior to SGP; IGP and SGP identical with peak at roof level
Cube	-45°	A	SGP lateral profile fits well with exception of roof top RCZ, SGP vertical profile is well fitted	DGP clearly shows roof top RCZ; SGP and IGP very similar with peak at roof level
Cube	0°	B	SGP good fitting to plume both directions with exception of ‘tails’	DGP marginally superior at ‘tails’; IGP marginally superior to SGP fitting – distinct elevated plume
Cube	-22.5°	B	SGP good fitting to plume in both direction, with exception of tails	DGP marginally superior than SGP; IGP similar to SGP with elevated peak
Cube	-45°	B	SGP good fitting to plume in both direction, with exception of tails	DGP marginally superior than SGP; IGP similar to SGP with elevated peak
EW clad	-22.5°	Vertex	SGP models detail of plume shape marginally worse than DGP	SGP and IGP very similar, with peak concentration close to roof level
EW unclad	-22.5°	Vertex	SGP plume very similar to DGP	SGP and IGP very similar, with peak concentration close to roof level

*- the North Wing Stair Tower position, close to the leading edge to the flow is described as the ‘vertex’ position for the EW clad and unclad cases

6.4.2 Concentration Profiles in the Main Recirculation Zone downwind of the Cube

Concentration profiles for the downstream plane (at $X=400\text{mm}$ from source) have been presented for the cube cases: the structure of the main plume can be readily distinguished from the main RCZ in the lee of the building. The crosswind spread at this distance is broad and is well modelled by both the DGP and the SGP. The vertical profiles require the IGP method to properly model the concentration closer to ground level, and the SGP method is not recommended for plume simulation there: a constant value for the well-mixed concentration field applies from the surface to a height somewhat greater than $H/2$ for the range of cube cases considered.

6.4.3 Concentration Weighted Dispersion Parameters: Variation with distance from Source

From the results shown the lateral crosswind normalised dispersion coefficient σ_y/X was a strongly varying function with release height: for the passive releases a clear pattern can be seen of increased dispersion parameter with decreasing distance from the roof surface plane. Further downstream (at the distance $X=1.67H$) further broadening is generally evident because of the interaction with the building wake. All values were significantly greater than the isolated plume comparator from report R-91. From the DGP method the deconvolution process gave a smaller magnitude of plume lateral spread, but nevertheless still greater than the R-91 comparator.

A clear pattern of increasing magnitude with decreasing distance from the roof plane is seen for the vertical plume spread σ_z/X assessed using the SGP method, with approximately constant values for positions over the roof i.e. $X < 1.4H$. The IGP method value is not determined from concentration weighted values of plume spread, and therefore may be subject to relatively higher weighting of concentrations at the edges of the measurement field, in some cases leading to larger spread values dependent on the characteristics of the flow field at those distal positions.

From Table 6.3 the spread parameters have been categorised with building, angle and release position. Approximate relative magnitudes from the downstream variation of lateral and vertical spread have been compared to respective isolated plume cases from R-91. Some broad inferences may be drawn from the results i.e. plume lateral plume spread is greater for the normal incidence cases and is reduced for the angulated cases to flow, and is greater for positions closed to the midline of the building i.e. position B. For the vertical spread the spread is greater for normal incidence and reduces with building angle. The EW cases are approximately intermediate i.e. the show enhanced lateral and vertical spreads (with IGP) compared to the most comparable cube case of $-22.5^\circ/A$ release position.

Table 6.3: Normalised Plume Spread Parameters: General Patterns in the Roof Zone

Case	Angle	Release Position (A/B/EW Vertex)	SGP*1: $\sigma_{y,cw}/X$	DGP*1: $\sigma_{y,cw}/X$	SGP*2: $\sigma_{z,cw}/X$	IGP*2: σ_z/X
Cube	0°	A	5	3	$Z_{0.1} < \sigma \approx Z_{1.0}$	$\sigma > Z_{1.0}$ (245/255mm) $Z_{0.1} < \sigma < Z_{1.0}$ (265/275)
Cube	-22.5°	A	5	3	$\sigma < Z_{0.1}$	$Z_{0.1} < \sigma < Z_{1.0}$ (245mm) $\sigma < Z_{0.1}$ (255/265/275)
Cube	-45°	A	5	3	$\sigma < Z_{0.1}$	$\sigma \approx Z_{0.1}$
Cube	0°	B	6	3	$\sigma > Z_{1.0}$ (245/255/265) $\sigma < Z_{0.1}$ (275mm)	$\sigma \approx Z_{1.0}$ (245/255/265mm) $Z_{0.1} < \sigma < Z_{1.0}$ (275mm)
Cube	-22.5°	B	5	3	$\sigma \approx Z_{1.0}$ (245/255mm) $Z_{0.1} < \sigma < Z_{1.0}$ (265/275mm)	$\sigma \approx Z_{1.0}$ (245/255mm) $Z_{0.1} < \sigma < Z_{1.0}$ (265/275mm)
Cube	-45°	B	5	3	$Z_{0.1} < \sigma < Z_{1.0}$ (all heights)	$Z_{0.1} < \sigma < Z_{1.0}$ (all heights)
EW clad	-22.5°	Vertex	5	3	$Z_{0.1} < \sigma < Z_{1.0}$ (245/255) $\sigma \approx Z_{0.1}$ (265/275/290mm)	$Z_{0.1} < \sigma < Z_{1.0}$ (all heights)
EW unclad	-22.5°	Vertex	6	3	$Z_{0.1} < \sigma < Z_{1.0}$ (245/255) $\sigma \approx Z_{0.1}$ (265/275/290mm)	$\sigma \approx Z_{1.0}$ (245mm) $Z_{0.1} < \sigma < Z_{1.0}$ (255-290)

*1- relative approximate average ratio against the R-91 benchmark cases for the lateral spread is expressed to one significant figure. *2- vertical profiles were assessed in comparison to the value of σ_z/X for the two ground roughness lengths: $z_0=0.1m$ and $1.0m$ at full scale, for which the values of plume spread are referred to as $z_{0.1}$ and $z_{1.0}$ respectively

In order to provide generalizable results, from the data set the concentration weighted normalised plume spread parameters $\sigma_{y,cw}/X$ and $\sigma_{z,cw}/X$, for both horizontal and vertical spreading of the plume respectively, were reduced by averaging over the distance from the source over the roof zone. In this way the plume spread laterally and vertically could be prescribed with two respective parameters for the range of release conditions investigated, and a clearer pattern could be established: these quantities were plotted against normalised plume height over the roof zone Z_{norm} . The ranges of values are presented in Table 6.4.

Table 6.4: Mean Normalised Plume Spread Parameters over Distance from Source*

Case	Angle	Release Position (A/B/EW Vertex)	SGP: $\sigma_{y,cw}/X$	DGP: $\sigma_{y,cw}/X$	SGP: $\sigma_{z,cw}/X$	IGP: σ_z/X
Cube	0°	A	0.092-0.169	0.069-0.108	0.084-0.132	0.097-0.139
Cube	-22.5°	A	0.082-0.158	0.060-0.112	0.060-0.072	0.068-0.081
Cube	-45°	A	0.098-0.149	0.051-0.101	0.058-0.081	0.054-0.077
Cube	0°	B	0.101-0.194	0.052-0.117	0.107-0.146	0.093-0.118
Cube	-22.5°	B	0.098-0.174	0.063-0.100	0.091-0.134	0.080-0.105
Cube	-45°	B	0.096-0.152	0.057-0.103	0.088-0.129	0.089-0.107
EW clad	-22.5°	Vertex	0.113-0.163	0.077-0.103	0.063-0.100	0.087-0.104
EW unclad	-22.5°	Vertex	0.115-0.189	0.066-0.088	0.066-0.088	0.088-0.117

*- smallest values correspond to passive release height 275mm and largest values the lowest release height of 245mm

Inspection of the results given in Table 6.4, Figures 6.38-6.51, and summary Figures 6.57-6.58 indicate that the lateral spread is systematically lower for the DGP method compared to the SGP method, and that both methods indicate a monotonic reduction of normalised plume spread parameter with normalised release height. All values were significantly greater than the R-91 comparator. It can also be seen that the plume spread is greatest for the normal incidence, with a general overall pattern of reduction with increasing angle of incidence of the flow to the cube. The extent of lateral plume spread was relatively high for the EW cases in comparison to the cube for the SGP method, being comparable to the values for cube at normal incidence, and overall generally similar for the DGP method.

Similarly, the SGP and IGP methods applied to the normalised vertical dispersion parameter indicate from Table 6.4, and the previous figures, that the vertical spread reduces with increasing plume height and is greatest for normal incidence to the cube for both 'A' and 'B' release position cases – where it can exceed for the lowest release heights values associated with an equivalent isolated plume in an environment with ground roughness length in the region of $z_0=1.0m$ at full scale. With increasing angle there is a general reduction in the plume vertical spread normalised parameter. For the 'A' release position oblique angles indicate an equivalent ground roughness length of $z_0=0.1m$. For the 'B' release position the equivalent ground roughness length of $z_0=1.0m$ is maintained with oblique angles: this indicates a significant difference in plume vertical spread parameter with release position in relation to the building.

The EW clad and unclad cases (Table 6.4, and Figures 6.44-6.55 and 6.50) indicate a reduction of normalised vertical plume spread parameter with release height. In comparison to the cube the values bear a greater similarity to the 'A' release case, but somewhat greater than the -

22.5°/A case and closer to the 0°/'A' values, but nevertheless within the overall range of cube values seen from the experimental results. Using the DGP method the EW values are closer to those of the cube normal for the 'A' position compared to the other angles - but are generally close to all of the 'B' release values.

6.4.4 Plume Deflection: Horizontal and Vertical

In order to be able to generalise the results and enable them to be used to calculate concentration values in a wider range of scenarios, the plume deflection normalised to distance from the release point was calculated and presented for all of the experimental conditions investigated. For the SGP and DGP methods the range of Y/X values for the plume maximum with distance from the source were averaged, generating a mean plume deflection for a given approach angle of flow, building, and release position for a given release height: these results have been presented graphically for all cases. Plume concentration maximum height was also obtained from the SGP and DGP analyses of the lateral crosswind profiles and these results have been presented, normalised to building height, so that they may be readily generalised from the release conditions considered in this study.

For the 'A' release position the plume deflection was seen to be moderately in the negative Y direction for the angles of 0° and -22.5°, but strongly so for the -45° angle case: these findings applied for the SGP and DGP method. For the 'B' release case the SGP case was neutral for 0° but moderately negative for the DGP case: for the -22.5° case the SGP and DGP methods showed moderate deflection in the negative Y -direction, and more strongly so for the -45° direction. The EW clad and unclad cases were assessed only at the -22.5° direction of approach flow: for both cases and for both the SGP and DGP plume fitting methods there is a strong negative Y direction deflection evident.

For the vertical deflection the 'B' position release case shows a strong upwards deflection for the three angles of approach flow. For the 'A' release case the pattern was more complex: strong upwards deflection for normal incidence at 0° for the SGP and DGP methods, changing to neutral (SGP) and moderate positive deflection (DGP) for the -22.5° case, and then consistently moderate upwards deflection for the -45° case for both analysis methods.

For the vertical deflection for the EW clad and unclad cases a clear pattern also emerged: moderate negative deflection as assessed by the SGP method, and moderate upwards deflection as assessed by the more sophisticated DGP method.

For the SGP method for cube 'A' position, the upwards deflection is greatest (normalised value just over 0.04) for normal incidence, then reducing through -45° to the lowest values at -22.5°: the EW clad and unclad cases show a large negative deflection for the intermediate release height of 255mm. The corresponding 'B' cases with SGP method show a large upwards deflection for all angles, with normal and -22.5° angles marginally greater.

The DGP analysis of plume deflection of the main plume shows that for the 'A' and 'B' cube cases the upwards deflection for normal incidence is of the same order of magnitude as the SGP cases, and this holds for the 'B' angled cases. However, for the 'A' and EW cases the pattern is more complex: upwards deflection is seen for the EW cases, reducing with the release height; for the 'A' cases a much larger deflection is seen at the greatest release heights of 265mm and 275mm for -45° and -22.5° respectively.

6.4.5 Variation of PCM with downstream distance

To obtain generalised rules that could be used to calculate plume centreline maximum concentration values from a release close to a building roof a reduction in the complex behaviour of the data set was necessary: a novel empirical formulation for the dimensionless plume concentration maximum (PCM) with an exponential decay factor was presented. From the results obtained the exponential decay factor was greatest (i.e. showing a more rapid decay with distance) for the DGP method: this is an expected result as the de-convolved main plume would be expected to follow an x^{-2} variation with downstream distance and a corresponding exponent decay factor close to -2. For the EW clad and unclad cases, the same overall pattern holds.

In Table 6.5 results for the log-log linear regression best fitting of the plume concentration maximum are presented for a release height $Z_{rh}=245\text{mm}$. For ease of reference equation [14] is reproduced, from earlier in this chapter, showing the terms for the intercept $\ln(\chi_1)$ and gradient, α , referred to in the table. It should be noted that χ_1 is specified at unit distance of 1 metre from the source.

$$\ln \chi(x) = \ln \chi_1 - \alpha \ln x \quad [14]$$

Table 6.5: Empirical Variation of PCM: $\ln(\chi)$ vs $\ln(x)$; for $Z_{rh}=49\text{m}$

Building Case	Angle	Release Position (A/B/Vertex*)	SGP gradient	SGP intercept	DGP gradient	DGP intercept
Cube	0°	A	-1.965	10.586	-2.082	10.803
Cube	-22.5°	A	-1.804	10.652	-1.858	10.649
Cube	-45°	A	-1.628	10.090	-2.130	11.683
Cube	0°	B	-1.901	10.287	-1.799	9.617
Cube	-22.5°	B	-1.653	9.349	-1.720	9.671
Cube	-45°	B	-1.656	9.459	-1.870	10.074
EW clad	-22.5°	Vertex	-1.459	8.883	-1.744	8.892
EW unclad	-22.5°	Vertex	-1.704	9.708	-2.033	10.137

*- the North Wing Stair Tower position, close to the leading edge to the flow is described as the vertex position for the EW clad and unclad cases

In Table 6.5 the values for gradient and intercept from the logarithmic fitting in equation [14] are presented for the lowest release height of $Z_{rh}=49\text{m}$ full scale, with the plotting against distance in metres from the source. The range of values is broadly similar to those compared to Iwai and Ijima (1970) which were previously discussed in section 6.2.4.4. It can be seen that the DGP generally shows a larger (negative) gradient i.e. a more rapid reduction in PCM concentration value with increasing distance from the source: this is to be expected if the DGP shows the de-convolved concentration in the main plume from the RCZ, and this main plume should be tending more to the theoretical inverse square fall-off with distance. The SGP shows a clear pattern of reduction in the magnitude of the gradient going from normal incidence through to -45°. The EW clad case shows a relatively small gradient value for the SGP value, but otherwise the EW cases lie somewhere within the range of gradient values calculated from the cube data. Inspection of Figures 6.38-6.47 indicates that the SGP fits to the data follow the linear model more closely, and the DGP graphs (after RCZ was de-convolved) show more variation with distance over the roof zone.

6.4.6 Rooftop Maximum Concentrations

Roof top concentrations have been presented for the range of conditions investigated, a chosen height of 1.5m above the roof plane. These results have been presented in dimensionless concentration in Figures 6.28-6.35, and summarised in Figures 6.59-6.61, so may readily be generalised to other types of releases where the dose is delivered by inhalation of the pollutant material. In Table 6.6 the maximum concentrations are given, irrespective of release height, for the range of approach angles, release positions and building cases.

For the cube with normal incidence, the ‘A’ release position leads to a maximum dimensionless concentration χ for the lowest release height of 245mm (1 metre at full scale above the roof plane) of approximately 39 for the SGP formulation and 29 with the DGP method with an associated RCZ concentration of 16. Peak concentrations (Figure 6.28) reduce monotonically with increasing release heights above this level but occur at increasing distances from the source. For the ‘B’ release position the corresponding values are respectively 37, 19 and 15 (Figure 6.33) with the peaks reducing monotonically with release height but at increasing distance from the source.

Table 6.6: Roof Top Maximum Concentrations***

Building Case	Angle	Release Position (A/B/Vertex*)	SGP: χ	DGP: χ	RCZ (or secondary plume): χ
Cube	0°	A	39	29	16
Cube	-22.5°	A	84	67	25
Cube	-45°	A	75	94	15
Cube	0°	B	37	19	15
Cube	-22.5°	B	23	18	11
Cube	-45°	B	32	30	10
EW clad	-22.5°	Vertex	109	57	67
EW unclad	-22.5°	Vertex	102	79	53

*- the North Wing Stair Tower position, close to the leading edge to the flow is described as the vertex position for the EW clad and unclad cases

**- interpolated or extrapolated values are given from the nearest values, to obtain a best estimated value at $Z_{rh}=247.5\text{mm}$. These differ slightly from Figures 6.28-6.35, where the values for the sampled height closest to 1.5m above roof level are given

For the cube with -22.5° incidence the ‘A’ release position leads to a maximum dimensionless concentration χ of approximately 84 for the SGP formulation, 67 with the DGP and associated RCZ concentration of 25. Peak concentrations (Figure 6.29) reduce monotonically with increasing release heights above this level but at increasing distances from the source. For the ‘B’ release position the corresponding values are respectively 23, 18 (at 255mm release height, Figure 6.34) and 11 following the same pattern. The values given in Table 6.6 differ slightly from the graphical results as these are based on interpolation or extrapolation to 1.5m height above the roof, whereas the graphs present the value from the nearest spatial sample position available from the data set.

For the cube with -45° incidence the ‘A’ release position leads to a maximum dimensionless concentration χ of approximately 75 for the SGP formulation, 94 with the DGP and associated RCZ concentration of 15. Peak concentrations (Figure 6.30) reduce monotonically with increasing release heights above this level but at increasing distances from the source. For the ‘B’ release position the corresponding values are respectively 32, 30 and 10 following the same pattern.

For the EW clad building with -22.5° incidence the maximum dimensionless concentration χ was approximately 109 for the SGP formulation, 57 with the DGP and associated RCZ concentration of 67. Peak concentrations (Figure 6.31) reduce monotonically with increasing release heights above this level but at increasing distances from the source. For the EW unclad building (Figure 6.32) the corresponding values were respectively 102, 79 and 53.

For the -22.5° angles the EW building (clad and unclad) maximum roof level concentrations are broadly similar to the cube 'A' release values at angles of both -22.5° and -45° . For normal incidence on the cube the maximum values are very approximately under half these values (except for the 'B' DGP case where the value is approximately one quarter). For -45° the 'B' release cases were approximately one third of the corresponding 'A' release values.

The overall pattern seen is that roof vortices at the leading edge of the building (refer to Chapter 5) act to cause advection of material down to lower levels at the oblique angulations to approach flow causing higher concentration levels closest to the roof. The release position 'A' near the leading vertex of the cube is significantly higher in concentration value compared to the 'B' case: this is due to the vortex generation near the leading edge, close to the release position, moving material vertically downwards. For the 'B' release position at oblique angulations the vortex system is reasonably well developed streamwise and the downwards advection less pronounced.

6.4.7 Downstream Main RCZ concentrations

Ground level concentrations downstream of the cube in the main RCZ (see Figure 6.62) were obtained for a range of release heights, angles of approach flow and for the two building release positions tested. Clear evidence of a well-mixed zone was seen with a distinct main plume above ground level for all angles of approach flow, passive release heights and building release positions investigated.

For the cube cases, a significant amount of data has been presented for the downwind main building recirculation zone, for the different release heights, release positions and angles of approach flow. For all the cube data considered the concentration approached an approximately uniform value when approaching ground level in the main RCZ: the well-mixed zone was clearly apparent in the data and this enabled a mean value to be established for the well-mixed zones for the approach angle of flow and the release height above the building. These are presented in Table 6.7.

Figure 6.62: Cube Recirculation Zones: Main and Roof Zone

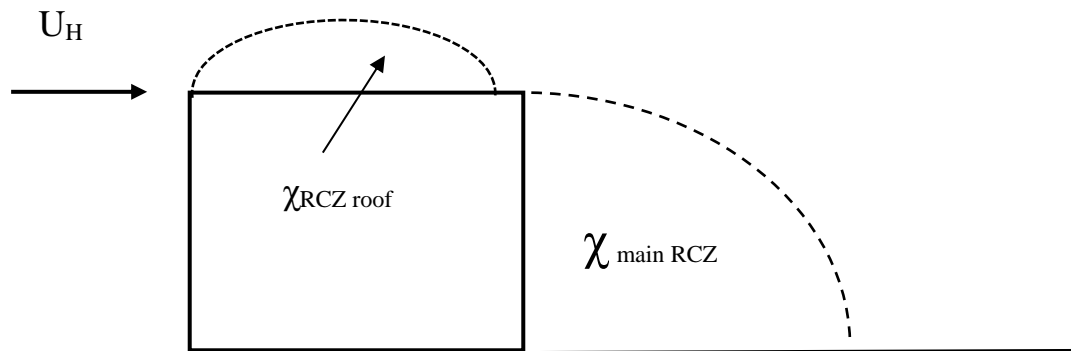


Table 6.7: Downstream Main RCZ Concentrations in the Well-Mixed Zone

Building Case	Angle	Release Position (A/B)	$\chi_{Z_{rh}=245\text{mm}}$	$\chi_{Z_{rh}=255\text{mm}}$	$\chi_{Z_{rh}=265\text{mm}}$	$\chi_{Z_{rh}=275\text{mm}}$
Cube	0°	A	2.572	1.978	1.761	0.905
Cube	-22.5°	A	2.800	2.079	2.819	0.908
Cube	-45°	A	3.298	3.026	1.998	1.225
Cube	0°	B	2.470	2.825	2.309	2.076
Cube	-22.5°	B	1.866	1.877	1.803	1.389
Cube	-45°	B	2.505	2.256	1.913	1.262

It can be seen from Table 6.7 that the greatest extent of entrainment was seen for the ‘A’ release case at -45° incidence with a dimensionless concentration value of approximately 3.3. For the ‘A’ release case the RCZ main concentrations reduced through angles of -22.5° through to normal incidence i.e. there was a distinguishable general increase in the RCZ well-mixed concentration moving from normal incidence to increased oblique angles of approach flow. As shown in Chapter 5 the stronger vortices with oblique angles of incidence are responsible for advection of material downwards into the main recirculation zone.

For the ‘B’ release case the pattern was more complex but appears to show a general tendency for the concentration to decrease with increasing stack height. For ‘B’ there are the combined effects of vortices and location of source relative to these with rotation of the building around the ‘B’ release position. However, it can be said that the greater downwards streamline deflection at oblique incidence will bring material closer to the roof and tend to increase the concentration value in the main RCZ.

6.5. Conclusions

Two methods have been presented in this work for the modelling of plume behaviour just above the roof of a building: the first being a single Gaussian plume (SGP) fitted to lateral and vertical profiles through the plume at different heights, crosswind positions and downstream planes from the release point; the second being a combination of two approaches: a Dual Gaussian Plume (DGP) to model the crosswind profiles, and for the vertical concentration profiles an Isolated Gaussian Plume (IGP) consisting of a well-mixed constant concentration zone just above the roof truncated at a given height above the roof superimposed with a single Gaussian profile. Both models have their relative advantages and disadvantages: the SGP is simpler and more robust because it is not subject to the uncertainty introduced when a concentration profile must be de-convolved into a main peak and secondary peak: the secondary peak in many cases corresponds to the roof top RCZ but could represent a bifurcation of the plume in a particular flow field situation. The DGP method has significant advantages where concentration values must be known at a position away from the plume main centreline e.g. at the position of a building air intake: plume broadening in the rooftop RCZ is well modelled with the DGP method. Plume rise, and upwards deflection in the active vertical releases investigated, was such that the plume was relatively well elevated above the building and the SGP method was a good approximation to the plume spread behaviour.

The SGP modelled lateral spread of concentration in the main recirculation zone - the downstream concentration in the main RCZ, extending down to ground level, for these releases that were just above roof level and with a release point only just upstream of the building. For

a release near ground level upstream of the building it may be more appropriate to use the DGP method, but this configuration was not considered in this work.

Values of the concentration weighted plume spread parameters, normalised for distance, were obtained for a range of conditions, such as release position in relation to the cube building, angle of approach flow and a range of passive release heights just above the roof the building. Lateral plume spread significantly increased with reduction of plume release height and was significantly greater than the established benchmark results in Report R-91. The vertical plume spread was generally greater than that which would be indicated for a plume with no building present in a turbulent flow with a ground roughness length corresponding to that used in the wind tunnel experiments, and this greater broadening was particularly evident at normal incidence to flow. The two 'real world' building cases considered (EW clad and unclad) were better modelled in terms of lateral plume spread by the DGP method.

Plume horizontal and vertical deflection for the cases considered have been presented for the main plume with both the SGP and DGP methods used. Horizontal deflection was generally towards the left driven by roof vortices flow, when viewing the approaching flow from a downstream position, except for the symmetric case of the cube at normal incidence with the midline release position ('B').

Mean vertical deflection of the plume, averaged over the roof zone, was strongly upwards for the cube midline release position and the normal incidence cases. A neutral vertical deflection was seen for the cube near vertex release position 'A' at the intermediate angle of approach flow of -22.5° which represents the transition from upwards directed flow for the normal case and the strong effect of vortices seen at the -45° case seen in the flow fields. For the EW clad and unclad buildings the SGP indicated plume downwash, but the DGP/IGP method indicated a small upwards deflection of the main plume once de-convolved from the roof top recirculation. This effect can be related to the strong variations with position of (W/U_{ref}) where it is easier to pick out a variation in the narrower plume relative to the release position (see Figure 6.55.)

The empirical method of modelling the downstream plume concentration maximum, using a power exponent model with distance and logarithmic fitting to the data, showed that the dimensionless concentration can be modelled well with this approach, and the gradient values yielded useful information concerning the dispersion of the tracer in the roof zone: it was found that the DGP results indicated a gradient closer to the expected (i.e. undisturbed flow) inverse square fall-off with distance.

Roof-top maximum concentrations were presented for the full range of passive release heights, building release positions, angles of approach flow and supplemented by results from the EW building cases. The overall magnitude of the dimensionless concentration at just above roof level was well established from these cases, and use of these results would enable a reasonable approximation of the overall magnitude to be made for intermediate cases.

The structure of the main recirculation zone near ground level just downwind of the building has been established: it has been possible to establish a robust overall level of concentration in this zone with a range of passive release heights close to the roof of the building. For the 'A' release position, near building vertex, the main RCZ concentration generally increases from the normal to increasing angles of obliquity (-22.5° then -45°) of the approach flow, for the 'B' midline case the general pattern was of a minimum at the intermediate angle of -22.5° .

Overall, it can be seen from the results that three of the major factors at play in determining the roof level maximum concentration are, in approximate relative order of importance:

- (a) Release height in relation to the roof of the building
- (b) Building release position, and position with respect to roof vortices
- (c) Angle of approach flow

Other factors include the building shape, angle of sides to approach flow, and there is some evidence from these experiments of the differences arising from the cases studied. The presence of roof top structures – especially those close to the release point may be another factor in the plume dispersion that affects the measurable maximum concentrations near roof level.

The parameters determined in this chapter have been used in the Monte Carlo program written as part of this thesis work to determine the radiation dose over the roof zone of the different experimental scenarios modelled in this work. The spatial parameterisation of the plume enables the plume to be described mathematically in terms of spatial distribution of concentration, and in turn these spatial variations in concentration have been used to compute radiation doses from inhalation, immersion and from gamma-ray radiation emitted from the radioactive material in the plume. The Monte Carlo methods and the results obtained have been presented later in this work.

CHAPTER 7: INTERMITTENT SHORT RELEASES IN THE FLOW FIELD

7.1 Introduction

The effects of source intermittency were investigated for a range of conditions – with the aim being to establish an understanding of the statistical variations of dose received with varying experimental conditions: in this context dose is defined generally as the integral of local concentration with time over a ‘puff’ release event. These experiments apply in the very near range within the roof zone and immediately beyond the building. A complementary series of results from experiments conducted as part of a parallel research project for short duration intermittent releases upwind of the cube model are presented elsewhere (Woodward, H, Gallacher, DJ, *et al*, 2021). However, some limited data from this project is presented in this chapter, covering the convergence to the mean of a time series of concentration values of sampled data from a continuous release. The aim was to show convergence in the limit of relatively long sample times of a continuous release. Further results are also presented for the cube model case showing the convergence with number of sampled puff releases of the statistical measures used, namely the mean dose from a series of puff releases and the coefficient of variation based upon the sampled standard deviation of the puff doses. The aim has been to establish statistical parameters that can be applied to short duration releases to estimate the confidence interval for doses arising from these puff release events.

7.2 Methods

The source intermittency effects were investigated for horizontal passive ‘puff’ release cases at a range of sample co-ordinates including the plume concentration maximum determined from the plume profiles. To obtain reliable dispersion statistics at each observation point, puff emissions had to be repeated many times, leading to very long overall run times per case studied. Consequently, it was necessary to restrict the number of cases investigated. Some additional data is presented from the related project run in parallel with this work (Woodward, H, Gallacher, DJ, *et al*, 2021). All data presented on the convergence to the mean for a continuous release data set were sampled at 400Hz.

7.2.1 Release durations for puff release experiment and dimensionless factors

The dimensionless concentration χ was used to generalise the measured concentration field values C obtained in the wind tunnel experiments, where U_{ref} was the flow velocity in the downstream direction at 1000mm from the tunnel floor corresponding to 200m full scale in the experiments, H was the building height and Q was the tracer release rate.

$$\chi = \frac{CU_{ref}H^2}{Q} \quad [1]$$

Equation [1] suits the continuous release case, however this requires modification when measuring a short intermittent ‘puff’ release as follows. Firstly, we define the release duration as ΔT and the time-varying measured concentration at the detector as $C(t)$. In equation [2] we define the mean dimensionless concentration for a puff release based on the time integral of concentration divided by the release time. In the limit of large ΔT the value of χ obtained will approach the steady-state release case. The upper limit on the time interval τ is set to integrate all tracer signal at the detector location and must be set multiple times greater than the puff release duration ΔT . The value of τ used in the experiments was limited by practical run time considerations but was set long enough so that the full dose integral of the concentration profile was obtained and that successive puff release events were independent in terms of eddy fluctuation timescales.

$$\chi = \frac{U_{ref} H^2}{Q \Delta T} \int_0^\tau C(t) dt \quad [2]$$

The individual time trace profiles for each puff release showed high levels of fluctuations of signal level versus time. The mean value of concentration for a given puff χ_i was obtained using equation [2] for a given sequence of puff release measurements $i=1$ to N , where N was the ensemble size for measurements under a given set of conditions.

To specify the fluctuation of the dimensionless concentration, and the mean dimensionless concentration per puff for a given set of conditions, the standard statistical measures for mean, sample standard deviation and coefficient of variation were obtained as follows:

$$\chi_{mean} = \frac{\sum_{i=1}^N \chi_i}{N} \quad [3]$$

$$\sigma_s = \left[\frac{\sum_{i=1}^N (\chi_i - \chi_{mean})^2}{N-1} \right]^{1/2} \quad [4]$$

$$C_v = \frac{\sigma_s}{\chi_{mean}} \quad [5]$$

The other statistical parameters used in the analysis were the 5th and 95th percentile from a normal distribution, using the mean and sample standard deviation.

To further generalise the analysis, the concept of the building scale normalised puff length scale was devised. This uses the puff release duration multiplied by the reference flow velocity to obtain a puff length scale (PLS): ‘scale’ is used in this context to reflect the fact that a release may not be at the same height in the tunnel as the reference velocity (1000mm). Since the flow velocity reduces when approaching the tunnel floor, and there are flow velocity field effects when in the vicinity of the building the actual length dimensions of the puff tracer may be different to the PLS. Nevertheless, PLS reflects the relative length of the tracer in the flow. The next step was to normalise the PLS for building size to determine the normalised puff length scale PLS/H , which is a dimensionless quantity which reflects the relative magnitude of the puff length to the building: further analysis was presented in terms of this quantity. In particular PLS/H was tested for values from well below one (i.e. with puff releases shorter in length terms than the sizes of the buildings being studied in the experiment) to greater than one.

The concept of puff length scale was used to generalise the results to a full-scale case using similarity principles, where the suffix ‘FS’ represents the quantities in the full-scale case.

$$\frac{PLS}{H} = \frac{U_{ref} \Delta T}{H} = \frac{U_{ref,FS} \Delta T_{FS}}{H_{FS}} \quad [6]$$

By re-arrangement of equation [6] we can obtain the relative puff release time in the wind tunnel and the full-scale case.

$$\frac{\Delta T_{FS}}{\Delta T} = \left(\frac{U_{ref}}{U_{ref,FS}} \right) \frac{H_{FS}}{H} \quad [7]$$

Insertion of some realistic values in equation (for model scale 1:200) indicates that for a downstream plane in the roof zone of the building with a wind tunnel reference velocity of 2ms⁻¹

¹ and a full-scale wind velocity of 4ms^{-1} (the latter at 200m height from ground level) the release time duration ratio would be 100; for the shortest puff release duration used in the tunnel of 0.025 seconds the equivalent time full scale would be just 2.5 seconds. Testing at the shortest possible puff release durations was carried out in order to investigate the effects of very short duration releases on the statistical parameters for the puff releases: i.e. the mean dimensionless concentration and the associated coefficient of variation over the samples, then leading to the equivalent dimensionless concentration values for the 5th and 95th percentiles treating the probability density function as approximately following the normal distribution.

The full range of sample times used in all experiments were as follows: $\Delta T = 0.025, 0.05, 0.10, 0.25, 0.5, 1.0, 2.0$ and 4 seconds to approach more closely a steady state release. Either the full range or a reduced subset of these release times was used in the experiments carried out with the cube and the East Wing (EW) building in either the clad or unclad form.

7.2.2 Short duration active puff vertical releases with cube

The cube model was investigated with a fixed release height and an active vertical release; i.e. with the tracer emission directed vertically upwards. The 'A' release position, corresponding to a release close to the leading-edge vertex was used. Three angles of approach flow were investigated: normal incidence (0°), and oblique incidences of -22.5° and -45° . A reduced subset of the puff release times was used, namely $\Delta T = 0.10, 0.25, 0.5, 1.0$. Wind tunnel reference velocity was 2ms^{-1} and the stack emission velocity was matched to the flow to give the same plume rise or upwards deflection as tested in previous cases. Four sampled downstream distances were measured, in model scale $X = 80, 160, 240$ and 400mm . At each downstream sampled plane the puff releases were measured at the plume concentration maximum (PCM), the position of which had been accurately determined from mapping the plume dispersion for a steady release case.

7.2.3 Short duration active puff vertical releases with EW Clad and Unclad Buildings

The EW clad and unclad models were investigated for the same fixed height active vertical release as the cube with the tracer emission from a position near the leading vertex of the EW building corresponding to the 'A' release position on the cube in terms of distance to the leading edge of the building. Only one angle of approach flow was investigated -22.5° . A fuller set of puff release times was used, namely $\Delta T = 0.025, 0.05, 0.10, 0.25, 0.5, 1.0, 2.0$ and 4.0 seconds. In this series of measurements, the wind tunnel reference velocity was 1ms^{-1} but the stack emission velocity was matched to the flow to give the same plume rise as for the cube case considered earlier. Only one downstream distance was sampled - in model scale at $X = 160\text{mm}$. At this single downstream plane the response was measured for the plume concentration maximum (PCM), but also with a range of offset positions, both crosswind and vertically in relation to the PCM position.

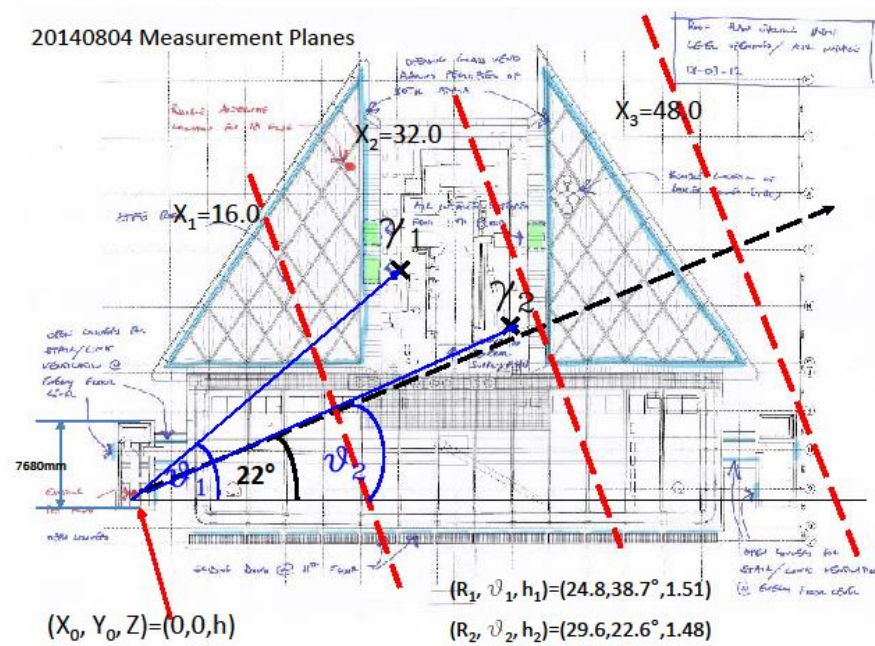


Figure 7.1 EW Clad Building: (-22.5°) Main Direction Studied (-22.5°)

Image by ARUP/Hopkins and ISG, with annotations by the author

7.2.4 Short duration passive puff releases with EW Clad and Unclad Buildings

The EW clad and unclad models were also investigated for horizontal passive puff releases with the tracer emission from a position co-ordinate directly below that used for the EW active vertical releases, at $Z_{RH}=245\text{mm}$. One angle of approach flow was investigated, -22.5° . As with the active release EW cases, $\Delta T=0.025, 0.05, 0.10, 0.25, 0.5, 1.0, 2.0$ and 4.0 seconds. In this series of measurements, the wind tunnel reference velocity was 1ms^{-1} and the emission velocity was matched to the flow. One downstream distance was sampled in model scale at $X=160\text{mm}$. At the single downstream plane the response was measured for the plume concentration maximum (PCM), but also with a range of offset positions, both crosswind and vertically in relation to the PCM position.

7.2.5 Convergence analysis of sampled data series

The number of sampled intermittent ‘puff’ releases was limited by experimental run time considerations given the number of cases that needed to be investigated. Consequently, it was necessary to check the convergence of the statistical parameters used to assess the variation in the dose per puff release. For a given series of puff releases, taken in the order that the puffs were measured, the mean and coefficient of variance were calculated on a cumulative basis consistently adding puff releases in the series into the data analysis. The convergence of the mean to the steady value towards the end of the series of sampled puffs was therefore assessed. Similarly, at each puff in the sampled series, the coefficient of variation (CV) was calculated based upon the sampled standard deviation divided by the mean puff dose, up to and including that puff release. The convergence of the CV with increasing number of puffs in the sequence was therefore also assessed.

7.3 Results

A representative sample of result is presented, along with supplemental results in Appendix 15.4.

7.3.1 Cube case: 0° incidence, stack position ‘A’ near vertex

$Z_{RH} = 255$ mm; fixed active vertical release; $\Delta T = 0.10, 0.25, 0.5, 1.0$ second; 144 puffs

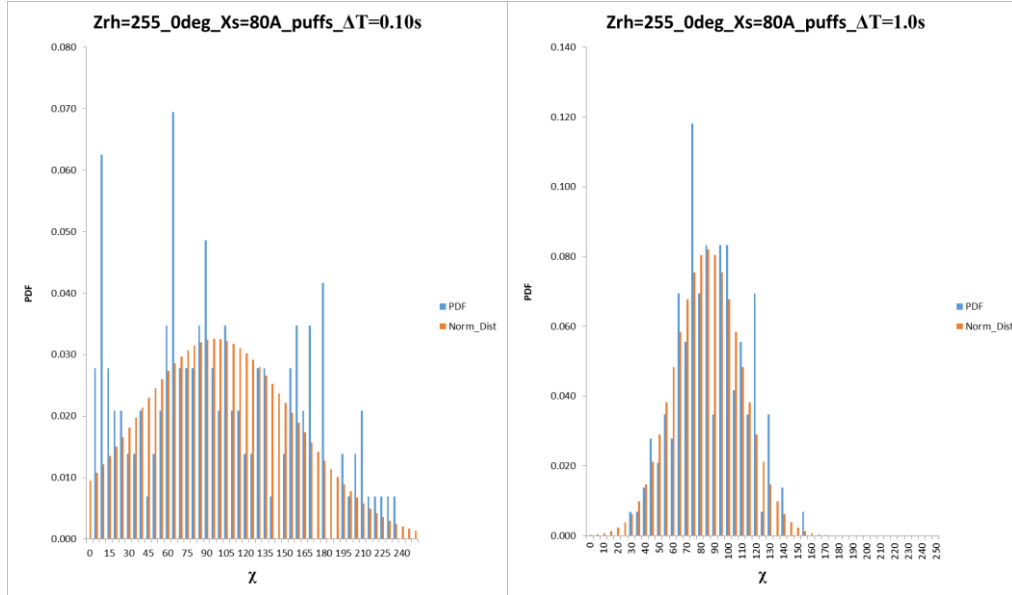


Figure 7.2(a/b): PDF of dimensionless concentration for cube; normal incidence, position ‘A’; $X=80$ mm; active vertical release; $Z_{RH}=255$ mm; normal Gaussian fitting best on mean and sampled standard deviation also shown. (a) 0.1s release (left); (b) 1.0s (right)

From Figures 7.2-7.5 we can see the progression of the probability density functions (PDF of dimensionless concentration) for the cube at normal incidence, with release at the ‘A’ position, with the different distances (X) measured from the source. The magnitude of the mean value of the dimensionless concentration χ reduces with increasing distance X as expected. From Figure 7.2 the longer release time (1.0s) shows a clear Gaussian distribution profile, whereas the much shorter release (0.1s) shows a much more uniform and ‘noisy’ distribution.

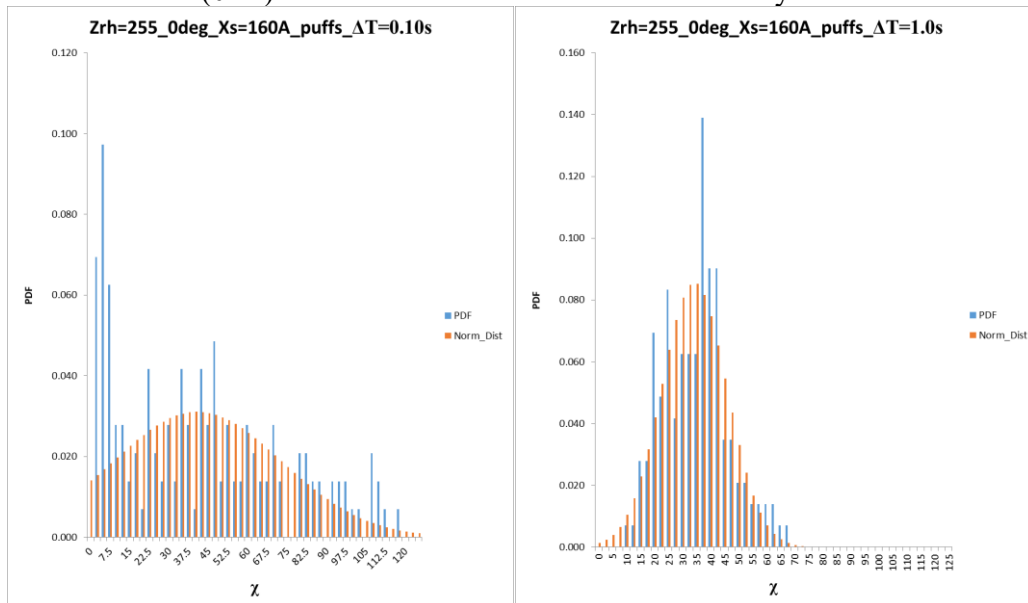


Figure 7.3(a/b): PDF of dimensionless concentration for Cube; normal incidence, position ‘A’; $X=160$ mm; active vertical release; $Z_{RH}=255$ mm; normal Gaussian fitting best on mean and sampled standard deviation also shown. (a) 0.1s release (left); (b) 1.0s (right)

At $X=160\text{mm}$ ($X/H=0.67$) in Figure 7.3 the same pattern is repeated, but there is evidence of a peak close to zero concentration for the 0.1s release, but evidence of greater values extending to a value of approximately 120. The longer release of 1.0s shows a similar mean value but maximum measured values of approximately 70.

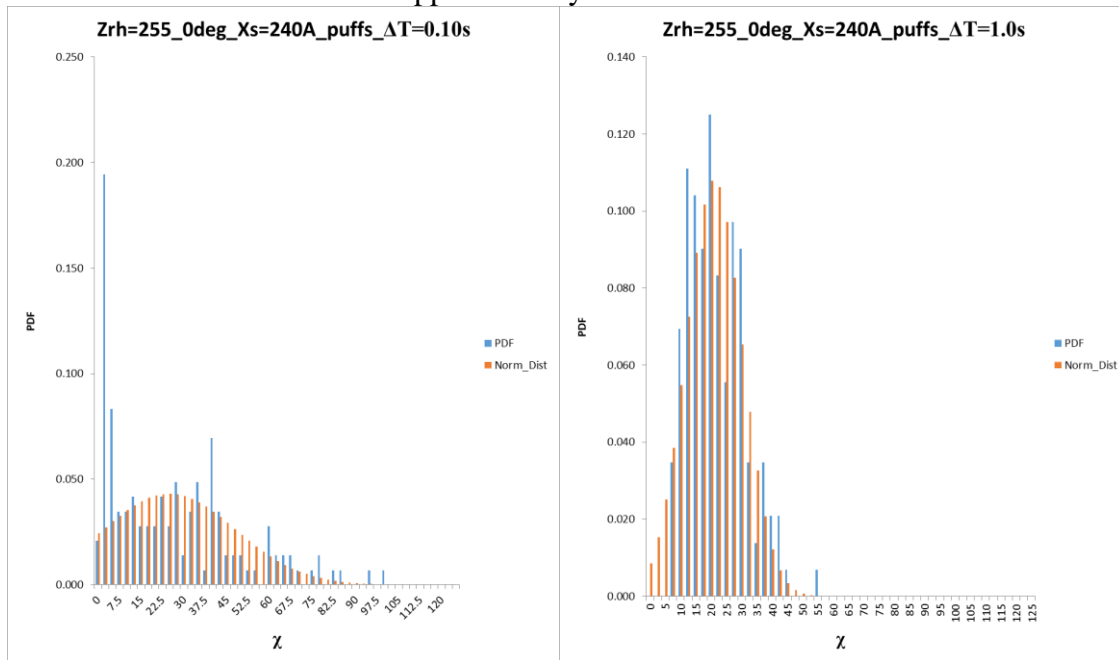


Figure 7.4(a/b): PDF of dimensionless concentration for Cube; normal incidence, position 'A'; $X=240\text{mm}$; active vertical release; $Z_{RH}=255\text{mm}$; normal Gaussian fitting best on mean and sampled standard deviation also shown. (a) 0.1s release (left); (b) 1.0s (right)

In Figures 7.4 and 7.5 at $X/H=1.0$ and 1.67 respectively, the same pattern holds but with a reducing mean with increasing distance from the source. Note that the 'spike' at zero concentration implies that zero concentration is observed, even on the centreline at the location of plume maximum mean concentration.

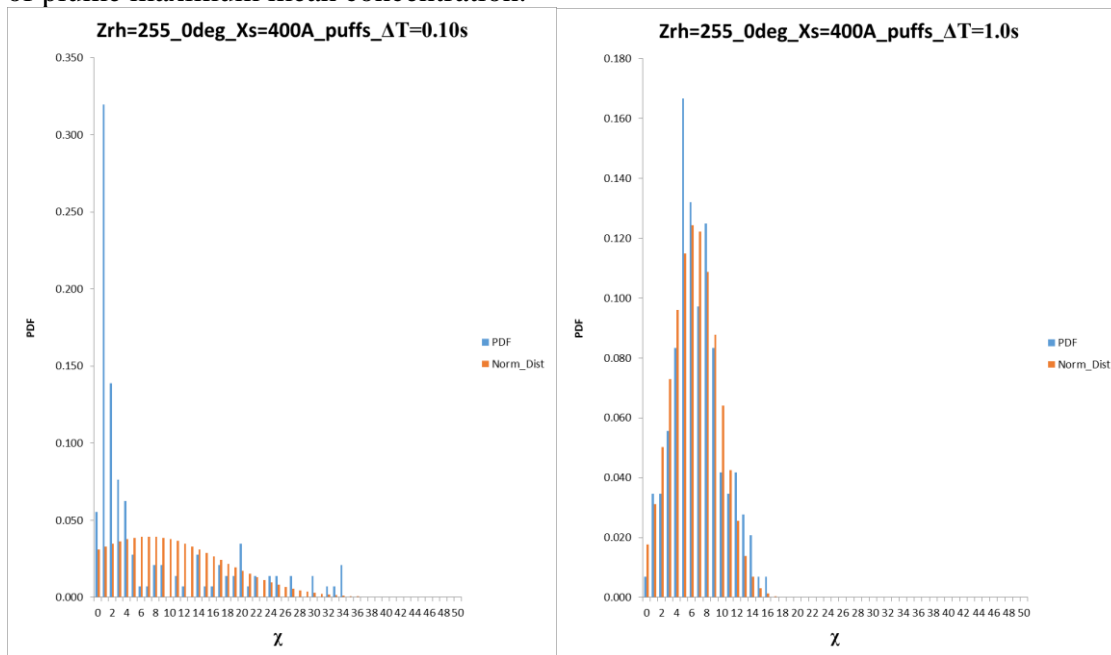


Figure 7.5(a/b): PDF of dimensionless concentration for Cube; normal incidence, position 'A'; $X=400\text{mm}$; active vertical release; $Z_{RH}=255\text{mm}$; normal Gaussian fitting best on mean and sampled standard deviation also shown. (a) 0.1s release (left); (b) 1.0s (right)

7.3.2 Cube case: -22.5° incidence, stack position ‘A’ near vertex

$Z_{RH} = 255$ mm; fixed active vertical release; $\Delta T = 0.10, 0.25, 0.5, 1.0$ second: 144 puffs

In Figure 7.6 three pdf's are presented for different release times of 0.1, 0.5 and 1.0 seconds for the cube at -22.5° oblique incidence and $X/H=0.67$. The low concentration spike is evident for the short release, and the progression through 0.5s to 1.0s shows the longer releases conforming closer to a Gaussian distribution: it should be noted that the mean values for all three distributions are similar. This figure shows that the sampled coefficient of variation will vary with release times.

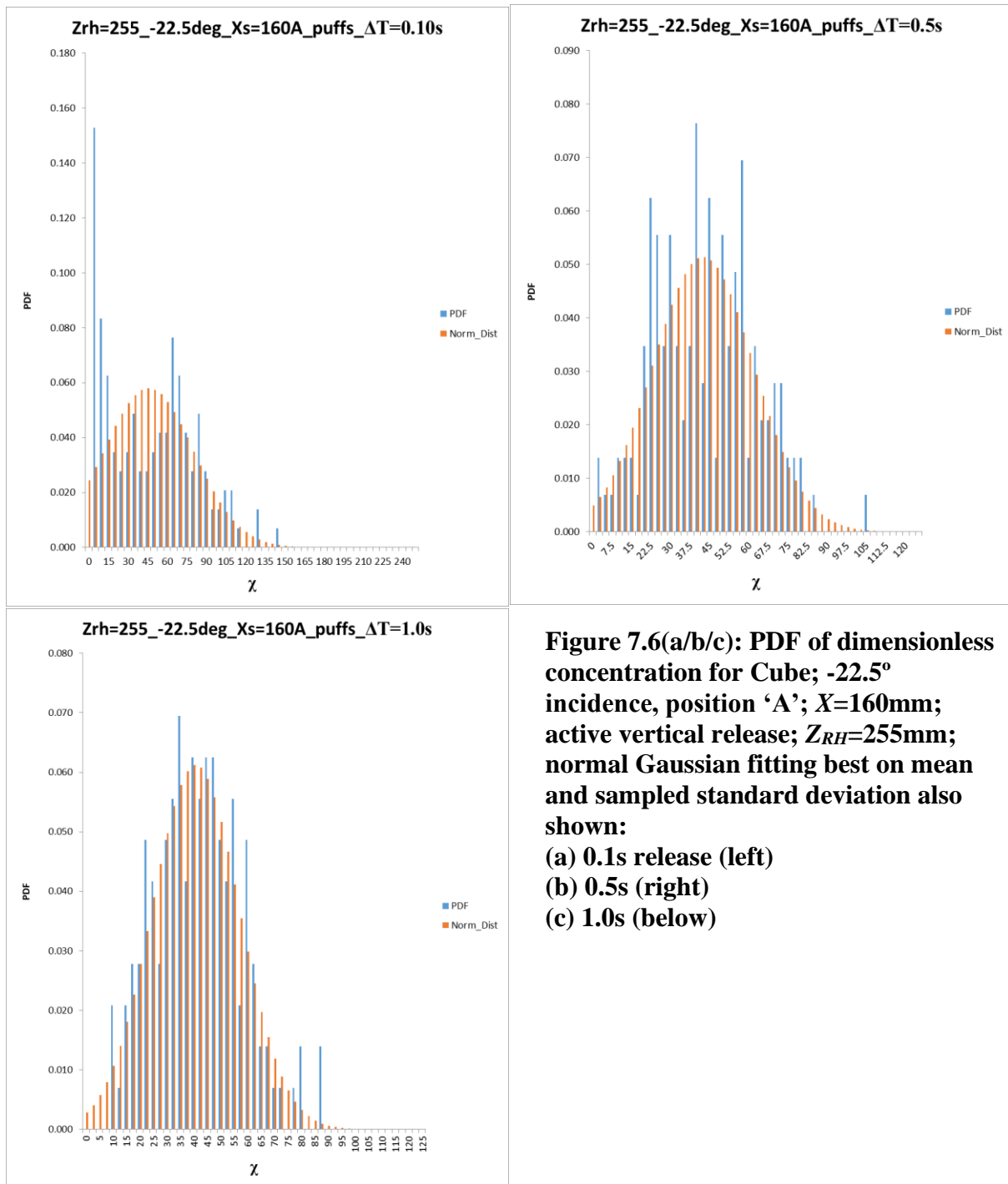


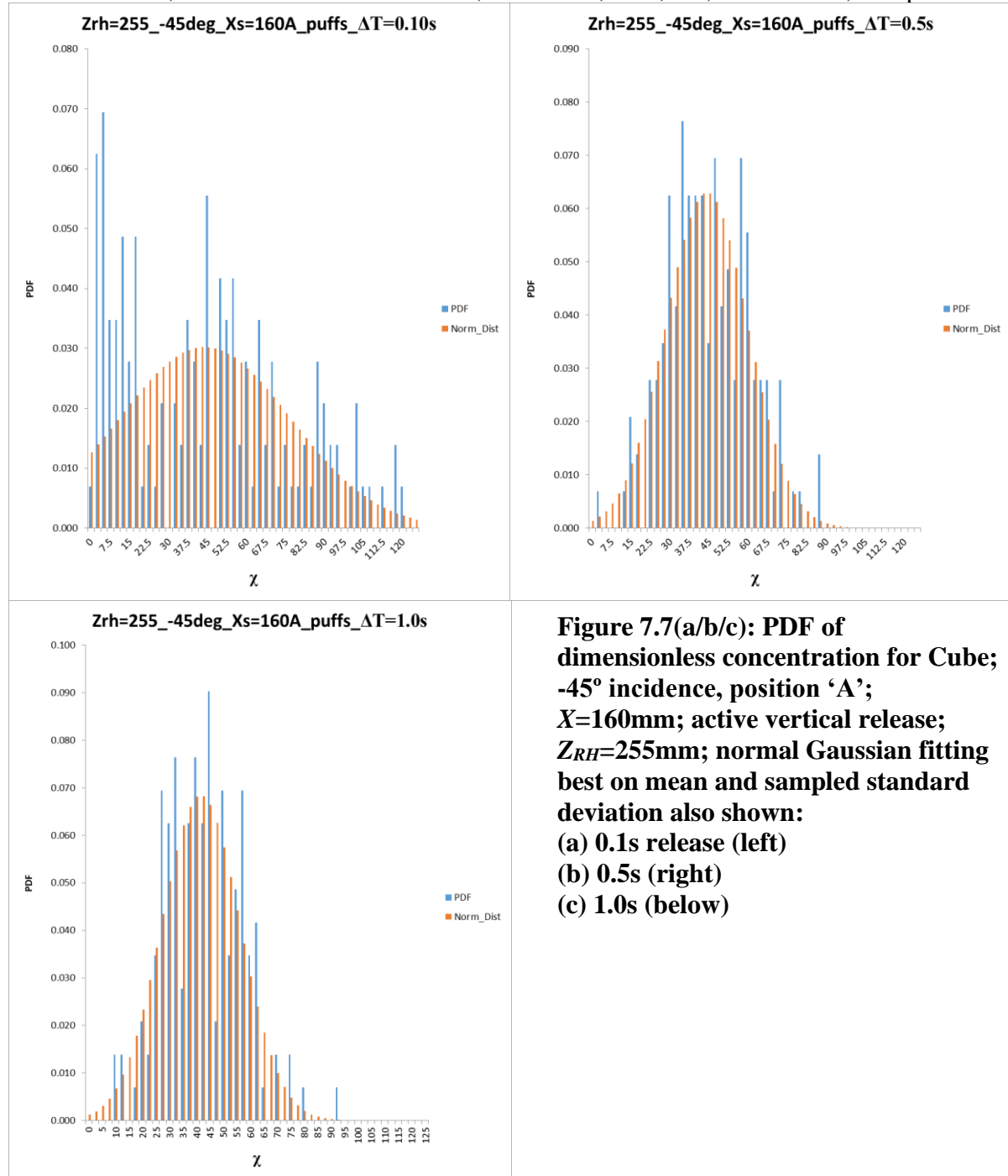
Figure 7.6(a/b/c): PDF of dimensionless concentration for Cube; -22.5° incidence, position ‘A’; $X=160$ mm; active vertical release; $Z_{RH}=255$ mm; normal Gaussian fitting best on mean and sampled standard deviation also shown:

- (a) 0.1s release (left)**
- (b) 0.5s (right)**
- (c) 1.0s (below)**

For the -45° incidence angle to the cube the same pattern is demonstrated in Figure 7.7 to the preceding figures, with increasing puff release durations from 0.1, 0.5 and 1.0 second.

7.3.3 Cube case: -45° incidence, stack position 'A' near vertex

$Z_{RH} = 255$ mm; fixed active vertical release; $\Delta T = 0.10, 0.25, 0.5, 1.0$ seconds; 144 puffs



The East Wing (EW) clad case results are presented in Figure 7.8, for an incidence angle of -22.5° and a release position close to the leading edge (to be similar to the cube in terms of distance to leading edge of the building). The same stack active vertical (AV) release height of 255 mm in model scale was used as the cube cases, so that they may be readily compared.

7.3.4 EW Clad case: -22.5° incidence, active vertical stack near leading edge vertex

$Z_{RH} = 255$ mm; fixed active vertical release; $\Delta T = 0.025, 0.05, 0.10, 0.25, 0.5, 1.0, 2, 4$ s

$X = 160$ mm, $Y = -7$ mm, $Z = 285$ mm

Puffs per ensemble = 178(0.025-0.10s); 160(0.25s); 138(0.5s); 107(1.0s); 74(2.0s); 46(4.0s)

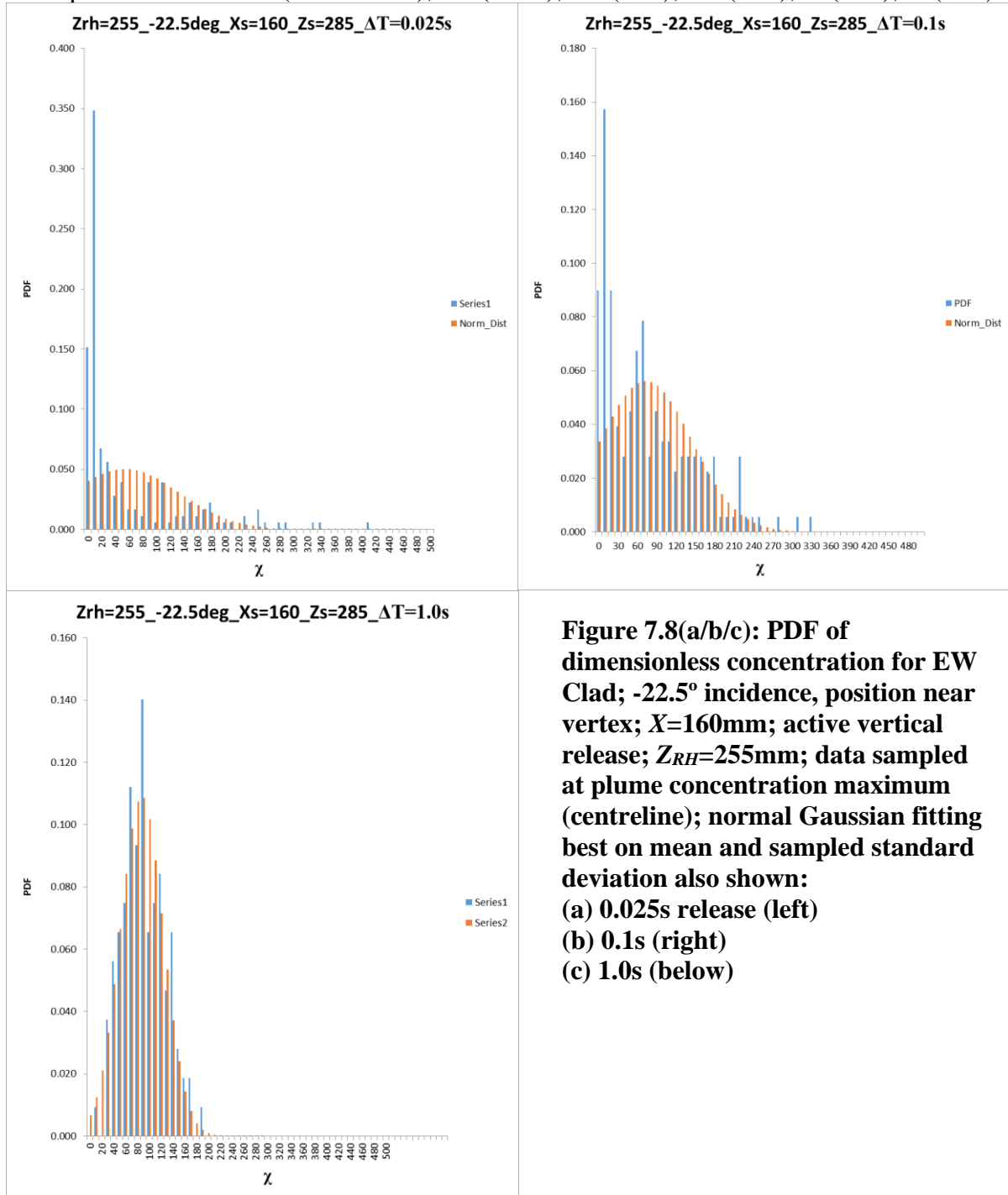


Figure 7.8(a/b/c): PDF of dimensionless concentration for EW Clad; -22.5° incidence, position near vertex; $X=160$ mm; active vertical release; $Z_{RH}=255$ mm; data sampled at plume concentration maximum (centreline); normal Gaussian fitting best on mean and sampled standard deviation also shown:
(a) 0.025s release (left)
(b) 0.1s (right)
(c) 1.0s (below)

A similar progression is seen in Figure 7.8, compared to preceding figures, through release times of 0.025s, then 0.1s and 1.0s for the pdf changing from a more exponential form with a large spike at the very low concentration range for the shortest release to a reasonably well-defined Gaussian form at the longest release time measured. For the EW unclad case, with other experimental conditions being kept the same, the pdf changes in a similar way to the EW clad case and the cube with a progression to a Gaussian profile at the longest puff duration release investigated (see section 15.4.5).

7.3.5 EW Unclad case: -22.5° incidence, active vertical stack near leading edge vertex

Refer to Appendix 15.4.5

7.3.6 EW Clad case: -22.5° incidence, passive stack near leading edge vertex

$Z_{RH} = 245$ mm; passive horizontal release; $\Delta T = 0.025, 0.05, 0.10, 0.25, 0.5, 1.0, 2, 4$ seconds
Per ensemble = 103(0.025s); 77(0.05-0.10s); 48(0.25s); 44(0.5s); 37(1.0s); 15(2.0s); 10(4.0s)

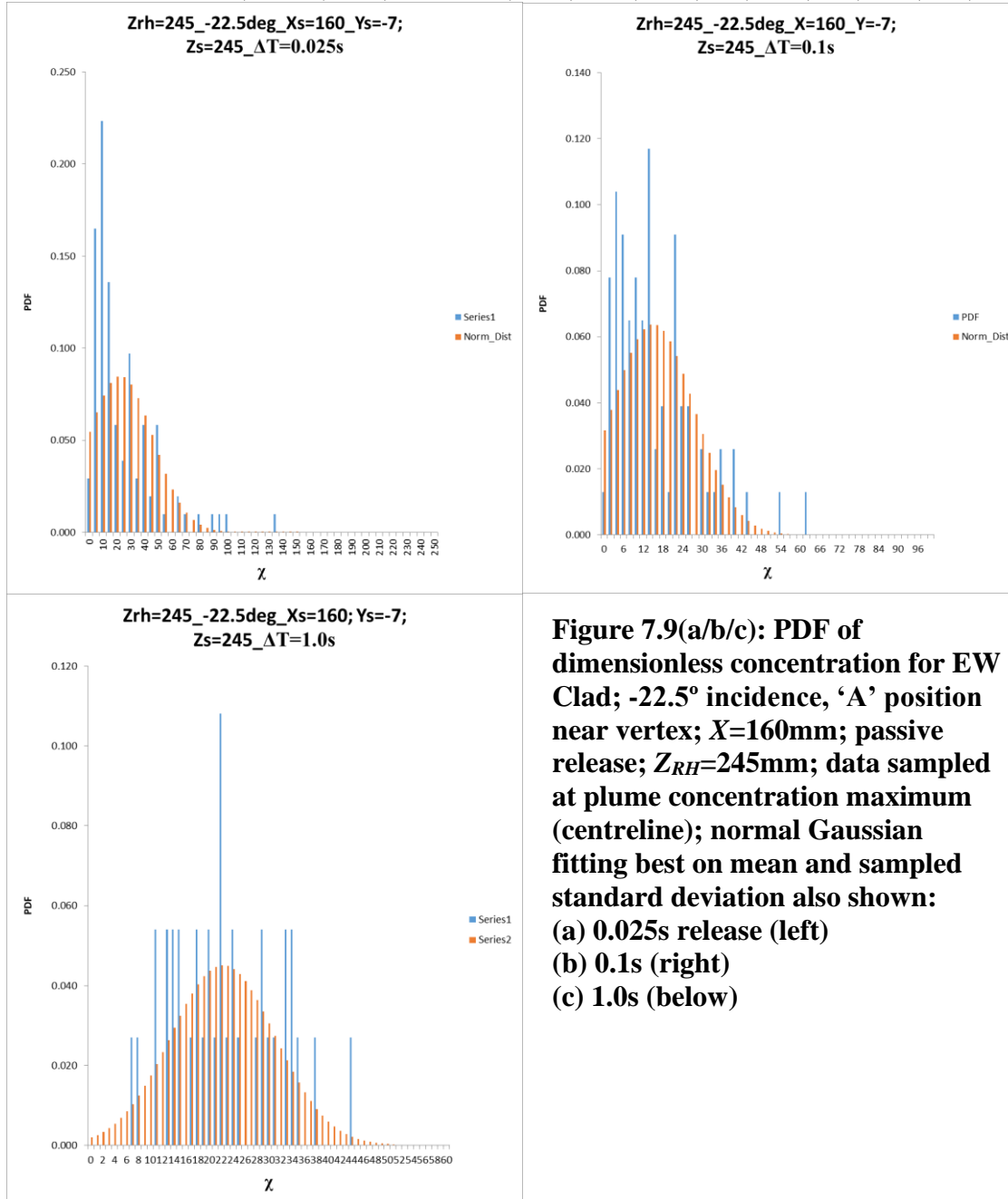


Figure 7.9(a/b/c): PDF of dimensionless concentration for EW Clad; -22.5° incidence, 'A' position near vertex; $X=160$ mm; passive release; $Z_{RH}=245$ mm; data sampled at plume concentration maximum (centreline); normal Gaussian fitting best on mean and sampled standard deviation also shown:
(a) 0.025s release (left)
(b) 0.1s (right)
(c) 1.0s (below)

A passive horizontal release was investigated for the EW clad building with a low release height of 245mm, which was just 5mm above the height of the building, and the results are shown in Figure 7.9. Although number of puff releases was limited, by considerations of experimental run time, this shows that the same broad overall pattern, as seen in previous figures in this chapter, is also demonstrated for a passive release very close to the roof of the building. Furthermore, an even shorter minimum release time of 0.025 seconds was used in this series of measurements, which clearly shows a more exponential-like distribution at the shortest release time.

7.3.7 EW Unclad case: -22.5° incidence, passive stack near leading edge vertex

$Z_{RH} = 245$ mm; passive horizontal release; $\Delta T = 0.025, 0.05, 0.10, 0.25, 0.5, 1.0, 2, 4$ seconds
Puffs per ensemble = 128(0.025-0.10s); 120(0.25s); 110(0.5s); 93(1.0s); 115(2.0s); 48(4.0s)
See 15.4.7 for graphical results. From Figure 15.4.3 for the EW unclad passive release measurements the pdf shows a similar pattern with increasing puff duration to the EW clad case, with the longest release showing a Gaussian profile. A similar pattern is seen for this EW unclad case with the pdf moving from a peaked concentration near the zero level for the shortest times through to a more Gaussian distribution for the longer puff release times.

7.3.8 Cube: coefficient of variation (CV) and 95th percentile of χ vs Puff Length Scale/H

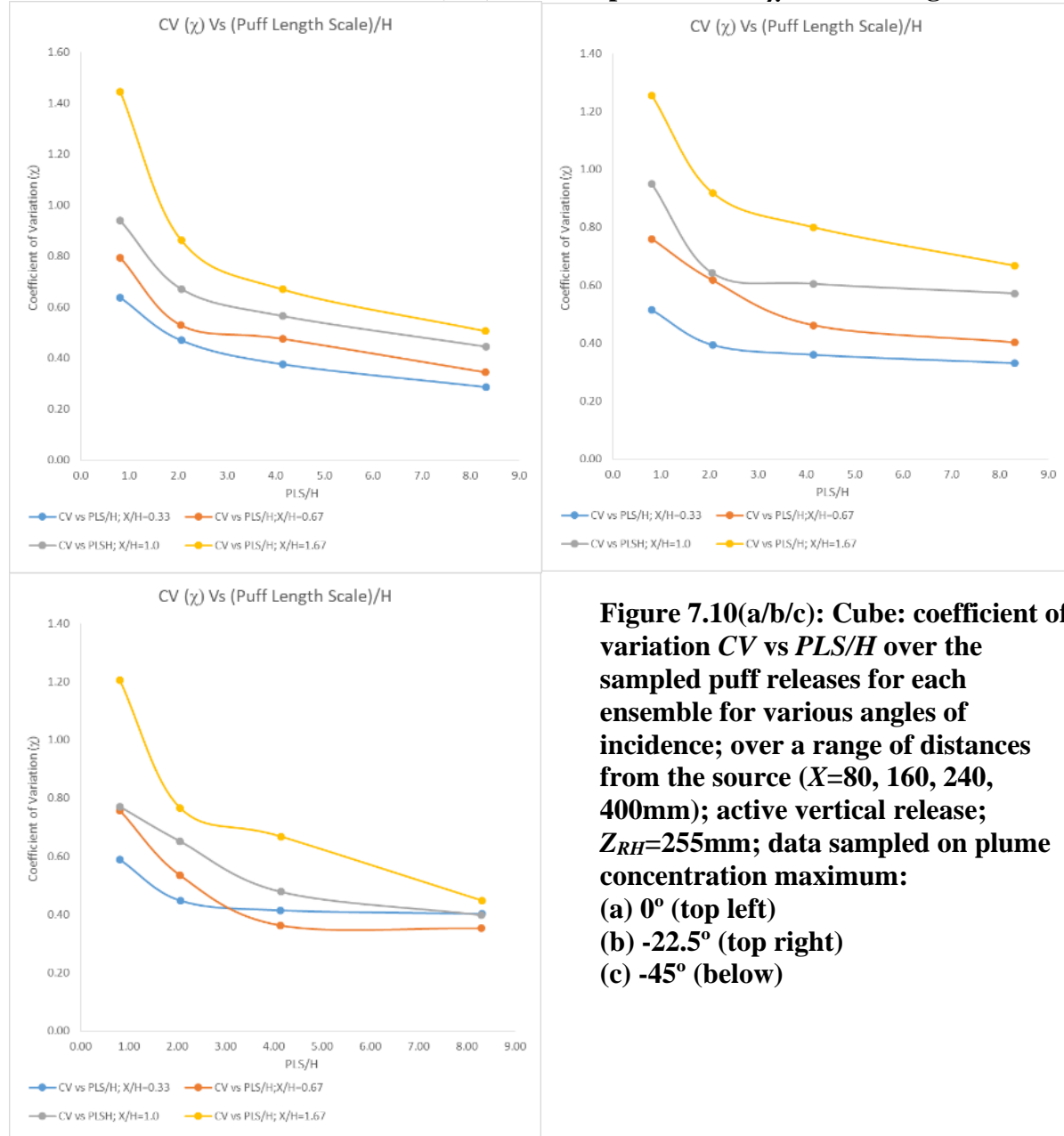
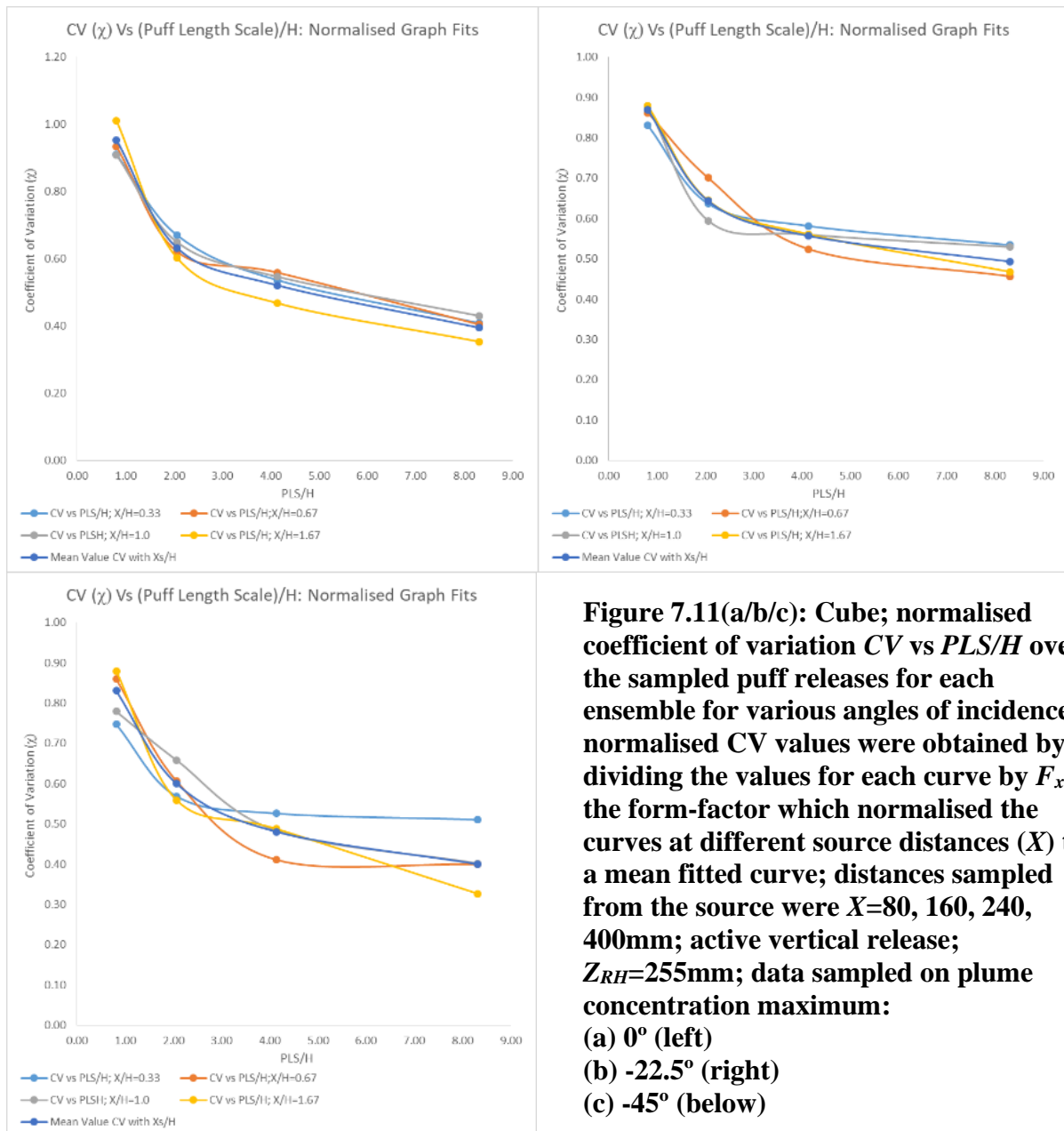


Figure 7.10(a/b/c): Cube: coefficient of variation CV vs PLS/H over the sampled puff releases for each ensemble for various angles of incidence; over a range of distances from the source ($X=80, 160, 240, 400$ mm); active vertical release; $Z_{RH}=255$ mm; data sampled on plume concentration maximum:
(a) 0° (top left)
(b) -22.5° (top right)
(c) -45° (below)

From Figure 7.10 we can see the coefficient of variation (CV) plotted against the puff length scale normalised to building height (PLS/H) for the three angles of incidence investigated in the experiments. The broad pattern is for the CV to reduce with PLS/H according to a similarly shaped characteristic curve. Inspection of the results shows that the magnitude of the CV depends on the distance of the measurement point from the source, with the overall magnitude

increasing with distance from the source. As part of this work, the nature of the characteristic curve determined from these measurements has been investigated.

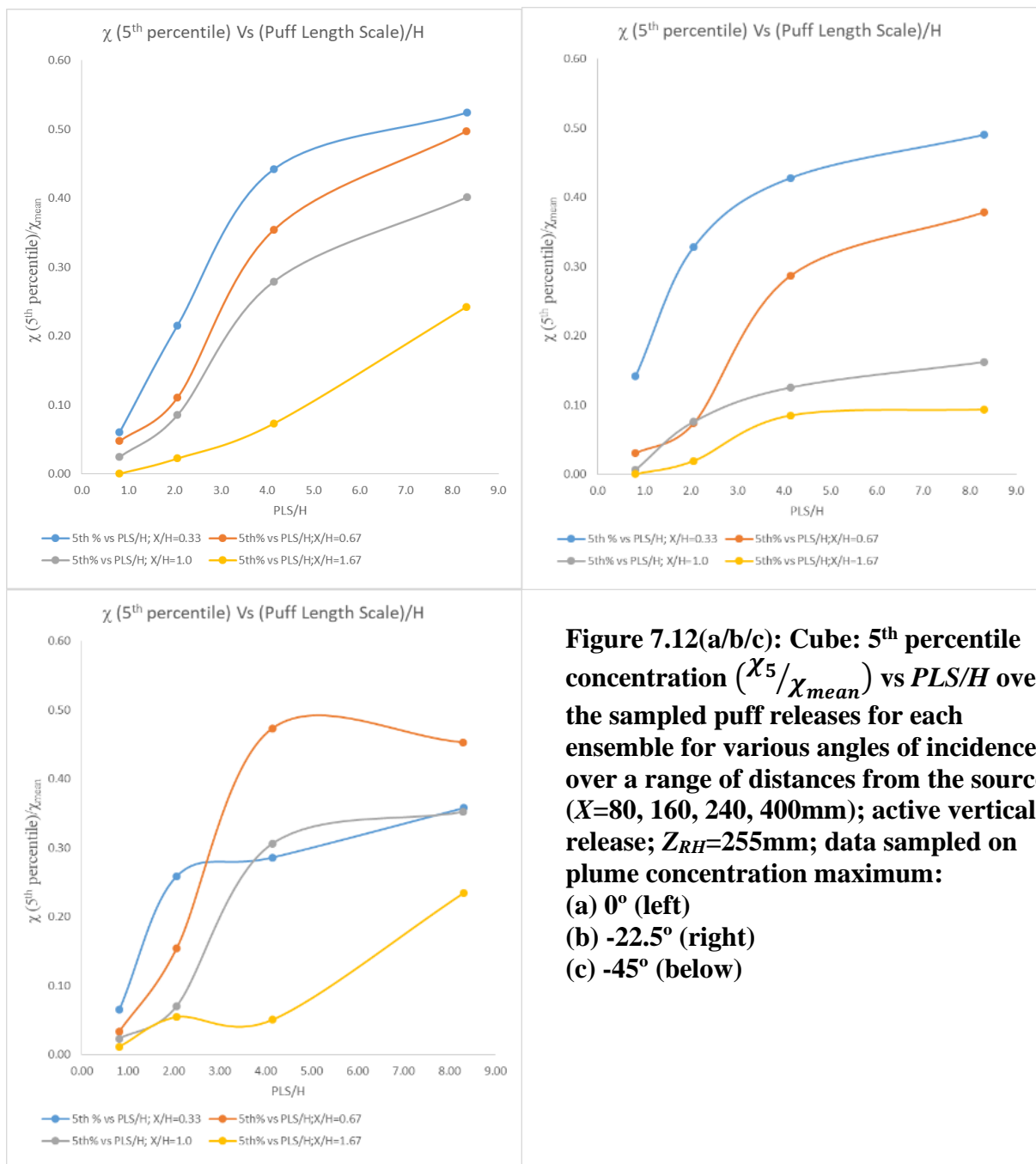
Note that, in a continuous plume, concentration fluctuations initially increase with fetch from the source, before reaching a maximum that is source-size dependent, and thereafter decay (Fackrell and Robins, 1982). Evidently, the results shown here correspond to the fetch over which fluctuations grow, and the increase with decreasing emission duration is akin to the increase with decreasing source size.



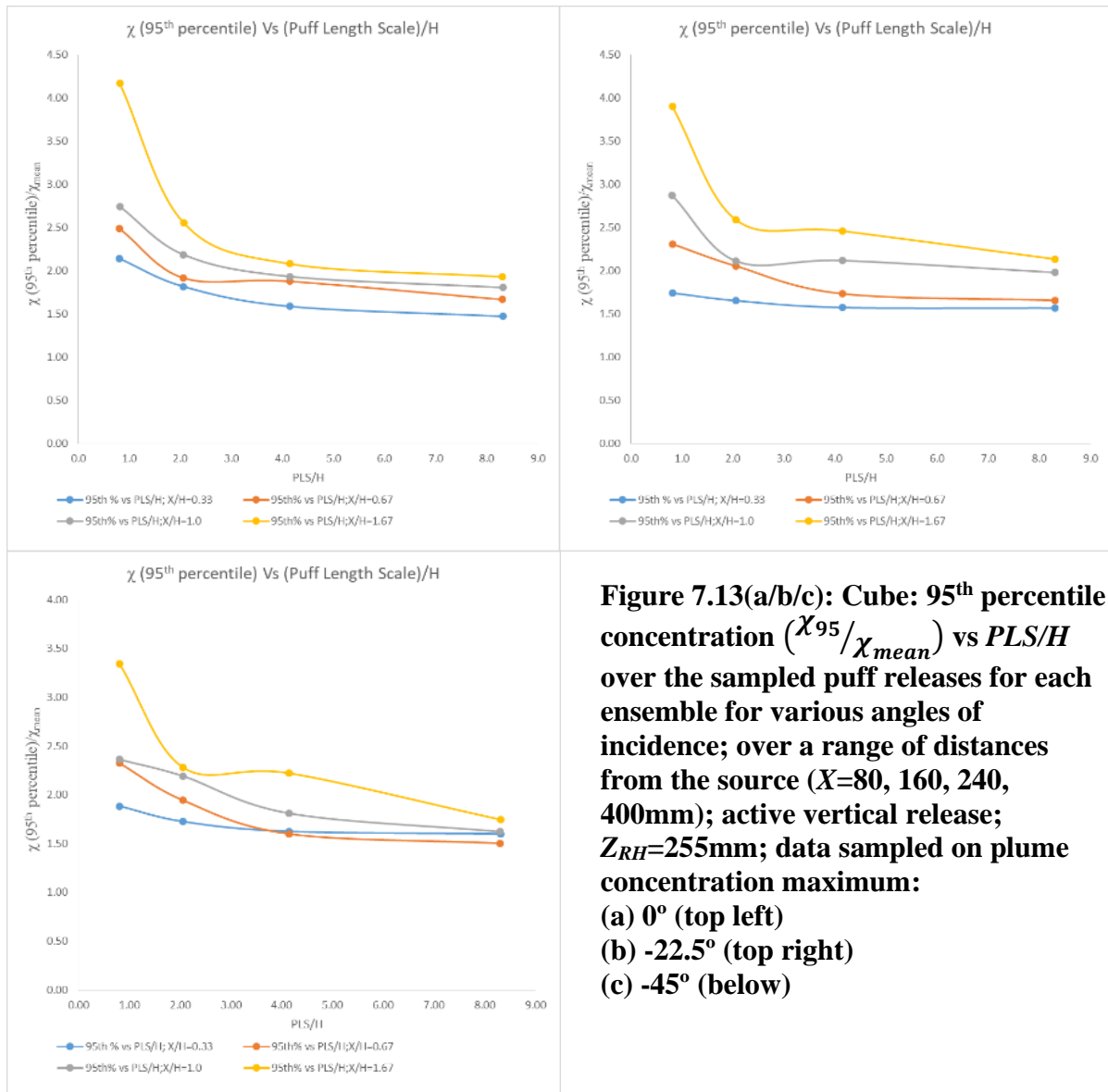
In Figure 7.11 the mean value of each of the three CV curves at each angle of incident flow has been determined for each sampled value of puff length scale. The mean characteristic has been plotted in each case, with the mean value extending to the furthest release point of $X/H=1.67$, representing a mean value over all distances sampled in the roof zone. It should be noted that for the -45° case the trailing edge of the building sits at $X/H=1.41$, so extending the range of sampled values to establish the mean out to $X/H=1.67$ was appropriate. Next, each curve representing variation with distance was scaled by a multiplicative 'form factor' F_x to provide

the best root mean square (RMS) residual minimised difference to the mean profile. The form-factor normalised plots are also shown; this demonstrated that a common distance invariant characteristic curve could be determined which fitted all cases. The mean curves for all three angles were close, showing a broad invariance with angle of approach flow and associated differences in flow conditions.

The analysis now addresses the extremes of concentration, as expressed through the 5th and 95th percentiles of the dimensionless concentration χ , although the 5th percentile is of less interest for determining a maximum expected concentration and most of the results for the 5th percentile will be presented in Appendix 15.4. Note that the nominal concentration fluctuation level at the source is zero.



From Figure 7.12 the fifth percentile value of χ divided by the mean χ per puff is plotted versus PLS/H for the three angles of approach flow. The curves show a similar profile with PLS/H with the greatest values being for points closest to the release position. The overall trend for each distance position sampled is that the dose, expressed as the 5th percentile concentration χ_{5th} divided by χ_{mean} , increased with the longer puff releases. Low signal levels in the $X/H=1.67$ data, caused by distance from the source, mean that the values for this distance should be treated with caution. In Appendix 15.4, Figure 15.4.4, the 5th percentile curves have been normalised to a mean curve using a scaling form-factor $F_{x,5th}$ which are functions of distance from the source.



In Figure 7.13 a similar approach is taken for the 95th percentile of the pdf expressed as χ_{95th} , again normalised to the mean dose per puff by taking the ratio χ_{95th}/χ_{mean} . The 95th percentile, in relation to the mean value of dose per puff, increases with distance from the source and the curve is broadly similar for all three angles of approach flow investigated. Normalised plots, in Figure 7.14, to the mean (RMS difference minimised), after dividing by a scaling form-factor $F_{x,95th}$, show that the curves follow a similar characteristic form. It was noted that the $X/H=1.67$ curve, being at the greatest distance, was to some extent more of an outlier to the general fit.

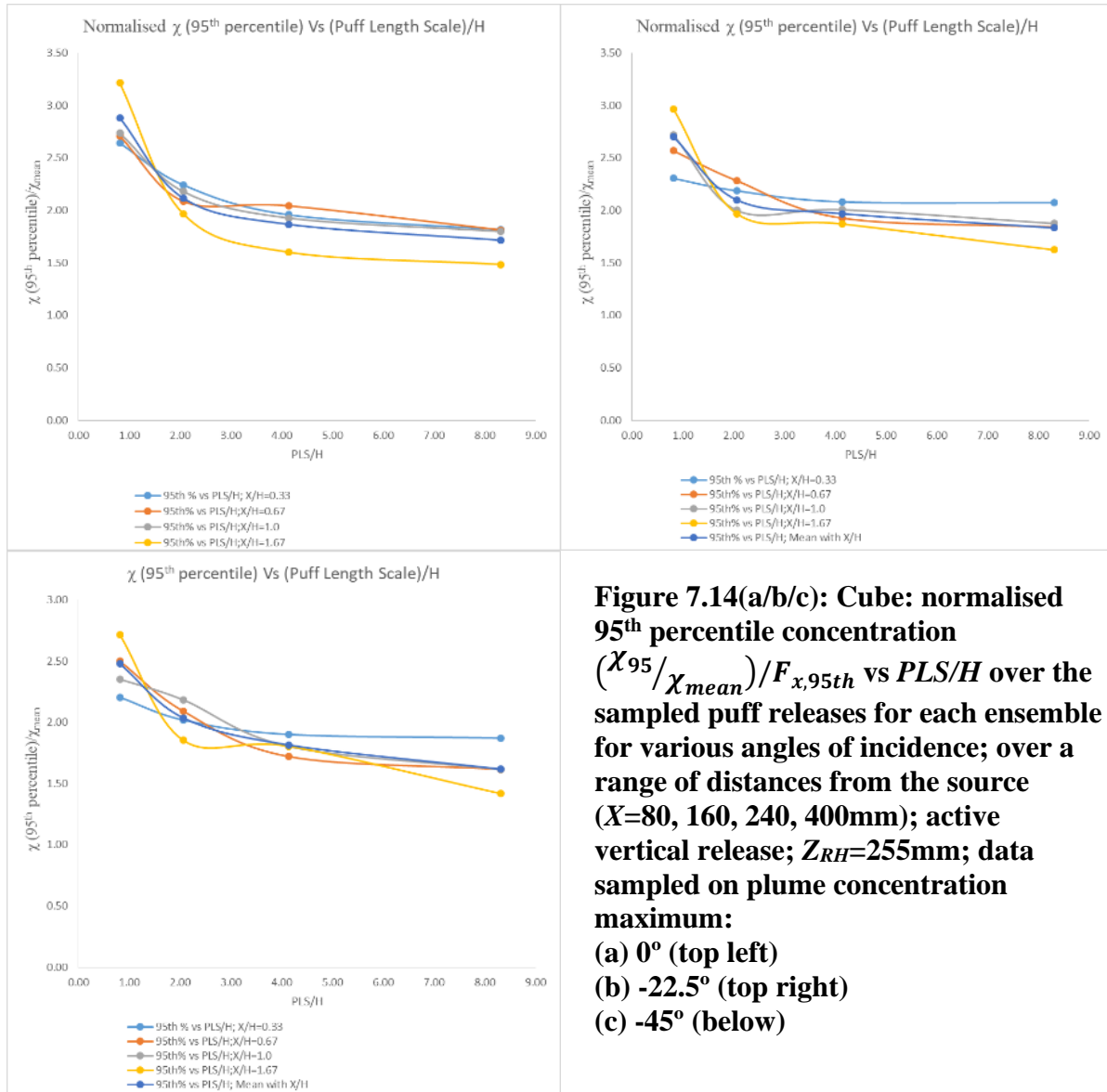
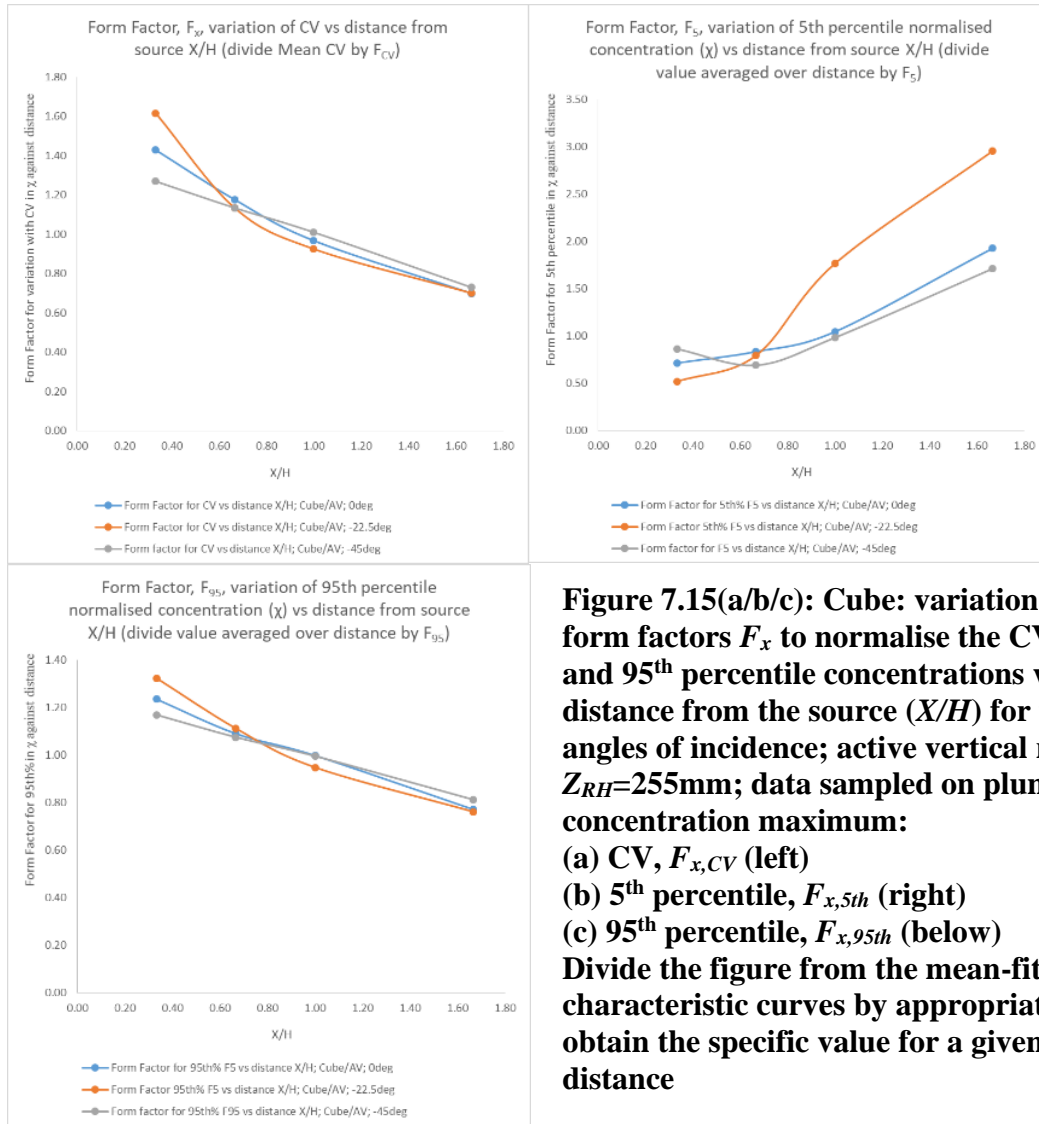


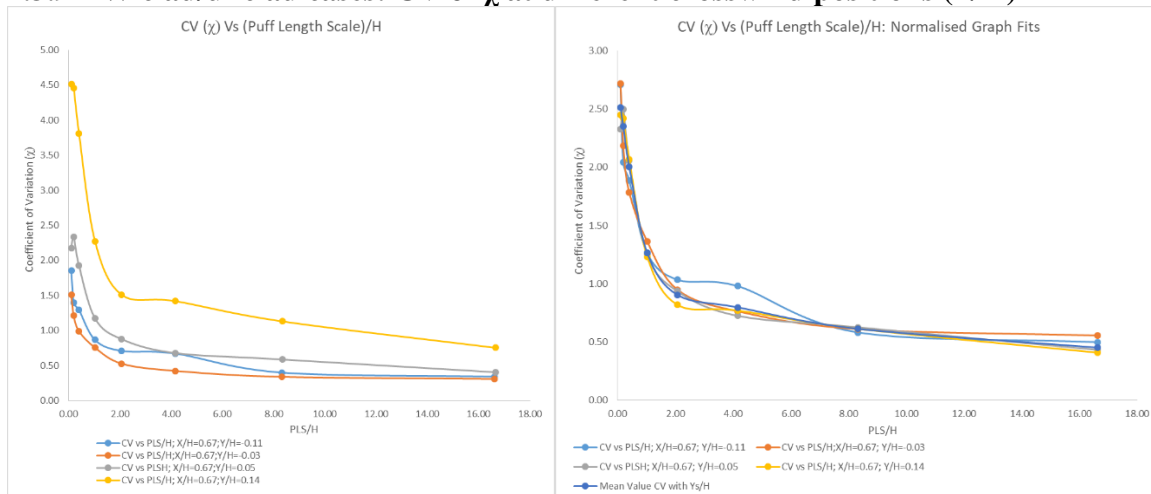
Figure 7.14(a/b/c): Cube: normalised 95th percentile concentration ($\chi_{95}/\chi_{\text{mean}}$)/ $F_{x,95th}$ vs PLS/H over the sampled puff releases for each ensemble for various angles of incidence; over a range of distances from the source ($X=80, 160, 240, 400\text{mm}$); active vertical release; $Z_{RH}=255\text{mm}$; data sampled on plume concentration maximum:
(a) 0° (top left)
(b) -22.5° (top right)
(c) -45° (below)

From Figure 7.14 the normalised $\chi_{95th}/\chi_{\text{mean}}$ curves follow the same general mean curve, largely invariant of the angle of approach flow, which may be taken as a general finding.

In Figure 7.15 the scaling, or form factors for distance are presented for the statistical quantities of CV, 5th and 95th percentile respectively. The mean general characteristic curve value (for a given PLS/H) must be divided by the distance form-factor to provide a value suited to the given distance from the source X/H of the position of interest. The scaling factor with distance indicates that the relative values of the CV and 95th percentile increase with distance from the source, relative to the mean characteristic curve. For the 5th percentile the opposite holds true.



7.3.9 EW clad/unclad cases: CV of χ at different crosswind positions (Y/H)



The crosswind variation of the CV with lateral co-ordinate (Y/H) is shown in Figure 7.16(a) for the EW clad case showing that the CV is greater at positions away from the plume centreline, where CV is a minimum. This again mirrors observations in continuous emissions. It is shown in Figure 7.16(b) that the overall magnitude of each curve may be scaled by a form-factor, F_y , related to horizontal position, and best-RMS fitted to the mean. A common characteristic mean curve is apparent in Figure 7.16(b), showing that the variation of coefficient of variation of χ with PLS/H has a generalizable nature. Similar findings were apparent for the EW unclad active vertical release case in shown in Appendix 15.4, Figure 15.4.5(a/b) and for the passive release case in Figure 15.4.6(a/b).

7.3.10 EW clad/unclad cases: CV of χ at different vertical positions $(Z_s-Z_{RH})/H$

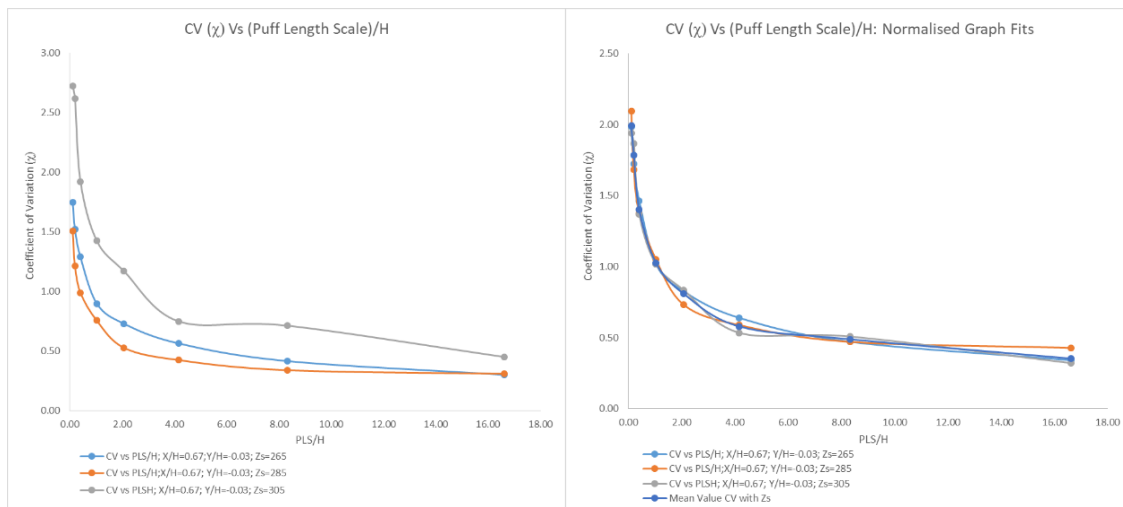


Figure 7.17(a/b): EW Clad: coefficient of variation CV vs PLS/H over the sampled puff releases for each ensemble for various normalised vertical measurement positions $(Z_s-Z_{RH})/H$; angle of incidence -22.5° ; $X=160\text{mm}$; active vertical release $Z_{RH}=255\text{mm}$; (a) measured values with $(Z_s-Z_{RH})/H$ (left); (b) normalised values with F_z form factor fitted to the mean (right)

From Figure 7.17(a) we see the EW clad case with different sampled heights for a fixed active vertical release, and in Figure 7.17(b) the normalisation to a common characteristic curve using the vertical scaling form-factor F_z .

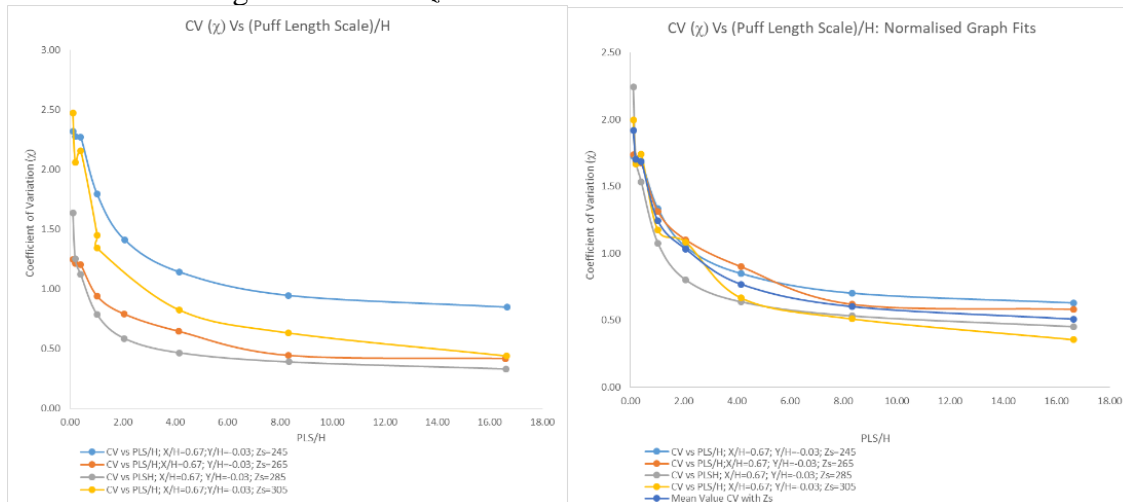


Figure 7.18(a/b): EW Unclad: coefficient of variation CV vs PLS/H over the sampled puff releases for each ensemble for various normalised vertical measurement positions $(Z_s-Z_{RH})/H$; angle of incidence -22.5° ; $X=160\text{mm}$; active vertical release $Z_{RH}=255\text{mm}$; (a) measured values with $(Z_s-Z_{RH})/H$ (left); (b) normalised values with F_z form factor fitted to the mean (right)

measured values with $(Z_s - Z_{RH})/H$ (left); (b) normalised values with F_z form factor fitted to the mean (right)

From Figure 7.18(a) we see that the EW unclad building has a range of CV values with different sampled heights for an active vertical release, and in this case the sample height of $Z=245\text{mm}$ was possible (due to the surface configuration of the roof of the building) showing larger CV values, corresponding to being further away from the centreline of the plume - which does influence the mean normalised value curve presented in Figure 7.18(b). It should be noted that, as before, the CV was a minimum close to the plume concentration maximum.

7.3.11 Overall Summary: Cube and EW clad/unclad: Normalised statistical parameters

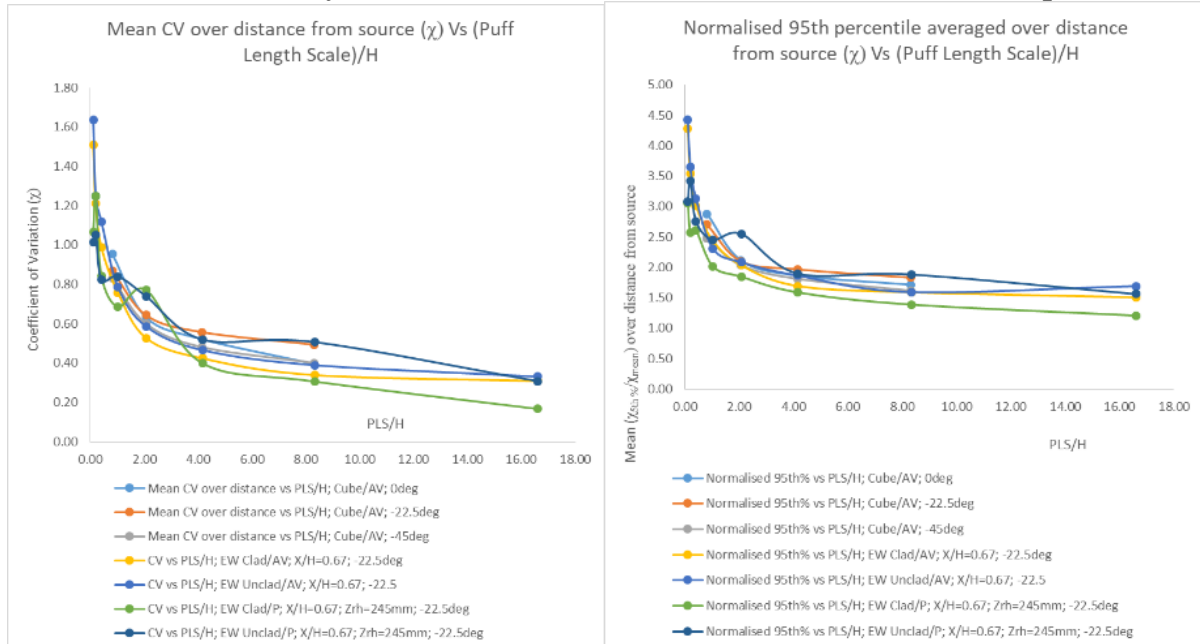


Figure 7.19(a/b): summary of statistical parameters vs PLS/H ; various angles of incidence; averaged over a range of distances from the source ($X/H=1/3, 2/3, 1, 5/3$); active vertical $Z_{RH}=255\text{mm}$; data sampled on PCM; EW active and passive release data at $X/H=0.67$ is presented for comparison; (a) CV (left); (b) 95th percentile (right)

All cases are shown for comparison in Figure 7.19(a/b): these are the normalised curves scaled to be best-fitted to the mean curve from all results - so must be divided by $F_{x,CV}$ and $F_{x,95th}$ form-factors respectively for (a) and (b) to determine the exact value required of CV or $\chi_{95th}/\chi_{\text{mean}}$. Results presented are for the cube with active vertical (AV) release for the cube with three angles of approach flow; EW clad and unclad AV releases at a fixed angle (-22.5°) for a distance near the middle of the roof zone, and EW clad and unclad passive releases at a low release height close to the roof surface (245mm above the roof surface at height 240mm). The figure shows the separate CV and 95th percentile characteristic curves: in all three, the same general characteristics are shown to be relatively insensitive to the different test conditions - these curves could be generally used to determine an approximate value for the statistical quantities at intermediate conditions.

Additional results showing the variation with crosswind position (Y/H) are shown in Appendix 15.4, section 15.4.11, which justify the application of a crosswind scaling form-factor F_y and present results in Figure 15.4.12 to enable this to be applied. These values could be used to adapt the mean value to give a more accurate solution for any individual case: one would divide by F_y to obtain a more accurate value of the statistical parameter from the mean curve.

Convergence properties of the puff release data series were assessed and some of the results are presented here. Results from the intermediate angle series at -22.5° with the cube for release position ‘A’ are presented in Figures 7.20(a/b) for the downstream plane at $X=160\text{mm}$, or $X/H=2/3$, which is approximately at the centre of the roof. Figure (a) shows the convergence of the mean value of χ with adding increasing number of puffs, in the acquired sequence order, and (b) shows the convergence of the coefficient of variation (CV) for the same sequence. Figure 7.20(a/b) shows that the mean and CV in the shortest puff, of release duration 0.1 seconds, converge to steady values within 80 puff samples.

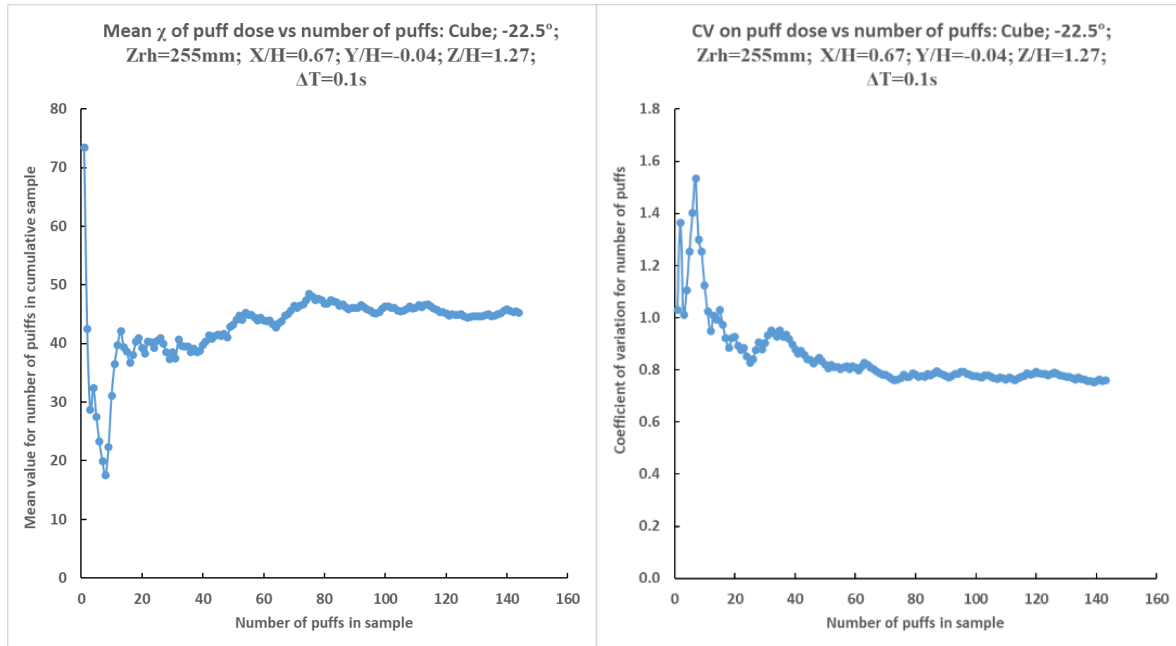


Figure 7.20(a/b): Convergence of statistical parameters with puff sequence; Cube; ‘A’; angle of incidence -22.5° ; $\Delta T=0.1\text{s}$; fixed distance from the source $X/H=0.67$; active vertical (AV) release at $Z_{RH}=255\text{mm}$; (a) mean; (b) CV

Additional results shown in Appendix 15.4, section 15.4.11, where Figure 15.4.15 shows that the number reduces to 60 for the puff of release duration 0.25 seconds, whilst Figures 15.4.16 and 15.4.17 show the numbers to be 40 for the 0.5 seconds puff release and 30-40 for the 1.0 second release respectively.

Figure 7.21 shows results at plume centre for a continuous tracer released from a source at height $Z=320\text{ mm}$ in the approach flow with no building model present: actually, a 30 second release. At the sample frequency of 400Hz this corresponds to 12,000 samples. Similar results were presented in Woodward and Gallacher *et al* (2021).

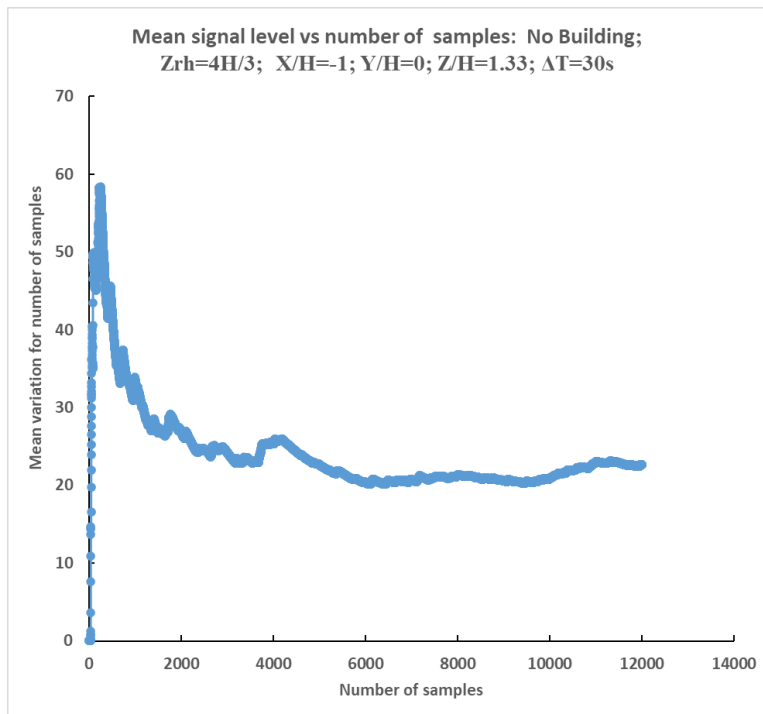


Figure 7.21: Convergence of FFID signal mean measurement with sample number: no upstream building; $\Delta T=30s$; $Z_{RH}=320mm$

The results in Figure 7.21 were derived from the time series of samples from the fast flame ionisation detector, sampled at 400Hz. Sample number is as a surrogate for time, although the samples are not independent as was the case for the puff releases shown previously. It can be seen from Figure 7.21 that convergence to a mean concentration value was achieved at approximately half of the total sample number, at 6,000 samples, which corresponds to 15 seconds in this case. For the continuous release cases this indicates that the mean value from 30 second sampled experiments were robust in terms of the evaluation of the mean concentration value.

7.4 Discussion

The statistical parameters associated with short duration ‘puff’ releases were investigated within the limitations of experimental wind tunnel run time and the number of cases investigated. From the equivalence of normalised emission durations, it was shown that the ‘real world’ puff durations investigated approach values as low as 2.5 seconds; i.e. short duration release cases. A number of experimental variables was investigated, such as the cube case at variable angles of incidence to the approach flow, and the EW clad and unclad models. Most of the measurements concentrated on the ‘real world’ active vertical stack release for the above cases, but there were some measurements for the passive release close to the building roof level.

Numerous probability density function (pdf) measurements have been presented showing the general features of the ‘puff’ release pdf under the range of conditions studied. With increasing distance from the source, the pdf shape varied from exponential-like at short range to near-Gaussian at the farthest downwind locations. The same pattern also holds for the pdf’s with the angled cube cases.

To show the independence of building shape, pdf's for the EW clad and unclad cases were also presented, with a fixed distance from the release point, and these showed the same distribution of a wide variation of dose per puff (in dimensionless concentration, normalised to puff duration) with a sharp peak at low values for the shortest duration releases, again tending to a normal distribution for longer puff releases. Statistical analysis, presented later, is required to draw out subtle differences in the distributions: the general findings are however clear, the pdf general profile is dependent primarily on the puff duration and distance downwind.

From Figures 7.11-7.15 the statistical analysis shows that for the different angles of flow incidence on the cube the coefficient of variation (CV) may be modelled to a given curve by applying a distance form factor, F_x , with the overall magnitude of the curve being a function of distance from the source. In this way the result may be generalised, by applying a distance related function F_x to refine estimates of the CV given the puff length (in the form of PLS/H) which can be readily determined from the wind velocity at the reference height, the duration of the release, and the height of the building. Figures 15.4.4 and 15.4.9 in Appendix 15.4 show that a similar approach can be applied to the 5th percentile of the puff dose, normalised to the mean, but given the limitations due to signal level and number of puff releases in each ensemble, which are particularly apparent in the furthest distance point sampled. Figures 7.13-7.15 show that the method can be applied readily to the 95th percentile values, and the values are similar for the 95th percentile curves for all angles of incidence investigated.

The form factor, F_x , reduces with distance from the source for both the CV and 95th percentile becoming linear in fetch far downwind. For the 5th percentile, where low signal level and lack of samples may be a hindering factor, an increasing function with distance is nevertheless evident.

The variation with CV against PLS/H crosswind laterally across the puff is shown in Figure 7.16(a) for the EW Clad building. As has been seen for the curves relating to the distance from source, the curves can be normalised to a common curve as shown in Figure 7.16(b). The same applies to supplemental results presented in Appendix 15.4: Figure 15.4.5(a/b) (AV) and Figure 15.4.6(a/b) (passive) for the EW unclad case.

For vertical plume sampling we see in Figure 7.17(a/b), for the EW clad case, that the CV versus PLS/H Figure 7.17(a) again collapses to a common curve on normalisation for scale with the form-factor F_z in Figure 7.17(b). The same applies for the AV releases with EW unclad in Figures 7.18(a/b) for the EW unclad case. In Figures 15.4.7(a/b) and 15.4.8(a/b) we see the close to roof releases for the EW clad and unclad cases respectively. In both cases a similar curve is demonstrated versus PLS/H when the form-factor F_z normalisation is applied in the respective (b) figures for these cases.

From the overall summary section 7.3.11, and supplemental results in Appendix 15.4, section 15.4.11, the range of results for the cases studied is summarised. These support the position that there is a common theme of a variation with PLS/H that is relatively invariant to building shape (cube, EW clad or unclad) and angle of approach flow. There is a correction factor F_x to be applied for distance from the source, and for crosswind distance, F_y , from the plume concentration maximum (PCM), and likewise for the distance vertically, F_z , from the PCM. More results to support this are presented in Appendix 15.4 section 15.4.11, with information on F_y in Figure 15.4.12 and F_z in Figure 15.4.14

7.5 Conclusions

The effect of short duration releases was investigated for both building cases at times short enough for dispersion to be affected by building generated turbulent eddies. These were investigated with active vertical stack puff releases, and for passive releases very close to the building roof, for a range of release times - ranging from very short releases equivalent to short length scales on the building to relatively long times approaching more closely to continuous release flow. The detected time traces were recorded at a number of locations ranging from proximal to the plume centreline and offset from this position, and for a limited range of cases at different downwind distances from the release position.

It has been shown generally that the pdf for the puff releases follows an exponential-like distribution with a high preponderance of puff releases doses at low signal level for the short puff releases. For longer duration pulses the pdf tends towards a Gaussian distribution and the length scales in relation to the building where this occurs are shown in this work. This pattern is shown for the cases investigated: the cube at variable incidence of angle of approach flow and the EW clad and unclad different building shapes.

A statistical analysis of the convergence of the mean and coefficient of variation (CV) with number of sampled puff releases indicates that the number of puff releases used in these experiments was sufficient to provide robust estimates of the mean and CV of the puff dose and normalised dimensionless concentration values calculated from these. For completeness, the time sequence of FFID values from a continuous release experiment was also presented which showed convergence to a robust measure of the mean value within the measurement durations used in previous experiments.

Furthermore, it has been possible to draw out some patterns from the data via the results presented. Using the statistical parameters of the coefficient of variation (CV) and the 5th and 95th percentile (from an assumed normal distribution with sampled standard deviation and mean value) it has been shown that the variation of these statistical parameters follows similar characteristic shapes when plotted against the normalised puff length against building height (PLS/H). It is therefore possible to use a characteristic curve based on the mean of the statistical parameter to determine a value of CV, 5th or 95th percentile of the normalised puff release concentration, against a mean value which tends to the continuous release case. Corrections are then required according to the form factors: F_x , F_y and F_z , to obtain values close to the ones experienced at the co-ordinates corresponding to the position of interest in the flow field.

This generalised method should enable, given the relative co-ordinates in the flow field, and in relation to the release height above the building, the determination of the correction factors to be applied when considering a short duration 'puff' release against the mean concentration values obtained from a continuous release of a pollutant tracer into the air stream. In terms of the particular values of interest, the 95th percentile value should enable the confidence interval for exposure to a particular dose threshold of a hazardous material to be set, or in the case of a radioactive material the typical expected maximum daily dose value from inhalation. An example of how the methods developed in this chapter can be applied to a given scenario is given in Chapter 12 covering practical applications of the methodology, where the 95th percentile dose was determined as a ratio against the mean dose for a longer duration release.

CHAPTER 8: MONTE CARLO COMPUTATIONAL METHODS

1. Introduction

The radiation dose received from the radioactive plume in various co-ordinate positions in the roof zone, and elsewhere in the vicinity of the building, was calculated using Monte Carlo (MC) methods. The following analysis deals with a constant radioactive release rate from the source. The plume concentration variation with spatial position had previously been measured from wind tunnel experiments, from which the concentration field had been fitted to parameters which described the steady-state mean Gaussian plume in the roof zone of the building. In this representation the Gaussian plume concentration field was described by parameters which were used to reconstruct the expected mean concentration field value at any spatial point in the simulation world-space. From a given source concentration at a given randomly sampled point in the world space the dose rate received at a given dose sampling point could be calculated, using the specific dose rate constant from the source radionuclide, and making the usual corrections for inverse square fall-off of dose rate with distance from a source and build-up factor in air, the latter also being a function of distance of the receptor point from the source. The methods of carrying out the evaluation of the dose rate integral over the sampled world space containing the plume are described.

Since dose rate from releases of radioactive gases containing positron (anti-electron) emitters were of particular interest, the immersion dose rate from beta (positron) particles was also calculated at a given dose receptor point. Also, the final source of dose in the problem being simulated was the dose received by a person in the concentration field from inhalation of the positron-emitting gases: this latter source of dose was calculated using the usual allowance for inhalation rate at a given receptor position. In this way all sources of dose to a position in the concentration field were calculated and a total dose rate was established corresponding to that receptor position for a given source release rate. Furthermore, the spatial variation of receptor dose was calculated using a sample mesh containing many sample points, including different sampling heights to allow for the vertical variation of concentration field and the sensitivity to height of an individual to the pertaining concentration field.

The parameterised values of the concentration field were available for a range of flow field cases from the wind tunnel experimental results: angle of approach flow to the cube, different release height and whether the release was active vertical or passive into the flow. The variation of dose rate received in the roof zone with these varying parameters could therefore be assessed with the MC code written for this work

8.2 Methods

A continuous and uniform rate of pollutant release has been taken as the source term for the Monte Carlo analysis. The dose rate analysis presented was therefore based on the time - averaged mean concentration field. The formulation of the MC analysis for external gamma-ray dose rate was derived from one of the fundamental texts in the field of MC computation namely Cashwell and Everett (Los Alamos, 1957), and using the gamma-ray dose Gaussian Plume formulation presented earlier (Ibid, Chapter 4 and Appendices 15.5 and 15.6).

8.2.1 Gamma plume-shine integral formulation

Plume gamma dose rate, based on the parameterised mean concentration field, is given by equation [1] which describes the dose kernel from a point source in space adapted from Imai

and Iijima (1970) and shown subsequently e.g. in Overcamp, TJ (1983, 1987, 1991, 2007). The formulation given here matches that provided used by ADMS (CERC, 2012a) and applies to a photon originating from the spatial co-ordinate for the nuclear disintegration. In this analysis we consider the dose arising from a concentration field containing positron emitting nuclei, from which the positron has a range in air before undergoing an annihilation reaction with an electron in air. However, for this analysis the dose kernel formulation for the annihilation gammas treats the gamma ray photons as arising from the same position as the decaying nucleus. This is an approximation, the effects of which will be investigated in further work.

Given the annihilation photon energy is E_γ (eV), positron yield per nuclear disintegration Y , K a constant that relates eV to energy in Joules, concentration $C(\underline{r}, t)$ (a function of time and spatial co-ordinates) we can determine the dose rate value at a given spatial point. The mass energy absorption coefficient term in equation [1] of $\left(\frac{\mu_a}{\rho}\right)$ is expressed as the absorbed dose in air - and the linear attenuation coefficient μ used applies to air. Absorbed dose in air was converted to effective dose using accepted conversion coefficients (CERC, 2012b).

$$\dot{D}_\gamma(t) = K Y E_\gamma \left(\frac{\mu_a}{\rho}\right) \iiint C(\underline{r}, t) B(E_\gamma, \mu r) \frac{e^{-\mu r}}{4\pi r^2} dv \quad [1]$$

Berger's formulation for the build-up is used in this analysis (equation [2]) that matches near-field conditions well (Raza and Avila, 2005) and further published details are reproduced in this work (Gallacher *et al*, 2016, Chapter 4, Ibid). The coefficients a , b are functions of the gamma photon energy E_γ and the mean free path-length (MFP) of the positron annihilation photons (511keV) which is approximately 90m in air.

$$B(E_\gamma, \mu r) = 1 + a \mu r e^{b \mu r} \quad [2]$$

Dimensionless concentrations χ for the concentration field were obtained from sample tracer concentration C , and evaluated with reference wind tunnel wind speed, U_{ref} , the building height, H , and tracer release rate, Q in equation [3].

$$\chi = \frac{C U_{ref} H^2}{Q} \quad [3]$$

From equation [3] the concentration and release rate can be expressed in terms of wind tunnel tracer values, and Q can be used in that context to determine the dimensionless concentration. This dimensionless quantity can be translated to radioactivity concentration C (Bqm⁻³) for a given release rate Q (Bqs⁻¹) and may be used to determine the value of χ for any given set of conditions relating to the radioactive concentration field.

The Monte Carlo (MC) method employs sampling from a probability distribution to obtain a solution value to a physical problem. In this case random co-ordinate sampling was used in a defined 'world-space' which encompassed the radioactive plume, to obtain estimates of the actual radiation dose at a given receptor point. We consider a mono-energetic photon energy E_γ of 511keV corresponding to the annihilation gammas from the positron electron interaction. The co-ordinate vectors \underline{R}_i and \underline{R}_p for the source element and the dose receptor point respectively were measured from the origin of the co-ordinate system at ground level below the source release position. The time variation has been dropped as the mean dose rate is calculated from the mean concentration value measured from the wind tunnel experiments. In this way the mean dose rate from the fitted Gaussian plume profile may be calculated.

$$\overline{\dot{D}_{\gamma,p}} = K Y E_{\gamma} \left(\frac{\mu_a}{\rho} \right) \iiint C(\underline{R}_i) B(\mu |\underline{R}_i - \underline{R}_p|) \frac{e^{-\mu |\underline{R}_i - \underline{R}_p|}}{4\pi |\underline{R}_i - \underline{R}_p|^2} d\mathbf{v} \quad [4]$$

For a given receptor dose point p the volume integral is evaluated over the world space for the MC calculation, given the spatial distribution of concentration. The integrand of equation [4] is expressed in equation [5].

$$\dot{D}_{\gamma,ip} = K Y E_{\gamma} \left(\frac{\mu_a}{\rho} \right) C(\underline{R}_i) B(\mu |\underline{R}_i - \underline{R}_p|) \frac{e^{-\mu |\underline{R}_i - \underline{R}_p|}}{4\pi |\underline{R}_i - \underline{R}_p|^2} \quad [5]$$

We have that, where the suffix i indicates integration over free space:

$$\overline{\dot{D}_{\gamma,p}} = \iiint \dot{D}_{\gamma,ip} d\mathbf{v} \quad [6]$$

Using the mean value theorem, we have that, where the integration is over the world space:

$$\overline{\dot{D}_{\gamma,p}} = \overline{\dot{D}_{\gamma,ip}} \iiint d\mathbf{v} \quad [7]$$

Next, the problem is reduced to the evaluation of the mean value of equation [5] using MC methods:

$$\overline{\dot{D}_{\gamma,ip}} = \frac{\sum_{i=1}^N \dot{D}_{\gamma,ip}}{N} \quad [8]$$

We have that we can easily obtain the volume space integral in equation [7] as the product of the dimensions of the sample world-space, L_x , L_y and L_z , where $V = (L_x L_y L_z)$. From equation [7] we obtain the mean dose rate over the space at the receptor point by taking the mean value of the integrand given in equation [5], provided by equation [8] multiplied by the volume of the world space V . The problem then reduces to evaluation of equation [8] over the range of conditions to be studied. The mean value of dose rate from a plume is then given by equations [7] and [8] and presented in equation [9].

$$\overline{\dot{D}_{\gamma,p}} = V \frac{\sum_{i=1}^N \dot{D}_{\gamma,ip}}{N} \quad [9]$$

Further analysis of the integrand equation [5] is required to achieve an effective method for the evaluation of the mean dose rate integral over the plume. It should be noted that increasing the volume of the world-space will result in the evaluation of the integrand in positions further away from the plume axis and the higher concentration zones, so that the mean value of the summation in equation [8] falls – but this is compensated by the increase of volume, V , in equation [9]. The aim of the MC summation must be to efficiently sample the space with sufficient sample point density to evaluate the integral where the concentration is highest near the plume centreline, but not have the sample space too small to miss contributions from outside of the world zone. Given the complexity of the integral being evaluated a straightforward uniform sampling density algorithm was used throughout the world space which avoided the problem of separate zones within the world space and weighting the contribution of these different zones into the integral evaluation: this enabled sampling multiple dose receptor points in the space without the risk of small discontinuities caused by receptor points being in different zones, particularly at the lateral extremes of the sampled receptor grids used.

8.2.2 Sampled receptor point grid

The sampled receptor point grid was chosen on the basis of a number of considerations such as sufficient sampling density to represent the variation of dose received with position in the roof zone of the building. On the basis of sample runs times of the MC code it was established that 0.5m point spacing in the horizontal (X,Y) plane could be achieved, coupled with three 0.5m sample points in the vertical (Z) direction, centred around the typical height of a person at 1.5m from the roof top level i.e. receptor dose points at heights of 1.0, 1.5 and 2.0m were achieved. The MC code was also written to evaluate the local concentration at all receptor dose points and separately calculate the contributions to radiation dose from the inhalation of the radioactive gases and the beta (positron, in this case) immersion dose at the receptor point. All three contributions were summed for the final analysis. It should be noted that the beta particle immersion dose was evaluated at the receptor point with the prevailing mean concentration field value at that point: consideration of beta particle range and the spatial concentration variation around the receptor point (over the range of approximately one metre in air) was not considered in this analysis. This approximation can be justified on the basis that the most significant contributions to radiation dose were inhalation and gamma shine dose and the contribution from beta particle immersion, and the dose to skin, was considerably smaller, so this approximation had a small effect on the overall dose value.

The receptor point grid was set symmetrically across the approaching wind direction, so that the maximum dose level ran approximately underneath the central axis of the grid space: however, it should be noted that there was plume deflection due to building effects and the resulting flow field and the rooftop recirculation zone was asymmetric and therefore also contributed to inhalation dose and gamma shine dose at a given receptor point. For the evaluation of the dose integrals, the dose was evaluated with respect to a co-ordinate system centred on the release position with the X-axis along the direction of the approaching wind. Therefore, all cases were evaluated using plume spread parameters appropriate for the release height, angle of approach flow and building case: the size of the roof top recirculation zone was inherent in the plume spread parameterisation used in each MC run case studied. For further analysis in this work it was necessary to use a co-ordinate transformation to evaluate the actual roof top position of receptor dose points i.e. to compare MC calculated gamma shine dose rate to that measured from 'sky shine' monitoring detectors placed on the roof of a real building. In most practical applications the dose with respect to the direction of wind will be the most readily applicable.

8.2.3 Co-ordinate sampling in the world-space

The receptor dose points (X_p, Y_p, Z_p) were sampled according to a uniform grid in the (X,Y) plane for a given height Z_p . The start and end points Z_0 and Z_1 were specified in the code parameter input page, along with the segmentation number of the range N_z i.e. the sample space to be divided into N_z intervals. For the loop calculations an integer parameter q was varied to change the receptor dose co-ordinate in the vertical (Z) direction resulting in (N_z+1) receptor point samples vertically.

$$Z_p = Z_0 + (Z_1 - Z_0) \frac{q}{N_z} \quad : q \in [0, N_z] \quad [10]$$

For the sampled space in the horizontal plane we have the indices m and n for X and Y respectively, and starting and ending values (X_0, X_1) and (Y_0, Y_1) , again selected on the parameter input page.

$$X_p = X_0 + (X_1 - X_0) \frac{m}{N_X} \quad : m \in [0, N_X] \quad [11]$$

$$Y_p = Y_0 + (Y_1 - Y_0) \frac{n}{N_Y} \quad : n \in [0, N_Y] \quad [12]$$

The world space, in most of the MC runs, was defined in terms of dimensions X_L , Y_L , Z_L , where the volume of the world space $V = X_L Y_L Z_L$. Three random numbers were generated in order to generate a co-ordinate in the world space at which the concentration was calculated, according to the model, and from which a gamma ray contribution to the integral summation could be evaluated.

$$X_{random} = r_1 X_L; Y_{random} = (r_2 - 0.5) Y_L; Z_{random} = (H + r_3 Z_L) : (r_1, r_2, r_3) \in [0, 1] \quad [13]$$

In all cases studied the world space was rectangular, symmetrical in the crosswind direction about the X -axis direction of approaching wind flow to the building and extending from the building roof level at height H from the origin centred at ground level below the source release point.

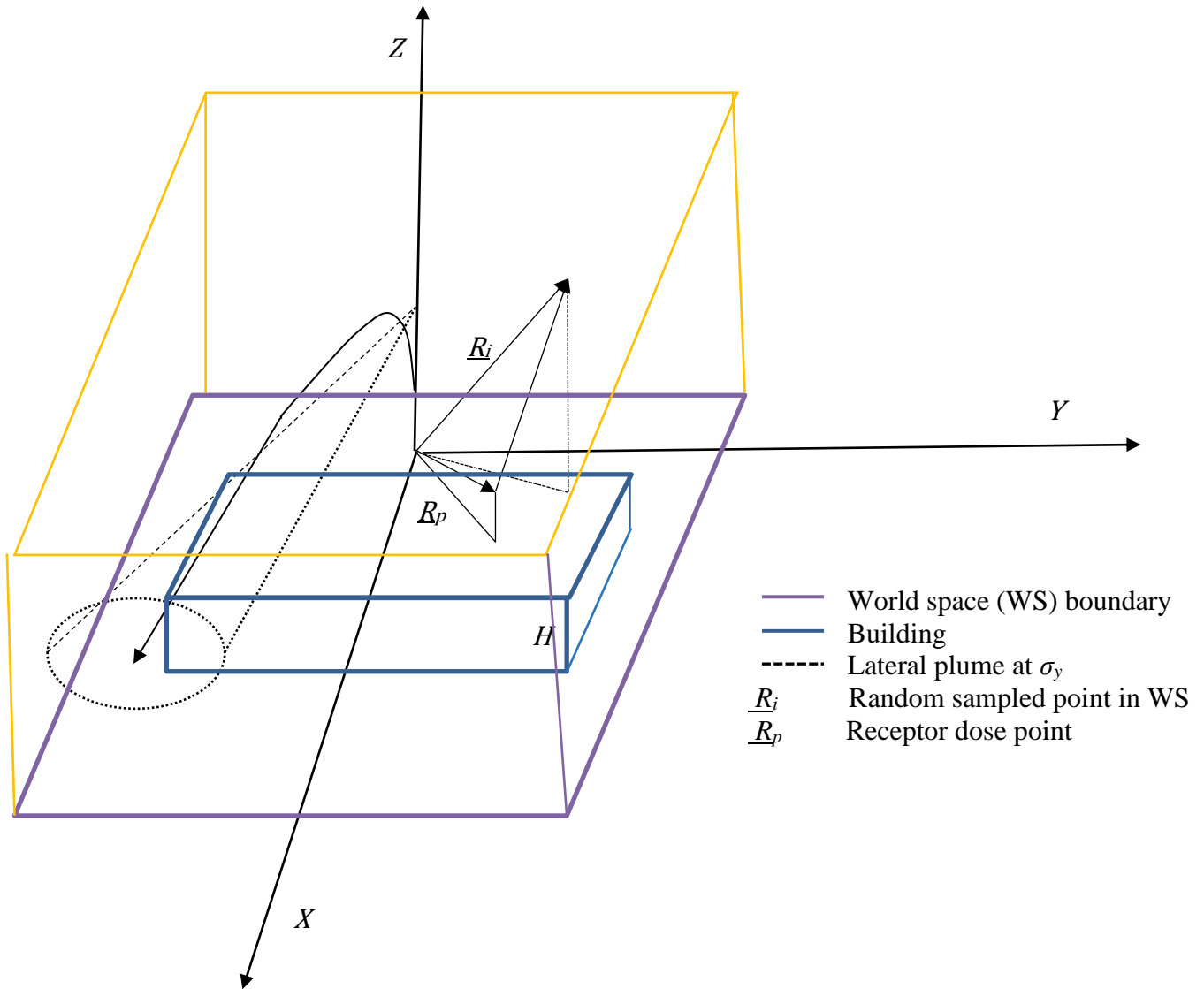


Figure 8.1. MC Calculation co-ordinate axes and plume geometry (Y-Z at ground level)

It should be noted that the world space as shown in Figure 8.1 has a lower boundary at the roof level of the building, and for the MC runs the upstream boundary was at the release point at $X=0$. The downstream boundary of the world space was selected so that it was beyond the maximum extent of the building (including for the angulated case of the cube at -45° to the direction of approaching flow) and further downstream so that all sampled receptor points lay within the world space, and secondly that the error in the gamma ray dose evaluation was acceptably small i.e. that the lost contribution from plume far downwind was an acceptably small fraction of the evaluated gamma ray shine dose level in the roof zone.

8.2.4 Main Recirculation Zone (RCZ) region

The main recirculation zone (RCZ) region in the lee of the building was handled as an extension and adjunct of the main world space. Since the main world space was defined with a lower margin at the roof of the building, it was decided to create the main RCZ, for the purposes of the MC calculation, as an adjunct space at the back of the building but nevertheless contributing to the dose received at any given receptor dose point in the roof zone. This main RCZ zone will be used in the current study as a means to calculate the gamma shine contribution to doses at the roof level proximal to the plume.

A 'line-of-sight' methodology was developed which allowed the gamma ray dose components from fluid elements containing a concentration of the pollutant gamma ray emitting gas to be added to the dose at a given receptor point in the roof zone. The main RCZ was taken to extend to the height of the building, H , and along a distance L_w beyond the back edge of the building length L_b , see Figure 8.2. The random sampled co-ordinate in the main RCZ was denoted (X_i, Y_i, Z_i) and the receptor point at which the gamma ray dose was determined by (X_p, Y_p, Z_p) . By solving the linear equation passing through fixed point $(L_b, 0, H)$ the equation for Z_{ls} the co-ordinates along the line-of-sight varying with X_i is given in equation [14], and the conditions for which the gamma ray dose contribution are added to the dose at the receptor point are also shown.

$$Z_{ls} = H + \frac{X_i - L_b}{X_p - L_b} (Z_p - H) \quad : \text{ if } \{X_i > L_b \text{ and } X_p \leq L_b\} \& \{Z_i > Z_{ls}\} \Rightarrow \gamma \text{ dose added [14]}$$

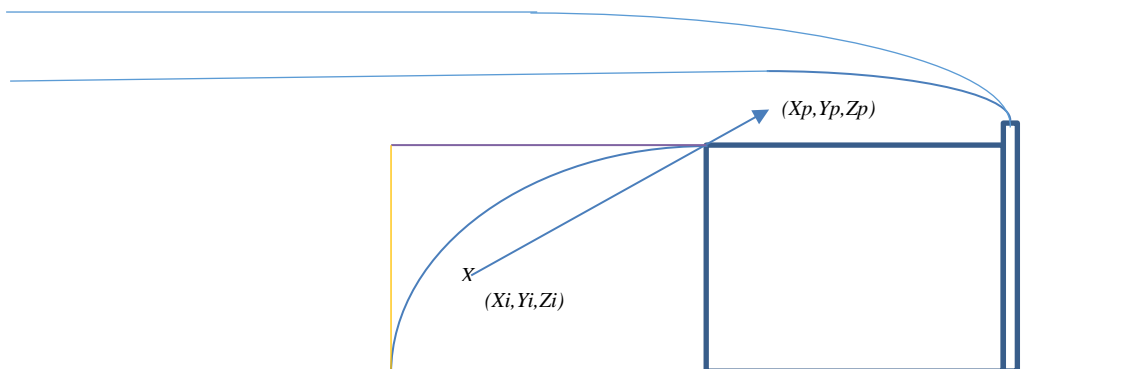


Figure 8.2 Line-of-sight geometry for the sampled points in the main RCZ

Equation [14] with associated conditions is used to determine if the Z co-ordinate of the sampled point in space is above the minimum height of the line-of-sight line and hence has a clear path not intercepted by the building trailing edge along which to contribute to the gamma ray dose integral. This equation is exact along $Y=0$ the central axis of symmetry, and for simplicity variations of Y_i and Y_p from the central axis have been neglected. Similarly, as an approximation for the angulated cases of the cube to which the MC code was applied the main

RCZ was taken to extend from the end of the building at the same distance L_b from the source. Given the relatively small contributions to the gamma ray dose from the main RCZ compared to the main plume immediately overhead of the roof this simplified approximation could be justified. If the MC model were further extended to other cases a more sophisticated model could be developed as further work.

To make best use of the three random numbers already generated to sample the main plume region above the roof these numbers were used again to sample the main RCZ cuboid region. The size of main RCZ region was determined by the three dimensions (X_{Lw} , Y_{Lw} , Z_{Lw}) which were set on the code parameter entry page, and equation [15] shows how the random sample co-ordinate was achieved. An error handling line in the code was made to cover the situation where the receptor point was at the back edge of the building so that $(X_p - L_b)$ was zero, causing an infinity in equation [14]: in these cases the gamma contribution was always added to the dose at the receptor point.

$$\begin{aligned} X_i &= (r_1 X_{Lw} + L_b) \\ Y_i &= (r_2 - 0.5) Y_{Lw} \\ Z_i &= r_3 Z_{Lw} \quad : (r_1, r_2, r_3) \in [0,1] \end{aligned} \quad [15]$$

8.2.5 Plume parameterisation and evaluation of the main plume concentration

The plume data used for the gamma shine dose calculation was based on a conical plume profile with a spread both vertically and horizontally based upon best-fitted values to the experimental data. The height of the main plume shown in equation [16] was set over the roof zone based upon the mean height of the plume concentration maxima (PCM), which was appropriate for a plume of neutral buoyancy, with the mean height reflecting vertical flow deflection effects. For the purposes of the code the normalised plume height Z_{norm} was entered in the parameter code page from which the height of the plume was determined for the MC calculations.

$$Z_{norm} = \frac{(Z_{pcm} - Z_{RH})}{H} \quad [16]$$

Using the conical plume shape means that the plume starts from a source of zero size i.e. at the point of origin. Given that the concentration of pollutant radioactive gas has a uniform value per unit length, with a constant wind velocity and emission rate, which gave rise to a point of infinite concentration at the release point at $(0, 0, Z_{RH})$. Sampling over the whole length of the plume therefore generated potential infinities in the MC dose calculation, or certainly very large values of dose contribution where a random sampled point landed close to the plume origin. A method was therefore developed to eliminate the infinities in the calculation by enabling a finite source size.

The classical Gaussian plume formulation for the problem is given in equation [17] where there is also an added reflection term from the surface of the roof. Since we are dealing with short ranges from the source there is no reflection term from the boundary or mixing layers aloft.

$$C(\underline{r}) = \frac{Q}{2\pi U_H \sigma_y \sigma_z} e^{-\frac{1}{2} \left(\frac{(y-y_0)^2}{\sigma_y^2} \right)} \left\{ e^{-\frac{1}{2} \left(\frac{(z-Z_{RH})^2}{\sigma_z^2} \right)} + e^{-\frac{1}{2} \left(\frac{(z+Z_{RH}-2H)^2}{\sigma_z^2} \right)} \right\} \quad [17]$$

Taking the gradient of the lateral and vertical plume spreads, which were based upon best-fitted concentration weighted values, and a mean value taken over the distance from the source over

the region of the roof, meant that single parameters S_y and S_z describe the conical plume spread in the near field region over the roof and these are used to replace the σ_y and σ_z terms in equation [17]. Both S_y and S_z are functions which are linear in X , and since the problem has been defined in terms of metres in full scale these take the same values at unit distance of 1 metre from the source. We next define an ‘offset distance’ from which the plume would diverge and give rise to a cross sectional area equal to that of the source when positioned at $X=0$ defining the size of the source as covering σ_y and σ_z of the Gaussian plume at that position, see Figure 8.3.

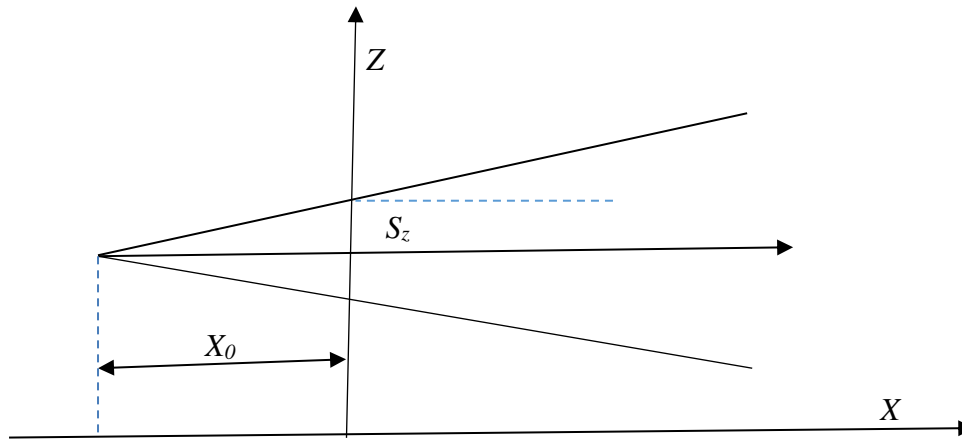


Figure 8.3. Offset distance resulting in the plume extent matching source size at $X=0$

If the physical aperture of the source has a diameter d_0 by equating the areas at $X=0$ we obtain equation [18].

$$(X_0 S_y)(X_0 S_z) = \frac{\pi d_0^2}{4} \Rightarrow X_0 = \frac{d_0}{2\sqrt{S_y S_z}} \quad [18]$$

For the purposes of defining the downstream distance for the calculation of plume centreline concentration we now define the distance from the virtual source as $X_s = (X_{random} + X_0)$. However, this would result in a reduction of concentration i.e. each point in the sample space would appear to be further from the source position. In order to correct for this effect, we modify the plume concentration equation, where we have that χ_1 is the dimensionless concentration at unit distance (1m). It can be seen that X_s is never zero (as X_0 is defined as a positive value) and $\alpha > 0$, hence there is no infinity for random sampled points in the plane of the origin and the dimensionless concentration is set correctly at unit distance from the source.

$$\chi(X_s) = \chi_1 \frac{(1+X_0)^\alpha}{X_s^\alpha} \quad X_s = (X_{random} + X_0) \quad [19]$$

The correction is nevertheless approximate but holds at unit distance and in the limit of large distance from the source, and the difference is acceptably small given the small source size (diameter 0.3m) evaluated in the MC calculations.

The spread of the plume was accounted for using the offset methodology as shown schematically in Figure 8.3. At each downstream position the dispersion parameter was calculated using X_s from equation [18] multiplied by the normalised for distance dispersion parameters S_y and S_z to obtain the Y_{sd} and Z_{sd} plume spread at any given downstream distance from the source. Furthermore, the co-ordinates in the roof zone for the lateral position of the

plume concentration maximum Y_{pcm} were determined based on the mean deflection of the plume established from the experimental data for each experimental condition assessed.

From equation [17] we also see that there is a reflection term from the roof. Given that the main world space only generated random co-ordinates down to the roof plane at height H from the ground it was decided to apply this equation in sampled regions of the world space further downstream than the immediate roof zone. The reason this choice was made was that otherwise the portions of the plume extending downwards past the building would not be accounted for in the sampled points and their contributions to the gamma dose integral would not be accounted for – applying the equation with the reflection term meant that the concentration would be reflected back into the sampled world-zone and would contribute to the gamma-ray dose summation. At sampled distances downstream from the building the distances to receptor points near the rooftop would be very similar compared with those for a plume that had been allowed to extend downwards in an extended world-zone: this approximation could therefore be justified, also on the basis that the dose rate from a given sample element falls with inverse square of the distance.

A number of factors were applied to calculate the value of the dimensionless concentration based upon the plume centreline value, itself a function of distance from the source as described. The factors were applied in the Y , Z directions and also a factor to account for the reflection term to correctly normalise this at the plume centreline. A factor was also added to radioactive decay with time of flight from the source.

$$F_y = e^{-\frac{1}{2} \left(\frac{(y-y_{pcm})^2}{Y_{sd}^2} \right)} \quad [20]$$

$$F_z = \left\{ e^{-\frac{1}{2} \left(\frac{(z-z_{pcm})^2}{Z_{sd}^2} \right)} + e^{-\frac{1}{2} \left(\frac{(z+z_{pcm}-2H)^2}{Z_{sd}^2} \right)} \right\} \quad [21]$$

$$F_h = \left\{ 1 + e^{-\frac{4(z_{pcm}-H)^2}{2Z_{sd}^2}} \right\} \quad [22]$$

Given the advection velocity U_{adv} applying at the plume concentration maximum, the time of flight for the distance T_d can be calculated as follows, and the decay factor on the concentration of radioactivity F_t in equation [23] given the half-life of the radionuclide $T_{1/2}$. For the low atomic number positron emitting radionuclides under consideration there is no radioactive daughter product to consider in the decay process. The short advection times to the points under consideration at very near distances would in any case largely eliminate this problem for other radionuclides were they considered: nevertheless, were it required the analysis could be extended to account for growth of daughter radionuclides in the advected flow with time of travel from the source.

$$F_t = e^{-\ln(2) \frac{T_d}{T_{1/2}}} \quad \text{where:} \quad T_d = \frac{X_s}{U_{adv}} \quad [23]$$

$$\chi(X_s) = \chi_1 \frac{(1+X_0)^\alpha}{X_s^\alpha} \left(\frac{F_y F_z F_t}{F_h} \right) \quad X_s = (X_{random} + X_0) \quad [24]$$

From equations [20]-[24] we can therefore calculate the concentration of the main plume in the world-space.

8.2.6 Roof Recirculation Zone

The roof recirculation zone was included in the MC analysis when the experimental results for modelling the Dual Gaussian Plume (DGP) were used. This was a technique by which the measured concentration profiles, at a range of downstream positions in the wind tunnel, were de-convolved into a main plume and a secondary plume. Generally, the secondary plume corresponded with a region in the roof zone where there would be some recirculation of flow and pollutant – or otherwise where there was a bifurcation of the plume due to splitting in the flow field for a given set of experimental conditions.

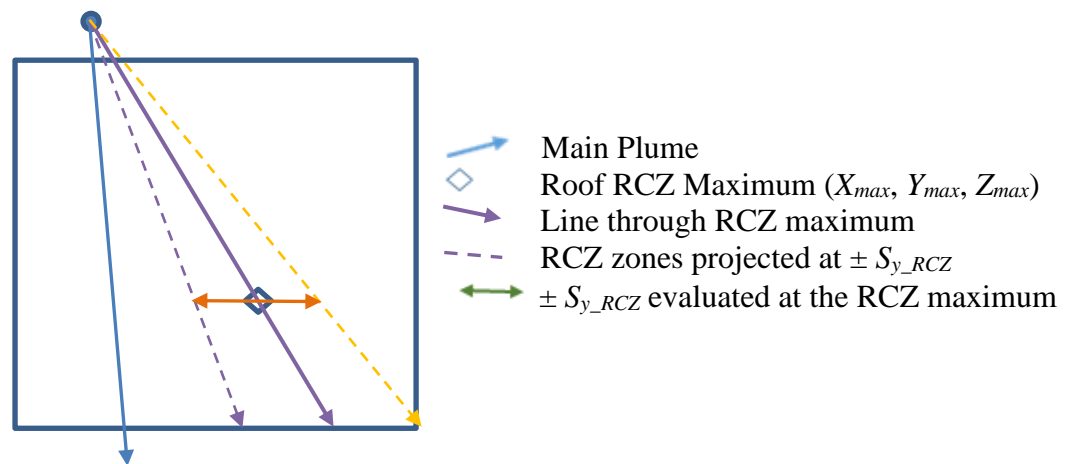


Figure 8.4(a). Roof recirculation zone (RCZ) co-ordinate and geometry

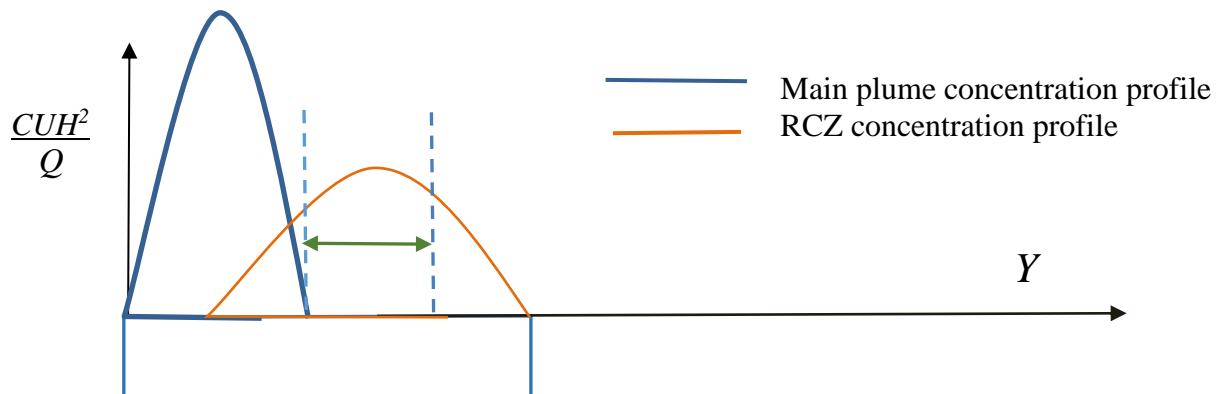


Figure 8.4(b). RCZ lateral deconvolved concentration profiles at $(X_{max}, Y_{max}, Z_{max})$

Figures 8.4(a) and 8.4(b) show how the roof top RCZ was modelled in the MC analysis. The maximum concentration was identified $(X_{max}, Y_{max}, Z_{max})$ and the lateral spread of the RCZ estimated at this point using the term S_{y_RCZ} i.e. the dispersion parameter σ_y applying for the RCZ, which were found to conform well to a Gaussian profile in the crosswind direction and was obtained from the experimental results for each case. Figure 8.4(b) shows schematically how the profiles of concentration vary with lateral distance (Y) and the figure is aligned with Figure 8.4(a) to show how the deconvolved profiles correspond spatially in the (X, Z) plane through the position of the RCZ maximum. The measured concentration field value is the superposition of the main plume and RCZ values at any point in the lateral profile.

Furthermore the gradient of the line, in the horizontal (X,Y) plane, from the origin through the RCZ maximum concentration point was determined and the width of the Gaussian RCZ lateral profile S_{y_RCZ} at different positions was determined by scaling with downstream distance from the source. The concentration was scaled according to a lateral fall-off Gaussian function F_{y_RCZ} given in equation [25].

$$F_{y_RCZ} = e^{-\frac{1}{2} \left(\frac{(y-y_{RCZ,max})^2}{S_{y_RCZ}^2} \right)} \quad [25]$$

The function was truncated at height Z_{RCZ} and at the downwind edge of the building. The RCZ was set with a uniform concentration along the centre line through the maximum concentration point along the path over the roof: the mean value was estimated from the maximum concentration at 1.5m from roof level (or the nearest available data point) and the maximum concentration at any height below Z_{RCZ} . This mean was to establish a value consistent with the well-mixed zone associated with a recirculation region.

8.2.7 Receptor point size and the dose point kernel (DPK) method

The receptor dose points close to the plume centreline were immersed within the plume, so there were high concentrations at or proximal to these points. As the dose point kernel (DPK) method involves an inverse-square term for the dose rate with distance between source and receptor point, a sampled source point co-incident with the receptor point would give rise to an infinity in the calculations: source points close to receptor points would give very large dose values skewing the dose results, given that the sampling density is still relatively sparse even with the high number of source events considered in this analysis. Initial runs without a correction for this effect showed high levels of spatial variation in calculated dose levels between adjacent receptor points. This was a statistical variation arising from some runs having higher numbers of simulated MC simulated events being close to a given receptor point – a consequence of the relatively sparse sampling. Radiation dose is a scalar quantity which is determined experimentally using the dose received inside an ICRU sphere of finite size (ICRU, 1998). A similar approach was adopted for the MC code where a sphere centred on the receptor point of radius ε was used to eliminate infinities: a generated sample point laying within the sphere was re-allocated a radial distance ε for the purposes of the dose calculation. In effect, the receptor was being given a finite size, from inside which radioactive emissions were excluded corresponding to a spherical volume in which doses were evaluated but small enough to not overly perturb the validity of the concentration field measurements. This follows the convention that radiation dose is evaluated as an integral quantity over a given volume but limiting values for smaller volumes can be extrapolated. The size of ε was set according to the size of the spacing between receptor points in the (X,Y) plane Δ_X and Δ_Y as follows in equation [26].

$$\varepsilon = \frac{\sqrt{\Delta_X \Delta_Y}}{5} \quad [26]$$

The sphere radius for ε was therefore set at a small fraction (one fifth) of the spacing between receptor points so as not to perturb the accuracy of the dose estimation. This factor was arrived at by analysis of repeated runs and an assessment of the impact on the dose results when calculated for a grid of receptor points.

8.2.8 Calculation of the dose rate levels from different zones

The dimensionless concentration was used according to equations [2], [3], [5] and [9] to evaluate the dose rate contribution from the plume gamma shine. All calculations were performed for a uniform release rate of radioactive material to determine a dose rate at the receptor point for a steady release with a given wind direction.

The contribution to the gamma-ray dose rate at a given receptor point from the roof RCZ was also determined separately as was the dose rate from the main RCZ extending to ground level beyond the downwind edge of the building.

Two other important contributors to the dose received (by a person at a given receptor point) were included in the analysis. Firstly, the inhalation dose based upon the concentration at a receptor point above the roof plane, and secondly the beta immersion dose from the cloud of activity around the receptor point. The inhalation dose is given in equation [27] where the local concentration C can be determined from the dimensionless concentration χ given by equation [3], where Q is the release rate (Bq.s^{-1}), \dot{V}_{inh} is the volume rate of inhalation taken as $1.2\text{m}^3\text{h}^{-1}$ consistent with light work and D_{inh} is a conversion coefficient from inhaled activity to effective dose (Sv.Bq^{-1}) both taken from ICRP Report 72 (ICRP, 1996).

$$\dot{E}_{inh} = C\dot{V}_{inh}D_{inh} \quad [27]$$

For the beta immersion doses (and for these MC experiments a positron emitting radionuclide was considered) the local dose is approximated to that arising from a uniform semi-infinite cloud (Piltingsrud and Gels, 1985). The beta/positron range is limited in air so that the concentration of the cloud around a receptor point being based upon the local concentration at the receptor point will be a justified assumption. Further developments in the model as part of further work would allow for the incorporation of a more complex beta range energy loss model. Equation [28] converts the local concentration at the receptor point to a beta-immersion effective dose according to the method presented in NRPB W-63 (MacDonnell, 1994)

$$\dot{D}_\beta = \left(\frac{2.3 \times 10^{-4}}{3600}\right)C\bar{E}_\beta w_T \quad [28]$$

Effective dose rate from beta particle immersion was \dot{D}_β ($\mu\text{Sv.s}^{-1}$) for a concentration determined from equation [3] for a given release rate Q (Bq.s^{-1}) and mean particle emission energy \bar{E}_β (MeV). The tissue weighting factor w_T that converts equivalent dose to skin to effective dose was 0.01 as determined from ICRP103 (ICRP, 2007).

A combined effective dose rate, including inhalation dose rate from the local concentrations, gamma-ray shine contributions and beta/positron immersion doses, was calculated for all cases. The inhalation and beta immersion doses were primarily calculated for a height of 1.5m above the roof level to represent the breathing height of a person standing on the roof of a building. The calculation of overall effective doses was performed for all receptor dose points in the sampled region, including for the heights of 1.0, 1.5 and 2.0m above the roof level. This calculation was also additionally performed at the maximum concentration in the roof zone and also for the maximum concentration point in the rooftop RCZ. In the series of MC calculations performed, where the main radionuclide of interest was the positron emitting ^{18}F the bulk of the received effective dose at the receptor points was from inhalation.

8.2.9 Practical considerations with respect to the MC code and runs

Specimen examples are presented in the results section. The MC runs shown were completed with $N=5 \times 10^5$ samples for each receptor point, with mesh spacing of 0.5m in the (X, Y) plane and Z-axis samples at 1, 1.5 and 2m from the roof plane of the building. The code parameter input page for the run is shown as follows in Table 1. The run over 24,000 receptor points took 10.5 hours on a quad core processor running C# via Microsoft Visual Studio 2017.

MC Run	Iterations	500000	Xdim_conc_1m	49164
Zrh(release height,m)	49.0		alpha	2.082
Ypcm/Xs	-0.0812		Xdim_conc.max_roof	32.149
Zpcm_norm	0.0556		Xs_max_conc/H	0.67
Sy/Xs	0.1075		Xdim_conc_RCZ_max	15.566
Sz/Xs	0.1391		Xs_max_conc_RCZ	32.0
Sy_RCZ/H	0.1705		Ys_max_conc_RCZ	5.460
Z_rcz/H	1.271		Zs_max_conc_RCZ	49.5
Zstart	49.0		Xdim_conc_RCZ_mean	12.02
Zend	50.0		X_length_main	150.0
Xstart	5.0		Y_length_main	50.0
Xend	55.0		Z_length_main	25.0
Ystart	-20.0		X_length_wake	48.0
Yend	20.0		Y_length_wake	48.0
mesh_Nx	100		Z_length_wake	48.0
mesh_Ny	80		Xdim_conc_wake	2.572
mesh_Nz	2		Uref (F/S at 200m) (m/s)	5.53
Q (Bq/s)	417000		d0 (m)	0.30
Radionuclide	F-18		Half-life (mins)	109.728
Roughness Z0 (m)	1.0		Ys_max_conc/H	-0.0529

Table 8.1: MC code parameter input page (where not otherwise specified distances are in metres)

8.3 Results

Specimen output from the MC code is included here to illustrate the results obtained. A systematic analysis is presented for all the results in the context of the experimental results in a later chapter of this work.

8.3.1 Combined dose rate from all routes (inhalation, positron immersion, gamma-rays)

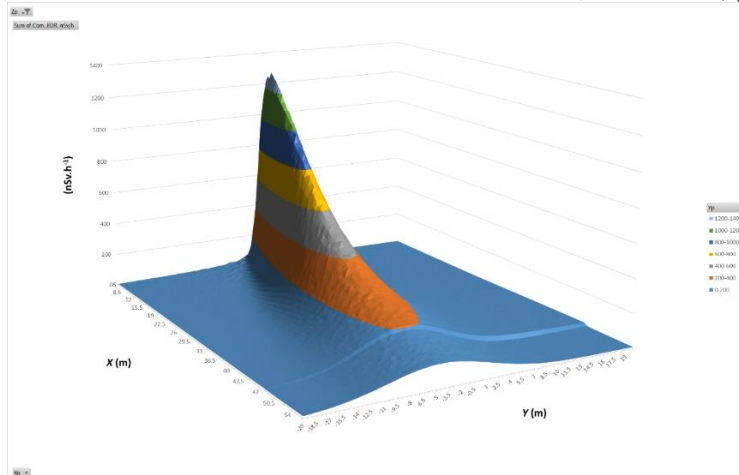


Figure 8.5. Cube, release position A, normal incidence of flow, $(Z_{rh}-H)/H=0.021$

From Figure 8.5 we can see that the total effective dose rate peaks at just over $1.2\mu\text{Sv h}^{-1}$ for all dose rate contribution terms. The receptor grid was defined at 5m to 55m from the source release position at $X=0\text{m}$, and release position A is defined at spacing $H/10$ from the vertex of the cube offset and laterally.

8.3.2 Combined dose rate from gamma-ray dose rate sources

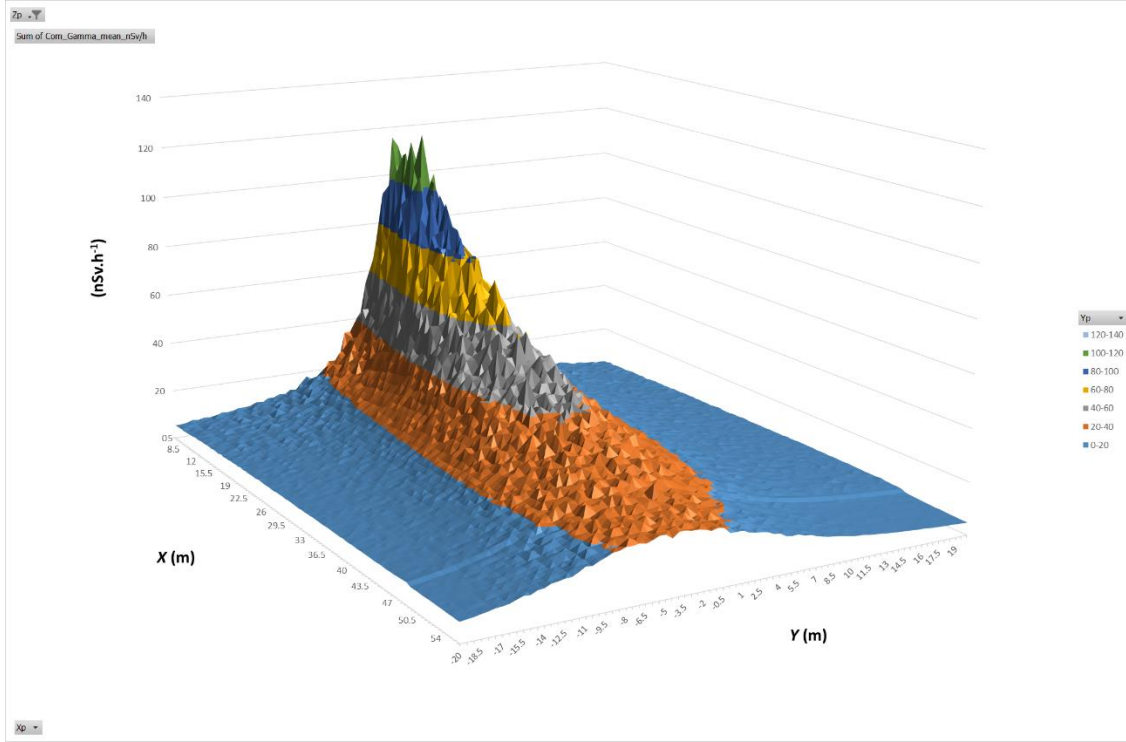


Figure 8.6. Gamma ray dose rate: cube/A, normal incidence of flow, $(Z_{rh}-H)/H=0.021$

From Figure 8.6 we see that the gamma ray peak dose rate is just under 10% of the peak dose rate from Figure 8.5, indicating that the inhalation dose rate for the case considered is a significant component of the dose rate. Fluctuations in the dose rate estimates with spatial position are evident and this was attributed to the relatively sparse sampling giving statistical variations between nearby sampled receptor points. The sampling density was nevertheless sufficient to give a good indication of the spatial variation of gamma-ray dose over the concentration field.

8.4. Discussion

A Monte Carlo (MC) code was developed based upon the dose point kernel (DPK) method for radioactive gases being emitted in the near-field of a building array. The calculations were based upon empirical data from wind tunnel experiments to determine the concentration field for various experimental conditions. The code was written to apply the methodology of the simplified conical Gaussian plume, using fitted parameters for plume spread based on concentrated weighted averages from the wind tunnel experimental data.

8.5 Conclusion

The dose point kernel estimates of dose rate from these calculations, based on a uniform release rate of pollutant, estimate the radiation dose rate in the near-field region of the roof zone of the emitting building, taking into account plume upwards and sideways deflection and spread in the horizontal and vertical directions. Adaptations were necessary in order to avoid infinities in the point sampled method to estimate the mean gamma-ray shine dose rate at the receptor points.

CHAPTER 9: MONTE CARLO RESULTS

9.1 Introduction

The results of the Monte Carlo (MC) calculations are presented in this chapter, following on from the previous chapter where the computational methods were detailed. Two main sets of results from running the MC code are presented: firstly, the total dose rate resulting from inhalation, immersion in the concentration field and gamma ray dose rate, and secondly the dose rate received from just gamma rays. In the case of the inhalation (and immersion) doses the most important factor is the concentration of pollutant around the receptor point (and three heights above the roof plane were chosen in this analysis) so the combined dose rate term reflected the concentration field spatial variation. The gamma ray dose is delivered at a distance from the point of radioactive disintegration, so the gamma ray dose at a receptor point depends on the spatial distance to the distribution of concentration overhead as well as being affected by local concentrations around the receptor point. This work extends that in the literature by being able to compute the local doses within and very close to the plume centreline or maximum concentration positions – analytical integral dose calculations from adapted Gaussian plume models attempting to calculate radiation dose close to the plume centreline are severely compromised (Overcamp, 1983, 1897, 1991, 2007) by poor convergence of the integrals close to the plume centreline and where the receptor point lays within the extent of the plume. The MC calculations presented in this work were not subject to the same convergence problems as the potential infinities were excluded (Ibid, Chapter 9) by use of a sample sphere analogous to the ICRU sphere (ICRU, 1992) for determining radiation dose in a radiation field.

The results given in this chapter represent the variation of the dose received with the range of parameters tested, such as angle of wind approach flow to the building, release position in relation to the building, release height, and building geometry. The approach taken has been to give the dose rates according to a fixed release rate of radioactive pollutant release (Gallacher *et al*, 2016a, Ibid Chapter 4 and Appendices 15.5/15.6) so that the relative dose rate variations can be seen. To obtain a dose rate normalised to unit release rate in any given case the dose rate may be divided by the release rate of radionuclide. All results are given for a fixed wind velocity determined upstream of the building and a straightforward correction to a different value of wind velocity would be required to generalise the results. The results are presented for a specific emission, ^{18}F , a positron emitting radionuclide which is very commonly produced (Kleck *et al*, 1991) in healthcare facilities using proton bombarding cyclotrons for use in positron emission tomography (PET) scanning of patients, and typically forms the bulk of production in many facilities (GE Healthcare, 2012).

Table 9.1. Monte Carlo cases analysed

#	Building	Metric	Z_{rh} (mm)	Angle	Method analysis	of	Release type	Position
1	Cube	EDR	**	0°, -22.5°	DGP		Passive	A
2	Cube	EDR	**	-45°	DGP/SGP		Passive	A
3	Cube	EDR	**	-45°	GA* DGP/SGP	–	Passive	A
4	Cube	EDR/ γ -ray	**	0°, -22.5°	DGP		Passive	A
5	Cube	EDR/ γ -ray	**	-45°	DGP/SGP		Passive	A

6	Cube	EDR/ γ -ray	**	-45°	GA* DGP/SGP	–	Passive	A
7	Cube	EDR/ γ -ray	245m m	0°, -22.5°,- 45°	DGP/SGP		Passive	A
8	Cube	EDR	255m m	0°,-22.5°,- 45°	DGP/SGP		Passive	A
9	Cube	EDR	265m m	0°,-22.5°,- 45°	DGP/SGP		Passive	A
10	Cube	EDR	275m m	0°,-22.5°,- 45°	DGP/SGP		Passive	A
11	Cube	EDR	**	0°, -22.5°	DGP		Passive	B
12	Cube	EDR	**	-45°	DGP/SGP		Passive	B
13	Cube	EDR	**	-45°	DGP/SGP		Passive	B
14	Cube	EDR/ γ -ray	**	0°, -22.5°	DGP		Passive	B
15	Cube	EDR/ γ -ray	**	-45°	DGP/SGP		Passive	B
16	Cube	EDR/ γ -ray	**	-45°	GA- DGP/SGP		Passive	B
17	Cube	EDR	245m m	0°,-22.5°,- 45°	DGP/SGP		Passive	B
18	Cube	EDR	255m m	0°,-22.5°,- 45°	DGP/SGP		Passive	B
19	Cube	EDR	265m m	0°,-22.5°,- 45°	DGP/SGP		Passive	B
20	Cube	EDR	275m m	0°,-22.5°,- 45°	DGP/SGP		Passive	B
21	EWC/UC	EDR	**	-22.5°	DGP		Passive	Vertex
22	EWC/UC	EDR	**	-22.5°	SGP		Passive	Vertex
23	EWC/UC	EDR	**	-22.5°	GA-DGP		Passive	Vertex
24	EWC/UC	EDR/ γ -ray	**	-22.5°	DGP		Passive	Vertex
25	EWC/UC	EDR/ γ -ray	**	-22.5°	SGP		Passive	Vertex
26	EWC/UC	EDR/ γ -ray	**	-22.5°	GA-DGP		Passive	Vertex
27	All	EDR/ γ -ray	255m m	-22.5°	GA-DGP		AV	V/A/B
28	Cube	EDR	255m m	0°, -22.5°, -45°	GA-DGP		AV	A/B
29	Cube	EDR/ γ -ray	255m m	0°, -22.5°, -45°	GA-DGP		AV	A/B
30	Cube	X_{max}	**	0°	DGP/SGP		Passive	A
31	Cube	X_{max}	**	-22.5°	DGP/SGP		Passive	A
32	Cube	X_{max}	**	-45°	DGP/SGP		Passive	A
33	Cube	X_{max}	**	0°	DGP/SGP		Passive	B
34	Cube	X_{max}	**	-22.5°	DGP/SGP		Passive	B

35	Cube	X_{max}	**	-45°	DGP/SGP	Passive	B
36	All	X_{max}	**	-22.5°	DGP/SGP	Passive	A/B/Vertex
37	Cube	ΔY	**	0°	DGP/SGP	Passive	A
38	Cube	ΔY	**	-22.5°	DGP/SGP	Passive	A
39	Cube	ΔY	**	-45°	DGP/SGP	Passive	A
40	Cube	ΔY	**	0°	DGP/SGP	Passive	B
41	Cube	ΔY	**	-22.5°	DGP/SGP	Passive	B
42	Cube	ΔY	**	-45°	DGP/SGP	Passive	B
43	Cube	ΔY	**	-22.5°	DGP/SGP	AV	B
44	Cube	EDR/ γ -ray	245m m	0°	DGP	Passive	A
45	Cube	EDR/ γ -ray	245m m	-22.5°	DGP	Passive	A
46	Cube Z=49.0m	EDR/ γ -ray	255m m	-45°	DGP	Passive	A
47	Cube Z=49.5m	EDR/ γ -ray	255m m	-45°	DGP	Passive	A
48	Cube Z=49.5m	EDR/ γ -ray	255m m	0°	DGP	Passive	B
49	EWC	EDR/ γ -ray	255m m	-22.5°	DGP	AV	Vertex
50	Cube Z=49.5m	EDR/ γ -ray	255m m	-22.5°	DGP	AV	A

*-GA: grid-averaged dose rates over 5m x 5m grid

** : various release heights sampled range over experiments

EDR: effective dose rate; EDR/ γ -ray: effective dose rate from gamma-rays

AV: active vertical release

9.2 Methods

A continuous and uniform rate of pollutant release has been taken as the source term for the Monte Carlo analysis. The dose rate results presented relate to the mean concentration field measured from wind tunnel experiments. Following on from the previous convention the real-world full-scale dimensions are stated in metres (m) and the wind tunnel dimensions are specified in millimetres (mm) which relate to wind tunnel model scale.

All results were specified with a release rate of 0.417MBq s^{-1} or 12GBq per assumed 8 hour working day, pro-rata of an annual total source term of 3TBq , assuming 250 working days per year. It is accepted that the pattern of release during any given day is time variant and is represented by a series of intermittent ‘puff’ releases. However, the mean dose from a series of puff releases has been shown (Ibid, Chapter 7) to converge to that from a continuous release, given sufficient puff releases, and the statistical variations of dose per puff have also been presented in that chapter with methods to evaluated likely upper bound doses in relation to the mean dose per puff. It follows that the inhalation and immersion dose components calculated from the MC analysis can be scaled according to the methods developed in Chapter 8. It will be seen that given the majority of the dose from the ^{18}F radionuclide investigated arises from inhalation the total effective dose rate from results in this chapter can be scaled to provide an approximate upper dose estimate: e.g. the 95th percentile dose.

Wind speed of the approaching flow was specified at 5.53ms^{-1} at 200m from ground level, or approximately at free stream. By use of a wind velocity power law exponent of $n = 0.2$, the wind velocity at 10m height corresponding to this velocity would be 2.76ms^{-1} , which matches the Heathrow five-year data set cited in previous publications (Gallacher *et al*, 2016a/b), where the pollutant release rate was also set the same, in order that all dose results may be directly compared.

In order to calculate a more broadly applicable dose rate level, the mean dose in a receptor grid (at each of the three receptor dose point heights) was calculated to simulate a situation where either the person receiving the dose is working at roof level in a certain region for a period of time, or to make an allowance for small fluctuations in the wind direction meaning that the concentration maximum location will move slightly over a period of time. These mean values were established over an 11 x 11 grid at the sample mesh spacing in the horizontal plane: given that the standard mesh spacing was 0.5m this corresponded to a 5m x 5m sample region in the (X, Y) plane. For double mesh sampling the corresponding sizes were 2.5m x 2.5m and for half mesh sampling 10m x 10m. The central value of the averaging grid was the local maximum for the combined effective dose rate. A separate grid was applied to the local maxima of the gamma ray dose where the positional co-ordinates in the (X, Y) were often in a different location to the maxima for the combined effective dose rate.

A large number of results are presented in this chapter. There are three main reasons for this. The first is to demonstrate the dependence of dose levels on the parameters investigated in the wind tunnel work – and then to interpret that in the context of actual emissions at a real site. The second reason is to provide comprehensive data that can be used, for example, by third parties to estimate doses in similar circumstances. Finally, the data can be used to help design wind tunnel or CFD work to apply the methodology to other sites of different character.

3. Results

Specimen data are presented from the MC code output to illustrate the results obtained. A systematic analysis is presented for all the results in the context of the experimental results in a later chapter of this work.

9.3.1 Variation of radiation dose rate with release height and angle

9.3.1.1 Cube with release position 'A'

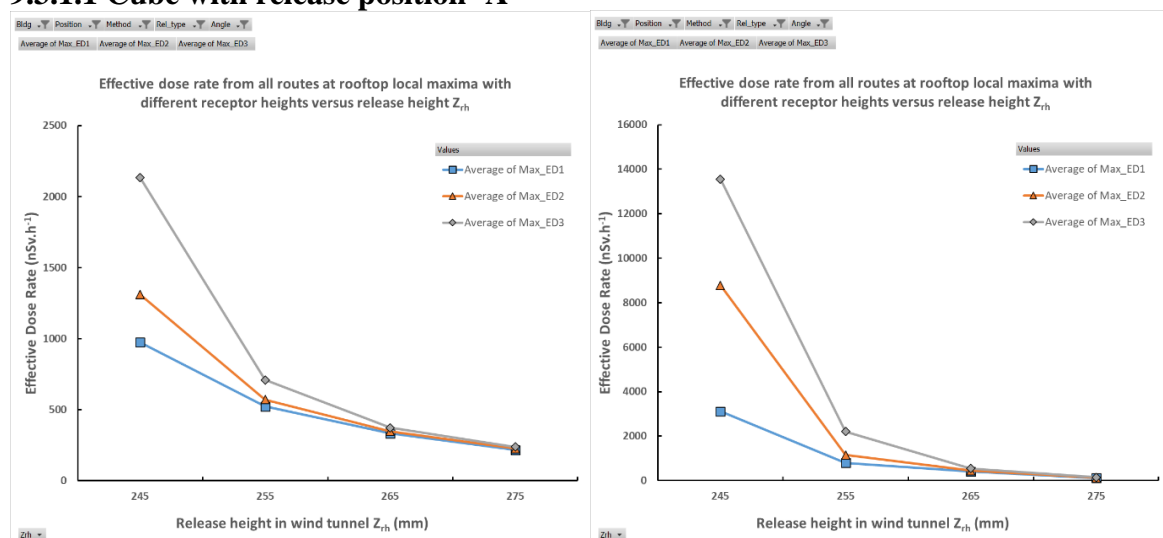


Figure 9.1(a/b). Cube, passive release, position 'A', DGP, dose rate maxima as function of release height (a) 0° ; (b) -22.5° . The terms ED1, ED2 and ED3 refer to effective dose at different heights from the roof: respectively 1.0, 1.5 and 2.0m above the roof.

From Figure 9.1(a/b) we can see that the total effective dose rate (from all dose rate contribution terms at the maxima receptor point) is greatest, at just under $14\mu\text{Sv h}^{-1}$, for the highest receptor point at 2m height from roof (ED3) in (b) at -22.5° and is lower for the peaks at 1.5m (ED2) and lowest for the receptor point closest to the roof at 1m height (ED1). The receptor grid was defined over 5m to 55m from the source release position at $X=0\text{m}$, and release position 'A' is defined at spacing $H/10$ from the vertex of the cube offset and laterally. For the normal incidence case in (a) the corresponding maxima are significantly lower, with the greatest value (ED3) at just over $2\mu\text{Sv h}^{-1}$. This can be attributed to the behaviour of the flow field where initial upwards deflection was observed for the normal incidence cases followed by modest downwards deflection when moving further over the roof zone in the streamwise direction. The -22.5° angled case in (b) shows the maximum for the ED3 receptor (2m above roof plane) because the plume has been advected down and mixed sufficiently to intercept a receptor on the roof, again seen in the flow field for the cube at this angle: in the simulation here the greater proportion of the dose arises from inhalation of the radionuclide so elevated concentration field value proximal to the detector will increase dose significantly and this is the reason for the large difference between the -22.5° maximum dose and that for normal incidence. In figures (a) and (b) the effective dose rate reduced with the height of passive release from 245mm (just 5mm above the roof level, or at 1m full scale) up to the greatest release height computed of 275mm (or 7m above the roof plane at full scale).

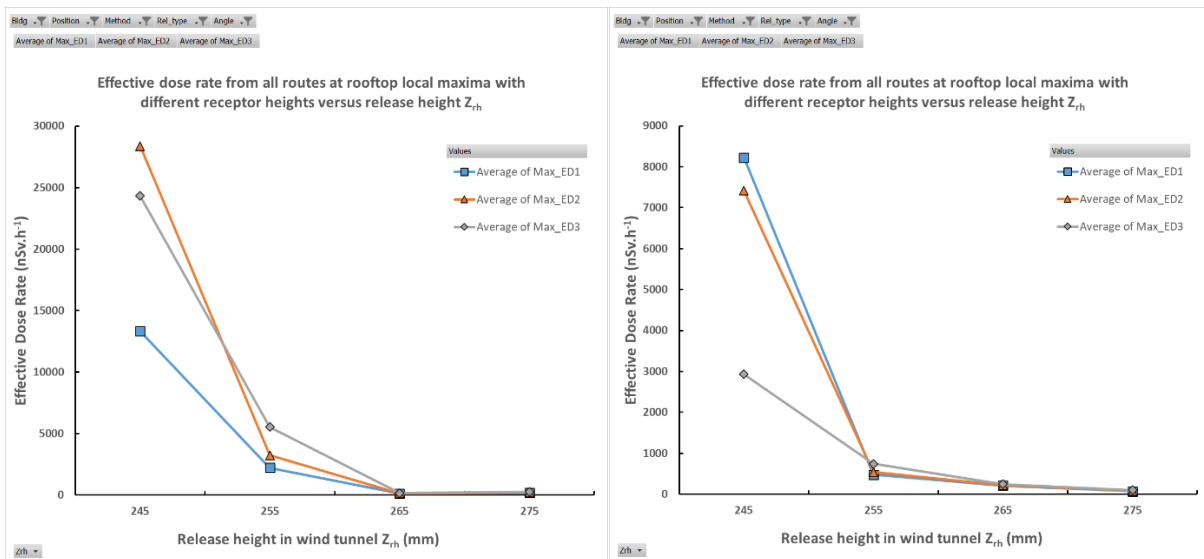


Figure 9.2(a/b). Cube, passive, position 'A'; -45° incidence, dose rate maxima as function of release height (a) DGP; (b) SGP

From Figure 9.2(a/b) (with the -45° angle of approach flow) it is seen that the peak level of dose for the DGP method in (a) was approaching $30\mu\text{Sv h}^{-1}$ for ED2 at 1.5m from the roof level at the lowest release height of 245mm and marginally greater than that at ED3 at 2m from the roof level at approximately $25\mu\text{Sv h}^{-1}$, a situation which reverses at the next highest release height of 255mm. By contrast the simpler SGP method only gives rise to peak dose rates (at the local maxima) in the region of $8\mu\text{Sv h}^{-1}$ for the 245mm release height. The bulk of this difference may be attributed to the broader and shallower concentration profiles needed to fit the complex flow field, including the recirculation region, to a single plume profile. It was seen in Chapter 6 that the dual peaks of the concentration field, whether attributed to plume bifurcation or the presence of a rooftop recirculation region, were better modelled with the DGP approach. In terms of the explanation from the flow field the -45° case has strong rooftop generated vortices which cause

advection and mixing of material downwards towards near the roof, which in this case means that the maximum dose rate occurs at ED2 (1.5m from the roof plane) rather than at ED3 (2m from the roof plane) seen in Figure 9.1(b) for the -22.5° case.

In Figure 9.3(a/b) we see the effect of taking the mean value of the effective dose rate over the sampled 11 x 11 grid in the (X, Y) plane using the DGP and SGP methods. The dose rates are reduced from averaging over the 5m x 5m grid in this case, for both the (a) DGP and to a lesser extent the (b) SGP case. Whichever of these two approaches needs to be supplied would depend on the safety case or radiological assessment being performed. In the case of a different pollutant where there was a maximum tolerable dose from a given release the more conservative peak dose at a receptor point could be adopted. In the case where the duration of release and occupancy of the working zone were over a longer period of time the dose rate averaged over the grid may be more appropriate.

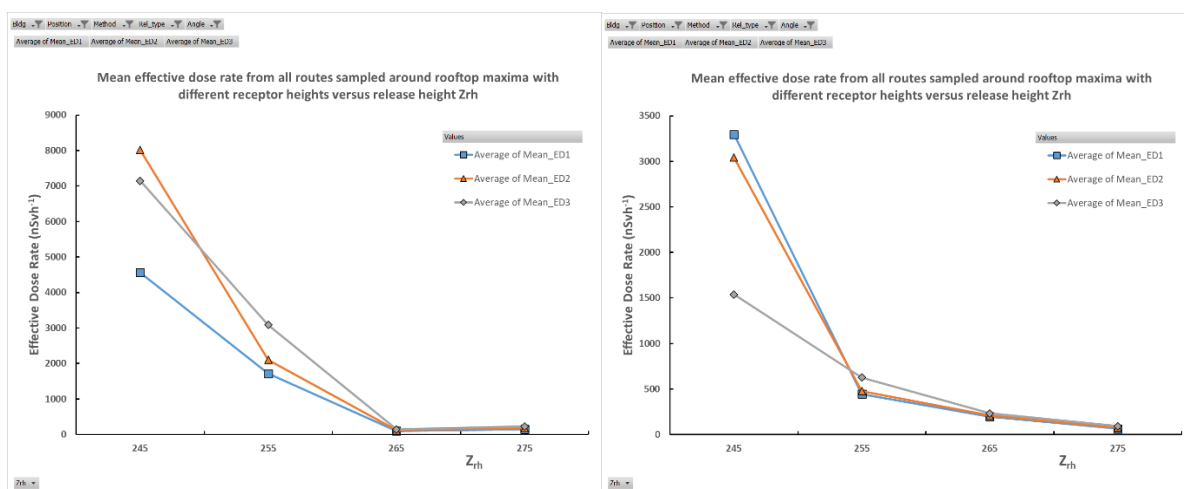


Figure 9.3(a/b). Cube, passive, position A; -45° incidence, dose rate mean, as function of release height (a) DGP; (b) SGP

Comparison of Figure 9.3(a/b) against Figure 9.2(a/b) indicates that using the 5m x 5m grid to calculate the mean dose reduced the effective dose rate to between approximately one half and one third of the values at the peak maxima shown in Figure 9.2. This spatial averaging may be an important factor when considering likely doses arising from exposure to the radioactive plume to a person working within a wider range of positions on the roof. This result is an expected consequence of spatial averaging of the dose arising from the concentration field for a relatively narrow plume close to the release position in a roof zone.

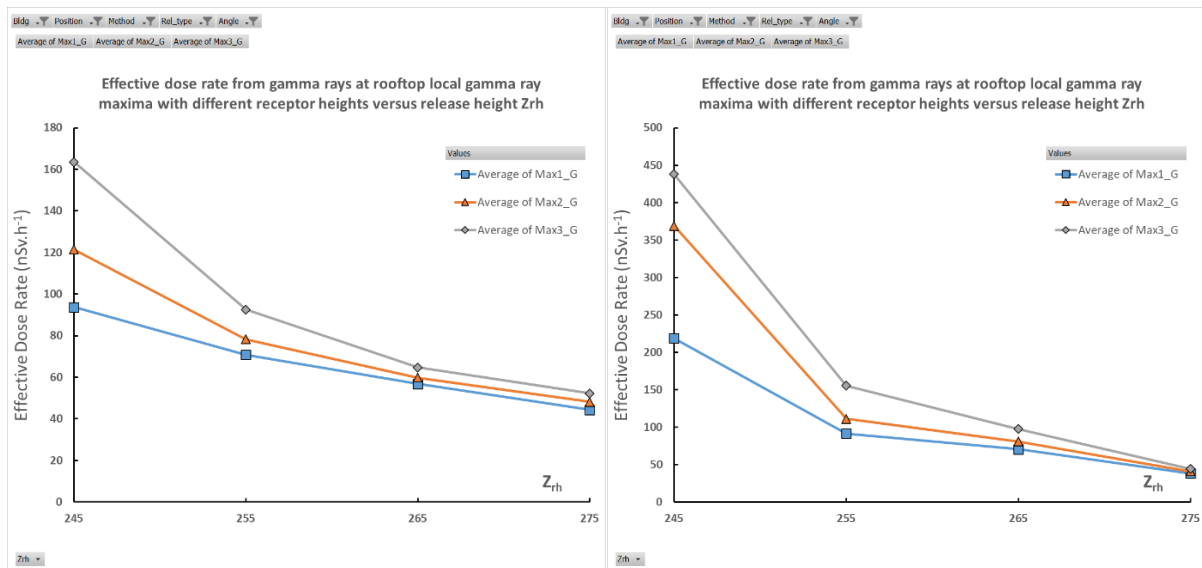


Figure 9.4(a/b). Gamma-ray maxima dose rates: cube/A, DGP, (a) 0°; (b) -22.5° as a function of release height

From Figure 9.4(a/b) we can see the gamma ray dose rate (maximum receptor dose point) for (a) normal incidence, and (b) -22.5° incidence of building to the approach flow. Max1_G refers to the maximum gamma ray dose rate point for sample point at 1m from the roof. Max2_G refers to 1.5m height and Max3_G refers to 2.0m height. For both cases the greatest doses were obtained at the most elevated receptor position (Max3_G) at 2m height, and the values at lower heights 1.5m (Max2_G) and 1.0m (Max1_G) were in order below that: Max1_G. The gamma ray dose rate reduces with increasing release height from a maximum at 245mm. The gamma ray dose rate in (b), approaching a maximum of around $0.3\mu\text{Sv.h}^{-1}$, is very approximately double that seen in (a), something which was attributed to the greater upwards deflection of the plume over the roof for the normal incidence case. Dose from gamma-rays reduces via the inverse square law from a point source and with inverse distance from a line source (see full exposition in Chapter 4 and Appendices 15.5/15.6) and the largest gamma ray doses are expected closest to the concentration maximum of the plume – in the cases given here the tallest receptor positions correspond to positions closest to the radiation source and this is reflected in the greater gamma ray dose values.

From Figure 9.5(a/b) we see the maximum point gamma ray dose rate for the -45° angulated case for the cube at release position ‘A’ and passive releases. From the DGP method shown in (a) the peak dose rates were seen for the 1.5m and 2.0m receptor heights at a release height of 255mm and broadly in the region of $0.8\mu\text{Sv.h}^{-1}$. This gamma ray dose rate reflects the receptor dose positions being inside the plume and closer to the plume centreline. By contrast, in (b) the SGP method shows a receptor dose maximum of approximately $0.3\mu\text{Sv.h}^{-1}$ similar to the -22.5° case. It should be noted that the DGP/IGP method has resolved a pattern of dose with varying release height that is different than the simple pattern of monotonic reduction of gamma ray dose with increasing release height of the plume because the DGP/IGP method has resolved the narrower peak concentration in the plume close to the 1.5m and 2.0m height dose receptor heights (referred to a Max G2 and Max G3 respectively) and this is reflected by the greater gamma ray dose values obtained by the DGP method.

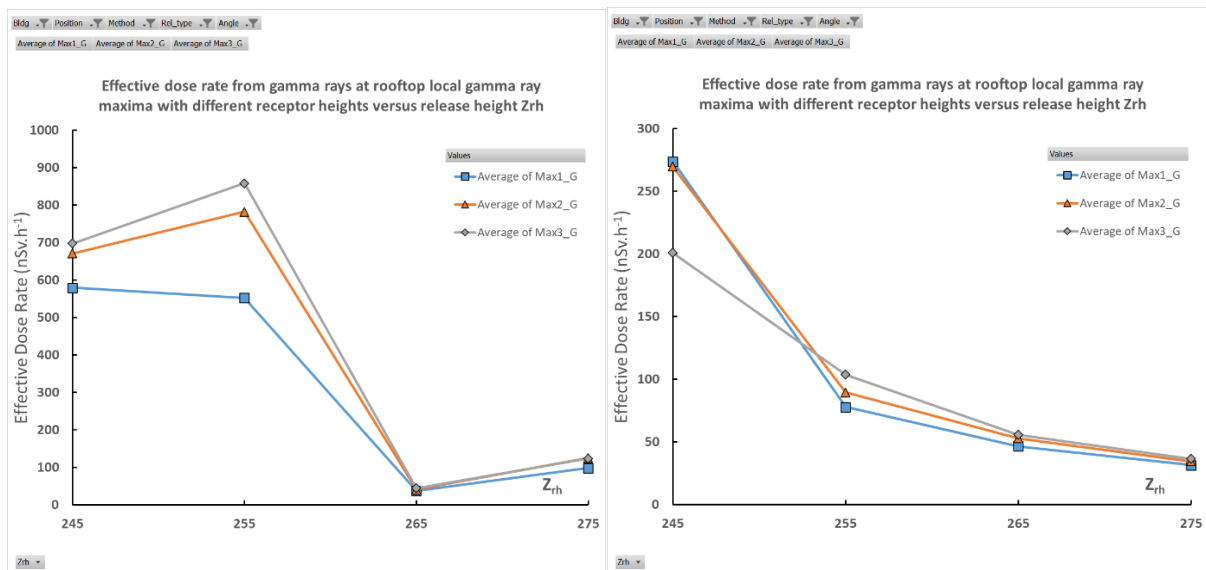


Figure 9.5(a/b). Gamma-ray maxima dose rates: cube/A, -45°; (a) DGP; (b) SGP

From Figure 9.6(a/b) the mean gamma ray dose rates averaged over the 11x11 (5m x 5m) grid are shown for DGP and SGP methods respectively and may be compared to the local maxima in Figure 9.5(a/b), where it is seen that the DGP/IGP method shows a reduction of approximately 35% to 60% by taking the mean gamma-ray dose rate over the sample grid. A similar level of reduction is seen in Figure 9.6(b) for the SGP method. The greater relative reduction for the lowest release height of 245mm in Figure 9.6(a), which shows the DGP method results, is attributed to movement of material, by the action of roof generated vortices, into the rooftop RCZ which reduces the radioactivity over the sampled grid in this case and the greater overall distance (over the 11 x 11 sample grid) of receptor points from higher concentration regions in the plume when sampled at Z=245mm to the plume compared to the Z=255mm sampled height.

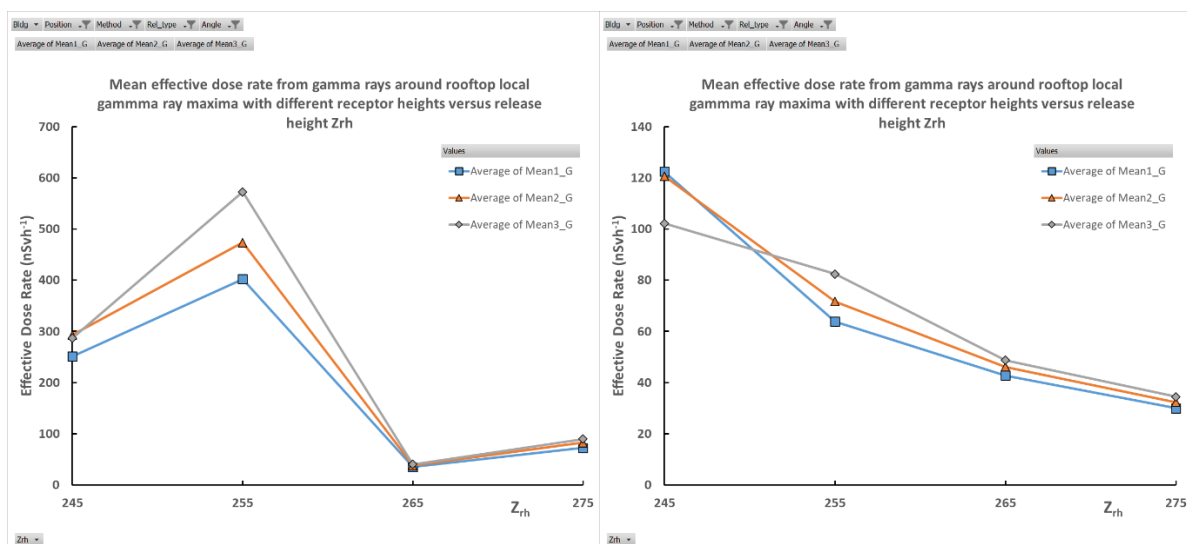


Figure 9.6(a/b). Gamma-ray mean dose rates: cube/A, -45°; (a) DGP; (b) SGP as a function of release height

The variation with effective dose rate at the dose maxima points is shown in Figures 7(a/b)-10(a/b), showing the results from increasing release heights 245, 255, 265 and 275mm in the wind tunnel (1, 3, 5 and 7m passive releases above the roof at full scale): the variation of dose with angle of approach flow is also shown.

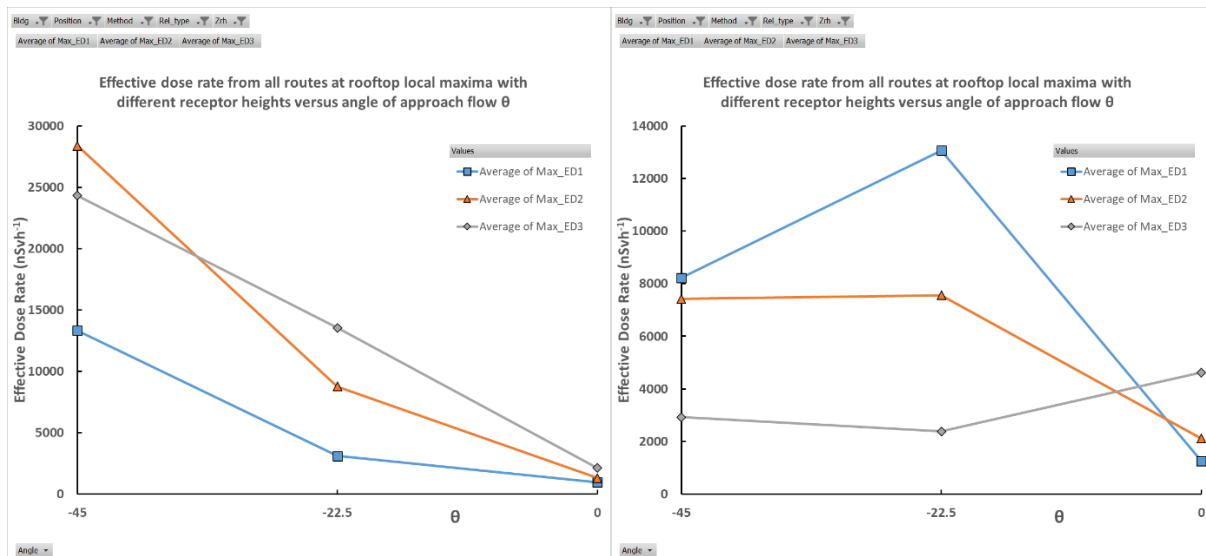


Figure 9.7(a/b). Effective dose rate: cube; ‘A’; passive release; $Z_{rh}=245\text{mm}$ (1m above roof at full-scale); (a) DGP; (b) SGP as a function of angle of approach flow

In Figure 9.7(a/b), for the lowest release height tested of $Z_{rh}=245\text{mm}$ in model scale, the maximum dose rate values from this sequence of figures can be seen. The dose rate can be seen in Figure 9.7(a) to be greatest for the most angled (-45°) approach flow, reducing with angle of flow obliquity to the cube to a minimum at normal incidence (0°), reflecting the changing flow and consequent dispersion conditions: the stronger roof top vortices and low upwards deflection for the -45° , and to a less extent the -22.5° , angled cases can be seen on the movement of material closer to the receptor dose positions above the roof plane. The SGP method in Figure 9.7(b) shows a maximum at ED1 (lowest sample height of 1m above roof) for the intermediate flow angle case (-22.5°) of approximately half the maxima in dose rate resolved by the DGP method in (a), but there is a less clear variation with angle, other than noting lowest dose rate values for normal incidence which may be accounted for by the upwards flow deflection for this case. It may be concluded that the DGP method, which models the concentration field spatially in a more accurate, gives rise to more accurate estimates of radiation dose rate obtained from the Monte Carlo method.

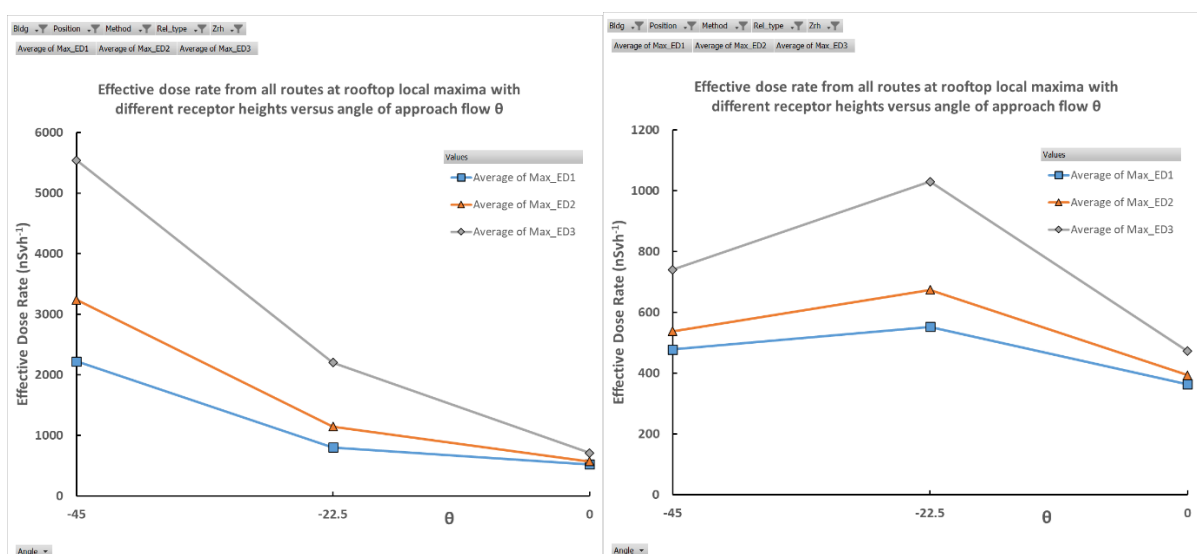


Figure 9.8(a/b). Effective dose rate: cube; ‘A’; passive release; $Z_{rh}=255\text{mm}$ (3m above roof); (a) DGP; (b) SGP as a function of angle of approach flow

From Figure 9.8(a/b) at the release height of $Z_{rh}=255\text{mm}$ we see a similar reduction of dose rate from the most oblique approach flow incidence angles going from -45° through to normal incidence. In this case the greatest dose rates were obtained at the tallest receptor position (ED3, 2m height) for all angles, followed by ED2 (1.5m) and the lowest dose rates at ED1 (1.0m). In Figure 9.8(b) for the SGP method the overall magnitude of dose is much smaller than Figure 9.8(a) and there is less overall variation with angle of approach flow reflecting the cruder concentration field fitting of the SGP method failing to resolve the peak of concentration field accurately compared to the DGP method.

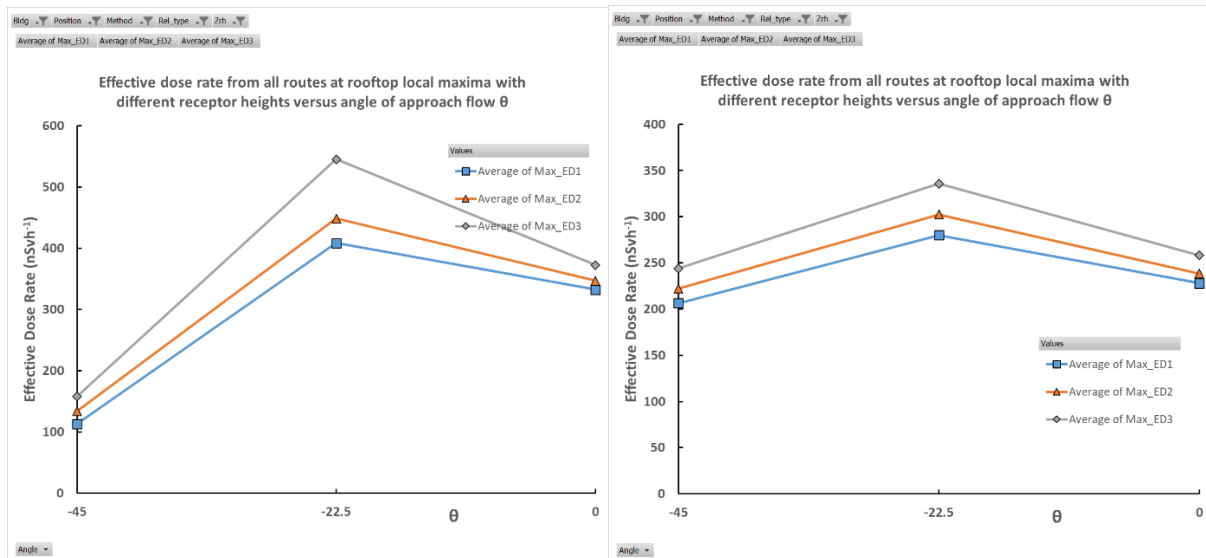


Figure 9.9(a/b). Effective dose rate: cube/A' , $Z_{rh}=265\text{mm}$ (5m above roof); (a) DGP; (b) SGP as a function of release height

From Figure 9.9(a) we see that the trend of dose increasing as one moves from the most oblique angle of incident flow (-45°) through to normal incident effectively reverses compared to the previous two sets of figures: the lowest down levels are seen at -45° , increasing to a maximum at -22.5° . The overall dose levels are much lower than was seen in previous figures reflecting the greater release height and reduced advection by vortices down to near roof level. The maximum at -22.5° correlates to the plume vertical deflection seen in Figure 6.56(a) where the concentration field for -22.5° shows an overall downwards deflection (compared to 0° and -45°) giving rise to more elevated concentration field values closer to the roof compared to the two other angles investigated. Figure 9.9(b) for the SGP method shows a similar pattern of relatively constant dose rate with angle compared to 9.8(b) with a monotonic increase of dose with receptor height going from ED1 (1m) through to ED3 (2m height) the latter being where the receptor is closer to the overhead plume and experiences an increased dose rate.

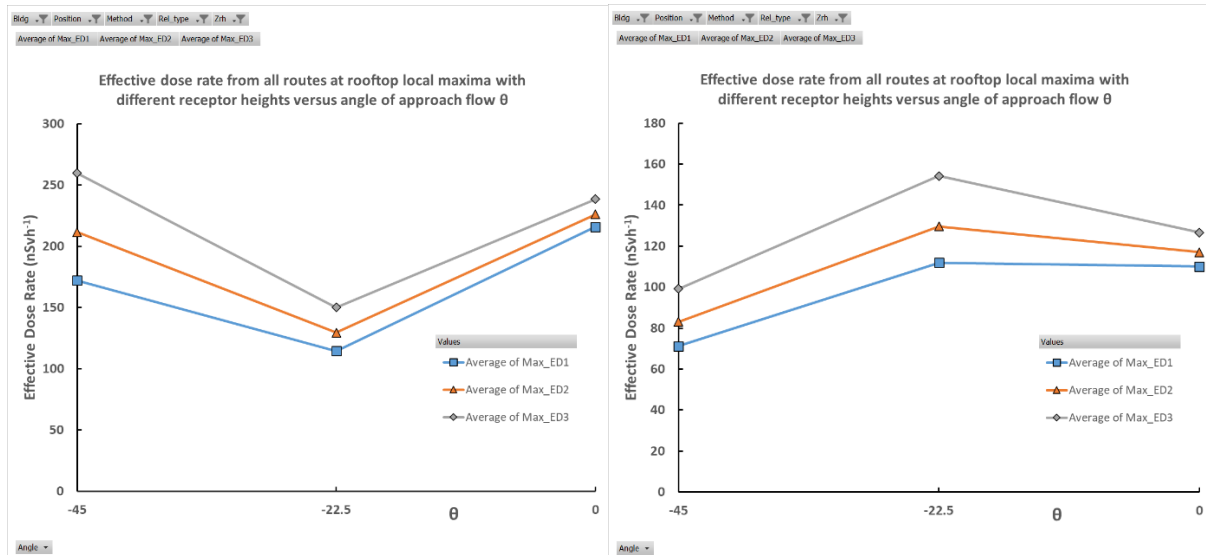


Figure 9.10(a/b). Effective dose rate: cube/'A', $Z_{rh}=275\text{mm}$ (7m above roof); (a) DGP; (b) SGP as a function of release height

Figure 9.10(a) shows an overall reduced level of dose rate with further increasing release height (275mm) compared to Figure 9.9(a); but with an inversion of dose rate with angle with the minima now occurring at -22.5° and the greatest values being at -45° and normal incidence. Again, this can be related to Figure 6.56(a), where the upwards deflection is now greatest for the -22.5° case compared to the 0° and -45° approach flow angles. The former (-45°) may be explained by increased advection to near roof level of the more elevated release from roof generated vortices compared to the -22.5° case but as seen in concentration field plots previously the maximum concentration peaks move further streamwise with increased passive release height and represent the bottom regions of a broadened plume at these distances. The normal incidence (0°) case reflects a further reduction with increasing height from the previous case. In Figure 9.10(b) the same pattern as previous SGP results is seen, with a further reduction in magnitude of dose.

9.3.1.2 Cube with release position B (midline to face)

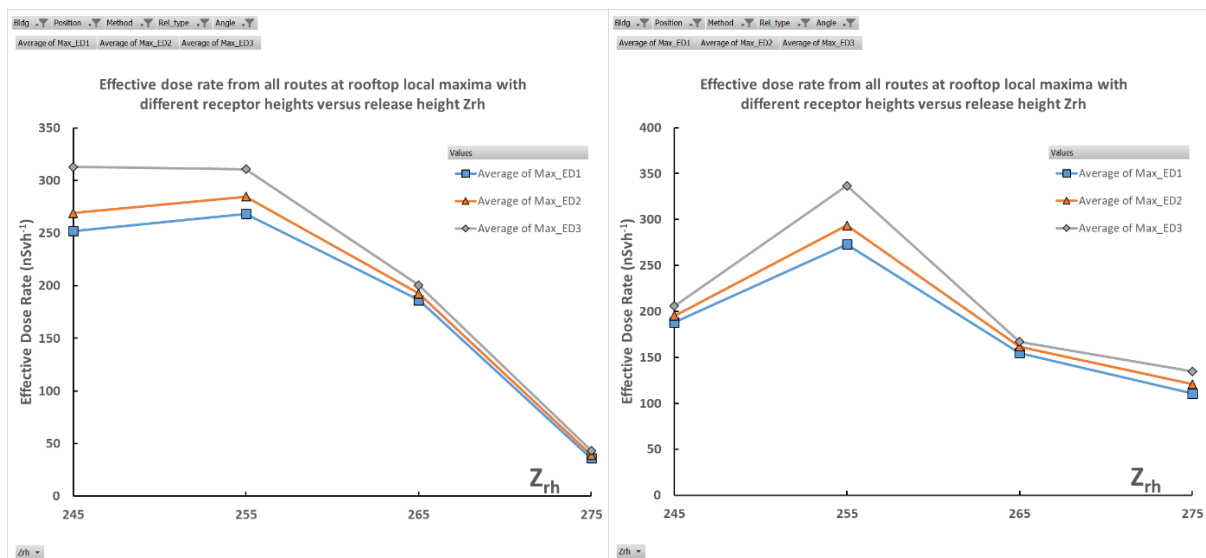


Figure 9.11(a/b). Cube, passive release, position 'B', DGP, dose rate maxima (a) 0° ; (b) -22.5° as a function of release height

From Figure 9.11(a/b) we can see that the total effective dose rate for the ‘B’ release position is considerably lower than the corresponding dose rates from the ‘A’ release case, at just over $0.3\mu\text{Svh}^{-1}$, for the highest receptor point at 2m height from roof (ED3). In (b) at -22.5° there is evidence of a peak at the 255mm release height which corresponds to the dip in upwards deflection seen for this angle compared to 0° and -45° in Chapter 6, Figure 6.56(b). In both (a) and (b) the overall pattern is for the receptor dose rate to be greatest for the highest receptor point reducing through to the lowest receptor point (ED1).

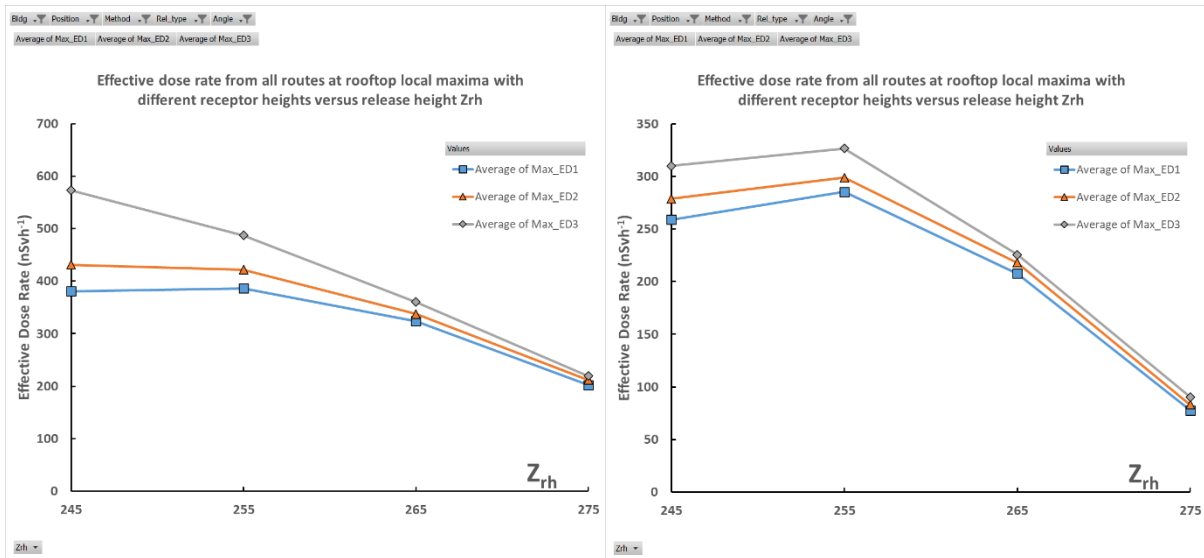


Figure 9.12(a/b). Cube, passive, position ‘B’; -45° incidence, dose rate maxima (a) DGP; (b) SGP as a function of release height

From Figure 9.12(a/b) (with the -45° angle of approach flow) it is seen that the peak level of dose for the DGP method in (a) was approaching $0.6\mu\text{Svh}^{-1}$ for ED3 at 2m from the roof level at the lowest release height of 245mm, compared to dose values considerably lower from Figure 9.11(a): this can be explained by the action of stronger vortices counteracting the strong upwards flow over the leading edge of the cube at this release position for the ‘B’ case (see Figure 5.20(a)) leading to higher levels of dose at the dose receptor positions. The reduction with increasing release height is much less pronounced than the variations seen with the ‘A’ release position. The simpler SGP method only gives rise to peak dose rates (at the local maxima) in the region of $0.3\mu\text{Svh}^{-1}$ for the 255mm release height.

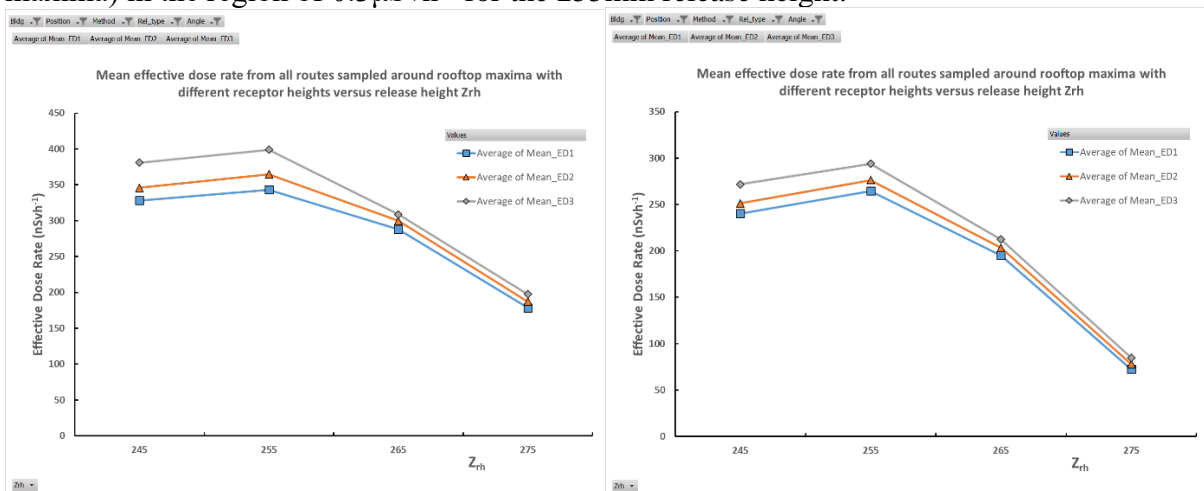


Figure 9.13(a/b). Cube, passive, position ‘B’; -45° incidence, dose rate mean: (a) DGP; (b) SGP as a function of release height

In Figure 9.13(a/b) we see the effect of taking the mean value of the effective dose rate over the sampled 11 x 11 grid in the (X, Y) plane. Comparison of Figure 9.13(a) against Figure 9.12(a) indicates that using the 5m x 5m grid to calculate the mean dose reduced the effective dose rate using the DGP method to approximately 20-30% lower than the peak maxima shown in Figure 13. The corresponding (b) figures showed only a marginal reduction from using the grid-averaging. The spatial averaging factor has a relative importance dependent upon the release position in relation to the building, which in turn determines the concentration field gradients near the receptor dose points which affect this result. The modest reduction due to spatial averaging over the grid can be explained by the relative elevation of the plume for the 'B' release cases making the calculated dose less sensitive to averaging of dose over an extended receptor dose grid below.

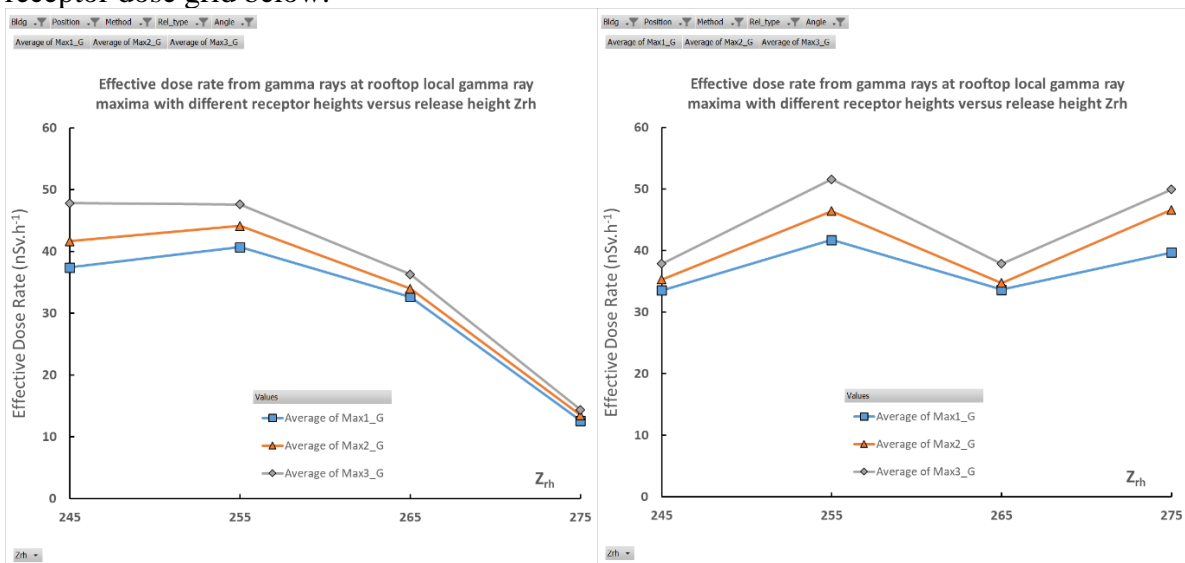


Figure 9.14(a/b). Gamma-ray maxima dose rates: cube; passive; release position 'B'; DGP: (a) 0°; (b) -22.5° as a function of release height

From Figure 9.14(a/b) we can see the gamma-ray dose rate (maximum receptor dose point) for (a) normal incidence, and (b) -22.5° incidence of building to the approach flow for release position 'B'. As with the 'A' release position for both cases the greatest doses were obtained at the tallest receptor dose position (Max_3G) at 2m height, and the values at lower heights 1.5m (Max2_G) and 1.0m (Max1_G) were in order below that. The gamma-ray dose rate was significantly lower than the values seen in the 'A' case, in (a) these values for the 'B' case are approximately one half to one third seen in the corresponding 'A' case, and for both of the angles of approach flow shown. This result is an expected consequence of the relative higher elevation of the plume caused by upwards deflection with an associated increase of distance down to the roof level receptor points.

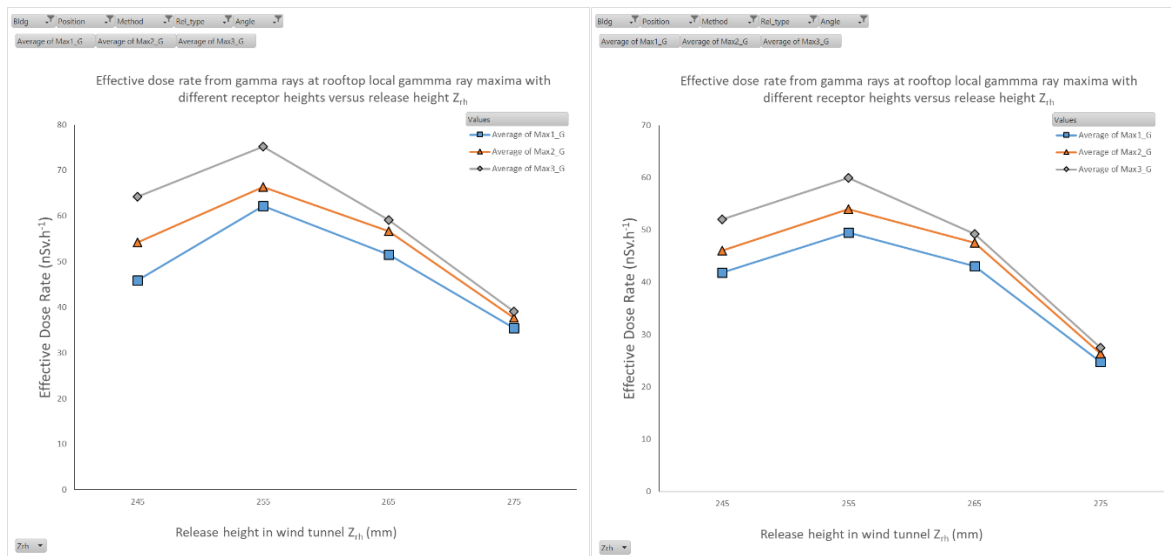


Figure 9.15(a/b). Gamma-ray maxima dose rates: cube; passive; ‘B’; -45°: (a) DGP; (b) SGP as a function of release height

From Figure 9.15(a/b) we see the maximum point gamma ray dose rate for the -45° angulated case for the cube at release position ‘B’ and passive releases. From the DGP method shown in (a) the peak dose rates were seen for the 2.0m receptor dose height (Max_3G) at release height of 255mm and broadly in the region of $0.07\mu\text{Sv.h}^{-1}$ greater than the 0° and -22.5° angles by the greater action of vortices counteracting the general greater upwards flow at this release position ‘B’. In (b) the SGP method by contrast shows a receptor dose maximum of approximately $0.06\mu\text{Sv.h}^{-1}$ only slightly greater than the -22.5° case. A reduction is seen above 255mm with increasing height.

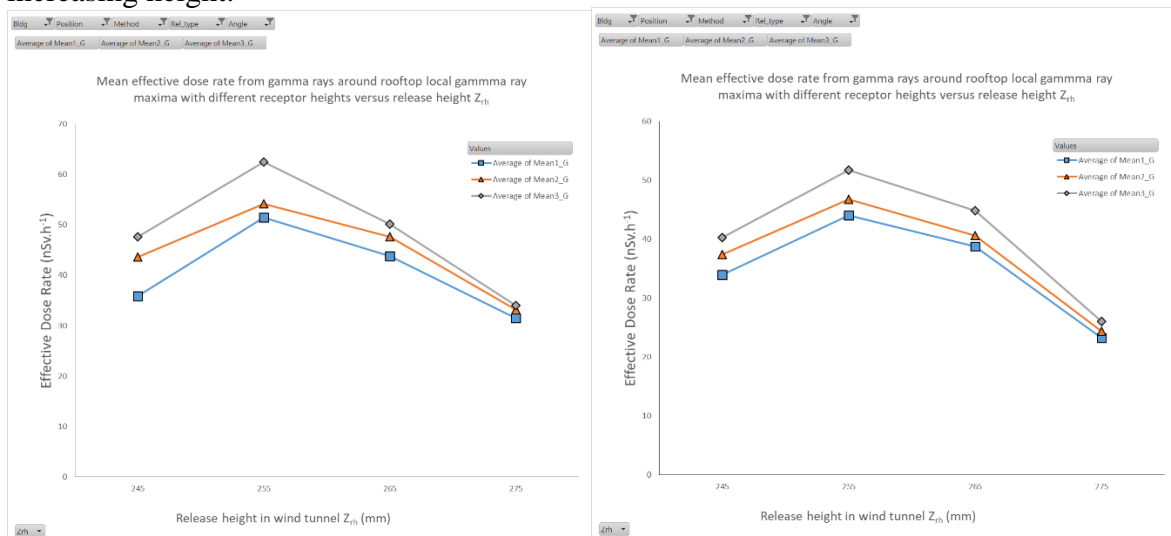


Figure 9.16(a/b). Gamma-ray mean dose rates: cube; passive; ‘B’; -45°: (a) DGP; (b) SGP as a function of release height

From Figure 9.16(a/b) the mean gamma ray dose rates averaged over the 11x11 grid are shown for DGP and SGP methods respectively and may be compared to the local maxima in Figure 9.15(a/b), where it is seen that both DGP and SGP methods show only a modest reduction from the local maxima by taking the mean gamma ray dose rate over the sample grid, with the explanation being the greater general elevation of the plume caused by upwards flow at this release position moving the plume away from the receptor grid

The variation with effective dose rate at the dose maxima points for the ‘B’ release position with angle of approach flow is shown in Figures 9.17(a/b)-9.20(a/b), the sequence of figures showing the results from increasing release heights 245-275mm.

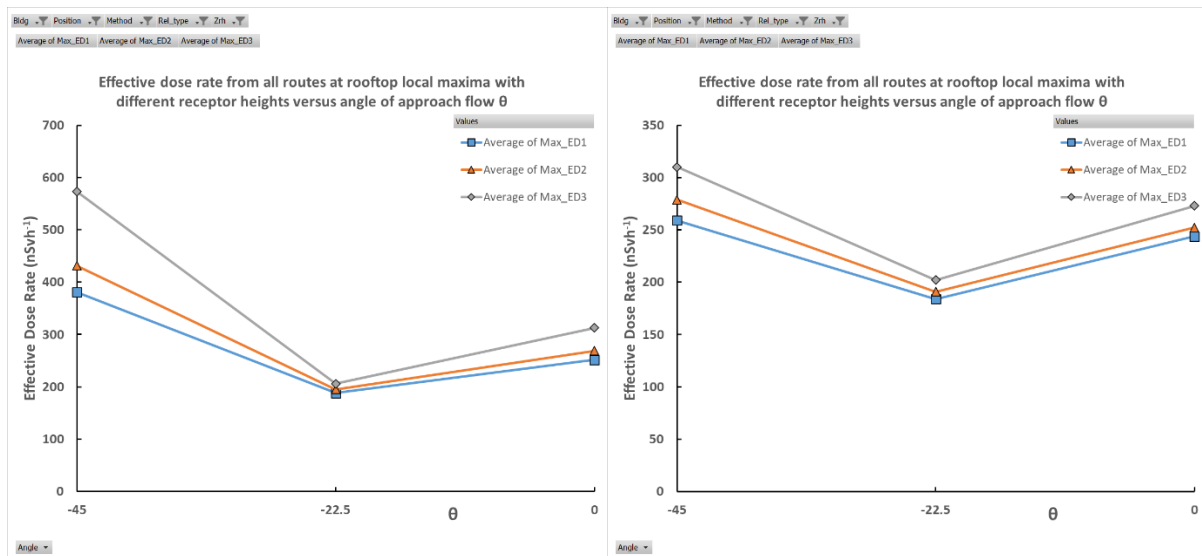


Figure 9.17(a/b). Effective dose rate: cube/'B'; $Z_{rh}=245\text{mm}$ (1m above roof); (a) DGP; (b) SGP

In Figure 9.17(a/b) at the lowest release height the maximum dose rate values of this sequence of figures can be seen. Both (a) and (b) show a dose minimum at the intermediate angle case, with the magnitude of the SGP dose rates somewhat below the DGP results. Variations can be explained by the lower plume upward deflection at -45° at this release height from Figures 6.56(a/b) for the DGP case in (a) and to a lesser extent for the SGP case in (b).

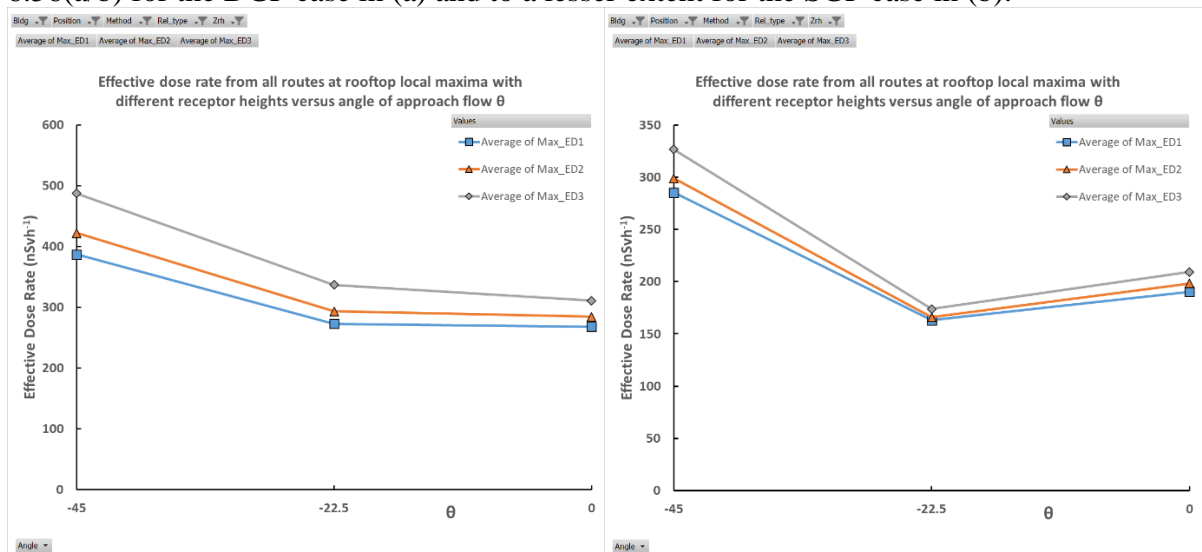


Figure 9.18(a/b). Effective dose rate: cube/'B', $Z_{rh}=255\text{mm}$ (3m above roof); (a) DGP; (b) SGP

From Figure 9.18(a/b) we see a similar reduction of dose rate from the most oblique flow incidence case through to normal incidence. The values for -45° are very approximately similar for the three angles, reflecting similar vertical deflections for this release height from the concentration field results from Figure 6.56(a/b). In 9.18(b) for the SGP method the overall magnitude of dose is smaller than seen in 9.18(a), but with the relative magnitude greater for the -45° angle, reflecting the reduced upwards deflection for this angle shown in Figure 6.56(a).

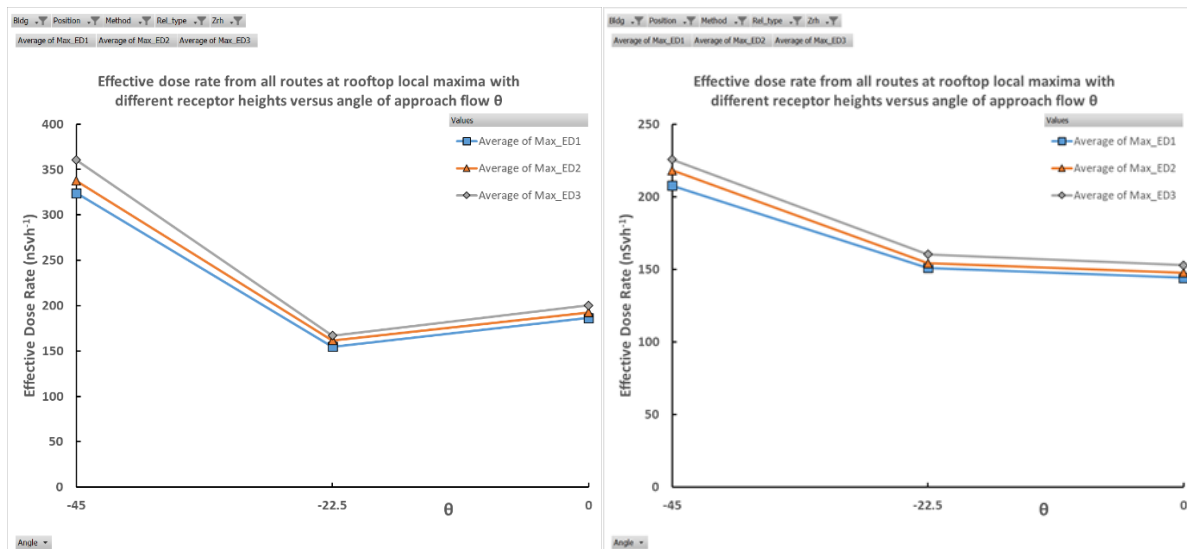


Figure 9.19(a/b). Effective dose rate: cube/'B'; $Z_{rh}=265\text{mm}$ (5m above roof); (a) DGP; (b) SGP

From Figure 9.19(a/b) we see that the dose rate has reduced with increasing release height compared to Figure 9.18(a/b). We also see a pattern of overall dose rate reduction going from angle -45° through to normal incidence with a similar explanation for these trends

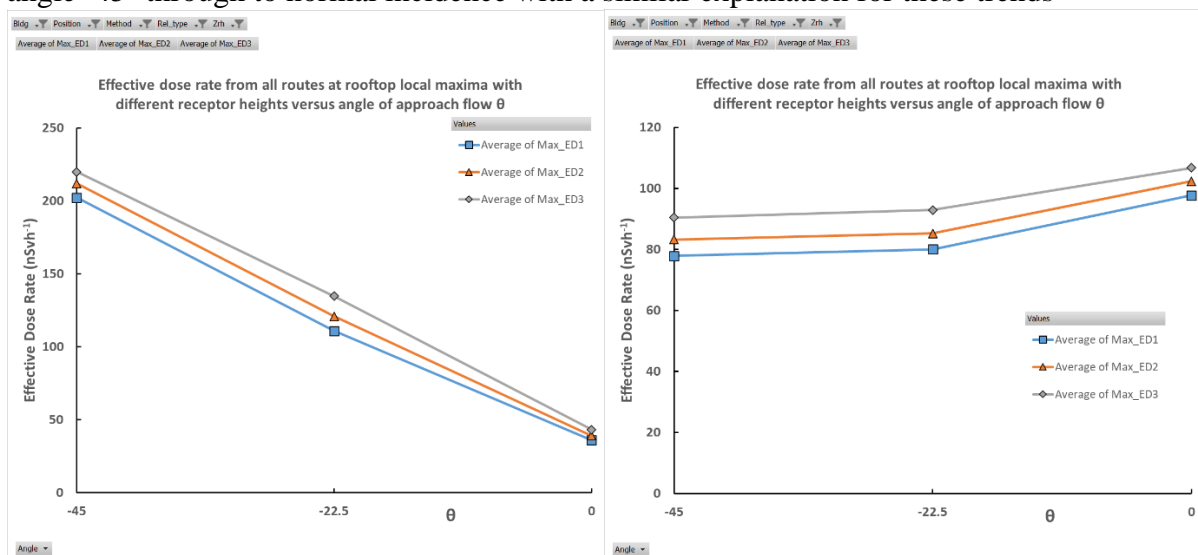


Figure 9.20(a/b). Effective dose rate: cube/'B'; $Z_{rh}=275\text{mm}$ (7m above roof); (a) DGP; (b) SGP

Figure 9.20(a) shows an overall reduced level of dose rate with further increasing release height (275mm) compared to Figure 9.19(a); but with a linear reduction of dose rate with angle with the minima occurring at normal incidence. This can be explained by the wide variation of upwards deflection Figure 6.56(b) with high upwards deflection for normal incidence (resulting in a large relative reduction in dose) and a small deflection at -45° , with -22.5° intermediate between these two cases. In Figure 9.20(b) the SGP shows an almost constant dose rate with angle: a consequence of very similar upwards deflection for these three angles Figure 6.56(a). Evidence from the flow fields chapter indicated that roof generated vortices were greatest for the -45° case and lesser so for the intermediate angle of -22.5° : these vortices are responsible for bringing material, from this more elevated release height, down closer to the receptor point and giving rise to greater effective dose from inhalation and gamma ray shine and this phenomena is coupled with the closer proximity of the plume to the roof receptor for the oblique

angulation cases due to reduced upwards deflection for these oblique cases, in particular the -45° case as seen in previous figures.

9.3.1.3 EW Clad and Unclad: Passive

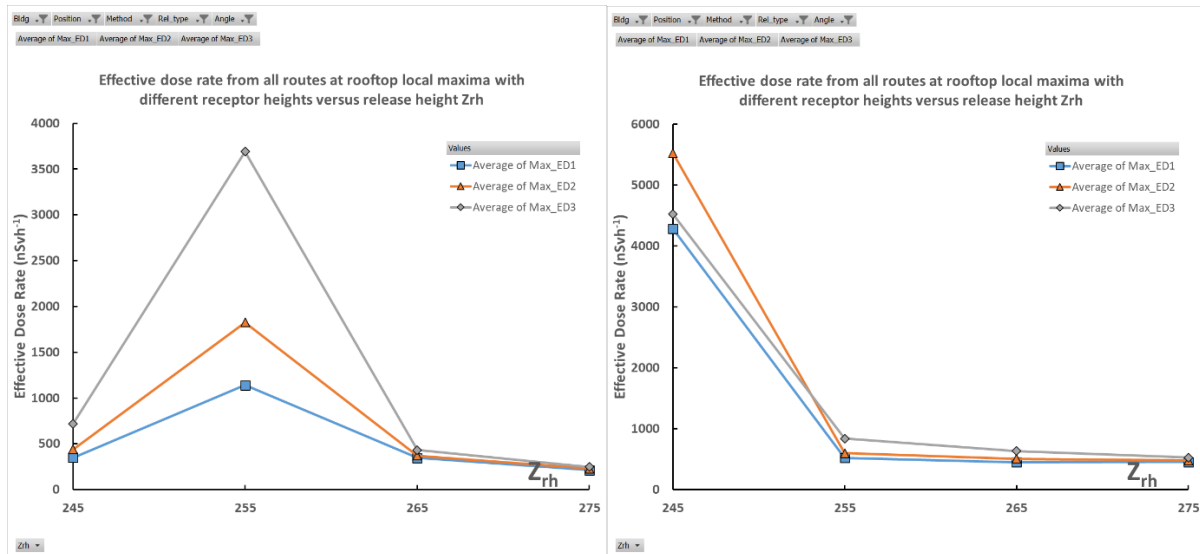


Figure 9.21(a/b). Effective dose rate at maxima vs Z_{rh} ; DGP: (a) EW Clad; (b) EW Unclad

In this section the differences between the EW clad and EW unclad building shapes are contrasted in terms of the effective overall dose rate and the gamma ray contribution to effective dose rate. From Figure 9.21(a) we see that the effective dose rate maxima occurred for the 255mm release, whereas in 9.21(b) this occurred at the lowest release height of 245mm. For the unclad building at 255mm release height the EDR was below 1000nSv.h⁻¹ compared to the maxima in (a) of over 3500nSv.h⁻¹ at the receptor height of 2m: the reading for the 1m receptor height was comparable to the general level at 255mm in (b). This figure shows the range of values encountered for two buildings which may be attributable to their different shapes: but the peak in 9.21(a) may be explained by strong downwards advection and mixing over the main roof zone seen in Figure 5.33(a), just above the roof projections (glass cladding triangular raised sections) where there is a recirculation zone from rooftop structures. The EW unclad case does not have these prominent rooftop structures, so the simple monotonic reduction with increasing height was seen similar to the cube cases shown previously.

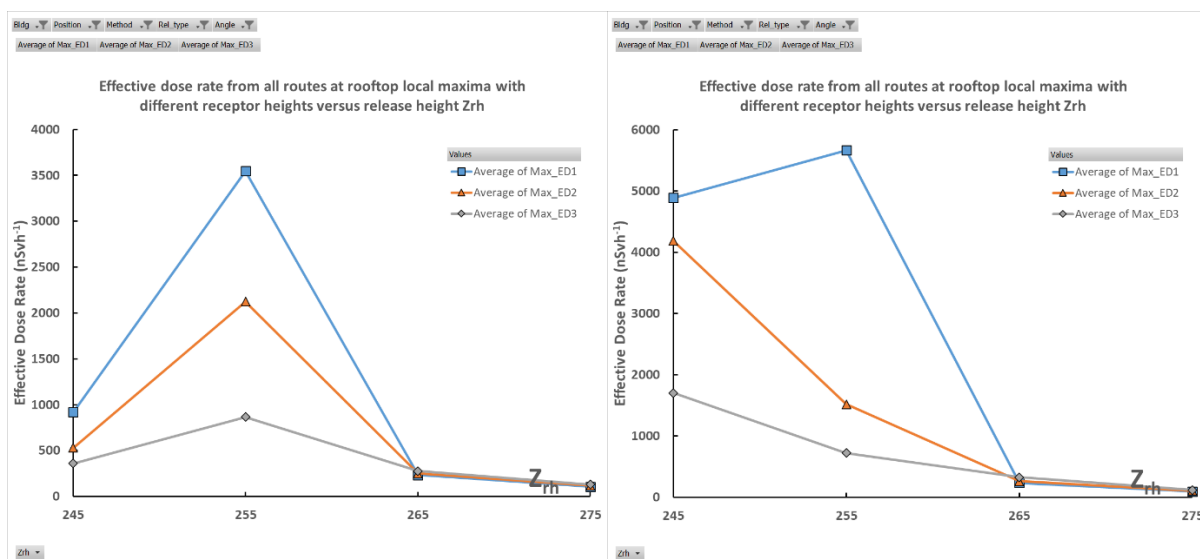


Figure 9.22(a/b). Effective dose rate at maxima vs Z_{rh} , SGP: (a) EW Clad; (b) EW Unclad

Figure 9.22(a/b) shows the two building shapes analysed with the simpler SGP method: a higher peak value for the near rooftop receptor (ED1) in (b) compared to the corresponding maxima in (a) for the same height receptor. The greater dose for the $Z=255\text{mm}$ height is clearly shown to be due to strong downwards deflection in the concentration field, seen for both EW clad and unclad cases, in Figure 6.55(a): this is of such extent that the plume maximum concentration was able to reach the lowest receptor height sampled (ED1) at 1.0m from the roof plane.

Figure 9.23(a/b) for the spatial sampled mean values over a grid shows the same overall pattern but with an overall reduction in magnitude to Figure 9.21. The effective dose correlates, averaged over an 11×11 sample grid, with the concentration field shown in Figure 9.21(a/b) for Figures 9.23(a) and 9.23(b) respectively. The significant reduction in magnitude of dose resulting from the grid averaging indicates that the plume has been advected relatively close to the roof level.

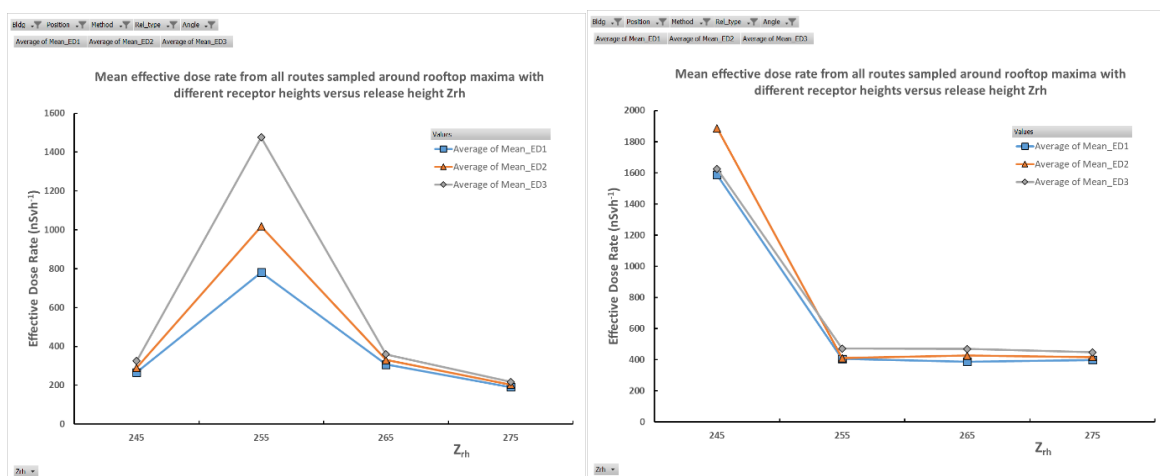


Figure 9.23(a/b). Effective mean dose rate vs Z_{rh} , DGP: (a) EW Clad; (b) EW Unclad

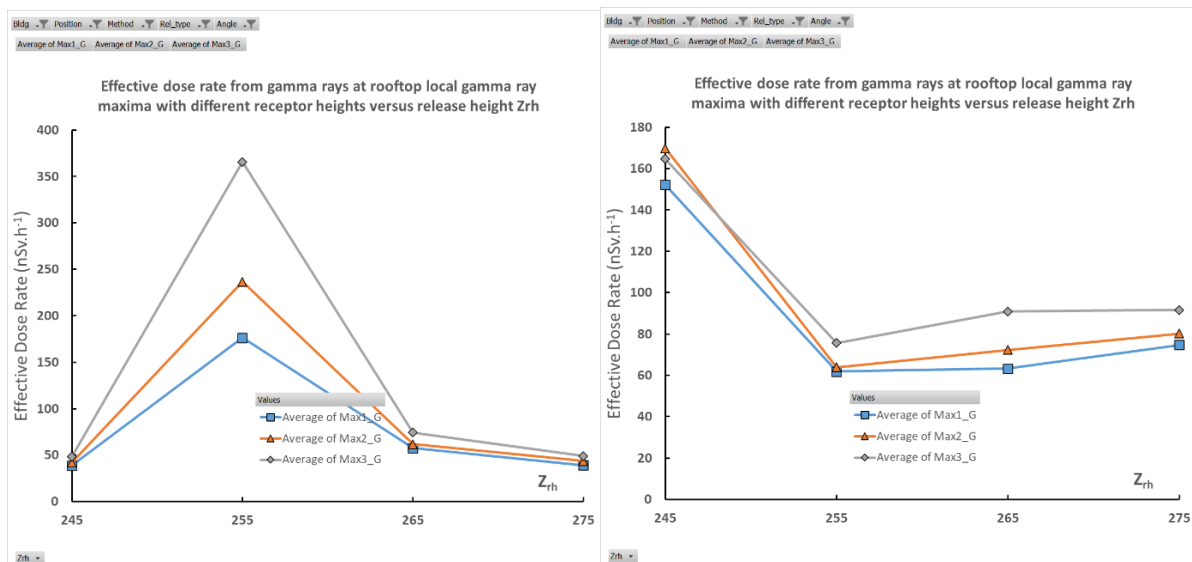


Figure 9.24(a/b). Gamma ray dose rate maxima vs Z_{rh} , DGP: (a) EW Clad; (b) EW Unclad

Figure 9.24(a/b) shows that for this experimental configuration the gamma ray dose contribution is a small component of the overall effective dose for the lower release heights. The trends with increasing release height follow the patterns seen in previous figures.

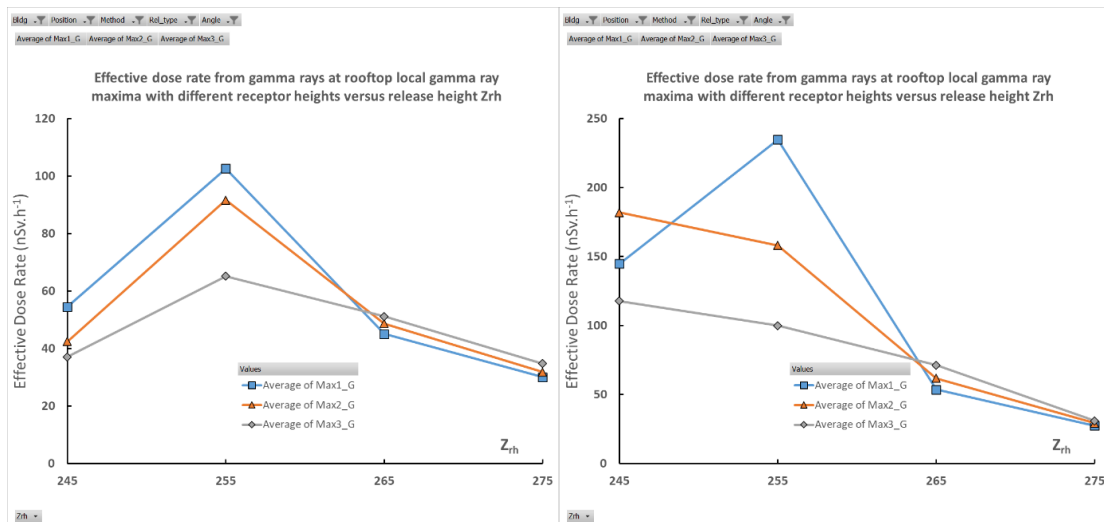


Figure 9.25(a/b). Gamma-ray dose rate maxima vs Z_{rh} , SGP: (a) EW Clad; (b) EW Unclad
 From Figure 9.25(a/b) using the SGP method the gamma ray dose rate peak is not determined to better than a factor of two for the clad case (a) compared to the DGP method in Figure 9.24(a). For (b) the lower release heights lead to a higher gamma ray dose estimate compared to the corresponding Figure 9.24(b): a consequence of the SGP method including RCZ concentration within a single broad peak closer to the maximum dose rate receptor

In Figure 9.26(a/b) the spatially averaged values in the receptor sample grid show a greater extent of reduction for the taller receptor position (2m) and for the lower release heights – this is to be expected as these receptor points are closer to the plume centreline and spatial averaging with act to sample points at greater relative distance which will have a greater effect due to the inverse square reduction of gamma ray dose rate from any sampled element.

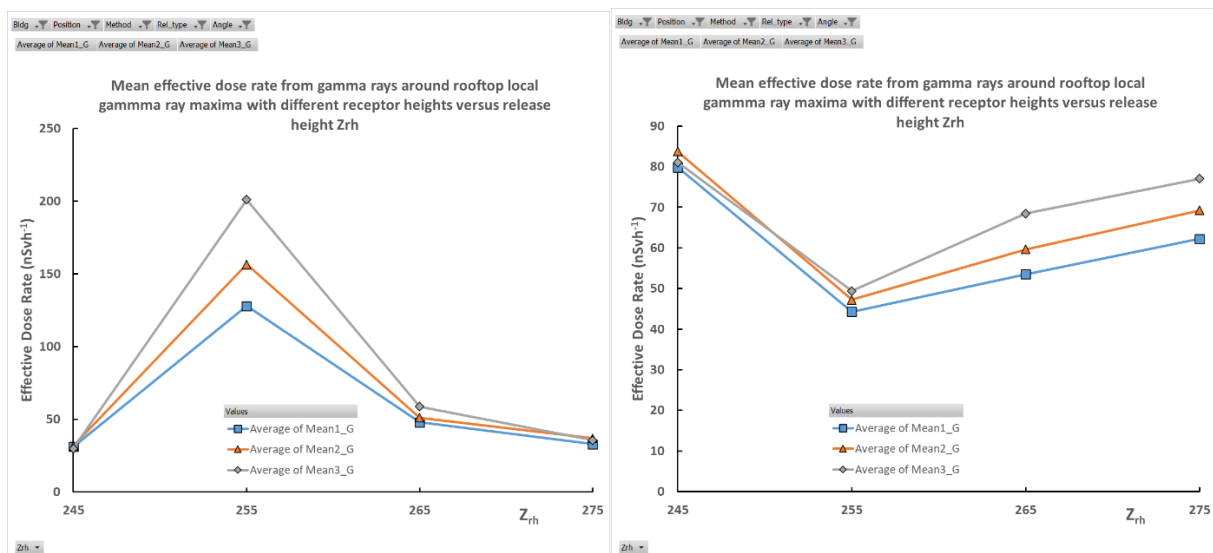


Figure 9.26(a/b). Gamma-ray dose rate mean vs Z_{rh} , DGP: (a) EW Clad; (b) EW Unclad

9.3.1.4 Active vertical releases: all cases

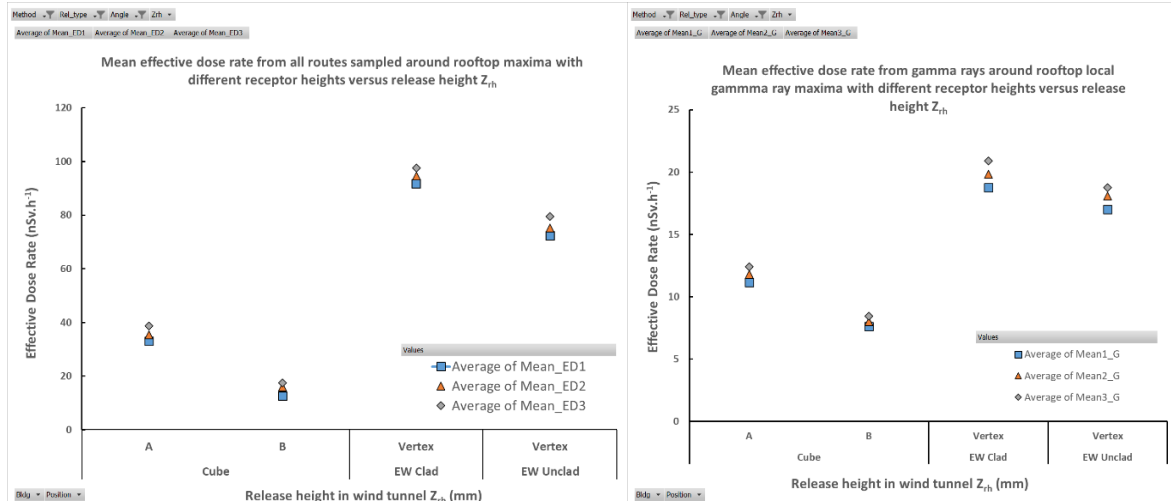


Figure 9.27(a/b). Mean dose rate; active vertical AV release; $Z_{rh}=255\text{mm}$; -22.5° ; DGP: (a) Effective; (b) Gamma-ray dose

From Figure 9.27(a/b) we see the effective dose rate (from all routes) and gamma-ray component of the effective dose rate sampled on the 11 x 11 grid for the active vertical release cases for cube and the EW building shapes at -22.5° . It can be seen that for the relatively elevated plume applicable for these cases that the cube A/B cases are clustered together and the EW clad and unclad cases are likewise clustered. The same pattern holds for the gamma-ray component shown in (b). The more elevated plume means that the concentration field has fallen off rapidly when considering the range of heights at which the rooftop dose is being estimated, and this in turn reduces the variation of dose with dose receptor height in all cases.

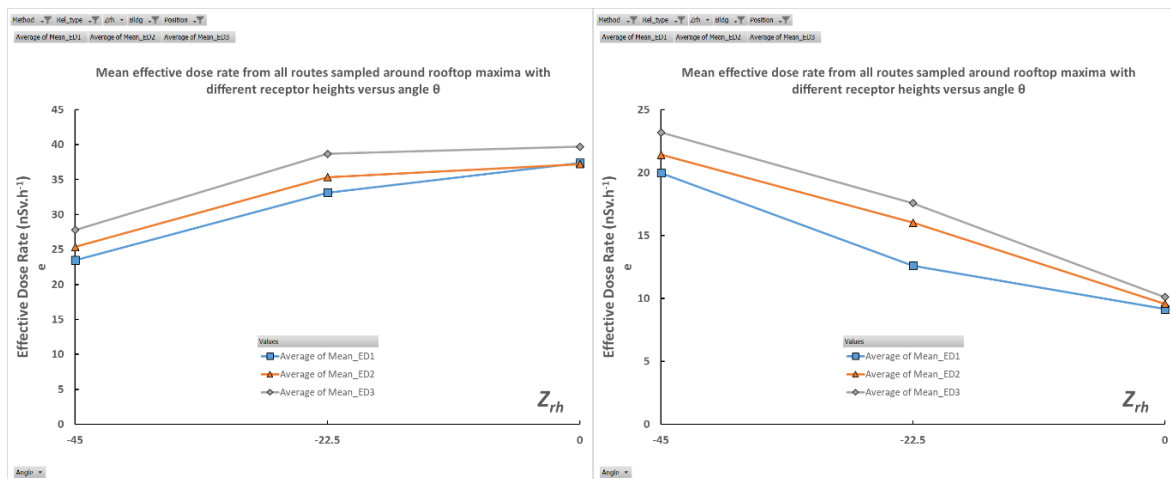


Figure 9.28(a/b). Effective dose rate vs θ ; Cube; AV release; $Z_{rh}=255\text{mm}$; DGP: (a) 'A'; (b) 'B'

Figure 9.28(a/b) shows general trends of changes in effective dose with increasing angle of rotation from -45° through to normal incidence for the active vertical (AV) case: for release at position 'A' the trend is for a modest increase in dose, for 'B' a reduction in dose. This trend is explained by the position of the roof top vortices in relation to the building and the release position. For the 'A' release position, but with the elevated AV release and associated plume height, the rooftop vortices may be less effective at advection of material downwards because the plume meets upwards vortex flow by the time it has moved streamwise to meet the perturbed flow over the building. For the 'B' release position in Figure 9.28(b) the different position of

release appears to indicate that downwards vortex flow is encountered, more strongly for the -45° angle case.

Figure 9.29(a/b) shows the same pattern for gamma-rays but the correlation is much less evident: the gamma ray dose component is less sensitive to the plume centreline position than the dose arising from inhalation in these cases studied.

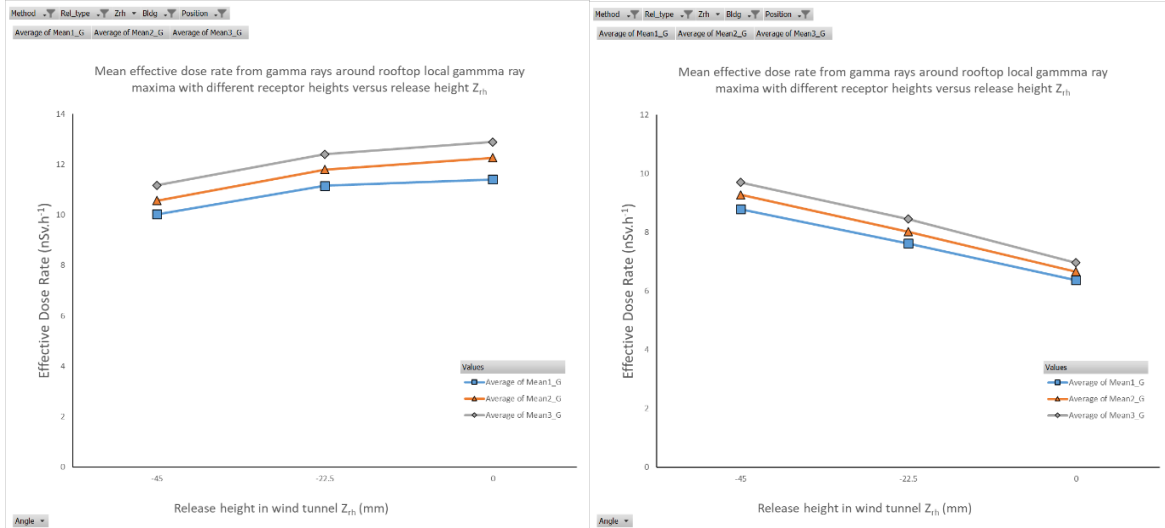


Figure 9.29(a/b). Mean gamma ray dose rate vs θ ; Cube; AV; $Z_{rh}=255\text{mm}$; DGP: (a) 'A'; (b) 'B'

Figure 9.29(a/b) indicates relatively modest changes with angle of approach flow for the 'A' and 'B' release position cases when averaged over the 11 x 11 grid.

9.3.1.5 Positional co-ordinates of effective dose rate and gamma-ray dose rates

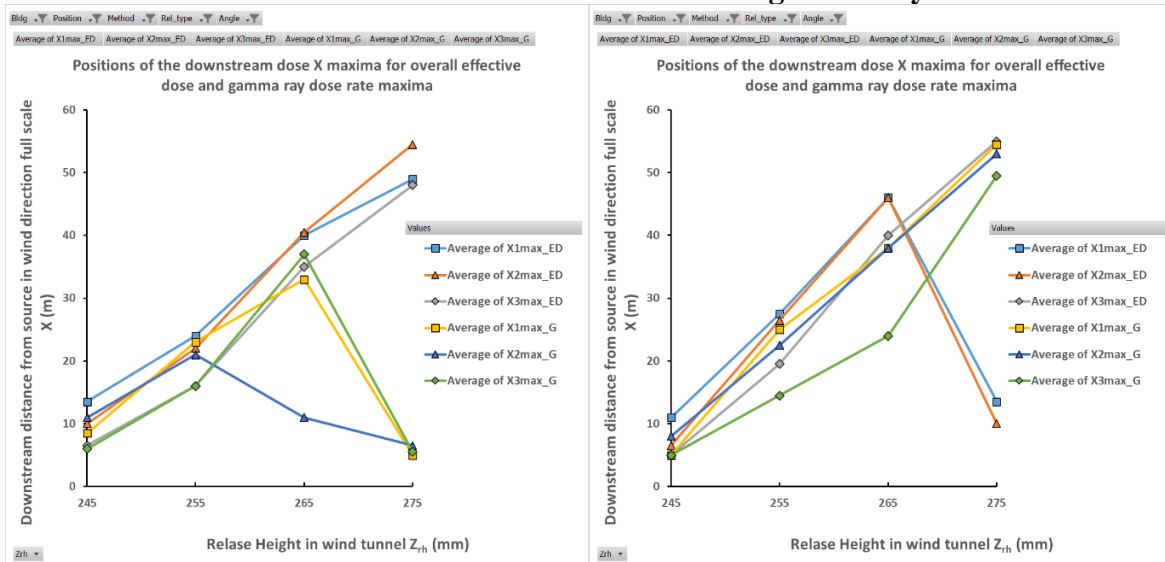


Figure 9.30(a/b). Downstream maxima positions; Cube; 'A'; passive; 0°; (a) DGP; (b) SGP as a function of release height. The suffices of X1, X2, X3 refer to receptor heights of 1.0, 1.5 and 2.0m respectively: 'ED' refers to maximum overall effective dose and 'G' refers to the maximum of the gamma ray dose (this labelling applies to all subsequent Figures 31-42).

In Figures 9.30(a/b) the streamwise maximum positions along the X axis are given in metres for the full-scale cases. Figure 9.30(a/b) shows a general trend for the effective dose rate maxima and gamma ray dose rate maxima downstream positions to have an increased distance

from the source corresponding to increased release height. The only exceptions to this trend were in cases where the release height was elevated: where the plume did not approach closely any part of the roof so the maxima gamma-rays doses occurred close to the source. It is also seen that the taller receptor points e.g. ED3 (2m tall) achieve the maxima for effective dose at a closer distance to the source i.e. they intercept the higher concentration regions in the plume closer to the source.

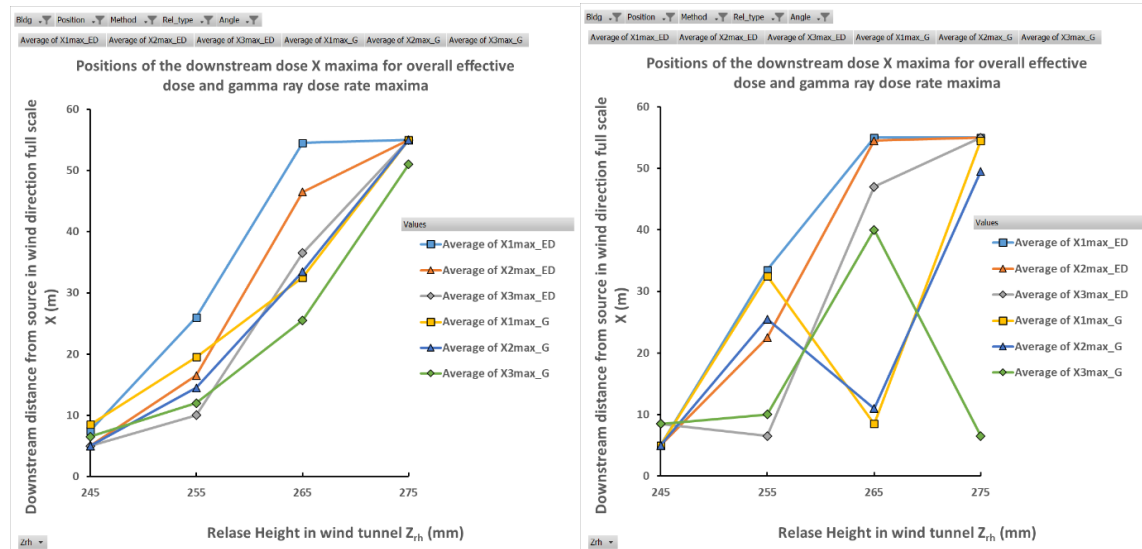


Figure 9.31(a/b). Downstream maxima positions; Cube; ‘A’; passive; -22.5°; (a) DGP; (b) SGP as a function of release height

Figure 9.31(a/b) for the angled cube at -22.5° and release position ‘A’ shows a general trend for the maxima distance to in downstream distance X to increase with release height using the DGP method shown in Figure 9.31(a).

For the SGP method shown in Figure 9.31(b) the pattern for the effective dose (ED) is for the maxima to occur close to the source taller receptor dose positions: X_3 (2m receptor height) is always closer to the source than X_1 (1m height). For the maxima of the gamma ray doses the pattern is more complex. For the receptor closest to the roof (X_{1_maxG}) with increasing release height the maxima moved downstream, and then reversed to be closer to the source as the gamma ray dose closer to the source is greater than the dose further along the X -axis with the more elevated plume associated with the greater release height. The pattern then re-established with the downstream maxima moving to the back edge of the building with a further increase in plume release height. The same pattern holds for the 1.5m receptor height (X_{2_maxG}) but with corresponding distances for the maxima closer to the source than the 1.0m receptor height case. For the tallest receptor (X_{3_maxG}) the competing factors of plume release height, with consequent elevation above the roof, and the fact that the receptor is 2.0m height so already closer to the plume at downstream positions nearer to the source: the interplay of these factors meant that the maxima stayed close to the source for the lowest two release heights, then moved much further streamwise for the next ($Z_{rh}=265\text{mm}$) release height considered, but then reverted back closer to the source at $Z_{rh}=275\text{mm}$ where the further elevation of the plume reduced gamma ray dose rate downstream such that the dose rate proximal to the source release position dominated.

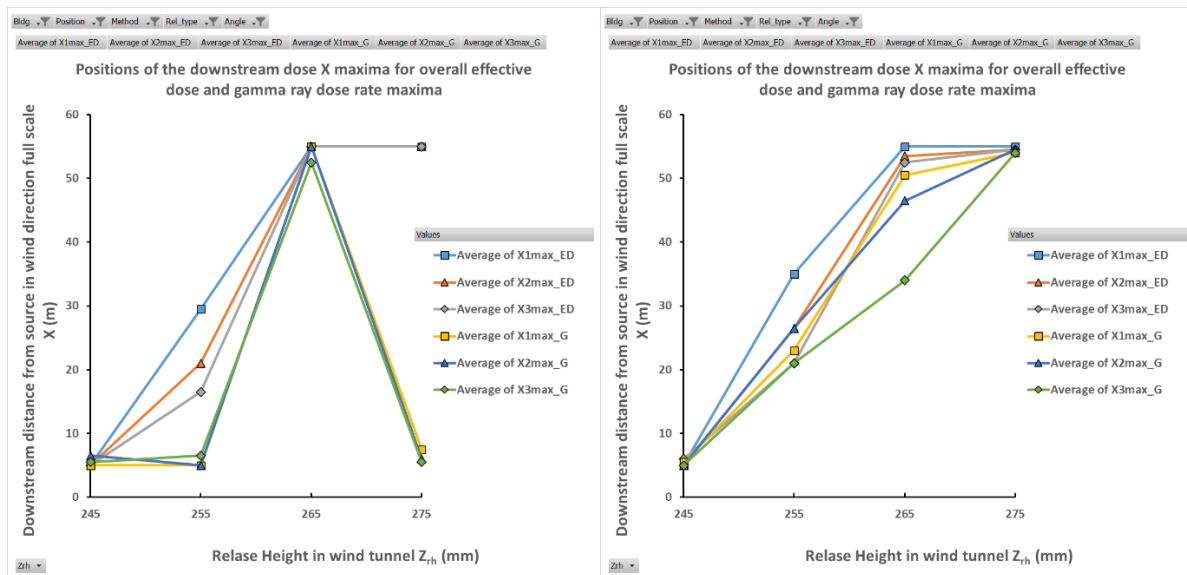


Figure 9.32(a/b). Downstream maxima positions; Cube; 'A'; passive; -45°; (a) DGP; (b) SGP as a function of release height

From Figure 9.32(a) for the DGP method with cube at -45° we see that the effective dose plots reach the furthest downstream distance used in the MC modelling when the passive release height reaches 265mm. This is general trend for lower release heights compared to the normal incidence and -22.5° cases. By contrast the gamma ray dose maxima stay close to the source for release heights up to and including 255mm and then switch to the furthest downstream distance from the source assessed (55m at full scale), then reverting to the nearest point assessed near the source of 5m at full scale. The reasons are as described before: as the plume release height increases the plume height tends to increase and the point of interception of the higher concentration region with the dose receptors increases, however if the plume rise is sufficiently great (as with $Z_{rh}=275$ mm in this case) the greatest gamma ray dose is obtained at positions closest to the source. Figure 9.32(b) with the SGP method shows a simpler pattern of behaviour with the distance to the dose maxima showing a general trend of increasing with passive release height of the plume and achieving comparable or greater distance to the maxima compared to the (a) figure.

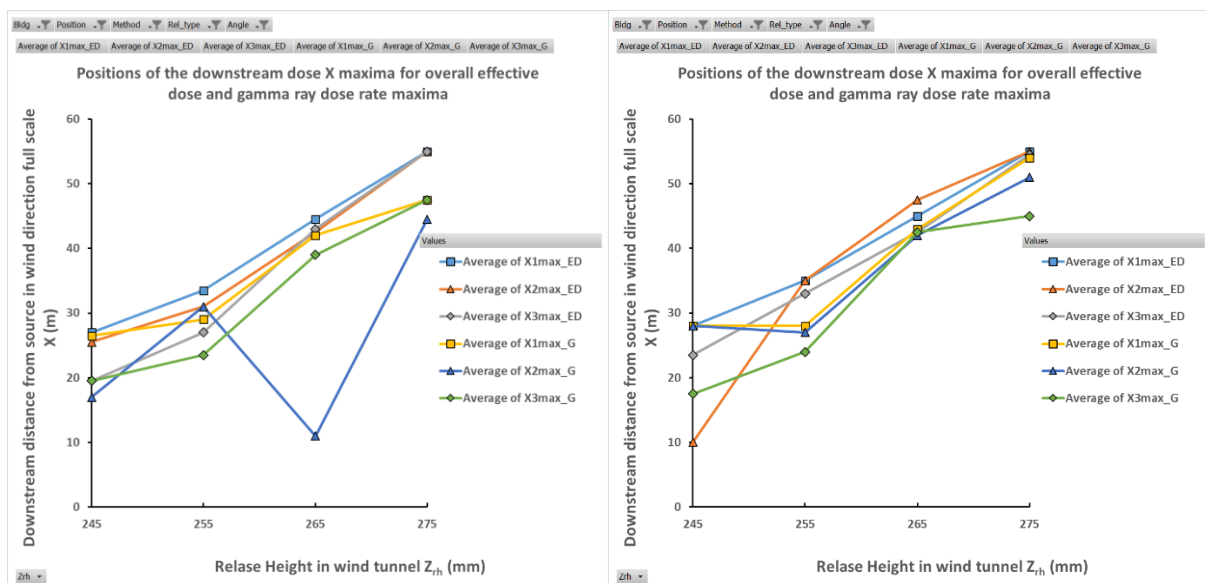


Figure 9.33(a/b). Downstream maxima positions; Cube; 'B'; passive; 0°; (a) DGP; (b) SGP as a function of release height

In Figure 9.33(a/b) we see the differences caused by the difference in the release position – in this case position ‘B’ at the midline of the cube face. Comparison of Figure 9.33(a/b) with Figure 9.30(a/b) for the ‘A’ release position at normal incidence shows the maxima for the ‘B’ release case are further downstream – this is particularly the case for the lowest passive release height of 245mm. This finding reflects the strong upwards deflection, particularly in the centre of the face at position ‘B’, of the flow taking the tracer away from the roof surface and moving the concentration maxima at the receptor points further downstream. This overall trend is also seen in Figure 9.33(b) for the SGP methods.

Figure 9.34(a/b) shows the ‘B’ release at the angle of -22.5° which may be compared with the corresponding case for the ‘A’ release position in Figure 9.31(a/b). In this case the maxima for the 245mm height passive release in (a) are much further downstream than the corresponding ‘A’ release case – which may again be largely attributed to upwards deflection for releases at this height. In contrast, the 255mm release maxima distances match those for the same height in Figure 9.31(a). The gamma-ray dose maxima are seen to change to positions close to the source for the tallest release height of 275mm, a feature not seen in Figure 9.31(a).

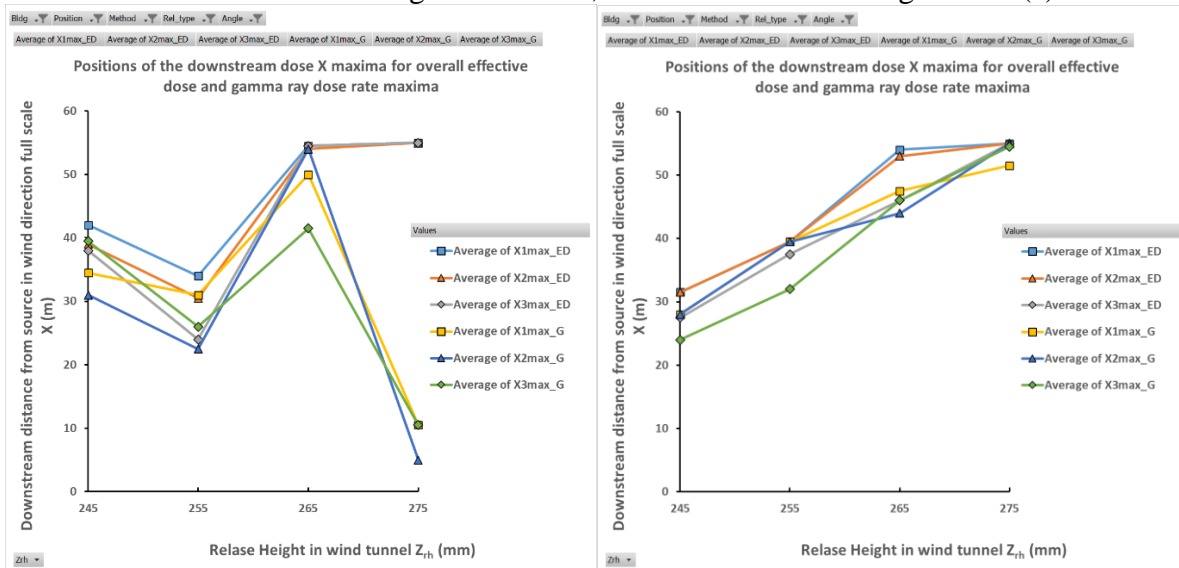


Figure 9.34(a/b). Downstream maxima positions; Cube; ‘B’; passive; -22.5° ; (a) DGP; (b) SGP as a function of release height

Figure 9.34(b) showing the SGP case shows, by comparison with Figure 9.31(b) a well-ordered transition of downstream maxima distance with increasing release height: in this case the upwards deflection of the plume centre meant that the SGP method was able to resolve the general plume centre shift upwards but lacks the detail of the DGP/IGP method in deconvolving the main plume from the rooftop recirculation zone region shown in Figure 9.34(a).

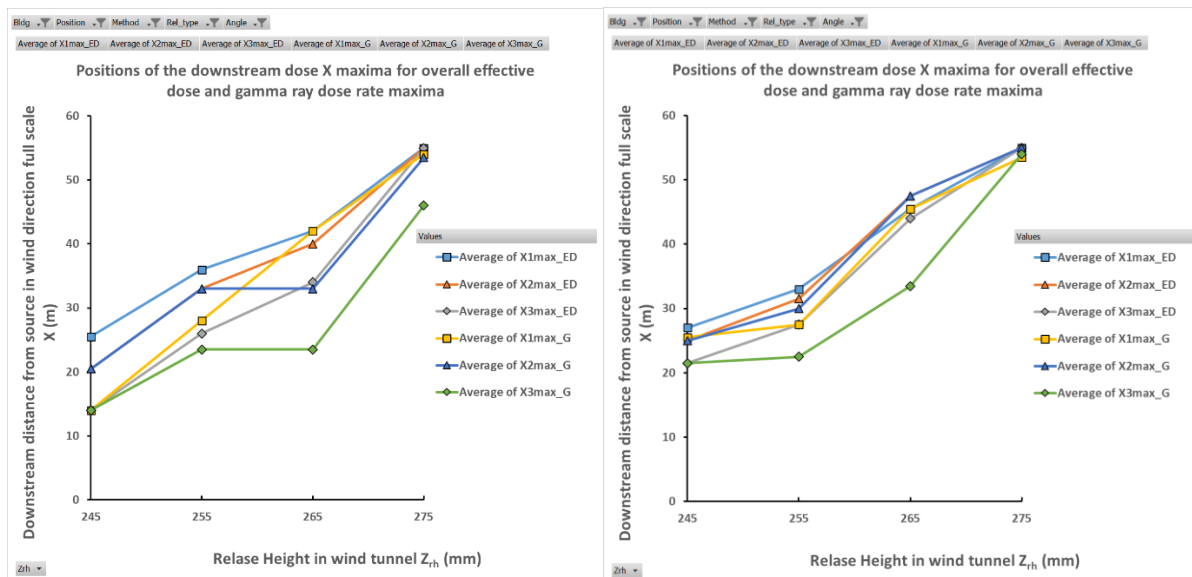


Figure 9.35(a/b). Downstream maxima positions; Cube; 'B'; passive; -45°; (a) DGP; (b) SGP as a function of release height

Figure 9.35(a/b) shows the 'B' release position at -45° and may be compared to Figure 9.32(a/b) for the 'A' release case. The corresponding effective dose maxima positions are further downstream in the 'B' case compared to the 'A' case. There is some complex behaviour for the gamma ray maxima positions, which show variation with receptor height, but nevertheless an overall trend of increasing maxima distance from the source with release height.

In Figure 9.36(a/b) the dose maxima downstream positions are presented for the cube A/B and EW clad/unclad cases all at the same angle of approach flow of -22.5°. For the 255mm stack height with a vertically upwards directed flow (AV) - with a matched Stack Velocity Ratio (SVR) to the downstream advection velocity at that height - the effects of considerable plume rise can be seen on the maxima positions. In (a) there was only one notable exception, being the 'A' release position for the tallest receptor point (ED3, 2m above roof level), where the local maxima was evaluated as closest to the source, the receptor point clearly being sufficiently close coupled with the particular flow conditions to give rise to the maxima at this proximal position at 5m from the source position.

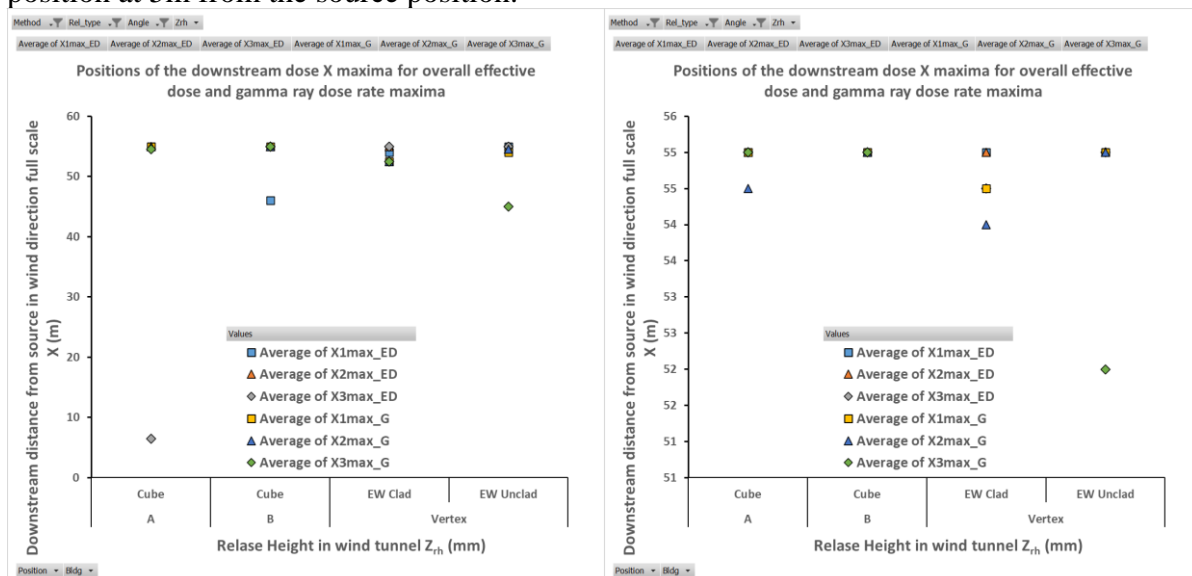


Figure 9.36(a/b). Downstream maxima positions; active vertical (AV); -22.5°; (a) DGP; (b) SGP (note different axes scaling)

Figure 9.36(b) shows downstream maxima generally at the furthest extent of the receptor plane evaluated (55m from the source position in full scale) but where the tallest receptor (G3, 2m from roof level) recorded the gamma ray maxima at approximately 53m for the EW cases.

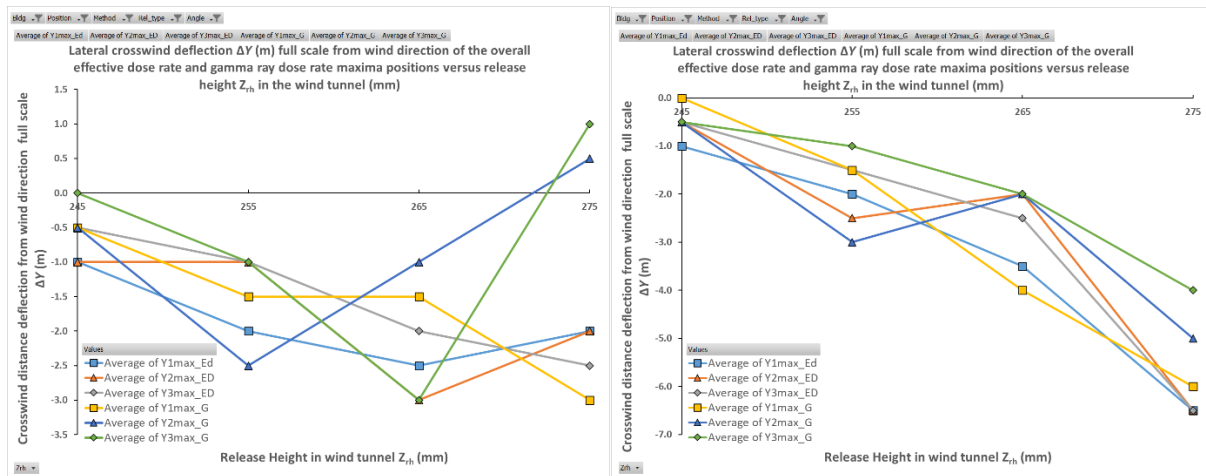


Figure 9.37(a/b). Lateral maxima positions; Cube; 'A'; passive; 0°; (a) DGP; (b) SGP

Figure 9.37(a/b) shows the lateral deflection crosswind from the line running downstream (the X-axis) in the direction of the approach flow for the cube 'A' case at normal incidence. From the DGP method shown in (a) we can see the effective dose rate maxima (ED) are generally deflected between 1-3m in the negative Y direction, the crosswind deflection of the maxima increasing with release height. The gamma ray maxima (G) follow the same pattern except for the Y₂_maxG (receptor at 1.5m height) and Y₃_maxG (receptor at 2m height) for the greatest release height of 275mm where the deflection was slightly positive. The gamma ray dose is a combination of dose rate delivered by the main plume and from the rooftop RCZ (which is towards the centre of the cube in relation to the 'A' release position), and for these positions the net effect is to shift the maxima laterally in the positive Y-direction as the elevated plume in these cases has somewhat less influence.

The SGP method in Figure 9.37(b) showed a stronger correlation of deflection ranging from approximately zero to 6m in the negative Y direction. It should be noted that the SGP method cannot de-convolve dual concentration peaks, for example for the rooftop RCZ, so the net effect is to show a single broader peak reflecting a simple overall best fit to the concentration data.

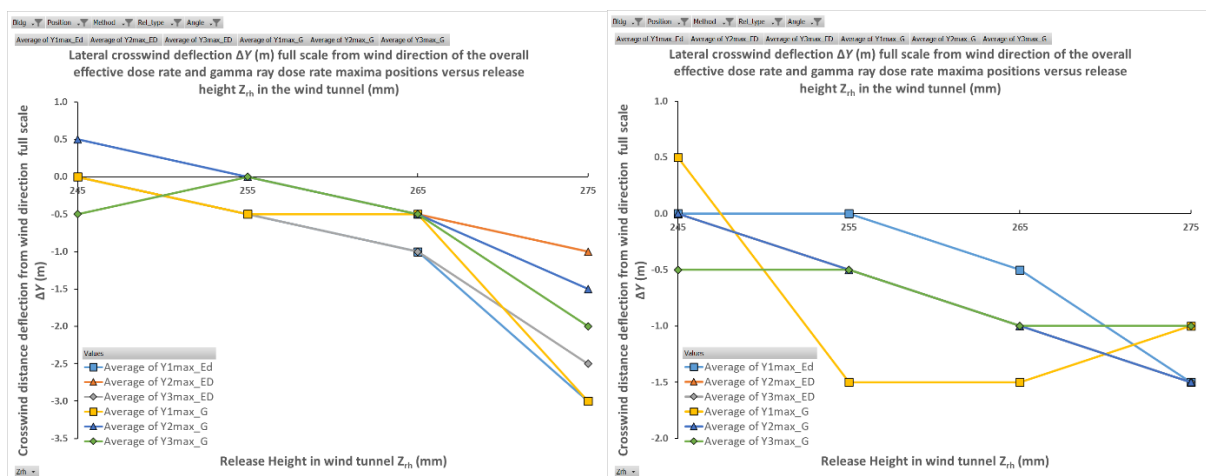


Figure 9.38(a/b). Lateral maxima positions; Cube; 'A'; passive; -22.5°; (a) DGP; (b) SGP as a function of release height

Figure 9.38(a) for the cube at ‘A’ release position with approach flow of -22.5° showed only a modest deflection of up to one metre except for the highest release height where the deflection could approach 3m. For Figure 9.38(b) the deflections were within 1.5m.

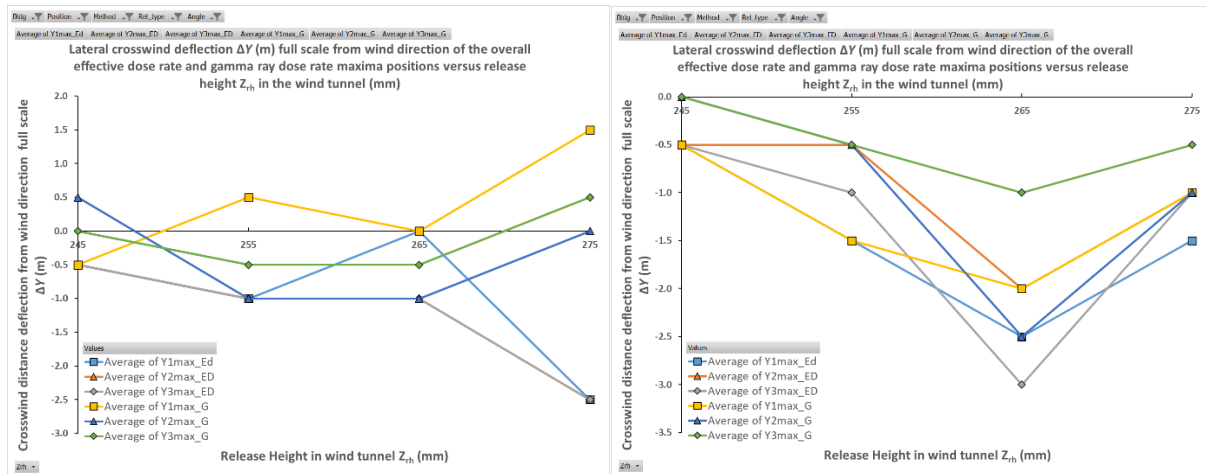


Figure 9.39(a/b). Lateral maxima positions; Cube; ‘A’; passive; -45° ; (a) DGP; (b) SGP as a function of release height

From Figure 9.39(a/b) for the cube release position ‘A’ at -45° the deflections of the maxima were all within 3 metres of the wind direction. For (a) the gamma ray maxima were marginally shifted towards the positive- Y direction, once again because of the effect of the RCZ as a contributory factor.

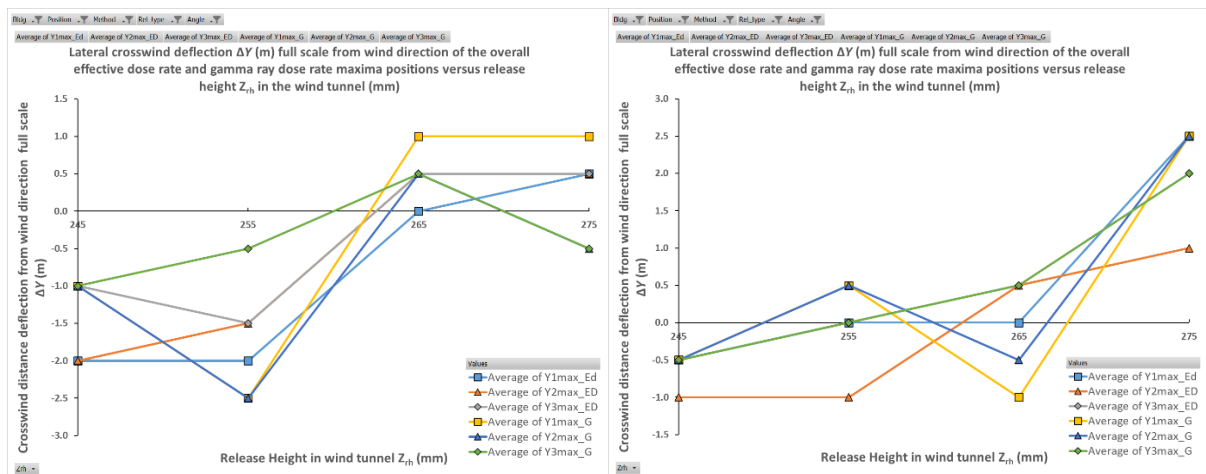


Figure 9.40(a/b). Lateral maxima positions; Cube; ‘B’; passive; 0° ; (a) DGP; (b) SGP as a function of release height

From Figure 9.40(a) the lower release heights were seen to be deflected into the negative Y direction by up to 2.5m, with taller release heights showing a modest positive deflection of up to one metre. This is the symmetrical ‘B’ release case for normal incidence but an explanation here would be that the more elevated plume has a slight bias in the direction towards the negative Y values, but that the gamma rays from the extensive RCZ have greater prominence for more elevated plumes and lower receptor heights (see Y_{1_maxG} at 1m height from the roof with the maximum positive Y deflection). The SGP method in (b) showed a maximum positive Y deflection of up to 2.5m for Y_{1_maxG} and Y_{2_maxG} (1.5m height) because of the influence of the rooftop RCZ on the gamma ray dose contribution for the most elevated plume at

$Z_{rh}=275\text{mm}$: a shift towards positive Y increased by fitting with a simple single Gaussian concentration profile.

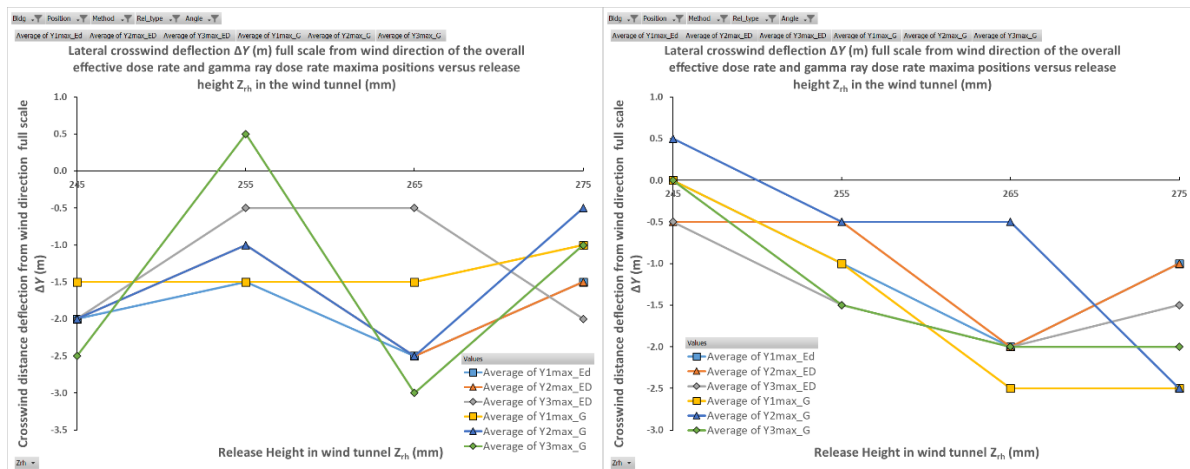


Figure 9.41(a/b). Lateral maxima positions; Cube; 'B'; passive; -22.5° ; (a) DGP; (b) SGP as a function of release height

Figure 9.41(a/b) for the cube 'B' case at -22.5° shows a general level of negative Y deflection in (a) of approximately 2m, with the (b) SGP case showing deflections in the same direction of up to 2.5m. The positive direction Y shift in (a) for Y_{3_maxG} (2.0m height) at $Z_{rh}=255\text{mm}$ is a notable feature and occurs for the tallest receptor point: for this gamma ray receptor the original pattern of negative Y deflection was re-established with increasing height at $Z_{rh}=265\text{mm}$ and 275mm . The positive Y -direction deflection for this point may be related to the influence of the rooftop RCZ as the same receptor (Y_{3_maxG}) does not show this pattern for the SGP method as shown in Figure 9.41(b).

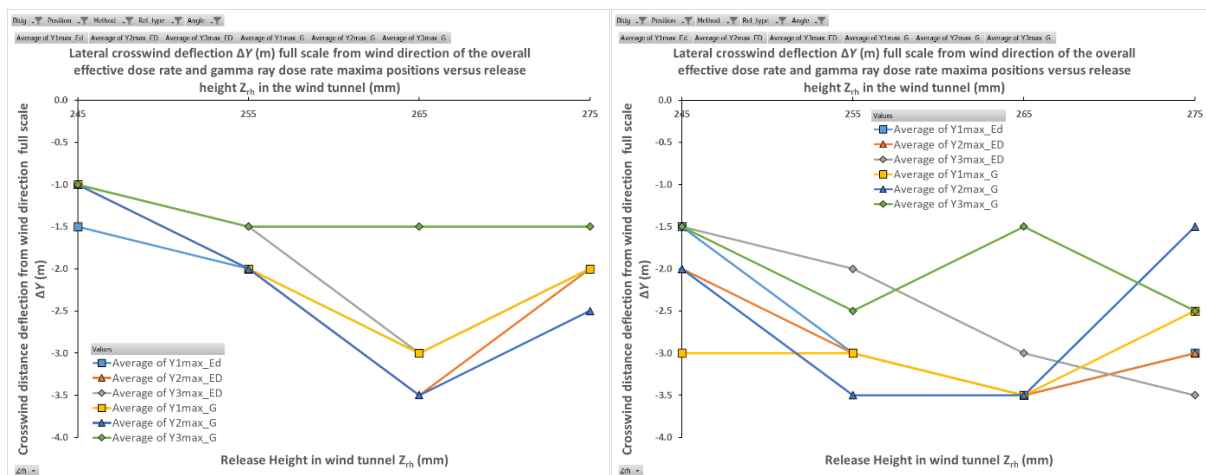


Figure 9.42(a/b). Lateral maxima positions; Cube; 'B'; passive; -45° ; (a) DGP; (b) SGP as a function of release height

Figure 9.42(a/b) for the cube 'B' case at -45° shows a general negative- Y deflection in the region of 1-3.5m for the (a) case and 1.5-3.5m for the (b) case.

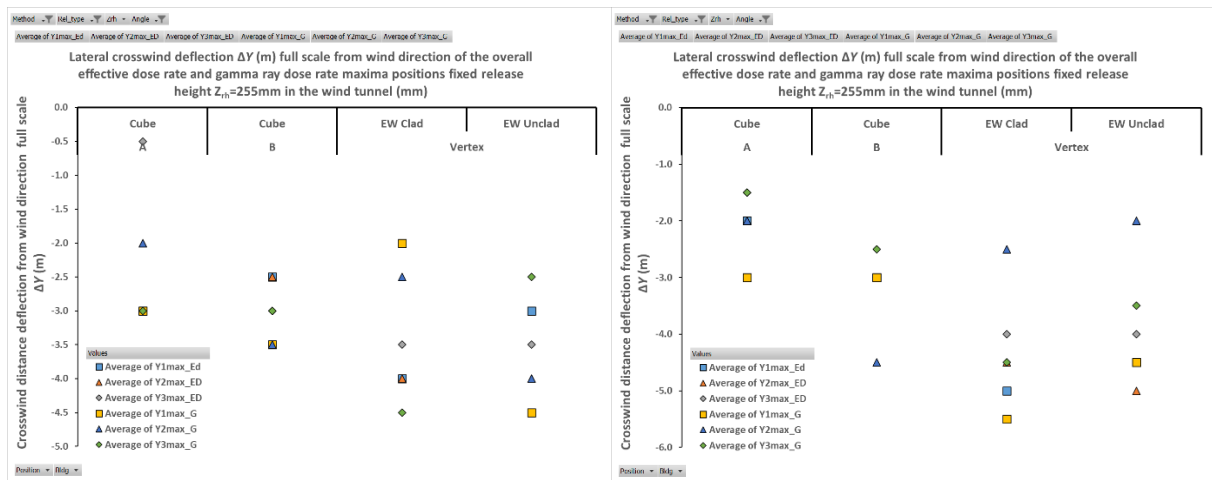


Figure 9.43(a/b). Lateral maxima positions; Active Vertical; -22.5°; (a) DGP; (b) SGP
 From Figure 9.43(a/b) for the active vertical stack releases showing the cube A/B and EW clad/unclad cases we see a general deflection in negative Y direction of between 2-4.5m in (a) and between 1.5-5.5m for the SGP method in (b) and for both cases there were no locations where the dose maximum was indicated in the positive Y co-ordinates.

9.3.2 Spatial variation of effective dose and gamma ray dose from Monte Carlo calculations

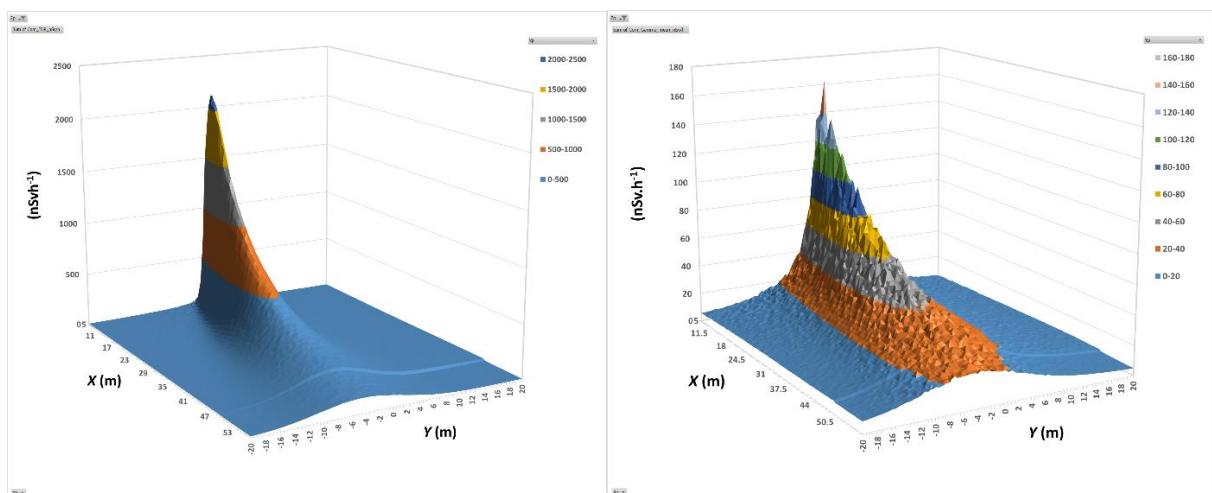


Figure 9.44(a/b). Cube/A/DGP; Passive; $Z_{rh}=245\text{mm}$; 0° ; $Z=50\text{m}$; (a) EDR; (b) Gamma-rays

From Figure 9.44(a) we see the spatial variation of the effective dose rate for the Cube 'A' release at normal incidence (corresponding to data shown in Figure 9.1(a) as line ED3) for a release height of 245mm and receptor point height of 250mm (50m at full scale height). The peak in effective dose is largely arising from the high component of the effective dose being inhalation dose, which in turn depends on the local concentration at the receptor point height. Figure 9.44(b) shows the same case but just showing the gamma ray dose contribution to effective dose which is just under 10% of the total effective dose for this point and set of conditions. Statistical fluctuations in the dose estimate are visible spatially across the receptor dose grid across which the dose values are shown.

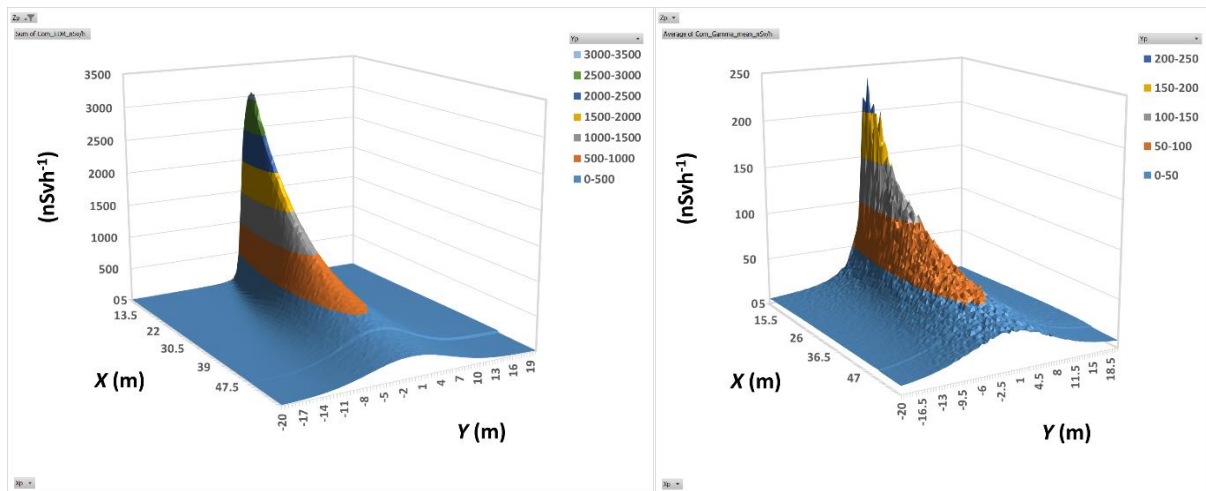


Figure 9.45(a/b). Cube/A/DGP; Passive; $Z_{rh}=245\text{mm}$; -22.5° ; $Z=49\text{m}$; (a) EDR; (b) Gamma-rays

From Figure 9.45(a/b) is shown the overall effective dose and contribution to effective dose from gamma rays for the cube 'A' case at release height 245mm and -22.5° approach flow, with in this case the receptor dose grid set at 245mm (49m height in full scale). The corresponding data for a/b is shown in Figure 9.1(b)/9.4(b) (for ED1/Max1_G at 1m height from roof). Once again, a well-defined plume has been demonstrated with a gamma ray dose component in the region of just under 10% of the effective radiation dose total.

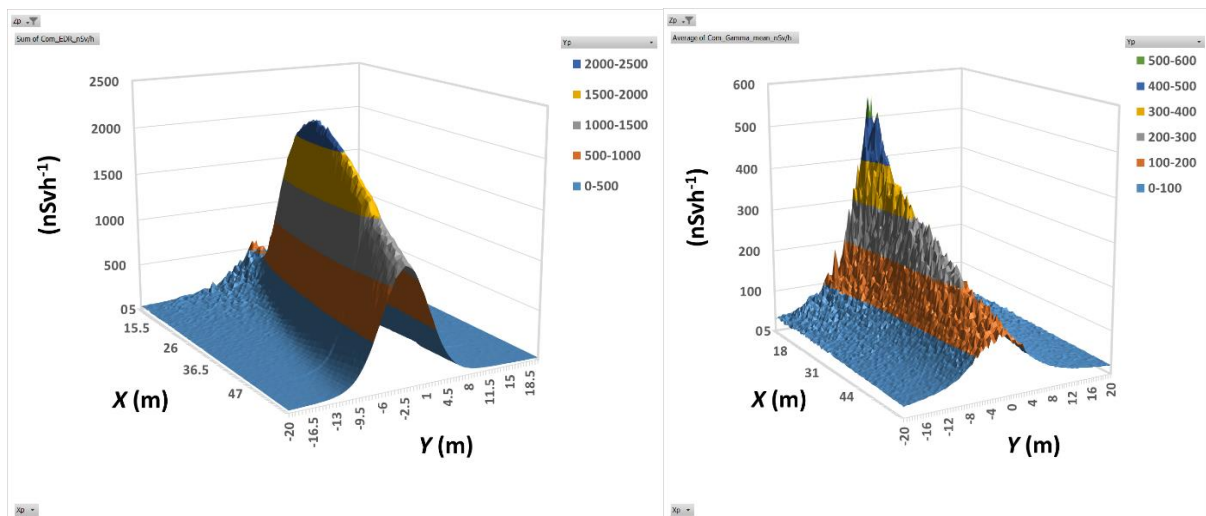


Figure 9.46(a/b). Cube/A/DGP; Passive; $Z_{rh}=255\text{mm}$; -45° ; $Z=49\text{m}$; (a) EDR; (b) Gamma rays

From Figure 9.46(a/b) can be seen some more interesting features of the dose variation spatially in the horizontal receptor grid plane: in this case relating to the cube with 'A' release position, angle of approach flow -45° with a passive release at 255mm (51m at full scale) but with the sampled receptor plane at 245mm (49m height in full scale, and just 1m above the roof plane). In Figure 9.46(a) the effective dose rate maximum (data point shown in Figure 3(a) as ED1) is shown as approximately 2000nSv h^{-1} at approximately 30m downwind of the source (Figure 32(a) applies for downstream distances from the source). However, in Figure 9.46(b) can be seen that the gamma ray dose rate peaks at approximately 550nSv h^{-1} but at a position much closer to the source. These figures indicate that the effective dose rate maxima can be located in a different spatial position to the gamma ray maxima point. The shape of Figure 9.46(a) with distance from the source reflects the distance from source required for the plume to spread downwards to the indicated receptor dose grid level.

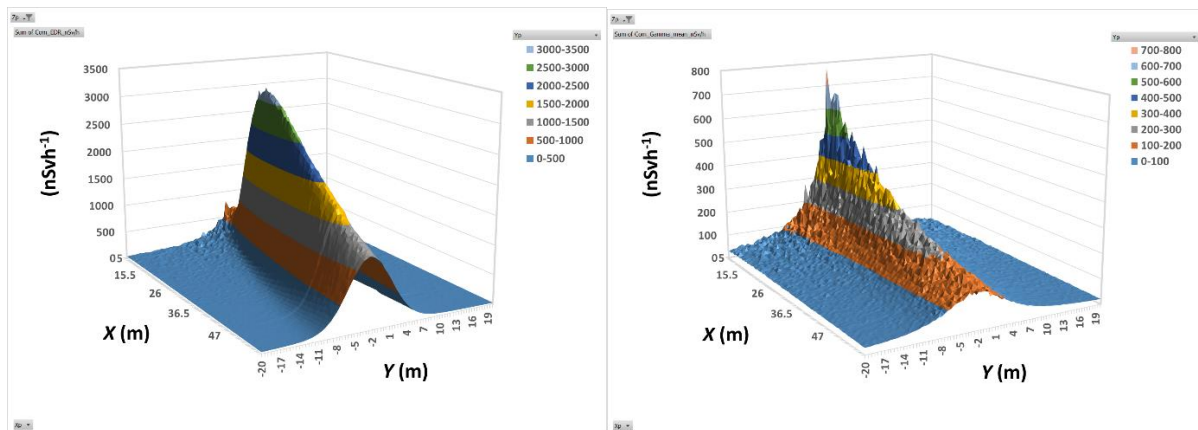


Figure 9.47(a/b). Cube/A/DGP; Passive; $Z_{rh}=255\text{mm}$; -45° ; $Z=49.5\text{m}$; (a) EDR; (b) Gamma-rays

Figure 9.47(a/b) shows the same configuration as Figure 46(a/b) except that the receptor dose plane is at 49.5m, or 0.5m above that shown previously. It can be seen (also in Figure 9.32(a)) that the effective dose rate maximum was at approximately 20m from the source (compared to 30m previously). Therefore, the positional change in the receptor dose grid has brought the effective dose rate maximum point 10m closer to the source: with the maximum value having increased by approximately 50% to just over 3000nSv h^{-1} . In Figure 9.47(b) the gamma ray dose rate is greater at just under 800nSv h^{-1} but still resides close to the source in a similar position to Figure 9.46(b).

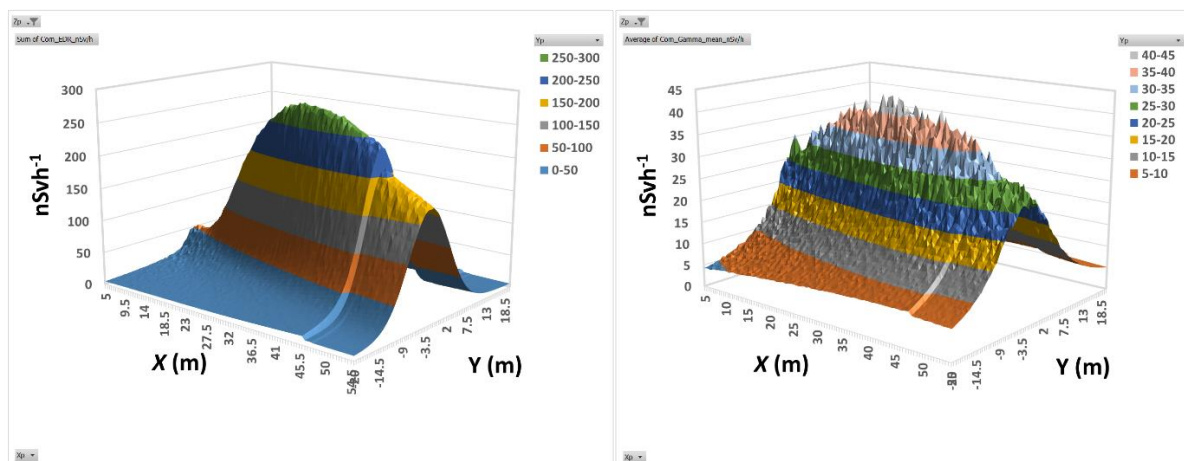


Figure 9.48(a/b). Cube/B/DGP; Passive; $Z_{rh}=255\text{mm}$; 0° ; $Z=49.5\text{m}$; (a) EDR; (b) Gamma rays

From Figure 9.48(a/b) can be seen the dose rates from the cube 'B' case at normal incidence for a passive release height of 255mm (51m full scale) and a receptor dose grid at height 49.5m (or 1.5m from the roof surface at full scale). This configuration gave rise to a significant rooftop recirculation zone, a wider Gaussian profile, which was superimposed on the narrow Gaussian plume due to the symmetry of normal incidence: this is shown in the broader profile of the effective dose plot. From Figure 9.48(a) the effective dose rate maxima of just over 250nSv h^{-1} (data shown in Figure 9.11(a)) occurs at a downstream distance from the source of approximately 30m (see Figure 9.33(a)). From Figure 9.48(b) in this case we see that the gamma ray contribution to effective dose rate peaks at approximately 45nSv h^{-1} at the same source distance. The truncation of the rooftop recirculation zone at the end of the roof (as per the MC code algorithm) can be seen in Figure 9.48(a) close to the roof edge, and the smaller effect of this concentration reduction can be seen in Figure 9.48(b) for the gamma ray dose.

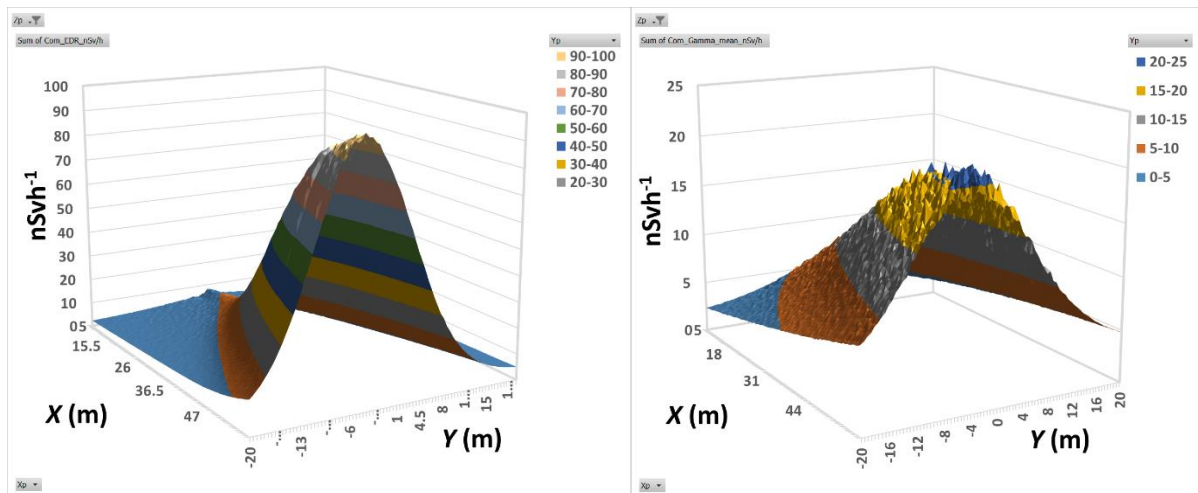


Figure 9.49(a/b). EW Clad/DGP; AV; $Z_{rh}=255\text{mm}$; -22.5° ; $Z=49.5\text{m}$; (a) EDR; (b) Gamma-rays

Figure 9.49(a) shows the effective dose from an active vertical (AV) release for the EW clad case, with a maximum value of just under 100nSv h^{-1} (see Figure 9.27(a) for data), which occurs at a downstream distance from the source of 55m (Figure 9.36(a)). Figure 9.49(b) shows the gamma ray contribution to the effective dose rate peaks at approximately 20nSv h^{-1} (data from Figure 9.27(b)) also at a downstream distance of approximately 55m (Figure 9.36(b)). These figures show that the elevated active vertical plume gives rise to highest level of dose at increased distances from the source.

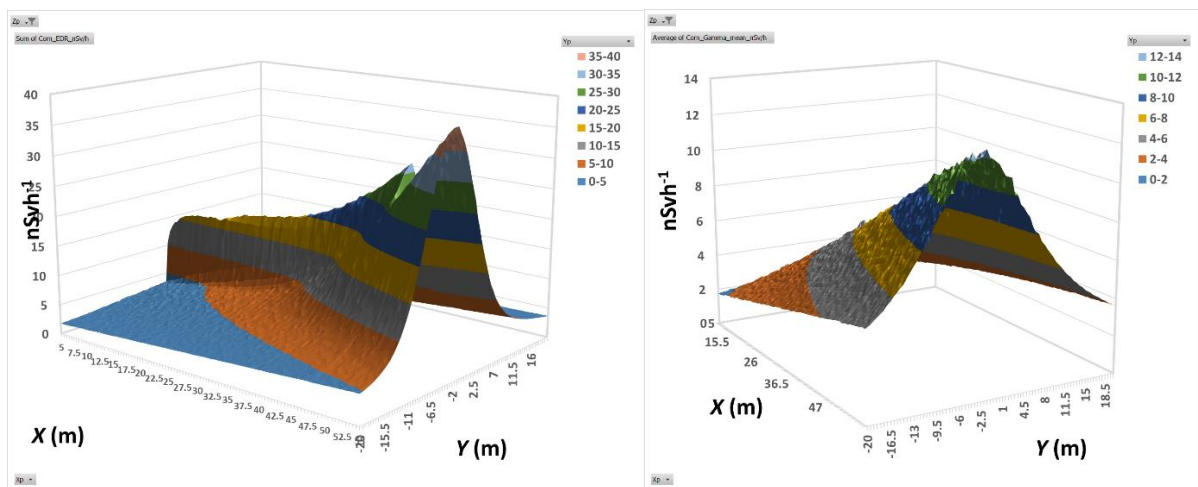


Figure 9.50(a/b). Cube/A/DGP; AV; $Z_{rh}=255\text{mm}$; -22.5° ; $Z=49.5\text{m}$; (a) EDR; (b) Gamma rays

Figure 9.50(a/b) shows the cube for an AV release at 'A' with an angle of flow of -22.5° with respective effective dose and gamma ray maxima of approximately (a) 35 nSv h^{-1} and (b) 11nSv h^{-1} respectively (see Figure 9.27(a/b)). Both maxima occur near the full MC receptor grid range evaluated at 55m downstream from the source. The interested feature shown is the rooftop recirculation zone (RCZ), truncated near the building trailing edge as per the MC code algorithm, lower in magnitude than the peak effective dose from the lower region of the main plume. Gamma ray contributions of the gaseous concentration cloud from both the main plume and RCZ are summed in (b) giving a relatively wide laterally but smoothed gamma ray dose distribution.

9.4 Discussion

Monte Carlo (MC) dose rate results have been presented based upon plume concentration field measurements made in wind tunnel experiments and best-fit parameterisations. Two sets of results have been presented for comparison, namely the simple Single Gaussian Plume fitted to a single Gaussian, and the dual Gaussian plume (with the Isolated Gaussian Plume method to determining the vertical profiles) with methods as detailed in Chapter 6. The methods take into account lateral deflection and mean upwards deflection for a range of conditions: building geometry, angle of approach flow, release position in relation to the building and the release height. Active vertical releases were simulated and the results were also presented from these cases.

Figures 9.1-9.3 show the variation with angle of approach flow and with receptor height at short range, particularly for the releases very close to the roof surface. These encompass a range of effective doses (the primary component of which being the concentration field value) within a factor of 2-3 between different cases: nevertheless, the range of conditions studied may enable setting of a range of expected values or for an estimate of a maximum: e.g. for intermediate cases. Figures 9.4-9.6 show the gamma ray component of the effective dose for the same cases, with the DGP/IGP method picking out variations against the trend of reduction of dose with increasing release height for the passive releases studied. In Figures 9.1-9.6 the DGP method shows features of the dose trends not apparent in the simpler SGP model. These are attributable to the deconvolution of bifurcated plumes, according to local flow features (such as the lead edge vertex) or rooftop recirculation zones, better handled by the more sophisticated DGP/IGP modelling approach.

Figures 9.7-9.10 show the variation of effective dose maxima with angle of approach flow for the near vertex release case 'A' with the cube. For the two lowest passive release heights tested ($Z_{rh}=245, 255\text{mm}$ or 1m or 3m above roof plane at full scale) there is a strong variation for increasing effective dose with angle of incidence moving from normal through to -45° . The SGP method picks out this trend with less clarity. For the two greater release heights studied ($Z_{rh}=265, 275\text{mm}$ or 5m and 7m above roof level) the pattern is complex but the trend reverses or tends to a very approximate constancy with angle. For the cube and midline 'B' release shown in Figures 9.11-9.16, the trend is broadly that the dose increases marginally as the release height increases from 245 to 255mm (1 and 3m at full scale) and then reduces with increasing release height: the same applies for the gamma ray component of dose. This is basically a consequence of the fall in inhalation dose as the difference between receptor and plume centre height increases. Variation of effective dose with angle in Figures 9.17-9.20 shows a general increase of dose moving from normal incidence to -45° , clearly picked out by the DGP method – the SGP method establishes this less clearly, indicating a very approximate constancy with angle in some of the cases.

The EW cases shown in Figures 9.21-9.26 show order of magnitude differences (in this context a factor of around 2-3) between these building cases for the dose maxima. The maximum values themselves are approximately within the same order of magnitude range when compared with the cube cases with near vertex (A) and midline release positions (B).

The active vertical releases (Figure 9.27) show clustered trends for the cube A/B and the EW building cases, with the EW building cases showing a greater dose, within approximately a factor of three of the corresponding cube cases. Variations with building angle were less pronounced with the elevated nature of these releases (Figure 9.28-9.29).

Downstream maxima positions were presented for all cases with significant dose, enabling the downstream maxima for overall effective dose and gamma ray component to be derived from Figures 9.30-9.36. There was evidence of some complex behaviour, particularly picked out by the more sophisticated DGP/IGP analysis method, but the broad finding was that as the release height increased the downstream maxima increased in distance from the source. Lateral crosswind maxima positions shown in Figures 9.37-9.43 were generally shown to be within a few metres of the approaching wind direction for the various cases investigated.

In Figures 9.44-9.50 various cases showing the spatial distribution of effective dose and gamma ray dose were shown with respective features of dose maxima occurring at further downstream positions due to more elevated release heights. The sensitivity to receptor dose height was shown as an important factor.

9.5 Conclusions

It can be seen from the results that the variations of dose are complex given the range of experimental conditions but some broad themes emerge. There is a wide range of values for the effective dose and the gamma ray component of the effective dose apparent in the results, leading to differences in dose of some orders of magnitude (defining this in the approximate range of a factor of 2-3 across the range of experimental cases modelled). The DGP method was seen to be more sensitive to conditions prevalent in the concentration field and their consequent effect on dose.

In summary, it can be seen from the results that for receptor dose positions close to the roof plane (up to 2 metres above the roof):

- (a) for a given wind direction, there is a strong dependence on release position with respect to the building with higher doses being evident with the near vertex release position (A) and lower doses where the release position was at the midline (B) where the greatest upwards direction of flow was encountered
- (b) there is a marked dependence upon release height, with a general pattern of reduction of dose rate with release height (but a countervailing factor for the very lowest release height studied attributed to the upwards deflection of flow and the resulting plume height relative to the receptor dose positions)
- (c) there is a marked dependence with angle of approach flow to the building, with the highest doses being evaluated for the more oblique angles of incidence; this is particularly apparent for a release which is closer to the leading upstream vertex of a building (position 'A' as compared to position 'B')
- (d) there was a significant response to the building shapes studied, broadly within the order of magnitude ranges specified
- (e) the active vertical releases studied for the cube and EW buildings configurations gave rise to plumes which were significantly elevated with respect to the roof plane, with associated small doses at near to roof level for all cases. The EW buildings gave effective dose values which were a factor of approximately three greater compared to the cube with near-vertex release position 'A'; which in turn was greater than maximum doses obtained for the 'B' release position by a factor of very approximately two
- (f) The downstream maxima positions for radiation dose depended upon release height – a greater release height tended to move the dose maxima positions downstream to where the plume dispersed downwards into the sampled height zone

- (g) Higher radiation dose maxima were generally attained for dose receptor positions farther from the roof surface (i.e. between short and tall individuals) within the assumptions of a steady-state plume averaged over time

For any given set of conditions with a cube building the results presented could be used to produce an estimate of the dose, or, from the basic data set which feeds the model, a value of maximum dimensionless concentration from which an estimate of 'real world' concentrations for a given situation can be evaluated knowing the pollutant release rate, building height and wind speed at the reference height and approach angle. Extending the model further to produce order of magnitude estimates of effective dose (or dose arising from pollutant through inhalation) could be made by interpolation of release position, release height and angle of approach flow and considering the relative variations in these parameters from the cases presented here. This may be particularly useful in an analysis for a safety case where an order of magnitude upper estimate needs to be evaluated together with an idea of the overall sensitivity to conditions in a given problem. In this respect the two 'real-world' cases of the East Wing (EW) building extend the data set further, giving an indication of the potential variation of dose and concentration field values in the presence of site building structures as opposed to the conventional cube building case.

The results of this analysis may be used to refine an assessment to narrow down and define the experimental cases that would need to be subjected to a detailed wind tunnel measurement or calculation using a Computational Fluid Dynamics (CFD) model in order to establish even more accurate concentration field values and ultimately more accurate dose assessments.

If there were an CFD module which enabled computation of radiation dose rates, then these results could use the data presented here as test cases to verify the accuracy of those simulations.

CHAPTER 10: FULL SCALE ROOFTOP GAMMA-RAY DOSE MEASUREMENTS

10.1. Introduction

Radiation dose levels arising from the emission of radioactive gases from the radiopharmaceutical production at St Thomas Hospital (STH) were measured in the roof zone of the East Wing (EW) building on the St Thomas Hospital (STH) site in central London. The released gases were positron emitting by products from the production of radiotracers used in patients undergoing Positron Emission Tomography (PET) scanning in the hospital. Two gamma ray dose detectors were placed at different locations on the EW roof. An ultrasonic anemometer was also placed near the flue stack in order to measure wind speed and direction just above the roof height. At the outset of these site measurements the EW building was undergoing cladding works which would significantly affect the shape of the building and have effects on the flow field and dispersion of the radioactive gases emitted from the stack. Workers were in the vicinity of the roof for considerable periods of time over a period of approximately one year and the measurements were necessary to confirm acceptably low radiation dose levels to those persons over that period of time in conformance to national regulations governing exposure to ionising radiation. The second reason was to provide data on the gamma ray dose rates to use as part of a radiological assessment of expected doses to persons inside the EW building (from intake of radioactive gases through air intakes on the roof) and to be able to confirm that the dose levels to persons inside this building, and elsewhere on the STH, were within acceptable levels with respect to regulations governing discharges of radioactive materials into the environment. With respect to this research the purpose of the measurements was to enable comparison of the full scale measured data with the Monte Carlo calculated data and to compare and contrast any differences between these methods of estimation of radiation dose.

10.2 Methods

10.2.1 EW Building Layout and detector placements

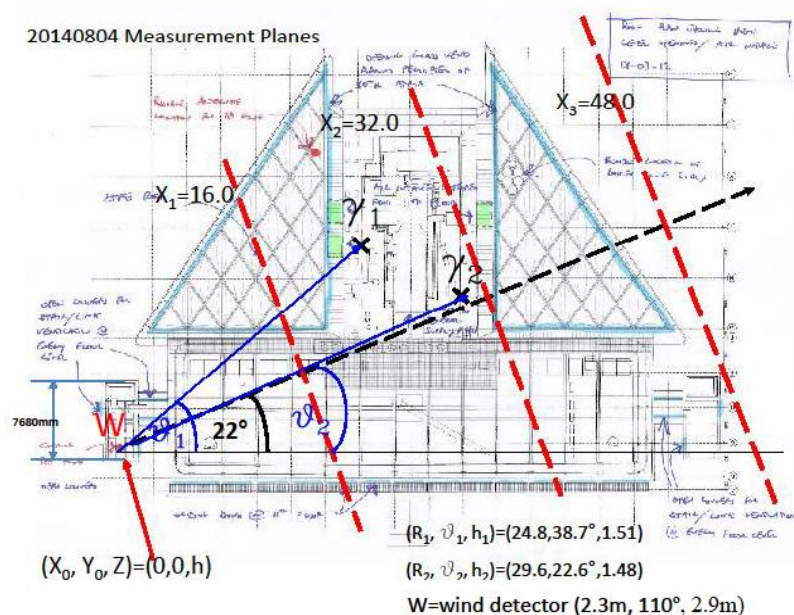


Figure 10.1 Gamma-Ray (γ_1 , γ_2) and Wind (W) detectors in relation to the EW roof
Image by ARUP/Hopkins and ISG, with annotations by the author

Figure 10.1 shows the EW roof zone and the positions of the two gamma ray detectors, positioned inwards in the main central section of the roof – the air intakes for the EW building were nearby and are shown with green colouration. The ultrasonic wind detector (W) is shown close to the stack on the North stair tower, at a radial distance of 2.3m from the centre of the stack, and a height of 2.9m above the base of the stair tower roof. In Figures 10.2(a) and 10.2(b) the two gamma detectors can be seen positioned with the probe pointing vertically upwards: the two detectors were positioned at a height of approximately 1.5m above the roof plane. The detector probes are shown with protective wrapping in place.



Figure 10.2(a/b): Gamma-Ray Detector 1 facing West/North

Figure 10.3(a) also shows the second gamma detector looking in a direction towards the South-East approximately in the direction of Lambeth Palace and Archbishop's Park.

The scaffolding seen in Figures 10.2(a), 10.2(b) and 10.3(a) was in place as part of the construction project to add the glass cladding layer to convert the East Wing (EW) unclad building into the EW clad building. The presence of the scaffolding is indicative that these working zones were occupied by construction operatives during these construction works – one of the main objectives of the measurements was to confirm levels of radiation dose during the project to those working there. The two glass triangular features visible in Figure 10.1, either side the central region where the EW air intakes and the two gamma-ray dose detectors were located, were installed as part of those cladding work and it should be noted that these projected above the central roof region where the detectors were located.

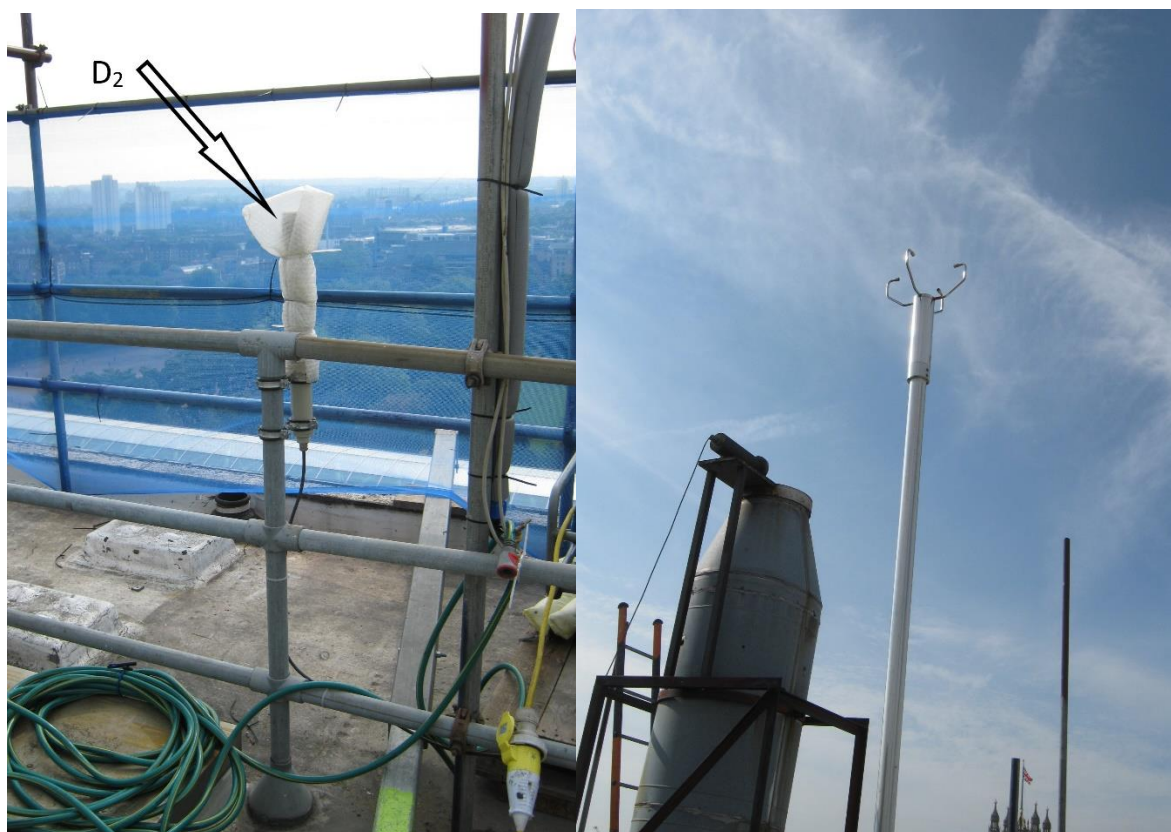


Figure 10.3(a/b). Detectors: (a) Gamma-ray Detector 2 facing SE; (b) Wind detector facing West

Figure 10.3(b) shows the four-pole ultrasonic anemometer positioned close to the flue stack on the EW North stair tower (the Houses of Parliament are just visible in the background).

10.2.2 Gamma-Ray Detectors

Berthold (Berthold GmbH, Bad Wildbad, Germany) installed two LB6360-H10 low dose rate gamma ray detectors for measurement of the gamma ray dose rate, a picture of which is shown in Figure 10.4(a) and the photon response shown in Figure 10.4(b).

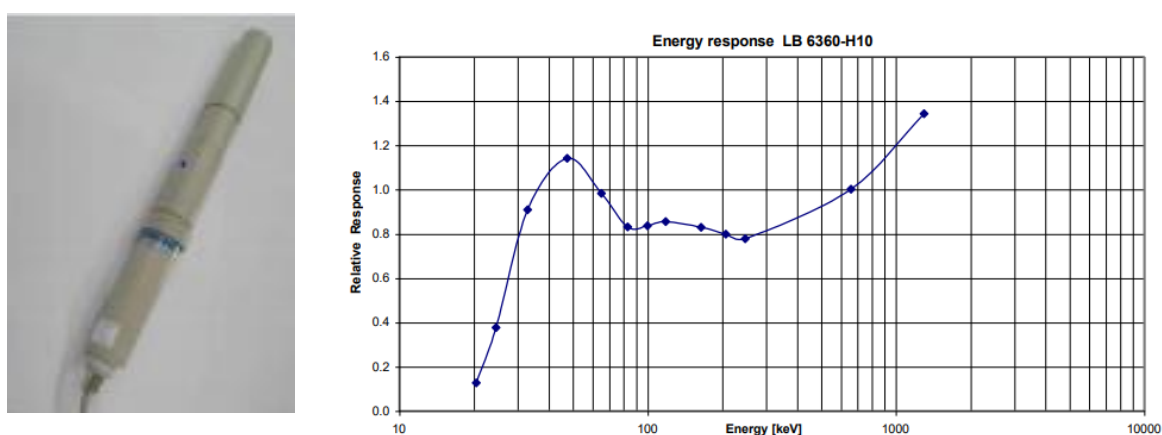


Figure 10.4(a/b): Gamma-ray detector: (a) LB6360-H10 Compensated Geiger Gamma Ray Detector; (b) Photon energy response: reproduced with the permission of Berthold UK Ltd.

The gamma ray dose rate meters were calibrated according to the ambient dose rate equivalent $H^*(10)$ (ICRU, 1992) which is the operational dose rate quantity, made in a radiation field, which most closely matches the effective dose received by a person in that radiation field. Furthermore, personal radiation dosimeters are calibrated to $H^*(10)$, so the measured quantity would match that recorded by dosimeters to personnel exposed to the radiation field. In this way the measured dose rate, and time integrated dose, from the roof gamma ray detectors may be compared directly to the Monte Carlo dose rate and integrated dose values. From the gamma-ray response factors shown in Figure 10.4(b) the energy response achieves a value of approximately 80% for photons of 53keV and is close to unity for photons above this energy value and extending up to beyond the positron annihilation gamma ray energy of 511keV. It may be therefore stated that the energy response of the detectors was suitable for the gamma-ray field measured, within an accepted tolerance on energy response of within +/-20%. Polar response of the detector was stated as being within stated tolerance ranges within +/-45° of the normal incidence at the calibration energy of 662keV applicable for ^{137}Cs (DDEP, 2014).

10.2.3 Ultrasonic Anemometer

The wind detector was the Thies Clima Ultrasonic Anemometer 2D (Thies Clima, Göttingen, Germany) which produced output data on wind speed and direction in the horizontal plane.

Ultrasonic anemometers work by measuring the time of an ultrasonic pulse to travel between a pair of transducers (The University of Manchester, 2021). The transducers work in parallel opposed pairs sending pulses backwards and forwards between them, and the wind velocity along the transducer axis is calculated using the values obtained from both directions. The speed of sound is also derived from the calculations. In these experiments two orthogonal directions in the horizontal plane were sampled.

Where the wind direction is travelling in the direction of the emitted pulse the transit time to the other transducer, T_1 , over a distance between detectors of L , is given in relation to the speed of sound, c , and the wind velocity in the direction of the axis of the sensors, v as follows in equation [1]. The corresponding return pulse in the other direction has a transit time T_2 as given by equation [2].

$$T_1 = \frac{L}{c+v} \quad [1]$$

$$T_2 = \frac{L}{c-v} \quad [2]$$

Solving for c from equations [1] and [2] we obtain equation [3] showing the wind velocity. Also, solving for v we obtain the speed of sound c in equation [4].

$$v = \frac{L}{2} \left(\frac{1}{T_1} - \frac{1}{T_2} \right) \quad [3]$$

$$c = \frac{L}{2} \left(\frac{1}{T_1} + \frac{1}{T_2} \right) \quad [4]$$

An estimated approximate temperature of the air in the beam path of the probe may be assigned by the ideal gas equation for the speed of sound in air with absolute temperature, as given in equation [5].

$$c = \sqrt{\frac{\gamma k T}{m}} \quad [5]$$

Where T is the absolute temperature in Kelvin, γ is the adiabatic index for air, k is Boltzmann's constant and m is the mass of a single molecule. Given the short time scales from release position to the measurement positions of the plume, and that radioactive decay processes are not affected by ambient temperature considerations, the temperature estimate data from the sonic anemometer were not analysed in the data analysis.

The detector was read using the MEVIS Communication Processor (Berthold GmbH, Bad Wildbad, Germany) which was operated at the shortest time base available between measurements of one minute. Outputs were available from the data polling system at one-minute intervals for mean wind speed and direction vector (angle with respect to North) in the horizontal plane and these data were taken forward for analysis.

10.2.4 Source release term

The release terms were estimated from a continuous logging system developed in-house at the Clinical PET Centre at St Thomas' Hospital. The Mini Instruments series 900 type 400 scintillation probe perpendicular to the effluent efflux direction is clearly visible in Figure 10.3(b). This detector was used to record the count rate at one second intervals during each day of radiopharmaceutical production. The data traces showing count rate of this detector over time were obtained for all noted gamma peaks in the MEVIS data traces. The detector was calibrated at periodic intervals using releases of liquid nitrogen cryogen-trapped $^{11}\text{C-O}_2$ from the ventilation system to the stack. These bolus releases of sublimated gas were trapped in a cryogenic Dewar flask inside a re-entrant radionuclide activity calibrator (Mirion, 2021) which was subject to periodic calibrations against NPL standards (NPL, 2021). A calibration factor relating released activity to integrated counts per second from the time trace was obtained from periodic series of measurements, and this factor was applied to all time traces (expressed as 'counts per second', or cps) to obtain the magnitude of releases in terms of MBq. It should be noted that integrated releases were recorded on a daily basis, and an accumulated tally calculated, in order to show compliance with daily and monthly discharge limits set down in the site emissions permit granted under national legislation (EPR2016, and amendment regulations).

2.5 Gamma ray-peak analysis

Experimental data was available from between August 2013 to September 2014. All data from the gamma ray traces available throughout the data sampling period was analysed. Since the data polling was set at one minute (the highest frequency sampling available with the MEVIS system) the wind and gamma-ray data was analysed from the synchronous output data set provided from the system output. From analysis of the release traces from the stack detector it was seen that the releases were 'spike' releases in nature, similar to those presented for other radiopharmaceutical production facilities of this kind (Kleck et al, 1991) with a duration of just a few minutes. Given the nature of the spike releases a method to analyse the integrated dose from the peaks of the release was devised as part of this experimental analysis.

Inspection of the gamma ray detected traces from the MEVIS system output indicated that the emission peaks during the synthesis processes was generally less than 4 minutes. Accordingly, a sample time window of five times this duration at 20 minutes duration was set for the analysis of the integrated gamma-ray dose for the system and the corresponding meteorological conditions pertaining during any given spike release under analysis. The 20 minute time window set for the analysis was set to satisfy the following conditions: (a) that the gamma ray dose rate background in the first three minutes was consistent with the temporal background

level immediately up to that point in time, and (b) the first three values were close to each other in magnitude i.e. the rising leading edge of the gamma ray peak did not affect those values – these values were used as the background gamma ray dose rate level against which to assess the excess dose rate arising from the radioactive release.

To assess the gamma-ray dose for a given release peak at the two detectors the approach taken was to integrate the excess dose above the initial background level over the 20-minute time window. Inspection of the gamma ray dose rate traces in all cases indicated that the excess dose rate had reduced to within $0.1\mu\text{Svh}^{-1}$ within the 20-minute window post the spike peak. Excess integrated dose values were recorded in nSv for each of the gamma-ray detectors used in the experiment.

10.2.6 Wind speed analysis

The magnitude of the horizontal wind velocity vector was available from the data logger at one-minute intervals. The mean value over the 20-minute sampling window was taken as a representative value of the wind speed over the experimental domain during each experimental time window.

10.2.7 Wind direction analysis

The wind direction was significant in terms of proximity of the plume to the detectors and hence the magnitude of the recorded dose at the gamma ray detectors. The MEVIS output was recorded in wind bearing from 0° at magnetic North to which the detector had been aligned, and this value was converted to the angle to the building to match the wind tunnel experimental data measured for the site models. Accordingly, the alignment of the West edge of the EW building at -7.5° to North (clockwise is positive) meant that a wind direction bearing of 345° (or -15°) against North resulted in an approach flow of -22.5° as measured from the building (this angle of approach wind is shown in Figure 10.1). All measured wind directions were likewise converted using the same approach so that the wind direction was expressed in relation to the angle of approach flow to the building, with 0° parallel to the long West face of the EW building.

There was generally considerable fluctuation in the one-minute wind direction samples over the 20-minute sample period containing the gamma ray dose rate peak. In order to accurately reflect the prevailing conditions when the plume was moving over the building, given the very short ranges of the gamma ray detectors in relation to the release point, the mean wind velocity direction was calculated over a four-minute window encompassing the dose rate peak value. This value was used as the actual direction of the plume during the interaction with the gamma ray detectors during the ‘peak catching’ event at the detectors and was also used in determining the position of the gamma ray detectors with respect to the plume when approaching the building from the determined wind direction over the four-minute sample window. In this way the Monte Carlo determined radiation dose rate at the detectors could be compared to the measured dose for each gamma ray peak event detected.

10.2.8 Comparison of measured dose values against Monte Carlo computations

In order to compare the gamma ray dose peak integrated values against the MC values, which were themselves calculated as mean dose rate values on the basis of a steady wind direction over an extended period of time, it was necessary to normalise and correct the integrated dose peak values. It was necessary to correct for the release rate assumed in the MC model and also the standard wind speed taken for those calculations.

An example of the calculation to determine the equivalent dose rate from a given gamma-ray peak detection event on the 24th April 2014 is given as follows in Table 10.1.

Table 10.1. Twenty-minute time-traces of γ_1 and γ_2 dose rates and wind speed/direction

Detector	γ_1	γ_2	Wind Speed	Direction
Net Dose Rate	($\mu\text{Sv/h}$)	($\mu\text{Sv/h}$)	(ms^{-1})	To Building
Time trace				θ_B
24/04/2014 15:48	-0.002	-0.001	0.600	161
24/04/2014 15:49	0.003	0.000	1.500	168
24/04/2014 15:50	-0.002	0.002	1.000	160
24/04/2014 15:51	0.044	0.023	0.300	134
24/04/2014 15:52	1.129	0.753	0.600	-87
24/04/2014 15:53	0.518	0.565	0.100	-22
24/04/2014 15:54	0.366	0.123	0.100	-58
24/04/2014 15:55	0.292	0.112	0.200	55
24/04/2014 15:56	0.232	0.085	0.400	166
24/04/2014 15:57	0.201	0.086	0.200	-5
24/04/2014 15:58	0.179	0.076	0.100	142
24/04/2014 15:59	0.155	0.066	0.600	-106
24/04/2014 16:00	0.141	0.059	0.200	-60
24/04/2014 16:01	0.122	0.053	0.200	-36
24/04/2014 16:02	0.104	0.048	0.200	-57
24/04/2014 16:03	0.099	0.044	0.300	-9
24/04/2014 16:04	0.090	0.039	0.300	-87
24/04/2014 16:05	0.073	0.029	0.200	-170
24/04/2014 16:06	0.063	0.026	0.400	-88
24/04/2014 16:07	0.048	0.024	0.100	112
			0.380	15.75
Dose (nSv)	64.36	36.76	0.349	109.8
		Four minute	θ_B	-27.8
		window	σ_{θ_B}	60.9

Table 10.1 shows data output for the two gamma-ray detectors over the standard 20-minute time trace used to analyse each peak catching event. Background dose rates are determined from the first three minutes at the start of the 20-minute window and then subtracted off all dose rate figures – net dose rates corrected for background radiation are shown in the table. The peak dose rate was identified and is shown in red figures. Next, a four-minute window is selected around the peak dose rate value – in this case the peak and following next three one-minute row entries and is highlighted in yellow. Wind speed figures are shown, with a mean value of 0.380ms^{-1} over the 20-minute time window, with a sample standard deviation of 0.349ms^{-1} over the same period. The mean wind direction in relation to the building, θ_B , is shown over the four-minute peak dose period as a value of -27.8° . The sample standard deviation of the wind direction over the four-minute peak window, σ_{θ_B} , is shown as a value of 60.9° . The cumulative dose at each of the two detectors γ_1 and γ_2 is expressed in nano-Sieverts (nSv) with respective values of 64.36nSv and 36.76nSv as shown in the table. This same methodology was consistently applied to all gamma-ray peaks analysed. Inspection of many time-traces indicated that the high levels of turbulence at the roof level, where the anemometer and gamma-ray

detectors were located on the EW building, gave rise to high levels of directional fluctuation in wind direction and variations in wind speed. The narrower four-minute window around the peak dose rate from these ‘spike’ releases was chosen to determine a more representative wind direction during which time the bulk of the dose accumulated at the detectors was received. The wind direction angle thus selected was then used to determine the dose rate applicable from the Monte Carlo calculations at the corresponding positions of the detectors with respect to the plume in terms of the streamwise and crosswind co-ordinates for that wind direction.

Table 10.2 shows correction factors for wind speed at height using the power-law formulation as shown in NRPB report R-91 (Clarke *et al*, 1979), given in equation [6]. In the paper reproduced in Appendix 15.6, the near free-stream velocity U_{ref} at height of 200m from the ground was taken from Heathrow data, a site at which $n=0.234$ would be applicable from R-91 with a corresponding ground roughness-length of $Z_0=0.2m$. From applying the power-law to the weighted-mean wind speed $U_{wm}=2.76ms^{-1}$ at Heathrow (from the paper in Appendix 15.6) this corresponds to $U_{ref}=5.53ms^{-1}$ at 200m height, the value used in all the Monte Carlo simulations. The quantity U_{10} is the wind speed at 10m height, and height z is expressed in metres in equation [6].

$$U(z) = U_{10} \left(\frac{z}{10} \right)^n \quad [6]$$

As an approximation, and at neutral stability conditions, treating U_{ref} as being the same at the STH site at 200m from ground level as at Heathrow and applying equation [6] with $n=0.386$ appropriate from R-91 for city locations (with a corresponding value of $Z_0=1.0m$) we obtain for an anemometer detector height of 50m on the EW roof:

$$U(200m) = 5.53ms^{-1} = U_{10}(200/10)^{0.386}$$

$$U(50m) = U_{10}(50/10)^{0.386}$$

Dividing to eliminate U_{10} , which is not required, we obtain V_{cf} the velocity correction factor from wind speed at 50m up to 200m, the height of U_{ref} at the STH site.

$$V_{cf} = U(200m)/U(50m) = (200/50)^{0.386} = 1.708$$

It can also be shown that at the STH site $U(50)=3.24ms^{-1}$ when $U_{ref}=5.53ms^{-1}$. Moreover, when we obtain wind speed values from the rooftop anemometer at the STH site they must be multiplied by V_{cf} to scale them to the U_{ref} height of 200m, where they can be compared to the U_{ref} value of $5.53ms^{-1}$ used in the MC calculations. The mean wind speed in Table 10.1 was $0.380ms^{-1}$ and when corrected by V_{cf} takes the value of $U_{ref,F/S} = 0.649ms^{-1}$.

Table 10.2. Wind speed values and velocity correction factor V_{cf}

Quantity	Value	Units	Explanation
V_{cf}	1.708	None	Wind speed correction from 50m to 200m at STH site
U_{mean}	0.380	ms^{-1}	Mean wind speed at 50m height from Table 10.1
$U_{ref,F/S}$	0.649	ms^{-1}	Wind speed from full-scale measurements at 50m height corrected to 200m height using V_{cf}
$U_{ref,MC}$	5.53	ms^{-1}	Value of U_{ref} used for all Monte Carlo calculations

The total release A_{rel} (in MBq) for the release was established from stack release data for the given spike release. The standard expected release rate per hour \dot{A}_{std} ($MBq.h^{-1}$) at the rate used

for all the MC calculations was also established. Next, the integrated dose at detector i , D_i , was converted into an equivalent mean dose rate that would pertain given the standard release rate of activity for the MC calculations. The measured mean speed at the building height U_{mean} (over the full 20-minute window of data) was converted using the correction factor V_{cf} to wind speed at the standard reference height of 200m using the appropriate power-law correction factors as given in Appendix 15.6, and as applied in equation [6] previously. Finally, the result was scaled by the reference wind speed at 200m height used in the MC calculations $U_{ref,MC}$. It has been shown in previous analysis, and from the paper reproduced in Appendix 15.6, that the dose rate from the plume is inversely proportional to the wind speed so the latter correction was necessary in order to be able to compare directly the measured doses at full-scale against the MC calculations applying for a different wind speed. The result of equation [7] is the measured dose rate at full-scale converted into a comparable equivalent dose rate $\dot{D}_{i,M}$ under the conditions used for the Monte Carlo calculation.

$$\dot{D}_{i,M} = D_i \frac{\dot{A}_{std}}{A_{rel}} V_{cf} \left(\frac{U_{mean}}{U_{ref,MC}} \right) \quad [7]$$

Table 10.3 shows the quantities involved in the example being given, and the application of equation [7] also using results from Tables 10.1 and Table 10.2.

Table 10.3. Release quantities corrected to Monte Carlo calculated steady release values

Quantity	Value	Unit	Explanation
\dot{A}_{std}	1501.2	MBq.h ⁻¹	Standard release rate for MC calculations
A_{rel}	5880	MBq	Spike release for event on 24/04/2014
$D_i (\gamma_1)$	64.36	nSv	Integrated dose from spike, detector 1
$D_i (\gamma_2)$	36.76	nSv	Integrated dose from spike, detector 2
$\dot{D}_{i,M} (\gamma_1)$	16.43	nSv.h ⁻¹	Equivalent dose rate from spike release to be compared to the steady state MC calculated dose rate: detector 1
$\dot{D}_{i,M} (\gamma_2)$	9.38	nSv.h ⁻¹	Equivalent dose rate from spike release to be compared to the steady state MC calculated dose rate: detector 2

Having established the dose rate values that would pertain to a release rate case and wind speed matching the calculations made for the MC case (an example has been given in Table 10.3) it was necessary to establish the MC values at the co-ordinate positions relative to the plume that would correspond to the two detector positions. Accordingly, a rotational co-ordinate transformation was applied to the detector positions, given the actual wind direction from the peak direction in relation to the building, to determine the actual positions relative to the plume and the source position. The wind tunnel data used to produce the plume data for the EW building was based upon measurements at a main wind direction of -22.5° (as per Figure 10.1): therefore, the -22.5° EW data sets, as applied through the MC calculations, were used to determine gamma-ray dose rate at detector positions corresponding to the detectors for different angles of incidence of wind on the building. There is an inherent limitation in this approach in that the plume upwards deflection and plume height could be expected to vary with angle of approach flow. However, results shown previously (Ibid, Chapter 6) indicate that for the active vertical releases considered from the wind tunnel data the plume is relatively elevated in relation to the building and the extent of plume lateral or vertical deflection would be expected to be significantly smaller than the passive release cases considered at low release heights in relation

to the roof. Therefore, the application of the -22.5° wind tunnel data in order to determine MC dose rates at detector positions corresponding to different angles of approach flow is considered to be a reasonable approximation.

Table 10.4 shows the application of a rotational co-ordinate transformation with the co-ordinates (X_1 , Y_1) applying to detector γ_1 and (X_2 , Y_2) applying to detector γ_2 in the non-rotated frame of reference at 0°. In the rotated frame-of-reference the primed co-ordinates (X_1' , Y_1') apply to detector γ_1 and (X_2' , Y_2') apply to detector γ_2 . From Table 10.1 the wind direction over the peak sampled 4-minute window was -27.8 and this is the rotation that has been applied in Table 10.4. The rotation of the co-ordinate system gives the (X , Y) values of the detectors when the X-axis has been rotated to the wind direction around the source position – since the MC calculations were all performed with the X-axis streamwise the transformed co-ordinates (X' , Y') show the streamwise distance from the source (X') and crosswind displacement (Y'). Therefore, the MC dose rate can be looked up for the (X' , Y') position of the detector from the MC data file.

Table 10.4. Rotation of the co-ordinate system to apply the MC calculated dose rate values

Position of detectors in co-ordinate systems		0 degrees	
X1 =	19.35 m	X2 =	27.33 m
Y1 =	15.51 m	Y2 =	11.38 m
Angle of rotation of co-ordinate system, θ_B =		-27.8 degrees	
X1' =	24.35 m	X2' =	29.49 m
Y1' =	4.72 m	Y2' =	-2.65 m

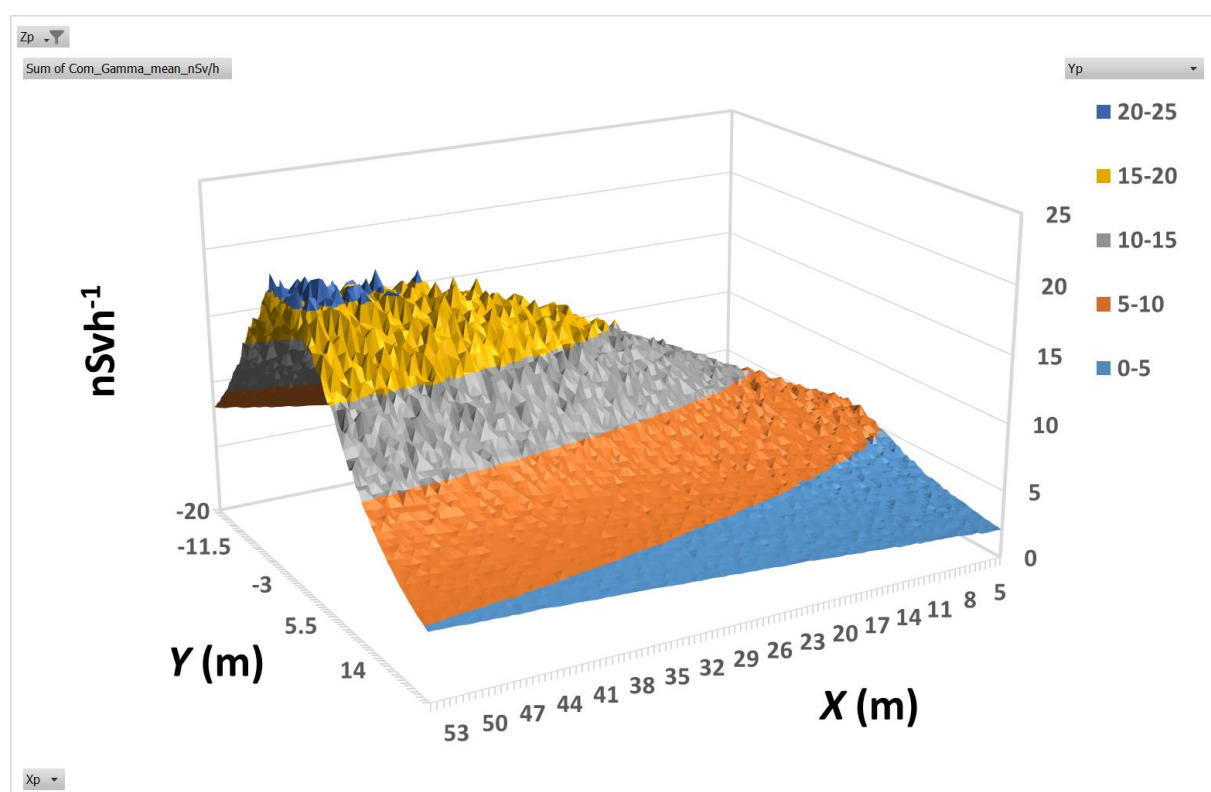
Four MC data sets were considered: EW clad and unclad, and for both the DGP and SGP analysis methods. For the purposes of this analysis the calculated dose rate from MC was compared against the measured values in a calculated/measured ratio (C/M) for each of these cases: the mean C/M ratio was determined averaging across all cases and the coefficient of variation across all cases was calculated. Inspection of the results indicated the mean (over the EW building cases) of coefficient of variation (CV) for the two detectors 1 and 2 (0.076 and 0.065 respectively) was much smaller than the variation inherent in the C/M ratio – it was therefore decided to pool the results across all the EW building cases and look at the mean response in comparison to the full-scale data.

Table 10.5 shows the (X' , Y') co-ordinates for the example being considered (wind direction of -27.8°) as given in Table 10.4 and the Monte Carlo (MC) dose rates at the detectors for the EW clad (EWC) and unclad (EW_UC) cases and for both the SGP and DGP plume modelling methods. The upper table is for detector 1 and the lower table for detector 2, all co-ordinates are at full-scale in metres. The dose rate values at the closest MC run angle (-22.5°) are also given for comparison for each of these detectors in the respective upper/lower tables. The ratios of the MC calculated dose rates over measured dose rates from Table 10.3 ($\dot{D}_{i,M}(\gamma_1)$ and $\dot{D}_{i,M}(\gamma_2)$) are given as the calculated-over-measured ratios (C/M) for each of the four cases. As above, the decision was to take the mean over all four cases considered and to calculate the sample standard deviation to evaluate the coefficient of variation (CV) to analyse the spread of these values. The mean C/M ratios are presented for detector 1 (0.528) and detector 2 (1.409) with respective CV values of 0.14 and 0.16 over the four cases (EWC, EW/UC, SGP, DGP).

Table 10.5. MC dose rates at the detectors under co-ordinate transform to wind direction

Dose Rate Match at co-ordinate points			(X ₁ ',Y ₁ ')	Detector	#1				
Sample DR angle	Co-ordinates			Dose rates (nSv.h ⁻¹)					
θ_b	X1' =	Y1' =		γ_{SGP_EWC}	γ_{DGP_EWC}	$\gamma_{SGP_EW_UC}$	$\gamma_{DGP_EW_UC}$		
-45	24.65	-2.72							
-22.5	23.81	6.92		6.314	7.608	6.479	8.181		
0	19.35	15.51							
-27.8	24.35	4.72		7.478	9.53	7.809	9.914	Mean	CV
		C/M		0.455	0.580	0.475	0.603	0.528	0.140
Dose Rate Match at co-ordinate points			(X ₂ ',Y ₂ ')	Detector	#2				
Sample DR angle	Co-ordinates			Dose rates (nSv.h ⁻¹)					
θ_b	X2' =	Y2' =		γ_{SGP_EWC}	γ_{DGP_EWC}	$\gamma_{SGP_EW_UC}$	$\gamma_{DGP_EW_UC}$		
-45	27.37	-11.28							
-22.5	26.23	0.06		10.492	14.406	10.95	14.226		
0	27.33	11.38							
-27.8	29.49	-2.65		11.223	15.176	11.56	14.91	Mean	CV
		C/M		1.196	1.617	1.232	1.589	1.409	0.160

Figure 10.5 shows the gamma-ray doses rates from the Monte Carlo run for the EW clad case using the DGP method: at (X₁', Y₁') co-ordinates (24.4, 4.7) the gamma-ray dose rate matches the figure in Table 10.5 at just under 10nSv.h⁻¹. The corresponding dose rate for detector 2 at co-ordinates (29.5, -2.7) takes a value of approximately 15nSv.h⁻¹ corresponding to the graph.

**Figure 10.5. Monte Carlo gamma-ray dose rate for EW clad DGP method**

10.3 Results

10.3.1 Anomalous results

The following data points were excluded from the analysis:

- 20140414: low reading, C/M anomalously high due to low release value or misidentified peak
- 20140508: low reading, C/M anomalously high due to low release value or misidentified peak
- 20140613: low reading, C/M anomalously high due to low release value or misidentified peak
- 20140710: low reading, C/M anomalously low due to suspected underestimated release peak

Inspection of the results indicated that all of the above figures were orders of magnitude different to the expected range of results – the subsequent results presented exclude the above data. In total there were 29 gamma peaks from which the further analysis of results was drawn.

10.3.2 Mean Gamma Dose Rate from MC compared against wind tunnel derived results

The procedure given in section 10.2.8 was repeated for all gamma-ray dose peaks producing a spread of C/M values which were analysed statistically. The mean C/M ratio for detectors 1 and 2 from the analysed data set were 0.74 and 1.26 respectively - providing the unexpectedly fortuitous result that averaged over both detectors the ratio of calculated dose from the MC analysis against the measured data was unity. This result however can be taken to infer that there was no significant bias affecting the results and that the overall magnitude of the dose calculation was approximately correct. The respective coefficients of variation (CV) for detector 1 and 2 were 1.17 and 1.14, which indicates a high extent of variability of the C/M ratio across the data set analysed for any individual puff release or spike release event.

10.3.3 Probability density function (pdf) for the measured full-scale results

Figure 10.6 indicates the probability density function of the ratio of the calculated (via MC analysis) dose rate against the measured dose rate at the respective detectors 1 and 2 (as covered in section 2.8) plotted against the C/M ratio. The mean values of the C/M ratio for both detectors and respective CV values have been stated in section 3.2.

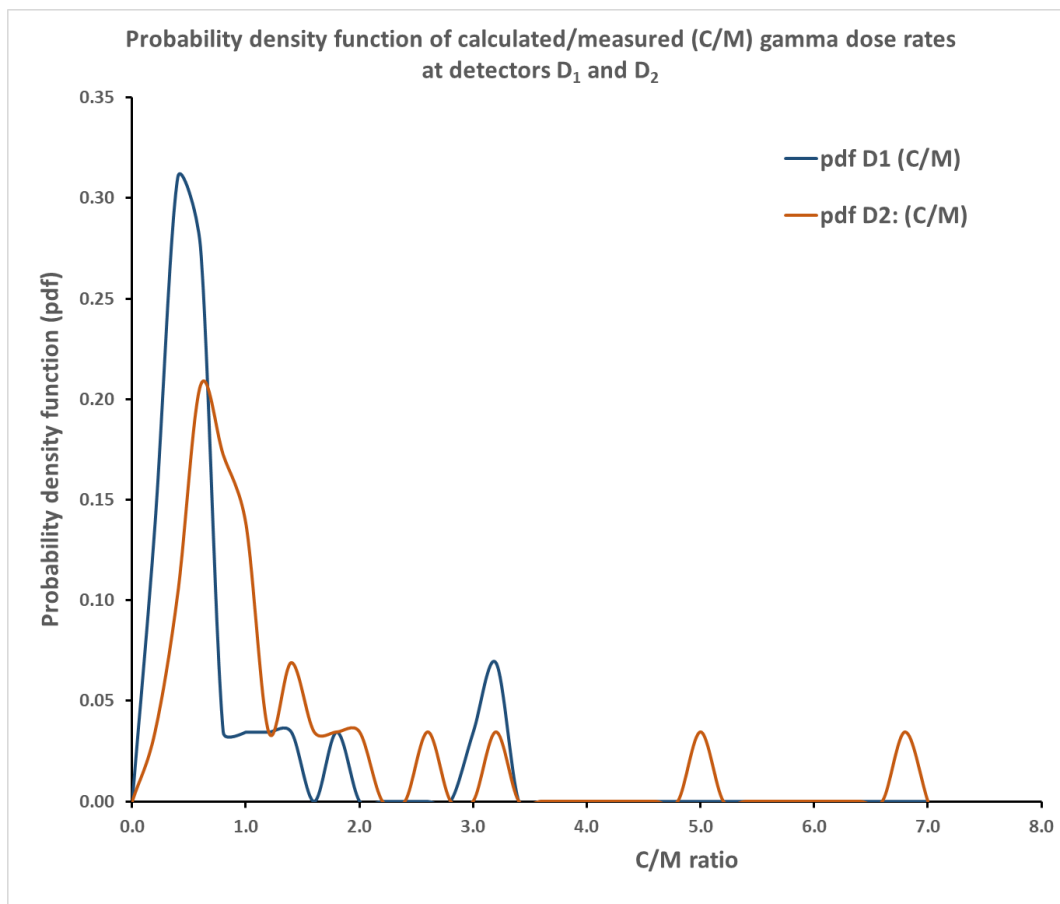


Figure 10.6. PDF of calculated/measured (C/M) values for Gamma Ray (γ_1 , γ_2) detectors

The probability density functions (pdf) for detectors 1 and 2 shows that there are significant peaks in the pdf at C/M values below unity i.e. a significant number of ‘plume catching’ events where the calculated dose rate from the MC analysis (which is based on an average dose rate

for sampling times significantly greater than those applicable for the full scale release events) was below that measured from the full scale case. However, there also exists a significant ‘tail’ in the pdf where in some cases the C/M ratio sits well above a value of unity and approaches a value of seven. The mean values, or first moments of the distribution, showed values where the overall mean difference between the methods was relatively small in magnitude. Figure 10.6 indicates therefore that the short time behaviour of the puff releases, over a period of four minutes, showed a significantly greater variability compared to the systematic differences between the EW case variability using the SGP or DGP methods, or between the EW clad and unclad cases. This justifies the approach in taking the average response across those cases and presenting the pdf across a mean of those cases.

3.4 Measured Gamma-Ray Dose rate corrected to standard release rate of pollutant

Figure 10.7 shows the measured dose rate (corrected to standard release rate of pollutant) across the range of wind directions sampled. The main features evident are the main central peaks, evident across both detectors, and the smaller ‘side-lobes’ which may be indicative of entrainment of radioactive material into the rooftop recirculation zone even at the greater angles of incidence compared to the main plume moving over the detectors. Peaks in the dose rate distribution can be seen corresponding to angular directions that would correspond to the plume blowing over the detector positions.

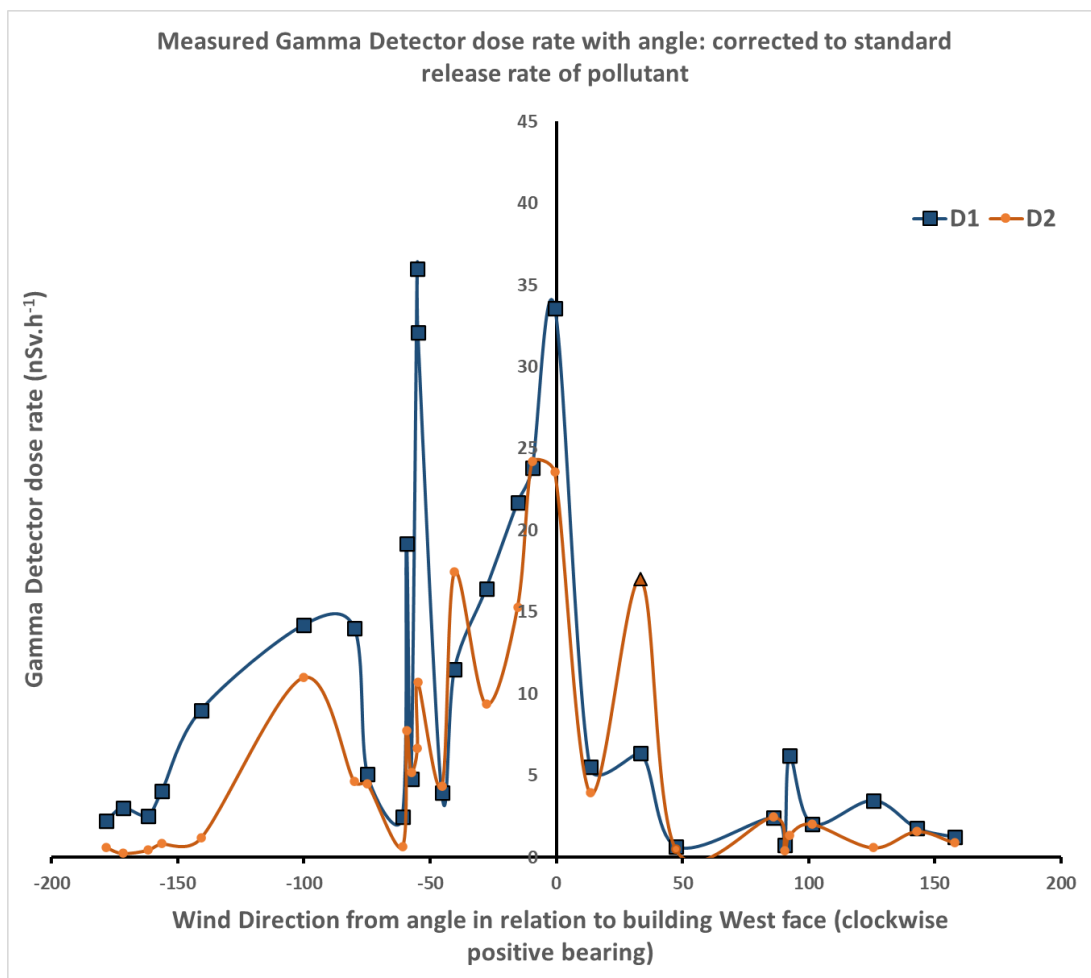


Figure 10.7. Measured Gamma Ray dose rate vs wind direction in relation to the building

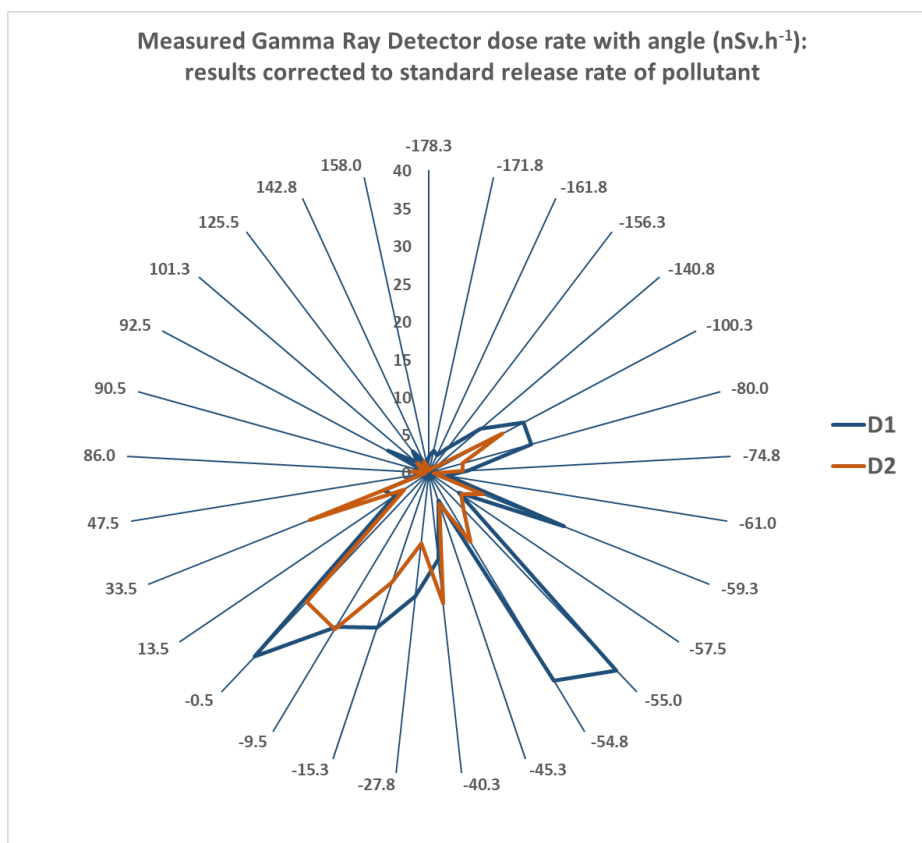


Figure 10.8. Angular polar plot of Measured Gamma-Ray dose rate vs wind direction

The polar plot of dose rate measured from the detectors 1 and 2 shown in Figure 10.8 shows the angular dependence very clearly. Both D_1 and D_2 show peaks with respect to wind directions ranging from 0° through to -40° (see Figure 10.1). However, another peak was detected with respect to D_1 in the direction of -55° which is also evident in Figure 10.7.

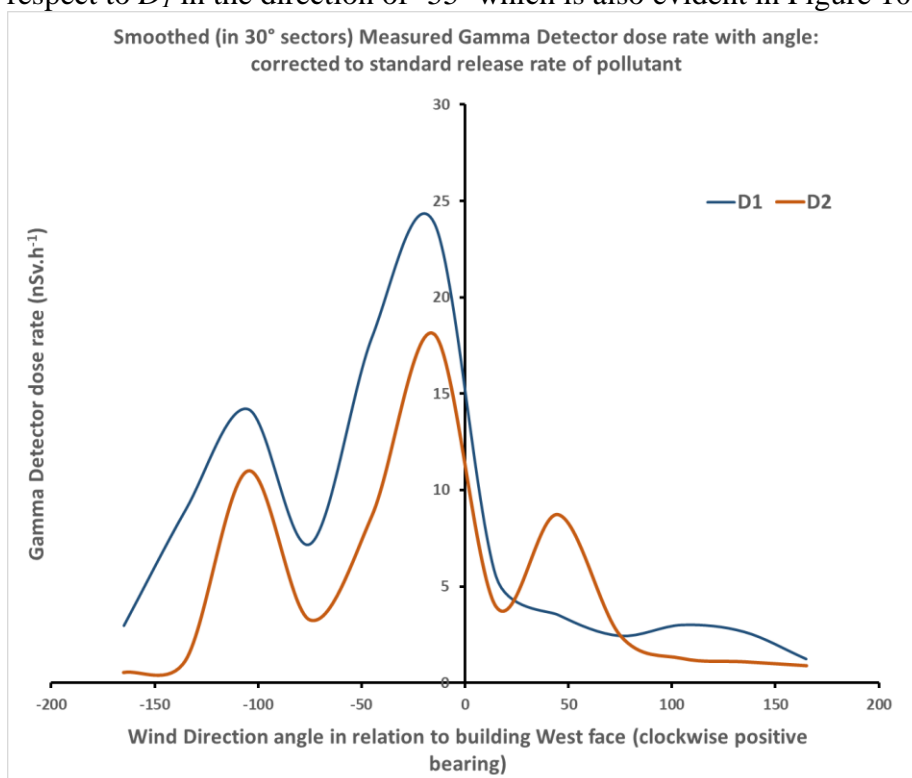


Figure 10.9 Measured Gamma-Ray dose rate vs wind direction averaged in 30° sectors

Figure 10.9 shows the experimental full scale dose rate data binned into 30° sectors. The distribution of dose rate with angle shows the trends more clearly: in particular the shape of the dose distribution matches that shown previously from an independent set of experiments using wind tunnel methods (Ibid, Chapter 4) with the presence of the two side-lobes to the dose distribution with angle of approaching wind flow. The main peaks are associated with the wind direction (in the region of -22.5°) where the approaching wind direction is towards the roof region where the detectors were located.

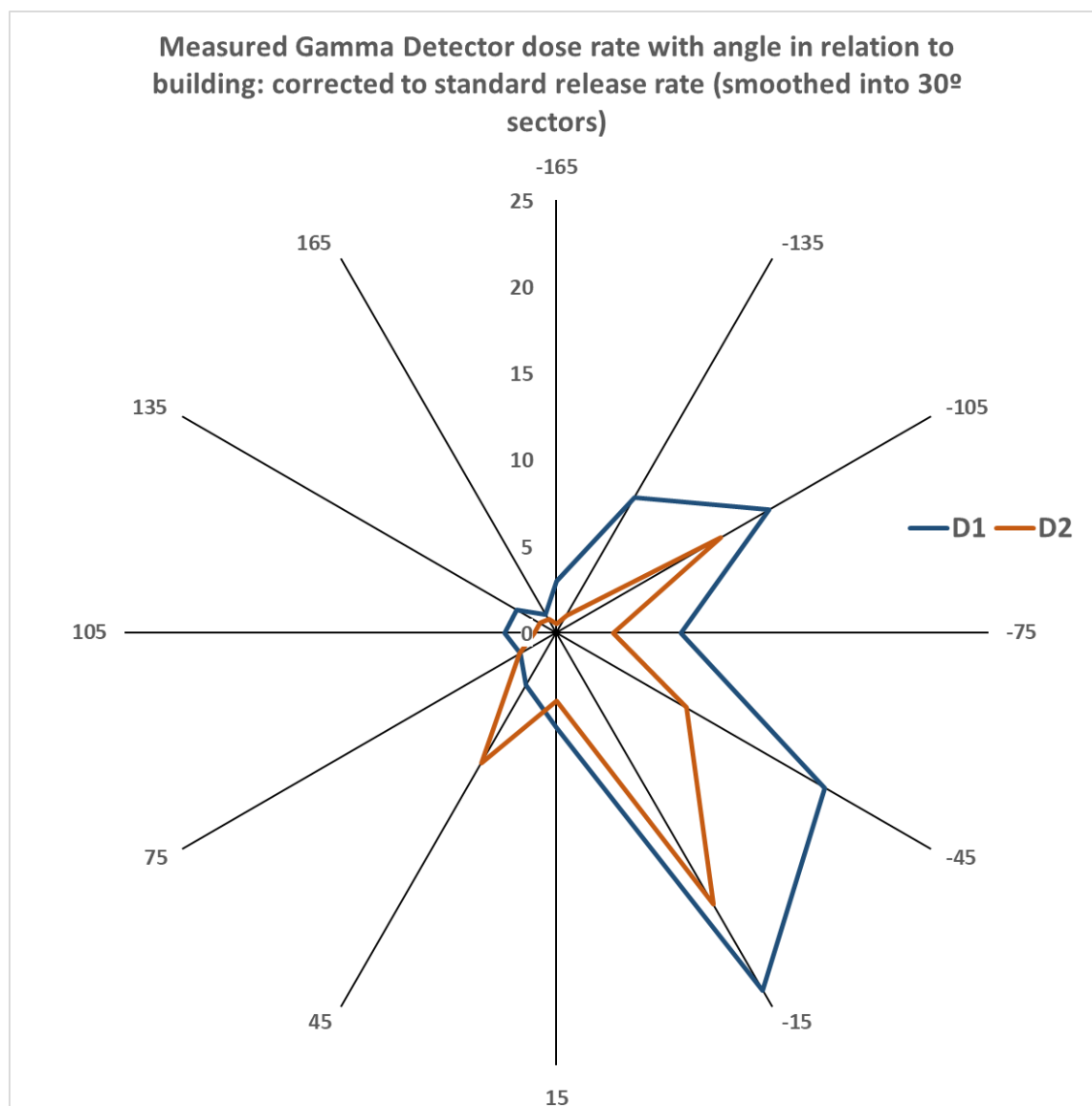


Figure 10.10 Angular polar plot of gamma-ray dose rate averaged in 30° sectors vs wind direction

Figure 10.10 shows the results from Figure 10.9 in a polar plot, again averaged over 30° sectors. The pattern is clearer than the respective Figure 10.8, with the peak around the main direction considered (-22.5°). Nevertheless, the side-lobes are evident to some extent.

10.3.5 Variability in wind direction over the sample period

Figure 10.11 shows the variation in one standard deviation of the wind direction angle (in degrees) over the 4-minute sample window encompassing the peak.

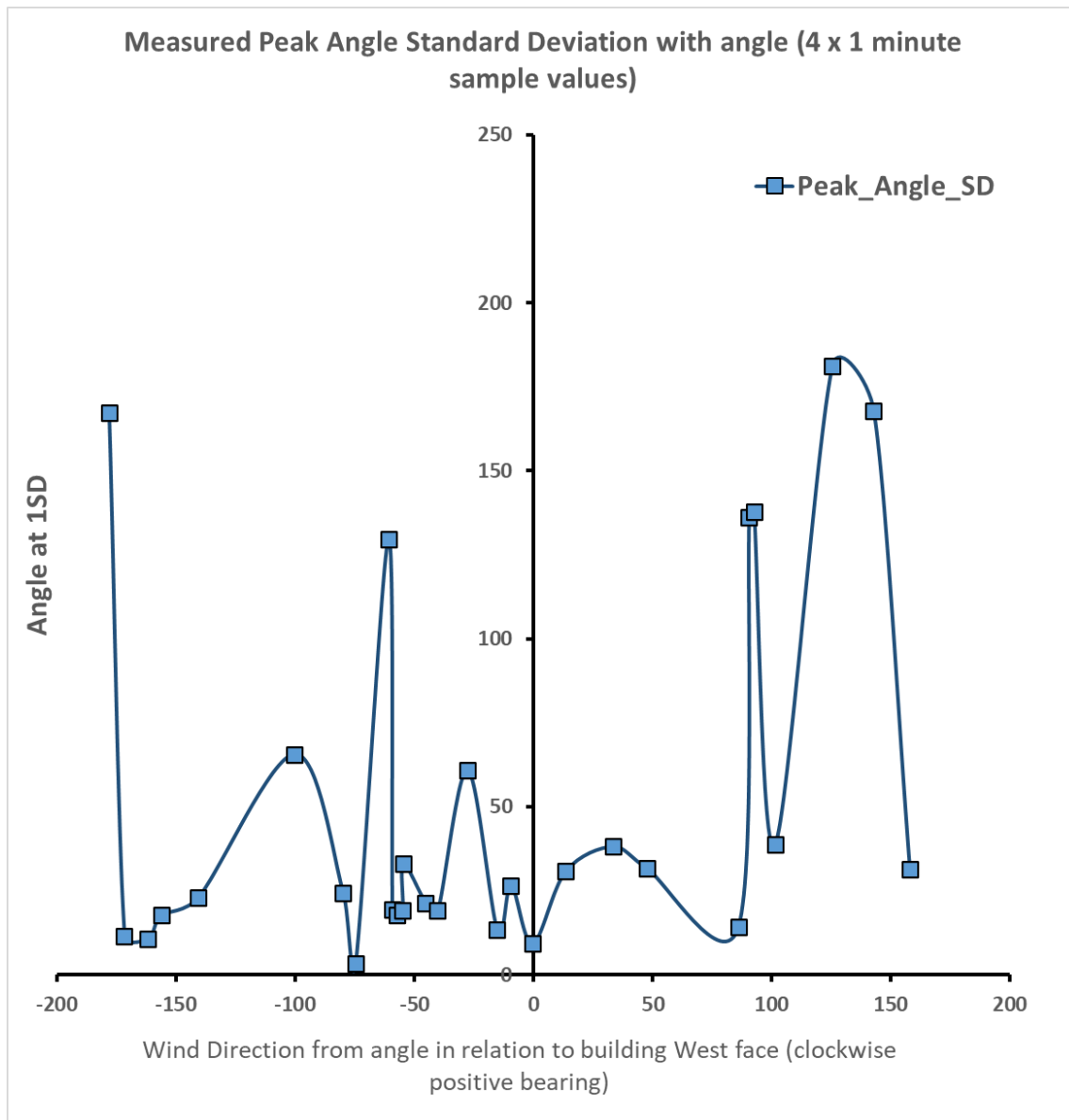


Figure 10.11. Peak dose rate angle Standard Deviation (SD) vs wind direction

The angular variation (even over four one-minute samples) can be quite significant: the effect that this would have on the plume would be to cause variability in direction – hence the larger sector averaging (over 30°) in Figures 10.9 and 10.10 showed a more consistent pattern consistent with the general wind direction for the detector positions. Radioactive material advection by the plume would be seen to follow a variable course in relation to the mean direction established by the four-minute average selected in this data analysis. By contrast the Monte Carlo mean gamma ray dose was based upon a mean direction for a continuous release established over a longer averaging time.

10.3.6 Variability in the velocity field: downstream and crosswind directions

From the sampled wind velocity, U , over the 20-minute sample period around the peak gamma release it was possible to determine the standard deviation of the wind speed and the crosswind velocity component. Normalised values of σ_U/U and σ_V/U are presented in Figure 10.12 smoothed into 30° sectors and plotted versus wind direction.

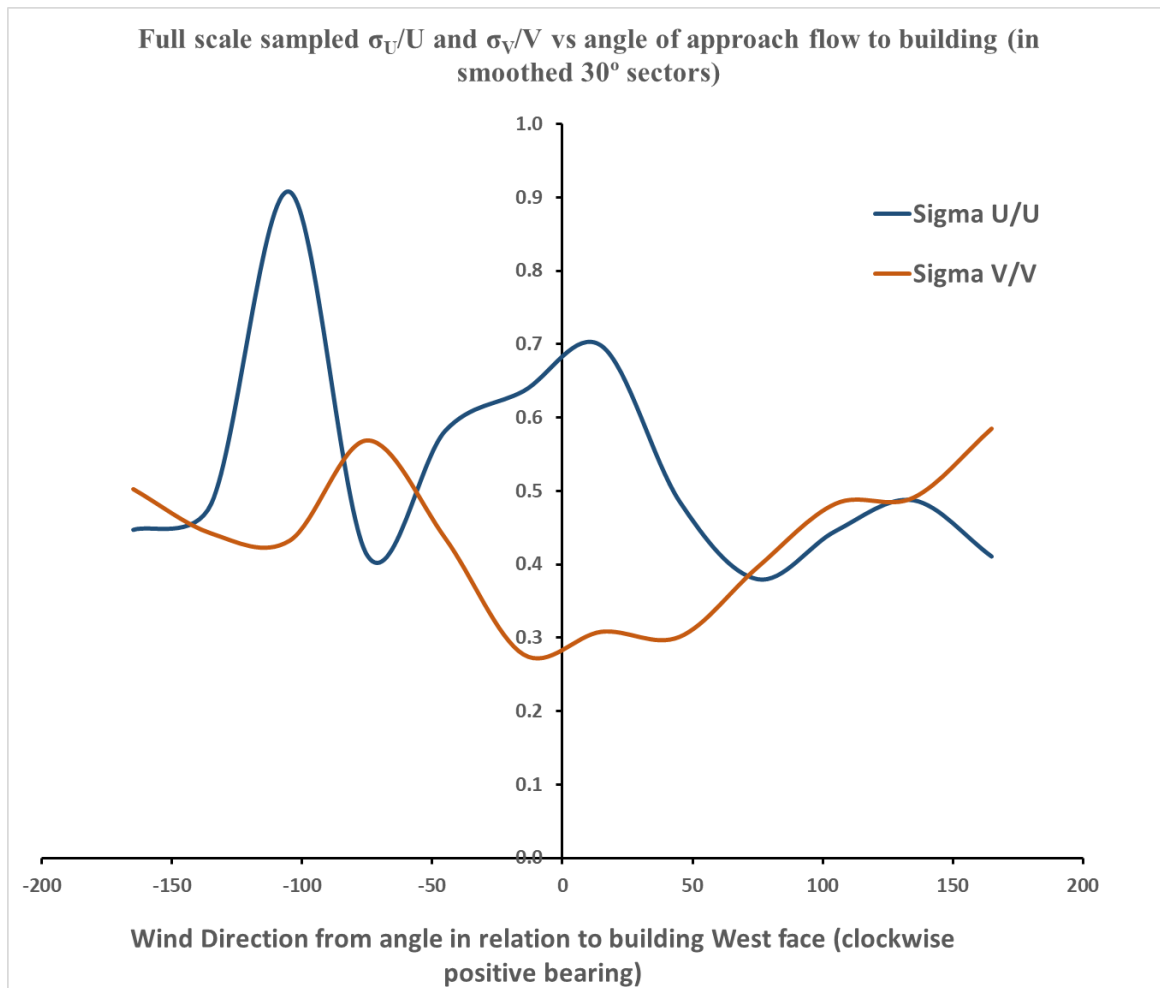


Figure 10.12. Variability of the velocity field components (σ_U/U) and (σ_V/U) averaged in 30° sectors vs wind direction

Figure 10.12 indicates that the downwind and crosswind samples standard deviations of velocity normalised to the magnitude of the wind speed show significant variations but were comparable in overall magnitude.

10.3.7 Turbulence intensity results

Figure 10.13 indicates the variation of calculated turbulence intensity based on the full scale measurement data. The reference wind velocity U_{ref} is that which would apply at the 200m height, estimated from applying the logarithmic power law with appropriate coefficients (Clarke *et al*, 1979).

It can be seen that the u'^2/U_{ref}^2 component peaks significantly along the main wind direction considered at -22.5°. The mean value across all directions was 0.107 with a sampled standard deviation of 0.090. The crosswind component v'^2/U_{ref}^2 was more consistent across the angular range, with a mean value of 0.078 and a sample standard deviation of 0.074.

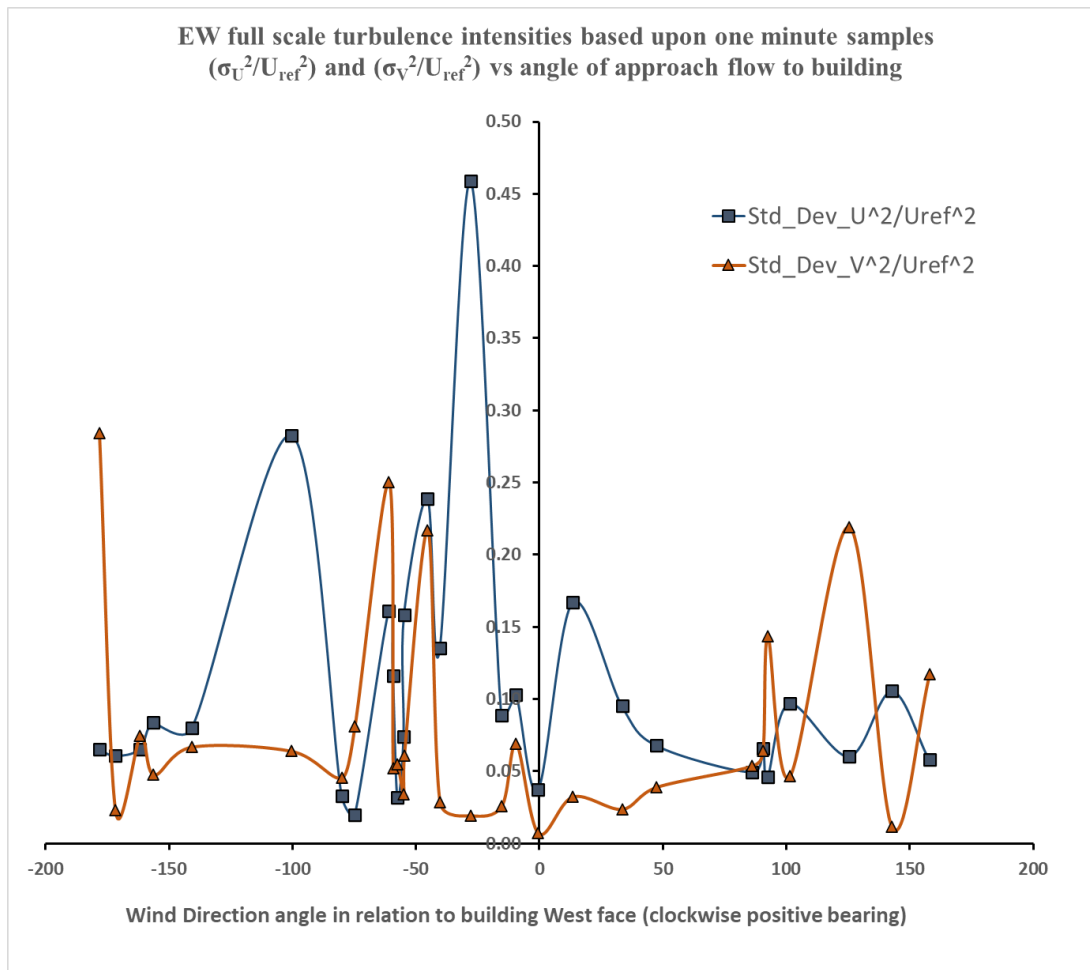


Figure 10.13. Estimates of turbulence intensity (σ_U^2/U_{ref}^2) and (σ_V^2/U_{ref}^2) based on the full-scale sampled values

10.4 Discussion

From the analysis it was seen that the probability density function (pdf) of the gamma ray dose rates showed a significant variation of the dose results compared to the Monte Carlo (MC) results based on a steady wind direction, but that overall the mean values of gamma-ray dose established from the full-scale measurements matched that established from the MC analysis.

For the four-minute time window over which ‘spike’ release occurs the puff length scale in dimensionless units can be calculated, $PLS/H = \Delta T U_{ref}/H$, using the mean value of the wind speed U_{ref} . The mean value is presented in Table 10.6 over the full-scale measurements results set, along with a sample standard deviation and coefficient of variation (CV): U_{ref} is calculated as before over the full 20-minute time window allocated to each ‘spike’ release. Values for the sampled turbulence intensities, based on the one-minute samples, are also presented in Table 10.6 for the downstream direction (U) and the crosswind component (V) and the statistical spread over the data set is presented as the sampled standard deviation (SD) and the associated coefficient of variation (CV).

Table 10.6. Statistical parameters from the full-scale data set

Quantity	$PLS/H^{(*1)}$	σ_U^2/U_{ref}^2	σ_V^2/U_{ref}^2	C/M Detector 1	C/M Detector 2	EW Clad/ AV ^(*2)	EW Unclad/ AV ^(*2)
Mean	13.6	0.107	0.078	0.74	1.26	--	--
Sampled SD: σ	6.6	0.090	0.074	0.87	1.44	--	--
CV	0.48	0.84	0.95	1.17	1.14	0.308	0.330

*1- the puff release ΔT has been taken as the nominal 4-minute window for the data analysis encompassing the main gamma spike measurement corresponding approximately to the maximum release rate over the 'spike'.

*2- WT puff release results presented for the closest data point available ($PLS/H=16.6$) for the EW clad and unclad cases with the active vertical (AV) release and angle of approach flow of -22.5° and sampled at $X/H=2/3$.

The CV for the full-scale data sets of calculated versus measured (C/M) dose rate (MC dose rate based on the continuous concentration measurement data for the wind tunnel divided by the equivalent dose rate from the 'spike' releases at full scale) can be compared to the CV from the wind tunnel puff releases for the EW active releases for clad and unclad cases. In both these cases the variation of dose rate arising from short releases is being compared to a mean value. In this context a 'spike' release will refer to the full-scale release time trace, and a 'puff' release will refer to the wind tunnel short release with a constant release rate, albeit of short duration. Analysis of the results presented in Table 1 indicates that the wind tunnel (WT) values for CV (for this approximate PLS/H in the region of 16.6, the closest data point available to the mean value of 13.6 for the full-scale data) were in the range 0.31-0.33, and the CV range of the C/M ratios for the gamma-ray detectors was 1.14-1.17. The larger value of CV associated with the full-scale case would be worthy of further investigation in future work, but some potential explanations for the differences against full scale values would be as follows.

- The spike releases show a temporal pattern with sometimes sharp release peaks over the nominal 4-minute window used in this analysis: this would feed through into higher spatial and temporal variations in the vicinity of the detectors when considering short term fluctuations in the flow field at full-scale, in particular for the crosswind variation over time – as evidenced by the sizeable value for σ_V^2/U_{ref}^2 in Table 10.6.
- The wind tunnel (WT) data relates to concentration reflects the variation in 'dose per puff' but based on the integral of concentration over time. The full-scale variation reflects the integral gamma-ray dose at the detectors but from a plume which is meandering and varying in direction minute-by-minute with the ambient wind velocity in the flow field over the building.
- The wind tunnel case was measured with neutral stability (class D), whereas the full-scale data was based on ambient conditions for surface heat flux and associated convective conditions and other varying meteorological conditions.

10.5 Conclusions

The calculated gamma-ray doses based upon the measured continuous release wind tunnel data compared well, within acceptable tolerances, to the measured gamma-ray doses from the full-scale measurement on the EW building.

The full-scale measurements, when presented as a probability density function expressed against the C/M ratio showed a high extent of variability e.g. as evidenced by the sampled standard deviation. When compared to the comparable variations in puff dose for the EW wind

tunnel models (concentration field) measurements the CV values were of the order of four times as great. This, at least in part, reflects the 'real world' meteorological conditions for the full-scale measurements which were achieved over many days of monitoring and the different temporal patterns for the real world 'spike' releases compared to well-controlled puff release experiments in the wind tunnel. The variation in wind direction, which could be significant even over the short time window of four minutes used to analyse the full-scale data, was another factor that would cause advection of the radioactive material into different trajectories with respect to the detectors. In the estimation of gamma-ray dose for a real-world case the application of a larger coefficient of variation (for any given spike release) to mean calculated doses would from these results be indicated in order to establish a more realistic range of probable value of dose arising from any given release. Naturally the wind direction and speed in relation to the building, along with the magnitude of the release would also need to be taken into account.

CHAPTER 11: SENSITIVITY ANALYSIS FOR BUILDING CASES

11.1 Introduction

Dispersion conditions in the vicinity of a building have long been known to be influenced by the presence of other buildings nearby (Meroney, RN, 1982)). Nearby buildings are expected to affect the flow field, including vertical velocity profiles, and the turbulence intensity levels in the flow. The complex of buildings at the St Thomas' Hospital site in central London was investigated with respect to levels of radioactive emissions from a stack on the East Wing building (Ibid, Chapter 4) using a full building model extending out to the site perimeter adjacent to the river Thames. Two geometries for the building closest to the release stack were investigated in the wind tunnel experiments, namely the East Wing Unclad (EWU) and East Wing Clad (EWC) buildings. Situated around these building in the wind tunnel was a range of other buildings, upstream, downstream and around the EW buildings. In this chapter, results are presented of selectively removing buildings from the full building model (FBM) set to investigate the effects on the flow field and concentration values at EW roof level. In this way the sensitivity of the obtained values to the presence, or absence of, surrounding buildings was investigated.

11.2 Methods

The building site plan, including adjacent buildings, was used to produce the wind tunnel model. Figure 11.1 shows the EW building and surrounding buildings in relation to the wind tunnel coverage of the site with the River Thames to the West.

11.2.1 Building Layouts investigated

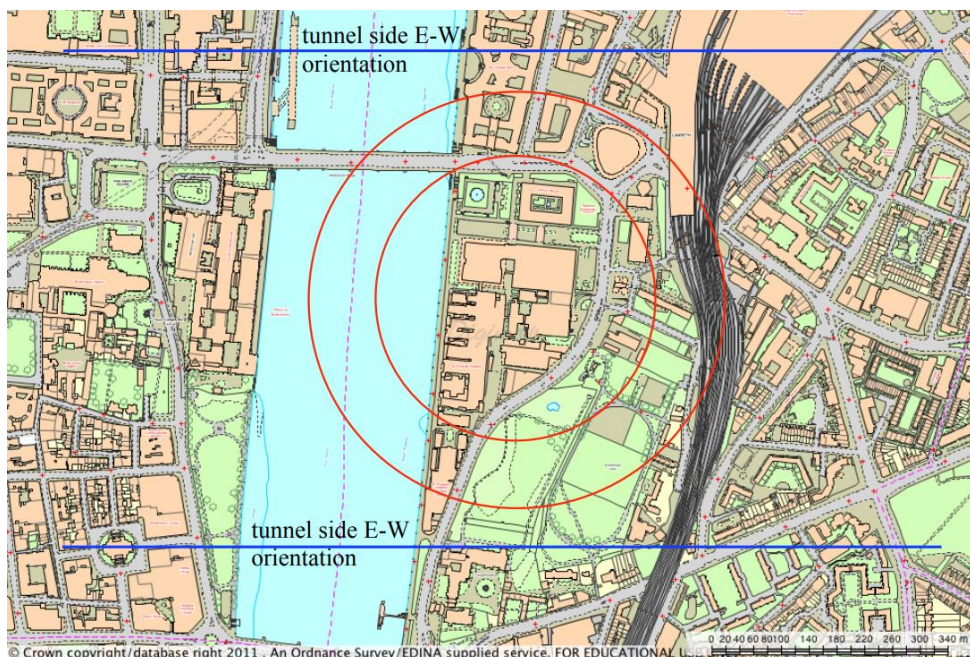


Figure 11.1 Wind tunnel model coverage. The red circles denote the extent of topography fitting the inner and outer turntable diameters.

Figure 11.1 shows the wind tunnel turntable dimensions superimposed on an Ordnance Survey EDINA (<https://digimap.edina.ac.uk/os>) map of the St Thomas Hospital site and surrounding region. The limits of the tunnel inner and outer turntable are shown with red circles, with the centre of rotation being the release point on the EW North Stair tower: i.e. the stack release position.

The buildings on the site are named in Figure 11.2 and their positions in relation to the EW building shown.



Figure 11.2 General site layout (reproduced with permission of Essentia Property Services)

Figure 11.2 shows the site layout of the buildings at the STH site used as information to construct the surrounding buildings to the East Wing clad and unclad models.

Figure 11.3 below shows the buildings used in the wind tunnel. Buildings marked in red were constructed for the model from accurate dimensions obtained from site records. The main wind direction chosen for the experiments is shown as an arrow at an angle of -22.5° to the West face of the EW building; geographical North is indicated by the direction of the vertical grid lines.

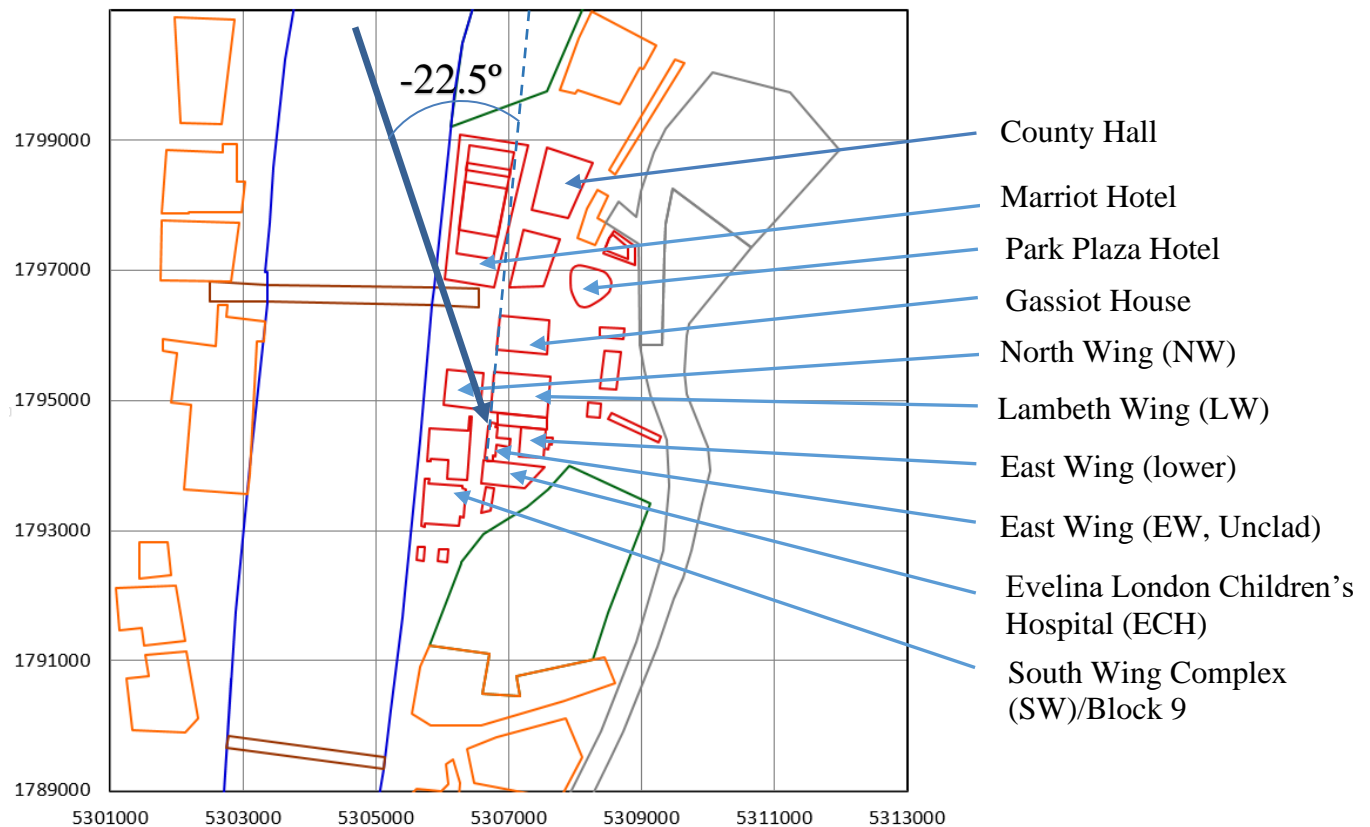


Figure 11.3 Constructed model (in red) for wind tunnel experiments (-22.5° wind direction marked)

Table 1. Building heights of the models used in the experiments

Building	Maximum Height (m)
Marriot Hotel (MH)	32.8
County Hall (CH)	31.1
Gassiot House (GH)	21.0
North Wing (NW)	51.7
Lambeth Wing (LW)	22.9
East Wing (EWL, lower section)	15.9
East Wing (EW, upper)	48.0
Evelina Children's Hospital (ECH)	34.0
South Wing (SW)	37.0

Table 11.1 shows the building heights of the surrounding buildings to the East Wing (EW) full building model (FBM). Important features of the main wind direction studied (i.e. -22.5° as shown in Figure 11.2) were the upwind presence of the North Wing building of approximately 52m height, taller than the EW building of 48m. The Lambeth Wing was approximately half the height of EW and immediately upwind. Immediately downstream, the ECH was 34m tall, or 71% of the EW height with a rounded canopy shape. Buildings further upwind (Marriot Hotel and County Hall) were of approximately two thirds of the height of the EW building.

11.2.2 Particular combinations in the building complex (STH) investigated in wind tunnel

Table 11.2 Building combinations measured in the wind tunnel

Case#	Building Combination	Angles of approach flow (bearing with respect to North)	Downstream distances from release point* (m)
1	EW Clad – Full Building Model (FBM)	-17.5°, -22.5°, -27.5°	16 – 240
2	EWClad+NW+LW+ECH+EWL	-22.5°	32 – 240
3	EWClad+NW+LW	-17.5°, -22.5°, -27.5°	32 – 240
4	EWU+NW+LW	-17.5°, -22.5°, -27.5°	32 – 240
5	EWClad+ECH+EWL	-22.5°	32 – 240
6	EWClad (clad only) – EW clad building	-22.5°	32 – 240
7	EWU (unclad only) – EW unclad building	-22.5°	32 – 240

*-specified in full scale

Table 11.2 specifies the building combinations investigated in the wind tunnel experiments. The case order list (1-7) reflects a general pattern of moving from a full building model (FBM) through to isolated buildings: i.e. EWClad or EWU alone. This pattern was chosen to approximately reflect the expected decreasing influence of external buildings on the measured parameters for the isolated buildings as those external buildings were selectively removed as one progresses through the analysed cases.

11.2.3 Measurements made in the wind tunnel

Measurements of the concentration field value and the flow field were made, in some cases simultaneously, at a wide range of positions in downstream planes from the source. Concentration field values were output in the form of CU_{ref}/Q , which must be multiplied by H^2 in order to obtain the dimensionless concentration χ . Mean velocity and turbulence intensity, e.g. w'^2/U_{ref}^2 , data were also available in a range of cases, and a selection of the full set of results will be presented.

11.3 Results

11.3.1 Concentration field maxima (across cases 1-8)

Table 11.3. Maximum Concentration field values: $X=160\text{mm}$ (32m); -22.5° ; $Z_{rh}=265\text{mm}$ (53m)

Case#	Building Combination	χ	$Y_{max}(mm)$	$Z_{max}(mm)$
1	EW Clad; the Full Building Model (FBM)	27.3	0	265
2	EWClad+NW+LW+ECH+EWL	38.9	-25	260
3	EWClad+NW+LW	30.4	-25	260
4	EWU+NW+LW	27.6	-25	260
5	EWClad+ECH+EWL	61.9	0	265
6	EWClad (clad only); EW clad building	67.3	0	265
7	EWU (unclad only); EW unclad building	44.9	-20	265

From Table 11.3, the largest concentration maximum values were obtained for the isolated EW clad and unclad buildings, with dimensionless concentration values of 67.3 and 44.9 respectively (cases 6 and 7, Table 11.3). In case 5 (with EWClad) the absence of a tall upwind building (North Wing, NW) led to maximum concentration value of a similar magnitude (61.9) for the isolated EW clad case (case 6). In reverse order in the table, cases 3 and 4 for the EW clad and unclad cases with NW and Lambeth Wing (LW) present showed a marked reduction in maximum concentration compared to the isolated building cases. Case 2 was an intermediate case with upstream and downstream buildings both present but not the full building model

(FBM). In this case the maximum concentration value was slightly greater than case 3. Case 1, EW FBM, showed the lowest concentration maximum in these series of experiments. The range of scale of the results was broadly within a factor of 2-3 between case 1 and case 6: i.e. the FBM compared to the isolated building case.

Table 11.4 Maximum Dimensionless Concentration χ vs X : -22.5° ; $Z_{rh}=265\text{mm}$

X (mm)	Case #1*	#2	#3	#4	#5	#6	#7
80	98.0	--	--	--	--	--	--
160	27.3	38.9	30.4	27.6	61.9	67.3	44.9
240	15.7	--	--	--	--	--	--
400	5.5	--	--	--	--	--	--
800	1.6	1.7	1.3	1.6	3.9	2.6	1.8
1200	1.1	1.5	1.1	1.1	2.0	1.7	1.4

*- cases are as specified in Table 3

Table 11.4 shows the variation with distance downstream of the source of the maximum dimensionless concentration. The salient feature observed here was that the higher concentrations seen for the cases #5 and #6 (the EW clad building with downstream buildings and as an isolated building) persisted downstream to distances of $X=800\text{mm}$ and $X=1200\text{mm}$. For all cases the reduction of maximum concentration with increasing distance from the source can be clearly seen.

11.3.2 Velocity Profiles in (U, W) for the EW Cases;: sensitivity to wind direction

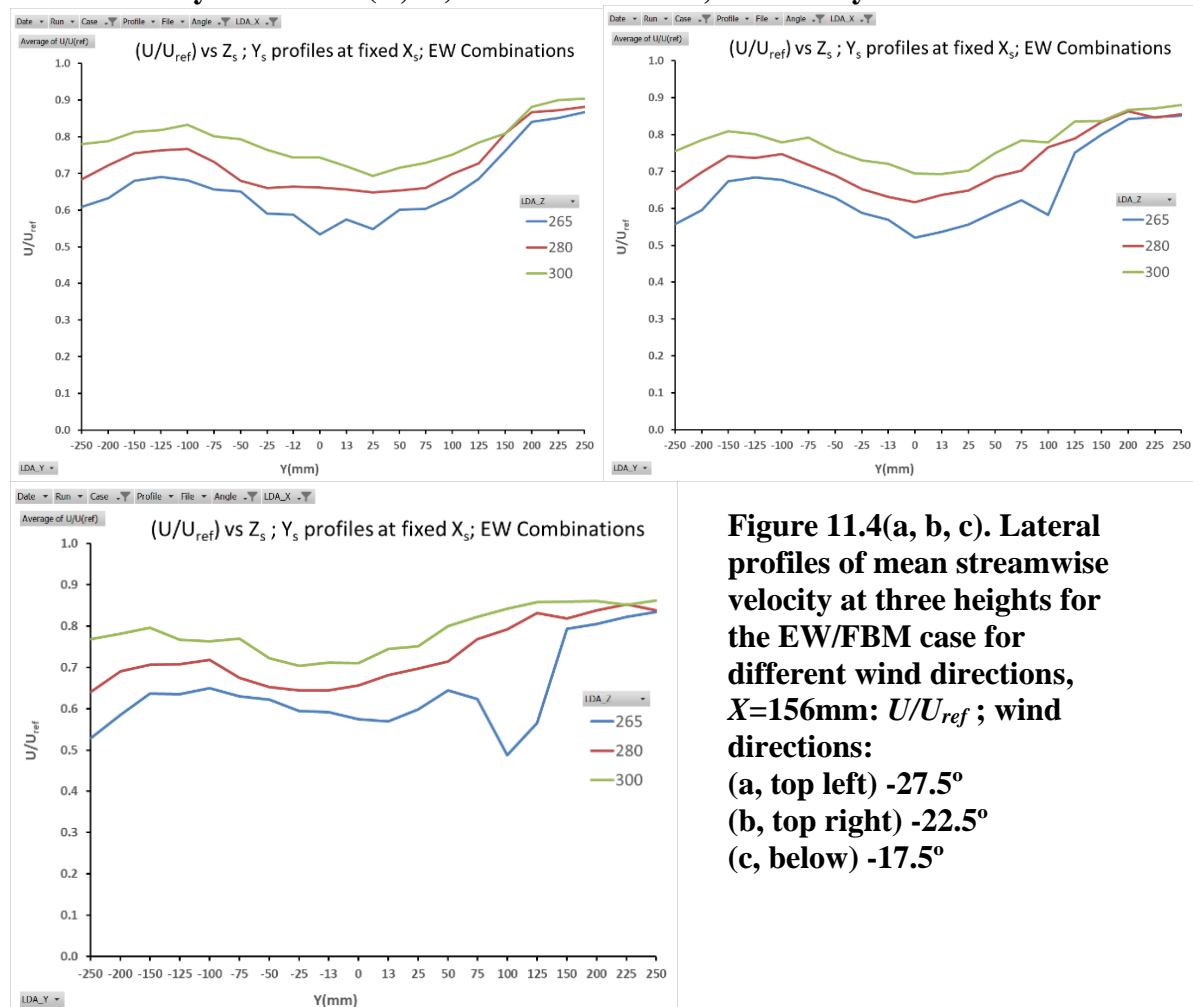


Figure 11.4(a, b, c). Lateral profiles of mean streamwise velocity at three heights for the EW/FBM case for different wind directions, $X=156\text{mm}$: U/U_{ref} ; wind directions: (a, top left) -27.5° (b, top right) -22.5° (c, below) -17.5°

Figure 11.4(a/b/c) shows lateral velocity profiles at three heights near the centre of the EW building roof, for the full building model set and wind directions $-22.5^\circ \pm 5^\circ$. The only significant difference is the velocity deficit feature which grows in moving from (b) -22.5° through to (c) -17.5° with U/U_{ref} locally reducing from approximately 0.6 to 0.5, and evident only on the lowest sample height of 265mm near $y = 125$ mm. This can be related to the roof geometry.

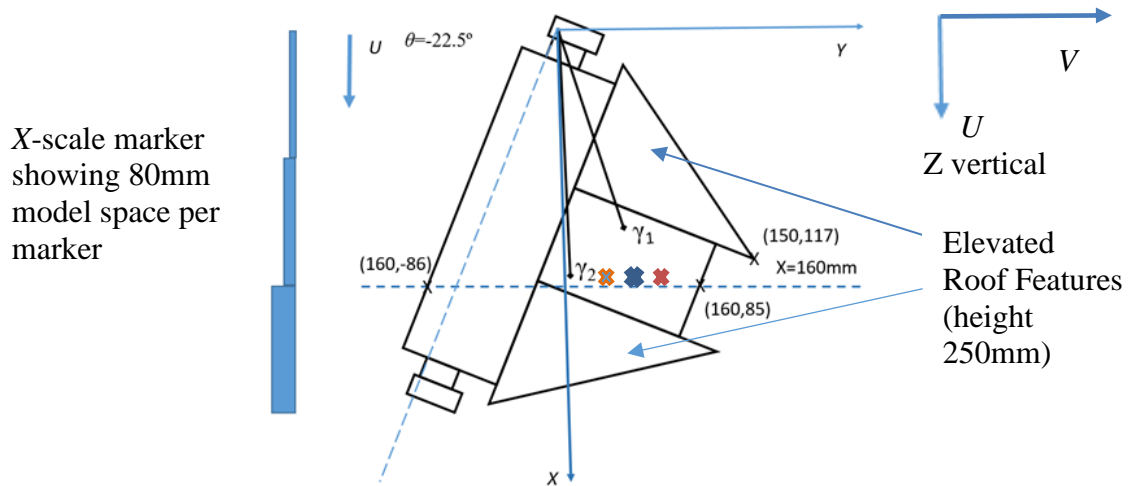
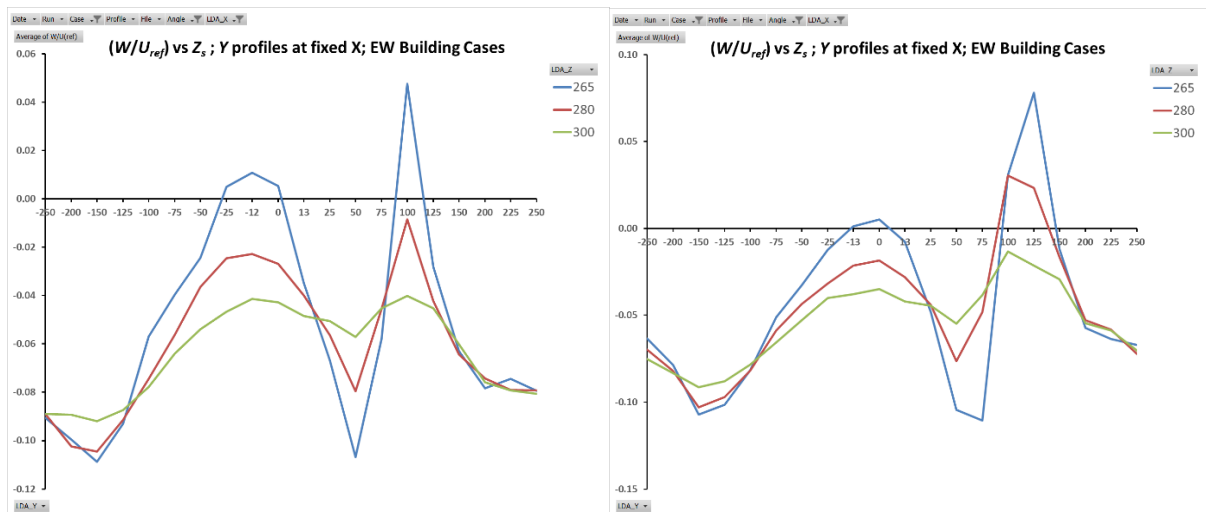


Figure 11.5 EW Clad building; $X=160$ mm; -22.5° ; showing point co-ordinates

From Figure 11.5 it can be seen that the velocity deficit at $Y \approx 100$ mm (indicated by the position of the blue cross) was measured in the recess (in which the gamma detectors γ_1 and γ_2 also resided) between two elevated roof features as shown. The flow here is evidently very sensitive to wind direction, unlike at the other locations shown, as were the turbulence levels and the mean vertical velocities shown below.



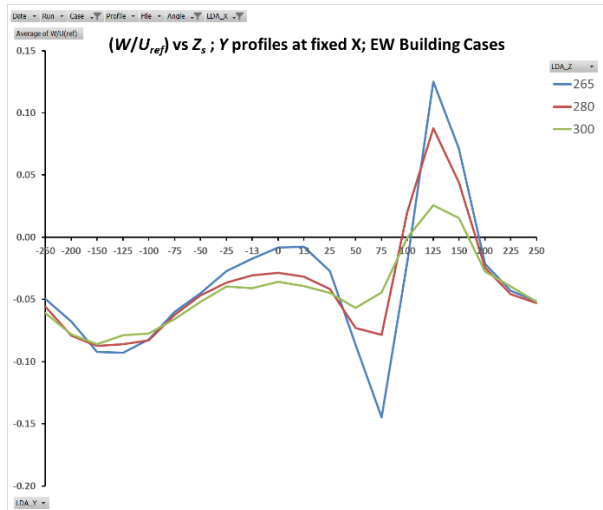


Figure 11.6. Lateral profiles of mean vertical velocity at three heights for the EW/FBM case, $X=156\text{mm}$: W/U_{ref} ; wind directions:
(a, top left) -27.5°
(b, top right) -22.5°
(c, below) -17.5°

Evidence of this feature is also seen in the vertical component of velocity shown in Figure 11.6, in which there is a strong positive upward deflection at $Y \approx 125\text{mm}$ (orange cross in Figure 11.5), and a strong downwards deflection at $Y \approx 60\text{mm}$ (green cross in Figure 11.4). As the magnitude of these deflections increase as one goes to the lowest sample height (265mm), and the magnitudes also increase as one moves from (a) -27.5° through to (c) -17.5° . It is clear therefore that these effects are related to the presence of the two elevated sections shown in Figure 11.5, and would therefore be classed as local building effect features in the flow field.

11.3.3 Vertical component of turbulence intensity

Table 11.5. Dispersion, mean flow and vertical turbulence intensity data at the position of maximum concentration: $X=160\text{mm}$ (32m); -22.5° ; $Z_{rh}=265\text{mm}$ (53 m)

Case#	Building Combination	U_{local}/U_{ref}	w'^2/U_{local}^2	χ_{max}	Y_{max} (mm)	Z_{max} (mm)
1	EW Clad – Full Building Model (FBM)	0.52	0.040	27.3	0	265
2	EWC+NW+LW+ECH+EWL	0.63	0.020	38.9	-25	260
3	EWC+NW+LW	0.57	0.029	30.4	-25	260
4	EWU+NW+LW	0.63	0.025	27.6	-25	260
5	EWC+ECH+EWL	0.54	0.040	61.9	0	265
6	EWC (clad only) – EW clad building	0.55	0.037	67.3	0	265
7	EWU (unclad only) – EW unclad building	0.45	0.059	44.9	-20	265

*- Z_{rh} = release height in model scale

The intensities of the vertical turbulence component, w'^2/U_{local}^2 , can be seen in Table 11.5 at a distance from the source approximately in the central region of the roof of the EW building ($X=160\text{mm}$) and given for the position corresponding to the plume concentration maximum (PCM): i.e. χ_{max} . The values range from 0.02-0.06 over the cases presented. The greatest values of vertical turbulence intensity corresponded to the isolated EWC and EWU building cases. The absence of nearby upwind buildings (NW/LW) for the EWC case indicated a relatively high level as well in the range of values presented. Overall, though, the range of values is not great and there is no obvious correlation with the χ_{max} values. Of course, the latter are a consequence of the whole flow field experienced by the dispersing plume, which might not be well represented by conditions at a single point.

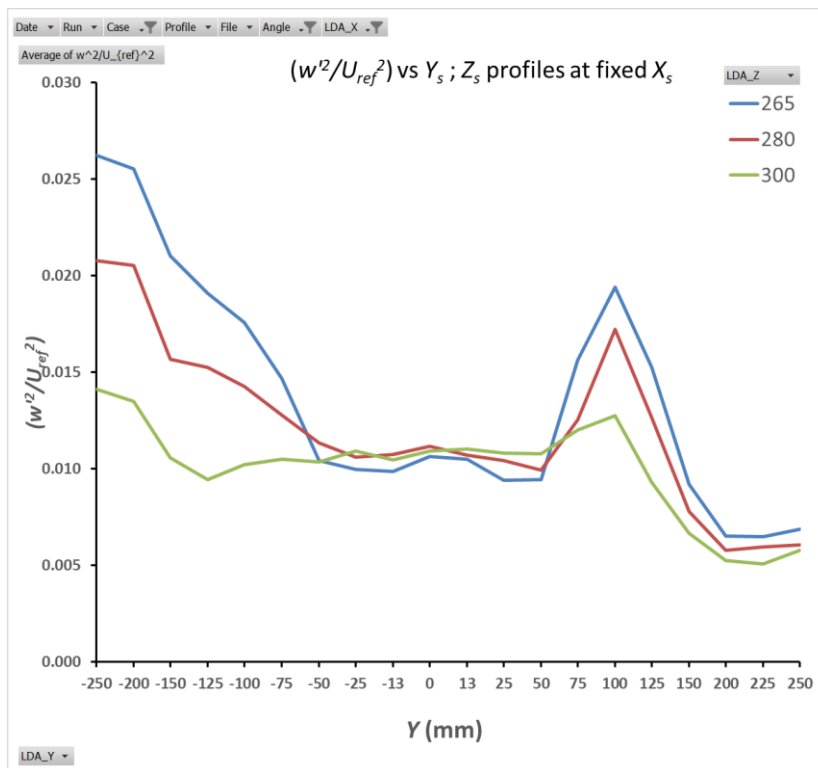
Table 11.6. Turbulence intensity w'^2/U_{ref}^2 vs angle of approach flow at the position of maximum concentration: $X=156\text{mm}$; $Z_{rh}=265\text{mm}$; $-27.5^\circ/-22.5^\circ/-17.5^\circ$

Case	Building Combination	-27.5°	-22.5°	-17.5°	Mean	CV	Y_{max}	Z_{max}
1	EW Clad – FBM	0.0104	0.0107	0.0098	0.0103	0.045	13,0,-13	265
3	EWClad+NW+LW	0.0096	0.0094	0.0092	0.0094	0.021	-12,-25,-25	260
4	EWU+NW+LW	0.0126	0.0100	0.0085	0.0104	0.200	-13,-25,-13	260 ^{*1}

*1: except for -27.5° where the sample height of the Plume Concentration Maximum (PCM) was 265mm

Table 11.6 shows the sensitivity of the vertical component of turbulence intensity w'^2/U_{ref}^2 to small changes in the angle of approach wind for three of the building configuration cases. The mean values at the plume concentration maximum (PCM) for each of the cases are similar. The coefficient of variation (CV) was notably greater, however, for case 4 compared to the other two cases.

Figure 11.7 shows the vertical component of the turbulence intensity w'^2/U_{ref}^2 for the EW Clad/FBM intermediate case of $X=156\text{mm}$ and -22.5° . The value peaks in the region of $Y \approx 100\text{mm}$ at just below 0.02, however the value presented in Table 11.6 is that for the PCM at around $Y \approx 0\text{mm}$, with a magnitude of approximately half this value. This illustrates the point that spatial variations in the flow field may affect the dispersion of pollutants from different release positions to different extents. As already noted, plume spread is affected by turbulence levels over the space occupied by the plume, which can smooth out the effects of local peaks in turbulence levels. The upstream North Wing building (see Figures 11.2 and 11.3) can be expected to have a significant influence, as seen in the results at large negative Y .



The edges of the roof are at approximately 120 and -86 mm, so the high values beyond $Y = -100\text{mm}$ are probably convected from upstream (N Wing, see Figure 11.3). The high values centred on $Y = 100\text{mm}$ are over the raised part of the roof.

Figure 11.7 East Wing Clad (FBM) lateral profile of the vertical component of turbulence intensity w'^2/U_{ref}^2 : $X=156\text{mm}$; -22.5°

11.3.4 Shear stress ($-u'w'/U_{ref}^2$): sensitivity to angle of approach flow

Table 11.7 shows the sensitivity of the shear stress $-u'w'/U_{ref}^2$ to small variations in the angle of approach wind for three of the building configuration cases. The mean values at the plume concentration maximum (PCM) for each of the cases are similar. The coefficient of variation (CV) was notably greater however for case 1 (EWC/FBM) compared to the other two cases, but the overall extent of variation was relatively high. The turbulence structure function, $w'^2/(-u'w')$, was typically of order 2 to 3 for Cases 3 and 4 but varied between 1.7 and 5 for Case 1. These values can be compared with 1.7 for a standard boundary layer, showing that the approach flow is heavily distorted by the local flow in the building canopy layer and, locally, over the roof of the East Wing.

Table 11.7. PCM shear stress $-u'w'/U_{ref}^2$: $X=156\text{mm}$; $Z_{rh}=265\text{mm}$; $-27.5^\circ/-22.5^\circ/-17.5^\circ$

Case	Building Combination	-27.5°	-22.5°	-17.5°	Mean	CV	Y_{max}	Z_{max}
1	EW Clad – FBM	0.0062	0.0033	0.0031	0.0041	0.54	13,0,-13	265
3	EWC+NW+LW	0.0018	0.0037	0.0038	0.0035	0.06	-12,-25,-25	260
4	EWU+NW+LW	0.0042	0.0036	0.0024	0.0031	0.23	-13,-25,-13	260* ¹

*1: except for -27.5° where the sample height of the PCM was 265mm

11.3.5 Sensitivity of Plume Concentration Maximum (PCM) to angle of approach wind

The sensitivity of the plume maximum concentration (PCM) to model configuration and wind direction is shown below. Building combinations 1, 3 and 4 were assessed over a range of distances downwind for a variation of $\pm 5^\circ$ around the nominal angle of approach flow. From Table 11.8 we can see that the mean values are broadly similar, but the CV values vary between 0.17-0.24 for cases 3 and 4, largely due to the higher concentration values recorded at the -17.5° angle of incidence. The root mean square (RMS) value of CV over the three building cases in Table 11.8 was 0.17. Nevertheless, the range of PCM is at most a factor of 1.3 and the table gives some details of the variation of PCM value with building configuration.

Table 11.8 Concentration maxima: χ_{max} ; $X=160\text{mm}$ (32m); $-17.5^\circ/-22.5^\circ/-27.5^\circ$; $Z_{rh}=265\text{mm}$

Case#	Building Combination	-27.5°	-22.5°	-17.5°	Mean	CV
1	EW Clad – FBM	28.6	27.3	28.8	28.2	0.029
3	EWC+NW+LW	29.4	30.4	39.9	33.2	0.174
4	EWU+NW+LW	21.9	27.6	35.2	28.2	0.236

*- Z_{rh} = release height in model scale

Table 11.9 Concentration maxima: χ_{max} ; $X=800\text{mm}$ (160m); $-17.5^\circ/-22.5^\circ/-27.5^\circ$; $Z_{rh}=265\text{mm}$; $Z=30\text{mm}$

Case#	Building Combination	-27.5°	-22.5°	-17.5°	Mean	CV
3	EWC+NW+LW	0.98	1.32	1.43	1.24	0.19
4	EWU+NW+LW	1.01	1.20	1.34	1.19	0.14

*- Z_{rh} = release height in model scale

From Table 11.9, at $X=800\text{mm}$, approximately 3.3 times the building height downstream from the release position, we can see that the mean and CV values are similar. This is evidence that the sensitivity to different building configurations (i.e. between EW clad and unclad) diminishes with distance from the source.

Table 11.10 Concentration maxima: χ_{max} ; $X=1200\text{mm}$ (240m); $-17.5^\circ/-22.5^\circ/-27.5^\circ$; $Z_{rh}=265\text{mm}$; $Z=30\text{mm}$

Case#	Building Combination	-27.5°	-22.5°	-17.5°	Mean	CV
3	EW C+NW+LW	0.91	1.05	1.17	1.04	0.12
4	EWU+NW+LW	0.93	1.05	1.14	1.04	0.10

*- Z_{rh} = release height in model scale

From Table 11.10, at $X=1200\text{mm}$, or five building heights downstream of the release point, we can see that the mean and CV values are close. This is further evidence that the sensitivity to different building configurations diminishes with distance from the source.

Table 11.11. Cube/A; χ_{max} ; $-45^\circ/-27.5^\circ/-22.5^\circ/-17.5^\circ/0^\circ$; $Z_{rh}=265\text{mm}$

X (mm)	-45°	-27.5°	-22.5°	-17.5°	0°	Y_{max}	Z_{max}	Mean	CV
76	--	157.9	181.7	170.7	--	-12/-13/-12	All 255	170.8	0.07
156	89.5	106.5	92.0	93.5	50.6	0/0/13/0/-13	All 245	86.4	0.28
236	50.8	--	41.6	--	24.6	0/--/25/--/0	All 245	39.0	0.31
396	3.68	--	2.93	--	4.57	0/--/120/--/25	265/--/120/--/265	3.73	0.31

*- Z_{rh} = release height in model scale

For the cube, Table 11.11 lists χ_{max} at various distances downwind of the source position. The root mean square value of the CV over the four distances above was 0.26. It should be noted that the sampling was achieved closer to the roof surface at 240mm, with the cube model, so that direct comparison with the EW cases at a sample height of 265mm is not possible. Nevertheless, comparison of the cube cases for coefficient of variation (CV) across the range of conditions presented in Table 11.11 shows that these are not much different to the maximum values presented in Table 11.8 for cases 3 and 4 in that table. It was noted for the plume concentration maxima (PCM) for the cube, that these were of the order of three times the values presented in Table 11.8 for the EW building at the downstream distance of 160mm: i.e. within the roof zone. It should however be noted that the EW measurements were conducted (for practical experimental reasons) at a greater height of 265mm or 25mm above the building roof surface, compared to 245mm, or 5mm above the building surface for the cube model.

11.4 Discussion

The concentration field and some aspects of the flow field were investigated for a range of conditions with a complex urban building model set, with a focus on a main wind direction corresponding to a release moving over the EW building, and a detailed assessment of roof level concentrations for the EW building. Additionally, some data are presented for the effects of experimental conditions further downstream than the immediate vicinity of the EW building.

Building cases (Table 11.2) numbered 1-7 broadly represent a transition from the EW full building model through to isolated clad and unclad versions of that building. Concentration field maxima near the midpoint of the roof of the EW building were shown to increase from case#1 (EW clad full building model), through the removal of peripheral buildings (case#2), through to removal of significant tall upstream buildings (case#5) through to a maximum concentration value in the roof zone for the isolated EW clad building case. Local building effects (i.e. the shape of the EW clad/unclad buildings) appeared to be part of the pattern, with the EW unclad building concentrations starting slightly lower than the corresponding EW clad

case (compare case#4 to case#3), culminating in a maximum concentration for the isolated EW unclad building ($\chi=44.9$, $Y=-20\text{mm}$, $Z=265\text{mm}$) being some way below the maximum concentration for the EW clad of $\chi=67.3$ (building case#7 compared to case#6). It is plausible therefore that the maximum concentrations values measured at roof level on the target (or pollutant source) building would be a function of two variables, namely local shape of the target building and the presence of buildings in the surrounding location – especially tall upwind buildings for the wind direction being considered.

Evidence presented here from Figures 11.4-11.6 show that it is plausible to relate features in the velocity flow field to small-scale building effects, showing that local building features are indeed important in the flow field near the roof of buildings. However, local flow field considerations will only become important in processes for the spatial distribution of pollutant material when the release position in relation to the building means that those processes come into effect in the advection and mixing distribution of pollutant releases: i.e. there is some importance placed on the release position with respect to flow field effects.

Local turbulence intensities at the plume concentration maxima (PCM) presented in Table 11.5 show that the turbulence levels in the roof zone are dependent, to some extent, on the building configurations tested, with the highest values recorded at the isolated EW buildings and configurations with the main buildings downstream. Further, the spread of pollutant and the reduction of plume centreline concentration by plume broadening is an integrated effect over the plume trajectory and volume. From Figure 7 for the EW/FBM, it can be noted that the maximum value of vertical turbulence intensity w'^2/U_{ref}^2 of approximately 0.026 occurs at $Y=-250\text{mm}$, outside of the position of the building, and in the wake of the North Wing. Sensitivity analysis of the roof zone vertical component of turbulence intensity w'^2/U_{ref}^2 at the PCM for cases #1/#3 and #4 (Table 11.6) indicated that the coefficient of variation (CV) was a highly variable quantity with respective values of 0.045, 0.021 and 0.200. In this respect the quantity appears to reflect variations in the local building geometry. A variation of angle of approach flow of $\pm 5^\circ$ around the main direction of interest at -22.5° does not indicate a significant variation with angle of approach flow. Figure 11.7 shows the spatial variability of this quantity with sample height and crosswind co-ordinate. Values normalised to local downstream advection velocity were approximately four times greater.

The shear stress $-u'w'/U_{ref}^2$ was also presented, showing, for the cases 1,3 and 4 investigated, that the value at the PCM is remarkably constant mean values of 0.004 through to 0.003. Once again, the CV varied widely from a value of 0.54 down to 0.06 with the modest change of angle of approach wind of $\pm 5^\circ$ around the main direction of interest at -22.5° . Analysis of the structure function, $w'^2/(-u'w')$, showed the turbulence to be highly distorted compared to the approach flow.

Table 11.8 shows the concentration maxima for the $\pm 5^\circ$ wind direction variation around the main wind direction of -22.5° ; we see that for the sampled position ($X=160\text{mm}$) in the central region of the roof of the EW building that the CV is low for case#1 (EW/FBM) at 0.029 rising to 0.174 and 0.236 for the cases #3 and #4 respectively. The mean dimensionless concentration values, across the three angles of approach flow tested, were however quite similar with respective values of 28.8, 33.2 and 28.2 for the angles of -27.5° , -22.5° , -17.5° respectively.

Data from limited cases were available for downstream cases at $X=800\text{mm}$ (Table 11.9) and $X=1200\text{mm}$ (Table 11.10) for cases 3 and 4, showing the variation between -27.5° and -17.5° . In both cases the mean dimensionless concentrations were quite similar, showing a minimal

difference between the downstream values at each distance between having the EW clad and unclad building models present. Of more interest is the CV of the values, which from Table 11.9 shows a range of only 0.14 to 0.19, and for Table 10 (at $X=1200\text{mm}$) of only 0.10-0.12. This gives some evidence to the claim that the sensitivity to angle of approach flow of the building cases diminishes rapidly with increased distance from the source.

In Table 11.11 the sensitivity analysis for different approach wind directions is shown for the cube model. For the closest downstream distance the CV is low at only 0.07. However, as the flow develops CV values of around 0.3 were seen at further downstream distances. This indicates that over the roof zone greater variation in measured concentration with angle of approach flow may be expected.

The cube concentration maximum was greater than that for the EW cases, although sampling for the cube was much closer to the roof surface (5mm above roof compared to 25mm) so local concentration effects in the EW cases cannot be excluded based upon this data. Limitations of access to close to the EW building roof plane were in effect due to the complex shape and projections above the roof surface extending to 10mm above the base plane of the EW roof.

5. Conclusion

Concentration and flow field measurements were made for a complex building system, and with various combinations of buildings present to evaluate the effects of changing upstream and downstream configurations. Of course, the exact buildings correspond only to one real-world case, but may serve to illustrate the range of variation that may be expected in concentration maxima from a plume of pollutant material at rooftop.

Turbulence intensity and shear-stress values at the plume concentration maxima were a highly variable quantity (in terms of coefficient of variation, CV) dependent on the angle of approach flow, although the mean quantities across the angles tested were relatively similar over $\pm 5^\circ$.

The results, although tentative and case-specific, indicate that the presence of upwind buildings has a significant effect on the maximum concentration values in the roof zone of the building under investigation: in this case the EW clad and unclad buildings. The maximum concentrations were measured for isolated buildings, and the presence of tall upwind buildings served to reduce the maximum measured concentrations. The results however indicate that a factor of 2-3 on maximum concentration values between the lowest value (for the FBM) and the isolated buildings would apply. The results presented give an indication of the likely variation in concentration maxima that may be expected in a similar experimental configuration. They also demonstrate that best estimates of dispersion parameters require the full site model and cannot be provided by a single building, as is common in many operation dispersion models.

CHAPTER 12: PRACTICAL APPLICATION OF METHODOLOGY

12.1 Introduction

Conventional dispersion models cannot be applied to very short-range dispersion over a building roof because of the complexity of the flow field and the resulting complexity of the concentration field. An empirical methodology has therefore been developed, based on understating of the key flow characteristics. The approaches developed in this work can be applied to provide an approximate estimate of the concentration field given the source term for an emission of pollutant that takes place close to and just above the roof level of a building. For short intermittent releases, statistical results have been presented which enable the range of expected dosage from a given puff release to be evaluated in terms of a statistical confidence interval. The methodology can be adapted to other circumstances of very short-range dispersion in complex flow, given a sufficient data base of dispersion data derived from either wind tunnel experiments or CFD simulations.

Two release positions were investigated for the cube model, their height and locations matched to the East Wing work. Dispersion behaviour was then determined in terms of the rooftop concentrations for a range of wind approach angles to the building. Mechanisms for the advection of material down to roof level via vortices provided an explanation of the range of near rooftop level concentration values. In any given scenario, the data at different angles of approach flow enables an estimate to be made of the range of expected near roof top level concentrations. In this chapter, a summary of the methodology will be presented, referencing previous parts of this work and recommending how best to apply the results and developed methodology to obtain estimates of the concentration field and then the dose to persons in the roof zone of the source building, and at some other locations should these also be required.

Radiation dose was evaluated by accounting for the dose from inhalation, immersion to beta particles or positrons from the local concentration field and from gamma ray shine from the surrounding concentration field of radioactive material. In this work, the pollutants being considered were those arising from a radiopharmaceutical production facility producing positron emitting radionuclides which were vented to air from an emission stack just above the roof of a building on a complex hospital site in an urban area. The calculation of doses from gamma rays, in this case from positron-electron annihilation events in the air above the building, was conducted by a Monte Carlo code into which the characteristics of the given radionuclides were entered. The Monte Carlo code used results on the measured plume concentration and spread from the wind tunnel experiments - plume horizontal and vertical spread parameters were available for a range of release heights, wind approach angles and building release positions in order that the MC model could accurately estimate the concentration field to be used in the gamma ray dose evaluation. The Monte Carlo code may be easily adapted for different gamma ray emitting radionuclides, but the results presented here may be used to gain an appreciation of the power of this method compared to cruder semi-infinite cloud approximations or integral solutions to the Gaussian plume formulation, where the convergence to a robust solution may become impossible due to the receptor point being within the actual plume.

12.2 Methods

Conversion of the dimensionless concentration given in equation [1] into concentration C of the pollutant requires the building height, H , the pollutant emission rate, Q , and the reference wind speed U_{ref} at 200m height from ground level to be known.

$$\chi = \frac{CU_{ref}H^2}{Q} \quad [1]$$

In the example below, and throughout this work, the reference wind speed has been taken to be the long-term average wind speed for the site in question. This has been carried out throughout the work to enable comparison across cases in a consistent way. Information on the evaluation of the long-term average wind speed is presented in Chapter 4 and associated Appendices 15.5 and 15.6.

12.2.1 Example case: cube building

The input data to the problem is specified in Table 1 below, showing the estimation of a roof top concentration from results presented in this work. To demonstrate the method, this example aligns to one case already in the results set.

Table 12.1: case input data

Parameter	Value	Unit
Building Height, H	48.0 (0.240m in model scale)	m
Surrounding buildings	No	--
Release position	$H/10$ offset from lead vertex (position 'A')	--
Wind Angle	-22.5	Degrees
Release Type	Passive	
Release duration	Puff release with $\Delta T = 10$ seconds at full scale releasing full daily amount of emission by this route	s
Release height Z_{rh}	49.0 (0.245m in model dimensions)	m
Wind speed: U_{ref} *	4.8	ms^{-1}
Pollutant release rate (mean rate over an 8-hour day)	4.17×10^5	Bqs^{-1}
Radionuclide	^{18}F (half-life 109 minutes)	--

*- specified at 200m from ground level

Table 12.1 specifies the wind speed U_{ref} at 200m from ground level, effectively close to the free-stream velocity. Chapter 4, and Appendices 15.5 and 15.6, detail the method to be applied to calculate the wind speed at 10m from ground level, or at the building height, based upon the ground roughness length z_0 applicable to the local conditions. Given local meteorological data measured at 10m from ground level the same method may be used to determine U_{ref} to be used in the calculations below. The half-life of the radionuclide, ^{18}F , for which the radiation doses were calculated by the Monte Carlo (MC) code is approximately 109 minutes and reduction in streamwise concentration due to radioactive decay of the emitted gas stream is not a consideration for this radionuclide due to the short distance ranges considered in this study. However, there are radionuclides emitted from PET radiopharmaceutical production and accelerator facilities such as ^{15}O , with a half-life of 2 minutes where this may become a consideration: the MC code does correct for the reduction in concentration with downstream

flow using the wind velocity at building height and the known distance to receptor points from the source.

Chapter 6, Figure 6.9 indicates (CU_{ref}/Q) value of approximately 1800m^{-2} , which using the model scale dimension in equation [1] in metres gives a maximum value of dimensionless concentration of $\chi = 104$ at $X/H = 2/3$ ($X = 32\text{m}$) at 1.5m from the roof level. This confirms the value read from Chapter 6, Figure 6.29(a) of χ of just over 100 for the Single Gaussian Plume (SGP) method at a downstream distance of approximately 32m . The Dual Gaussian Plume (DGP) graph in Figure 6.29(b) gives a value of $\chi = 90$ for the same downstream distance, with the roof top Recirculation Zone (RCZ) from Figure 6.29(c) returning a maximum value of $\chi = 20$ at the same downstream distance.

The lateral and vertical spreads are also obtained from results presented in Chapter 6. Figure 6.40(a) for the SGP method gives a value of $\sigma_y/X = 0.14$ at $X/H = 0.67$, and Figure 6.40(b) returns $\sigma_z/X = 0.060$ at the same distance. For $X = 32\text{m}$, the position of peak concentration, we have $\sigma_y = 4.5\text{m}$ and $\sigma_z = 1.9\text{m}$ at this distance.

Using the results from Chapter 6, Figure 6.41(a/b) for the DGP and Isolated Gaussian Plume (IGP) method (the latter IGP method applying to the procedure to deconvolve the vertical spread from the rooftop recirculation zone) we obtain $\sigma_y/X = 0.10$ and $\sigma_z/X = 0.080$ from Figures 6.41(a) and 6.41(b) respectively, leading to $\sigma_y = 3.2\text{m}$ and $\sigma_z = 2.6\text{m}$ at the same distance of $X = 32\text{m}$ for the plume concentration weighted estimates of the plume dispersion parameters at this distance.

To feed in values into a Monte Carlo analysis for the gamma ray dose component evaluation the mean values of σ_y/X and σ_z/X over the roof zone need to be determined: these are mean spread parameters over the region of the roof zone. Ascribing these values enables a best fitted ellipsoidal Gaussian conical plume, with an adjacent rooftop recirculation zone, with appropriate spatial spread parameters to be used in the calculations. For the example under consideration Chapter 6, Figure 6.49(a/b), concentration weighted values of σ_y/X and σ_z/X from the over the roof region are given plotted against the normalised release height given in equation [2].

$$Z_{norm} = \frac{(Z_{rh}-H)}{H} \quad [2]$$

Given a value of $Z_{rh} = 0.021$ for the case given above by applying equation [2] from Figure 6.49(a/b) values of $\sigma_y/X = 0.155$ (0.11) and $\sigma_z/X = 0.07$ (0.08), where values given in brackets are from the DGP/IGP analysis method. These values are averaged with distance over the roof zone. Evaluated at $X=32\text{m}$ they give $\sigma_y = 5.0\text{m}$ (3.5m) and $\sigma_z = 2.6\text{m}$ (2.6m) for the SGP method with the DGP/IGP values being presented in brackets. The DGP spread values evaluated in this way from the mean fitted curves are similar to the values of 3.2m and 2.6m for lateral and vertical spreads estimated from Figure 6.41(a/b) above.

Plume horizontal deflection of the concentration maximum is obtained from Chapter 6, Figure 6.52(a), in this case for the SGP method, and yields a value of $Y_p/X_s = -0.03$, where Y_p is the Y co-ordinate of the peak and X_s is the distance from the source, yielding $Y_p = -0.96\text{m}$ measured crosswind of the plume approach flow direction along the X -axis extending from the source position. A similar estimation from Figure 6.53(a) with the DGP/IGP yields $Y_p = -0.32\text{m}$.

The lateral position of the rooftop RCZ maximum is given from Chapter 6, Figure 6.54(a) using $Z_{norm}=0.021$ and reading off the result for cube; A; -22.5° yielding a value of $Y_{max}/X_{max}=0.27$. Coupled with the value of $X_{max}/H=0.67$ from Chapter 6, Table 6.1 the value of $X_{max}=32.0\text{m}$ and follows that $Y_{max}=8.6\text{m}$. These values of (X_{max}, Y_{max}) thus obtained for the rooftop RCZ maximum concentration position are used in the Monte Carlo computation.

The normalised height of the plume Z_{PCM} is given in equation [3] and is the normalised mean height of the plume concentration maximum (PCM) with distance over the roof zone, and Z_{pcm} is the height of the plume concentration maximum measured from ground level.

$$Z_{PCM} = \frac{(Z_{pcm} - Z_{rh})}{H} \quad [3]$$

From Chapter 6, Figure 6.55(a) we obtain $Z_{PCM}=0$ given $Z_{norm} = 0.021$, for the SGP case, which indicates minimal plume upwards or downwards deflection from the release height in this example. Figure 6.56(a) for the DGP/IGP analysis yields $Z_{PCM}=0.02$, from which $Z_{pcm} = 50.0\text{m}$, a mean upwards deflection of 1.0m over the roof zone from the release height of 49.0m .

From Chapter 6, Figure 6.61(a) we obtain an RCZ (vertically-mixed) concentration of $\chi = 17$ for the example given here with $Z_{norm}=0.021$, and this value is taken forward in the Monte Carlo analysis: this value is arrived at by taking the mean of the RCZ concentration close to roof level (at 1.5m height) and the RCZ rooftop value at the main plume height in this (X, Y) position: it represents an approximation of the mean value of the RCZ concentration up to the rooftop RCZ truncation height Z_{RCZmax} . This concentration is appropriate for carrying out gamma ray dose rate computation from radioactive gas in the rooftop RCZ. Values for the rooftop RCZ χ (at 1.5m height) at the rooftop RCZ concentration maximum (X_{max}, Y_{max}) are given in Chapter 6, Table 6.6: in this case $\chi=25$. Additionally, Table 6.7 of that chapter gives a value of $\chi = 2.8$ for the main recirculation zone which extends to ground level downwind of the building.

The daily radiation dose may be evaluated using the methods given in Chapter 4 for the inhalation and positron immersion (in this case) based upon a continuous release at a known rate and scaling the dose rate for the full period of exposure over 8 hours operation in this example. The MC method may be applied to calculate the additional dose rate due to the gamma rays from the continuous release, again scaling the dose rate at the release rate given above to the dose received over a period of 8 hours.

12.2.2 The intermittent short release method

In the example given above we have posed the problem that all the daily activity is released in one short duration burst of 10 seconds. In this case we have calculated the dose received based upon a steady wind direction and a duration of 8 hours.

It is then necessary to determine the confidence interval on the dose received because the release happened over a short duration as follows. Chapter 7, equation [6] gives the pulse length scale from the full-scale release as follows for this example, where the release duration is 10 seconds, which indicates a value of $PLS/H = 1$, as below.

$$PLS/H = U_{ref} \Delta T/H = 4.8\text{ms}^{-1} \times 10\text{s}/48.0\text{m} = 1.0$$

From Figure 7.10(b) in Chapter 7 we obtain the coefficient of variation (CV) as a value of 0.75 corresponding to $X/H = 0.67$, the position where we have found the maximum inhalation dose in our example, and from Figure 7.13(b) the 95th percentile value of χ divided by the mean value of χ as 2.3. We may therefore state that the dose received could be up to 2.3 times greater than the dose calculated assuming a steady release of the same total amount of pollutant over an 8h period. We ascribe a 95% confidence value on the dose not being greater than 2.3 times the dose value calculated based on the steady continuous release. Information on the fluctuation of gamma-ray dose from the measured results for the full-scale building in Chapter 10 may be useful in estimating the likely fluctuations in the gamma ray dose from a spike or puff release, which forms part of the total dose received from a puff or spike release event.

12.3 Discussion

The application of methods given in this work has been demonstrated in outline for a given example showing a release at an oblique angle of -22.5° to the cube building, with a release position near the leading edge of the cube (position 'A' in previous experiments), and with a passive release into the flow at a height of 245mm model scale above the cube roof at 240mm from ground level. An intermittent release was also considered where the total daily release, based upon the mean release rate averaged over an 8h period, occurred in a single 10 second 'spike' release: in this case results provided in this work enabled a statistical estimate of the 95th percentile dose estimate as a ratio to the mean dose based on a longer 8 hour release of the same total quantity of pollutant. It was also possible to evaluate the plume dimensions in terms of the lateral and vertical spread parameters and evaluate these at the maximum concentration region near the roof. Furthermore, the plume vertical and horizontal deflections were evaluated, and as such the information obtained supplied parameters to the Monte Carlo model to carry out the gamma ray dose calculation. Methods for converting concentration field values into radiation dose estimates have been provided in detail in previous chapters and have not been reproduced again here.

12.4 Conclusions

This chapter has provided an example of how to use the results presented in this work for a case matching one of those considered in the wind tunnel experiments with the cube model. Experimental data has also been provided in previous chapters for the two 'real world' building configurations investigated in the wind tunnel, namely the EW clad and unclad cases. In Chapter 11 results of an analysis of the sensitivity to the experimental conditions, concerning changes to the building model set with these cases, were also presented to provide evidence on the likely variation in maximum concentrations with changes to the presence and configuration of surrounding buildings.

The question arises as to how the methods and results presented in this work could be generalised to apply to a different building close to a release stack of pollutant material. The method proposed, based on the results of this work, would be to consider the following factors for the case under investigation. Factors (a)-(c) require critical evaluation prior to applying the model.

- (a) Information on the source term
- (b) Critical features in the roof zone where concentration values may be significant such as air intake vents to the air conditioning system

- (c) Shape of the building such as whether this may be approximated by a cube model in terms of the expected flow and shape of the rooftop and main recirculation zone
- (d) Release position in relation to the building
- (e) Height of release, either passive or effective release height for an active vertical release
- (f) Angle of approach flow to the building
- (g) Duration of the release
- (h) Presence of surrounding buildings

Item (e) requires evaluation of the effective stack height for an active vertical release. There are several formulae in the literature that might be applied, taking account of upwards momentum and, if necessary, momentum and buoyancy (e.g. see the ADMS-BUILD model specification, CERC, 2020). Where the model may be applied, the release position may be parameterised in terms of length alongside: two release positions ‘A’, near the vertex at $H/10$ along the leading-edge length and ‘B’ midline at $H/2$ have been presented. For a given case methods for position ‘A’ and ‘B’ may be applied to determine concentration field values and dose estimates as required. Otherwise, the methodology can be applied but acquisition of a site-specific dispersion dataset would be part of that activity.

The solution is attained by interpolation in terms of the normalised source height, the wind direction, source location etc., leading to a first estimate of the concentration field maxima and expected dose levels. A statistical estimate can then be made of the 95th percentile dose from a puff or spike release in relation to the value obtained from the steady-state continuous release concentration field or dose estimate.

Estimation can be made of the general effect of surrounding buildings in terms of an analogy to the cases considered in this work: it may be that there is some degree of generalisation possible and an estimate of a factor to account for the presence or absence of nearby surrounding buildings may be possible.

Having considered the above factors a range of results for concentration field maximum and expected maximum dose for the different configurations can be made. In some cases, the spread of results may provide sufficient information to provide an order of magnitude estimate of the likely concentration maximum in the roof zone, or elsewhere, for a safety case and provide information on which cases may require further investigation – enabling better deployment of wind tunnel or CFD computational time.

CHAPTER 13: CONCLUSIONS AND FURTHER DEVELOPMENTS

The practical motivation for the work described here was to provide good estimates of radiation dose over the roof of a large building due to stack emissions from the building. The methods developed in this body of work are empirical, based on extensive wind tunnel experimentation, and justified by the underlying complexity of the topic which takes it well beyond the capability of existing operational dispersion models. Evaluating the dose required detailed understanding of flow and dispersion behaviour, sufficient to characterise the concentration field in the region of interest. Although the context was radioactive emissions from cyclotron facilities, there are numerous examples where the same understanding is required. These generally revolve around a requirement to avoid reingestion of emissions into ventilation systems, and include many HVAC design issues, fume cupboard exhaust systems, distributed power generation stack design, and so on. What at first glance appears to be a very parochial research matter has, in fact, a rather widespread value. The methods developed in this body of work are empirical, based on extensive wind tunnel experimentation, and justified by the underlying complexity of the topic.

13.1 Conclusions

This work has provided the results of a series of extensive and detailed experimental measurements in a wind tunnel of dispersion of tracer to simulate the dispersion near to buildings in a specific full-scale case, and a more generic case derived from it. The operation of the wind tunnel and LDA are described in some detail in Chapter 3 on experimental methods, with details of the experimental conditions used. The dispersion measurements encompassed releases at different heights, different positions with respect to the nearest building and different angulations of approach flow in relation to the buildings. A detailed measurement of the fluid flow characteristics with Laser Doppler Anemometry (LDA) was carried out to understand the flow processes in terms of direction of advection of material in the roof zone just above the buildings and to quantify the turbulence levels, as these also affect the dispersion of pollutant material close to roof and downstream of a building. The literature review indicated that there has been no systematic and detailed measurement of pollutant levels in the very-near field of a pollutant emitting stack near to the roof zone of a building – therefore, this work provides important and detailed new evidence to increase the sum of knowledge in this area.

Two scientific papers have been published in the course of this work in the *Journal of Radiological Protection* by the author working in collaboration with others (Gallacher *et al.*, 2016a, 2016b) and these are reproduced in Chapter 4 and associated Appendices 15.5 and 15.6 of this thesis. The papers deal with the initial work around the comparison of radiation dose predictions using different techniques with a given source term of radioactive material released into the environment, and the development of methods to convert spatially measured concentration field data from wind tunnel tracer release experiments into estimates of radiation dose to persons in the roof zone and other locations close the release point of radioactive material. The initial wind tunnel experiments, which provided data for these two papers had the limitation of the concentration field only being measured in one horizontal plane at 265mm height (5 metres in full scale above the roof level) above the wind tunnel floor. Limited information from additional experiments enabled estimates of the plume vertical and crosswind dispersion to be made in these two initial papers from which the gamma ray dose contribution could be estimated. The total effective doses based upon a fixed wind direction are given in Table 1 from this initial work. It should be noted that the same release rate of pollutant has been used throughout this thesis based upon that specified in the published papers; this enables ready

comparison of the relative levels of dose. Results presented may be scaled to a different release rate as required.

Table 13.1: Chapter 4 estimates of the total radiation dose at 5m above the roof from the ^{18}F release

Building	Release position	Angle of flow (degrees)	Normalised Release height*: $(Z_{rh}-H)/H$	Release height (mm)	Effective dose per year ($\mu\text{Sv.y}^{-1}$)
EW clad	Vertex	-22.5	0.063	255	630
EW clad	Vertex	-22.5	0.104	265	1498
EW unclad	Vertex	-22.5	0.063	255	292
EW unclad	Vertex	-22.5	0.104	265	876

*- where H is the height of the building, receptor height was 5metres above roof level or $Z=265\text{mm}$ height in model scale from the ground plane

Chapter 5 gave results of detailed measurements of the flow field around the cube and EW buildings in an approach flow that was fully turbulent and independent of Reynold's number. It was established that the flow field was complex and highly dependent on angle of approach flow. The presence of roof top vortices, generated at the building edges leading into the flow, was seen to progress from corner edge vortices at the normal incident case, through to developments of asymmetrical vortices for the intermediate -22.5° case, to strong near-symmetrical experimentally observed vortices for the -45° case. From the flow fields seen in the (V, W) plots at each downstream plane the vortices were seen to be important features in the downwards advection of pollutant material (or tracer) towards near roof level, more strongly with the greater incidence angles of the building to the flow. The upstream approach flow was characterised in terms of the flow velocity with height, but also in terms of the normalised components of the unsteady part of the flow velocity: u'^2/U_{ref}^2 , v'^2/U_{ref}^2 , w'^2/U_{ref}^2 , $-u'w'/U_{ref}^2$ and $v'w'/U_{ref}^2$. Analysis of the measured turbulent intensity components in the three orthogonal directions indicated a high extent of building generated turbulence introduced by the buildings which would act to increase dispersion of released pollutant material still further in addition to advective processes.

Chapter 6 gives detailed results of the concentration field measurements made during this work. The values are presented in, or may easily be converted to, dimensionless concentration χ from which the results may easily be generalised to buildings of different heights, different speed of approach flow (U_{ref}) and different source release rates Q . The results may therefore be used to determine values of concentration of other pollutants, for example from chemical processes. The variations of wind tunnel measured dispersion parameters horizontally, vertically and downstream were parameterised according to the Gaussian Plume Model (GPM) so that these parameters could be used in the Monte Carlo computations. To account for the rooftop recirculation zones (RCZ) encountered in flows over the building models, a novel Dual Gaussian Plume (DGP) method was devised to supplement the simpler Single Gaussian Plume (SGP) and enable the parameterised concentration field immediately over the roof of the building to better describe the concentration field for evaluation of local doses to persons in the roof zone (or at roof level ventilation intakes). A similar Isolated Gaussian Plume (IGP) method was used to deconvolve the overlapping rooftop plume vertical profile from a recirculation well-mixed volume immediately above the roof.

Chapter 7 details the experimental results from intermittent or puff releases, and the effect on dose received at different locations for these kinds of releases. A method was developed to normalise the puff doses in terms of release duration, U_{ref} and building height, H to provide a dimensionless parameter, Puff Length Scale/ H (termed PLS/H), which enables generalisation of the findings to real world conditions where U_{ref} and release duration are known in the full-scale case. The coefficient of variation (CV), and 95th percentile level of dose per puff, were obtained from statistical analysis of puff dose histograms for a range of experimental conditions and presented. From this analysis values of the 95th percentile dose per puff against an equivalent value obtained from a continuous release have been given: this practical method enables a confidence interval (95th percentile dose per puff) to be established compared to a simple analysis considering only a constant steady state release.

Chapter 8 gives details of the Monte Carlo code written by the author to determine the gamma ray dose from the measured and parameterised concentration field for the range of experimental conditions investigated. Full details of how the Dose Point Kernel (DPK) method was applied to the computational problem of calculation of the external gamma ray dose were presented in this chapter.

Extensive results from the Monte Carlo computations were presented in Chapter 9, showing how the effective dose values – including components from inhalation, beta (positron) immersion and external gamma ray dose – varied with position, angle, release height and building under investigation. Values from the simpler SGP parameterisation were compared to the more sophisticated DGP/IGP methods.

More refined dose estimates, based on an accurate evaluation of the plume spread horizontally, vertically and with downstream travel, are presented in Table 13.2 with which the earlier values, from the published papers covered in Chapter 4, and reproduced in Appendices 15.5 and 15.6, and presented in Table 13.1, can be compared. Table 13.2 shows the best estimates from the extensive concentration field mapping and Monte Carlo computations of gamma ray external dose using the Dual Gaussian Plume (DGP) method. It should be noted that one refinement of the model was that dose levels have been evaluated closer to the roof plane where persons would actually be standing and where air intakes could be located: accordingly the values in Table 2 correspond to a height of 1.5m from the roof level or a height above the ground plane in model scale of 247.5mm – these should be contrasted to the conditions in Table 1 where the height above the roof was 5m or a total height of 265mm from ground level in model scale.

Table 2: Best estimates of the EW model total radiation dose at 1.5m from the roof level from the ^{18}F release**

Building	Release position	Angle of flow (degrees)	Normalised Release height*: $(Z_{rh}-H)/H$	Release height (mm)	Effective dose per year ($\mu\text{Sv.y}^{-1}$)
EW clad	Vertex	-22.5	0.063	255	3,650
EW clad	Vertex	-22.5	0.104	265	741
EW unclad	Vertex	-22.5	0.063	255	1,201
EW unclad	Vertex	-22.5	0.104	265	1,016

*- where H is the height of the building

** - receptor height was at 1.5m from roof level or 247.5mm height in model scale from the ground plane

From Table 13.2 can be seen that the refined estimates using MC indicate dose levels generally larger than the simpler less extensive initial analysis. However, it should be noted that the refined analysis presents results much closer to the roof surface and represents more accurately expected doses to a representative person at nose/mouth breathing height of 1.5m from roof level.

Table 13.3 summarises results from the cube measurements with different release heights all with the DGP method. Results from two release positions, 'A' near the vertex and 'B' level with the cube midline, are given along with variation with angle at one height.

The results in Table 13.3 indicate that the dose levels are lower, in some case much lower, for the midline 'B' release position compared to the 'A' release position near the vertex of the cube. For the 'A' release data, the dose at 1.5m rapidly decreases with release height above the roof: for the 'B' case the dose peaked at the intermediate release height investigated (255mm or 51m full scale). With respect to angle of approach flow there was a marked increase of dose with the 'A' case going from normal incidence through to -45°. For the 'B' case normal incidence and -22.5° gave similar doses but the angle -45° showed a marked increase, reflecting changes in the roof-top flow structure.

Table 13.3: Best estimates of the total cube model radiation dose at 1.5m height from the roof plane from the ^{18}F release**

Building	Release position	Angle of flow (degrees)	Normalised Release height*: $(Z_{rh}-H)/H$	Release height (mm)	Effective dose per year ($\mu\text{Sv.y}^{-1}$)
Cube	A	-22.5	0.021	245	17,557
Cube	A	-22.5	0.063	255	2,294
Cube	A	-22.5	0.104	265	897
Cube	A	0	0.063	255	1,142
Cube	A	-45	0.063	255	6,472
Cube	B	-22.5	0.021	245	391
Cube	B	-22.5	0.063	255	587
Cube	B	-22.5	0.104	265	323
Cube	B	0	0.063	255	569
Cube	B	-45	0.063	255	844

*- where H is the height of the building

** - receptor height was at 1.5m from roof level or 247.5mm height in model scale from the ground plane

The general conclusions were that the radiation doses, which are closely related to the maximum concentration field values near the roof level in these cases, depends strongly on release position with respect to the building and release height – with a general pattern of reduction in dose with increasing height of the release - and on angle of approach flow. With respect to approach flow normal incidence gave rise to the lowest dose levels, the -22.5° case was intermediate, and the greatest dose levels were seen with the highest angulation investigated of -45°.

The differences of results for the EW clad and unclad, and cube, cases for a given stack are clearly significant and would not be reproduced by operational models that reduce the real buildings to an equivalent cuboid building.

A component of the work was real world gamma ray dose measurements from two gamma ray detectors on the roof of the EW building, coupled with wind direction and velocity measurements from an anemometer also located on the roof of this building presented in Chapter 10. Methods were presented to enable the results of the full-scale gamma measurements to be compared with the MC dose results by normalisation of known spike emission releases coupled with wind direction and velocity data. Although only limited data were obtained from the full-scale case, the results, averaged over both detectors, did not indicate a systematic bias from the dose results calculated from the MC method for the mean dose continuous release - in this way the field measurements provided support to the results obtained from the wind tunnel and computational results. The fluctuations of real-world dose values reflected the high levels of turbulence that were seen in the flow field measurement. These may be used to estimate variations in the measured gamma ray dose in a full-scale scenario for short duration puff releases.

A sensitivity analysis to measurement conditions was presented in Chapter 11, showing how maximum roof top concentration levels varied when moving from the EW full building model through to isolated buildings in the flow. Variations were seen due to local effects, in this case the tall North Wing building on the site, but also the presence of other upstream and to a lesser extent downstream, buildings. The variations in peak concentration were seen to be very approximately a factor of two. Variations in maximum rooftop concentrations χ_{\max} to sensitivity of approach flow, from small variations of wind approach angle, were also shown here and in earlier chapters and the root mean square (RMS) value of the coefficient of variation (CV) was 0.17, indicating variations of up to approximately $\pm 20\%$ for wind angle direction changes of $\pm 5^\circ$. For the cube case (with release position 'A') a range of cases with variations of wind approach angle between -45° to 0° , and streamwise distances from the source of between $H/3$ to $5H/3$, measured at the plume concentration maximum yielded an RMS value of CV of 0.26 or 26%. This information may be useful when deciding how many wind directions to experimentally measure in a wind tunnel experiment to accurately determine rooftop maximum concentrations.

Results between the DGP and SGP methods were found to be significantly different, especially for releases close to roof level, and numerically differences in concentration field value and radiation dose can be large between these two methods. However, the SGP will suffice for elevated releases in terms of accuracy where the plume does not interact with the building rooftop recirculation zone. For cases where greater accuracy is required, for example releases relatively close to the level of the roof, the DGP method is required to give reasonable accuracy of predicted roof top concentrations and their spatial distribution: e.g. the location of the peak concentration in the roof zone and the position of the rooftop RCZ.

The justification for using the more sophisticated methods developed in this work over simpler models can be stated as follows:

- (a) Use of these methods, especially the DGP methods, will enable many cases to be given an initial analysis prior to commencing extensive wind tunnel or computational fluid dynamics (CFD) work as part of the design of a new facility. A range of estimates can be achieved easily for a given case using different parameters (wind direction, stack release position, release height) and values for any given intermediate case obtained by interpolation of the results. A range of likely variation can then be estimated. In some cases, this may be sufficient information to justify a safety case and avoid extensive, and potentially expensive, further investigations.

- (b) The methods presented may enable the case to be made to avoid potentially costly and disruptive additional abatement measures for facilities already in operation. This could include avoiding the fitting of taller and more expensive release stacks or the fitting of gas capture or filtration systems to trap radioactive releases (or other pollutants) before stack emission.
- (c) The methods presented will provide evidence to regulators for a radiological assessment of given levels of discharge into the environment and will enable an operator of a local site permit to justify the radiation dose to persons in the immediate environment of the radioactive releases, and thereby legally maintain the use of the permit to continue production.

An example of how the practical methodology may be formed from results presented in this work was given in Chapter 12, and proposals put forward for methods that could be applied to specific cases not matching exactly any of the measured cases in this work.

In conclusion, detailed results have been presented on the evaluation of radiation dose, and concentration field, from radioactive releases in the very-near field of buildings, and for complex building cases – including for real world modelled scenarios. The results have been presented for a known release rate of certain pollutants, principally ^{18}F , arising from production in a radiopharmaceutical laboratory facility. The methods could be applied to different release scenarios by modification of parameters in the input models to allow for different radionuclides.

The methods developed in this work will enable quicker, efficient and effective design of many facilities that emit gaseous pollutants, not only radioactive emissions but also chemical and biological pollutants. Different design scenarios of release height, considerations of stack location in respect of a building, and wind directions using wind rose data can be investigated at the drawing board stage and estimates of near field pollutant levels obtained. This in turn will enable the options for design to be quickly reduced to a limited number of cases, which in turn can then be subjected to detailed specific investigations as appropriate via, for example, wind tunnel experiments or CFD. In some cases, the methods will enable design to be achieved without more extensive investigation by judicious use of design parameters for stack height and location.

The sophisticated techniques, and associated data, provide new and detailed knowledge of the concentration field in the very near field of buildings nearby to pollutant emissions: helping to fill the gap in knowledge between very near-scale effects and the widely studied dispersion of pollutants over larger regions such as the surrounding local street scale environments and then further outwards over cities (or regions with different topography) at even greater distances from a source of pollutant.

The spread of the plume was characterised in terms of fitting to a Gaussian Plume Model, but with highly specific concentration weighted plume spread parameters allowing for the exact scenario being simulated in terms of building, release position, release height and angle of approach flow to be used in further computation.

In terms of the concentration field this has been measured and results presented in generalisable non-dimensional quantities, so these results may be used for pollutants of other, possibly non-radioactive, materials. The results presented may be used as benchmarking test cases to

compare pollutant dispersion and advection results from Computational Fluid Dynamics (CFD) simulations. To enable benchmarking of the cases investigated in this work the data and results have been made available through the electronic repository of the University of Surrey.

13.2 Further developments

The evaluations presented here were based on the long-term mean wind speed for the site in question and a wind direction that carried the plume over the rooftop. A neutrally stable atmospheric boundary layer was assumed, being the most likely at the wind speed studied. Together, these two assumptions defined the velocity ratio of the emission and, hence, any plume rise that might occur through upwards momentum. Natural developments of this work would be to extend the methodology to cover a wider range of emission and meteorological conditions. The former would be relatively easily treated by applying the methods discussed in Chapter 12 to calculate an effective stack height, being the physical height plus the plume rise, and then using a passive source at that height. Whether or not the data compendium presented here could then be used would depend on the degree of plume rise in any particular case. Otherwise, wind tunnel or CFD modelling would need to be undertaken with the appropriate stack height and emission velocity ratio to compile the basic dispersion data to enable the impact analysis to be completed – in this case, a radiological dose assessment.

The first aspect of the meteorology that might be addressed could well be wind direction as the procedure would be relatively straightforward. Wind direction probability and associated long-term wind speeds would be required using, say, twelve 30° sectors. The assessment methodology would then be repeated for each sector. This would clearly lead to considerably more work. In the present case, most wind directions carry the plume away from the roof area of interest, implying that the inhalation dose would be zero for most wind directions. The gamma dose would remain but again the expectation is that it would be small as the plume is carried away from the rooftop. Doses experienced on the surfaces of adjacent buildings might though be of interest.

The next aspect of the meteorology than could be readily treated is the wind speed – rather than assuming the long-term mean, a range of assessments could be undertaken at different wind speeds. If it is assumed that boundary layer conditions are still neutral, then this would amount to using data for different effective stack heights and then combining results according to the probability of each occurring. Finally, a wider range of boundary layer states might be treated. The work involved in doing this would be substantial – modelling non-neutral conditions, whether in a wind tunnel or in CFD – is far from straightforward. However, it is feasible and could be undertaken if there were a compelling reason to do so. The effort to do so should not though be underestimated. A much more realistic undertaking would be to carry out the analysis only for the critical wind direction.

Some other areas for further investigation have been considered and are listed here.

- (a) Further investigation of the parameters affecting the boundary layer height that may affect the plume dispersion in the near field.
- (b) Analyse the effect of different source stack release positions in relation to the cube and the EW building.
- (c) Analyse the situation where the dispersion parameters used to describe the Gaussian plume take larger values ($H/4 < \sigma_y < H$, $H/3 < \sigma_z < H$) where the plume dispersion reaches this range of values at the distal edges of the site. To then compare the results of wind

tunnel experiments with computationally modelled approaches (ADMS) in this intermediate region. Note: there are some limited results presented for doses at the edge of the site in the publication reproduced in Appendix 15.5 of this work, but the primary focus of this thesis was on behaviour of the plume very close to the building and on doses of radiation received to persons in the roof zone.

- (d) Investigate wind velocities below 0.5ms^{-1} in terms of the effect on radiation dose term. For low wind speeds, atmospheric conditions may be unstable during daytime conditions, where the stability class parameter $P < 3.6$, corresponding to Pasquill A, B, C conditions (Pasquill, 1974). To look further at the effect on doses to a roof-workers in the near field region where low wind speed conditions apply.
- (e) The Gaussian Plume Model (GPM) is a solution to turbulent eddy diffusion equations that assumes turbulent flow is fully developed and homogenous, and the turbulence intensities are constant (Pasquill, 1974). For zero-wind conditions further work may be carried out on the solution to the diffusion equation with a hemispherical control boundary to develop further the hemisphere model presented in Appendix 15.6.
- (f) Radioactive tracer release measurements give information about the radiation doses received from the plume but also information about the dispersal of the plume pollutant gases including residence time in the rooftop recirculation zone and in the near-field region. A more detailed analysis using equipment that could investigate the energy spectrum and photon-counting at a higher temporal sampling rate could prove valuable in further investigations.
- (g) Further investigations could provide information on variations of the local background level of radiation dose in this location of London along with more information on local wind direction and velocity data measured at rooftop level.

Finally, it is worth noting that the empirical approach to describing the concentration field is a consequence of using sparse data. The wind tunnel time was used to cover a range of wind directions, geometries, etc., at the expense of obtaining highly resolved measurements. If the measurements were well resolved, then empiricism would not be necessary, and the Monte Carlo calculations could make direct use of the data. This raises the possibility of including those calculations within the suite of data analysis programmes that form part of the tunnel operating software. Alternatively, the methodology could be added to a high fidelity CFD method, again automating the analysis procedure. Other models such as ADMS could potentially benefit from use of Monte Carlo computational algorithms to calculate radiation dose from exposure to plume where the region of interest is close to or within the plume.

[14] REFERENCES AND BIBLIOGRAPHY

The citation list also includes those presented for the pair of papers from the author which were published in the Journal of Radiological Protection in December 2016, which are also cited in the list below for completeness. These represent citation lists applicable at that time relevant to the research questions in this thesis, and applicable to those published papers. To preserve the text of those papers the list of citations was also presented along with each paper as discussed in Chapter 4, and reproduced in Appendices 15.5 and 15.6, where they are shown in their complete form.

[14.1] References

Andronopoulos, S, Bartzis, JG, 2010, A gamma radiation dose calculation method for use with Lagrangian puff atmospheric dispersion models used in real-time emergency response systems, *J Radiol Prot*, 30, 747-759

ASHRAE 2007, Building Air Intake and Exhaust Design, Chapter 44, *ASHRAE Applications Handbook*, Atlanta: American Society of Heating, Refrigeration and Air-Conditioning Engineers, Inc. Atlanta, GA.

ASHRAE 2011, Building Air Intake and Exhaust Design, Chapter 45, *ASHRAE Applications Handbook*, Atlanta: American Society of Heating, Refrigeration and Air-Conditioning Engineers, Inc. Atlanta, GA.

Barlow, JF, Dunbar, TM, Nemitz, EG, Wood, CR, Gallagher, MW, Davies, F, O'Connor, E, Harrison, RM, 2011, Boundary layer dynamics over London, UK, as observed using Doppler lidar during REPARTEE-II, *Atmos.Chem.Phys.*, 11(2011) 2111-2125

Basit, A, R, Raza, S, Irfan, N, 2006, *J Radiol Prot*, 26, 375-387

Basit, A, Espinosa, F, Avila, R, Raza, S, Irfan, N, 2008, Simulation of atmospheric dispersion of radionuclides using an Eulerian-Lagrangian modelling system, *J Radiol Prot*, 28, 539-561

Becerra, VM, Vajpayee, V, Bausch, N, Santhosh, TV, Vinod, G, Deng, J, 2020, Estimation of Radioactivity Release Activity Using Non-Linear Kalman Filter-Based Estimation Techniques, *Energies*, 13, 3985

Berthold GmbH, Bad Wildbad, Germany, <https://www.berthold.com/en/radiation-protection/products/dose-and-dose-rate/geiger-mueller-dose-rate-probe-lb-6500/>, last accessed 02/10/2020

Berthold GmbH, Bad Wildbad, Germany, <https://www.berthold.com/en/radiation-protection/products/nuclear-data-processing/measurement-and-visualization-software-mevis/>, last accessed 09/09/2020

Blocken, B, Stathopoulos, T, Carmeliet J, Hensen, JLM, 2011. Application of computational fluid dynamics in building performance simulation for the outdoor environment: an overview, *Journal of Building Performance Simulation*, 4:2, 157-184, DOI: 10.1080/19401493.2010.513740

Britter, RE, Hanna, SR, 2003, 'Flow and dispersion in urban areas', *Annu.Rev.Fluid.Mech.*, 35, 469-96

Bronkhorst Ltd., <https://www.bronkhorst.com/en-gb/products/gas-flow-en/controllers/>, last accessed 14th July 2021

Buchave, P, George, WK, Lumley, JL, 1979, The measurement of turbulence with the laser-doppler anemometer, *Ann Rev Fluid Mech*, 11, 443-503

Burt, A., Robins, A.G., Hayden, P., 2012, 'Flow and Dispersion of Radioactive Tracers at St.Thomas' Hospital', MEng Thesis, Faculty of Engineering and Physical Sciences, University of Surrey

Calais, PJ, 2017, Gaussian plume atmospheric modelling and radiation exposure calculations following the cremation of a deceased thyroid cancer patient treated with iodine-131, *J Radiol Prot*, 37, 247-265

Calandrino, R, del Vecchio, A, Todde, S, Fazio, F, Measurement and control of the air contamination generated in a medical cyclotron facility for PET radiopharmaceuticals, 2007, *Health Physics* 92(5), 870-877

Cambridge Environmental Research Consultants (CERC), 'Dispersion Modelling of radioactive emissions at St.Thomas' Hospital', CERC, Cambridge, 2012a

Cambridge Environmental Research Consultants (CERC), 2012b, P20/01M/12, http://www.cerc.co.uk/environmental-software/assets/data/doc_techspeg/CERC_ADMS5_P20_01.pdf, last accessed 10/07/2014

Cambridge Environmental Research Consultants (CERC), 2020, Modelling of buildings effects in ADMS, P16/01X/20, https://www.cerc.co.uk/environmental-software/assets/data/doc_techspeg/P16_01.pdf, last accessed 21/08/2021

Cambustion Ltd, <https://www.cambustion.com/products/knowledgebase/fast-fid-principles>, last accessed 16/05/2021

Carruthers, DJ, Holroyd, RJ, Hunt, JCR, Weng, WS, Robins, AG, Apsley, DD, Thomson, DJ, Smith, FB, UK-ADMS: a new approach to modelling dispersion in the earth's atmospheric boundary layer, 1994, *J.Wind Engineering&Ind.Aer.*, 52, 139-153

Cashwell, ED, Everett, CJ, A Practical Manual of the Monte Carlo Method for Random Walk Problems, Los Alamos Scientific Laboratory, *Physics and Mathematics TID-4500*, 13th Edition Supplement, University of California, 1957

Chavez, M, Hajra, B., Stathopolous, T., Bahloul, A., Near-field pollutant dispersion in the build environment by CFD and wind tunnel simulations, *Journal of Wind Engineering and Industrial Aerodynamics* 99(2011) 330-339

Clarke, R.H., et al, A Model for Short and Medium Range Dispersion of Radionuclides Released to the Atmosphere, 1979, NRPB R-91, Chilton, UK

- Cochran, WG, 1963, Sampling Techniques, 2nd Edition, John Wiley and Son Ltd.
- Contini, D, Cesari, D, Donato, A, Robins, AG, 2009, Effects of Reynolds number on stack plume trajectories simulated with small scale models in a wind tunnel, *Journal of Wind Engineering and Industrial Aerodynamics*, 97, 468-474
- Crick, MJ, Linsley, GS, 1982, An assessment of the radiological impact of the Windscale reactor fire, October 1957, NRPB, Report R-135, Chilton, UK
- Crick, MJ, Linsley, GS, 1983, An assessment of the radiological impact of the Windscale reactor fire – Addendum to report NRPB R135, 1983, NRPB, Addendum to Report R-135, Chilton, UK
- Decay Data Evaluation Project (DDEP), Laboratoire National Henri Becquerel, http://www.nucleide.org/DDEP_WG/DDEPdata.htm, last accessed 10/07/2014
- Delacroix, D, Guerre, JP, Leblanc, P, Hickman, C., 2002, Radionuclide and Radiation Protection Data Handbook 2002, *Radiation Protection Dosimetry*, 98(1)
- Dantec Dynamics, <https://www.dantecdynamics.com/solutions-applications/solutions/fluid-mechanics/laser-doppler-anemometry-lda/measurement-principles-of-lda/>, last accessed 16/05/2021
- Dey, R, Patni, HK, Singh, KD, Kulkarni, MS, Anand, S, 2019, Effective dose conversion coefficient for gamma ray exposure from an overhead plume, *Phys Med Biol*, 64, 155001
- Di Ronco, A, Giacobbo, F, Cammi, A, 2020, A Kalman Filter-Based Approach for Online Source-Term Estimation in Accidental Radioactive Dispersion Events, *Sustainability*, 12, 10003
- Eckerman, KF, Ryman, JC, *External Exposure to Radionuclides in Air, Water and Soil*, Federal Guidance Report No.12, EPA-402-R-93-081, 1993
- EnFlo, 2016, Meteorological Wind Tunnel, www.surrey.ac.uk/mes/research/fluids/enflo
- Enflo, 2021, Centre for aerodynamics and environmental flow, <https://www.surrey.ac.uk/centre-aerodynamics-environmental-flow/research-centres/environmental-flow-research-centre>, last accessed 11/04/2021
- Environment Agency, 2010, *RSR permitting – prospective radiological assessments for human health and wildlife (habitats)*, Operational Instruction 338_04, Version 6, <https://publications.environment-agency.gov.uk>
- Environment Agency/SEPA/NIEA/FSA/HPA, 2012, *Principles for the assessment of prospective public doses arising from Authorised Discharges of Radioactive Waste to the Environment*, (Cumbria, Environment Agency), <https://publications.environment-agency.gov.uk/ms/EPSSyx>
- Fackrell, JE, Robins, AG, 1982, Concentration fluctuations and fluxes in plumes from point sources in a turbulent boundary layer, *Journal of Fluid Mechanics* 117, 1-26

Fawaz, A, Waller, E, Design of a hybrid computational fluid dynamics-Monte Carlo radiation transport methodology for radioactive particulate resuspension studies, 2014, *Health Physics*, 107(4), 311-317

Gallacher, D.J., Chadwick, S., Robins, A.G., Burt, A., Hayden, P., Williams, M, Halstead, P., Woods, E., Aerodynamic Models of Radioactive Gas Discharges on the St.Thomas' Hospital Site, South East EA/RPA Liaison Meeting 15th June 2012 at University College London

Gallacher, D.J., Robins, A.G., Burt, A., Chadwick, S, Hayden, P., Williams, M, 2016a, Dispersion of positron emitting radioactive gases in a complex urban building array: a comparison of dose modelling approaches, *Journal of Radiological Protection*, 36 (2016), 746-784

Gallacher, DJ, Robins, AG, Hayden, P, 2016b, Conversion of wind tunnel simulated radioactive pollutant gas concentrations for a complex building array into radiation dose, *Journal Radiological Protection*, 36 (2016), 785-818

Garland, JA, Wakeford, R, Atmospheric emissions from the Windscale accident of October 1957, 2007, *Atmospheric Environment* 41, 3904-3920

Gayev, Y.A., Hunt, J.C.R. (Eds.), 2007, Flow and Transport Processes with Complex Obstructions, NATO science series II Vol.236, Springer, Netherlands

GE Healthcare, 2012, PETtrace 800 series site planning guide, Direction 2102960-100

Gill Instruments Ltd,
<http://www.gillinstruments.com/products/anemometer/windobserver.html>, last accessed 14th July 2021

GSTFT, Guy's and St Thomas' NHS Foundation Trust,
<https://www.guysandstthomas.nhs.uk/Home.aspx>, last accessed 11/04/2021

Guy's and St.Thomas' NHS Foundation Trust, 2016, Medical Physics Department,
<http://www.guysandstthomas.nhs.uk/our-services/medical-physics/team.aspx>, last accessed 14/12/2015

Hajra, B., Stathopoulos, T., Bahloul, A., 2010, Assessment of pollutant dispersion from rooftop stacks: ASHRAE, ADMS and wind tunnel simulation, *Building and Environment* 45(2010) 2768-2777

Hajra, B., Stathopoulos, T., 2012, A wind tunnel study on the effects of downstream buildings on near-field pollutant dispersion, *Building and Environment* 52(2012): 19-31

Hajra, B., Stathopoulos, T., Bahloul, A., 2013, A wind tunnel study on the effects of adjacent buildings on near-field pollutant dispersion from rooftop emissions in an urban environment, *Journal of Wind Engineering and Industrial Aerodynamics* 119(2013) 133-145

Hajra, B., Stathopoulos, T., Bahloul, A., 2014, Performance of ASHRAE models in assessing pollutant dispersion from rooftop emissions, *HVAC&R Research* (2014) 20, 72-79

- Hawkley, G, 2014, Evaluation of near field atmospheric dispersion around nuclear facilities using a Lorentzian distribution methodology, *Health Physics*, 107(6), 514-522
- Matthews, JC, Wright, MD, Martin, D, Bacak, A, Priestley, M, Bannan, TJ, Silva, HG, Flynn, M, Percival, CJ, Shallcross, DE, 2020, *Boundary-Layer Meteorology*, 175: 113-134
- Hort, MC, Robins, AG, 2002, The dispersion of fugitive emissions from storage tanks, *J.Wind.Eng&Ind.Aer.*, 90, 1321-1348
- Hosker RP, 1984, Flow and diffusion near obstacles. In: D.Randerson, ed. Atmospheric Science and Power Production. Office of Scientific and Technical Information, United States Department of Energy
- ICRP, 1994, Publication 68, Dose coefficients for intakes of Radionuclides by Workers, *Annals of the ICRP Vol.24/4*, Elsevier
- ICRP Publication 72, 1996, Age-dependent doses to the members of the public from intake of radionuclides Part 5, compilation of ingestion and inhalation coefficients, *Annals of the ICRP Vol.26/1*, Elsevier
- ICRP Publication 103, The 2007 recommendations of the International Commission on Radiological Protection, 2007, *Annals of the ICRP Vol.37, Nos.2-4*, Elsevier
- ICRU, 1992, Measurement of Dose Equivalents from External Photon and Electron Radiations, ICRU Report 47, Bethesda, Maryland, US
- ICRU, 1998, Conversion coefficients for use in radiological protection against external radiation, ICRU Report 57, Bethesda, Maryland, US
- Ionising Radiations Regulations 2017, SI2017/1075
- Imai, K, Iijima, T, 1970, Assessment of gamma-exposure due to a radioactive cloud released from a point source, *Health Physics* 18, 207-216
- Irwin, HPAH, 1981, The design of spires for wind simulation, *Journal of Wind Engineering and Industrial Aerodynamics*, 7, 361-366
- Jeong, H, Kim, E, Park, M, Jeong, H, Hwang, W, Han, M, 2014, Numerical simulation of air pollutant dispersion using an *in situ* tracer experiment at a nuclear site, *Annals of Nuclear Energy*, 73, 1-6
- Jones, JA, 1980, ESCLOUD: A Computer Program to Calculate the Air Concentration, Deposition Rate and External Dose Rate from a Continuous Discharge of Radioactive Material to Atmosphere, NRPB Report R-101, Harwell, Didcot, Oxon
- Jones JA, 1983, Models to Allow for the Effects of Coastal Sites, Plume Rise and Buildings on Dispersion of Radionuclides and Guidance on the Value of Deposition Velocity and Washout Coefficients, NRP Report R-157, Chilton, Didcot, Oxon
- Kearfott, KJ, 1983, Radiation absorbed dose estimates for positron emission tomography (PET) inert gases ^{19}Ne and ^{77}Kr , *Health Physics* 44(3), 235-241

- Kleck, JH, Benedict, SH, Cook, JS, Birdsall, RL, Satyamurthy, N, 1991, Assessment of ^{18}F gaseous releases during the production of ^{18}F -Fluorodeoxyglucose, *Health Physics* 60(5), 657-660
- Lahti, GP, Hubner, RS, Golden, JC, 1981, Assessment of gamma-ray exposures due to finite plumes, *Health Physics* 41(August), 319-340
- Leelőssy, A, Lagzi, I, Kovacs, A, Mészáros, R, 2018, A review of numerical models to predict the atmospheric dispersion of radioactivity, *J Env Radioactivity*, 182, 20-33
- Lim, HC, Thomas, TG, Castro, IP, 2009, *Journal of Wind Engineering and Industrial Aerodynamics*, 97, 96-109
- MacDonnell, C., 2004, Radiological Assessments for small users, NRPB W-63, Chilton, UK
- McNaughton, MW, Gillis, JM, Ruedig, E, Whicker, JJ, Fuehne, DP, 2017, Gamma-Ray dose from an overhead plume, *Health Physics*, 112(5), 445-450
- McNaughton, MW, Gillis, JM, Ruedig, E, Whicker, JJ, Fuehne, DP, 2017, Accuracy of Cloudshine Gamma Dose Calculations in the CAP-88 Dispersion Model, *Health Physics, Operational Topic*, 414-419
- Meroney, RN, 1982, 'Turbulent diffusion near buildings', In: Plate, E (Ed.), *Engineering Meteorology*, Elsevier, pp 481-525
- Mirion Technologies, <https://capintec.com/support/manuals/crc-127r-dose-calibrator-manual/>, last accessed 20th June 2021
- Moore, DJ, Calculation of ground level concentrations for different sampling periods and source locations, 1978, *Atmospheric Pollution*, 51-60
- Nakayama, H, Nagai, H, Development of local-scale high-resolution atmospheric dispersion model using large eddy simulation. Part 1: turbulent flow and plume dispersion over flat terrain. 2009, *Journal of Nuclear Science and Technology*, Vol.46, No.12, 1170-1177
- Nakayama, H, Nagai, H, Development of local-scale high-resolution atmospheric dispersion model using large eddy simulation. Part 2: turbulent flow and plume dispersion around a cubical building. 2011, *Journal of Nuclear Science and Technology*, Vol.48, No.3, 374-383
- Nakayama, H, Jurcakova, K, Nagai, H, Development of local-scale high-resolution atmospheric dispersion model using large eddy simulation. Part 3: turbulent flow and plume dispersion in building arrays. 2013, *Journal of Nuclear Science and Technology*, Vol.50, No.5, 503-519
- Nakayama, H, Leidl, B, Harms, F, Nagai, H, Development of local-scale high-resolution atmospheric dispersion model using large eddy simulation. Part 4: turbulent flow and plume dispersion in an actual urban area. 2014, *Journal of Nuclear Science and Technology*, Vol.51, No.5, 626-638

Nicholson, KW, The Dispersion, Deposition and Resuspension of Atmospheric Contamination in the Outdoor Urban Environment, in *Airborne Radioactive Contamination in Inhabited Areas*, Ed. Anderson, KG, Radioactivity in the Environment, Vol.15, Elsevier, 2009

National Physical Laboratory (NPL), <https://www.npl.co.uk/products-services/radioactivity/medical-radionuclides>, last accessed 20th June 2021

Oura, M, Ohba, R, Robins, A, Kato, S, 2018, Validation Study for an Atmospheric Dispersion Model, Using Effective Source Heights Determined from Wind Tunnel Experiments in Nuclear Safety Analysis, *Atmosphere*, 9, 111, 1-20

Overcamp, TJ, Fjeld, RA, 1983, An exact solution of the Gaussian cloud approximation for gamma absorbed dose due to a ground-level release, *Health Physics* 44(4), 367-372

Overcamp, TJ, Fjeld, RA, 1987, A simple approximation for estimating centreline gamma absorbed dose rates due to a continuous Gaussian plume, *Health Physics* 53(2), 143-146

Overcamp, TJ, 1991, Modelling gamma absorbed dose due to meandering plumes, *Health Physics* 61(1), 111-115

Overcamp, TJ, 2007, Solutions to the Gaussian cloud approximation for gamma absorbed dose, *Health Physics* 92(1), 78-81

Pasquill, F, Atmospheric Diffusion: The Dispersion of Windborne Material from Industrial and other Sources, 2nd Ed., 1974, William Clowes and Sons, London

Pecha, P, Pechova, E, 2014, An unconventional adaptation of a classical Gaussian plume dispersion scheme for the fast assessment of external irradiation from a radioactive cloud, *Atmospheric Environment*, 89, 298-308

Pilkingsrud, HV, Gels, GL, 1982, Evaluation of Xe-133 radiation exposure dosimetry for workers in nuclear medicine laboratories, *Health Physics* 42(6), 837-848

Pilkingsrud, HV, Gels, GL, 1985, An evaluation of the external radiation exposure dosimetry and calculation of maximum permissible concentration values for airborne materials containing ¹⁸F, ¹⁵O, ¹³N, ¹¹C and ¹³³Xe, *Health Physics* 49(5), 805-824

Raza, S, Avila, R, A 3D Lagrangian particle model for direct plume gamma dose rate calculations, *J.Radiol.Prot.*21(2001), 145-154

Raza, S, Avila, R, 2005, Calculation of immersion doses from external exposure to a plume of radioactive material, *Health Physics*, 89(3): 247-254

Rishel, JP, Keillor, ME, Arrigo, LM, Baciak, JE, Detwiler, RS, Kernan, WJ, Kirkham, RR, Milbrath, DB, Seifert, A, Seifert, CE, Smart, JE, 2016, Using atmospheric dispersion theory to inform the design of a short-lived radioactive particle release experiment, *Health Physics*, 110(5), 526-532

Robins, A.G, MacDonald, R., 2001, Review of Flow and Dispersion in the Vicinity of Groups of Buildings, Annexe B, Atmospheric Dispersion Modelling Liaison Committee, Annual Report 1998/99, NRPB R-322, Chilton

Robins, AG, Castro, IP, 1977a, A wind tunnel investigation of plume dispersion in the vicinity of a surface mounted cube – I. The flow field, *Atmospheric Environment* Vol.11, 291-297

Robins, AG, Castro, IP, 1977b, A wind tunnel investigation of plume dispersion in the vicinity of a surface mounted cube – II. The concentration field, *Atmospheric Environment* Vol.11, 299-311

Robins, AG, Castro, IP, 1977a, A wind tunnel investigation of plume dispersion in the vicinity of a surface mounted cube – I. The flow field, *Atmospheric Environment* Vol.11, 291-297

Robins, AG, Castro, IP, 1977b, A wind tunnel investigation of plume dispersion in the vicinity of a surface mounted cube – II. The concentration field, *Atmospheric Environment* Vol.11, 299-311

Robins, AG, Carruthers, D, McHugh, C, 1997, The ADMS building effects module, *Int.J.Environment and Pollution*, Vol.8, Nos.3-6, 705-717

Robins, AG, McHugh, C, 2001, Development and evaluation of the ADMS building effects module, *Int.J.Environment and Pollution*, Vol.16, Nos.1-6, 161-174

Robins, A.G, MacDonald, R., 2001, Review of Flow and Dispersion in the Vicinity of Groups of Buildings, Annexe B, Atmospheric Dispersion Modelling Liaison Committee, Annual Report 1998/99, NRPB R-322, Chilton

Satoh, D, Nakayama, H, Furuta, T, Yoshihiro, T, Sakamoto, K, 2021, Simulation code for estimating external gamma-ray doses from a radioactive plume and contaminated ground using a local-scale atmospheric dispersion model, *PLoS ONE*, 16(1), e0245932

Smith, JG, Simmonds, JR, 2009, The methodology for assessing the radiological consequences of routine releases of radionuclides to the environment used in PC-CREAM 08, HPA-RPD-058, Chilton, UK

Snyder, WH and Castro IP, 2002. The critical Reynolds number for rough-wall boundary layers, 2002. *J. Wind Eng. and Industrial Aero.*, 90, 41-54.

Soulhac, L, Salizzoni. P, Cierco, F,-X, Perkins, R, 2011, The model SIRANE for atmospheric urban pollutant dispersion; part I presentation of the model, *Atmospheric Environment*, 45, 7379-7395

Srinivas, CV, Venkatesan, R, Somayaji, M, Indira, R, 2009, A simulation study of short-range atmospheric dispersion for hypothetical air-borne effluent releases using different turbulent diffusion methods, *Air Qual Atmos Health*, 2, 21-28

Tarasov, VI, 1993, A factorization procedure for calculations of gamma exposure from radioactive clouds, *Health Physics* 65(5), 535-538

The University of Manchester, |Centre for Atmospheric Science,
<http://www.cas.manchester.ac.uk/restools/instruments/meteorology/sonic/>, last accessed 20th June 2021

Thielen, SV, Turcanu, C, Camps, J, Keppens, R, 2015, Optimising the calculation grid for atmospheric dispersion modelling, *J Env Radioactivity*, 142, 103-112

Thies Clima, Göttingen, Germany, <https://www.thiesclima.com/en/Products/Wind-Ultrasonic-Anemometer/?art=145>, last accessed 09/09/2020

Thompson, JM, Poston, JW, 1999, Absorbed Dose from Traversing Spherically Symmetric, Gaussian Radioactive Clouds, *Health Physics*, 76(6): 639-643

Uchiyama, K, Miyashita, M, Sato, H, Tanishima, Y, Maeda, S, Yoshikawa, J, Kimura, S, 2015, A study of ¹³¹I activity of five human subjects exposed to a radioactive plume at Tamura city in Fukushima, *Health Physics*, 109(6), 573-581

Vervecken, L, Camps, J, Meyers, J, 2015, Dynamic dose assessment by Large Eddy Simulation of the near-range atmospheric dispersion, *J Radiol Prot* 35(2015), 165-178

Vickers, L, 2015, An update on a Spreadsheet Method for Computing Consequences to the Nearest Maximally Exposed Offsite Individual in compliance with DOE-STD-3009-94, *Health Physics*, Operational Topic, S42-S49

Wood, CR, Lacser, A, Barlow, JF, Padhra, A, Belcher, SE, Nemitz, E, Helfter, C, Famulari, D, Grimmond, CSB, 2010, Turbulent flow at 190m height above London during 2006-2008: a climatology and the applicability of similarity theory, *Boundary Layer Meteorology*, 137:77-96

Woodward, H, Gallacher, DJ, Robins, AG, Seaton, M, ApSimon, H, A review of the applicability of Gaussian modelling techniques to near-field dispersion, *Air Dispersion Modelling Liaison Committee, ADMLC-R11*, 2021,
https://admlc.files.wordpress.com/2021/01/short_range_gaussian_finalised-1.pdf, last accessed 12/05/2021

Xie, Z-T, Castro, IP, 2009, 'Large-eddy simulation for flow and dispersion in urban streets', *Atm.Env.*, 1-12

[2] Bibliography

The following publications were used for background and contextual information but not cited directly in the text or in the published papers associated with this work.

Environment Agency, 2006a, *Initial radiological assessment methodology – part 2 methods and input data*, Science Report SC030162/SR2, (Bristol, Environment Agency),
<https://publications.environment-agency.gov.uk>

Environment Agency, 2006b, *Initial radiological assessment methodology – part 1 user report*, Science Report SC030162/SR1, (Bristol, Environment Agency), <https://publications.environment-agency.gov.uk>

Environmental Permitting Regulations (England and Wales), 2010, SI2010/675

Environmental Permitting (Amendment) Regulations, 2011, SI2011

HSE 2000 Work with ionising radiation: Ionising Radiations Regulations 1999 Approved code of practice and guidance Publication L121 (Norwich: HSE Books)

ICRP 2008a, Publication 106, Radiation Dose to Patients from Radiopharmaceuticals, 3rd Amendment to ICRP Publication 53, Annals of the ICRP Vol.38/1-2, Elsevier

ICRP 2008b, Publication 107, Nuclear Data for Dosimetric Calculations, Annals of the ICRP Vol.38/3, Elsevier

GE Healthcare, 2012, PETtrace 800 series site planning guide, Direction 2102960-100

Smith, JG, Simmonds, JR, The methodology for assessing the radiological consequences of routine releases of radionuclides to the environment used in PC-CREAM 08, HPA-RPD-058, Chilton, UK

Veselko, AV, Gorshkov, VE, Tarasov, VL, 1996, A reduced integral solution to the dose rate due to a non-stationary release, *Rad.Prot.Dos.* 64(4), 259-268

APPENDIX 15.1: Wind tunnel experimental methods – indicative data sampling positions

The experimental sample position co-ordinates and release heights have been specified in model scale (mm) in this appendix so that should further research investigations be carried out these positions can be replicated.

15.1.1 EW clad and unclad experimental measurement positions

These are referenced in Table 3.3. Note: the original experiment code numbering scheme specified in Table 3.3 has been retained below for this section and is shown in square brackets.

[2.2.1.1] EW clad passive release sampling positions (in model scale)

$Z_{RH} = 245, 255, 265, 275, 290\text{mm}$

$X=80\text{mm}$;

$Y_I = -50, -40, -10, 0, 10, 40, 50\text{mm}$

$Z = 245\text{--}320\text{mm}$, sampled over 10 evenly spaced samples.

$X=160\text{mm}$;

$Y_I = -50, -40, -10, 0, 30, 40\text{mm}$

$Z = 245\text{--}340\text{mm}$, sampled over 10 evenly spaced samples.

$X=240\text{mm}$;

$Y_I = -70, -40, -30, 0, 10, 20, 50, 60\text{mm}$

$Z = 245\text{--}345\text{mm}$, sampled over 10 evenly spaced samples.

[2.2.1.2] EW unclad passive release sampling positions (in model scale)

$Z_{RH} = 245, 255, 265, 275, 290\text{mm}$

$X=80\text{mm}$ (Trace gas at 1.0%);

$Y = -50, -40, -10, 0, 10, 40, 50\text{mm}$

$Z = 245\text{--}320\text{ mm}$, sampled over 9 evenly spaced samples.

$X=160\text{ mm}$ (Trace gas at 1.5%);

$Y = -50, -40, -10, 0, 30, 40\text{mm}$

$Z = 245\text{--}330\text{ mm}$, sampled over 9 evenly spaced samples.

$X=240\text{ mm}$ (Trace gas at 2.0%);

$Y = -70, -40, -30, 0, 10, 20, 50, 60\text{mm}$

$Z = 245\text{--}323\text{ mm}$, sampled over 8 evenly spaced samples.

[2.2.2.1] EW Clad building: active vertical release

The release height was fixed at $Z_{RH} = 255\text{mm}$. Four minute sampling times were used at each point.

$X=80\text{mm}$ (tracer gas 0.5%);

$Y = -50, -40, -30, -20, -10, 0, 10, 20, 30, 40, 50\text{mm}$

$Z = 245\text{--}310\text{mm}$ (9points)

$X=160\text{ mm}$ (0.75% tracer gas);

$Y = -50, -40, -30, -20, -10, 0, 10, 20, 30, 40\text{mm}$

$Z = 245\text{--}320\text{ mm}$ (9 points)

$X=240\text{ mm}$ (1.0% tracer gas);

$Y = -70, -40, -30, -20, -10, 0, 10, 20, 30, 40, 50, 60\text{mm}$

$Z = 245\text{--}325\text{ mm}$ (9 points)

$Q = 0.64\text{litres/min}$

Approximate run time $3 \times 11 \times 9 \times 4 = 1188\text{minutes} \sim 20\text{ hours}$.

[2.2.2.2] EW Unclad building: active vertical release

$X=80\text{mm}$ (tracer gas 0.5%);

$Y=-50, -40, -30, -20, -10, 0, 10, 20, 30, 40, 50\text{ mm}$

$Z=245\text{-}295\text{mm}$ (9points)

$X=160\text{ mm}$ (0.75% tracer gas);

$Y=-50, -40, -30, -20, -10, 0, 10, 20, 30, 40\text{ mm}$

$Z=245\text{-}307\text{ mm}$ (9 points)

$X=240\text{ mm}$ (1.0% tracer gas);

$Y=-70, -40, -30, -20, -10, 0, 10, 20, 30, 40, 50, 60\text{ mm}$

$Z=245\text{-}312\text{ mm}$ (9 points)

$Q = 0.64\text{ litres/min}$

Approximate run time $3 \times 11 \times 9 \times 4 = 1188\text{minutes} \sim 20\text{ hours}$.

[2.2.3.1] EW Clad case: fixed release height with various release times

$Z_{RH} = 255\text{ mm}$

$X=160\text{ mm}$;

$Y=-27, -7, 13, 33\text{mm}$

$Z=245, 265, 285, 305\text{mm}$

ΔT release time, minimum $=0.025\text{s}$

Runs for: $\Delta T = 0.025, 0.05, 0.10, 0.25, 0.5, 1, 2, 4\text{s}$

Ensemble sizes: 4 minutes

[2.2.3.2] EW Unclad case: fixed release height with various release times

$Z_{RH} = 255\text{ mm}$

Runs for: $\Delta T = 0.025, 0.05, 0.10, 0.25, 0.5, 1, 2, 4\text{s}$

$X=160\text{ mm}$;

$Y=13, 33\text{mm}$ (plume centreline)

$Z=285\text{ mm}$ (plume maximum)

[2.2.4.1] EW Clad with passive puff releases

$Z_{RH} = 245\text{ mm}$

$X=160\text{ mm}$;

$Y=-27, -7\text{mm}$ (centreline), also 13, 33mm for $Z=245\text{mm}$

$Z=245, 265, 285, 305\text{mm}$

ΔT release time, minimum $=0.025\text{s}$

Runs for: $\Delta T = 0.025, 0.05, 0.10, 0.25, 0.5, 1, 2, 4\text{s}$

Ensemble sizes: various

[2.2.4.2] EW Unclad with passive puff releases

$Z_{RH} = 245\text{ mm}$

$X=160\text{ mm}$;

$Y=-27, -7\text{mm}$ (centreline), also 13, 33mm for $Z=245\text{mm}$

$Z=245, 265, 285, 305\text{mm}$

ΔT release time, minimum $=0.025\text{s}$

Runs for: $\Delta T = 0.025, 0.05, 0.10, 0.25, 0.5, 1, 2, 4,$

Ensemble sizes: 5minutes

[2.2.5.2] EW Unclad; position offset sequence

$Z_{RH} = 245\text{ mm}$

$Y=-3.7\text{mm}$, $Z=246.8\text{mm}$ (corresponds to nozzle position)

$\Delta T = 0.10\text{s}$ (for all samples)
Runs for: $\Delta X = 2, 5, 10, 20, 40, 80, 160\text{mm}$
Ensemble sizes: 5 minutes

[2.2.6.1] No building: active vertical continuous release
 $Z_{RH} = 255\text{ mm}$
 $X = 160\text{mm}$
 $Y = -50, \dots, 70\text{mm}$ (20mm increment)
 $Z = 195\text{--}315\text{mm}$ (13 sample points, 10mm increment)

[2.3.1.1A] Cube model with wind direction 0° ; no surrounding buildings, passive release position A
 $Z_{RH} = 245, 255, 265, 275, 290\text{mm}$
 $X = 80\text{mm};$
 $Y_{1\&2} = -60, -50, -40, -30, -20, -10, 0, 10, 20, 30, 40, 50\text{mm}$ (requires updating)
 $Z = 245\text{--}325\text{mm}$, sampled over 9 evenly spaced samples.
 $X = 160\text{mm};$
 $Y_{1\&2} = -60, -50, -40, -30, -20, -10, 0, 10, 20, 30, 40, 50\text{mm}$ (requires updating)
 $Z = 245\text{--}340\text{mm}$, sampled over 9 evenly spaced samples.
 $X = 240\text{mm};$
 $Y_{1\&2} = -80, -70, -60, -50, -40, -30, -20, -10, 0, 10, 20, 30, 40, 50, 60, 70\text{mm}$ (requires updating)
 $Z = 245\text{--}345\text{mm}$, sampled over 9 evenly spaced samples.
 $X = 400\text{mm};$
 $Y_{1\&2} = -100, \dots, 90\text{mm}$ (requires updating)
 $Z = 150\text{--}400\text{mm}$, sampled over 9 evenly spaced samples.

[2.3.1.1B] Cube model with wind direction 0° ; no surrounding buildings, passive release position B
 $Z_{RH} = 245, 255, 265, 275, 290\text{mm}$
 $X = 80\text{mm}$
 $Y_{1\&2} = -60, -50, -40, -30, -20, -10, 0, 10, 20, 30, 40, 50\text{mm}$ (requires updating)
 $Z = 245\text{--}325\text{mm}$, sampled over 9 evenly spaced samples.
 $X = 160\text{mm}$
 $Y_{1\&2} = -60, -50, -40, -30, -20, -10, 0, 10, 20, 30, 40, 50\text{mm}$ (requires updating)
 $Z = 245\text{--}340\text{mm}$, sampled over 9 evenly spaced samples.
 $X = 240\text{mm}$
 $Y_{1\&2} = -80, -70, -60, -50, -40, -30, -20, -10, 0, 10, 20, 30, 40, 50, 60, 70\text{mm}$ (requires updating)
 $Z = 245\text{--}345\text{mm}$, sampled over 9 evenly spaced samples.
 $X = 400\text{mm}$
 $Y_{1\&2} = -100, \dots, 90\text{mm}$ (requires updating)
 $Z = 150\text{--}400\text{mm}$, sampled over 9 evenly spaced samples.

[2.3.2.1A] Cube model with wind direction 0° ; no surrounding buildings, passive release position A
 $Z_{RH} = 255\text{mm}$
 $X = 80\text{mm}$
 $Y_{1\&2} = -60, -50, -40, -30, -20, -10, 0, 10, 20, 30, 40, 50\text{mm}$ (requires updating)
 $Z = 245\text{--}345\text{mm}$, sampled over 9 evenly spaced samples.
 $X = 160\text{mm}$
 $Y_{1\&2} = -60, -50, -40, -30, -20, -10, 0, 10, 20, 30, 40, 50\text{mm}$ (requires updating)

Z= 245-345mm, sampled over 9 evenly spaced samples.
 X=240mm
 Y_{1&2}= -80,-70, -60, -50, -40, -30, -20, -10, 0, 10, 20, 30, 40, 50, 60, 70mm (requires updating)
 Z= 245-345mm, sampled over 9 evenly spaced samples.
 X=400mm
 Y_{1&2}= -100, ..., -10, 0, 10, ..., 80, 90mm (requires updating)
 Z= 150-400mm, sampled over 9 evenly spaced samples.
 [2.3.3.1A] Experiment#3/A. Cube case at 0° incidence, stack position A near vertex
 Z_{RH} = 255 mm
 X=160 mm
 Y=-40, -30, -20, -10, 0, 10, 20, 30mm
 Z= 245, 265, 285, 305, 325mm
 ΔT release time, minimum =0.025s
 Runs for: ΔT = 0.10, 0.25, 0.5, 1.0 second
 Ensemble sizes: 1 minute

[2.3.4.1-2-3] Experiment #4. Repeated EW Clad model (no surrounding buildings) with different wind directions

Z_{RH} = 255mm
 X=80mm
 Y_{1&2}=-60, -50, -40, -30, -20, -10, 0, 10, 20, 30, 40, 50mm (12 positions)
 Z= 245-325mm, sampled over 9 evenly spaced samples.
 X=160mm
 Y_{1&2}=-60, -50, -40, -30, -20, -10, 0, 10, 20, 30, 40, 50mm (12 positions)
 Z= 245-340mm, sampled over 9 evenly spaced samples.
 X=240mm
 Y_{1&2}=-80,-70, -60, -50, -40, -30, -20, -10, 0, 10, 20, 30, 40, 50, 60, 70mm (14 positions)
 Z= 245-345mm, sampled over 9 evenly spaced samples.
 X=400mm
 Y_{1&2}=-100, ..., -20, -10, 0, 10, 20, ..., 80, 90mm (20 positions)
 Z= 150-400mm, sampled over 9 evenly spaced samples.

15.1.2 Cube experimental measurement positions (with additional EW data)

These are referenced in Table 3.4. Note: the original experiment code numbering scheme specified in Table 3.4 has been retained below for this section and is shown in square brackets.

[2.2] Passive Releases

[2.2.1] Cube – Passive Releases

Release Position A

Z_{RH} = 245, 255, 265, 275, 290mm
 X=80mm; Y_{1&2}=-60, ..., +50mm; Z= 245-325mm, over 9 evenly spaced samples.
 X=160mm; Y_{1&2}=-60, ..., +50mm; Z= 245-340mm, over 9 evenly spaced samples.
 X=240mm; Y_{1&2}=-80, ..., +70mm; Z= 245-345mm, over 9 evenly spaced samples.
 X=400mm; Y_{1&2}=-100, ..., +90mm; Z= 150-400mm, over 9 evenly spaced samples.

Release Position B

Z_{RH} = 245, 255, 265, 275, 290mm
 X=80mm; Y_{1&2}=-60, ..., 50mm; Z= 245-325mm, over 9 evenly spaced samples.
 X=160mm; Y_{1&2}=-60, ..., 50mm; Z= 245-340mm, over 9 evenly spaced samples.
 X=240mm; Y_{1&2}=-80, ..., 70mm; Z= 245-345mm, over 9 evenly spaced samples.

$X=400\text{mm}$; $Y_{1\&2}=-100, \dots, 90\text{mm}$; $Z=150-400\text{mm}$, over 9 evenly spaced samples.

[2.2.2] EW Clad – Passive Releases

$Z_{RH} = 245, 255, 265, 275, 290\text{ mm}$

$X=80\text{ mm}$; $Y_I=-50, \dots, +50\text{mm}$; $Z=245-320\text{mm}$, over 10 evenly spaced samples.

$X=160\text{ mm}$; $Y_I=-50, \dots, +40\text{mm}$; $Z=245-340\text{ mm}$, over 10 evenly spaced samples.

$X=240\text{ mm}$; $Y_I=-70, \dots, +60\text{mm}$; $Z=245-345\text{ mm}$, over 10 evenly spaced samples

[2.2.3] EW Unclad – Passive Releases

$Z_{RH} = 245, 255, 265, 275, 290\text{mm}$

$X=80\text{ mm}$ (trace gas 1.0%); $Y=-50, \dots, +50\text{mm}$; $Z=245-320\text{ mm}$, 9 evenly spaced samples.

$X=160\text{mm}$ (trace gas 1.5%); $Y=-50, \dots, +40\text{mm}$; $Z=245-330\text{ mm}$, 9 evenly spaced samples.

$X=240\text{mm}$ (trace gas 2.0%); $Y=-70, \dots, +60\text{mm}$; $Z=245-323\text{ mm}$, 8 evenly spaced samples.

[2.3] Active Vertical Releases

[2.3.1] Cube – Active Releases

$Z_{RH} = 255\text{mm}$

$X=80\text{mm}$; $Y_{1\&2}= -60, \dots, +50\text{mm}$; $Z=245-345\text{mm}$, over 9 evenly spaced samples

$X=160\text{mm}$; $Y_{1\&2}= -60, \dots, +50\text{mm}$; $Z=245-345\text{mm}$, over 9 evenly spaced samples

$X=240\text{mm}$; $Y_{1\&2}= -80, \dots, +70\text{mm}$; $Z=245-345\text{mm}$, over 9 evenly spaced samples

$X=400\text{mm}$; $Y_{1\&2}= -100, \dots, +90\text{mm}$; $Z=150-400\text{mm}$, over 9 evenly spaced samples

[2.3.2] EW Clad – Active Vertical Releases

Measurement positions were as follows.

$Z_{RH} = 255\text{mm}$

$X=80\text{mm}$; $Y=-50, \dots, +50\text{mm}$; $Z=245-310\text{mm}$ (9 points)

$X=160\text{ mm}$; $Y=-50, \dots, +40\text{mm}$; $Z=245-320\text{mm}$ (9 points)

$X=240\text{ mm}$; $Y=-70, \dots, +60\text{mm}$; $Z=245-325\text{ mm}$ (9 points)

[2.3.3] EW Unclad – Active Vertical Releases

$Z_{RH} = 255\text{mm}$

$X=80\text{mm}$; $Y=-50, \dots, +50\text{mm}$; $Z=245-295\text{mm}$ (9 points)

$X=160\text{mm}$; $Y=-50, \dots, +40\text{mm}$; $Z=245-307\text{mm}$ (9 points)

$X=240\text{ mm}$; $Y=-70, \dots, +60\text{mm}$; $Z=245-312\text{mm}$ (9 points)

APPENDIX 15.2: Flow field further results

These results are shown additionally to supplement those in Chapter 5.

15.2.1 Cube at 0° to approach flow

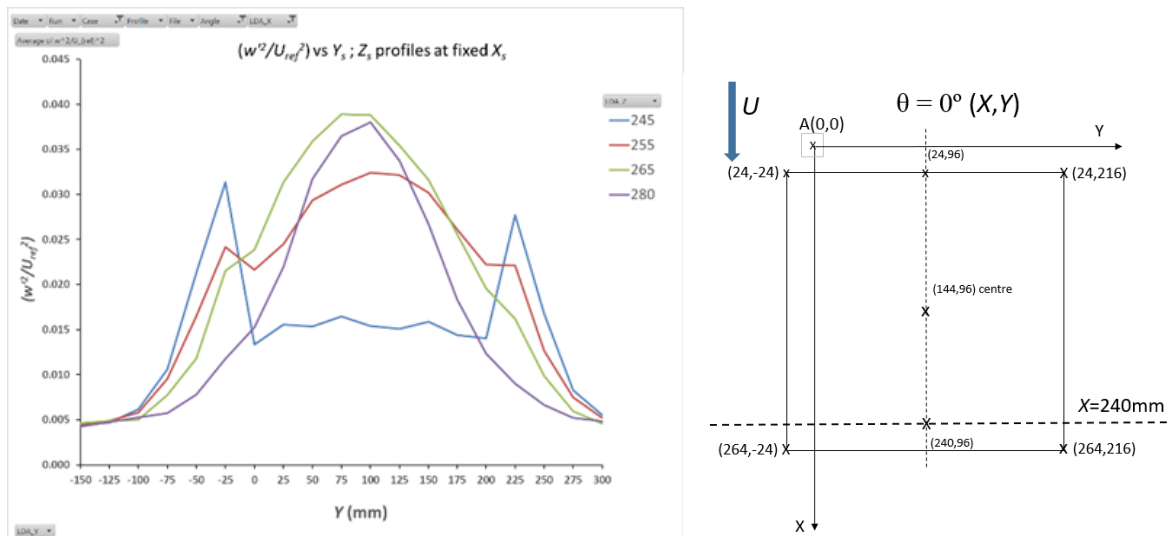


Figure 15.2.1(a/b). Cube/A; 0°; $X=236\text{mm}$; (a) (w^2/U_{ref}^2) (b) schematic layout

Figure 15.2.1(a) shows increased turbulence intensity for the lowest height sampled of $Z=245\text{mm}$ just outside the side-edges of the cube at $Y=-50\text{mm}$ and $Y=225\text{mm}$ as seen by comparison to 15.2.1(b), with reduced turbulence just above the middle section of the roof at this downstream plane. At other sampled heights the turbulence peaks near the centre of the cube along $Y=96\text{mm}$.

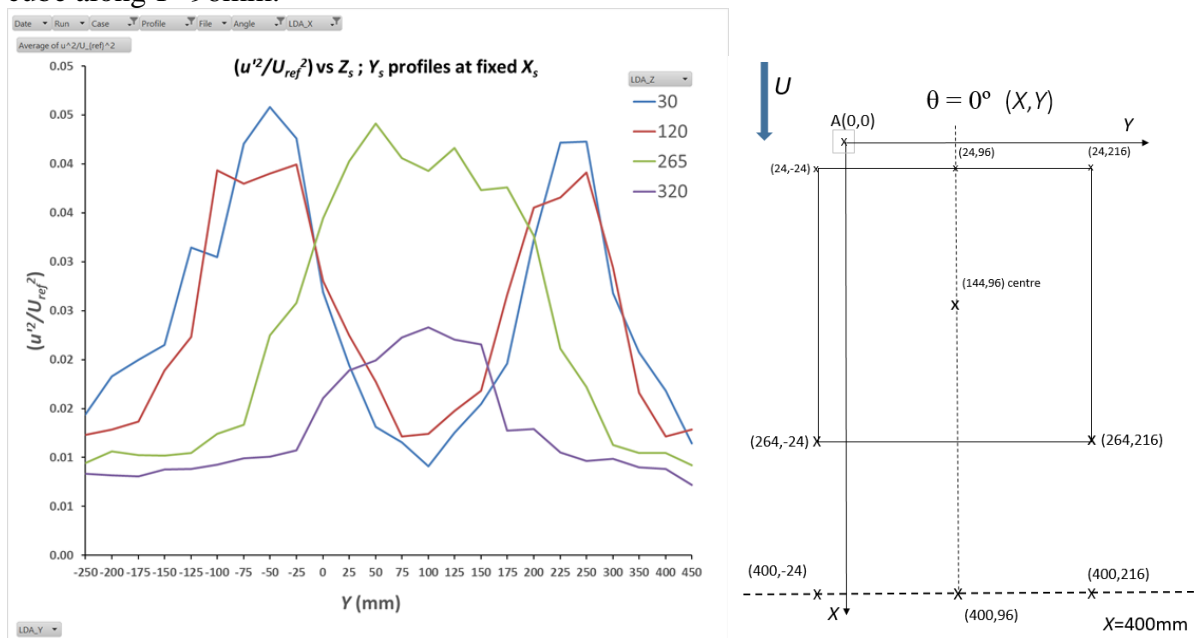


Figure 15.2.2(a/b). Cube/A; 0°; $X=396\text{mm}$; $X/H=1.65$; (a) (u^2/U_{ref}^2) ; (b) schematic

Figure 15.2.2(a) shows the streamwise component of turbulence intensity beyond the end of the building at $X/H=1.65$ as shown in the orientation Figure 15.2.2(b). Lowest sampled heights of $Z=30\text{mm}$ and $Z=120\text{mm}$ height ($Z/H=1/8$ and $1/2$ respectively) show reduced values in the main RCZ down to near ground level but pronounced peaks at $Y=-75\text{mm}$ and $Y=225\text{mm}$ at the edges of the cube as shown in (b).

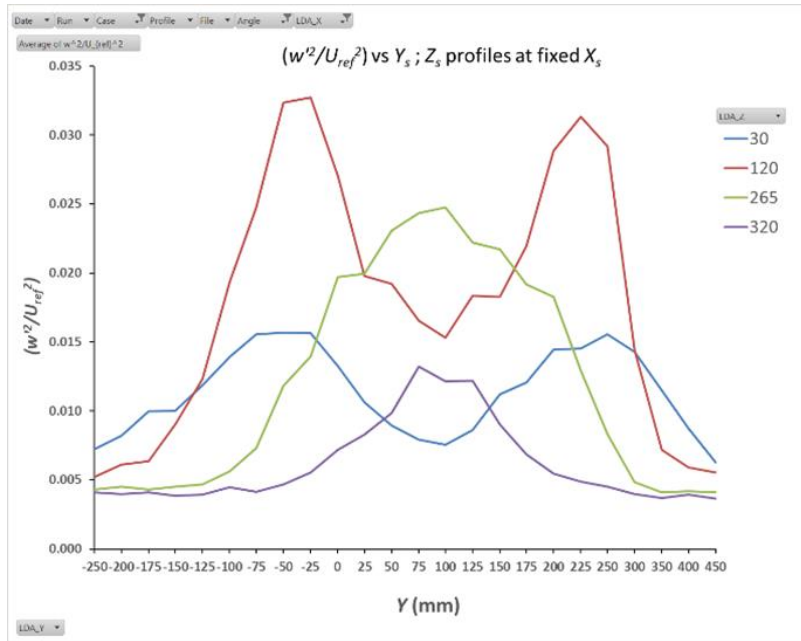


Figure 15.2.3. Cube/A; 0°; $X=396\text{mm}$; $X/H=1.65$: (w'^2/U_{ref}^2)

Figure 15.2.3 showing the vertical component of turbulence intensity may also be compared to Figure 15.2.2(a) at the sample sampled streamwise plane with orientation shown in 15.2.2(b). Pronounced peaks may again be seen at $Y=-75\text{mm}$ and $Y=225\text{mm}$ at the edges of the cube as shown for height $Z/H=1/2$ and to a lesser extent for $Z/H=1/8$.

15.2.2 Cube at -45° to approach flow

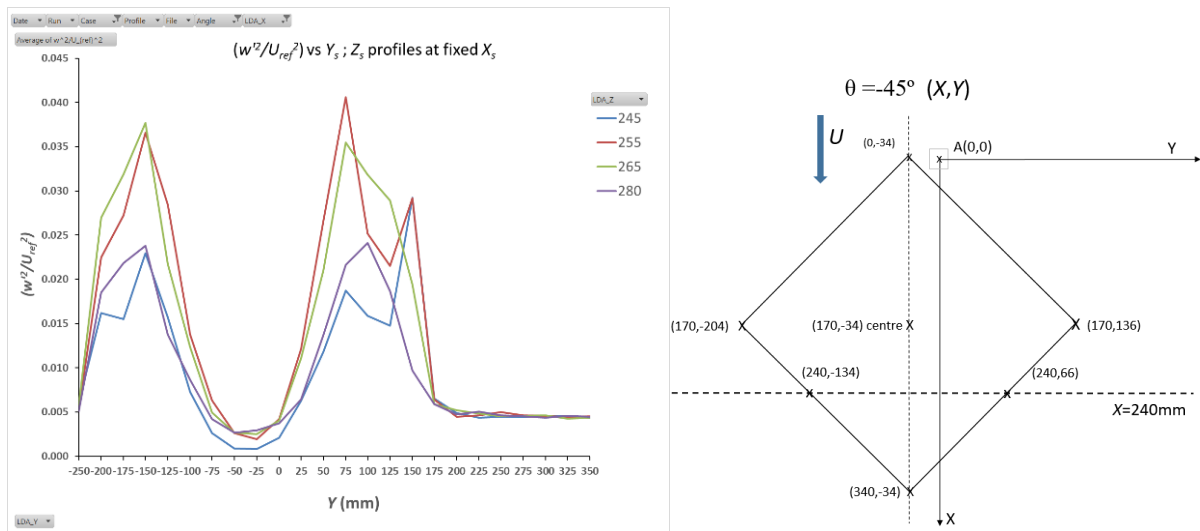


Figure 15.2.4(a/b). Cube/A; -45°; $X=236\text{mm}$; $X/H=0.98$: (a) (w'^2/U_{ref}^2) ; (b) schematic

Figure 15.2.4(a) shows the cube orientated at -45° to the approach flow with the sampled plane as a dotted line in Figure 15.2.4(b) where the contact points with the sample plane are at Y -axis co-ordinates of $Y=-134\text{mm}$ and $Y=66\text{mm}$: from Figure 15.2.4(a) these locations can be seen to correspond to peaks in the vertical turbulence intensity particularly evident for $Z=255\text{mm}$ and $Z=265\text{mm}$.

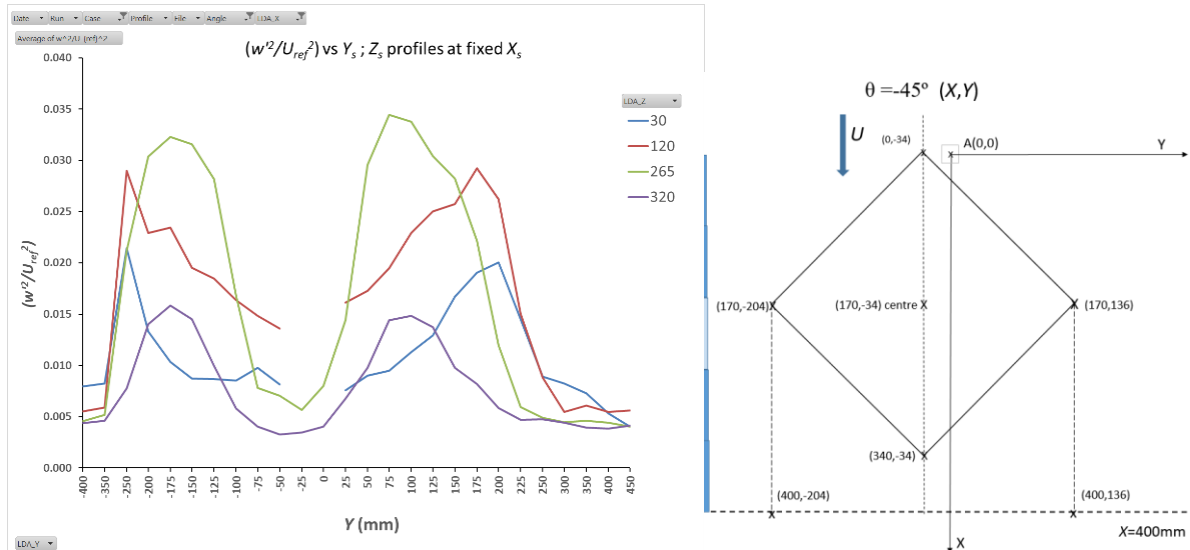


Figure 15.2.5(a/b). Cube/A; -45°; $X=396\text{mm}$; (a) (w^2/U_{ref}^2) ; (b) schematic

Figure 15.2.5(a) shows streamwise progression from the previous figure to $X/H=1.65$, past the back-edge of the building, as seen in (b), of w^2/U_{ref}^2 that shows peak intensities at $Y=-175\text{mm}$ and in the region of $Y=125\text{mm}$: from 15.2.5(b) these Y -axis locations are just inside the projected lateral corners of the cube with Y -axis co-ordinates of $Y=-204\text{mm}$ (left in the figure) and $Y=136\text{mm}$ (right in the figure).

15.2.3 Cube at -22.5° to approach flow

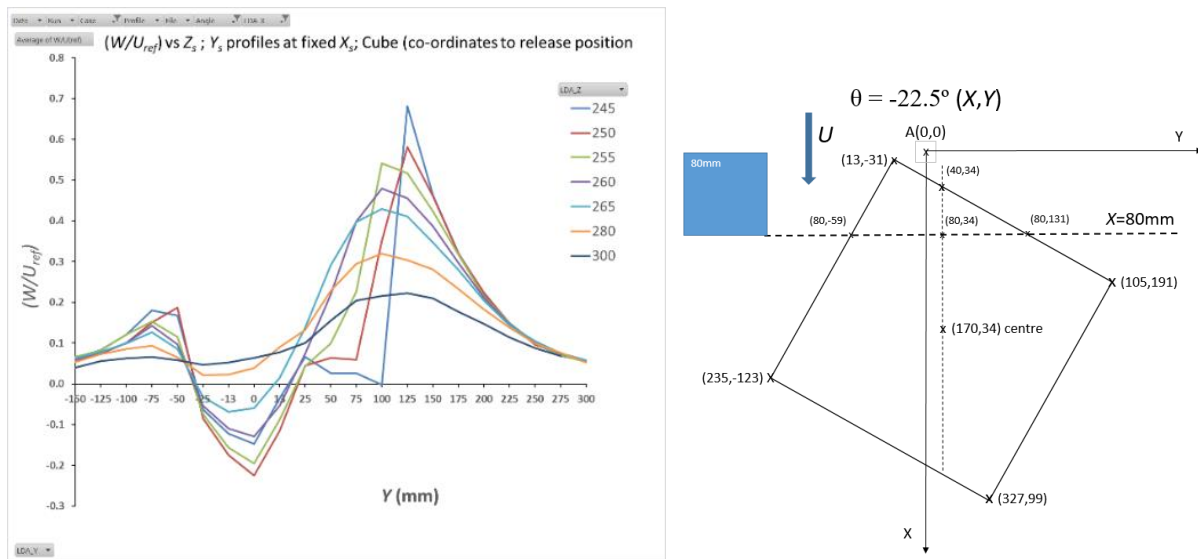


Figure 15.2.6(a/b): Cube/A; -22.5°; $X=76\text{mm}$; $X/H=0.32$: (a) (U/U_{ref}) ; (b) schematic

Figure 15.2.6(a) shows the vertical component of flow W/U_{ref} at a sampled plane close to the lead-edge vertex of the cube at $X/H=0.32$ at an approach flow of -22.5°. Strong vertical deflection upwards was seen in the region of $Y=125\text{mm}$, close to the contact point of the sampled plane with the leading edge at $Y=131\text{mm}$ shown in Figure 15.2.6(b). A downwards directed flow is seen at $Y=0\text{mm}$ suggesting the action of a leading-edge vortex.

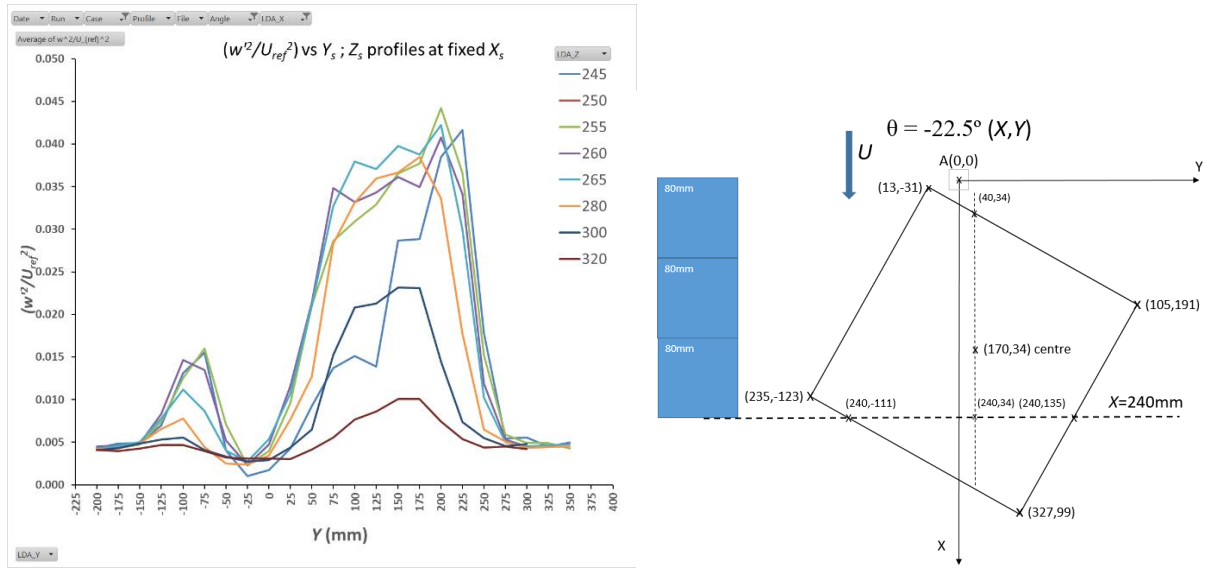


Figure 15.2.7(a/b). Cube/A; -22.5° ; $X=236$ mm; $X/H=0.98$: (a) (w'^2/U_{ref}^2) ; (b) schematic

Figure 15.2.7(a) shows vertical turbulence intensity for the cube at -22.5° flow and for a sampled plane at $X/H=0.98$ near the back end of the cube to the approaching flow. Pronounced turbulence was seen in the region of $Y=150$ mm which corresponds from Figure 15.2.8(b) to the location of the contact point of the sampled plane with the trailing edge of the cube to the flow at $Y=135$ mm and downwind of the right-corner at $Y=191$ mm.

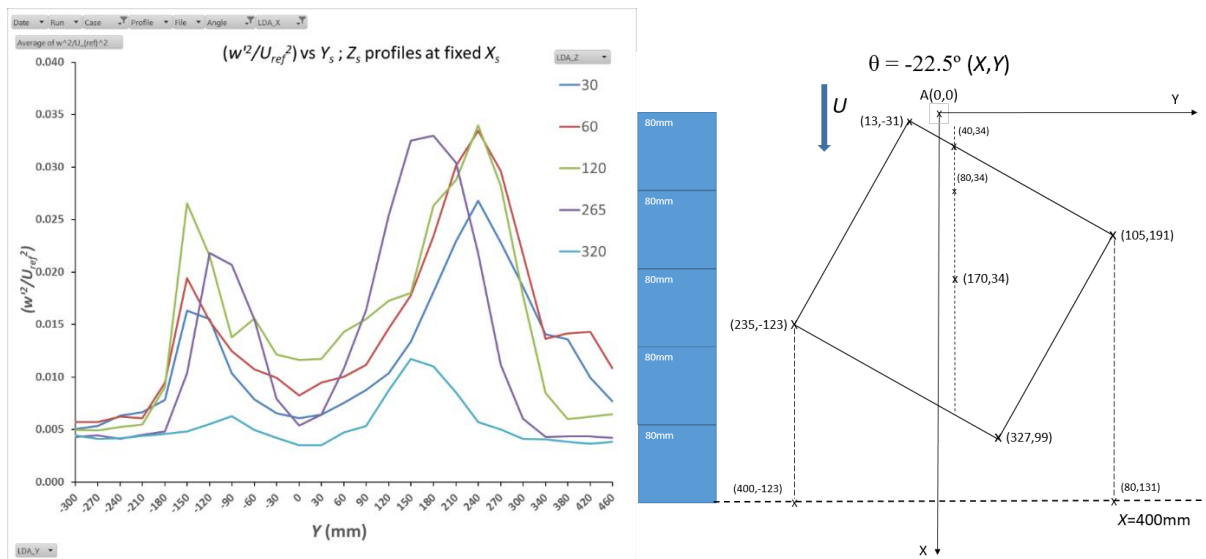


Figure 15.2.8(a/b). Cube/A; -22.5° ; $X=396$ mm; (a) (w'^2/U_{ref}^2) ; (b) schematic

Figure 15.2.8(a) shows the further streamwise plane sampled past the back-edge of the cube at -22.5° to the approach flow as can be seen from Figure 15.2.8(b). In Figure 15.2.8(a) the peaks in turbulence are located at $Y=-150$ mm and around $Y=240$ mm: from Figure (b) these are located just outside of the projections of corners of the cube at $Y=-123$ mm (left in the figure) and $Y=191$ mm (right in the figure).

15.2.4 EW clad at -22.5° to approach flow

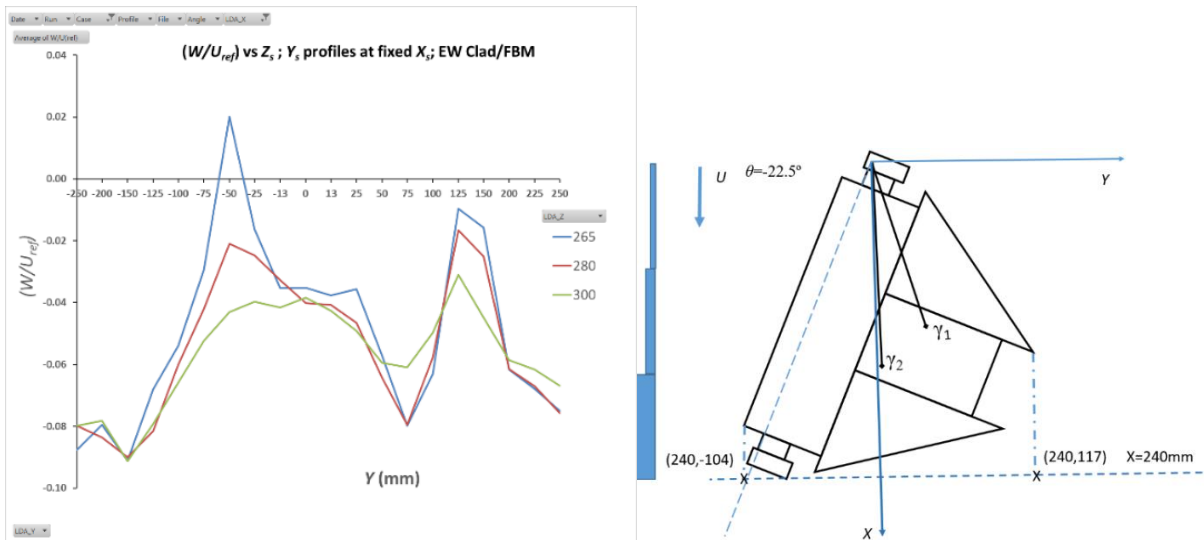


Figure 15.2.9(a/b). EW Clad/FBM; -22.5° ; $X=236$ mm; $X/H=0.98$: (a) (W/U_{ref}) ; (b) schematic

Figure 15.2.9(a) shows the vertical component of flow velocity for the EW clad full building model (FBM), at $X/H=0.98$, with a co-ordinate schematic showing the sampled place as a dotted line in Figure 15.2.9(b) just beyond the back-edge of the building to the approach flow. Pronounced downwards directed flow can be seen at this sampled plane.

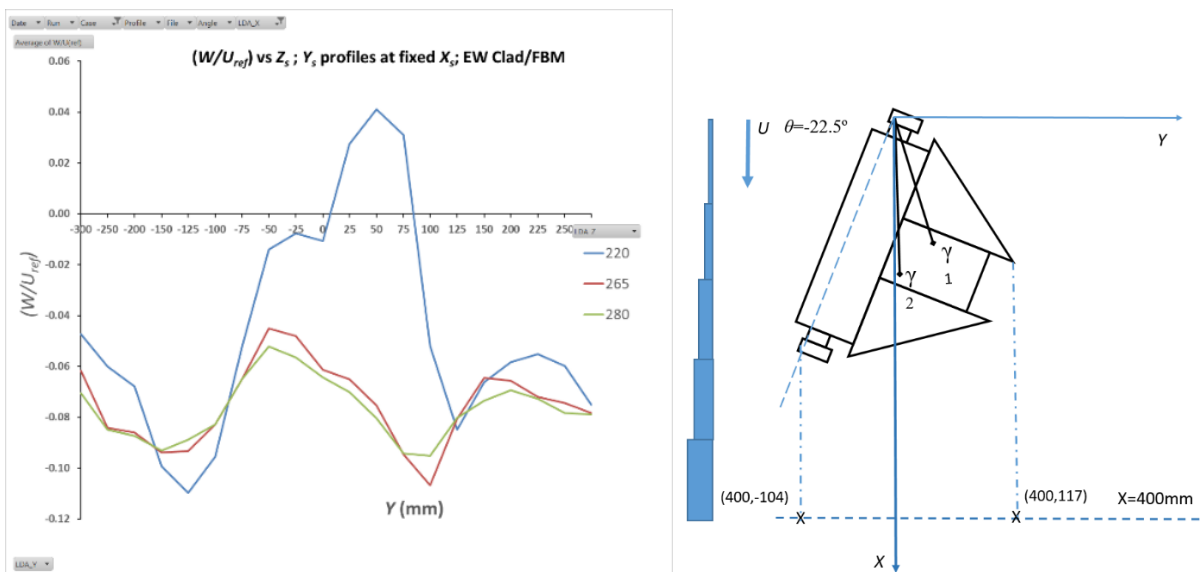


Figure 15.2.10(a/b). EW Clad/FBM; -22.5° ; $X=396$ mm; $X/H=1.65$: (a) (W/U_{ref}) ; (b) schematic

Figure 15.2.10(a) shows the vertical component of flow velocity for the EW clad full building model (FBM), at $X/H=1.65$, with a co-ordinate schematic in Figure 15.2.10(b) showing that the sampled plane is beyond the back-edge of the building in the direction of the approach flow. Some upwards directed flow is seen at $Y=50$ mm, close to the centre of the building for the lowest sampled height of $Z=220$ mm. Otherwise, the flow shows an overall negative (downwards) velocity component in this direction.

APPENDIX 15.3: Concentration field supplementary results

15.3.1 Concentration Profiles: Supplementary Results

This appendix contains supplemental results to those presented in Chapter 6 on the concentration field.

15.3.1.1 Cube: Concentration Profiles - Passive Releases

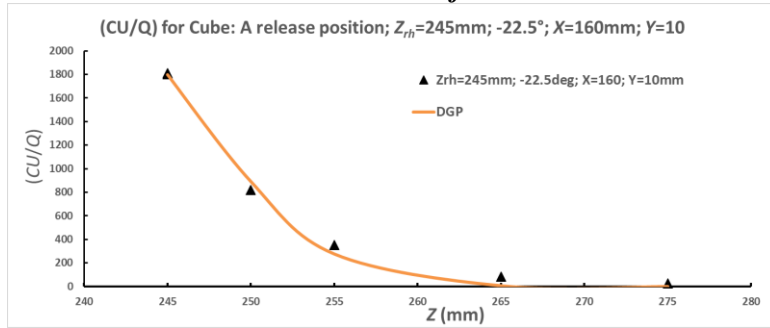


Figure 15.3.1:
(CU/Q) variation
with release height $Z_{rh}=245\text{mm}$;
release position 'A' (near cube
vertex); angle -22.5° to cube
face; Z range sampled at
 $Y=10\text{mm}$

From Figure 15.3.1 the vertical profile close to the plume centreline showed no distinct plume centre with height, but concentration increasing to a maximum value nearest the cube roof plane. In this case both IGP and SGP converged to the same fitted line, with only one shown.

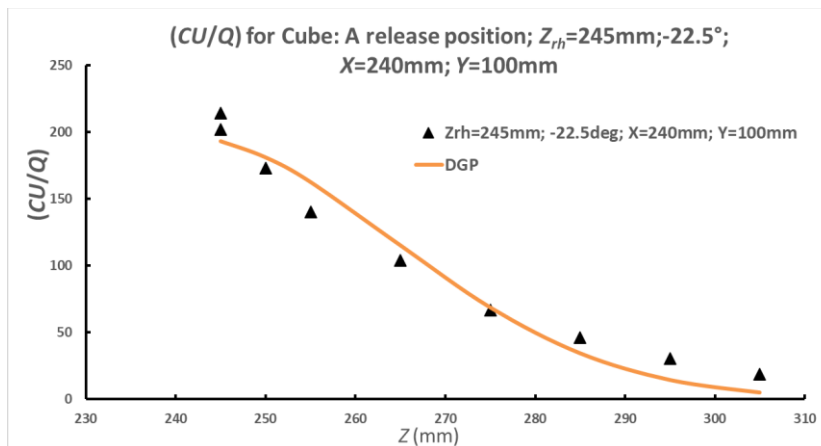


Figure 15.3.2
(CU/Q) at $X=240\text{mm}$;
release height $Z_{rh}=245\text{mm}$
(5mm above model roof
plane), release position 'A';
 -22.5° to cube face; Z range
sampled at $Y=100\text{mm}$
corresponding to the
rooftop RCZ

In Figure 15.3.2, the vertical profile was taken at $Y=100\text{mm}$, corresponding to the profile through the secondary peak (RCZ): the SGP and DGP converge in this case and no distinct elevated peak was present – evidence of the structure of the secondary peak, whether this is considered a bifurcated plume or a building rooftop RCZ.

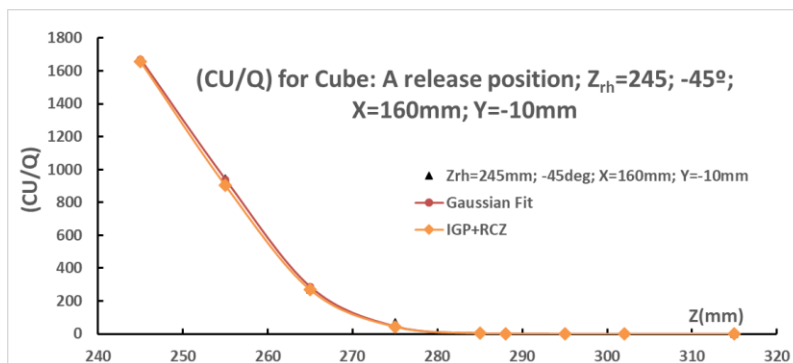


Figure 15.3.3:
(CU/Q) variation, at $X=160\text{mm}$,
release height $Z_{rh}=245\text{mm}$
(5mm above model roof plane),
at position 'A'; -45° to cube
face; Z range sampled at
 $Y=10\text{mm}$ corresponding to the
roof RCZ

It can be seen in Figure 15.3.3 for an angle of approach flow of -45° to the building, cube release position 'A', the vertical profile along the plume centreline does not show a distinct elevated peak in concentration, similar to the -22.5° case, with the maximum value in close proximity to the roof plane. The SGP and IGP methods give very similar results.

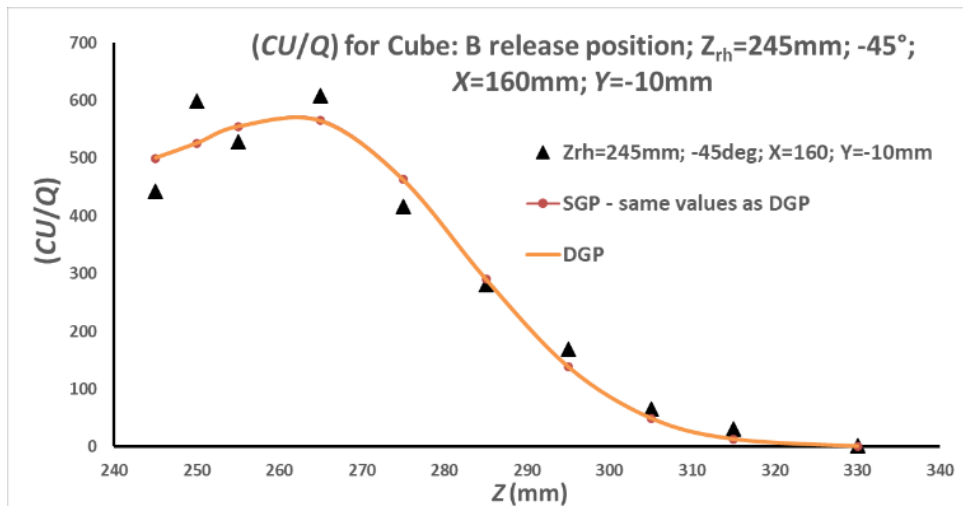


Figure 15.3.4
(CU/Q) at
 $X=160\text{mm}$;
 $Z_{rh}=245\text{mm}$;
midline position
‘B’; -22.5° to cube
face: Z range
sampled at
 $Y=10\text{mm}$
corresponding to
the roof RCZ

From Figure 15.3.4 with the ‘B’ release position the graph shows a distinct elevated peak above the roof plane, but with no difference between the SGP and IGP fitted curves which are coincident.

15.3.1.2 Cube: Concentration Profiles - Active Vertical Releases

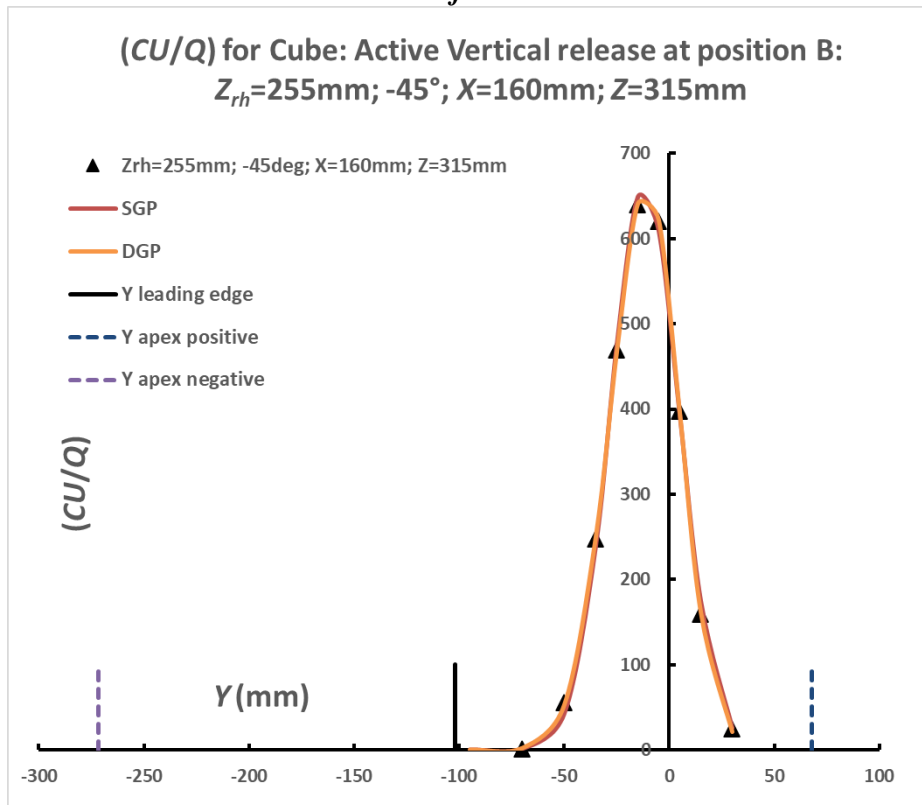


Figure 15.3.5:
(CU/Q) variation for
plume concentration
maximum profiles at
 $X=160\text{mm}$; release
height $Z_{rh}=255\text{mm}$;
active vertical release
at position ‘B’ (midline
of cube); crosswind co-
ordinate Y sampled at
 $Z=315\text{mm}$; -45°
incidence to cube face

Figure 15.3.5 shows the concentration profile for the cube with an active vertical release at position ‘B’ and angulation to flow of -45° . Release height was 255mm. The lead vertex of the cube and the two corner edges are shown with vertical marker lines in the figure. This is an example of an elevated plume, as a result of the active vertical release, where the SGP and DGP fitted methods are convergent because of the greater effective plume height from the active vertical release.

15.3.1.3 EW Clad and Unclad: Concentration Profiles - Passive Releases

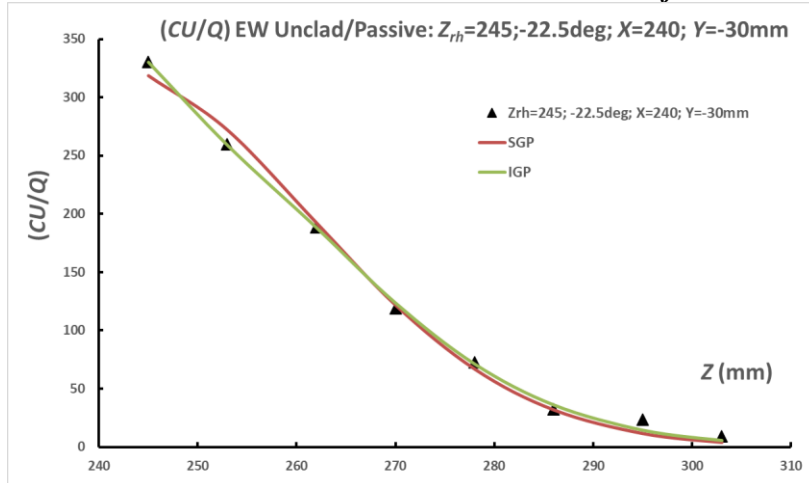


Figure 15.3.6

EW Unclad (CU/Q) variation for plume concentration maximum profiles at $X=240\text{mm}$ with passive release height $Z_{rh}=245\text{mm}$: sampled $Y=-30\text{mm}$.

The vertical profile in Figure 15.3.6 for the EW unclad case near the plume centreline does not show an elevated peak, and the SGP and IGP fitting formulations have given rise to curves which are very similar.

15.3.2 Plume Concentration Maximum (PCM) variation with downstream distance: Supplementary Results

15.3.2.1 Cube: 'A' position: PCM variation with downstream distance

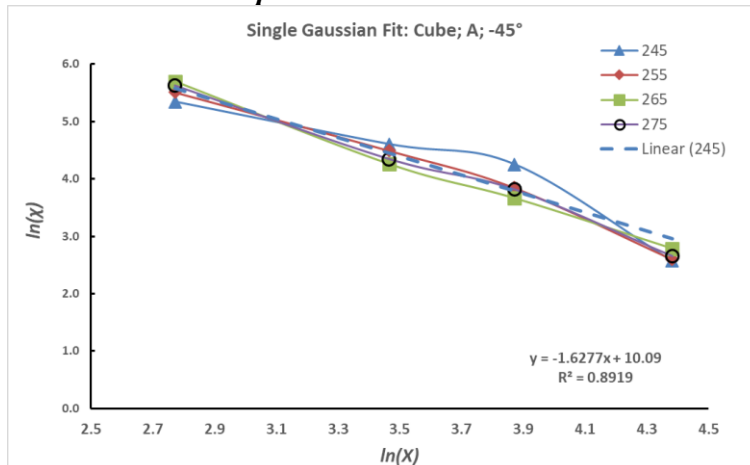
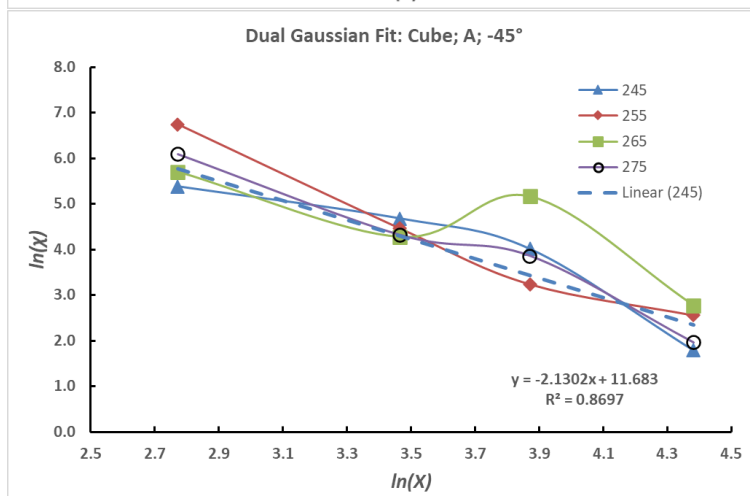


Figure 15.3.7(a, top/b, below):
 $\ln(x)$ variation with $\ln(X)$ for different release heights Z_{rh} for the PCM with downstream distance; vertex position 'A'; incidence -45° to cube face:

(a) SGP

(b) DGP

Regression trend line is presented for $Z_{rh}=245\text{mm}$, lowest release height case



From Figure 15.3.7 the cube at 'A' release position, with incidence -45° is shown. The SGP (a) shows a robust linear characteristic with high correlation coefficient, but the DGP (b) shows a generally poorer correlation with the linear fit model. It should be noted that the gradient of the regression line is lowest for this configuration for the SGP case: this shows that the extent of variation with distance for SGP fitted concentrations is reduced with increasing angles of approach flow.

15.3.2.2 EW Unclad releases: PCM variation with downstream distance

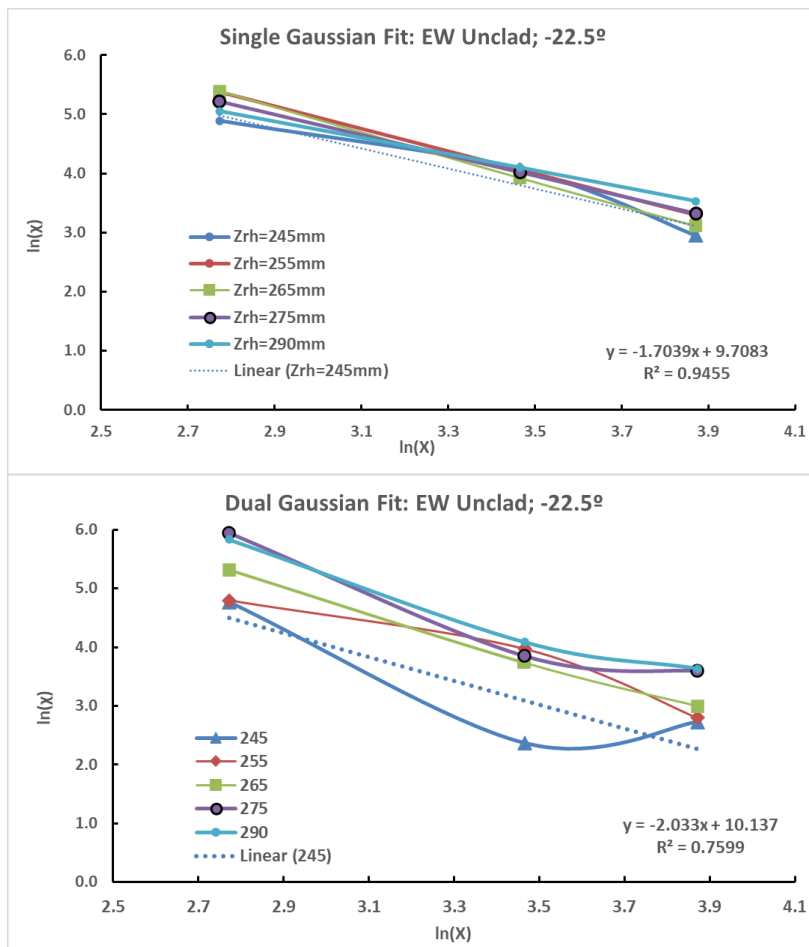


Figure 15.3.8(a, top/b, below): $\ln(\chi)$ variation with $\ln(X)$ for different release heights Z_{rh} for the PCM with downstream distance; vertex position 'A'; incidence -22.5° to EW Unclad face:

(a) SGP

(b) DGP

Regression trend line is presented for $Z_{rh}=245\text{mm}$, lowest release height case.

Figure 15.3.8 for the EW unclad building for (a) SGP and (b) DGP show an enhanced gradient compared to the EW clad cases for the same -22.5° angle of approach flow when comparing to Figure 6.26(a/b).

15.3.2.3 Cube centreline 'B' position: PCM variation with downstream distance

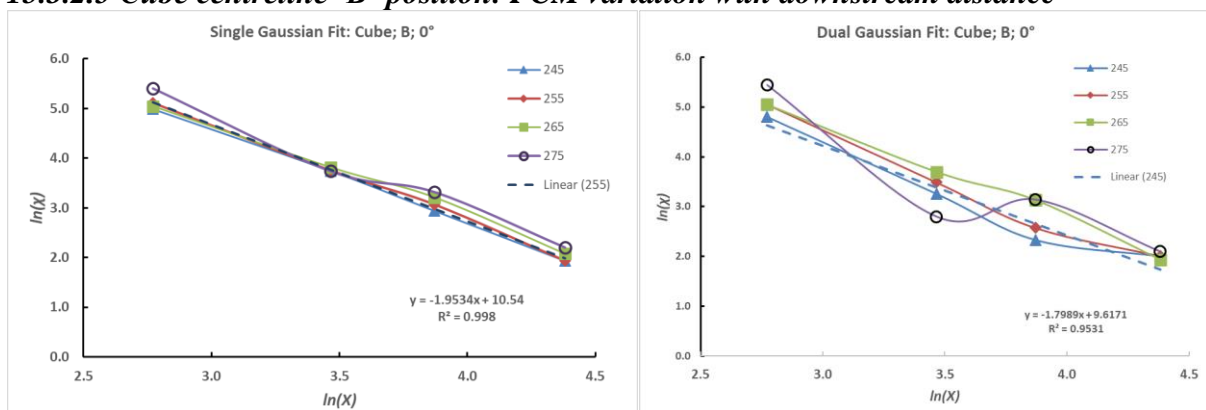


Figure 15.3.9(a/b): $\ln(\chi)$ variation with $\ln(X)$ for different release heights Z_{rh} for the PCM with downstream distance; centreline position 'B'; incidence 0° to cube face; (a) SGP; (b) DGP. Regression trend line is presented for $Z_{rh}=245\text{mm}$, lowest release height case

Figure 15.3.9 for the cube centreline 'B' release position for (a) SGP and (b) DGP show similar gradients compared to the cube 'A' release position cases for the 0° angle of approach flow.

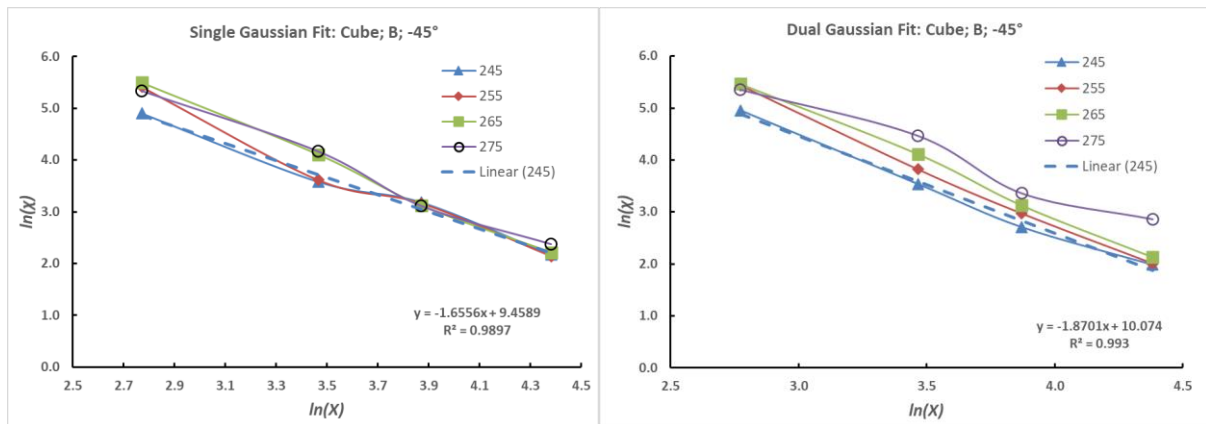


Figure 15.3.10(a/b): $\ln(\chi)$ vs $\ln(X)$ with release heights Z_{rh} for the PCM with downstream distance; position 'B'; -45° to cube face; (a) SGP; (b) DGP. Regression line presented for $Z_{rh}=245\text{mm}$, lowest release height case. Note: The data for release position 'B' shows similar regression line gradients compared to the 'A' case for angle -45° .

15.3.3 Concentration Weighted Dispersion Parameters: variation with distance from the source - SGP and DGP/IGP formulations with release height

15.3.3.1 EW Unclad: concentration weighted dispersion parameters

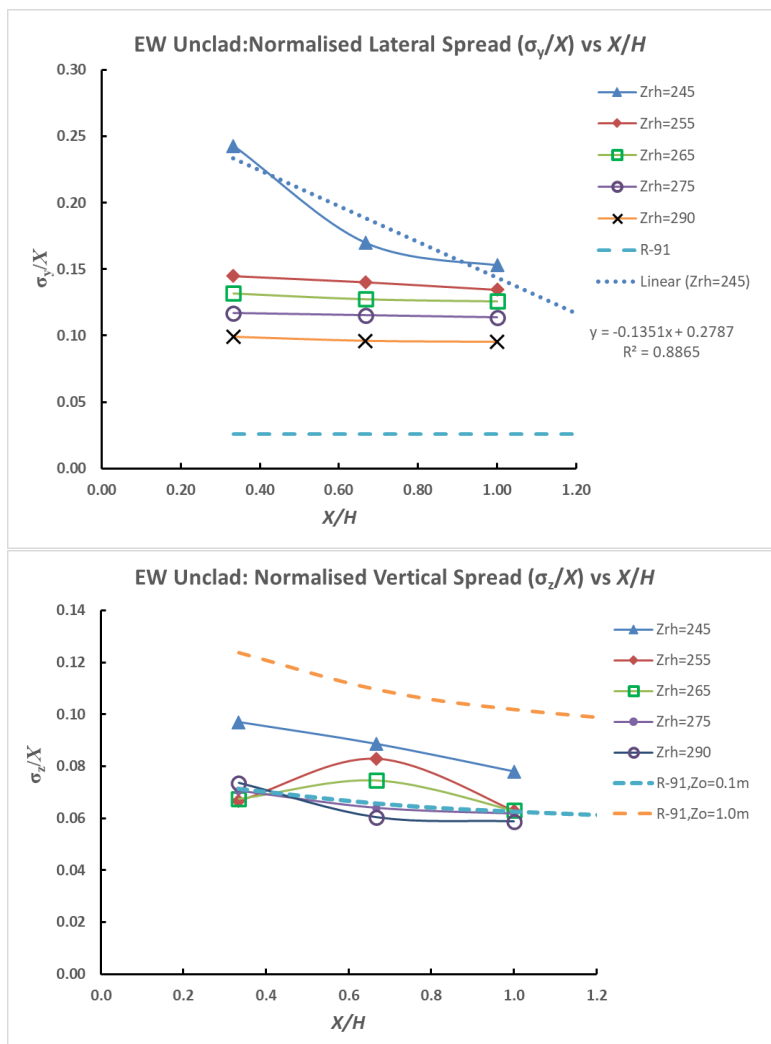


Figure 15.3.11(a, top)/(b, below): EW unclad release; -22.5° ; $\sigma_{y,cw}/X$ and $\sigma_{z,cw}/X$ variations with normalised distance from release X/H for the SGP model. Error bars are given as the sampled standard deviation of the value over range of downstream distance

The EW unclad building in Figure 15.3.11 shows a clear monotonic relationship between the release height and the lateral spread with the SGP method: this is broadly similar to the EW clad case. Vertical dispersion parameters are generally similar to the EW clad case, but with evidence of being somewhat smaller in magnitude.

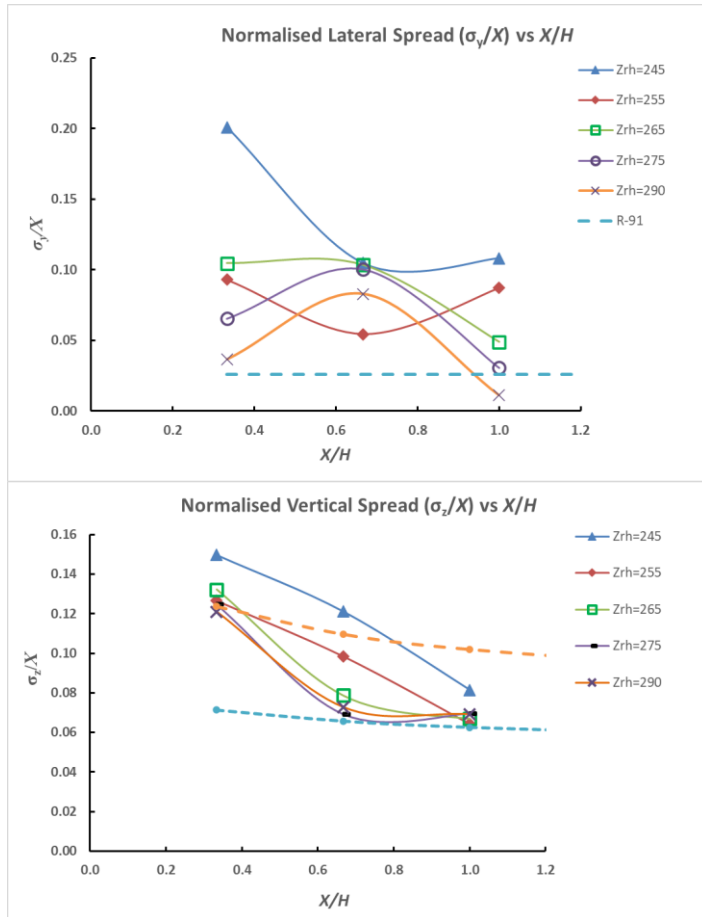


Figure 15.3.12(a, top)/(b, bottom): EW unclad release, -22.5°; $\sigma_{y,cw}/X$ and $\sigma_{z,cw}/X$ variations with normalised distance from release X/H for the DGP/IGP models.

Figure 15.3.12 shows the reduced plume spread evident from the plume DGP/IGP de-convolution process: the monotonic relationship is less pronounced with release height for the lateral spread.

Conversely, the DGP/IGP method shows enhanced values of vertical spread for this angle of approach flow.

15.3.3.2 Cube: 'B' release position - concentration weighted dispersion parameters

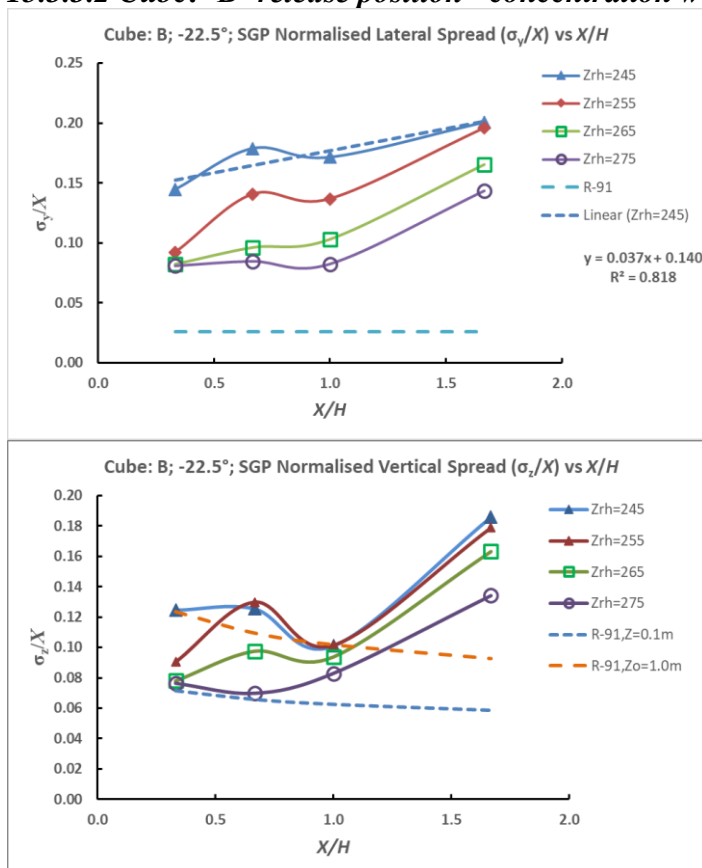


Figure 15.3.13(a, top)/(b, bottom): cube release; position 'B'; -22.5°; $\sigma_{y,cw}/X$ and $\sigma_{z,cw}/X$ variations with normalised distance from release X/H for the SGP model.

For the 'B' release position from Figure 15.3.13 the degree of lateral plume spread with the SGP model is significantly greater than the corresponding 'A' case at the two lowest release heights, but similar for the 265 and 275mm heights. The vertical spread is also significantly larger for all release heights.

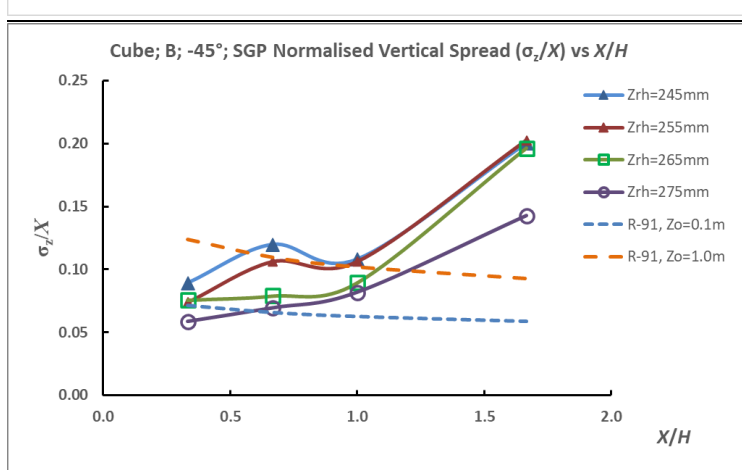
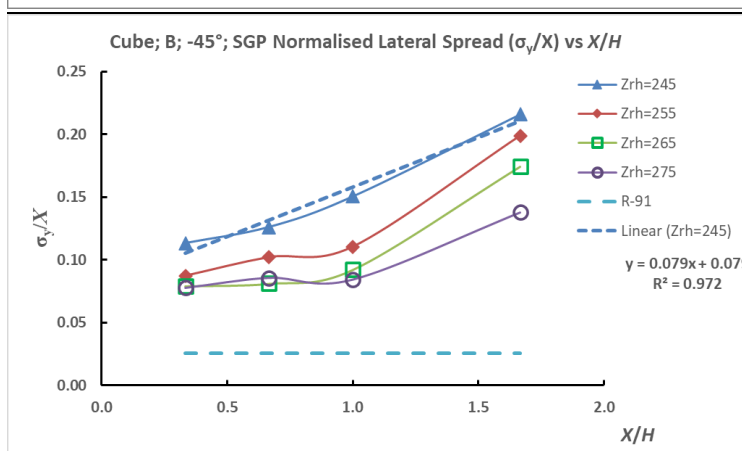
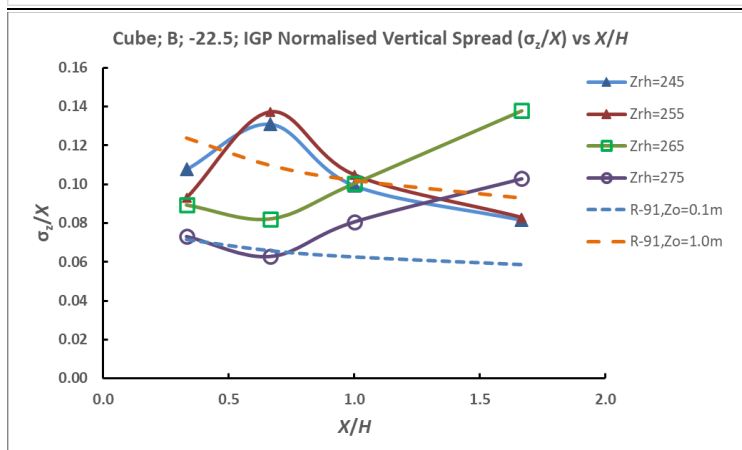
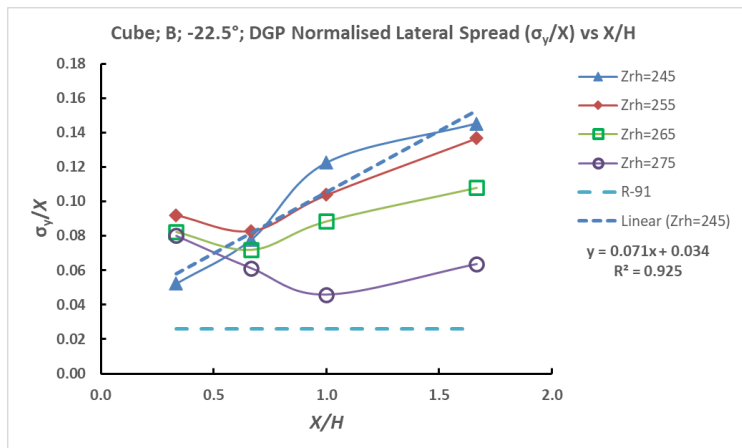


Figure 15.3.14(a, top)/(b, below): cube release; position 'B'; -22.5°; σ_y/X and σ_z/X variations with normalised distance from release X/H for the DGP/IGP models.

For the 'B' release position from Figure 15.3.14 the degree of lateral plume spread with the SGP model is broadly similar to the corresponding 'A' case. The vertical spread of the 'B' release case is significantly greater than the 'A' case.

Figure 15.3.15(a, top)/(b, lower): cube release; position 'B'; -45°; $\sigma_{y,cw}/X$ and $\sigma_{z,cw}/X$ variations with normalised distance from release X/H for the SGP model.

From the SGP model in Figure 15.3.15 the 'B' case shows enhanced plume spread with respect to the 'A' case for lateral and vertical spread especially for the lowest two release heights tested.

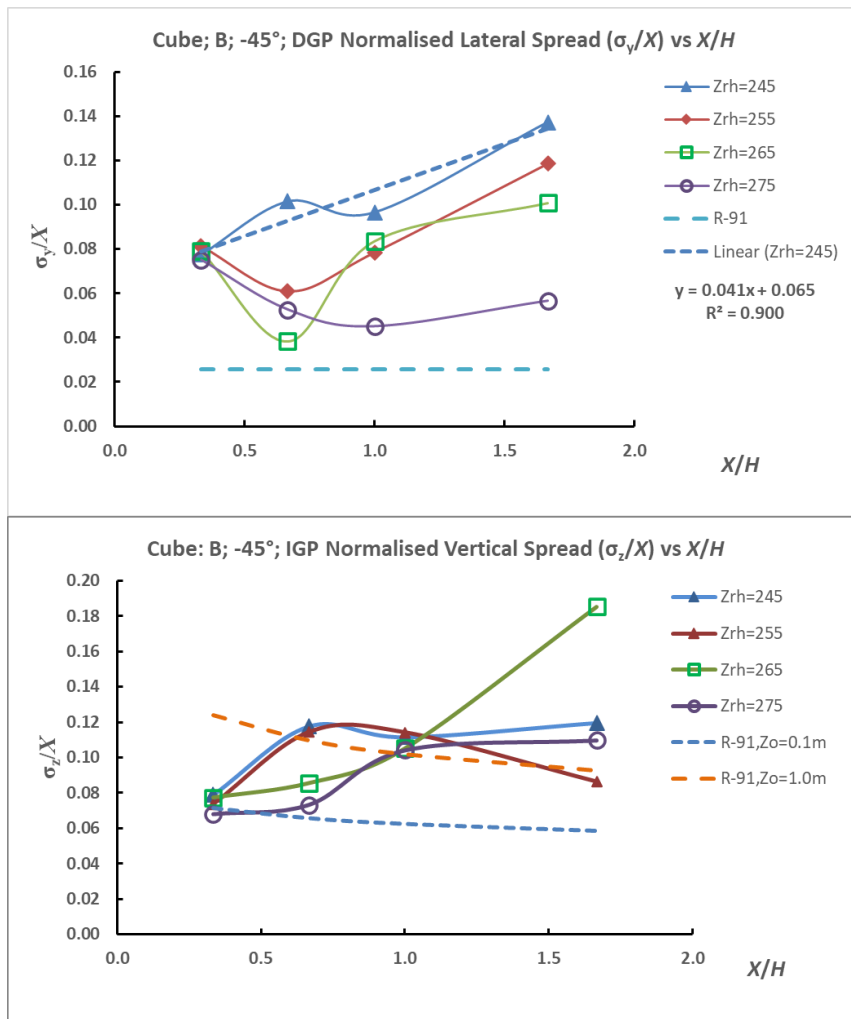


Figure 15.3.16(a, top)/(b, bottom): cube release; position 'B'; -45°; σ_y/X and σ_z/X variations with normalised distance from release X/H for the DGP/IGP models.

From Figure 15.3.16 'B' release position the lateral spread values are broadly similar to the 'A' release case. For the vertical spread parameters the values are significantly larger than the 'A' release case.

15.3.4 Concentration Weighted Dispersion Parameters: Mean values over distance from the source of SGP and DGP/IGP formulations: Supplementary Results

15.3.4.1 Cube: 'A': Mean dispersion parameters over distance from source

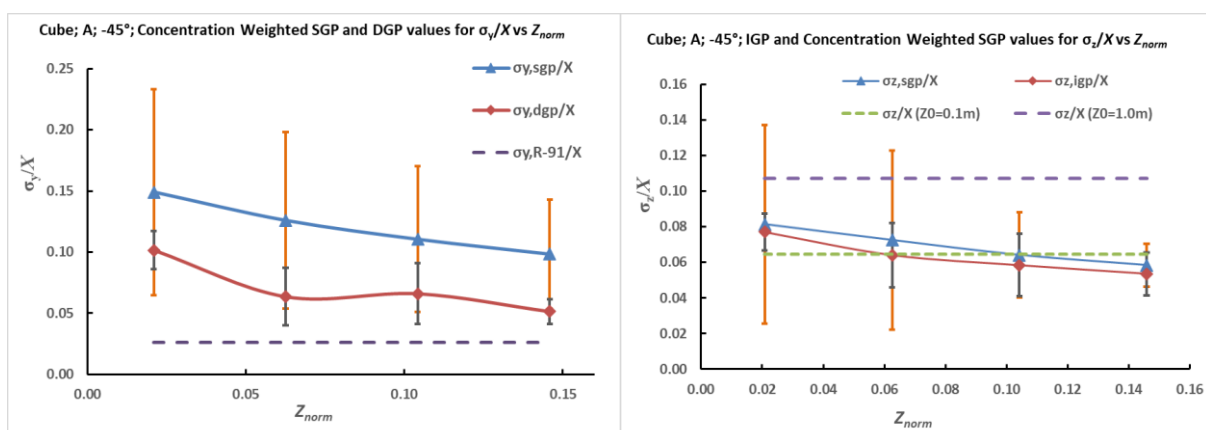


Figure 15.3.17(a, left)/(b, right): cube release, position A, -45°; σ_y/X and σ_z/X variations with normalised passive plume release height $Z_{norm}=(Z_{rh}-H)/H$ for both the SGP and DGP/IGP models. Error bars are given as the sampled standard deviation of the value over range of downstream distances

15.3.4.2 EW Unclad: Mean dispersion parameters over distance from the source

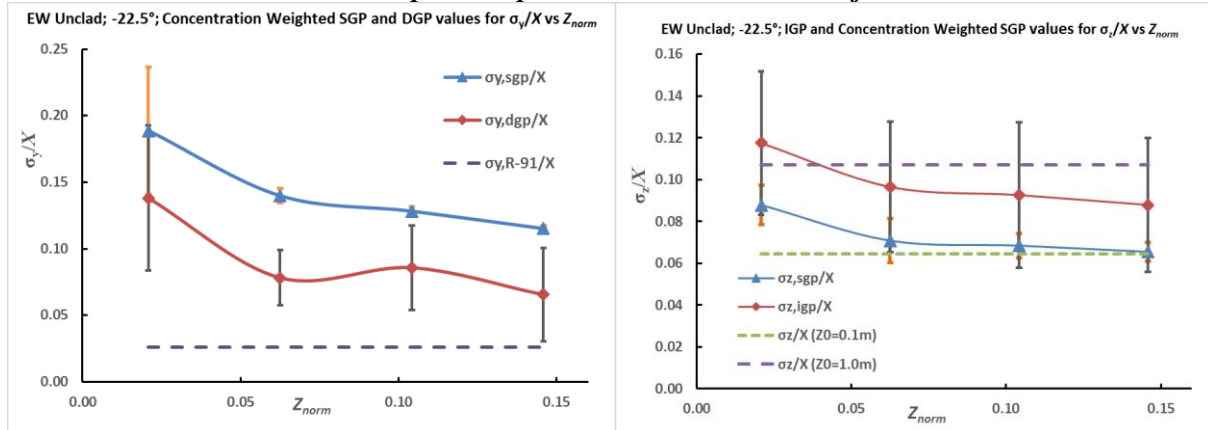


Figure 15.3.18(a,left)/(b,right): EW Unclad release, position NW stair tower, -22.5°; σ_y/X and σ_z/X variations with normalised passive plume release height $Z_{norm} = (Z_{rh} - H)/H$ for both the SGP and DGP/IGP models. Error bars are given as the sampled standard deviation of the value over range of downstream distances

15.3.4.3 Cube: 'B': Mean dispersion parameters over distance from the source

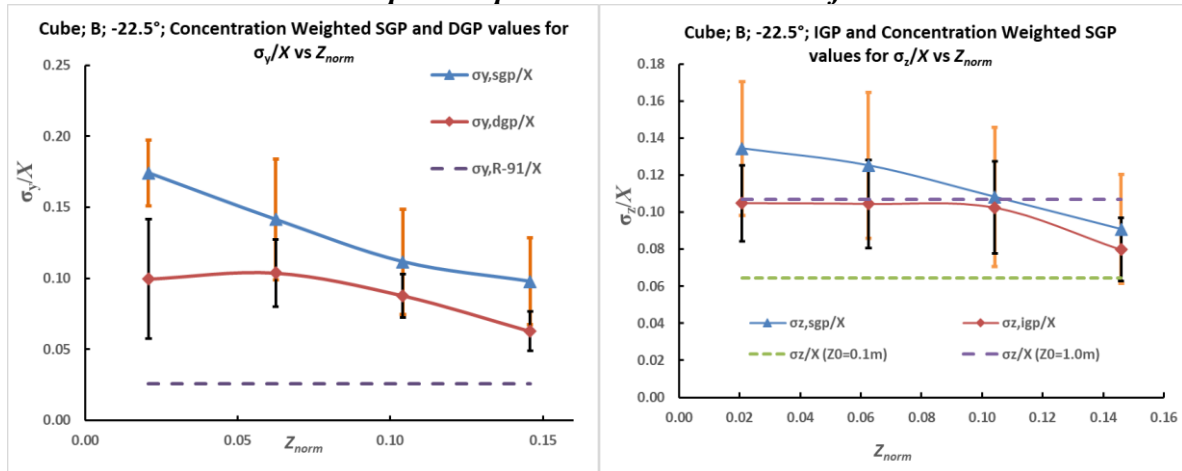


Figure 15.3.19(a,left)/(b,right): cube release, position B, -22.5°; σ_y/X and σ_z/X variations with normalised passive plume release height $Z_{norm} = (Z_{rh} - H)/H$ for both the SGP and DGP/IGP models. Error bars are given as the sampled standard deviation of the value over range of downstream distances

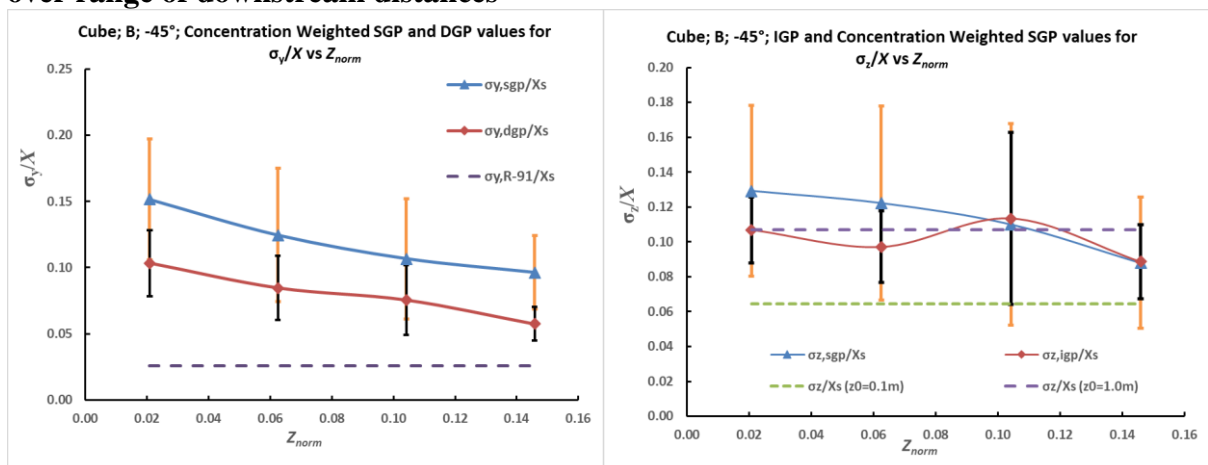


Figure 15.3.20(a,left)/(b,right): cube release, position B, -45°; $\sigma_{y,cw}/X$ and $\sigma_{z,cw}/X$ variations with normalised passive plume release height $(Z_{rh} - H)/H$ for both the SGP and DGP/IGP

models. Error bars are given as the sampled standard deviation of the value over range of downstream distance

15.3.5 Concentration Weighted Dispersion Parameters: Summary data over 'B' release positions

15.3.5.1 Concentration Weighted Dispersion Parameters: Summary data over 'B' release positions for SGP formulation with normalised release height

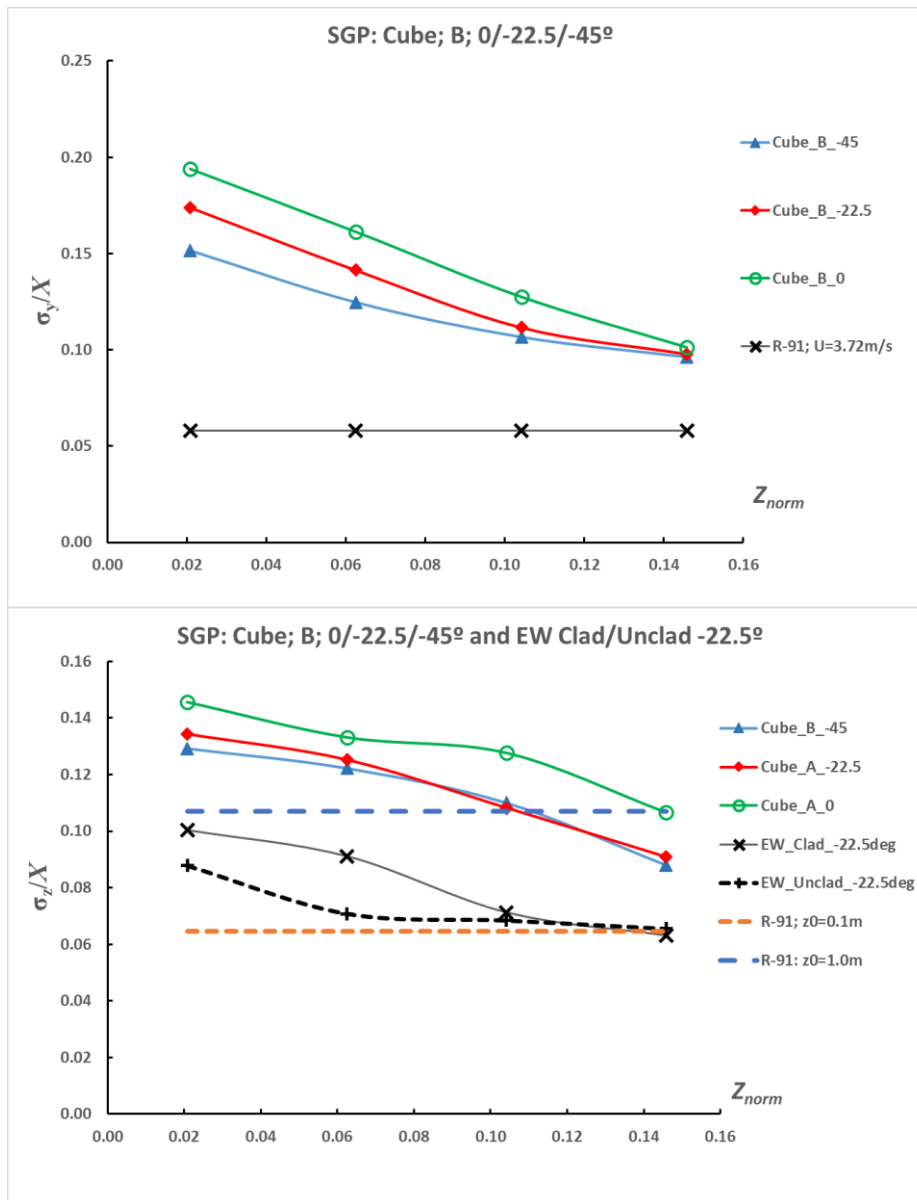


Figure 15.3.21(a, top)/(b, lower): cube release; position 'B'; 0/-22.5/45°

(a) σ_y/X

(b) σ_z/X

Variations with normalised passive plume release height $Z_{norm}=(Z_{rh}-H)/H$ for the SGP model.

EW clad/unclad values are also presented for comparison in (b)

Data represents mean values with distance X over the roof zone and immediate vicinity of the roof

15.3.5.2 Concentration Weighted Dispersion Parameters: Summary data over ‘B’ release position cases for DGP/IGP formulations with normalised release height

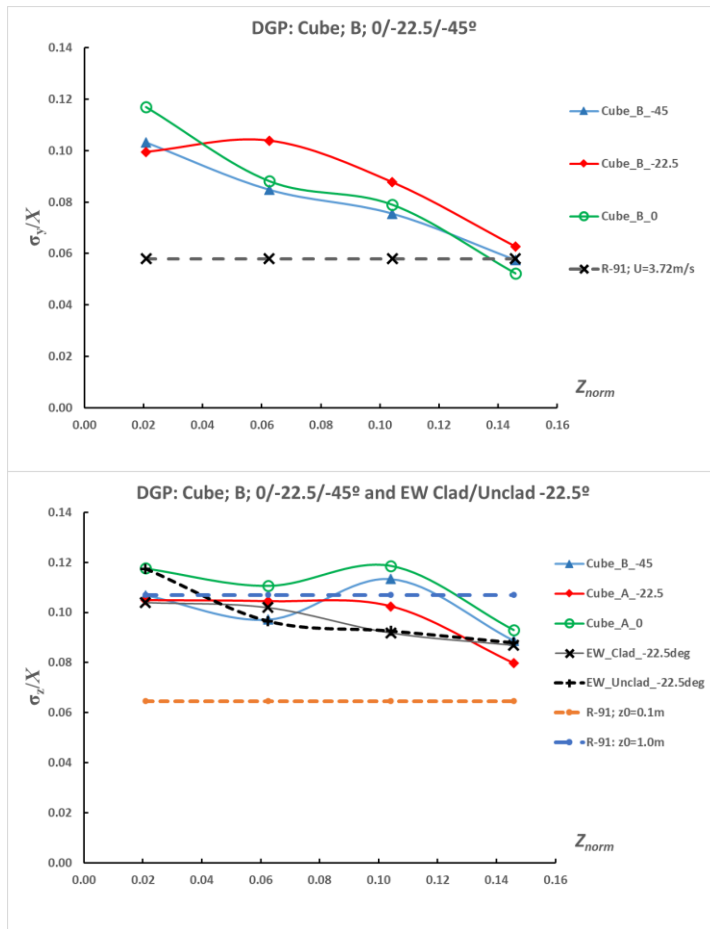


Figure 15.3.22(a, top)/(b, below):
cube release; position ‘B’; 0/-22.5/-45° and -22.5° EW clad and unclad cases:

(a) σ_y/X

(b) σ_z/X

Variations with normalised passive plume release height $Z_{norm}=(Z_{rh}-H)/H$ for the DGP model.

Data represents mean values with distance X over the roof zone and immediate vicinity of the roof. EW results are also presented in (b) to enable direct comparison

APPENDIX 15.4: Intermittent short release further results

15.4.1 Cube case: 0° incidence, stack position ‘A’ near vertex (section 7.3.1 refers)

Z_{RH} = 255 mm; fixed active vertical release; ΔT = 0.10, 0.25, 0.5, 1.0 second; 144 puffs

Sample co-ordinates for Figures 7.2-7.5.

Figure 7.2: X= 80mm, Y= -5mm, Z=305mm

Figure 7.3: X= 160mm, Y= -10mm, Z=315mm

Figure 7.4: X= 240mm, Y= -5mm, Z=305mm

Figure 7.5: X= 400mm, Y= 0mm, Z=315mm

15.4.2 Cube case: -22.5° incidence, stack position ‘A’ near vertex (section 7.3.2 refers)

Z_{RH} = 255 mm; fixed active vertical release; ΔT = 0.10, 0.25, 0.5, 1.0 second: 144 puffs

Sample co-ordinates for Figure 7.6: X= 160mm, Y= -10mm, Z=305mm

15.4.3 Cube case: -45° incidence, stack position ‘A’ near vertex (section 7.3.3 refers)

Z_{RH} = 255 mm; fixed active vertical release; ΔT = 0.10, 0.25, 0.5, 1.0 second: 144 puffs

Sample co-ordinates for Figure 7.7: X= 160mm, Y= -10mm, Z=305mm

15.4.4 EW Clad case: -22.5° incidence, active vertical stack near leading edge vertex (section 7.3.4 refers)

Z_{RH} = 255 mm; fixed active vertical release; ΔT = 0.025, 0.05, 0.10, 0.25, 0.5, 1.0, 2, 4s

X= 160mm, Y= -7mm, Z=285mm

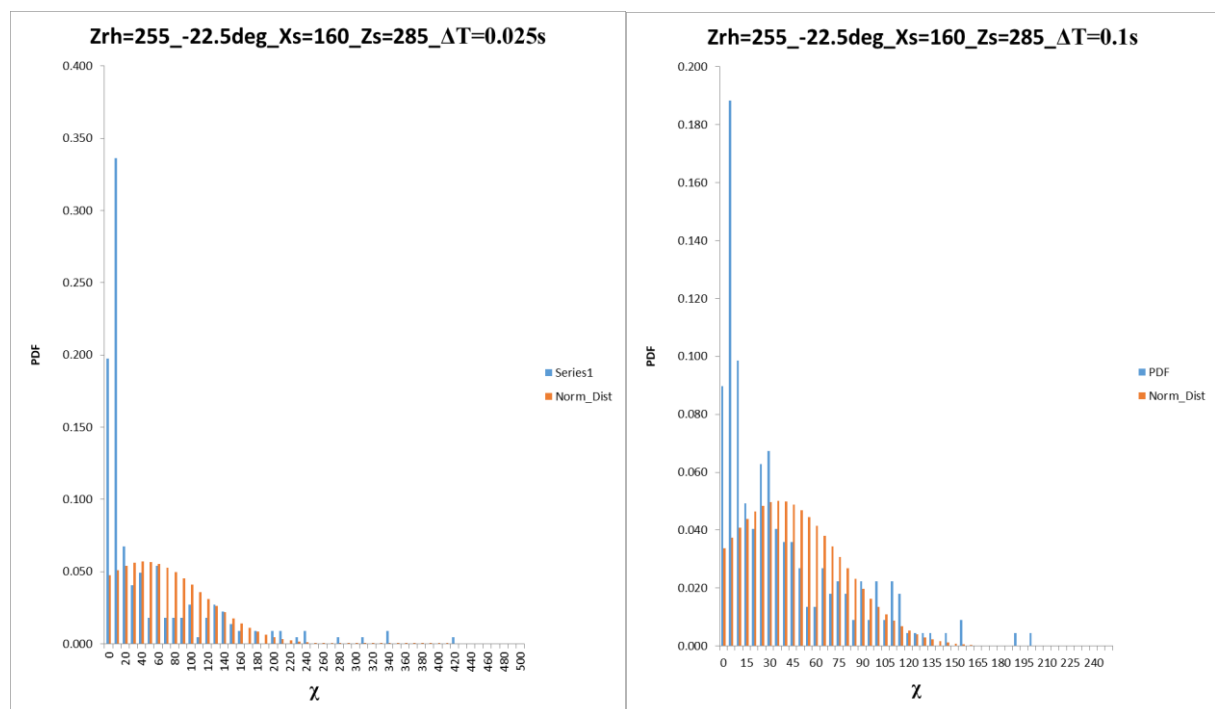
Puffs per ensemble = 178(0.025-0.10s); 160(0.25s); 138(0.5s); 107(1.0s); 74(2.0s); 46(4.0s)

15.4.5 EW Unclad case: -22.5° incidence, active vertical stack near leading edge vertex (section 7.3.5 refers)

Z_{RH} = 255 mm; fixed active vertical release; ΔT = 0.025, 0.05, 0.10, 0.25, 0.5, 1.0, 2, 4 seconds

X= 160mm, Y= -7mm, Z=285mm

Puffs per ensemble = 223(0.025-0.10s); 200(0.25s); 172(0.5s); 134(1.0s); 93(2.0s); 58(4.0s)



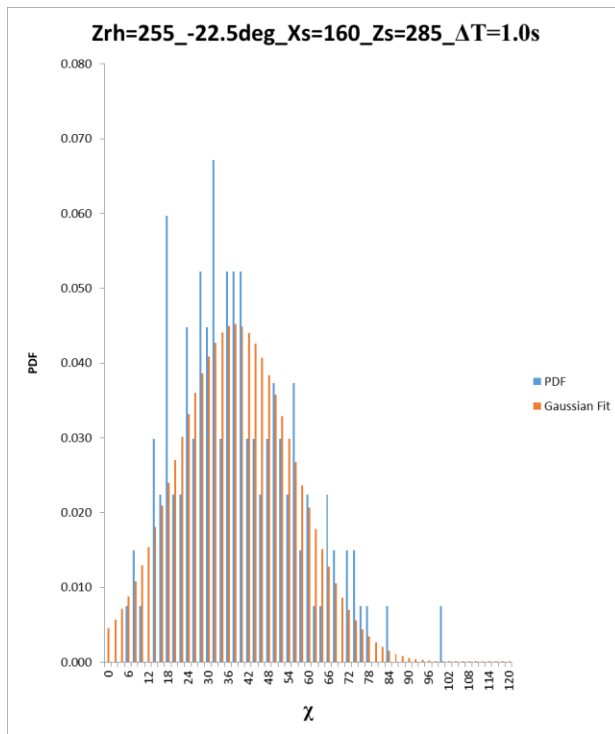


Figure 15.4.1(a/b/c): PDF of dimensionless concentration for EW Unclad; -22.5° incidence, position near vertex; $X=160\text{mm}$; active vertical release; $Z_{RH}=255\text{mm}$; data sampled at plume concentration maximum (centreline); normal Gaussian fitting best on mean and sampled standard deviation also shown. (a) 0.025s release (left); (b) 0.1s (right); (c) 1.0s (below)

15.4.6 EW Clad case: -22.5° incidence, passive stack near leading edge vertex (section 7.3.6 refers)

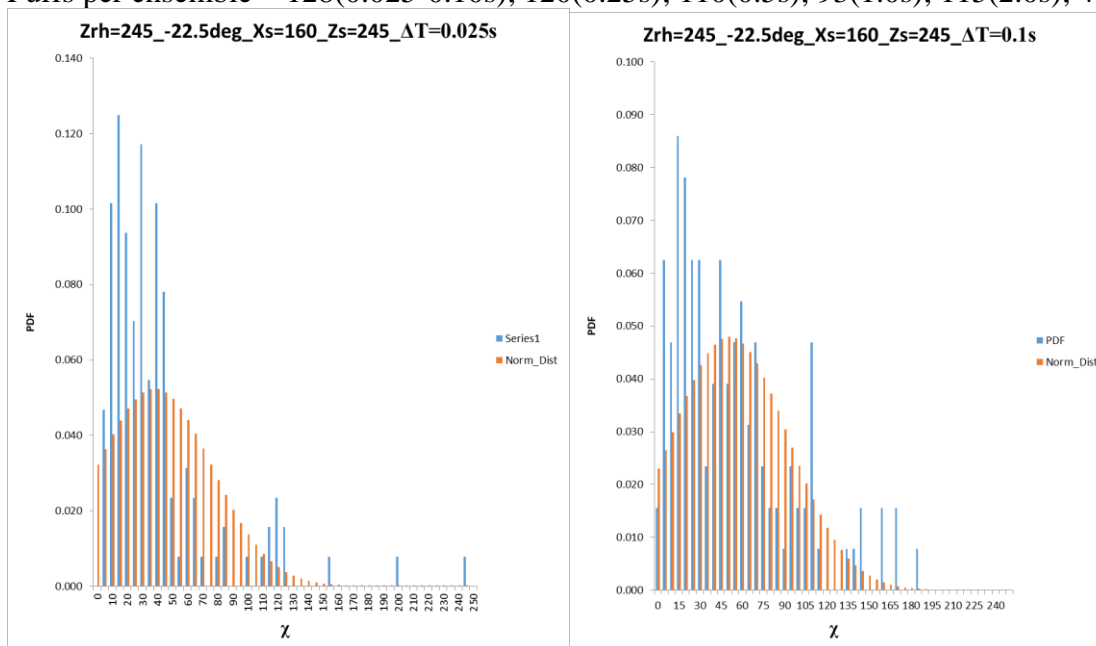
$Z_{RH} = 245\text{ mm}$; passive horizontal release; $\Delta T = 0.025, 0.05, 0.10, 0.25, 0.5, 1.0, 2, 4\text{ seconds}$
 $X = 160\text{mm}$, $Y = -7\text{mm}$, $Z = 245\text{mm}$

Per ensemble = 103(0.025s); 77(0.05-0.10s); 48(0.25s); 44(0.5s); 37(1.0s); 15(2.0s); 10(4.0s)

15.4.7 EW Unclad case: -22.5° incidence, passive stack near leading edge vertex (section 7.3.7 refers)

$Z_{RH} = 245\text{ mm}$; passive horizontal release; $\Delta T = 0.025, 0.05, 0.10, 0.25, 0.5, 1.0, 2, 4\text{ seconds}$
 $X = 160\text{mm}$, $Y = -7\text{mm}$, $Z = 245\text{mm}$

Puffs per ensemble = 128(0.025-0.10s); 120(0.25s); 110(0.5s); 93(1.0s); 115(2.0s); 48(4.0s)



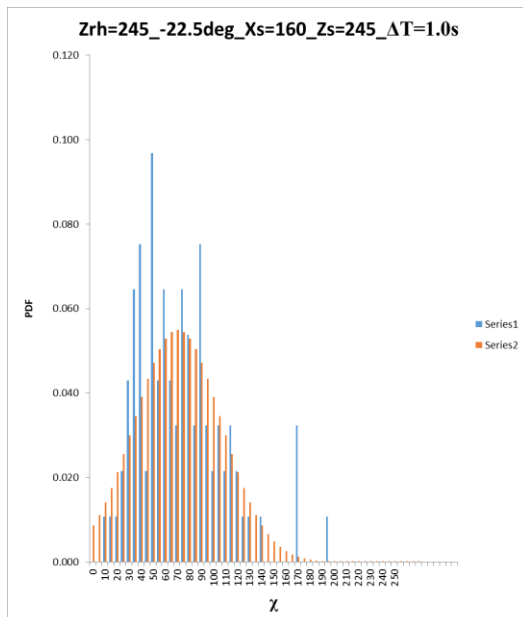


Figure 15.4.2(a/b/c): PDF of dimensionless concentration for EW Unclad; -22.5° incidence, position near vertex; $X=160\text{mm}$; passive release; $Z_{RH}=245\text{mm}$; data sampled at plume concentration maximum (centreline); normal Gaussian fitting best on mean and sampled standard deviation also shown

(a) 0.025s release (top left)

(b) 0.1s (top right)

(c) 1.0s (below)

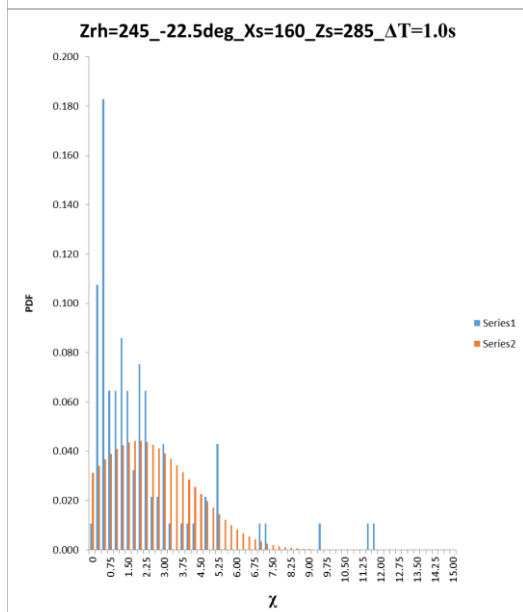
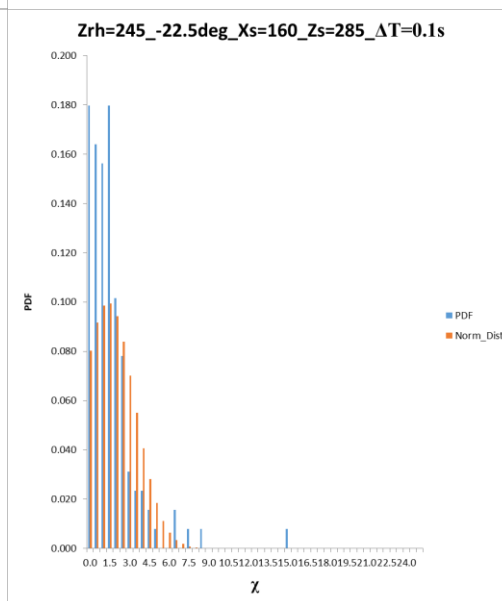
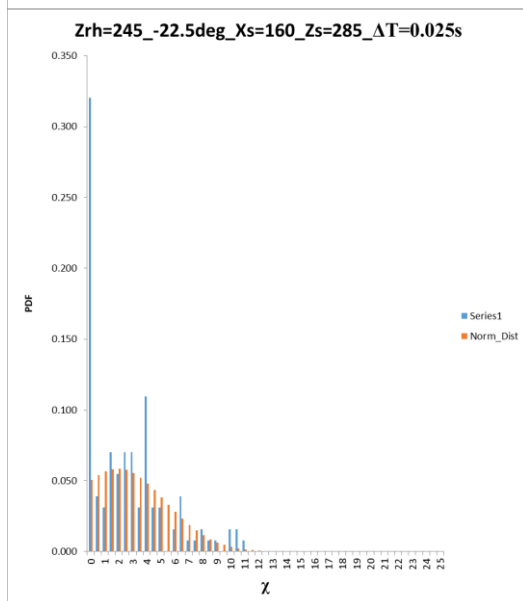


Figure 15.4.3(a/b/c): PDF of dimensionless concentration for EW Unclad; -22.5° incidence, position near vertex; $X=160\text{mm}$; passive release; $Z_{RH}=245\text{mm}$; data sampled at an off-axis position (+40mm vertical offset to plume concentration maximum); normal Gaussian fitting best on mean and sampled standard deviation also shown:

(a) 0.025s release (top left)

(b) 0.1s (top right)

(c) 1.0s (below)

15.4.8 Cube: statistical parameters for various angles of incidence, AV releases and at different source distances

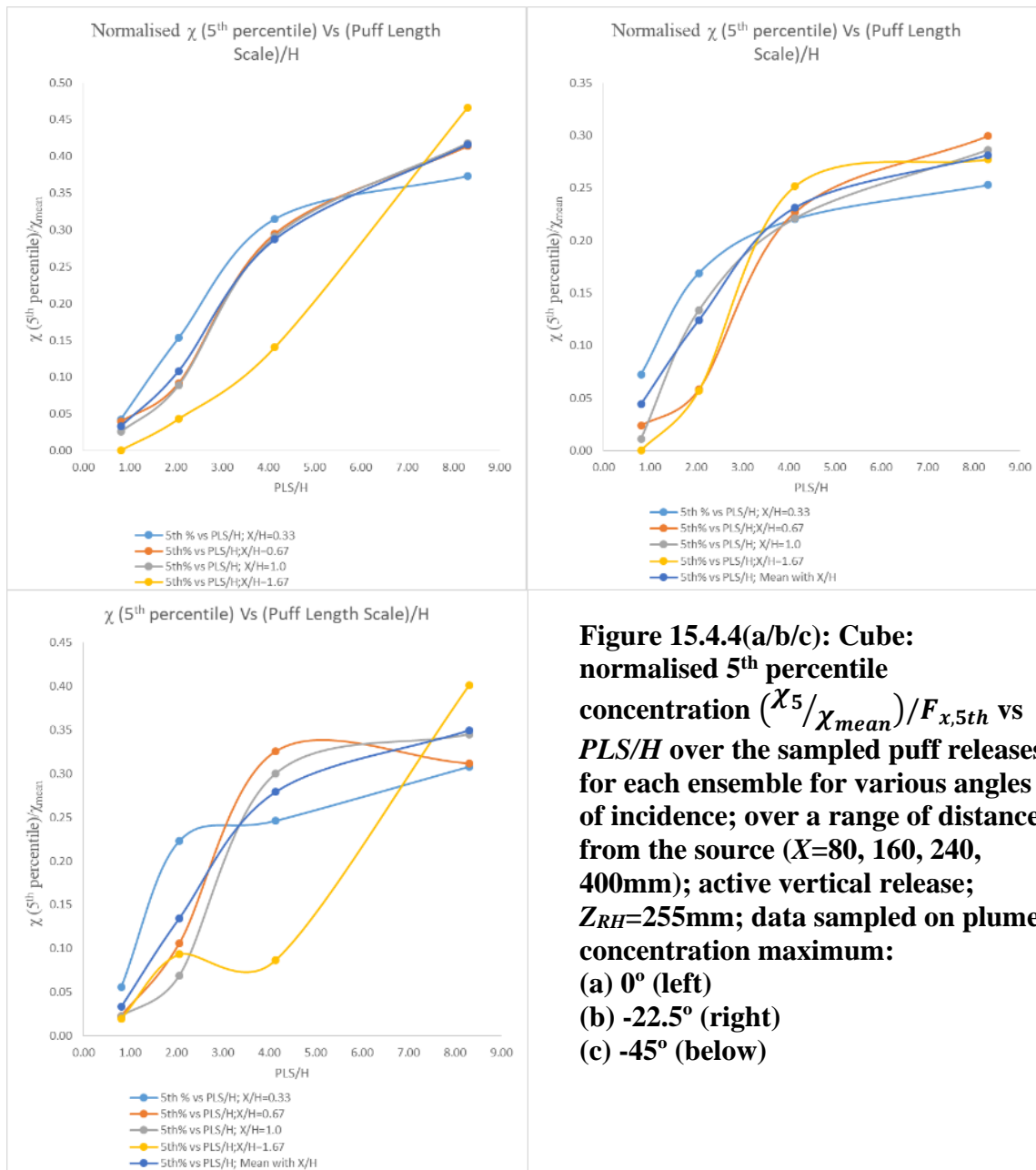


Figure 15.4.4(a/b/c): Cube:
normalised 5th percentile
concentration ($\chi^5/\chi_{\text{mean}}$)/ $F_{x,5th}$ vs
 PLS/H over the sampled puff releases
for each ensemble for various angles
of incidence; over a range of distances
from the source ($X=80, 160, 240,$
 400mm); active vertical release;
 $Z_{RH}=255\text{mm}$; data sampled on plume
concentration maximum:
(a) 0° (left)
(b) -22.5° (right)
(c) -45° (below)

In Figure 15.4.4 scale normalisation (by dividing each set of points on a curve by a scaling form-factor $F_{x,5th}$) which scales to the mean characteristic curve (the average curve over the available data) has been plotted. Apart from the outlier at $X/H=1.67$, which is thought to be related to low signal levels at this distance and insufficient puff measurements available within the limitations on experiment run time to better determine this curve, the normalised curves follow the mean curve and show a characteristic form which may be taken as a general finding, invariant to the angle of approach flow.

15.4.9 EW clad/unclad cases: CV of χ at different crosswind positions (Y/H)

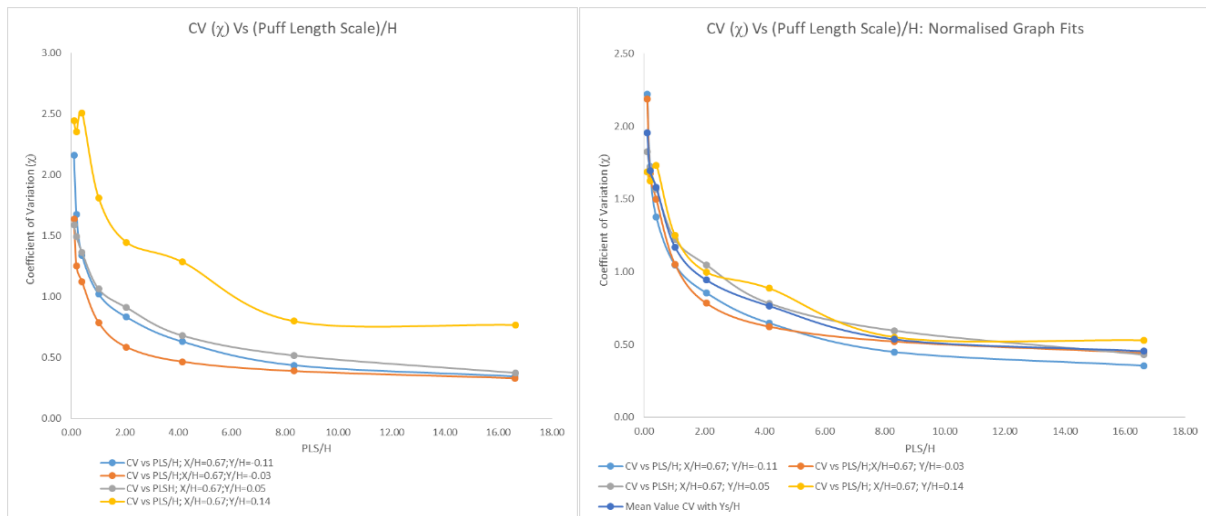


Figure 15.4.5(a/b): EW Unclad: coefficient of variation CV vs PLS/H over the sampled puff releases for each ensemble for various normalised crosswind positions (Y/H); angle of incidence -22.5° ; $X=160\text{mm}$; active vertical release $Z_{RH}=255\text{mm}$; (a) measured values with Y/H (left); (b) normalised values with F_y form factor fitted to the mean (right)

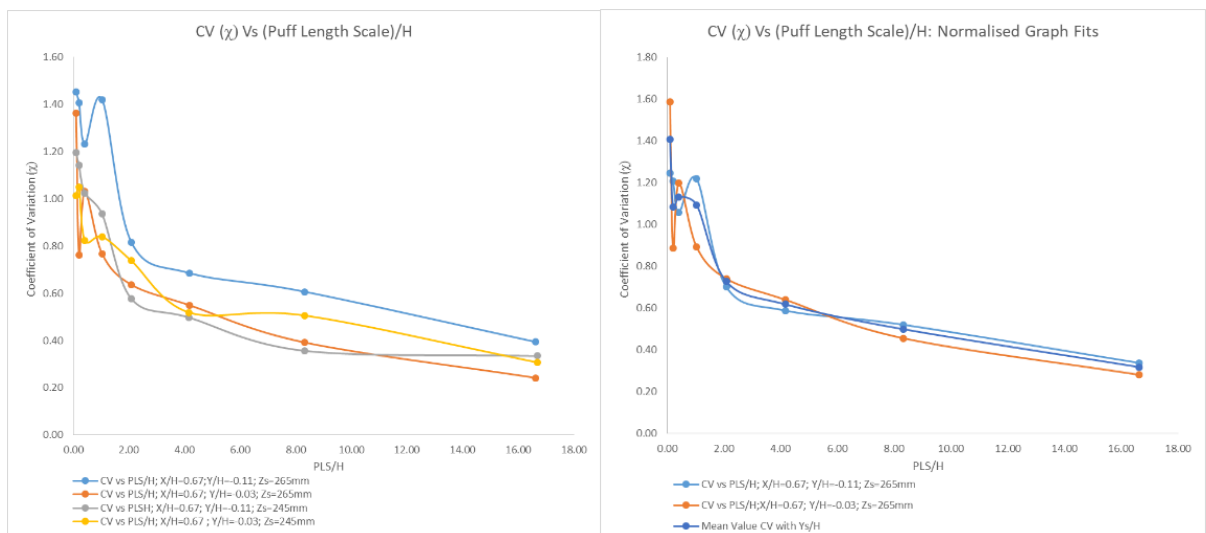


Figure 15.4.6(a/b): EW Unclad: coefficient of variation CV vs PLS/H over the sampled puff releases for each ensemble for various normalised crosswind positions (Y/H); angle of incidence -22.5° ; $X=160\text{mm}$; passive releases $Z_{RH}=245\text{mm}$; (a) measured values with Y/H (left) and two sampled heights $Z_s=245/265\text{mm}$; (b) normalised values for sampled height $Z=265\text{mm}$ with F_y form factor fitted to the mean (right)

In Figure 15.4.6(a) for the EW unclad case the CV is presented versus PLS/H for two passive release heights, for comparison purposes to previous figures. It can be seen from Figure 15.4.6(b) that upon normalisation the curves collapse into a common characteristic curve when normalised to the mean.

15.4.10 EW clad/unclad cases: CV of χ results at different vertical positions $(Z_s-Z_{RH})/H$

Passive release data are shown for the EW clad case in Figure 15.4.7 for a release very close to the building roof at $Z_{RH}=245\text{mm}$. The low values of CV can be seen for the heights sampled close to the roof zone, and greater values of CV can be seen at the greatest sampled height away from the plume concentration maximum height. The magnitude of the CV value curve can be seen as broadly similar to that seen in Figure 7.17(a/b) for the active vertical release. Figure 15.4.8 for the EW unclad passive release shows a similar pattern.

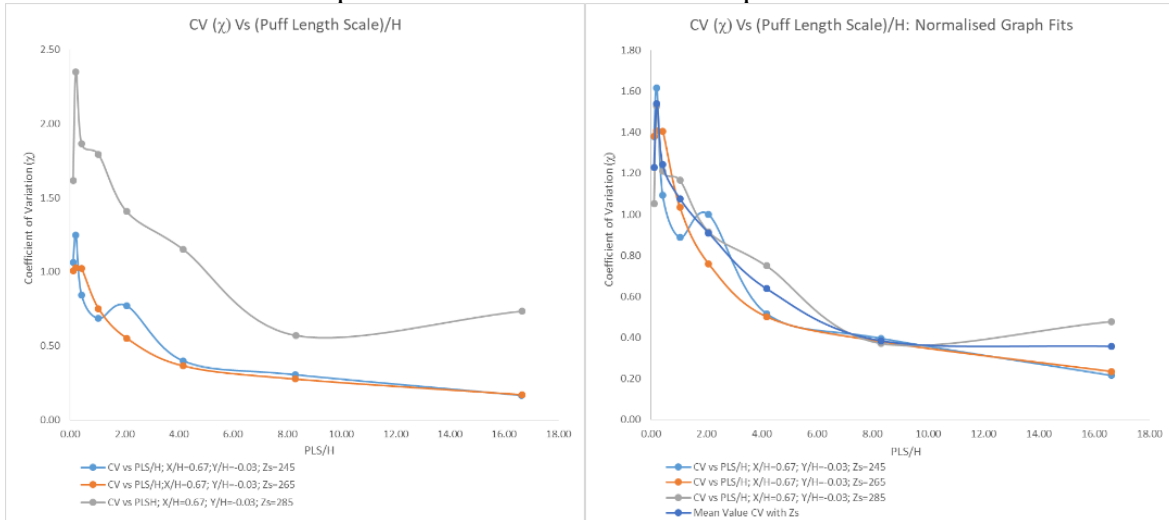


Figure 15.4.7(a/b): EW Clad: coefficient of variation CV vs PLS/H over the sampled puff releases for each ensemble for various normalised vertical measurement positions $(Z_s-Z_{RH})/H$; angle of incidence -22.5° ; $X=160\text{mm}$; passive releases at $Z_{RH}=245\text{mm}$; (a) measured values with $(Z_s-Z_{RH})/H$ (left); (b) normalised values with F_z form factor fitted to the mean (right)

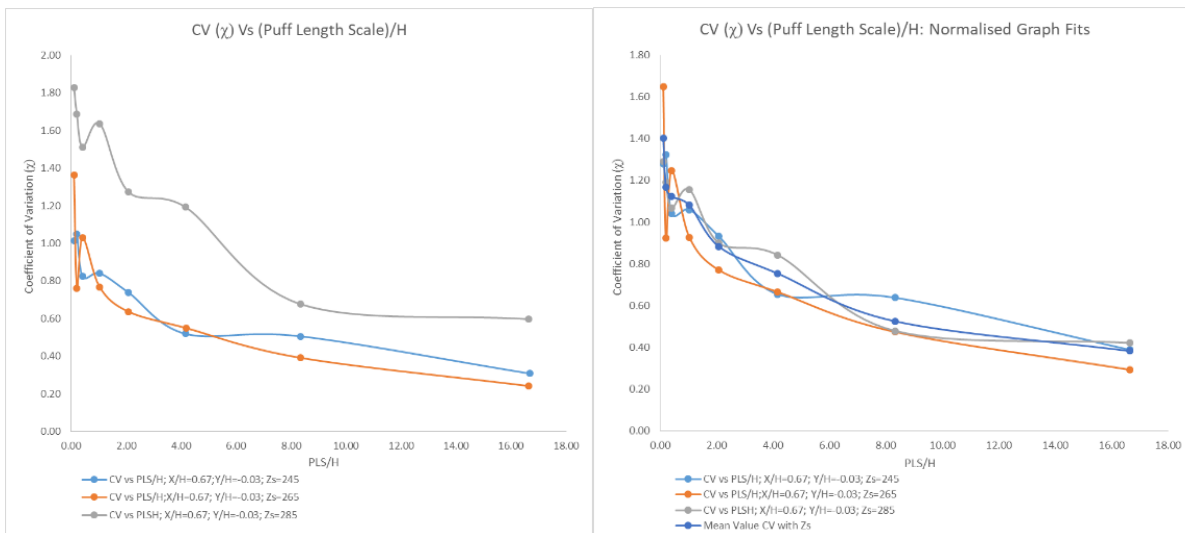


Figure 15.4.8(a/b): EW Unclad: coefficient of variation CV vs PLS/H over the sampled puff releases for each ensemble for various normalised vertical measurement positions $(Z_s-Z_{RH})/H$; angle of incidence -22.5° ; $X=160\text{mm}$; passive releases at $Z_{RH}=245\text{mm}$; (a) measured values with $(Z_s-Z_{RH})/H$ (left); (b) normalised values with F_z form factor fitted to the mean (right)

15.4.11 Overall Results Summary: Cube and EW clad/unclad cases: statistical parameters

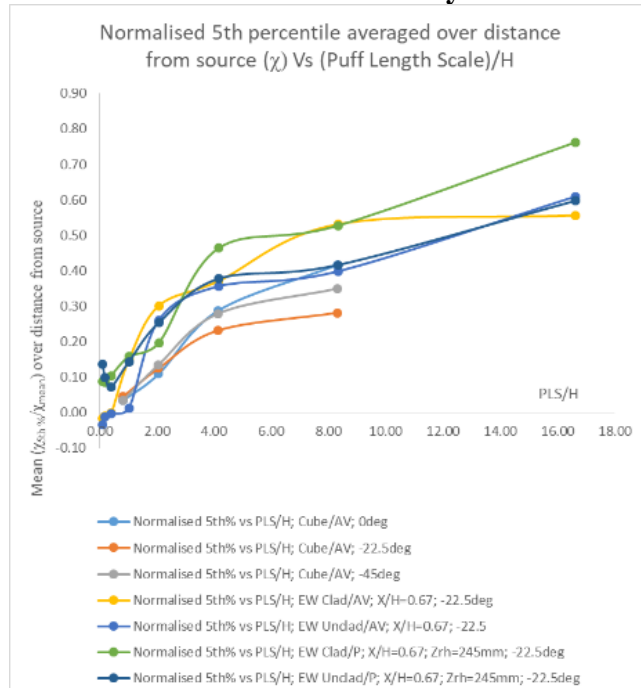
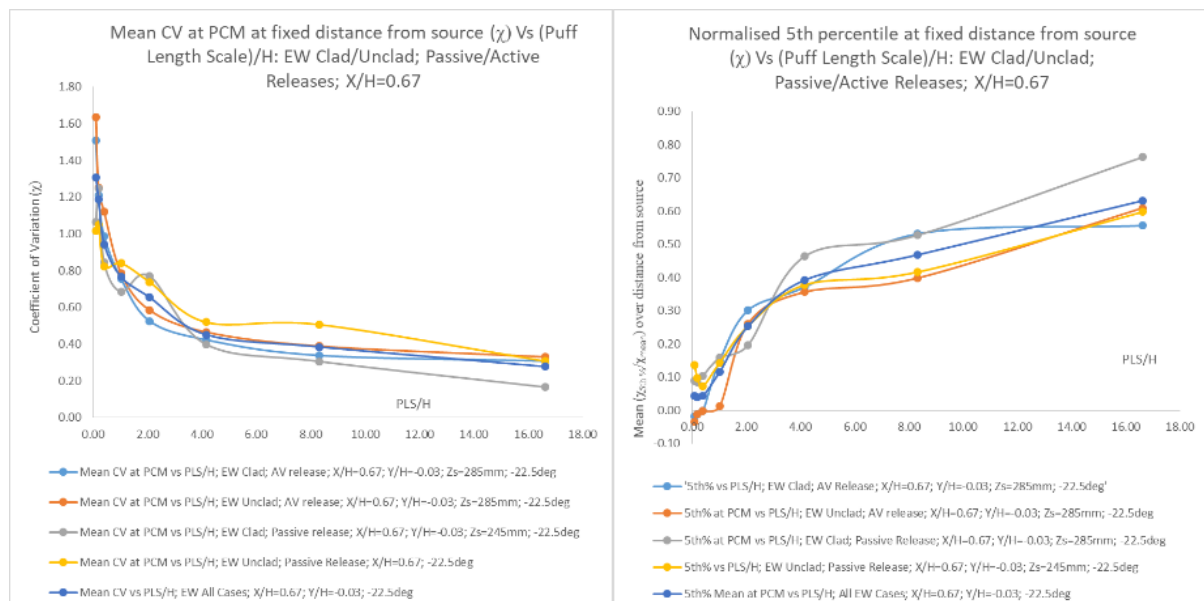


Figure 15.4.9: Summary of 5th percentile of χ_{5th}/χ_{mean} vs PLS/H ; various angles of incidence; averaged over a range of distances from the source ($X/H=1/3, 2/3, 1, 5/3mm$); active vertical $Z_{RH}=255mm$; data sampled on PCM; EW active and passive release data at $X/H=0.67$ is presented for comparison

All cases are shown for comparison in Figure 15.4.9 for χ_{5th}/χ_{mean} versus PLS/H : these curves are normalised to the mean of all the 5th percentile results so must be divided by the scaling form-factor $F_{x,5th}$ to obtain a more accurate determination at a known distance from the source. Cases presented: active vertical (AV) release for the cube with three angles of approach flow; EW clad and unclad AV releases at a fixed angle (-22.5°) for a distance near the middle of the roof zone, and EW clad and unclad passive releases at a low release height close to the roof surface (245mm). The figure shows the separate 5th percentile characteristic curves where the same general characteristics are shown to be relatively insensitive to the different test conditions.



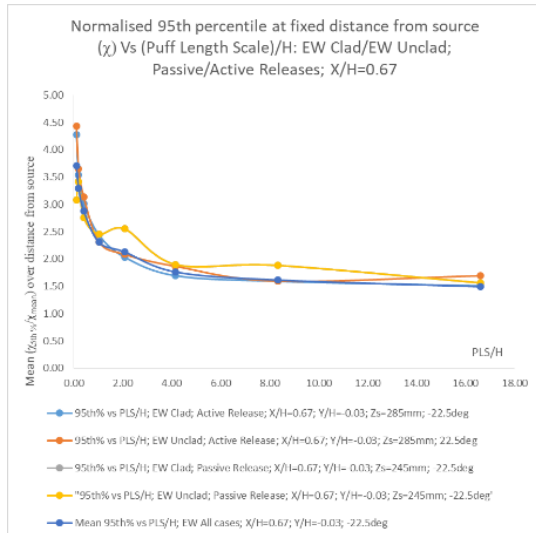


Figure 15.4.10(a/b/c): EW passive and active vertical release data - summary of statistical parameters vs PLS/H : fixed angle of incidence - 22.5° ; fixed distance from the source $X/H=0.67$; active vertical $Z_{RH}=255mm$; passive $Z_{RH}=245mm$; data sampled at PCM:
(a) CV (top left)
(b) 5th percentile (top right)
(c) 95th percentile (below)

From Figure 15.4.10 we see the EW clad and unclad results showing passive and AV releases at a range of sampling heights and normalised to the best-fitted mean of all the curves. It can be seen that the statistical descriptors used show a range of variation within a relatively narrow range after the scaling form-factor F_z is applied, meaning that there is a general characteristic pattern for these parameters that is relatively insensitive to the individual cases: i.e. different building shapes.

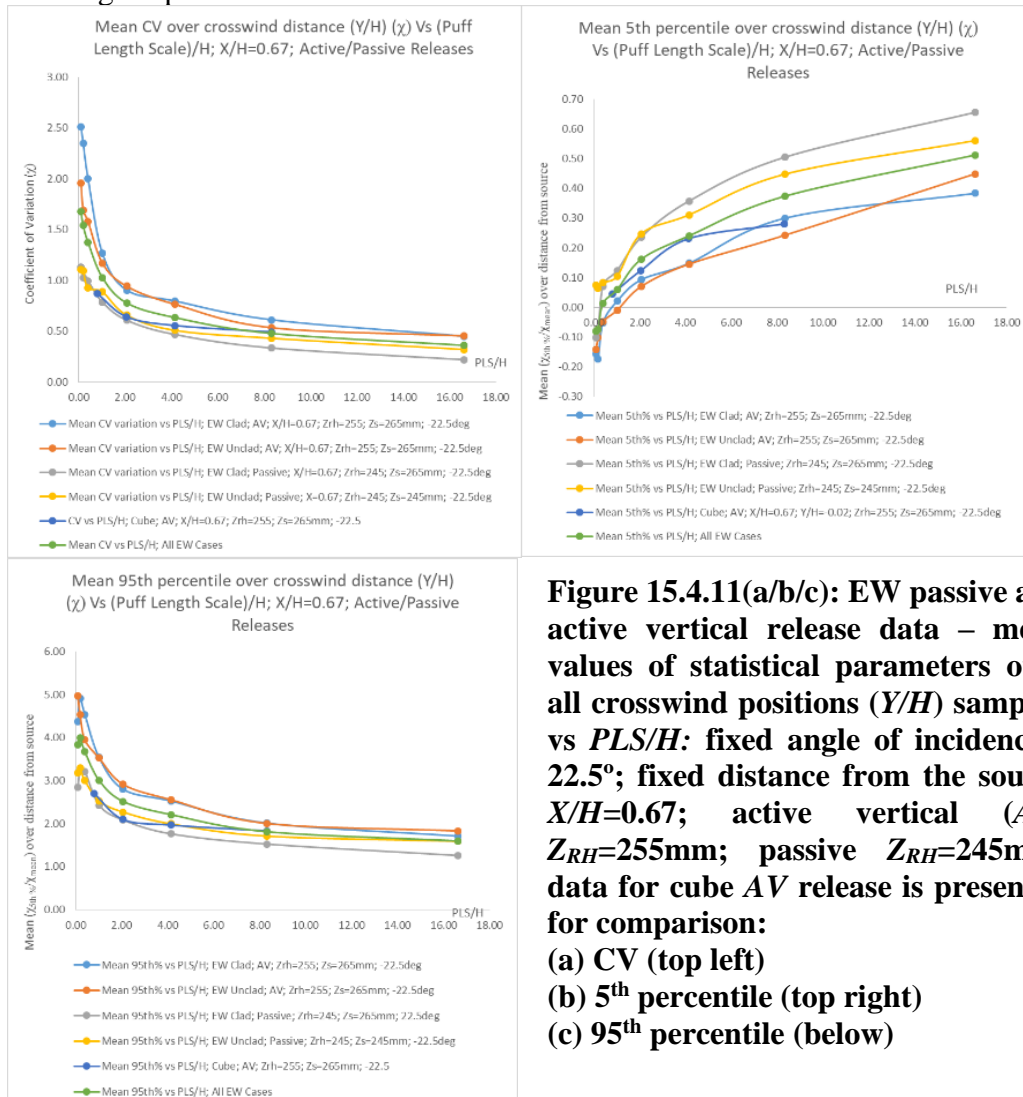


Figure 15.4.11(a/b/c): EW passive and active vertical release data – mean values of statistical parameters over all crosswind positions (Y/H) sampled vs PLS/H : fixed angle of incidence - 22.5° ; fixed distance from the source $X/H=0.67$; active vertical (AV) $Z_{RH}=255mm$; passive $Z_{RH}=245mm$; data for cube AV release is presented for comparison:
(a) CV (top left)
(b) 5th percentile (top right)
(c) 95th percentile (below)

Additional results showing the variation with crosswind position (Y/H) are shown in Figure 15.4.11 for the EW clad and unclad cases being the mean value over the measured co-ordinates. They may be further corrected to obtain a more accurate result by dividing by the form-factor F_y for the crosswind variation as shown in Figure 15.4.12. The peak values of F_y occur for the CV and 95th percentile slightly to the negative- Y crosswind co-ordinate. The 5th percentile values are more open to interpretation as the values were obtained from low signal levels in puffs and with the inherent limitations of finite ensemble number of puffs leading to much increased statistical uncertainty: these results should be considered speculative.



Figure 15.4.12(a/b/c): EW passive and active vertical results – crosswind form factor F_y vs Y/H : fixed angle of incidence -22.5°; fixed distance from the source $X/H=0.67$; active vertical (AV) $Z_{RH}=255\text{mm}$; passive $Z_{RH}=245\text{mm}$; (a) CV (top left); (b) 5th percentile (top right); (c) 95th percentile (below)

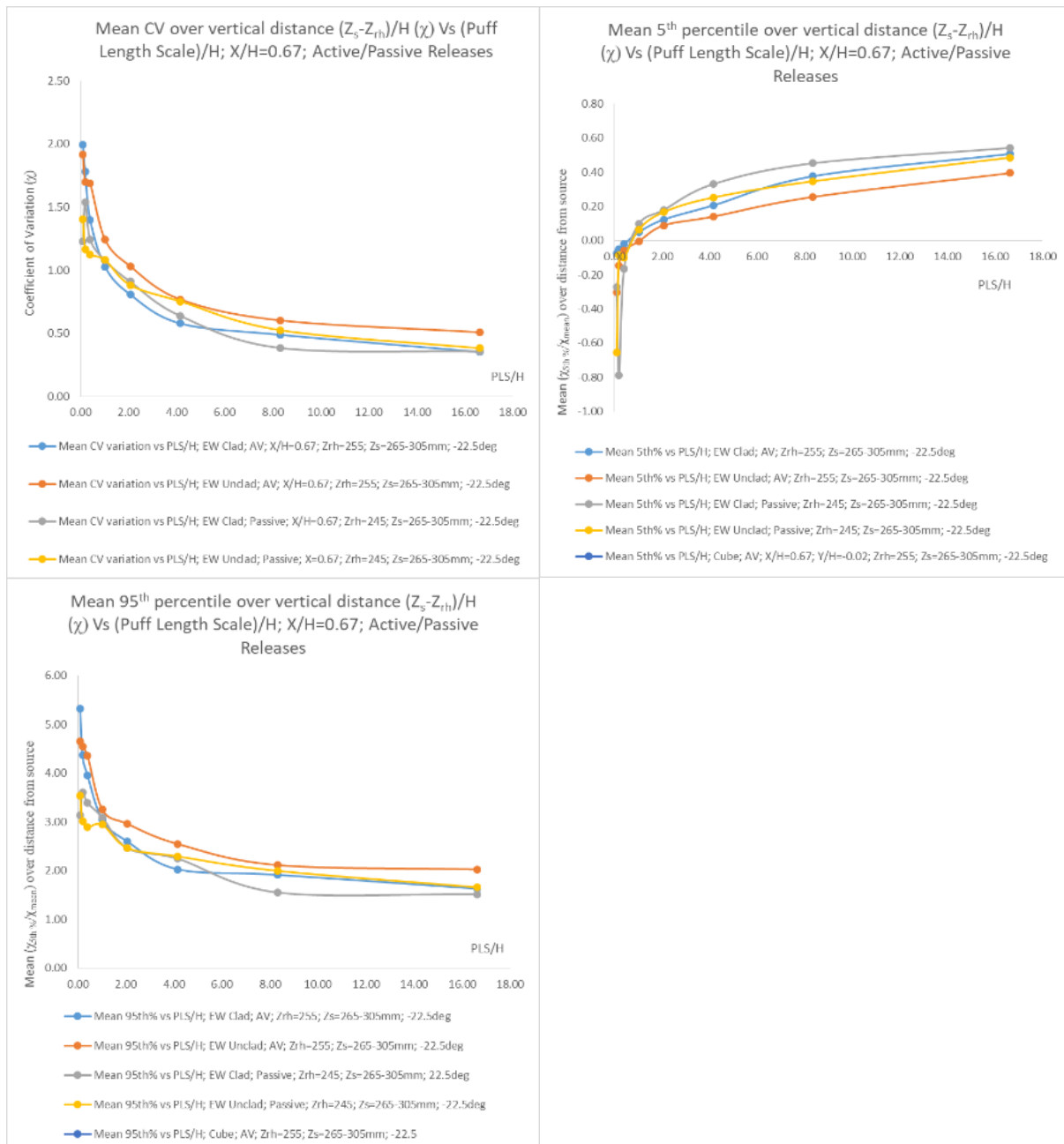


Figure 15.4.13(a/b/c): EW passive and active vertical release data – mean values of statistical parameters over all vertical measurement positions (265-305mm) sampled vs PLS/H : fixed angle of incidence -22.5° ; fixed distance from the source $X/H=0.67$; active vertical (AV) $Z_{RH}=255$ mm; passive $Z_{RH}=245$ mm; (a) CV (left); (b) 5th percentile (right); (c) 95th percentile (below)

Figure 15.4.13 shows the variation with vertical sample position (normalised against release height and building height) for the range of EW clad, unclad and passive and AV cases. The same general characteristics for PLS/H are seen compared as in the previous examples.

Figure 15.4.14 shows that the form factor for the vertical direction F_z shows a peak for passive releases this is close to the surface of the roof, but for the active vertical releases at greater height. These curves may be used to correct the mean value of the statistical parameters i.e. the CV and 95th percentile according to vertical distance of the sample in relation to the release

height. The 5th percentile, because of the limitations in the data discussed before, may be considered speculative.

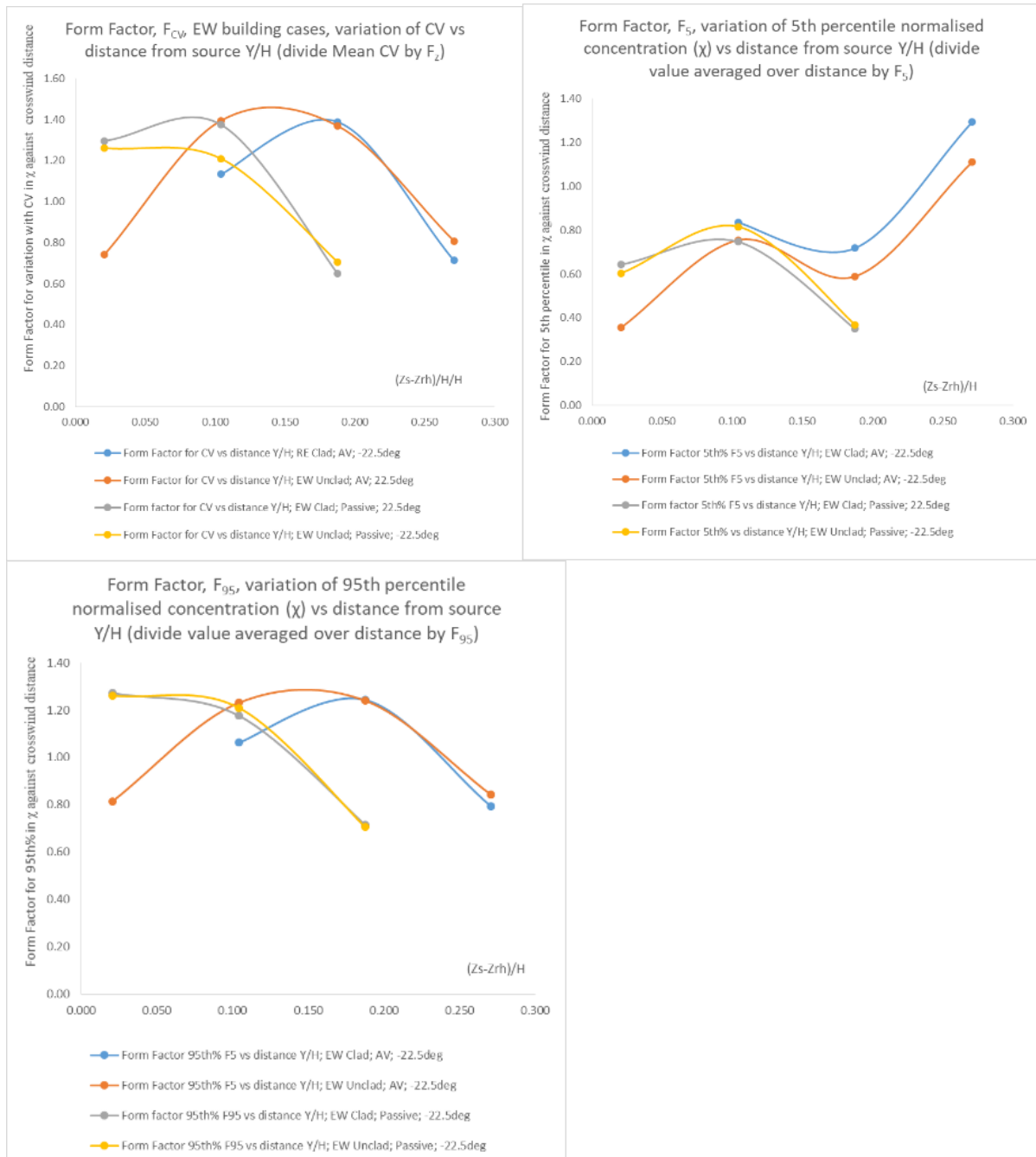


Figure 15.4.14(a/b/c): EW passive and active vertical results – vertical form factor F_z vs Y/H ; fixed angle of incidence -22.5°; fixed distance from the source $X/H=0.67$; active vertical (AV) $Z_{RH}=255\text{mm}$; passive $Z_{RH}=245\text{mm}$; (a) CV (left); (b) 5th percentile (right); (c) 95th percentile (below)

Supplemental results for the convergence of the statistical quantities of the mean and coefficient of variation (CV) for a sequence of puffs, in the order in which they were obtained experimentally, are presented in Figures 15.4.15 through to 15.4.17, which are additional to those presented in Figure 7.20(a/b) and show the speed of convergence with increasing puff duration ΔT .

Figure 15.4.15 shows that the number reduces to 60 for the puff of release duration 0.25 seconds, whilst Figures 15.4.16 and 15.4.17 show the numbers to be 40 for the 0.5 seconds puff release and 30-40 for the 1.0 second release.

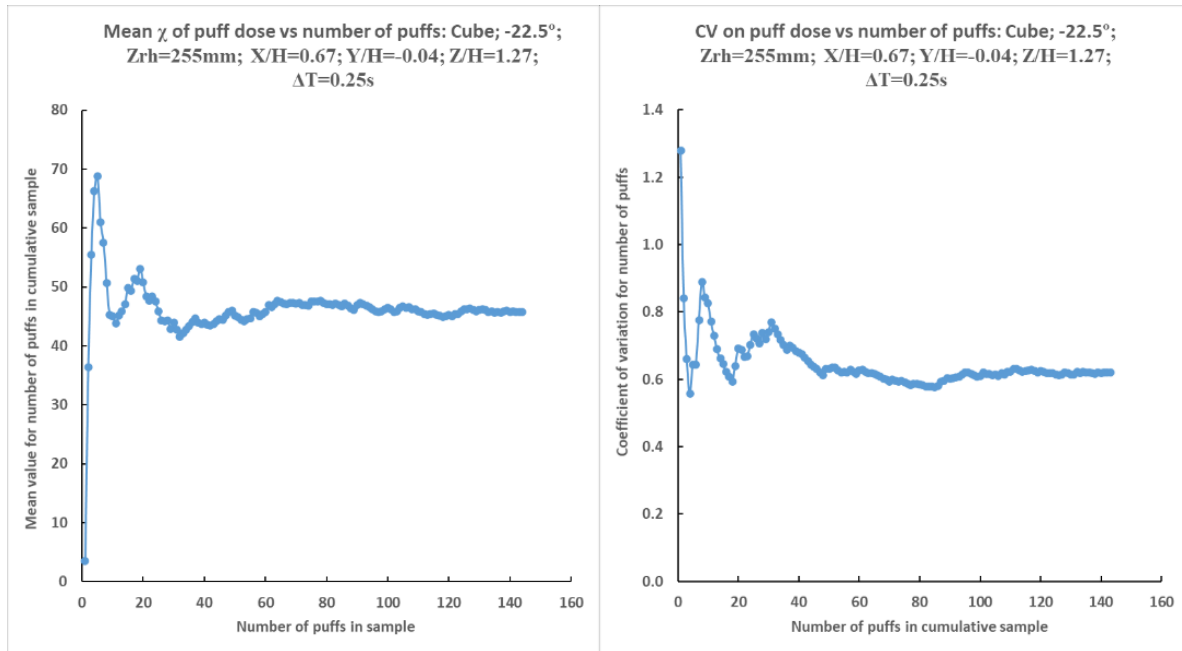


Figure 15.4.15(a/b): Convergence of statistical parameters with puff sequence: Cube; ‘A’; angle of incidence -22.5° ; $\Delta T = 0.25$ s; fixed distance from the source $X/H = 2/3$; active vertical (AV) release at $Z_{RH} = 255$ mm: (a, left) mean; (b, right) CV

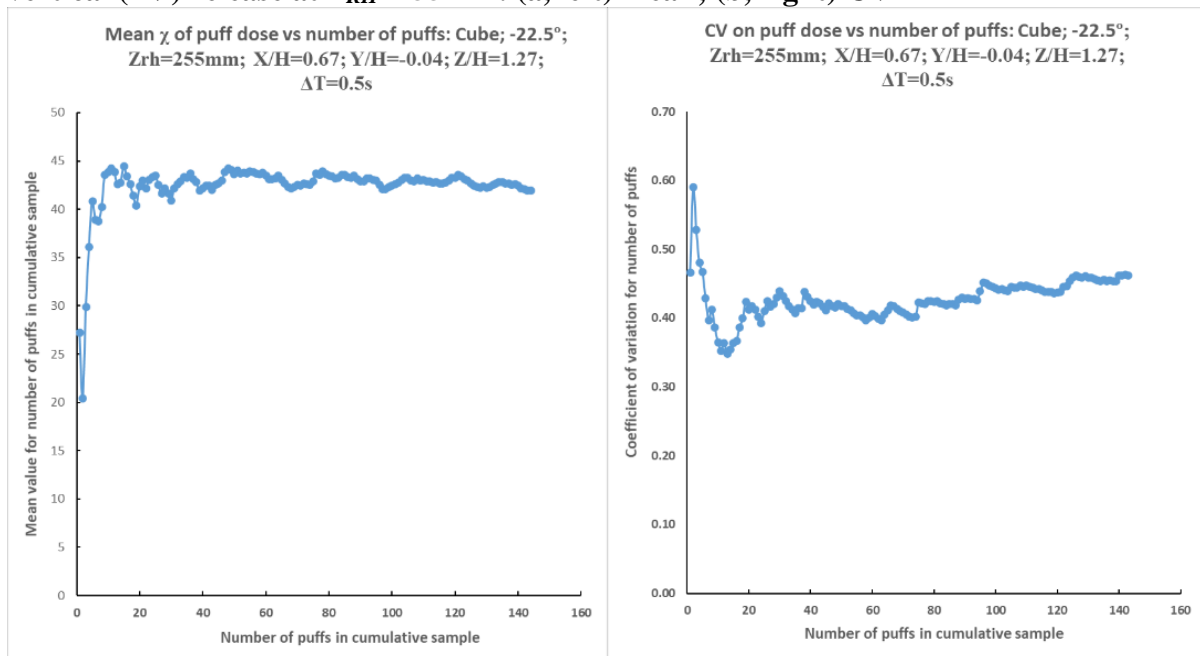


Figure 15.4.16(a/b): Convergence of statistical parameters with puff sequence; Cube; ‘A’; angle of incidence -22.5° ; $\Delta T = 0.5$ s; fixed distance from the source $X/H = 2/3$; active vertical (AV) release at $Z_{RH} = 255$ mm: (a, left) mean; (b, right) CV

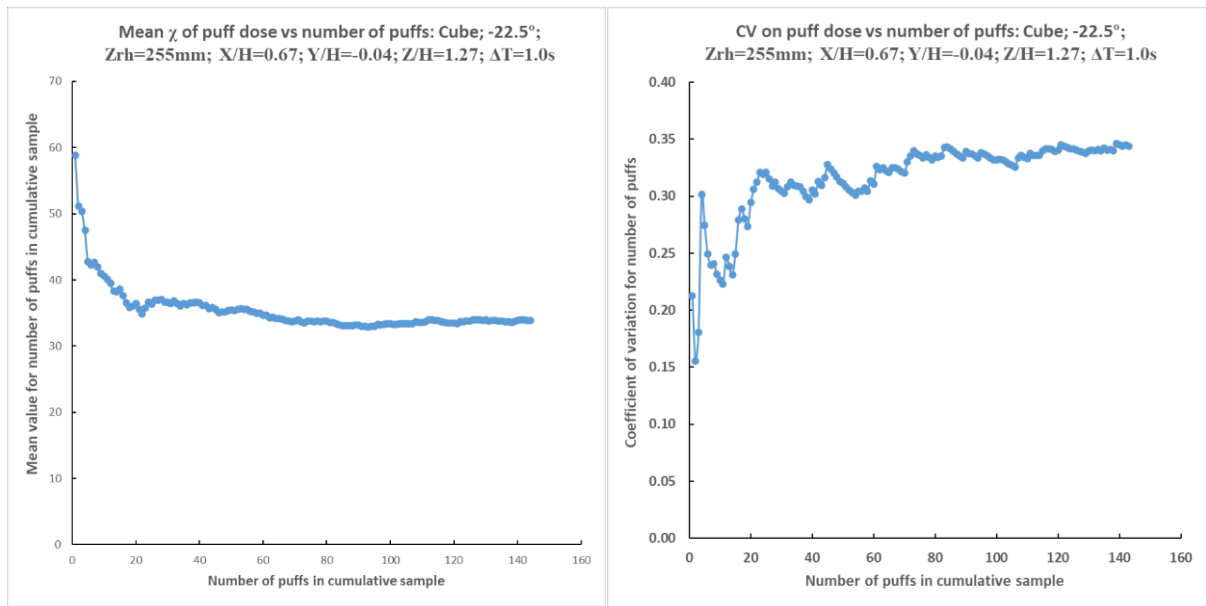


Figure 15.4.17(a/b): Convergence of statistical parameters with puff sequence: Cube; 'A'; angle of incidence -22.5°; $\Delta T=1.0s$; fixed distance from the source $X/H=2/3$; active vertical (AV) release at $Z_{RH}=255mm$; (a, left) mean; (b, right) CV

Appendix 15.5: Paper 1

'This is the Accepted Manuscript version of an article accepted for publication in Journal of Radiological Protection. IOP Publishing Ltd is not responsible for any errors or omissions in this version of the manuscript or any version derived from it. The Version of Record is available online at <https://doi.org/10.1088/0952-4746/36/4/746>.'

DISPERSION OF POSITRON EMITTING RADIOACTIVE GASES IN A COMPLEX URBAN BUILDING ARRAY: A COMPARISON OF DOSE MODELLING APPROACHES

DJ Gallacher¹, AG Robins², A Burt², S Chadwick¹, P Hayden², M Williams³

1-Medical Physics Department, Guy's and St. Thomas' NHS Foundation Trust

2- Enflo, Faculty of Engineering and Physical Sciences, University of Surrey

3- Cambridge Environmental Research Consultants (CERC), Cambridge

E-mail: david.gallacher@gstt.nhs.uk

Abstract

A radiological assessment was carried out on the release of positron-emitting radioactive gases from a roof-level stack at a central London site. Different modelling approaches were performed to investigate the range of radiation doses to representative persons. Contributions from plume inhalation, gamma shine and immersion to effective dose were taken into account. Dry and wet surface deposition on the roof, and exposure from contamination on the skin of roof-workers, added only a mean 4.7% to effective dose and were neglected. A 1:200 scale model, consisting of the stack and surrounding buildings, was tested in a wind tunnel to simulate pollutant dispersion in the near-field region i.e. rooftop. Concentration field measurements in the wind tunnel were converted into effective dose, including for roof-workers installing glass cladding to the stack building. Changes in the building shape, from addition of the cladding layer, were investigated in terms of the near-field flow pattern and significant differences found between the two cases. Pollutant concentrations were also modelled using ADMS and the results used to calculate the effective dose using the same meteorological data set and source release terms. Sector averaged wind tunnel dose estimates were greater than the ADMS figure by approximately a factor of two to three. Different stack release heights were investigated in the wind tunnel and ADMS simulations in order to determine the best height for the replacement flue stack for the building. Other techniques were investigated: building wake models, modified Gaussian plume methods and uniform dilution into a hemispherical volume to show the wide variation in predicted dose possible with different approaches. Large differences found between simpler analytic approaches indicated that more robust radiological assessments, based on more complex modelling approaches, were required to achieve satisfactory estimates of radiation dose to representative groups in adjacent buildings and on the building rooftop.

1. Introduction

Ventilation air from the cyclotron facility that serves the Clinical PET Centre at St Thomas' Hospital (STH) in central London is discharged to the atmosphere from a short stack on the roof of the highest site building, the 50m East Wing (EW). Emissions intermittently contain small amounts of short half-life radioactive materials. Assessing the resulting radiation doses received by representative persons is a challenge, chiefly because of the complexity of the buildings on site and near to the release point, but also because discharges are intermittent. Although a number of desk based dose calculation methods are recommended for use in the

UK (MacDonnell, 2004), most are not well suited to this task. Other methods, commonly used in air pollution analysis are available, including wind tunnel (WT) simulation (e.g. Hajra *et al*, 2012) and advanced atmospheric dispersion models such as ADMS (CERC, 2012a). All methods have their limitations and the need to assess the impact of the cyclotron emissions was taken as an opportunity to compare their performance and examine their applicability.

The assessment was undertaken because STH was planning to clad the EW building in a glass envelope for the EW Cladding Project (Figure 1), which would significantly alter the appearance, shape and height of the building. It was anticipated that these changes would alter the characteristics of plume dispersion around the building, affecting doses to persons inside and outside the EW from the stack discharges. The radiological assessment would have to include doses to workers carrying out the cladding work in the near field zone (Figure 2) on the roof of the EW building over significant periods of time during the eighteen month construction period. Of particular interest would be the maximum air concentration values near the air handling intakes for EW (in the upper middle section of Fig.2), which were close to the recorded plume concentration maximum for the main wind direction studied, where the wind was blowing directly over the EW building. During the EW cladding construction phase workers could be located anywhere in the general roof area. The installation of new radiochemistry laboratories and an additional 16MeV proton beam cyclotron (GE, 2012), with expected increase of workloads, required the height of the replacement flue stack to be determined. The analysis provided an assessment of doses to representative persons (EA, 2012) from aerial discharges required under the Environmental Permitting Regulations (EPR, 2010) and Amendment Regulations 2011 (EPR, 2011), under which the site gaseous discharge limits were set, and a risk assessment under the Ionising Radiations Regulations 1999 (IRR, 1999). Existing gaseous discharge limits were used as the source term for the emissions.

2. Methods

Methods used in the analysis are described in the accompanying paper (Gallacher *et al*, 2016) and summarised in 2.4 with further details of their application to the emission of positron-emitting radioactive waste gases from the site flue stack. Releases occurred intermittently during cyclotron bombardment and subsequent radiochemical tracer production. The existing flue was 3m above the top platform of the EW North stair tower (Figure 3). The replacement stack would handle an increase of exhaust flow rate from $1.48\text{m}^3\text{s}^{-1}$ to $6.6\text{m}^3\text{s}^{-1}$ but with an increased diameter to limit the efflux velocity to 13ms^{-1} . Three stack positions were considered: existing stack position #1 and positions #2 and #3 (Fig.2) though only results from #1 are required in this analysis.

Physical constants (DDEP, 2014) and parameters used in the models for converting concentration values into effective dose are given in Table I. Table II shows site-specific model parameters. Source terms for the emissions are listed in Table III in terms of total annual release and equivalent constant release rate between 07:00-15:00 daily i.e. over 2000 hours per annum (5 days per week and 50 weeks per year).

Fourteen estimates were made of representative person annual effective doses from the discharges (Table IV). Models used ranged from simple hemispherical gas ball models, where spherical cloud geometries have been described in the literature (Thompson, 1999), Gaussian plume modelling (GPM), building wake models, WT simulations and ADMS. The GPM and building wake approaches were based on NRPB W-63 (MacDonnell, 2004) which follows on from the dispersion models originally presented in NRPB R-91 (Clarke *et al*, 1979). ADMS is a GPM with advanced features i.e. with a building effects module and allowance for

atmospheric stability and meteorological conditions, and is referred to as a separate method for this reason.

2.1 Source Term

Continuous monitoring of radioactive releases throughout cyclotron operation and radiochemical production ensured that the site operated within permitted daily and annual cumulative limits. Radiological impact assessments are based on the source term which is characterised by the nature, magnitude and frequency of the discharge. For all models it has been assumed that the full permitted annual activity is released in each listed radionuclide category over the course of each calendar year. Daily discharge was taken as the pro-rata fraction of the annual limit (Table III). The ^{18}F , ^{13}N and ^{11}C group was modelled on ^{18}F as a 'worst case' scenario, as ^{18}F gives the greatest representative person dose because of its greater inhalation dose conversion coefficient and longest half-life (Table I). The ^{15}O group ($t_{1/2}=2.04\text{min}$) was treated as a separate source term.

2.2 Representative Person Selection

The representative person approach will be used as defined by the Environment Agency (2012), which replaces the formerly used concept of the 'critical group'. The representative person is defined accordingly as the most appropriate person for which the dose is calculated for comparison with site constraints and dose limits. All of the workers on the roof and surrounding the EW building must be considered as individuals not working directly with ionising radiation, and were therefore treated as being members of the public: they will however be referred to as 'roof workers' for the purposes of this work. Workers employed by the host organisation for the area within the perimeter of the STH site are taken to also be non-radiation workers and will be treated in the same way: these will be referred to as 'adults'. For all representative persons the assumption made is that they spend all of their time, during the period of daytime emissions 07:00-15:00 on weekdays, at or close to the receptor point at which the dose term is calculated. No special protective measures are assumed in terms of skin contamination for the roof workers other than building site standard personal protective equipment (PPE). At other locations on site the skin deposition and contamination will be significantly lower than the roof workers and has been neglected. The STH site does treat child patients: there is a crèche, in which children will be assumed to stay for the period of daytime emissions. These patients and children will be taken to reside in the location of the receptor point e.g. crèche, over the full year. In Table IV, methods 1-9 were modelled for both adults and one year old infants and methods 10-14 for adults only. The difference between the two representative persons is the greater dose coefficient (Sv.Bq^{-1}) for infants (ICRP, 1996), though this is offset by the lower breathing volume rate (MacDonnell, 2004). Breathing rates for adults were taken for nose-breathing and light work, according to the figures given in ICRP Report 68 (ICRP, 1994). The EW air intakes were on the roof (in the stem of the 'T' section) close to the maximum concentration position recorded in the wind tunnel. Roof worker effective doses may be taken as an upper estimate of the doses to persons inside the EW, because some reduction from gamma shine doses could be expected due to attenuation in the roof materials and air concentration values inside the building will not exceed those occurring externally.

2.3 Wind Conditions

The prevailing wind condition in this part of England is 55% Pasquill D from the South West, as per NRPB W-63 (MacDonnell, 2004). Although in practice the release is intermittent, a constant release rate was assumed for models 7-14 (Table IV), and the dose assessed by taking account of a range of wind directions and speeds. Models 7-9 assume a uniform wind rose and 10-14 use 5 years of sector averaged meteorological data which takes into account hourly

figures for wind direction and speed. Models 3-6 are consistent with a fixed wind direction and a short term release and hemisphere models 1 and 2 assume very short release durations and rapid dilution into a given volume.

2.4 Modelling Approaches

Effects of local buildings on the pollutant dispersion patterns were unknown but were expected to be significant (Robins and MacDonald, 2001, Fackrell and Robins, 1982). There is limited knowledge about the effects of complex building arrays on the dispersion patterns of plumes from elevated sources as most studies to date have analysed only simpler cases of a single building or ground level emissions in urban areas (i.e. traffic pollution). In the case of a building with a rooftop stack, it has been shown that many Gaussian plume dispersion models give rise to overly conservative (i.e. excessive) air concentration values when compared with data obtained from WT or ADMS simulations (Hajra *et al*, 2010). Factor of ten differences have been found between simple Gaussian plume dispersion models (e.g. ASHRAE, 2007), WT and CFD simulations (Chavez *et al*, 2011). Related studies have shown the significant effect of downstream buildings on dispersion from rooftop stacks, with similar orders of magnitude differences between simple GPM, WT and CFD studies (Hajra *et al*, 2012). Significant effects of adjacent and upwind buildings on plume dispersion have also been demonstrated (Hajra *et al*, 2013). By using a more sophisticated model (ASHRAE, 2011) with respect to R-91 (Clarke *et al*, 1979), which takes better account of plume dispersion with ground roughness, plume rise and downwash effects it is possible to produce better estimates of pollutant dispersion: but even this method is sensitive to building spacing and wind direction (Hajra *et al*, 2014). In general, a wide variation has been shown between various standard approaches that vary from being overly conservative to near best estimate, depending on the local conditions. Considerable uncertainty was therefore ascribed to simple approaches based on GPM dispersion without analysis and allowance for building effects (Robins and McHugh, 2001). Due to the position of the representative persons (Figure 4), it was important to understand plume behaviour over the site buildings, especially entrainment in the near-wakes of the larger buildings. An accurate 1:200 scale site model was therefore constructed for the wind tunnel plume dispersion studies.

The existing stack projected 3m above the former (2013-14) EW roof level, a total height of 53m above site datum to the West of the EW. EW was the tallest building in a complex local building array, but with other buildings in the immediate vicinity expected to affect local flow and dispersion. Figures 3 and 4 show the EW building and environment.

Photon build-up factors in air were taken into account using Berger's formulation (Raza and Avila, 2005) where it was concluded that an accurate determination of external dose rate needed to account for build-up effects from source distances of less than several photon mean free path lengths. Methods of applying the build-up factors for the 511keV annihilation gamma rays are detailed in Gallacher *et al* (2016).

Contributions to EW roof worker effective doses from (a) dry and wet surface deposition on the EW roof building surfaces, over which the plume was passing in the primary direction studied, and (b) doses from deposition of radionuclides on (limited) exposed surfaces to skin were considered. Contributions from both these processes were estimated using the parameters described elsewhere in this work but using the estimated concentration values near roof level from the wind tunnel experiments. The evaluation was carried out at the plume concentration maximum (PCM) position from the wind tunnel experiments in the roof plane. The basic methodology followed W-63 (MacDonnell, 2004) with the wet deposition occurring 10% of the time, consistent with Pasquill-D conditions, plus 100% dry deposition. The release was

taken as a single spike release, halfway through the working day and the cumulative dose over the remaining four hours integrated to a worker standing near the plume concentration maximum throughout this period. Skin deposition was allowed to integrate out to full effective decay, with no end of shift washing or decontamination assumed. Surface concentrations were estimated based on the crosswind and downwind WT concentration profiles and an averaging factor was applied over the Gaussian profile out to 2σ in the downwind direction. The crosswind profile out to 2σ at the PCM matched the primary sector used for the wind tunnel experiments, so the weighted wind velocity appropriate to this sector was used to evaluate the wet deposition term. The skin contamination term was taken to be the same for exposed skin surfaces as the roof surfaces, but limited skin coverage was assumed (anterior head and upper uncovered forearms) as personal protective equipment (PPE) usage on site required helmet, hi-visibility tabard, gloves and protective visor. The dose arising from the deposited radionuclide was estimated using factors for 0.5MeV photons (corresponding closely to the positron annihilation gamma energy of 0.511MeV) tabulated in Eckerman and Ryman (1993) for the semi-infinite plane. Doses from skin contamination were estimated from the uniform contamination factor for ^{18}F from Delacroix *et al* (2002). The evaluation was carried out over all stack heights investigated and for clad and unclad building models. The contribution from ^{15}O contamination to the dose could be neglected due to the much shorter half-life compared to ^{18}F . Reactive-form inorganic ^{131}I was chosen as the surrogate radionuclide to approximate reactive ^{18}F in accordance with Nicholson (2009) who reported figures for dry deposition velocity of approximately 0.01ms^{-1} for gaseous reactive iodine and washout coefficient of 10^{-4}s^{-1} for iodine vapour: these figures are the same as presented in W-63(MacDonnell) and were used in the basic analysis carried out.

The total dose for deposition and skin contamination processes was between 2.3-12% of the inhalation, immersion and gamma shine doses with a mean ratio of 4.7%. Given the wide range of dose values from the different methods presented in this work it was therefore decided to neglect the contribution from these source terms, without affecting the general accuracy to any significant extent.

The positron immersion cloud doses were calculated for full body skin immersion, without any correction applied for protective clothing. This approximation was justified on the grounds that the contribution from this source term to effective dose was small from this source term, and that this follows the methodology presented in W-63 (MacDonnell, 2004). The omission of a beta skin dose protection factor from clothing to some extent offsets the small contributions from dry and wet deposition, and skin contamination, which were neglected in the analysis.

Given the close proximity of the EW roof in relation to the stack, the decay of ^{15}O ($t_{1/2}=2.04\text{mins}$) was not a significant factor in the WT estimates of roof-top doses but would become more important further downwind of the release. For the downwind distal point analysis of the WT data (at the edge of the site) the activity of ^{15}O was decay corrected using the transit time from the release point. Decay correction was applied for both hemisphere models. For the building wake models the recirculation zones were either on the rooftop or over the building so ^{15}O decay was not applied in the near field. Decay correction was not applied for the fixed wind direction or for the continuous release models (Table IV). In these cases the concentration maximum values were provided by the graphical data at some hundreds of metres downstream, but that concentration value was taken to apply in the near field of the release at near rooftop level, so that a correction for ^{15}O decay was deemed not necessary. The EA model (2006a, 2006b, 2010) did not specify whether a decay correction had been applied, nor did it specify the downstream distance at which the dose was evaluated.

2.4.1 Model 1- Static Hemisphere

This model assumes that a hemisphere of uniformly dispersed gas, centred at ground level at stack position, was formed instantaneously after a spike emission of zero duration. The full daily pro-rata release was assumed to calculate the daily dose. A radius of 75m was taken that contained the stack top (53m), and the whole of the EW building, with an allowance for plume rise in low wind conditions. Building attenuation effects were neglected for the proportion of the volume contained inside other buildings within this radius, and it was assumed that the concentration inside those buildings matched that outside. The static hemisphere of gas was decay corrected over the following 8 hour working day to give the accumulated effective dose from gamma cloud shine, inhalation and skin beta dose. For the distal point at the edge of the site (selected to show the difference between models further from the release point) a hemisphere of radius 175m was used to encompass the receptor points used for the WT and ADMS analysis available at this distance. The larger hemispherical volume resulted in a lower concentration from the same fixed release.

2.4.2 Model 2 – Moving Hemisphere

To make the static model more realistic the 75m radius hemisphere was assigned a translation velocity of 0.02ms^{-1} . A transit time would therefore be expected to occur in just over one half-life of the predominant radionuclide: a different drift velocity could be selected for the model. The assumption was that persons would be exposed at a location while a full diameter of the hemisphere moved over them. For simplicity it was assumed that the dose rate was the same as that calculated for the hemisphere centre, though in practice this would be an overestimate. Decay of the radionuclides was taken into account and it was assumed that no dose was received either before entering the hemisphere volume or after exiting it. The same scheme was applied with a 175m radius hemisphere for the distal point analysis.

The positron ranges for the energies given in Table I are limited to less than approximately 0.6g.cm^{-2} (Delacroix, 2002), corresponding to full absorption in air for range up to $1.76\text{m} (^{18}\text{F})$ and $6.22\text{m} (^{15}\text{O})$ at sea level (Pilkingsrud and Gels, 1985). Edge effects caused by positron irradiation outside the hemisphere volume and the slightly larger effective source volume caused by the positron range in air (since the gamma rays come from the annihilation event positions) have been neglected.

2.4.3 Model 3 – Ground Release (Fixed Wind Direction, W-63 Model)

NRPB W-63 (MacDonnell, 2004) was used to calculate the effective dose to an adult and infant on site 8 hours per day during the full discharge period. For releases in the vicinity of buildings the peak concentration with range was read from the graphs provided and used for the roof zone. Given an assumed fixed wind direction with the receptor point downwind, a short daily ‘spike’ release (of the daily release term) gives rise to a time integrated concentration (Bq.s.m^{-3}) equal to that for the same activity uniformly released over the working day, leading to the same cumulative dose for both cases. The dispersion constant, $C_{\text{plume}}(\text{s.m}^{-3})$, was taken at the peak concentration maximum occurring at a downwind distance of 30m; a figure lying approximately within the near-field region under consideration. W-63 recommends that a ground release model be applied where complex building topologies result in significant plume entrainment and an isolated stack discharge point is unrealistic. For the distal point the concentration (C_{plume}) per unit release was taken from the graphs at the downwind distance of 175m, and was considerably lower than the maximum value selected for the roof zone at 30m.

2.4.4 Model 4 – Building Wake Model: 3m Roof Top Structure (RTS) Recirculation Zone

W-63 includes a building wake method for calculating plume concentrations in the wake of an isolated building, as originally presented in NRPB R-157 (Jones, 1983). The method calculates a concentration based on a plume that forms and re-circulates on the building face that is downwind of the discharge point. The model assumes a rectangular block building geometry and no allowance was therefore possible for the different cross sectional shapes of the EW. For simplicity, the model used here assumed a flat face of 45m wide by 20m deep and 50m high: dimensions for EW were taken from archive record drawings. The concentration in the recirculation zone may be estimated by using the standard approach which is applied in 2.4.5. However, to obtain an estimate of the concentration and dose from the plume entrainment in the roof top structure (RTS) recirculation zone a new method was proposed (Gallacher *et al*, 2016) using assumptions about flux balance, similarity scaling and entrainment velocities in the respective zones. The RTS height of 3m was selected for the calculation, corresponding to the height of the clad sections of building above the level of the North stair tower (Figs.1,2,3) and approximately the height of the EW air handling units near the building air intakes (in the stem of the EW 'T' section, Fig.2). A wind speed of 3.24ms^{-1} was selected, corresponding to the mean weighted wind speed from bearing 345° at the building height.

2.4.5 Model 5 - Building Wake Model (W-63): 50m Building Height

To obtain a more realistic estimate of the doses to persons at ground level from plume entrainment and downwash, the building wake model calculations were repeated with the EW building height of 50m with other dimensions as Model 4.

2.4.6 Model 6 - Fixed Wind Direction/Short Term Release (W-63): 53m Isolated Stack

Calculations in Model 3 were repeated for a fixed wind direction and a 53m release height. The plume concentration maximum (PCM) at ground level was taken (corresponding to 500m downwind of the release point) to provide an upper-bound estimate to apply to the roof top zone. For the distal point analysed at the edge of the site the concentration value used corresponded to an actual range of 175m and stack height 58m, consequently less than the maximum, but was considered more appropriate to this case.

2.4.7 Model 7 - Continuous Discharge/Uniform Windrose (W-63): 53m Isolated Stack

Continuous discharge is assumed in this model, which is then sector averaged with a uniform wind-rose at 55% Pasquill D atmospheric stability. The daily short releases are treated as a continuous release then averaged over varying wind directions over the year. The PCM was found to occur at approximately 400m downwind, and this figure was used in the calculations as an upper bound estimate. As with Model 6, the lower concentration value corresponding to 175m from the release point was used for the distal point calculation, but with stack height 58m selected to match to the WT and ADMS analyses.

2.4.8 Model 8 – EA Discharge Model: 0m (ground release)

Because of the known significant errors in these simple models, the EA (2006a) advise a ground release calculation using their supplied proprietary IRAT spreadsheet; i.e. zero stack height with no plume rise as a conservative allowance for the effect of nearby buildings on air dispersion patterns. The model used $^{99\text{m}}\text{Tc}$ as a surrogate radionuclide for ^{18}F and ^{15}O and the downwind distance was assumed to be 100m (EA, 2006b).

2.4.9 Model 9 – EA Discharge Model: 53m (elevated stack release)

The IRAT spreadsheet was also used to calculate doses from an elevated release. A simple GPM was assumed; i.e. not allowing for building effects. A ground level dilution factor is used to take account of the elevated stack release (EA, 2010).

2.4.10 ADMS Simulations: Models 10, 11

An ADMS (version 4.2.2) computer simulation of the site, release conditions and source term was undertaken. The programme uses vertical wind velocity profiles based on estimated surface roughness, and in order to take account of the different characteristics of the meteorological site, a surface roughness value of 0.2m was used based on Heathrow. A Gaussian plume release profile with a fraction of the plume entrained into the building wake was also inherent in the ADMS model (CERC, 2012b). However, it only takes into account the presence of one effective building (Robins and McHugh, 2001) and therefore ignores the effects on flow and dispersion of other nearby buildings.

Key receptor dose locations were positioned around the site, as defined by Figures 3 and 4 based on representative person locations and geographical coverage (CERC, 2012c). The model used a single composite building and a surface roughness length of 1.0m appropriate for a city location (Wood *et al*, 2010). Five years of hourly meteorological wind data (2007-2011) from Heathrow were run through the model and associated hourly flow and dispersion conditions simulated. Discharges were spread over 8 hour intervals during the peak production periods from 07:00-15:00.

ADMS only calculates gamma shine doses at the ground plane (CERC, 2012a). In practice, the gamma doses to persons on the EW roof site were calculated using a raised ground plane set at the building height of 50m with the stack set at a height above this e.g. the 53m unclad building stack was 3m above the raised ground plane, but took into account plume upwards efflux velocity. Gamma doses for receptor points at true ground level were calculated with the correct stack release height in relation to the site datum. Intermediate height points were interpolated using the method described in Gallacher *et al* (2016).

The ADMS simulation gave air concentrations (Bq.m^{-3}) and gamma shine doses. These required conversion into effective dose for each radionuclide by inhalation and positron (beta) cloud immersion by the method described in Gallacher *et al* (2016) using coefficients from Table I. Air inhalation and beta immersion doses were calculated using the air concentration values for the receptor points with the true stack height in relation to the buildings.

Point r24a(Fig.4) was selected from the ADMS analysis and was the furthest downwind in approximately the primary wind direction studied (345°); lay within the sector of integration for the WT(Table V), and was 218m from the release position. The dose at this position was compared to the other methods also applied at the distal point.

2.4.11 Wind Tunnel Simulation Measurements (Models 12, 13, 14)

WT modelling was carried out at the EnFlo laboratory at the University of Surrey (EnFlo, 2016). Wind directions listed in Table V were investigated, as these were expected to carry the plume over critical locations on-site (Burt *et al*, 2012). Note: a) that the directions (30, 90, 125, 205, 260, 280 and 345°) are measured from true North and denote the bearing from which the wind blows and b) that 345° was termed the primary wind direction, as releases from the stack blew directly over the roof area. The full range of wind directions was modelled using a single stack release height equivalent to 58m full scale. Two different EW models were available, one clad the other unclad. To investigate the effects of adding the cladding layer on concentrations in the roof zone, and elsewhere, measurements of pollutant concentration were carried out for both building shapes.

The effect of varying stack release height was also examined in the primary wind direction for unclad and clad cases. A passive release was selected as the most appropriate, so the stated release height matches the effective release height for the plume. Since the EW models were made to be correct in relation to the ground level on their East aspect (i.e. with a ground level 2m below datum) there was the equivalent of a 2m offset between the model height in the WT and the stated height against the ground plane datum. To allow for this difference, measurements in the WT were adjusted to the actual height of the model: therefore 240mm corresponds to 50m above the datum level at full size (model 1:200 scale). Effective stack release heights between 53 and 58m (from ground datum) were modelled.

Air concentrations were measured in the WT for a continuous release of tracer gas and sampling on a pre-programmed uniform square element mesh. EW roof level concentrations were measured at a height of 265mm (55m full scale), corresponding to a worker standing on top of the glass cladding. Six sample meshes were measured for the primary wind direction, and nineteen for other wind directions, for both clad and unclad cases. Sample concentrations, C , were converted into standard dimensionless concentrations, χ , using the reference WT wind speed, U , the building height, H , and tracer release rate, Q ; where:

$$\chi = \frac{CUH^2}{Q} \quad [1]$$

Methods were developed in Gallacher *et al* (2016) for converting the WT data into field concentrations of a radioactive pollutant at each co-ordinate point and converting inhalation and positron immersion cloud doses into effective dose. WT results showed a clear concentration maximum point on the EW roof. Since inhalation dose was the largest component of effective dose from ^{18}F , at the plume concentration maximum (PCM) in the EW roof zone, this position was chosen to evaluate the overall maximum dose including the external gamma ray cloud shine dose and positron immersion dose. This follows as the gamma ray dose was calculated from the grid of measured concentration values just above roof level as detailed in Gallacher *et al* (2016).

Wind rose data relating to the Heathrow site (2007-2011) were used in the calculation of effective dose for different wind directions and wind speeds. Adjustments were made for the vertical wind velocity profile and the differences expected between the Heathrow site and the STH site in terms of ground roughness length.

For the distal point analysis downwind concentration profiles (in the crosswind Y axis direction) were analysed for wind in the primary direction in both the clad and unclad cases. It was found that the two positions of concentration maximum were sufficiently close spatially to treat the dose point as the geometric centre. These points lay within the primary direction wind sector (Table V). The dose calculated at this point (R=175m) was compared to the relatively nearby ADMS point r24a to gain an understanding of the convergence, or otherwise, of the modelling approaches at more distant receptor points from the stack.

3. Results

3.1 Models 12, 13, 14: Wind Tunnel Simulation of Top of East Wing

The wind-rose data analysis is detailed in Gallacher *et al* (2016), showing the range of effective wind velocity values with direction (weighted for the reciprocal of wind velocity, from a bivariate distribution of frequency and velocity) and giving the methodology used to convert the measured concentration values from WT data into effective dose at the PCM in the roof area. The seven (unequal) wind sectors were derived from the seven WT directions tested (Table V). These directions were chosen to investigate the effects of the two EW building shapes i.e. clad and unclad in terms of the flow field differences. The primary direction, bearing 345° (sector width 50°, bearing 320° through to 10°) contributes by far the largest proportion to the effective dose for workers in the roof area. The weighted wind velocity for this sector was 2.75ms⁻¹ and the wind direction probability was 0.114 i.e. 11.4%. Contributions from other wind directions to the overall dose totals were possible from data from the other WT directions studied, which enabled a comparison with ADMS.

Normalised mean concentrations (i.e. the concentration per unit release rate) at the EW roof-top level are listed in Table VI for both the clad and unclad buildings. The concentration maximum was measured in a horizontal plane 2m above the roof level of the clad building, approximately at the breathing height of a worker on the roof cladding. These figures apply to the wind bearing of 345° (i.e. 15° to NNW from N), which corresponds to a plume maximum directly over the roof area. The effective doses shown in Table VI have been calculated assuming the wind was 100% from this direction. It is interesting to note that the relatively smaller contribution from inhalation doses to the total effective dose for the ¹⁵O dose term leads to the external dose rate from this radionuclide to dominate for lower release heights. This explains the dose maximum occurring at a release height of 255mm, compared to ¹⁸F where the dose maximum depends more on the air concentration and the maximum dose occurs at release height of 265mm.

The variation of the maximum effective dose in the roof area for the full source term release is shown in Figure 5 showing the contributions to the total effective dose (weighted for wind direction probability) as a function of wind direction. The continuous smoothed lines represent a stack effective release height of 280mm in the WT (58m full scale). Clearly, the maximum dose in this area occurs for the primary wind direction tested, of 345°. This is referred to also as the ‘main’ direction, by virtue of it blowing directly over the EW roof, and giving rise to the inhalation dose term in the wind tunnel analysis. Doses that would be experienced by a roof worker are considerably reduced when the wind comes from other directions. For wind directions between 100° (from E) and 200° (SSW), doses for the unclad case, though small, are larger than for the clad case: it may be hypothesised that the presence of the ‘T’ cross section in the unclad case gives rise to greater flow recirculation over the unclad building for this wind direction range, giving rise to higher concentrations in the roof area and a greater gamma cloud shine component. Dose levels for each wind direction are given in Table VII (columns 2-4 for the unclad and 5-7 for the clad case), assuming steady conditions. These results are converted into wind sector weighted components in columns 9-11 and 12-14, respectively.

Table VIII presents contribution to annual effective dose for the primary wind direction (345°) from one sector and a range of effective release heights, 53-58metres (equivalent to 255-280mm in the WT). These results are also plotted in Figure 5 at the angular position of 345°. The maximum dose for the clad case was 180μSvy⁻¹ compared to the maximum for the unclad case of 110μSvy⁻¹.

By adding the small contributions from other wind directions (by making the assumptions that the doses from other sampled positions distant from the roof location can be approximated by the data collected for the 280mm releases in different directions) in Table VII; the total effective dose, weighted for wind velocity and direction probability, over the full source term at uniform discharge is given in Table IX, and shown in Figure 6. It can be seen that for the lower release heights (53-55m) the concentration is greatest for the clad building whereas for release heights of 56-58m the converse is true. The results clearly demonstrate that the roof-top pollutant maximum for a passive release occurs when the release is at the same level as the measurement plane on the roof (height 55m, or 265mm in WT). It is thought that this difference may be due to local building effects between the un-clad and clad cases.

3.2 ADMS Computer Simulation Model of Site (Models 10, 11)

The ADMS model was run for a range of ten different source and building parameters detailed in Table X (CERC, 2012c). Three stack heights were modelled (53, 58, 60m) as one aim of the study was to determine the appropriate height for the proposed new stack which, although of similar efflux velocity was of significantly larger diameter, meaning the efflux momentum (m^4s^{-2}) was approximately five times greater. The same set of meteorological data was used as for the WT dose estimation (Heathrow, 2007-2011, 07:00 to 15:00h each day). Table XI shows results at roof-top (maximum concentrations of the receptor points at roof level) for each case, for which Table XII gives the corresponding concentrations converted into effective dose. The maximum dose for the unclad case with existing stack parameters was estimated to be $22\mu\text{Svy}^{-1}$, reducing to $7.4\mu\text{Svy}^{-1}$ for a taller 58m stack and, with the higher efflux momentum for the new stack, reducing further to $13.3\mu\text{Svy}^{-1}$ and $4.9\mu\text{Svy}^{-1}$, respectively (Fig.6). Since ADMS did not calculate gamma cloud shine doses at elevated heights, the height of the effective ground plane for these calculations was taken as the roof of the EW building and the doses calculated from an effective stack height release above this level; i.e. with the stack effectively above a raised ground level. It can be seen that the near-field gamma shine doses are up to $6\mu\text{Svy}^{-1}$ for the ^{18}F source component and around half that for the ^{15}O component. The spread of results for ADMS is smaller than that from the wind tunnel: possible reasons for this are that ADMS does not account for local building effects (as it is based on a simple cuboid geometry building), and that only a limited number of stack heights was evaluated with ADMS; these topics are the subject of further investigation.

As ADMS is designed to calculate doses only on a ground plane, the method given in Gallacher *et al* (2016) was used to interpolate between (a) the raised ground plane approach used to estimate doses at roof level and (b) the true ground plane dose estimate based upon an elevated plume and a single effective building. In this way, the cloud gamma shine component was calculated at intermediate receptor heights further out from the EW roof zone, as required. Figure 7 shows the ground level maximum 8-hour average concentration from a daily release (the maximum occurred during 2011 from the 5 years studied) from the existing 53m tall stack with the unclad building. For the same conditions Figure 8 shows the cumulative annual gamma shine dose for 2011. From Table XIII predicted doses decrease rapidly with distance from the release location and annual values are generally below $1\mu\text{Svy}^{-1}$ off-site.

Table XIII shows maximum annual mean concentrations (over 5 years simulated) for ^{18}F and ^{15}O at a selection of receptor positions. The greatest daily 8-hour average concentrations are significantly larger than the corresponding mean values and both show a rapid decrease with distance from the source. Figure 9 shows corresponding annual doses (existing 53m stack, unclad building); the annual dose was $22\mu\text{Svy}^{-1}$ at EW roof-top, and below $1\mu\text{Svy}^{-1}$ off-site. Table XIV and Figure 10 provide an interesting comparison by showing the taller clad building

(53.4m), but with the proposed 58m stack with greater efflux momentum, at a range of locations. In the latter case the dose to a person on the roof would be reduced to below $10 \mu\text{Svy}^{-1}$ and doses to persons elsewhere on-site were estimated to be below $2 \mu\text{Svy}^{-1}$.

Tables XIII and XIV include details of the dose contributions from external gamma cloud shine, inhalation and skin beta exposure. These are dominated by gamma shine except at roof-top locations. The beta component contribution to effective dose is negligible everywhere. There is an interesting difference between the two cases at roof-top, where inhalation is the major component for the existing stack and the unclad building but makes only a minor contribution in the other case. This is a simple consequence of the stack heights relative to roof level, being 3m for the existing stack and building and 5m for the new stack and (3m taller) clad building. In the latter case, the plume passes overhead and workers are only exposed to its lower edge, whereas the lower plume from the existing stack leads to much greater inhalation exposure.

3.3 Summary of Model Results for the Roof-Top Location

A summary of the results of all the different methods for the EW roof top location, ranked in order of Table IV is presented in Table XV and Figure 11. The highest dose value of $2151 \mu\text{Svy}^{-1}$ was given by Model 4, which assumed a fully entrained emission in the RTS recirculation zone; a release of the daily fraction of the annual source term, repeated daily and with the wind always in the critical direction (i.e. a person always downwind on the building). The result decreased to $258 \mu\text{Svy}^{-1}$ when the full building height was used in the building wake calculation (Model 5), largely as a consequence of the increased recirculation-wake volume. A ground release, assuming the plume concentration peak downwind is equivalent to that attained in the region of the roof (Model 3), gave rise to an estimate of $1860 \mu\text{Svy}^{-1}$ under similar assumptions of short duration daily releases and always being downwind of the release. The static and moving hemisphere approximations (Models 1 and 2) gave rise to estimates of 1000 and $576 \mu\text{Svy}^{-1}$ respectively and represent models based on very pessimistic assumptions about plume entrainment and dispersion about the site in a very low wind velocity condition. Table XVI shows the corresponding doses to a one year old for models 1-9 in the roof top location. This approach is justified on two grounds: paediatric patients are treated in hospital buildings and the inhalation dose is a significant component of the effective dose (the EW air intakes are proximal to the plume concentration maximum for the main direction). These figures set an upper bound on the doses for those representative persons. In each case these are lower than the adult dose figures and show that the lower expected child inhalation rate offsets the greater SvBq^{-1} conversion factor applicable to this age. These child dose figures presented could be scaled down with occupancy factors, and roof shielding, as required, to achieve a more realistic effective dose for a child patient over an assumed course of treatment.

The other cluster of models in Table XV and Figure 11 comprises modelling approaches based on more realistic assumptions: fixed wind direction 53m stack ground level dose (Model 6), the EA spread-sheet model for a ground release (Model 8) at $15.4 \mu\text{Svy}^{-1}$ being reasonably close to the estimates from the WT of $39 \mu\text{Svy}^{-1}$ (Model 12, 53m stack, unclad) and $84 \mu\text{Svy}^{-1}$ (Model 13, 53m stack, clad). The taller 58m stack estimate from the WT gave rise to a dose of $11 \mu\text{Svy}^{-1}$ (Model 14, clad). ADMS Models 10 and 11 gave 22 and $9 \mu\text{Svy}^{-1}$ respectively.

There were two further outliers based on idealised source and building conditions that did not account for local complex effects. These were Model 7 (uniform wind rose, 53m isolated stack) and Model 9 (EA discharge model, 53m isolated stack). Both of these estimates can be discounted in terms of predictive value for roof workers in the complex flow and dispersion conditions caused by building effects and release in near proximity.

More detailed comparisons were made between ADMS and WT derived dose estimates by consideration of the variation in roof-top dose with stack height and building configuration. The comparison is shown in Figure 6. Differences range from about a factor of three to ten which is predicted of such a comparison (e.g. see Robins and McHugh, 2001). The wind tunnel results showed a maximum where the plume height corresponds to the receptor height. ADMS only uses a simple cuboid building which loses information from the full geometry and the flow field it creates. At short distances from the release the plume, although broadened by building generated turbulence, is still relatively narrow compared with its height above the surface. The differences between these methods i.e. wind tunnel and ADMS may be also partly due to differences in plume rise and building deflection. It is expected that a broadly equivalent maximum would be predicted by ADMS but calculations were not performed for the relevant stack heights and this is an items for ongoing investigation.

3.4 Summary of Model Results for the Distal Point at edge of site

Table XVII shows the results of models applied to receptor points downwind in the primary direction considered (345°). The wind tunnel models are referred to as 14a and 14b for the clad and unclad cases respectively: both apply for a 58m stack. These results are also shown in Figure 12. It can be seen that the WT and ADMS methods (11, 14a, 14b) converge to within a factor of two at the more distal points from the release point and are clustered together. The hemisphere and fixed wind ground release models (1, 2, 3) form another cluster with significantly larger doses by some orders of magnitude. The other cluster of elevated release, isolated stack models (6, 7, 9) are significantly lower in terms of dose than the WT and ADMS analyses.

3.5 Other Operational Radiation Monitoring Considerations

It may not be practicable to conduct air sampling measurements to support operational radiation protection for workers in the roof area. However, use of an electronic personal dosimeter (EPD) that responds to Personal Dose Equivalent $H_p(10)$ (ICRU,1992) could be used to estimate total effective dose to a worker with an appropriate scaling factor by scaling up the external dose to include the inhalation and beta immersion dose components and thus estimate the overall effective dose. In Table XVIII the total effective dose (from inhalation, gamma shine and positron skin irradiation) is presented as a ratio against the contribution from external gamma shine dose. The ratio differs depending on whether ^{18}F or ^{15}O is considered, being greater for ^{18}F because of the larger inhalation component. For ^{18}F , and in the roof top region, the scaling ratio estimated from ADMS methods indicates a value of approximately 1.9. For the wind tunnel at the plume concentration maximum the ratio could take a value of up to approximately 30, but a potential scaling factor between, or even outside, of these two factors (2 - 30) indicates a wide range of potential effective dose based on personal external radiation dosimeter readings alone. A factor at the lower end of the range might be appropriate for a roof top worker who may not be at PCM at all times, especially considering wind direction changes over the working day, but this requires substantiation.

By using an isotropic conversion factor (for photons of 511keV) to convert air kerma to effective dose of 0.675(ICRU,1998) and the ratio of $H_p(10)$ to kerma of at the same energy of 1.256(ICRU,1992), it may be shown that when converting from $H_p(10)$ to effective dose a multiplier of 0.537 should be used. The conversion factor from measured $H_p(10)$ with an EPD to effective dose for a roof worker might therefore, from the scaling factor range quoted above, be in the range 1.0-16: but this is a wide range and gives considerable uncertainty when being used for operational radiation protection purposes. Further work is being carried out using a

pair of gamma ‘plume shine’ detectors on the roof of the EW building, coupled with a digital anemometer mounted just above the roof, to provide more evidence in the real world case of the correlation of gamma doses with wind direction and to provide further evidence on the dose levels encountered in this zone.

4. Discussion

Models for calculating annual dose levels in complex urban conditions should take into account the source and the topographical and the meteorological conditions. None of the methods examined here fully meets this specification, though two come close and, in combination, can produce an adequate assessment. The two are wind tunnel modelling and ADMS. The former can include a detailed model of the site buildings and emission conditions but generally only covers a limited range of meteorological conditions, in particular atmospheric stability. The latter provides a comprehensive treatment of meteorology (5 years of hourly data were used here) but greatly simplifies the buildings to an effective building. The results from the distal point analysis for WT and ADMS ($R=175\text{m}$ and 218m , respectively), in the same primary wind sector, in a nearby park situated south east of the release point, provide some evidence for the convergence of these models further from the release point. More data is required to further support this hypothesis.

Other methods not examined here could also prove satisfactory; e.g. the use of another advanced atmospheric dispersion model in place of ADMS or computational fluid dynamics instead of the WT. Methods 1–9 in Table IV are much simpler approaches, or attempts to adapt a simple approach to complex conditions. Methods 1 and 2 have limited physical basis and are clearly inappropriate for predicting long term averages and have little value as estimators of extreme short-term doses because no probability of occurrence is recognised. Models 3 and 8 assume a ground level emission and can be adapted to give reasonably sensible estimates of roof-top exposure. Model 3 assumes steady meteorological conditions and, as a result, predicts very large dose levels, whereas model 8 takes better account of meteorological variability and provides a result that is consistent with the ADMS and WT results. However, it is obvious that neither approach can be applied to the wider problem of the whole site. Models 6, 7 and 9 are dispersion models for an isolated stack and, not surprisingly, predict by far the lowest dose levels. Methods of this kind can be adapted to provide dose levels downwind by replacing the actual source height by an effective height that accounts partially for the effects of the buildings, but this is somewhat arbitrary and has not been attempted here. Finally, there are the building wake models, 4 and 5. These assume that the emission is fully entrained into the recirculation region that forms around the building and implicitly assume that the receptor is also within that region. The volume of the recirculation region is a key parameter in such modelling and this largely explains the differences in the results given by the two methods. Given the location of the stack, the assumption of full entrainment is inappropriate as only a fraction of the emission will, in practice, enter the recirculation region, the remainder passing over or around it. ADMS models this process explicitly, if somewhat simply, and it is a key feature of the wind tunnel simulation.

Models 1-14 lead to a very wide variation of results ranging from $2151\mu\text{Svy}^{-1}$ to $0.062\mu\text{Svy}^{-1}$ (Table XV). Of the models shown in Figure 11, models 10, 12 and 13 give results in the range 22 to $84\mu\text{Svy}^{-1}$ for the existing stack configuration of 53m height, and models 11 and 14 approximately $10\mu\text{Svy}^{-1}$ for the taller proposed 58m stack. Both ranges are reasonably consistent with model 8 which gave a result of $15\mu\text{Svy}^{-1}$.

There is evidence from the WT simulation that, all other factors being equal, doses are increased in the near field of the EW roof by the introduction of the glass cladding layer (for the current stack height) which changes the air flow patterns around that building. It is postulated that the WT may provide the better estimate of roof-top doses because the measurements were carried out with accurate models of the unclad and clad buildings, in a surrounding environment of buildings that match the actual site. It is interesting to note that the ADMS simulation and the EA model (with ground release conditions) gave rise to effective dose figures that were comparable within an order of magnitude with the figures derived from the wind tunnel analysis. This is to be expected for ADMS, as already noted, but must be regarded as fortuitous for the EA model because that model (as applied in this case) is based on a ground release that does not match the conditions under consideration; i.e. at roof-top level on a building.

5. Conclusion

The results indicate that the models that took into account the presence of nearby buildings and realistic meteorological conditions appeared to give convergent results that agreed within an order of magnitude of each other. This gives some confidence as to the robustness of the estimates when being used for an assessment of doses to representative persons in a radiological assessment: a factor of two to three appears to be indicated from these results.

The doses to representative adults at the different locations around the site (as per Table XIII, under the assumptions already specified) are generally well below the $20\mu\text{Svy}^{-1}$ threshold above which further abatement of emissions may be sought (EA, 2012) and were lower for the infant representative persons included in the assessment. The dose levels assessed in this study relate to the full discharge of the site permitted source term over the course of a year as a continuous discharge. Some of the simpler models do make assumptions about downwind fixed wind direction conditions, but the more robust models i.e. wind tunnel and ADMS take into account the direction and wind velocity from reasonably local data.

There is evidence from the WT simulation that the addition of the cladding to the EW building does affect the representative person doses to persons working on the roof of that building. Furthermore the presence of air intakes proximal to the concentration maximum on the roof indicates that for the primary wind direction in the study the doses to persons inside the EW building may be a significant fraction of the dose assessed for the roof area. If the WT estimates are taken as the most reliable estimates the $39\mu\text{Svy}^{-1}$ representative person dose level for the current 53m stack could potentially increase to $84\mu\text{Svy}^{-1}$ on completion of the cladding works, if discharges were occurring at the full site permitted level. The proposed taller 58m stack, with greater efflux momentum, would reduce the representative person doses (including those to persons inside the EW building) to approximately $10\mu\text{Svy}^{-1}$ i.e. to below the range of regulatory scrutiny (EA, 2012). It would therefore be an effective measure to reduce representative person doses to persons in the near-field of the stack and was therefore specified for installation on-site.

Acknowledgements

With special thanks to Phil Halsted in the Mechanical Engineering section of the Medical Physics Department, Guy's and St. Thomas' NHS Foundation Trust, for the construction of the model for use in the wind tunnel experiments.

References

ASHRAE 2007, Building Air Intake and Exhaust Design, Chapter 44, *ASHRAE Applications Handbook*, Atlanta: American Society of Heating, Refrigeration and Air-Conditioning Engineers, Inc. Atlanta, GA.

ASHRAE 2011, Building Air Intake and Exhaust Design, Chapter 45, *ASHRAE Applications Handbook*, Atlanta: American Society of Heating, Refrigeration and Air-Conditioning Engineers, Inc. Atlanta, GA.

Burt, A., Robins, A.G., Hayden, P., 2012, 'Flow and Dispersion of Radioactive Tracers at St. Thomas' Hospital', MEng Thesis, Faculty of Engineering and Physical Sciences, University of Surrey

Cambridge Environmental Research Consultants (CERC), 2012a, P20/01M/12, http://www.cerc.co.uk/environmental-software/assets/data/doc_techspeg/CERC_ADMS5_P20_01.pdf, last accessed 10/07/2014

CERC, 2012b, http://www.cerc.co.uk/environmental-software/assets/data/doc_techspeg/CERC_ADMS5_P17_11.pdf, accessed 04/03/2016

CERC, 2012c, 'Dispersion Modelling of radioactive emissions at St. Thomas' Hospital', CERC, Cambridge

Chavez, M, Hajra, B., Stathopolous, T., Bahloul, 2011, A., Near-field pollutant dispersion in the build environment by CFD and wind tunnel simulations, *Journal of Wind Engineering and Industrial Aerodynamics*, 99, 330-339

Clarke, R.H., et al, A Model for Short and Medium Range Dispersion of Radionuclides Released to the Atmosphere, 1979, NRPB R-91, Chilton, UK

Decay Data Evaluation Project (DDEP), Laboratoire National Henri Becquerel, http://www.nucleide.org/DDEP_WG/DDEPdata.htm, last accessed 10/07/2014

Delacroix, D, Guerre, JP, Leblanc, P, Hickman, C., 2002, Radionuclide and Radiation Protection Data Handbook 2002, *Radiation Protection Dosimetry*, 98(1)

Eckerman, KF, Ryman, JC, *External Exposure to Radionuclides in Air, Water and Soil*, Federal Guidance Report No.12, EPA-402-R-93-081, 1993

EnFlo, 2016, Meteorological Wind Tunnel, www.surrey.ac.uk/mes/research/fluids/enflo

Environmental Permitting Regulations (England and Wales), 2010, SI2010/675

Environmental Permitting (Amendment) Regulations, 2011, SI2011/

Environment Agency, 2006a, *Initial radiological assessment methodology – part 2 methods and input data*, Science Report SC030162/SR2, (Bristol, Environment Agency), <https://publications.environment-agency.gov.uk>

Environment Agency, 2006b, *Initial radiological assessment methodology – part 1 user report*, Science Report SC030162/SR1, (Bristol, Environment Agency), <https://publications.environment-agency.gov.uk>

Environment Agency, 2010, *RSR permitting – prospective radiological assessments for human health and wildlife (habitats)*, Operational Instruction 338_04, Version 6, <https://publications.environment-agency.gov.uk>

Environment Agency/SEPA/NIEA/FSA/HPA, 2012, *Principles for the assessment of prospective public doses arising from Authorised Discharges of Radioactive Waste to the Environment*, (Cumbria, Environment Agency), <https://publications.environment-agency.gov.uk/ms/EPSSyx>

Fackrell, JE, Robins, AG, 1982, Concentration fluctuations and fluxes in plumes from point sources in a turbulent boundary layer, *Journal of Fluid Mechanics* 117, 1-26

Gallacher, DJ, Robins, AG, Hayden, P, 2016, Conversion of wind tunnel simulated radioactive pollutant gas concentrations for a complex building array into radiation dose, In Preparation, *Journal of Radiological Protection*

GE Healthcare, 2012, PETtrace 800 series site planning guide, Direction 2102960-100

Hajra, B., Stathopoulos, T., Bahloul, A., 2010, Assessment of pollutant dispersion from rooftop stacks: ASHRAE, ADMS and wind tunnel simulation, *Building and Environment* 45(2010) 2768-2777

Hajra, B., Stathopoulos, T., 2012, A wind tunnel study on the effects of downstream buildings on near-field pollutant dispersion, *Building and Environment* 52(2012): 19-31

Hajra, B., Stathopoulos, T., Bahloul, A., 2013, A wind tunnel study on the effects of adjacent buildings on near-field pollutant dispersion from rooftop emissions in an urban environment, *Journal of Wind Engineering and Industrial Aerodynamics* 119(2013) 133-145

Hajra, B., Stathopoulos, T., Bahloul, A., 2014, Performance of ASHRAE models in assessing pollutant dispersion from rooftop emissions, *HVAC&R Research* (2014) 20, 72-79

ICRP, 1994, Publication 68, Dose coefficients for intakes of Radionuclides by Workers, *Annals of the ICRP* Vol.24/4, Elsevier

ICRP, 1996, Publication 72, Age-dependent doses to the members of the public from intake of radionuclides: Part 5, compilation of ingestion and inhalation coefficients, *Annals of the ICRP* Vol.26/1, Elsevier

ICRP, 2008, Radiation Dose to Patients from Radiopharmaceuticals – Addendum 3 to ICRP Publication 53, ICRP Publication 106, *Annals of the ICRP* Vol. 38(1-2), Elsevier

ICRU, 1992, Measurement of Dose Equivalents from External Photon and Electron Radiations, ICRU Report 47, Bethesda, Maryland, US

ICRU, 1998, Conversion coefficients for use in radiological protection against external radiation, ICRU Report 57, Bethesda, Maryland, US

Ionising Radiations Regulations 1999, SI1999/3232

Jones HA, 1983, Models to Allow for the Effects of Coastal Sites, Plume Rise and Buildings on Dispersion of Radionuclides and Guidance on the Value of Deposition Velocity and Washout Coefficients, NRPB Report R-157, Chilton, Didcot, Oxon

MacDonnell, C., 2004, Radiological Assessments for small users, NRPB W-63, Chilton, UK

Nicholson, KW, The Dispersion, Deposition and Resuspension of Atmospheric Contamination in the Outdoor Urban Environment, in *Airborne Radioactive Contamination in Inhabited Areas*, Ed. Anderson, KG, Radioactivity in the Environment, Vol.15, Elsevier, 2009

Pilkingsrud, HV, Gels, GL, 1985, An evaluation of the external radiation exposure dosimetry and calculation of maximum permissible concentration values for airborne materials containing ^{18}F , ^{15}O , ^{13}N , ^{11}C and ^{133}Xe , *Health Physics* 49(5), 805-824

Raza, S, Avila, R, 2005, Calculation of immersion doses from external exposure to a plume of radioactive material, *Health Physics*, 89(3): 247-254

Robins, A.G, MacDonald, R., 2001, Review of Flow and Dispersion in the Vicinity of Groups of Buildings, Annexe B, Atmospheric Dispersion Modelling Liaison Committee, Annual Report 1998/99, NRPB R-322, Chilton

Robins, AG, McHugh, C, 2001, Development and Evaluation of the ADMS Building Effects Module. *Int. J. Environment and Pollution*, 16, 1-6, 161-174

Thompson, JM, Poston, JW, 1999, Absorbed Dose from Traversing Spherically Symmetric, Gaussian Radioactive Clouds, *Health Physics*, 76(6): 639-643

Wood, CR, Lacser, A, Barlow, JF, Padhra, A, Belcher, SE, Nemitz, E, Helfter, C, Famulari, D, Grimmond, CSB, 2010, Turbulent flow at 190m height above London during 2006-2008: a climatology and the applicability of similarity theory, *Boundary Layer Meteorology*, 137:77-96

Figure 1. Guy's and St Thomas' East Wing cladding scheme showing the glass cladding envelope around the original T-shaped building

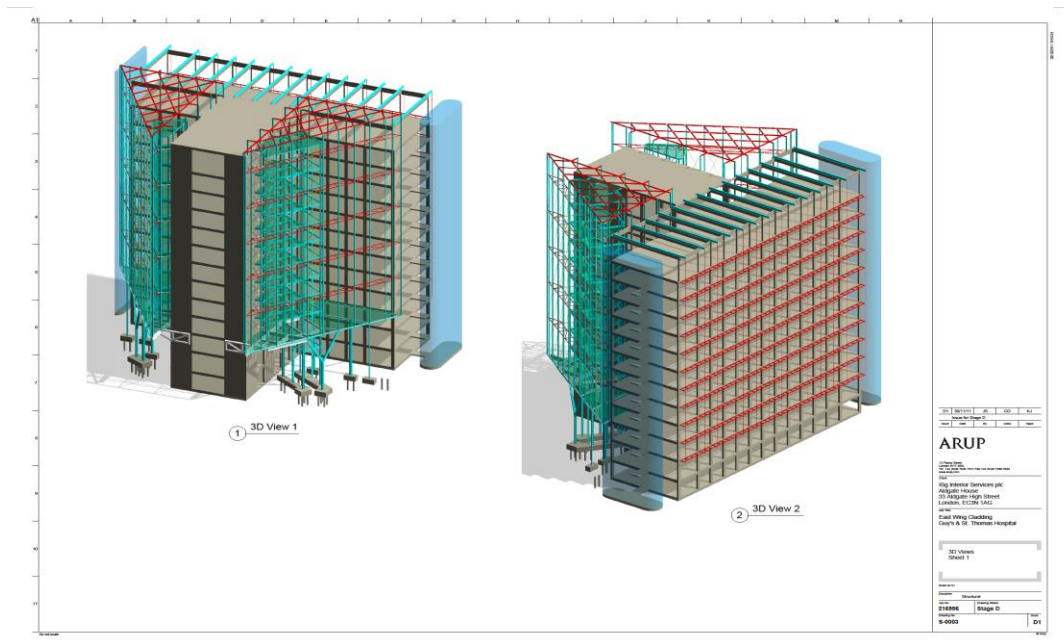


Image by ARUP/Hopkins and ISG PLC

Figure 2. EW Plan view: possible positions for the replacement flue stack (#1 modelled in this study)

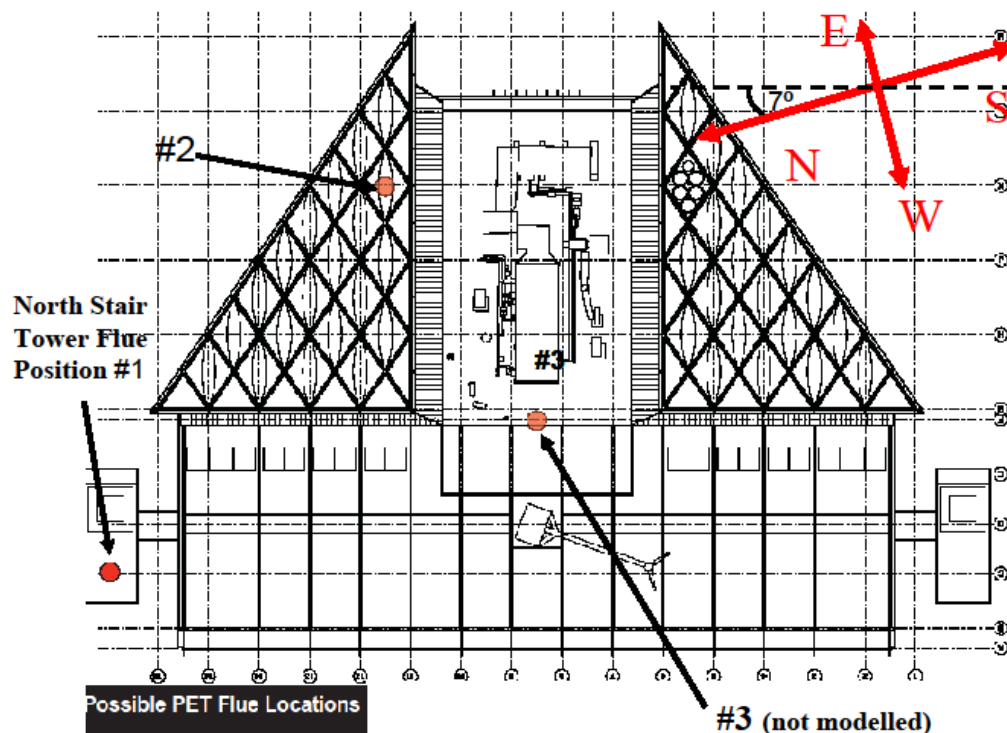


Image by ARUP/Hopkins and ISG PLC, with additional annotation by the authors

Figure 3. Points selected from 3-D mapping for ADMS analysis

Sampling points on the EW were of particular relevance to contract workers on the Cladding Project.

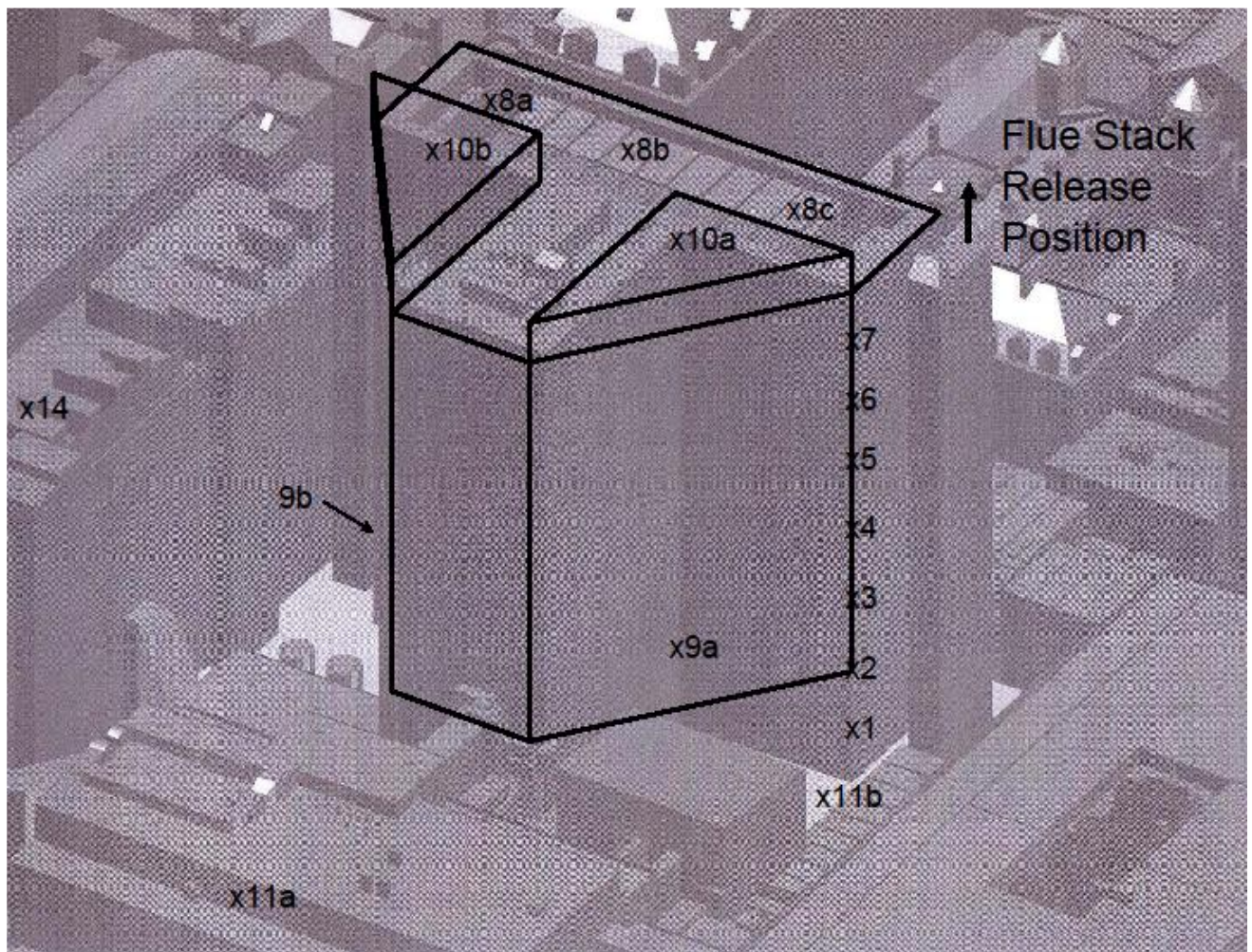


Figure 4. Receptor points for ADMS dose analysis

Sampling points were located at critical positions on-site and off-site at adjacent hotels, offices and accommodation blocks (r24a in SE sector was chosen for the edge of site analysis)

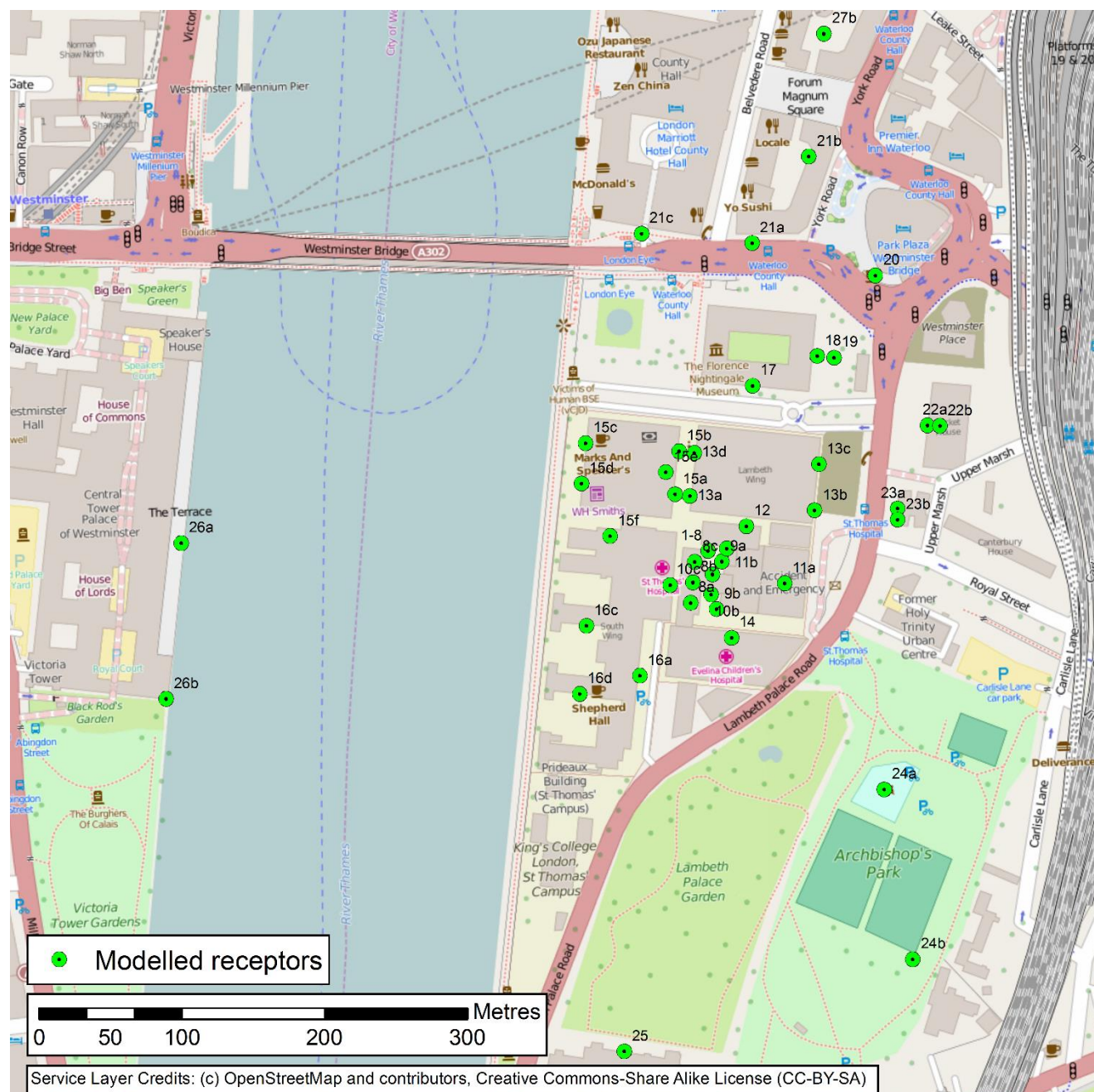


Figure 5. Effective dose contributions at the roof concentration maximum point derived from wind tunnel dispersion data for different building configurations and release heights taking into account the weighting for wind direction probability

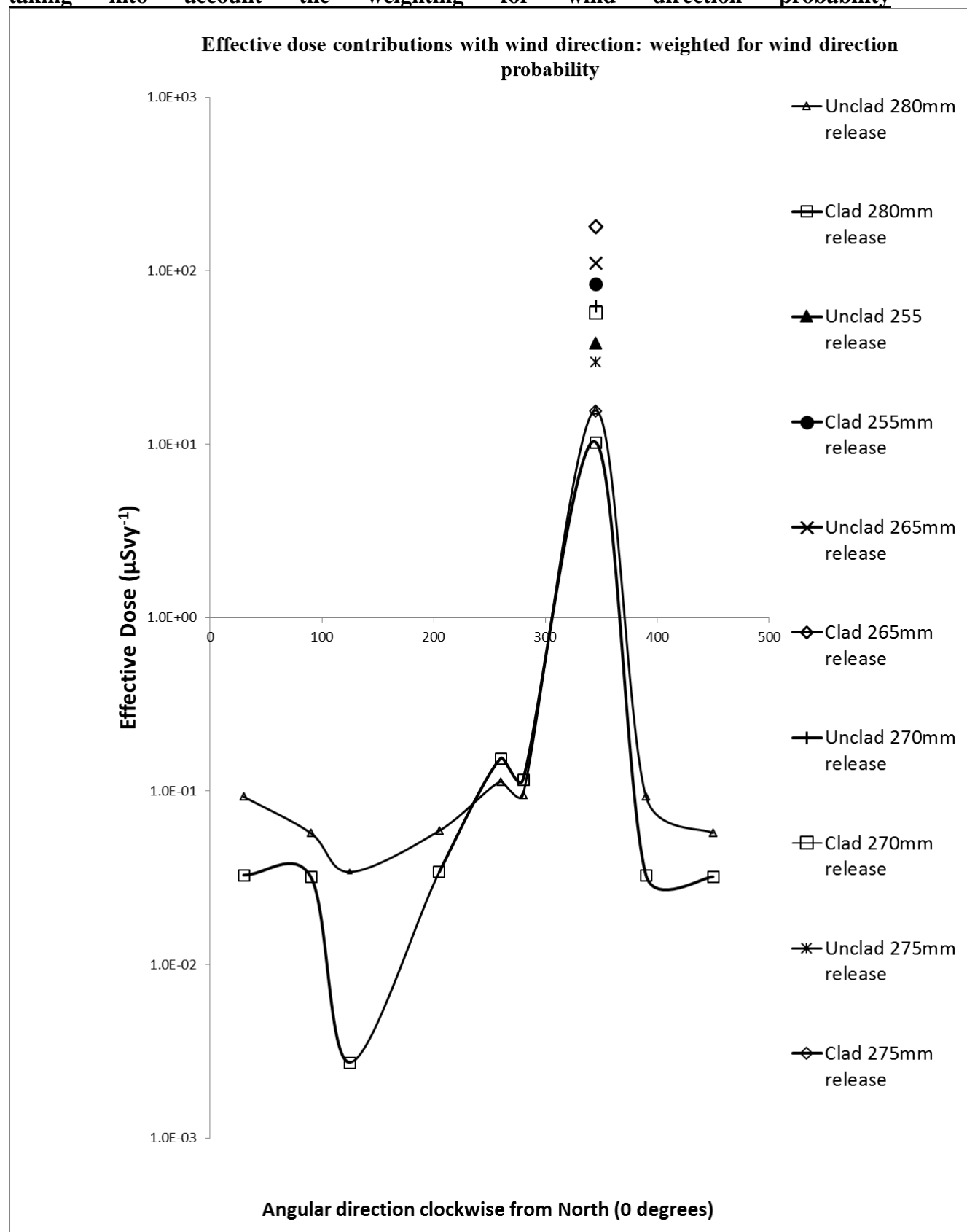


Figure 6. Comparison of predicted effective dose (gamma shine, inhalation, positron skin irradiation) at point of measured roof maximum concentration from ADMS and wind tunnel; weighted for all wind directions; clad building with new stack and unclad building with existing stack; stack heights 53-60m

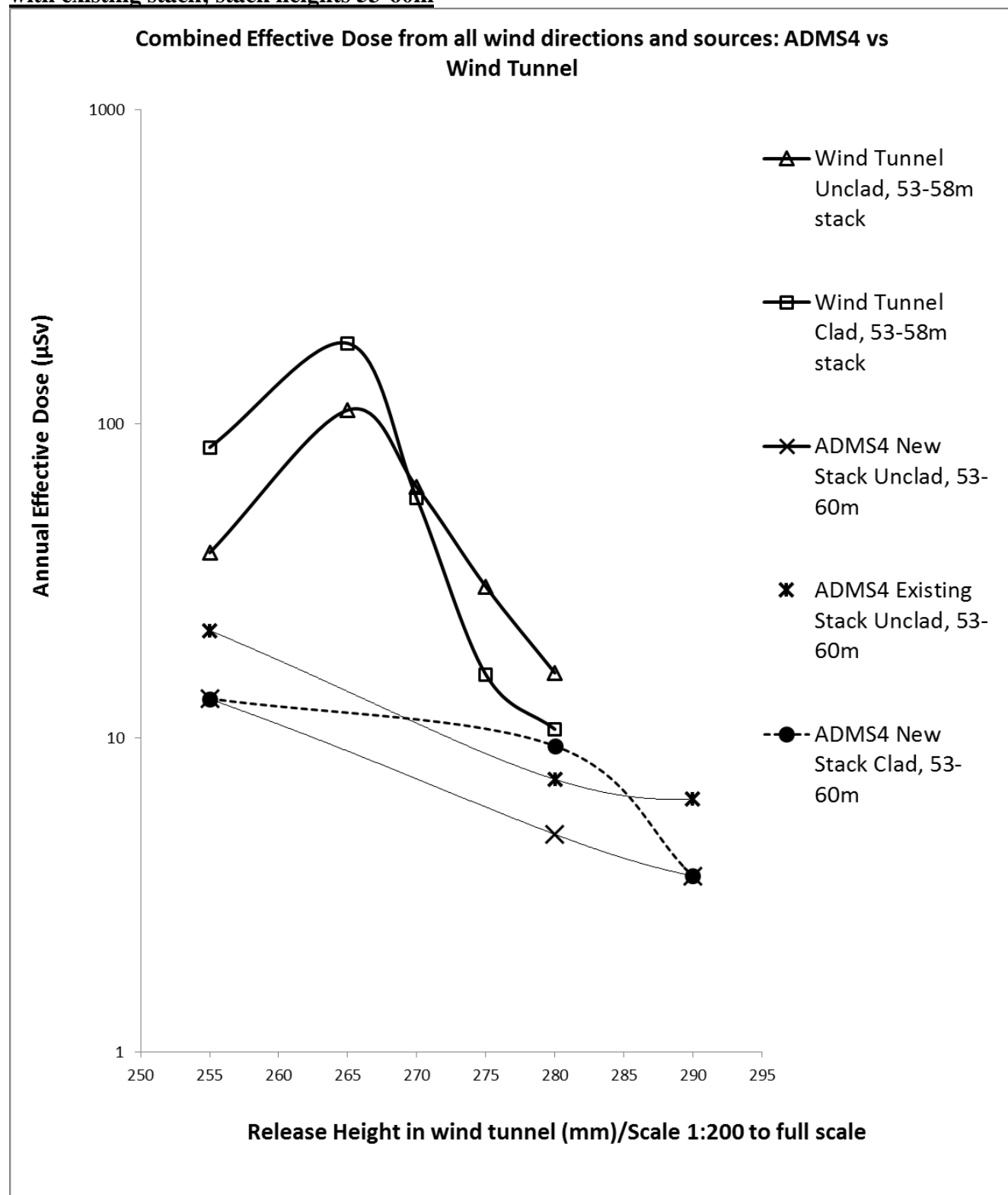


Figure 7. ADMS prediction of maximum 8 hour concentration values at ground level ($Bq\cdot m^{-3}$) for ADMS scenario#1 (existing stack of 53m height, exit diameter 0.354m, unclad building of height 50m). This is the highest concentration average over one 8 hour day and occurred during the 2011 meteorological data set

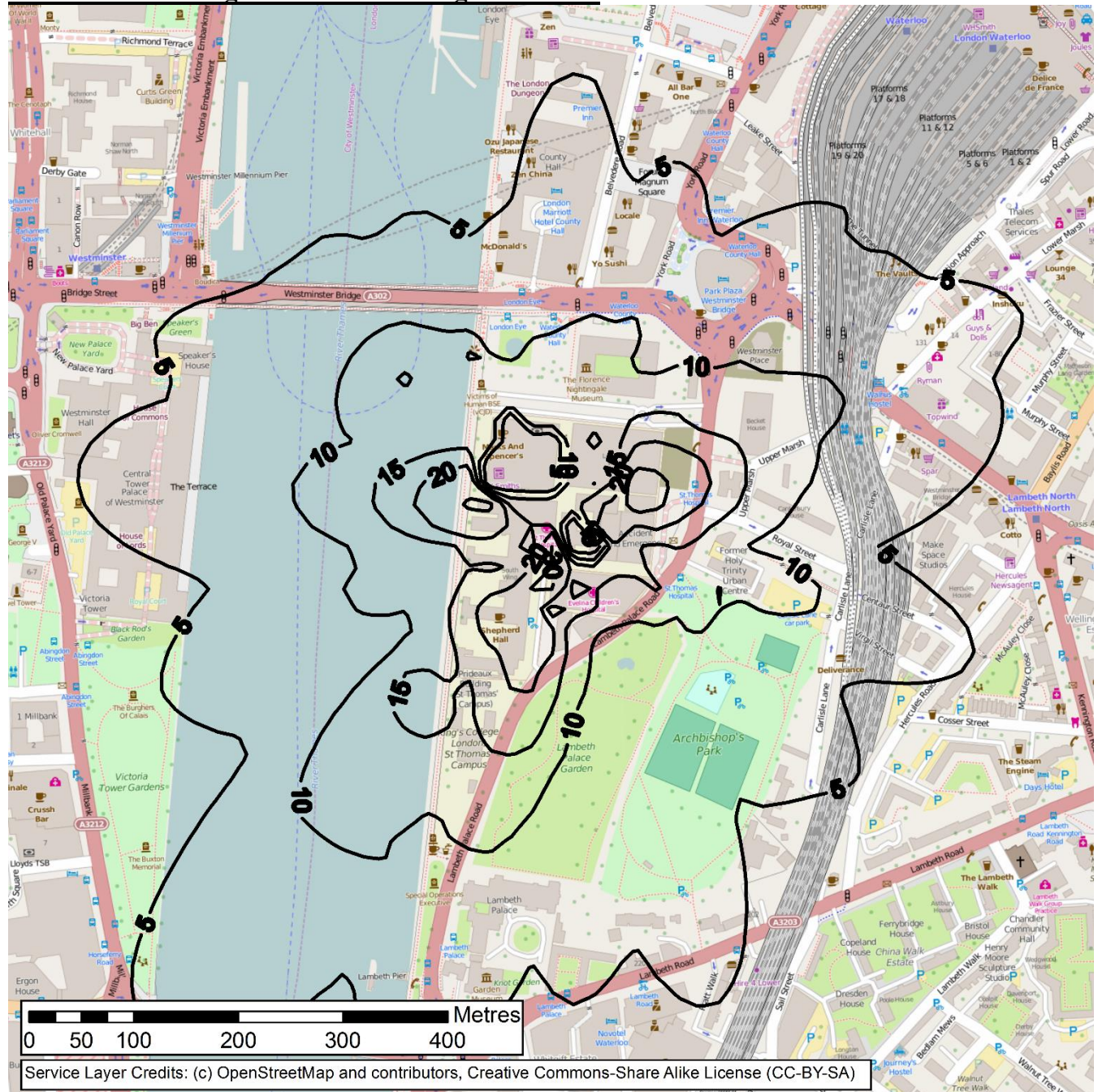


Figure 8. ADMS predictions of annual accumulated gamma dose at the ground plane ($\mu\text{Sv.y}^{-1}$) for ADMS scenario#1 (existing stack of 53m height, exit diameter 0.354m, unclad building of height 50m, 2011 data)

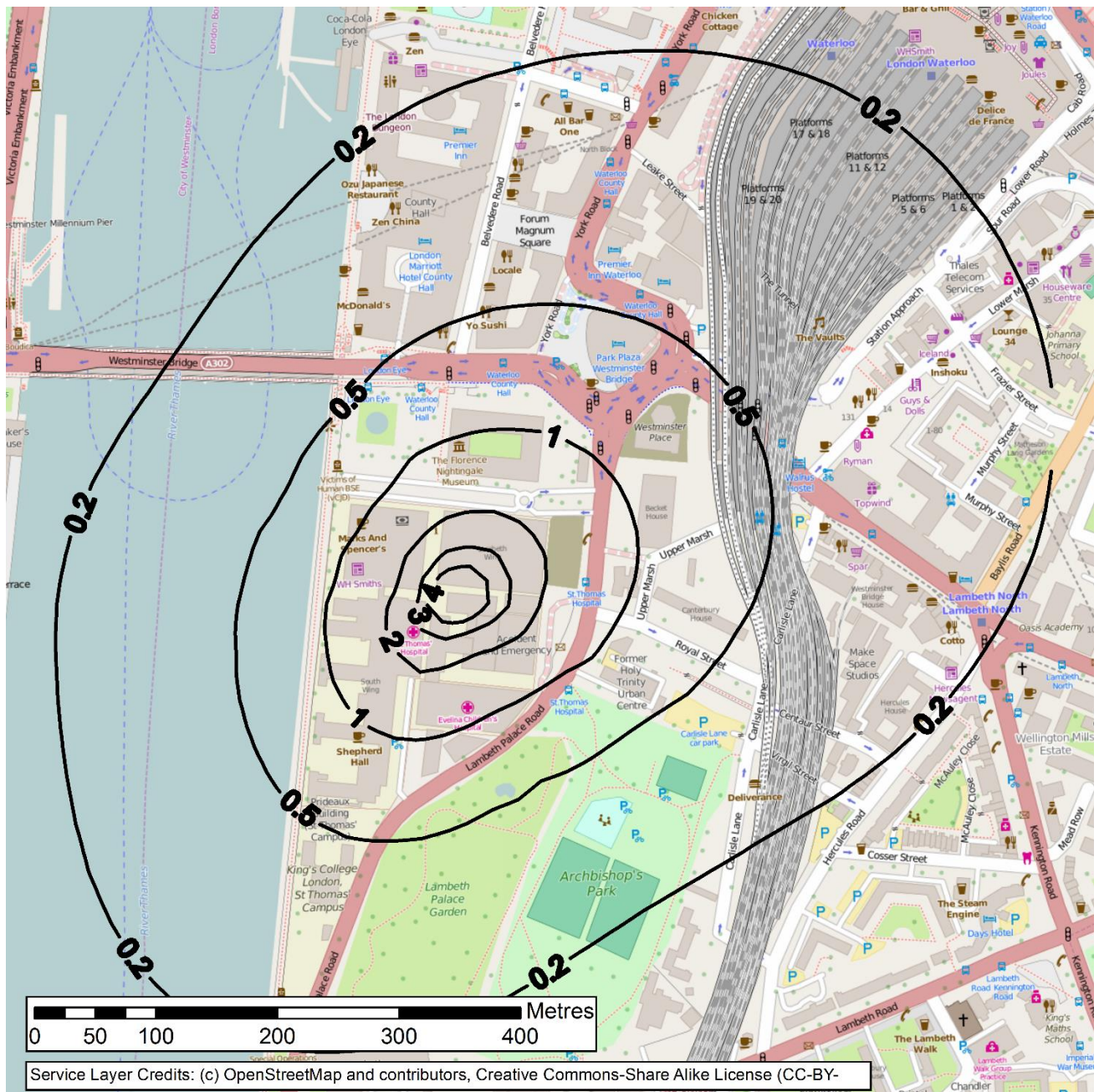


Figure 9. Effective doses estimated from ADMS scenario 1 data on air concentration figures and cloud gamma shine: existing 53m stack with lower efflux momentum and unclad 50m building height (Table XIII); simulation was using 5 years of meteorological data (2007-2011) between 07:00-15:00 daily; source term has been assumed continuous uniform discharge to average over the wind direction and velocity conditions

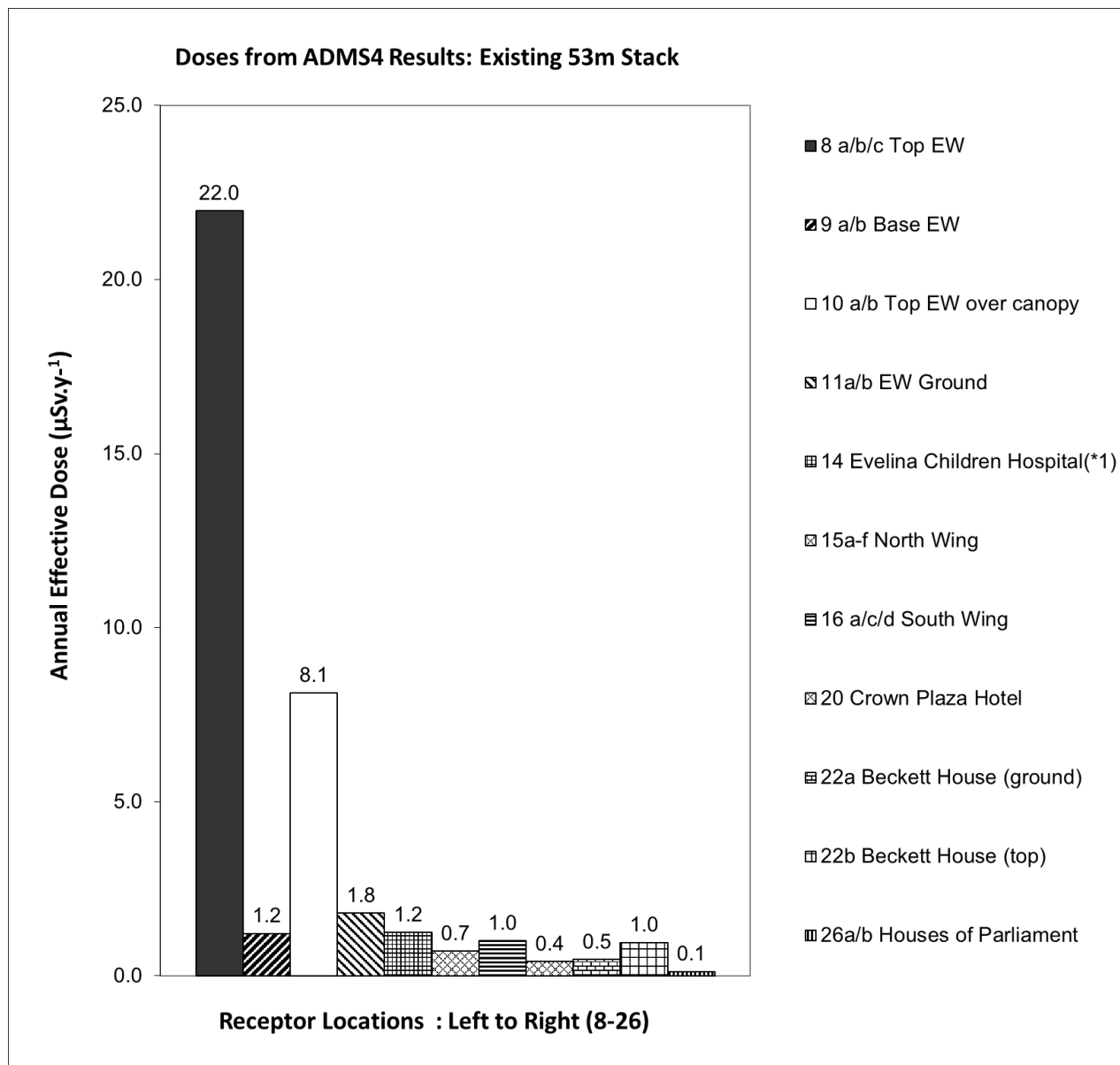
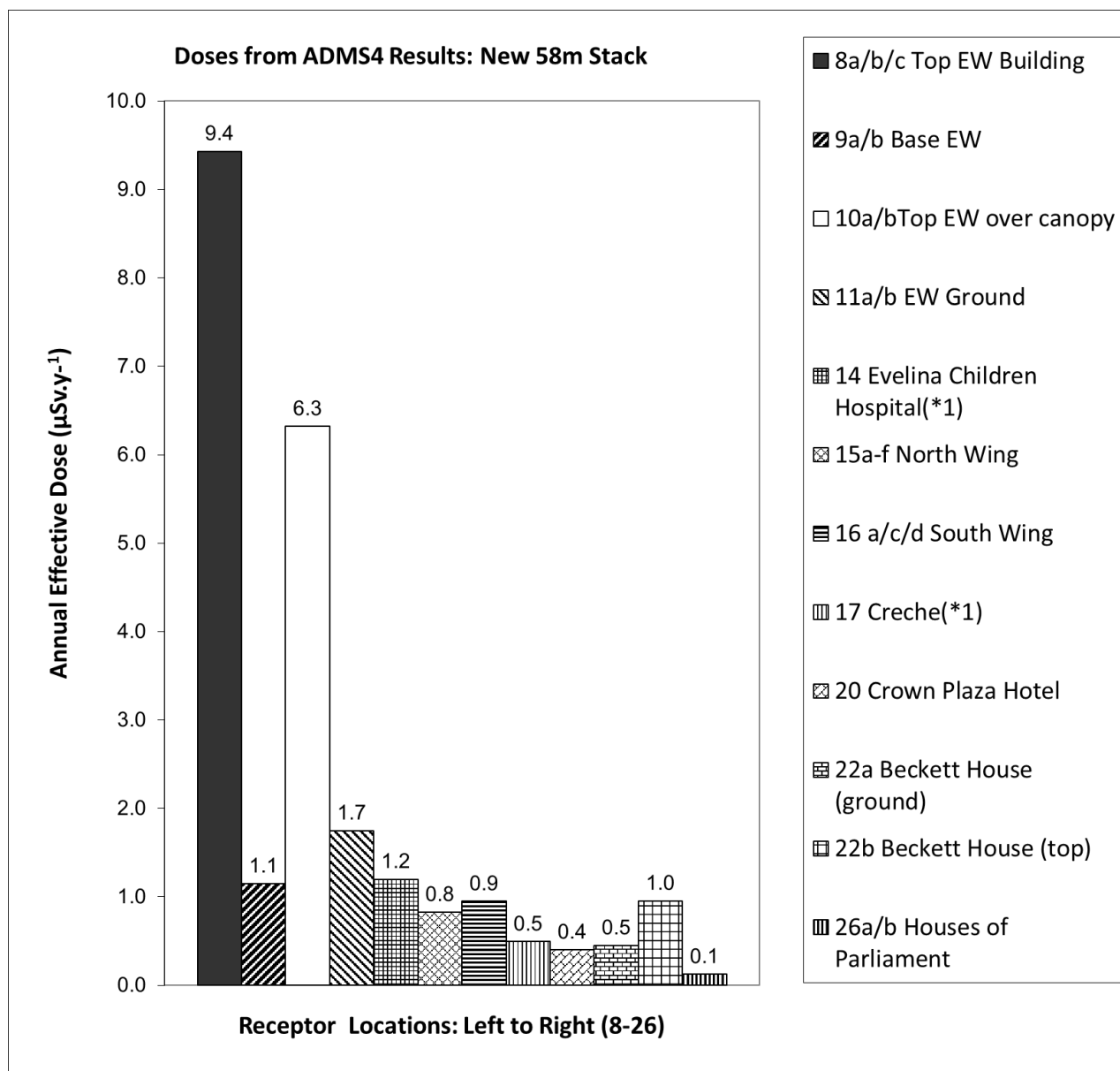


Figure 10. Effective doses estimated from ADMS Scenario 7 data on air concentration figures and cloud gamma shine: new recommended stack height of 58m with higher efflux momentum and clad 53.4m building height (Table XIV); simulation was using 5 years of meteorological data (2007-2011) between 07:00-15:00 daily; source term has been assumed continuous uniform discharge to average over the wind direction and velocity conditions



Annual Effective Doses from different modelling approaches Nos.1-14

Method	Dose ($\mu\text{Sv}\cdot\text{y}^{-1}$)
1	1000
2	576
3	1860
4	2151
5	258
6	2.79
7	0.0624
8	15.4
9	0.066
10	22.0
11	9.4
12	38.9
13	84.1 (+/-90% error bars)
14	10.7

Figure 12. Comparison of predictions of effective doses at distal point at edge of site (ADMS r24a): a range of radiation dose modelling approaches and model parameters for a uniform release source term

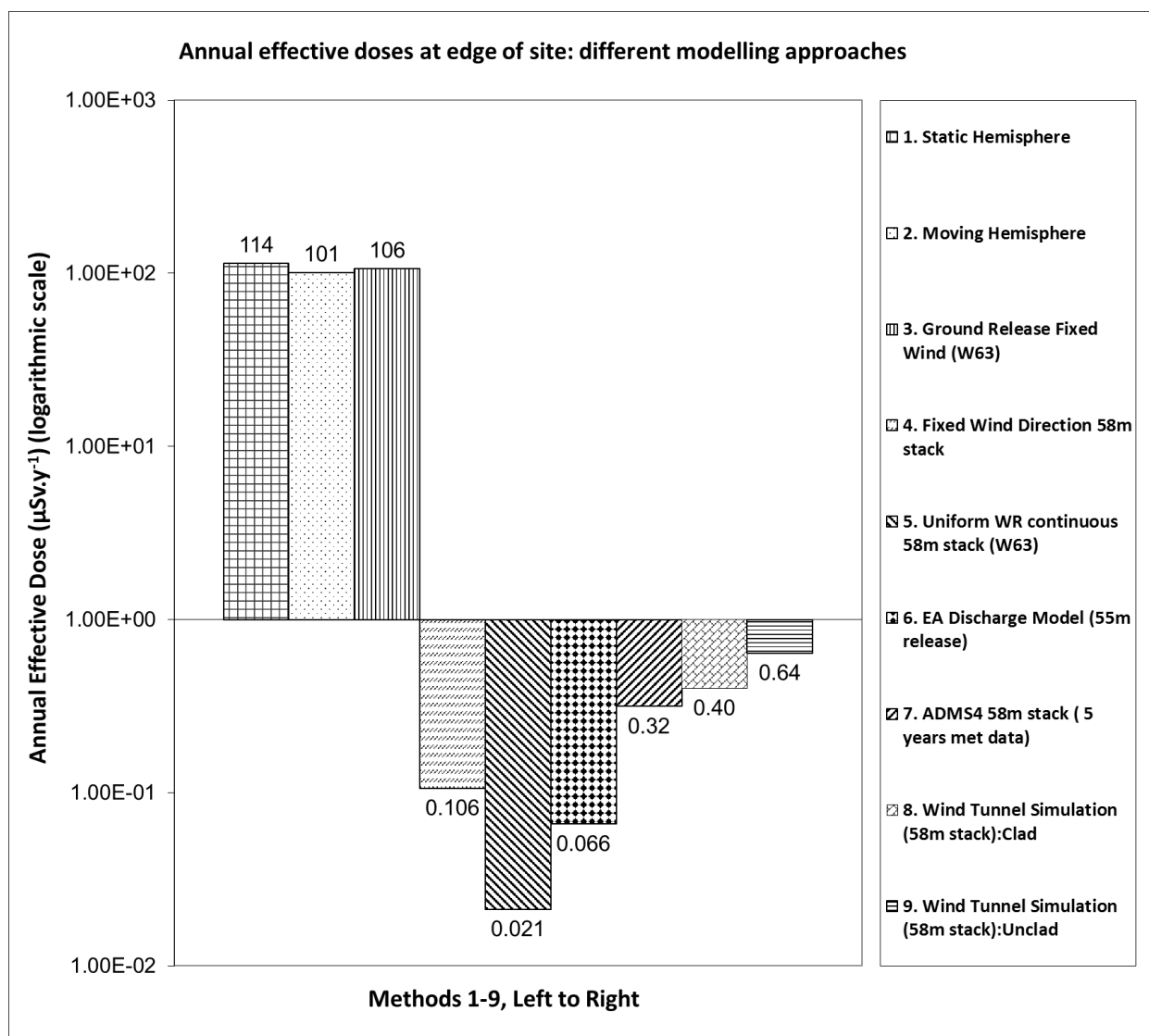


Table I. Physical constants and parameters used in modelling

Parameter/Constant Name	Value	Source
¹⁸ F: Infant Inhalation Coefficient (1 year old) D _{inh}	3.10x10 ⁻¹⁰ Sv/Bq	ICRP72
¹⁵ O: Infant Inhalation(*1) Coefficient (1 year old) D _{inh}	7.70x10 ⁻¹² Sv/Bq	ICRP106
¹⁸ F: Adult Inhalation Coefficient D _{inh}	5.90x10 ⁻¹¹ Sv/Bq	ICRP72
¹⁵ O: Adult Inhalation(*1) Coefficient D _{inh}	1.10x10 ⁻¹² Sv/Bq	ICRP106
Infant Breathing Rate (m ³ h ⁻¹)	0.22 m ³ h ⁻¹	ICRP72 (one year old)
Adult Breathing Rate (m ³ h ⁻¹)	1.20 m ³ h ⁻¹	ICRP 72 (light work)
Positron Yield of Radionuclide: ¹⁸ F	0.9686	DDEP
Positron Yield of Radionuclide: ¹⁵ O	0.9989	DDEP
Mean Beta Energy: ¹⁸ F	0.2493 MeV	DDEP
Mean Beta Energy: ¹⁵ O	0.7368 MeV	DDEP
F-18 half life	1.8288(3) h	DDEP
O-15 half life	2.041(6) mins	DDEP
Annihilation Gamma Energy	0.511 MeV	DDEP

(*1) ¹⁵O: there is no D_{inh} for ¹⁵O specified in ICRP72, instead we have used the coefficient from intravenous injection of ¹⁵O₂ in the form of water (ICRP106). Given the short residence time in the lungs of the order of 11s this approximation can be justified.

Table II. Model specific parameters used in the modelling

Existing Stack Height	53m	Site drawings
Existing Building Height (East Wing Roof)	50.0 m	Site drawings
Proposed New Clad Building Height (East Wing Roof)	53.4 m	Site Proposal Drawings
Hemisphere Radius	75m (175m for the edge of site analysis)	Cautious Estimate
Hemisphere Volume	883,573 m ³ (R=75m)	2/3πr ³
Discharge duration	8 hours (continuous)	Clinical PET Centre
Occupancy Infant (in creche or Evelina Children's Hospital-ECH)	100% duration during daily release periods over one year	Site Information
Wind Speed (Moving) Hemisphere Model	0.02 ms ⁻¹	Cautious Estimate
Wind Speed (Building Wake Model)	3.24ms ⁻¹	Heathrow Wind Rose Data

Table III Source term: pro-rata annual discharge limit figures

Radionuclide Group	Annual Limit GBq	Pro-Rata Discharge MBq	Daily Release Rate ^(*) (Bqs ⁻¹)	Constant
¹⁸ F ^(*)	3000	12,000	4.17 x 10 ⁵	
¹⁵ O	1600	6,400	2.22 x 10 ⁵	

(*) Site Permit includes grouped radionuclides ¹³N and ¹¹C. Since these have lower dose coefficients per Bq the source term for this group has been taken to be completely ¹⁸F.

(*) Assumes uniform discharge over 8 hour working days (07:00-15:00) for 250 working days per annum

Table IV. Dose assessment methods

Model Number	Basis	Wind Direction	Representative Person Adult	Representative Person Child	¹⁵ O Decay Correction Applied
1	Static Hemisphere	Downwind	Yes	Yes	Yes
2	Moving Hemisphere	Downwind	Yes	Yes	Yes
3	Ground Release Fixed Wind (W63)	Downwind	Yes	Yes	No
4	Building Wake Recirculation Model (3m height)	Downwind	Yes	Yes	No
5	Building Wake Model (50m height)	Downwind	Yes	Yes	No
6	Fixed Wind Direction 53m stack	Downwind	Yes	Yes	No
7	Continuous 53m stack (W63 method) at 55% Pasquill D	Uniform Wind Rose	Yes	Yes	No
8	EA Discharge Model (0m release)	Uniform Wind Rose	Yes	Yes	No
9	EA Discharge Model (55m release)	Uniform Wind Rose	Yes	Yes	No
10	ADMS: Scenario 1; 53m stack (5 years met. data)	5 years met data	Yes	Yes	Yes
11	ADMS: Scenario 7; 58m new stack (5 years met. data)	5 years met data	Yes	Yes	Yes
12	Wind Tunnel Simulation (Stack 53m): Unclad	5 years met data	Yes	No	No
13	Wind Tunnel Simulation (Stack 53m): Clad	5 years met data	Yes	No	No
14	Wind Tunnel Simulation (Stack height 58m): Clad	5 years met data	Yes	No	No**

** - except for edge of site receptor point R=175m

Table V. Wind directions used in wind tunnel studies and associated sector sizes

Status	Bearing (degrees)	Lower Half Sector (LL)	Upper Half Sector (UL)	Range (UL+LL)	Rounded Sector Margins	Rounded Sector Margin	Zone	Annual Probability	SD	U _{wm} (ms ⁻¹)	SD (ms ⁻¹)
Secondary	30	22.5	30	52.5	20	50	1	0.125	0.009	3.106	0.175
Secondary	90	30	17.5	47.5	60	100	2	0.084	0.004	3.245	0.101
Secondary	125	17.5	40	57.5	110	160	3	0.075	0.004	3.507	0.172
Secondary	205	40	27.5	67.5	170	230	4	0.277	0.008	4.679	0.168
Secondary	260	27.5	10	37.5	240	260	5	0.160	0.010	4.716	0.212
Secondary	280	10	32.5	42.5	270	310	6	0.165	0.005	3.262	0.125
Primary*	345	32.5	22.5	55	320	10	7	0.114	0.006	2.745	0.157
Total	--	--	--	360	--	--	ALL	1.000	---	---	---

*- primary direction is where the plume is blowing directly over the roof from the source

Table VI. Dose calculation from wind tunnel simulations: annual effective dose at the point of maximum concentration at EW roof level; clad and unclad cases; wind direction 345°

Building	Release	Full Scale Release Height (*2)	$C_{\text{plume}}^{(*)1}$ (s.m ⁻³)	¹⁸ F Doses				¹⁵ O Doses				TOTAL (μSv.y ⁻¹)
				E _{ext} (μSv.y ⁻¹)	E _{inh} (μSv.y ⁻¹)	E _{beta} (μSv.y ⁻¹)	Sub-Total (μSv.y ⁻¹)	E _{ext} (μSv.y ⁻¹)	E _{inh} (μSv.y ⁻¹)	E _{beta} (μSv.y ⁻¹)	Sub-Total (μSv.y ⁻¹)	
(Y/N)	(mm)	(m)		(F-18)	(F-18)	(F-18)	(F-18)	(O-15)	(O-15)	(O-15)	(O-15)	(ALL)
Y	255	53	1.339E-03	176.9	449	3.6	630	97.3	4.5	5.7	107	737
Y	265	55	7.882E-04	104.2	1382	11.2	1498	57.3	13.7	17.6	89	1586
Y	270	56	1.643E-04	21.7	458	3.7	484	11.9	4.6	5.9	22	506
Y	275	57	1.979E-05	2.6	128	1.0	132	1.4	1.3	1.6	4	136
Y	280	58	1.142E-05	1.5	85	0.7	87	0.8	0.8	1.1	3	90
N	255	53	2.597E-04	34.3	256	2.1	292	18.9	2.5	3.3	25	317
N	265	55	7.600E-04	100.4	769	6.2	876	55.2	7.6	9.8	73	949
N	270	56	1.377E-04	18.2	485	3.9	507	10.0	4.8	6.2	21	528
N	275	57	3.548E-05	4.7	227	1.8	234	2.6	2.3	2.9	8	241
N	280	58	1.413E-05	1.9	110	0.9	112	1.0	1.1	1.4	4	116

(*1) C_{plume} is the air concentration in Bqm⁻³ per unit release rate Bq.s⁻¹.

(*2) Full scale release heights differ from equivalent heights at wind tunnel scaling (1:200) due to a 2 metre datum offset for the EW building.

Table VII. Contributions to the effective dose at the point of maximum recorded concentration at roof-top: release height at 280mm in wind tunnel (full size 58m)

Run Data	Annual effective doses with the wind blowing 100% in the direction indicated over one full year with full source term						Doses weighted for wind direction: annual effective doses						
Bearing	¹⁸ F	¹⁵ O	Total (μSv)	¹⁸ F	¹⁵ O	Total (μSv)	Sector	¹⁸ F	¹⁵ O	Total (μSv)	¹⁸ F	¹⁵ O	Total (μSv)
(degrees)	Un-Clad	Un-Clad	Un-Clad	Clad	Clad	Clad	Probability	Un-Clad	Un-Clad	Un-Clad	Clad	Clad	Clad
30	0.479	0.263	0.742	0.169	0.093	0.262	0.125	0.060	0.033	0.093	0.021	0.012	0.033
90	0.440	0.242	0.682	0.246	0.135	0.382	0.084	0.037	0.020	0.057	0.021	0.011	0.032
125	0.295	0.162	0.457	0.023	0.013	0.036	0.075	0.022	0.012	0.034	0.002	0.001	0.003
205	0.138	0.076	0.213	0.080	0.044	0.123	0.277	0.038	0.021	0.059	0.022	0.012	0.034
260	0.457	0.251	0.709	0.623	0.343	0.965	0.160	0.073	0.040	0.114	0.100	0.055	0.155
280	0.374	0.206	0.580	0.457	0.252	0.709	0.165	0.062	0.034	0.096	0.075	0.041	0.117
345 (other locations*1)	14.11	7.76	21.88	0.313	0.172	0.485	0.114	1.602	0.881	2.484	0.036	0.020	0.055
345 (main run)	112.47	3.52	115.98	87.32	2.763	90.08	0.114	12.769	0.339	13.169	9.914	0.314	10.23
345 (sub-total)	126.6	11.28	137.9	87.6	2.94	90.6	0.114	14.37	1.28	15.65	9.95	0.33	10.28
Sum(*2)	128.8	12.5	141.2	89.2	3.8	93.0	1.000	14.7	1.44	16.1	10.2	0.47	10.7

(*1) – ‘other locations’ refers to the gamma shine received from the downwind plume once it has moved away from the roof zone. No dose from beta immersion or inhalation is added for these locations

(*2) – the sum presented in columns 9-14 represents the expected dose received. The sum presented in columns 2 – 7 is presented for reference, but is not realisable as these figures must be weighted by the wind direction probability in order not to over-estimate the total dose received from all directions.

Table VIII. Estimated effective dose at roof-top based on wind tunnel data for clad and unclad building cases for the primary wind direction only; annual averages obtained by applying wind direction probability factor for 345 at the concentration maximum point

Run Data			Doses weighted for wind direction: annual Effective Doses from the primary wind direction listed						
Bearing	Release Height	Full Scale Release Height	Applied Sector	¹⁸ F	¹⁵ O	Total* (μSv)	¹⁸ F	¹⁵ O	Total* (μSv)
(degrees)	(mm)	(m)	Probability	Un-Clad	Un-Clad	Un-Clad	Clad	Clad	Clad
345	255	53	0.114	33.1	2.8	38.4	71.5	12.2	83.8
345	265	55	0.114	99.5	8.3	110.2	170.0	10.1	180.2
345	270	56	0.114	57.5	2.4	62.4	54.9	2.5	57.5
345	275	57	0.114	26.5	0.9	29.9	15.0	0.5	15.5
345	280	58	0.114	12.8	0.4	15.7	9.9	0.3	10.3

*- the total figure includes a small additional gamma shine contribution from sampled volumes away from the roof top zone

Table IX. Summary of wind tunnel results: combined annual effective dose at roof maximum concentration point from all directions allowing for wind direction probability and weighted velocity in each sector

Wind Tunnel Release Height (mm)	Full Scale Release Height (m)	Total Effective Dose (μSv) Un-Clad	Total Effective Dose (μSv) Clad
255	53	38.9	84.1
265	55	110.6	180.5
270	56	62.9	57.9
275	57	30.3	15.9
280	58	16.1	10.7

Table X. Summary of ADMS run parameters sets: scenarios 1-10

Modelling Scenario	Stack Height (m)	Stack Diameter (m)	Efflux Velocity (ms ⁻¹)	Exhaust Flow Rate (m ³ s ⁻¹)	Building Height (m)	Clad
ting	4	3	0			
ting	4	3	0			
ting	4	3	0			
ting	4	3	0			
			0			
			0			
			0			
			0			

Table XI. ADMS results for air concentration values in roof zone (location 8; 5 years of meteorological data, 2007-2011)

ADMS Scenario (from Table X)	Stack	Clad (Y/N)	Stack Height	Full Scale Release Height	Annual Concentration (highest year in 5 years period) ¹⁸ F	Mean concentration (averaged over a single 8h period) ¹⁸ F	Maximum daily concentration (averaged over a single 8h period) ¹⁵ O	Annual Concentration (highest year in 5 years period) ¹⁵ O	Mean (highest concentration over a single 8h period) ¹⁵ O	Maximum daily concentration (averaged over a single 8h period) ¹⁵ O
			(mm)	(m)	(Bq.m ⁻³)	(Bq.m ⁻³)	(Bq.m ⁻³)	(Bq.m ⁻³)	(Bq.m ⁻³)	(Bq.m ⁻³)
1	Existing	N	255	53	89.27	3022.7	46.67			1590.1
5	Existing	N	280	58	6.58	259.1	3.33			130.7
8	Existing	N	290	60	3.5	176.6	1.76			84.5
2	New	N	255	53	48.59	1479.9	25.47			778.3
6	New	N	280	58	3.31	111.6	1.68			54.4
9	New	N	290	60	2.04	77.3	1.01			37.7
3	Existing	Y	255	53	89.17	3022.1	46.61			1589.8
4	New	Y	255	53	48.58	1481.5	25.46			779.5
7	New	Y	280	58	3.31	111.6	1.68			54.4
10	New	Y	290	60	2.04	77.3	1.01			37.7

Table XII. ADMS results for air concentration values converted to effective dose on roof (location 8, 5 years of meteorological data, 2007-2011)

ADMS Scenario (from Table X)	Stack	Clad (Y/N)	Stack Height	Full Scale Release Height	E _{ext}	E _{inh}	E _{beta}	Sub- Total	E _{ext}	E _{inh}	E _{beta}	Sub- Total	OVERALL TOTAL
			(mm)	(m)	¹⁸ F	¹⁸ F	¹⁸ F	(μSv.y ⁻¹) ¹⁸ F	¹⁵ O	¹⁵ O	¹⁵ O	(μSv.y ⁻¹) ¹⁵ O	(μSv.y ⁻¹) ALL
1	Existing	N	255	53	5.96	12.64	0.099	18.70	2.99	0.12	0.158	3.27	22.0
5	Existing	N	280	58	4.27	0.93	0.007	5.21	2.15	0.01	0.011	2.17	7.4
8	Existing	N	290	60	3.92	0.50	0.004	4.42	1.97	0.00	0.006	1.98	6.4
2	New	N	255	53	4.13	6.88	0.054	11.06	2.08	0.07	0.086	2.23	13.3
6	New	N	280	58	2.96	0.47	0.004	3.43	1.49	0.00	0.006	1.50	4.9
9	New	N	290	60	2.23	0.29	0.002	2.52	1.11	0.00	0.003	1.12	3.6
3	Existing	Y	255	53	5.96	12.63	0.099	18.69	2.99	0.12	0.158	3.27	22.0
4	New	Y	255	53	4.13	6.88	0.054	11.06	2.08	0.07	0.086	2.23	13.3
7	New	Y	280	58	5.94	0.47	0.004	6.41	2.99	0.00	0.006	3.00	9.4
10	New	Y	290	60	2.23	0.29	0.002	2.52	1.11	0.00	0.003	1.12	3.6

Table XIII. Summary of ADMS simulation results for air concentration converted to annual effective dose: scenario 1; existing stack, 53m tall, unclad building, range of site locations given

ADMS Run scenario = 1			Building Height=50m		Stack Parameters = Existing										
Location (Figures 3, 4)	Description	Measured	Mean	Max.	Mean	Max.	¹⁸ F				¹⁵ O				ALL
		Conc.(*2)	Conc.(*2)	8h conc.	Conc.(*2)	8h conc.	E _{ext}	E _{inh}	E _{beta}	Total	E _{ext}	E _{inh}	E _{beta}	Total	TOTAL
		Height (m)	¹⁸ F (Bqm ⁻³)	¹⁸ F (Bqm ⁻³)	¹⁵ O (Bqm ⁻³)	¹⁵ O (Bqm ⁻³)	(μSv.y ⁻¹)				(μSv.y ⁻¹)				(μSv.y ⁻¹)
8	Top EW (a,b,c)	55	89.27	3022.7	46.67	1590.1	5.96	12.64	0.099	18.70	2.99	0.12	0.158	3.27	22.0
9	Base EW (a,b)	5	1.2	30.6	0.62	16	0.70	0.17	0.001	0.87	0.34	0.00	0.002	0.34	1.2
10	Top EW over canopy (a,b)	53.5	14.32	502.6	7.28	260.3	4.08	2.03	0.016	6.12	1.96	0.02	0.025	2.00	8.1
11	EW Ground	14	0.93	28.7	0.48	14.9	1.12	0.13	0.001	1.25	0.55	0.00	0.002	0.55	1.8
14	ECH(*1)	34	0.82	27.8	0.38	10.6	0.79	0.11	0.001	0.90	0.34	0.00	0.001	0.34	1.2
15	North Wing	4	0.29	17.6	1.76	119.2	0.44	0.04	0.000	0.48	0.21	0.00	0.006	0.22	0.7
16	South Wing (a,c,d)	35	1.06	40.3	0.49	15.4	0.60	0.15	0.001	0.75	0.25	0.00	0.002	0.25	1.0
17	Creche(*1)	5	0.63	24.3	0.29	7.4	0.31	0.08	0.001	0.39	0.13	0.00	0.001	0.13	0.5
20	Crown Plaza Hotel	5	0.43	16.7	0.18	5.3	0.25	0.06	0.000	0.32	0.09	0.00	0.001	0.10	0.4
22a	Beckett House (ground)	2	0.57	14.4	0.25	4.7	0.28	0.08	0.001	0.36	0.11	0.00	0.001	0.11	0.5
22b	Beckett House (top)	44	0.53	17.5	0.22	6.4	0.64	0.08	0.001	0.71	0.25	0.00	0.001	0.25	1.0
26	Houses of Parliament (a,b)	0	0.09	8.7	0.03	1.9	0.09	0.01	0.000	0.10	0.02	0.00	0.000	0.02	0.1

(*1) Use infant 1y.o. coefficients for the Evelina Children's Hospital location and the site creche

(*2) Highest concentration annual mean value over 5 years of meteorological data shown

Table XIV. ADMS Simulation Results for air concentration converted to annual effective dose: scenario 7; new stack, 58m tall, clad building, range of site locations given

Location (see Figs 3, 4, Table XIII)	Meas. Height (m)	Mean	Max.	Mean	Max.	¹⁸ F				¹⁵ O				TOTALS (μSv.y ⁻¹)
		Conc. (*2) ¹⁸ F (Bqm ⁻³)	8h conc. ¹⁸ F (Bqm ⁻³)	Conc. (*2) ¹⁵ O (Bqm ⁻³)	8h conc. ¹⁵ O (Bqm ⁻³)	E _{ext}	E _{inh}	E _{beta}	Total (μSv.y ⁻¹)	E _{ext}	E _{inh}	E _{beta}	Total (μSv.y ⁻¹)	
8	55	3.31	111.6	1.68	54.4	5.96	0.47	0.004	6.43	2.99	0.00	0.006	3.00	9.4
9	5	0.72	17.6	0.37	8.8	0.70	0.10	0.001	0.81	0.34	0.00	0.001	0.34	1.1
10	53.5	1.93	66.5	0.96	33.4	4.08	0.27	0.002	4.36	1.96	0.00	0.003	1.97	6.3
11	14	0.58	17.6	0.3	9.2	1.12	0.08	0.001	1.20	0.55	0.00	0.001	0.55	1.7
14(*1)	34	0.48	16.4	0.22	6.5	0.79	0.06	0.001	0.86	0.34	0.00	0.001	0.34	1.2
15	4	1.17	50.1	0.58	25.3	0.44	0.17	0.001	0.61	0.21	0.00	0.002	0.22	0.8
16	35	0.66	23.9	0.29	8	0.60	0.09	0.001	0.70	0.25	0.00	0.001	0.25	0.9
17(*1)	5	0.39	17.9	0.18	5.9	0.31	0.05	0.000	0.36	0.13	0.00	0.001	0.13	0.5
20	5	0.37	9.8	0.15	3.3	0.25	0.05	0.000	0.31	0.09	0.00	0.001	0.10	0.4
22a	2	0.45	8.4	0.19	3.3	0.28	0.06	0.000	0.34	0.11	0.00	0.001	0.11	0.5
22b	44	0.49	14.5	0.21	5.7	0.64	0.07	0.001	0.71	0.25	0.00	0.001	0.25	1.0
26	0	0.08	6.4	0.02	1.6	0.09	0.01	0.000	0.10	0.02	0.00	0.000	0.02	0.1

(*1) Use infant 1year old coefficients

(*2) Highest annual mean concentration value over 5 years of meteorological data shown

Table XV. Comparison of modelling approaches for roof top doses: adult representative person subject

Model Number	Receptor Location	Release Height	C _{plume}	¹⁸ F				¹⁵ O				ALL
				E _{ext}	E _{inh}	E _{beta}	Total	E _{ext}	E _{inh}	E _{beta}	Total	TOTAL
				(Table IV)								
		(m)	(s.m ⁻³)				(μSv.y ⁻¹)				(μSv.y ⁻¹)	(μSv.y ⁻¹)
1	Hemisphere	53	1.02E-02	387.2	603.7	4.7	996	4.2	0.1	0.2	4.4	1000
2	Hemisphere	53	5.87E-03	222.1	346.3	2.7	571	4.2	0.1	0.2	4.4	576
3	Downwind PCM	0	7.000E-03	925.2	413.0	3.2	1341	508.8	4.1	5.3	518.2	1860
4	Recirculation zone	3	8.096E-03	1070	477.6	3.7	1551	588.5	4.7	6.1	599.3	2151
5	Recirculation zone	50	9.715E-04	128.4	57.3	0.4	186	70.6	0.6	0.7	71.9	258
6	Downwind PCM	53	1.050E-05	1.4	0.6	0.0	2	0.8	0.0	0.0	0.8	2.8
7	PCM/Uniform WR	53	2.350E-07	0.0311	0.0139	0.0001	0.0450	0.0171	0.0001	0.0002	0.0174	0.062
8	PCM/Uniform WR	0	n/a				12				3.4	15.4
9	PCM/Uniform WR	55	n/a				0.052				0.014	0.066
10	ADMS r8 (maximum)	53	2.14E-04	5.96	12.6	0.10	18.7	2.99	0.12	0.16	3.3	22.0
11	ADMS r8 (maximum)	58	7.94E-06	5.96	0.47	0.00	6.43	2.99	0.00	0.01	3.0	9.4
12	Rooftop PCM	53	2.597E-04				35.04				3.8	38.9
13	Rooftop PCM	53	1.339E-03				71.78				12.3	84.1
14	Rooftop PCM	58	1.142E-05				10. 19				0.4	10.7

Table XVI. Comparison of modelling approaches: 1 year old child subject (models 1-9)^(*1)

Model Number (Table IV)	Description of method used	Receptor Location	Release Height (m)	C _{plume} (s.m ⁻³)	¹⁸ F			¹⁵ O				GRAND	
					E _{ext}	E _{inh}	E _{beta}	Total (μSv.y ⁻¹)	E _{ext}	E _{inh}	E _{beta}	Total (μSv.y ⁻¹)	TOTAL (μSv.y ⁻¹) (ALL)
1	Static Hemisphere	Hemisphere	53	1.02E-02	387.2	573.6	4.7	966	4.2	0.1	0.2	4	970
2	Moving Hemisphere	Hemisphere	53	5.87E-03	222.1	329.0	2.7	554	4.2	0.1	0.2	4	558
3	Ground Release Fixed Wind (W63)	Downwind PCM	0	7.000E-03	925.2	392.4	3.2	1321	508.8	5.2	5.3	519	1840
4	Building Wake Model (3m height)	Recirculation zone	3	8.096E-03	1070	453.8	3.7	1528	588.5	6.0	6.1	601	2128
5	Building Wake Model (50m height)	Recirculation zone	50	9.715E-04	128.4	54.5	0.4	183	70.6	0.7	0.7	72	255
6	Fixed Wind Direction 53m stack	Downwind PCM	53	1.050E-05	1.4	0.6	0.0	2	0.8	0.0	0.0	0.8	2.8
7	W-63 method (55% Pasquill D)	PCM/Uniform WR	53	2.350E-07	0.0	0.0	0.0	0	0.0	0.0	0.0	0	0.062
8	EA Discharge Model (0m release)	PCM/Uniform WR	0	n/a				12				3.4	15.4
9	EA Discharge Model (55m release)	PCM/Uniform WR	55	n/a				0.052				0.014	0.066

(*1) See Table XIII for ADMS child representative person doses

Table XVII. Comparison of modelling approaches: receptor point at edge of site

Model (Table IV)	Receptor Location	Release Height (m)	Cplume (s.m ⁻³)	Eext(*) (μSv/y) (F-18)	Einh (μSv/y) (F-18)	Ebeta (μSv/y) (F-18)	Total (μSv/y) (F-18)	Eext(*) (μSv/y) (O-15)	Einh (μSv/y) (O-15)	Ebeta (μSv/y) (O-15)	Total (μSv/y) (O-15)	TOTAL (μSv/y) (ALL)
1	Hemisphere	58	8.05E-04	65.5	47.5	0.4	113	0.7	0.0	0.0	0.7	114
2	Hemisphere	58	7.12E-04	57.9	42.0	0.3	100	0.7	0.0	0.0	0.7	101
3	WTPCM	0	4.000E-04	52.9	23.6	0.2	77	29.1	0.2	0.3	29.6	106
6	WTPCM	58	4.000E-07	0.053	0.024	0.0002	0.077	0.029	0.0002	0.0003	0.030	0.106
7	WTPCM	58	8.000E-08	0.0106	0.0047	0.0000	0.0153	0.0058	0.0000	0.0001	0.0059	0.021
9	PCM/Uniform WR	55	n/a				0.052				0.014	0.066
11	ADMS r24a	58	6.48E-07	0.21	0.038	0.0003	0.25	0.069	0.0002	0.0003	0.070	0.32
14a	WTPCM	58	1.425E-06				0.35				0.05	0.40
14b	WTPCM	58	3.245E-06				0.56				0.08	0.64

14a – clad case, 14b – unclad case; WTPCM= wind tunnel distal point at edge of site; ADMS r24a is closest point to distal WTPCM point

Table XVIII Comparison of modelling approaches: total effective dose ratio to external gamma cloud shine

Model (Table IV)	Description	¹⁸ F: E _{tot} /E _{ext}		¹⁵ O: E _{tot} /E _{ext}	
		Mean	±SD	Mean	±SD
#1-#2	Hemisphere models	2.571	--	1.064	--
#3-#7	Simple Gaussian plume models	1.450	--	1.018	--
#10-#11	ADMS roof-top models (various stack/building heights)	1.85	0.93	1.037	0.041
#12-14	Wind tunnel cases (existing stack/building clad and unclad)	30.4	22.2	2.20	0.91
#15	ADMS all doses on-site (adult)	1.27	0.41	1.014	0.025

(*) a multiplier of 0.537 must be applied to these figures to establish a conversion factor from measured *Hp(10)* to effective dose.

Appendix 15.6: Paper 2

'This is the Accepted Manuscript version of an article accepted for publication in Journal of Radiological Protection. IOP Publishing Ltd is not responsible for any errors or omissions in this version of the manuscript or any version derived from it. The Version of Record is available online at <https://doi.org/10.1088/0952-4746/36/4/785>'

CONVERSION OF SIMULATED RADIOACTIVE POLLUTANT GAS CONCENTRATIONS FOR A COMPLEX BUILDING ARRAY INTO RADIATION DOSE

DJ Gallacher¹, AG Robins², P Hayden²

1-Medical Physics Department, Guy's and St. Thomas' NHS Foundation Trust

2- Enflo, Faculty of Engineering and Physical Sciences, University of Surrey

E-mail: david.gallacher@gstt.nhs.uk

Abstract

Methods used to convert wind tunnel and ADMS concentration field data for a complex building array into effective radiation dose were developed based on simulations of a site in central London. Pollutant source terms were from positron emitting gases released from a cyclotron and clinical PET radiotracer facility. Five years of meteorological data were analysed to determine the probability distribution of wind direction and speed. A hemispherical plume cloud model (both static and moving) was developed which enabled an expression of gamma-ray dose, taking into account build-up factors in air, in terms of analytic functions in this geometry. The standard building wake model is presented, but this is extended and developed in a new model to cover the concentration field in the vicinity of a roof top structure recirculation zone, which is then related to the concentration in the main building wake zone. For all models presented the effective dose was determined from inhalation, positron cloud immersion and gamma ray plume contributions. Results of applying these models for determination of radiation dose for a particular site are presented elsewhere.

1. Introduction

The use of wind tunnel (WT) modelling to simulate dispersion of pollutant gases around buildings is an established technique to determine likely concentrations and environmental exposures (Robins and Castro, 1977a, 1977b, Robins and MacDonald, 2001, Hajra *et al*, 2010, Hajra and Stathopoulos 2012, Hajra *et al*, 2013, 2014, Chavez *et al*, 2011). In the case of radioactive gases, pollutant concentrations may be converted into effective dose to human subjects using known conversion factors for inhalation (ICRP, 1994, 1996). For positron or beta particle emitters the immersion dose to the skin should also be taken into account (Pilkingsrud and Gels, 1985). There is also a need to calculate the other component of effective dose resulting from plume gamma shine (Raza and Avila, 2005). For this latter calculation the spatial and temporal distribution of radioactive gas must be known in relation to the point of dose estimation and the build-up properties of the emissions at the photon energy considered (Jones, 1980, Lahti *et al*, 1981, Overcamp and Field, 1983, 1987, Overcamp, 1991, 2007). Measured concentration field data from the wind tunnel must be converted into effective dose, which requires the model to take into account temporal variation of wind speed and direction from changing meteorological conditions (Clarke *et al*, 1979, Jones, 1980, Smith and Simmonds, 1980). The case studied here related to positron emitting gases which result in a pair of 511keV gammas from the electron-positron annihilation event; 511keV being the rest-

mass energy of the electron. In this work a constant release source term will be assumed to model a release train of intermittent releases that would occur over an extended period of time. The methods used to convert a number of concentration distributions into effective doses are described. The results of that analysis for a particular site are presented in an accompanying paper (Gallacher *et al*, 2016).

2. Methods

The methods used to treat the various model parameters are described in sections 2.1-2.8. A continuous and uniform rate of pollutant release has been assumed over the working day of radiopharmaceutical production. Intermittent or short duration ‘puff’ releases will be analysed in further work.

2.1 Wind Conditions

Five years (2007-11) of meteorological data (Heathrow, 25km south west of the site, 07:00-15:00 daily) were used. Data were analysed in a bivariate probability distribution model where the two pseudo-random variables were the wind speed (horizontal component) and the wind direction in relation to North. Data were binned into integer values of wind speed at 10m from ground level (ms^{-1}) and angular sectors of 10° .

The Heathrow data set was chosen as the only one available providing 5 years of continuous London data for the ADMS analysis, and since the aim of the study was to compare wind tunnel and ADMS the same data set was used in the wind tunnel analysis. Velocity profile corrections are based on data from the urban boundary layer consistent with Wood *et al* (2010) for built up conditions in the London area; the profile for the wind tunnel was well established, and the data for Heathrow was chosen consistent with a site of that type. Use of the urban ground roughness length of 1m indicates a 19% reduction in wind speed relative to Heathrow at the building height under consideration (50m). Although the urban roughness sub-layer in the vicinity of buildings may add some uncertainty to the effective displacement height the slow down factor is thought to be approximately correct and not inconsistent with the other experimental sources of error in the techniques employed.

The atmospheric boundary layer depth is known to depend on a number of factors such as incoming solar radiation, cloud cover and wind speed (Clarke *et al*, 1979), and heterogeneous roughness due to different building heights is also thought to be a factor. The boundary layer over London has been investigated with Lidar techniques (Barlow *et al*, 2011) with daytime values being typically significantly greater than 200m. For the purpose of velocity profile corrections in this work we treat the free stream at Heathrow as being at 200m from ground level, at the same effective height as in the wind tunnel, and take this as the free stream height at the St. Thomas’ Hospital (STH) site. The local value of the power law coefficient is then used to calculate the required wind velocity at the building height.

Wind speed was taken to vary with height above ground level according to the standard power-law profile in NRPB Report R-91 (Clarke *et al*, 1979) that applies for neutral stability atmospheric conditions. In this model the wind speed $U(z)$ at height z is related to the standard height of 10m, U_{10} , in equation [1]. The power-law coefficient n is largely dependent on ground roughness length z_0 , but also to some extent on atmospheric stability.

$$U(z) = U_{10} \left(\frac{z}{10} \right)^n \quad [1]$$

The log-law representation is given in equation [2] for the neutral stability case, where u_* is the friction velocity over the ground, and k is von Karman's constant.

$$U = \frac{u_*}{k} \ln \left(\frac{z}{z_0} \right) \quad [2]$$

From equations [1] and [2], given z_0 , the corresponding value of coefficient n can be determined. A range of values of z_0 applicable to London have been presented in Wood *et al* (2010). In this study wind velocity corrections with height were applied between the three cases studied using equation [1]: between the wind data measurement site at Heathrow airport ($z_0 = 0.2\text{m}$, $n=0.234$), the wind tunnel itself ($z_0 = 0.1\text{m}$, $n=0.201$) and the STH site under investigation in central London ($z_0 = 1.0\text{m}$, $n=0.386$). The wind tunnel (WT) measurements were made at neutral atmospheric stability corresponding to Pasquill category D (Pasquill, 1974), and as an approximation the power law coefficients applied for ground roughness between the sites were those appropriate for the neutral case. Wind tunnel measurements, made without ground heating elements and therefore no surface heat flux, match the neutral stability case corresponding to cloudy and windy conditions which apply to Pasquill-D conditions best suited to typical London conditions (MacDonnell, 2004). Velocity profiles were therefore chosen to match these conditions as being the most representative of the case under consideration.

2.2 Wind Tunnel Simulation Measurements

The wind tunnel measurements were carried out in the Enflo laboratory at the University of Surrey (EnFlo, 2016). WT simulations are an established method of investigation for complex flows, including those involving the dispersion of pollution in an urban environment in the vicinity of buildings (Robins and MacDonald, 2001). The method rests on the use of dimensionless similarity parameters that relate the flows at full scale to those of the model employed. An important parameter in wind tunnel studies (Contini *et al*, 2009) is the Reynolds number of the background flow $(Re)_F = U_{ref} H_{BL} / \nu_a$, where U_{ref} is the reference wind velocity at the boundary layer height H_{BL} in the tunnel (1.0m) and ν_a is the kinematic viscosity of air. At the operating speed used for these experiments of 2ms^{-1} $(Re)_F$ takes a value of 1.32×10^5 which is significantly greater than the critical Reynolds value of 2000 which marks the transition from laminar to turbulent flows. In terms of the flow dynamics, scale insensitivity is normally considered in relation to the obstacle Reynolds number $(Re)_b$ where $(Re)_b = U_{ref} H_b / \nu_a$ and H_b is the obstacle length scale. Hort and Robins (2002) reported that the differences between full scale and model are negligible for sharp edged buildings for $(Re)_b > 4000$: for cylindrical structures that criterion is far greater. For the model configurations in this study, the emitting building (unclad and post addition of surface cladding) and all others in the immediate near field have sharp edged shapes. In practice the Reynolds number of the full scale case would be significantly larger than for the wind tunnel case but both would be well above the lower threshold of 4000 for scale insensitivity.

Another important aspect of the flow in the wind tunnel is the simulation of an atmospheric boundary layer and this was achieved artificially in a standard way with five vortex generating 1.26m tall spires located at 50mm from the tunnel inlet, and a staggered distribution of 20mm tall roughness elements covering the floor of the tunnel. The resultant vertical velocity profile in the tunnel matched that corresponding to $n=0.20$ well ($R^2=1.00$).

The upstream roughness elements generated a well-defined turbulent boundary layer in the approach flow to the experimental buildings. Buildings were modelled to at least 400m (in full scale) upstream of the East Wing (EW) building release point and 300m downstream for all wind directions studied. Approach flows for the most critical (main) wind direction studied

(bearing 345°, blowing directly over the EW roof) had scale building models of the surrounding region extending 500m (full scale) into the upwind fetch. The equivalent radius of the tunnel turntable (centred on the EW release point) was 300m and scale model buildings, corresponding to the STH site, were in place laterally out to this radius. The wind tunnel width was equivalent to 700m in full scale.

The two cases studied in the experiment were for different building shapes of the EW (emitter) building on which the release stack was mounted. The shapes studied are referred to as ‘unclad’ (a ‘T’ cross-section building, approximately 50m tall) and the same building after the addition of a glass panel cladding layer, changing the section to a triangular shape, the ‘clad’ building with new closed canopy sections 53m tall. For all seven wind directions studied the surface roughness elements in the approach flow, coupled with upstream and downstream buildings, were deemed sufficient to simulate the necessary boundary layer, building generated turbulence and flow dynamics to model the full scale scenario. Wind directions studied in the wind tunnel experiment (expressed as a positive bearing from geographical North) were: 30°, 90°, 125°, 205°, 260°, 280° and 345° (main direction). The WT directions were chosen on the basis of (a) an investigation of the features of the flow dynamics and pollutant dispersion for both unclad and clad building cases, and (b) to sample the concentration distribution over the full angular range, with sufficient samples, to enable a comparison with ADMS which uses the meteorological data set with wind from all directions. Further details are given in Gallacher *et al* (2016) the accompanying paper.

Propane tracer gas mixed with air in a known calibrated concentration was released from the stack position horizontally in a passive release i.e. at the same velocity as the approaching flow in the tunnel (a tracer volume release rate of 0.00453 l.min⁻¹) with a density effectively the same as air. The tracer gas concentrations, upon further dilution in the flow over and around the buildings, were measured using a FFID (fast flame ionisation detector, HRF400 Cambustion Ltd.) mounted on a robotically controlled traverse arm in the tunnel and used to sample different co-ordinate locations. Sampling of the flame ionisation detector signal was at 400Hz, and sample times at each location were set sufficiently long to attain a standard error on the mean concentration value of a few percent for a steady state release at each measured location (Burt *et al*, 2012).

Sample tracer concentrations, C , were converted into standard dimensionless concentrations, χ , using the reference wind tunnel wind speed, U_{ref} , the building height, H , and tracer release rate, Q ; where:

$$\chi = \frac{CU_{ref}H^2}{Q} \quad [3]$$

Note that in equation [3] the concentration and release relate to wind tunnel tracer values, and Q is used in that context to determine the dimensionless concentration. The dimensionless concentration is then transferred between the wind tunnel and full scale case without any ambiguity over quantities. When considering the full scale case concentration and release rate are expressed in the units given below. Therefore using wind tunnel dimensionless concentration values at each co-ordinate location, equation [3] may be used to determine the concentration C (Bqm⁻³) for a given release rate Q (Bqs⁻¹) and a given value of full scale reference velocity U at the corresponding height to the 1:200 scale of the model (200m).

Extensive measurements were made of the roof-top level concentrations on a sample grid for clad/unclad building cases and for effective stack release heights. A number of other wind

directions were also assessed and the gamma ray dose contribution to the roof-top doses was added from these other directions. A method is presented here where the contribution to gamma dose rate at the roof concentration maximum position is calculated using the available sample concentrations in the horizontal sampling plane. To do this the vertical spread of the plume must be taken into account. In the primary wind direction, with the plume blowing directly over the roof, the vertical dispersion coefficient, σ_z , was measured for a range of effective release heights for both clad/unclad building cases. The plume vertical concentration profile was measured at plume centre-line and two adjacent crosswind positions, and for three downstream positions along the direction of flow. Resultant values of dispersion coefficient take into account plume reflection from the building surface and were compared with conventional methods for calculating the vertical dispersion from an isolated stack release (Clarke *et al*, 1979).

For directions other than the primary wind direction suitable volume elements were selected for all cases and wind directions studied, given the spacing of sample points of concentration and taking into account the relatively low concentration values experienced outside of the main plume direction. Only the gamma shine dose component was added from these points relatively far from the EW roof zone. The vertical, horizontal and stream-wise profiles studied in general enabled the concentration to be evaluated at one point in a cube of 10m side. These volume elements were assumed to be at the same concentration as the sample point contained within the volume; i.e. the volumes were well mixed. Given the small contribution from volume elements away from the roof this approximation can be justified.

2.3 Modelling Approaches

2.3.1 Inhalation

The concentration at a given point C (Bqm^{-3}) divided by the release rate Q (Bqs^{-1}) defines the normalised quantity C_{plume} (s.m^{-3}) as given in equation [4].

$$C_{plume} = \frac{C}{Q} \quad [4]$$

Contribution to effective dose rate \dot{E}_{inh} via inhalation is expressed in terms of breathing volume rate, \dot{V}_{inh} (m^3s^{-1}), dose conversion coefficient Sv.Bq^{-1} of D_{inh} , both of which are age dependent, and concentration (Bqm^{-3}), which is given by the product of C_{plume} and release rate Q (Bqs^{-1}). Equation 5 has been adapted from NRPB W-63 (MacDonnell, 2004) to explicitly show the release rate as a term and the units expressed in a different form.

$$\dot{E}_{inh} = C_{plume} \dot{V}_{inh} D_{inh} Q \quad [5]$$

2.3.2 Beta skin immersion dose

Exposure to beta or positron emitting gases gives rise to skin doses. The equation in W-63 (MacDonnell, 2004) was adapted as in equation [6]. The dosimetry assumes immersion in a uniform semi-infinite cloud (Piltingsrud and Gels, 1985). In practice the beta/positron range is limited so that the extent of the cloud around a receptor point (or person) need only be approximately the particle range in air for the equation to hold true.

$$\dot{D}_\beta = \left(\frac{2.3 \times 10^{-4}}{3600} \right) C_{plume} \bar{E}_\beta w_T Q \quad [6]$$

Effective dose rate from beta particle immersion is \dot{D}_β ($\mu\text{Sv.s}^{-1}$) given release rate Q (Bq.s^{-1}) and mean particle emission energy \bar{E}_β (MeV). The tissue weighting factor w_T that converts equivalent dose to skin to effective dose is 0.01 from ICRP103(2007).

2.3.3 Gamma plume shine

Plume gamma dose rate is given by equation [7] which describes the dose kernel from a point source in space adapted from Imai and Iijima (1970) and shown subsequently, e.g. in Overcamp(1987). An assumption of this dose kernel formulation is that the annihilation gammas from a positron emitting source originate from the same position as the decaying nucleus. In reality the gamma emission is from a sphere centred at the release point at position vector \underline{r} corresponding to the range of the positrons in air (Piltingsrud and Gels, 1985) but as an approximation we will treat the emissions as coming from the site of nuclear decay. The annihilation photon energy is E_γ (eV), positron yield per nuclear disintegration Y , and K a constant that relates eV to energy in Joules. Concentration $C(\underline{r}, t)$ is a function of spatial co-ordinate and time. The mass energy absorption coefficient $\left(\frac{\mu_a}{\rho}\right)$ is expressed as the absorbed dose in air, and the linear attenuation coefficient μ used applies to air. The absorbed dose in air was converted to effective dose using accepted conversion coefficients (CERC, 2012b).

$$\dot{D}_\gamma(t) = K Y E_\gamma \left(\frac{\mu_a}{\rho}\right) \iiint C(\underline{r}, t) B(E_\gamma, \mu r) \frac{e^{-\mu r}}{4\pi r^2} dv \quad [7]$$

Time-varying concentration and volume element can be expressed in spherical polars:

$$dv = r^2 \sin \theta dr d\theta d\phi \quad [8]$$

$$C(\underline{r}, t) = C(r, \theta, \phi, t) \quad [9]$$

The build-up factor B is given by Berger's formulation (equation [10]) that matches near-field conditions well (Raza and Avila, 2005) such as considered in this application (Gallacher *et al*, 2016). Coefficients a , b are functions of the gamma photon energy E_γ . The mean free path-length (MFP) of the positron annihilation photons (511keV) considered is approximately 90m in air.

$$B(E_\gamma, \mu r) = 1 + a \mu r e^{b \mu r} \quad [10]$$

2.4 Model: Static Hemisphere

Uniform dispersion into a bounded hemisphere is assumed, radius R , with radial centre at ground level and pollutant reaching uniform concentration distribution instantaneously.

2.4.1 Inhalation doses

Release activity A_{rel} (Bq) may be considered to be uniformly distributed into a hemispherical volume $V = \frac{2}{3} \pi R^3$ with release at $t=0$. The subsequent activity concentration in air will be given by $C(t)$ with λ as the radioactive decay constant of the radionuclide in question.

$$C(t) = \frac{3A_{rel}}{2\pi R^3} e^{-\lambda t} \quad [11]$$

Inhalation dose rate at time t following release was obtained by substitution of equations [4] and [11] into equation [5].

$$\dot{E}_{inh} = \frac{3e^{-\lambda t}}{2\pi R^3} \dot{V}_{inh} D_{inh} A_{rel} \quad [12]$$

By integration of the dose rate with time the effective dose from inhalation is obtained, where τ is the dose accumulation time.

$$E_{inh} = \frac{3(1-e^{-\lambda\tau})}{2\lambda\pi R^3} \dot{V}_{inh} D_{inh} A_{rel} \quad [13]$$

2.4.2 Beta skin immersion dose

Effective dose rate from beta (positron) immersion will be given from equations [4], [6] and [11]:

$$\dot{D}_\beta = \left(\frac{2.3 \times 10^{-4}}{3600} \right) \frac{3e^{-\lambda t}}{2\pi R^3} \bar{E}_\beta w_T A_{rel} \quad [14]$$

2.4.3 External Gamma Shine dose rate

From equations [7], [8], [9] and [10] we evaluate the integral over the angular co-ordinates (θ, ϕ) from which concentration C is independent. Emissions considered consisted only of positron annihilation photons of electron rest mass energy, therefore build-up factor is stated for this energy only, as is the linear attenuation coefficient, μ .

$$\dot{D}_\gamma = \frac{K Y E_\gamma \mu_a}{2\rho} e^{-\lambda t} \int_0^R C(r) B(\mu r) e^{-\mu r} dr \quad [15]$$

Given uniform concentration in the hemisphere, the integral has been evaluated analytically, with the Berger build-up formulation, to give an analytic expression for the gamma dose rate. It is however necessary to use an energy-conservation relation between the linear attenuation coefficient μ and the mass energy absorption coefficient μ_a expressed in terms of the build-up equation [10] coefficients, a and b . Considering a point source of activity A we can write the dose-kernel equation [16] where integration is over all space.

$$\iiint \dot{D}_\gamma \rho dv = K Y E_\gamma \left(\frac{\mu_a}{\rho} \right) \iiint A B(\mu r) \frac{e^{-\mu r}}{4\pi r^2} \rho dv \quad [16]$$

The right-hand side is the total energy emission rate from the source expressed in terms of the annihilation photon energy E_γ (eV), positron yield per nuclear disintegration Y , and K a constant that relates eV to energy in Joules. The dose rate is expressed in Gy (J.kg^{-1}) so the volume integral on the left is an integration of the energy absorbed per unit mass, $K Y E_\gamma A$, where A is the activity in Bq within the source. Setting the energy balance, with further rearrangement and integration over the polar angles:

$$K Y E_\gamma A = K Y E_\gamma \left(\frac{\mu_a}{\rho} \right) \iiint A B(\mu r) \frac{e^{-\mu r}}{4\pi r^2} \rho dv \quad [17]$$

Following integration over (θ, ϕ) :

$$\frac{1}{\mu_a} = \int_0^\infty B(\mu r) e^{-\mu r} dr \quad [18]$$

The functional form of B (equation [10]) may be evaluated analytically to give the following relation between μ and μ_a :

$$\mu_a = \frac{\mu}{\left[1 + \frac{a}{(1-b)^2}\right]} \quad (a \neq 0, b \neq 1) \quad [19]$$

So equation [15] may be evaluated to yield:

$$\dot{D}_\gamma = \frac{3K Y E_\gamma A_{rel}}{4\pi\rho R^3} e^{-\lambda t} \left\{ 1 - \frac{F(R)}{[a + (1-b)^2]} \right\} \quad [20]$$

Where the function $F(R)$ is given by:

$$F(R) = a e^{-(1-b)\mu R} + a(1-b)\mu R e^{-(1-b)\mu R} + (1-b)^2 e^{-\mu R} \quad [21]$$

It is interesting to investigate equation [22] where we write the concentration C as a constant.

$$\dot{D}_\gamma = \frac{K Y E_\gamma C}{2\rho} \left\{ 1 - \frac{F(R)}{[a + (1-b)^2]} \right\} \quad [22]$$

For the constant concentration case as the sphere radius increases the dose rate tends to an asymptotic limit i.e. $\lim_{R \rightarrow \infty} F(R) = 0$, where; $[a + (1-b)^2] \neq 0$, and where $a \neq 0, b \neq 1$.

As the hemisphere radius tends to zero the gamma dose rate also reaches the physically expected value of zero for no radioactive gas containment i.e. $\lim_{R \rightarrow 0} \frac{F(R)}{a + (1-b)^2} = 1$, such that $\dot{D}_\gamma \rightarrow 0$.

We have that the gamma-shine dose tends to the semi-infinite uniform case given in Pilkingsrud and Gels (1985) and also assumed in W-63 (MacDonnell, 2004). We are interested in the finite radius model case and must use the more complex formulation given here in equations [20]/[21]. In the near-field case the build-up factor is small as the photon mean free path may be large compared to the source hemisphere radius, R . Decay data and positron energy for the calculations was obtained from DDEP(2014) and conversion to effective dose was based on CERC(2012b), itself consistent with ICRU57(1998).

2.5 Model: Moving Hemisphere

We make the same assumptions as the static hemisphere but consider a slowly moving hemisphere of diffusing gas at ground level with uniform concentration: the dose terms can be expressed as analytic functions, and we also evaluate the contributions from inhalation and immersion skin dose from beta (positron) particles. The model differs from that presented by Thompson and Poston (1999) where an aircraft flew through a spherically symmetric cloud of gamma emitting fission products, with air concentration taking Gaussian form, with only numerical evaluations of external gamma ray dose.

The dose receptor point is assumed downstream (distance R) of the release point: the uniform hemisphere moves with a velocity of v ; and a complete diametrical traverse is carried out over the dose reference point taking a time $\tau = 2R/v$. Dose from inhalation (owing to the uniform concentration) is given by equation [13] where τ is the traverse time. Beta/positron immersion dose is given by equation [23].

$$D_{\beta} = \left(\frac{2.3 \times 10^{-4}}{3600} \right) \frac{3(1-e^{-\lambda\tau})}{2\pi\lambda R^3} \bar{E}_{\beta} w_T A_{rel} \quad [23]$$

An upper estimate of the gamma shine dose can be evaluated by using equation [20] and evaluating over time τ , with the function $F(R)$ given by equation [21]. This treats the gamma shine dose as being constant along a diameter of the hemisphere volume.

$$D_{\gamma} = \frac{3K Y E_{\gamma} A_{rel}}{4\pi\lambda\rho R^3} (1 - e^{-\lambda\tau}) \left\{ 1 - \frac{F(R)}{[a+(1-b)^2]} \right\}, \quad \tau = \frac{2R}{v} \quad [24]$$

2.6 Model: Standard Building Wake Model (W-157)

Wind speed at the building height of U_H was selected (3.24ms^{-1}) corresponding to the mean weighted wind speed (bearing 345°) for the primary wind direction in the wind tunnel experiment.

C_{plume} (C/Q from equation [4]) is given from NRPB R-157(Jones, 1983) and applies where the release is on, or close to, the roof surface and the concentration applies to the value inside the roof recirculation zone.

$$C_{plume} = \frac{B T_r}{A U_H \lambda_r} \quad [25]$$

B is a shape factor, typically taken as 0.5 for many cases; A is the cross sectional area of the building normal to the direction of flow; T_r is the normalised residence time of material in the building wake, and λ_r is the normalised wake length (Jones, 1983). The building height and width are W and H respectively. The latter two quantities are given in equations [26] and [27].

$$T_r = \frac{11 \left(\frac{W}{H} \right)^{1.5}}{[1 + 0.6 \left(\frac{W}{H} \right)^{1.5}]} \quad [26]$$

$$\lambda_r = \frac{1.8 \left(\frac{W}{H} \right)}{\left(\frac{L}{H} \right) [1 + 0.24 \left(\frac{W}{H} \right)]} \quad [27]$$

Selection of building height affects the concentration significantly. The inhalation dose will be given by using the value of C_{plume} in equation [5].

Beta particle immersion dose was also calculated according to the method from W-63 (MacDonnell, 2004) for the assumed uniform concentration in the recirculation zone:

$$\dot{E}_{\beta} = w_T \dot{H}_{\beta} = C_{plume} \dot{D}_{\beta, cloud} Q \quad [28]$$

$$\dot{D}_{\beta, cloud} = \left(\frac{2.3 \times 10^{-16}}{3600} \right) Y \bar{E}_{\beta} \quad [29]$$

Dose rates are in $\mu\text{Sv.s}^{-1}$ with mean beta energy expressed in MeV.

The cloud gamma method in NRPB W-63 was used to calculate the external gamma-shine dose, being appropriate to a semi-infinite source above the ground plane. Adapting that formulation we may write the gamma-shine dose in equations [30] and [31].

$$\dot{E}_{ext} = C_{plume} \dot{E}_{\gamma, cloud} Q \quad [30]$$

$$\dot{E}_{\gamma, cloud} = \left(\frac{1.6 \cdot 10^{-16}}{3600} \right) Y E_{\gamma} \quad [31]$$

Dose rates ($\mu\text{Sv.s}^{-1}$) and energy (0.511MeV) are for annihilation gammas. Gamma-ray yield per disintegration Y is the probability of positron emission per nuclear transformation multiplied by a factor of two for the gamma-ray pair produced in each positron annihilation event.

2.7 Model: Building Wake Model for the Roof Top Structure recirculation zone

2.7.1 Well mixed wake zones

The model used in ADMS (Robins and McHugh, 2001) and similar codes for concentrations in the well-mixed recirculation region, for example in the wake immediately behind a building, is expressed in terms of an entrainment fraction, the geometry of the recirculation region and a pollutant residence time. The standard result for a fully entrained release is:

$$\chi = \frac{C U_H A}{Q} = \beta \frac{\tau}{\lambda} \quad [32]$$

where τ is the dimensionless pollutant residence time, λ the dimensionless length of the recirculation region and β a constant; see Appendix A for a full derivation. As shown in Appendix A, the theory can be recast in terms of an entrainment velocity, w_E , acting over the surface area, S , of the recirculation region, leading to:

$$\frac{C U_H A}{Q} = \frac{A}{S} \frac{U_H}{w_E} \quad [33]$$

With $A = HW$, $S = sW$ and W the building width, the entrainment velocity is related to the standard parameters by equation [34], where H/s is a shape parameter:

$$\frac{w_E}{U_H} = \frac{1}{\beta} \frac{H}{s} \frac{\lambda}{\tau} \quad [34]$$

ADMS distinguishes between two forms of recirculation region, one where separation takes place at the trailing edge of the roof (see Fig.1) and another with separation from the leading edge. A simple criterion based on building geometry (Robins *et al*, 1997, Robins and McHugh, 2001) is used to select the appropriate form. If $L_B \geq \min\left(H, \frac{W}{2}\right)$, where L_B is the building length (in the direction of the oncoming flow), then the roof flow reattaches and separation is from the downwind edge of the roof. The concentration is then calculated on the basis of the entrained fraction into the recirculation zone on the leeward side of the building. This is the case in the accompanying paper (Gallacher *et al*, 2016) where the length of the building in the direction of flow in the primary wind direction was greater than $W/2$. In the converse case, where the building is shorter, the flow is taken to separate from the leading edge of the building and reattach to the ground downwind of the building.

Figure 1 shows the flow regime of interest, with the main recirculation region forming downwind of the building and a small recirculation region over the roof, commencing at the leading edge and reattaching before the trailing edge, the roof well-mixed zone. The

entrainment velocity approach can be used to derive a model for concentrations in this region, or any other formed by roof-top structures, due to material released or entrained into the region of interest.

2.7.2 A well-mixed roof zone (RTS model)

The model derivation for the roof zone, suffix 'r', is expressed in terms of the entrainment speed as follows, and is shown fully in Appendix A.

$$\frac{d(VC)_r}{dt} = Q - w_E S_r C_r \quad [35]$$

The steady state concentration follows as:

$$\chi_r = \frac{C_r U_H A}{Q} = \frac{A}{S_r} \frac{U_H}{w_E} = \frac{H}{s_r} \frac{U_H}{w_E} \quad [36]$$

If the entrainment speed is taken to be the same as for the main wake, then:

$$\chi_r = \frac{C_r U_H A}{Q} = \beta \frac{H_r}{s_r} \frac{s}{H} \frac{H}{H_r} \frac{\tau}{\lambda} = \beta \delta \frac{H}{H_r} \frac{\tau}{\lambda} \quad [37]$$

which is more conveniently written as:

$$\chi_r = \delta \frac{H}{H_r} \chi \quad [38]$$

where $\delta = \frac{H_r}{s_r} \frac{s}{H}$ is another shape factor. The classical wake model assumes separation from the downwind edge of the roof (a half-ellipse, Fig.1) and the roof model separation from the leading edge and reattachment onto the roof (full ellipse) for the building dimensions under consideration. This suggests that the shape factor δ should be approximately 0.5 considering the relative volumes enclosed by the shapes. Taking this value leads to:

$$\chi_r = \frac{1}{2} \frac{H}{H_r} \chi \quad [39]$$

This equation provides a direct link between the two dimensionless concentrations, assuming that the entrainment speed is the same in both cases. It can be seen that the recirculation concentrations in the RTS recirculation zone will be greater than the main wake concentration if $H > 2H_r$, which will always be the case; e.g. ASHRAE (2011) provide an estimator for the ratio H/H_r , which is typically about 5.

2.8 Model: ADMS Simulations

The ADMS4 (CERC, 2012a) simulations were run with the same set of wind data as used for the wind tunnel study, so direct comparison was made. Receptor points were selected over the whole of the site, and in particular the roof of the East Wing (EW) building. Additionally, some points offsite in adjacent locations were selected in order to test the convergence of ADMS and wind tunnel dose estimates. Mean annual concentrations were obtained, along with maximum daily concentrations, over the 5 years of wind data. For the purposes of the dose calculation to persons (on and off-site) the maximum of the five years mean annual average concentrations was selected. ADMS gave output in air concentration (Bq.m^{-3}). For inhalation and plume immersion dose from positrons these concentrations were converted into contributions to effective dose using equations [5]/[6].

For the annihilation gamma component of dose it was noted that ADMS had the limitation of plume gamma shine dose rate only being calculated at ground level (CERC, 2012b). Since the doses at elevated positions on the roof of the building were a prime consideration, a second set of plume gamma-shine doses was calculated using an effective raised ground plane at the building height of H=50m for the unclad (existing) building and H=53m for the clad building. Dose tallies were then obtained for elevated receptor points at the EW roof height (Gallacher *et al*, 2016), whereas standard ADMS output was used at the ground level. The following formulation was applied to estimate doses at intermediate height receptor points.

The plume gamma-shine dose rate may be approximated by a line source, where the plume is assumed to progress horizontally along the aligned X-axis originating from position (0,0,Z_{RH}) at the effective plume height (Figure 2). Equation [7] may be written in terms of the activity per unit length C_L (Bq.m⁻¹), where \underline{r}_p is the position vector of the receptor point, and \underline{r} the vector pointing to the line source element length dx along the plume line.

$$\dot{D}_\gamma = K Y E_\gamma \left(\frac{\mu_a}{\rho} \right) \int C_L B(\mu |\underline{r} - \underline{r}_p|) \frac{e^{-\mu |\underline{r} - \underline{r}_p|}}{4\pi |\underline{r} - \underline{r}_p|^2} dx \quad [40]$$

It can be shown that $C_L = Q/U_H$ where Q is in Bq.s⁻¹ and U_H is the wind velocity at building height (ms⁻¹). By defining the distance vector from source to receptor point as $\underline{R} = (\underline{r} - \underline{r}_p)$ we write:

$$R^2 = |\underline{r} - \underline{r}_p|^2 = (x - x_p)^2 + (z_{RH} - z_p)^2 \quad [41]$$

Using substitutions $w = (x - x_p)$ and $h = (z_{RH} - z_p)$ the integral simplifies as follows.

$$\dot{D}_\gamma = K Y E_\gamma \left(\frac{\mu_a}{\rho} \right) \frac{Q}{U_H} \int_{w=-x_p}^{w=\infty} B(\mu R) \frac{e^{-\mu R}}{4\pi R^2} dw \quad [42]$$

As an approximation we set $B=1$ and neglect photon interactions along the length R , so that $\exp(-\mu R) \approx 1$. Equation [42] reduces as follows.

$$\dot{D}_\gamma = K Y E_\gamma \left(\frac{\mu_a}{\rho} \right) \frac{Q}{4\pi U_H} \int_{w=-x_p}^{w=\infty} \frac{1}{h^2 + w^2} dw \quad [43]$$

So that:

$$\dot{D}_\gamma = K Y E_\gamma \left(\frac{\mu_a}{\rho} \right) \frac{Q}{4\pi h U_H} \left[\frac{\pi}{2} + \tan^{-1}(x_p/h) \right] \quad [44]$$

Where the ratio (x_p/h) is sufficiently large the simplified form is:

$$\dot{D}_\gamma = K Y E_\gamma \left(\frac{\mu_a}{\rho} \right) \frac{Q}{4\pi h U_H} \quad [45]$$

From equation [45] it can be seen that the dose rate at the receptor points depends on the perpendicular distance between the receptor point and the line source, h . Given the uncertainty in the value of z_{RH} after plume rise has been taken into effect we write, for the data fitting regimen, a functional form of the type given in equation [45] where η is an effective value of the plume height above ground plane level.

$$\dot{D}_\gamma(z_p) = \frac{\Lambda}{\eta - z_p} \quad [46]$$

where $\dot{D}_{\gamma g} = \frac{\Lambda}{\eta}$ and $\dot{D}_{\gamma e} = \frac{\Lambda}{\eta - H}$

Where $\dot{D}_{\gamma g}$ and $\dot{D}_{\gamma e}$ are the output values of ground and elevated plane gamma shine dose. From equation [46] it may be shown that an interpolated value of the gamma dose rate at an elevated height z_p is given by equation [47].

$$\dot{D}_\gamma(z_p) = \frac{H\dot{D}_{\gamma g}\dot{D}_{\gamma e}}{[H\dot{D}_{\gamma e} - (\dot{D}_{\gamma e} - \dot{D}_{\gamma g})z_p]} \quad [47]$$

Inspection of the equation shows that it meets the boundary conditions. As expected in all cases, we have that $\dot{D}_{\gamma e} > \dot{D}_{\gamma g}$, the dose at the elevated plane being greater than at the ground plane.

2.9 Model: Wind Tunnel Simulation

2.9.1 Inhalation Dose Calculation

Knowing the dimensionless concentration χ at the corresponding sample point (equation [3]) in the WT we can calculate the full scale case. The wind velocity U will be the wind speed at the full scale height equivalent to the reference height in the WT.

$$C(x, y, z, \theta, U) = \frac{\chi Q}{UH^2} \quad [48]$$

For wind speed U we use the inverse velocity weighted mean over the meteorological conditions U_{wm} corrected to the equivalent height at full scale corresponding to the reference height in the WT (200m). We have that θ is the direction of wind approaching the dose calculation point measured clockwise from North. At the point of interest (x, y, z) one would therefore use the calculated value of the concentration C (equation [48]) to determine the effective dose from inhalation from the release with wind direction θ .

To determine the dose over an extended period of time from a steady continuous release it is necessary to integrate equation [5] over the wind velocity from bivariate probability distribution $p(\theta, U)$ which represents the wind rose data (Smith and Simmonds, 2009). In this context U represents the wind speed measured at the conventional 10m from the ground plane at the reference site.

We have that for normalisation the probability density function $p(\theta, U)$ must conform to:

$$\iint p(\theta, U) d\theta dU = 1 \quad [49]$$

We define the inverse weighted velocity as a function of wind direction bearing as follows.

$$\frac{1}{U_{wm}(\theta)} = \int_{U_{min}}^{\infty} \frac{p(\theta, U)}{U} dU \quad [50]$$

We select $U_{min} > 0$, but the numerical integration is performed using meteorological data where integer values of $U (ms^{-1})$ are specified: $U=0$ is excluded from the summation. The inability to include still wind conditions is a limitation on all the currently available models, including

ADMS and wind tunnel, with the exception of the hemisphere models presented in this work, owing to the singularity created by the division by zero wind velocity. Allowance could be made for zero wind speed conditions by adding a contribution from a hemisphere model assumption, but the consequence needs to be carefully assessed, and this will be the subject of further work.

Each value of the inverse weighted wind velocity in a given direction is given by equation [51].

$$\overline{U_{wm}}(\theta_j) = \frac{\sum_i p(\theta_j, U_i)}{\sum_i \frac{p(\theta_j, U_i)}{U_i}} \quad [51]$$

The sum of the wind direction probabilities for each sector θ_j will add to unity (after summation over the velocity bins, so the wind velocity dependence is removed) and the sectors are contiguous, so that:

$$\sum_j p(\theta_j) = 1 \quad [52]$$

$$\sum_j \theta_j = 2\pi \quad [53]$$

Where $\overline{U_{wm}}(\theta)$ is the inverse weighted mean velocity for the wind direction θ used for the value of U in equation [48] once corrected to the reference height full scale using the power-law vertical velocity profile in equation [2]. The term V_{cf} is a correction factor between the two wind velocities at different heights from the ground.

$$\overline{U_{wm}}(\theta) = (z/10)^{-n} U = V_{cf} U \quad [54]$$

Where $z=200\text{m}$, and $n=0.386$ is the coefficient for roughness length $z_0=1.0\text{m}$ appropriate for the full scale site.

We have that the effective dose term can be written by adapting equation [3] to take into account the weighted wind velocity and applying angular sector integration over all directions over the release duration since U and θ are implicitly functions of time. Since we assume a uniform release rate Q over time T_y the integration is just over U and θ , and the total release over the sample period is given by the product QT_y .

$$E_{inh}(x, y, z) = \iint \frac{\chi(x, y, z)}{UH^2} \dot{V}_{inh} D_{inh} Q T_y p(\theta, U) d\theta dU \quad [55]$$

Integration over wind velocity using equation [55] and substitution of equation [54] yields the following simplification. The probability density function is expressed as the probability of wind direction and velocity. It is expressed as the probability in each binned velocity range (1ms^{-1} intervals) and angular sector (10 degrees). Integration over both of these variables, over the course of one year, adds to unity. As stated, $U=0$ was excluded from the analysis. Mean values over 5 years were taken at each angular sector and wind speed, the bi-variate distribution of probability representing the expected mean probability in each value of wind velocity and direction. Given the integration is over a continuously varying function across wind speed and direction, the double integration could be performed speed or direction first, over the same probability distribution. There is some error introduced by the discrete sampling of wind sectors (over which the mean wind speed is assessed), which was a limitation of the finite number of

directions sampled in the wind tunnel. The summations could be done for the same angular sector for each wind speed, and then the contributions from each (inverse weighted) wind speed added leading to the same result.

$$E_{inh}(x, y, z) = V_{cf} \int \frac{\chi(x, y, z)}{U_{wm}(\theta)H^2} \dot{V}_{inh} D_{inh} Q T_y p(\theta) d\theta \quad [56]$$

Where $p(\theta)$ is the marginal probability after integration over U for a given value of angular co-ordinate θ . Given that only a limited number of finite wind directions were sampled we must evaluate this integral numerically. T_y is the time over which the integration is carried out (one year) and over which the wind direction probability $p(\theta_j)$ is specified.

$$E_{inh}(x, y, z) = V_{cf} \sum_j \frac{\chi(x, y, z)}{U_{wm}(\theta_j)H^2} \dot{V}_{inh} D_{inh} Q T_y p(\theta_j) \quad [57]$$

The dose term will be calculated over the duration of the whole release, but taking into account the variation of wind speed and direction. From wind tunnel studies (where experimental running time can be significant) it was necessary to limit the number of directions from which the dispersion was assessed. Numerical integration from a finite number of experiments was necessary, for which the integral can be approximated by the summation given in equation [57]. The effective dose contribution from inhalation, assessed at the dose calculation point, will be given according to equation [57] with the breathing rate assumed constant.

2.9.2 Positron/Beta Immersion Dose Calculation

Given the concentration at the dose point it is possible to calculate the immersion dose at that point. It was assumed that the concentration value at the point extends uniformly out to the positron particle range i.e. range energy and beta dose calculations have not been attempted from adjacent sampled concentration measurement points. The effective dose contribution ($\mu\text{Sv.s}^{-1}$) is given according to release rate Q (Bq.s^{-1}) and the total time of emission T_y (s), and particle mean emission energy \bar{E}_β (MeV). Equation [6] is adapted using equations [4] and [57].

$$D_\beta(x, y, z) = \left(\frac{2.3 \times 10^{-4}}{3600}\right) V_{cf} \sum_j \frac{\chi(x, y, z)}{U_{wm}(\theta_j)H^2} \bar{E}_\beta w_T Q T_y p(\theta_j) \quad [58]$$

2.9.3 Plume Gamma Shine Calculation from measured concentration field

Measured values of concentration from the wind tunnel were on a co-ordinate sampled grid ($i=1$ to N points), where $C(x_i, y_i, z_i)$ is the concentration from equation [3]. For a given wind direction equation [7] can be expressed in terms of a finite sum of dose arising from discrete volume elements, where each volume element is centred on the co-ordinate at which the sample was made. This model effectively places the activity contained within the volume element at the centre of that element to carry out the gamma dose rate calculation. The simplifying approximation made for positrons was that the annihilation gamma-rays from positron annihilation in air were assumed to come from the position of the originating radioactive atom. No such approximation is necessary for a gamma-emitting radionuclide. For the positron emitting atoms considered, the maximum range in air could be as great as 1.76m(^{18}F) and 6.22m(^{15}O) (Piltingsrud and Gels, 1985) in standard density air.

The Gaussian plume dispersion equation is stated in [59] (Imai and Iijima, 1970), however without the ground reflection term, which may not be appropriate for near-field positions, especially on the building roof. Plume reflection from the building roof is taken into account in

the lateral and vertical dispersion parameters which were fitted to the measured plume dispersion coefficients. The plume is travelling with the wind in the x-axis direction, with y being the crosswind co-ordinate horizontally and the z-axis pointing vertically (Figure 2). The value of concentration at a point $\underline{r}(x,y,z)$ is given by equation [59], where σ_y and σ_z are the lateral crosswind plume and vertical dispersion coefficients respectively, each of which is a function of downstream distance x i.e. they both increase with downstream distance due to plume broadening. Quantities y_0 and z_{RH} are the plume lateral centre line and the effective release height of the plume accounting for plume rise and downwash effects. Once the plume rise to z_{RH} has been attained it is assumed the progression in the near-field is at constant height, given the neutral buoyancy assumption.

$$C(\underline{r}) = \frac{Q}{2\pi U_H \sigma_y \sigma_z} e^{-\frac{1}{2} \left\{ \frac{(y-y_0)^2}{\sigma_y^2} + \frac{(z-z_{RH})^2}{\sigma_z^2} \right\}} \quad [59]$$

We have that in Cartesian co-ordinates the distance from the point of interest of a dose receptor point p will be given by:

$$|\underline{r} - \underline{r}_p|^2 = (x - x_p)^2 + (y - y_p)^2 + (z - z_p)^2 \quad [60]$$

Figure 2 shows the plume geometry, and the position vectors. Rewriting equation [59] and substituting in equation [7] we obtain equation [61]. It should be noted that $C(x, y, z_{RH})$ expresses the concentration in a horizontal plane at the level of the plume centreline at constant height, which is a function of x and y only: σ_z in this analysis is only a function of downwind distance x , as per R-91 (Clarke *et al*, 1979). The z-varying component is expressed as the exponent term in z .

$$\dot{D}_\gamma = K Y E_\gamma \left(\frac{\mu_a}{\rho} \right) \iiint C(x, y, z_{RH}) e^{-\left\{ \frac{(z-z_{RH})^2}{2\sigma_z^2} \right\}} B(\mu |\underline{r} - \underline{r}_p|) \frac{e^{-\mu |\underline{r} - \underline{r}_p|}}{4\pi |\underline{r} - \underline{r}_p|^2} d\mathbf{v} \quad [61]$$

A method of reducing the gamma dose rate equation to a form suitable for the evaluation of gamma dose rate from the sampled grid is detailed in Appendix B.

We define the effective height of the integration zone of radioactive gas above the measured value in the plane $z = z_m$ as H_{vol} , given in equation [62]:

$$H_{vol} = \frac{C(x_p, y_p, z_{RH})}{C(x_p, y_p, z_m)} \int_{z=H}^{z=\infty} e^{-\left\{ \frac{(z-z_{RH})^2}{2\sigma_z^2} \right\}} dz \quad [62]$$

The total area of the sampling grid Ω will be given in equation [63], where (x_{min}, y_{min}) and (x_{max}, y_{max}) define the extent of the rectangular sample grid above the roof plane of the building. The integration volume is given by the product ΩH_{vol} , where all sampling area elements $\Delta_i = \Delta$, a constant value.

$$\Omega = \sum_{i=1}^N \Delta_i = N\Delta = (y_{max} - y_{min})(x_{max} - x_{min}) \quad [63]$$

We therefore write from Appendix B the gamma shine dose rate equation:

$$\dot{D}_\gamma = K Y E_\gamma \left(\frac{\mu_a}{\rho} \right) \frac{\Omega H_{vol}}{N} \sum_{i=1}^N C(x_i, y_i, z_i = z_m) B(\mu R_{p_i}) \frac{e^{-\mu R_{p_i}}}{4\pi R_{p_i}^2} \quad [64]$$

Equation [64] could easily be adapted to a Monte Carlo simulation, although this is not the aim of the current work. In a similar way to section [2.9.1] the different wind directions, with their associated probability and weighted inverse wind velocity, are taken into account to produce the accumulated gamma dose given over time T_y . Dimensionless concentrations determined from the measurements are specified for a given wind direction θ_j . Summation was carried out over suffix i for each wind direction in the first instance, then dose values were weighted for wind probability in the summation over j . Equation [65] was used to determine the annual dose contribution from the release as simulated by the wind tunnel experiment.

$$D_\gamma = K Y E_\gamma \left(\frac{\mu_a}{\rho} \right) \frac{\Omega H_{vol}}{N} V_{cf} \sum_j \sum_{i=1}^N \frac{\chi(x_i, y_i, z_i = z_m, \theta_j)}{U_{wm}(\theta_j) H^2} B(\mu R_{p_i}) \frac{e^{-\mu R_{p_i}}}{4\pi R_{p_i}^2} Q T_y p(\theta_j) \quad [65]$$

H_{vol} used in the integration is evaluated from equation [62]. Using the exponential term fall-off from the plume centre line at z_{RH} and re-arrangement of terms we obtain:

$$H_{vol} = \sqrt{2\pi} \sigma_z e^{\left\{ \frac{(z_m - z_{RH})^2}{2\sigma_z^2} \right\}} \int_{z=H}^{z=\infty} \frac{1}{\sqrt{2\pi} \sigma_z} e^{-\left\{ \frac{(z - z_{RH})^2}{2\sigma_z^2} \right\}} dz \quad [66]$$

It can be seen that by letting $\sigma_z \ll (z_{RH} - H)$ the integral tends to unity, representing a full plume integration. The integral may be evaluated using the special error function $erf(x)$. By letting $\sigma_z \ll (z_{RH} - H)$ the integral tends to one, as required. For $z_{RH} = H$ the integral takes a value of $1/2$ as expected with integration over the half-plume. Equation [67] gives the height of the integration volume.

$$H_{vol} = \sqrt{\frac{\pi}{2}} \sigma_z e^{\left\{ \frac{(z_m - z_{RH})^2}{2\sigma_z^2} \right\}} \left[1 + \operatorname{erf} \left(\frac{z_{RH} - H}{\sigma_z} \right) \right] \quad [67]$$

3. Results

3.1 Wind Conditions

Table I presents reference site wind-rose data, in terms of the weighted-inverse velocity as calculated by equation [67], presented for the conventional 10m from the ground. Fig.3 gives the five year mean, with error bars shown at two standard deviations over the five years of data, showing significant differences of weighted wind velocity with direction. The highest weighted velocities correspond to the sector quadrant 180° (S) through to 270° (W) i.e. were experienced from the South West. For the primary wind direction (345° , in which the plume is blown directly over the building) the wind speed is relatively low. This would lead to higher concentrations and a greater dose rate compared to higher wind speeds. In terms of radiological assessment the value of using actual wind data is apparent.

Table II gives the probability distribution of wind direction, in 10° sectors. Data presented relate to 07:00-15:00 daily, the likely hours of emission. Zero wind velocity values were excluded from the analysis: these comprised only 0.05% of hours in the sample data. Valid, non-zero data comprised 98.1% of the sample, the remainder being invalid, missing or zero data. Fig.4 shows the probability density function plotted with bearing from North (N). The most probable sector is from the SW, with the NE also prominent. NW and E are less probable directions. This

is significant as the primary wind direction (345°) is also one of the least probable directions for wind. This shows the value of using appropriately weighted wind direction probabilities in the analysis.

3.2 Hemisphere Model

Fig.5 shows the gamma-ray dose factor for 0.511MeV annihilation gamma-rays following equations [21] and [22], increasing to the normalised asymptotic limit for a uniform concentration hemisphere. The asymptotic tendency is consistent with the findings of Pilkingsrud and Gels (1985) for positron emitting gases. The limitations of using a semi-infinite approximation are clear from Fig.5 in terms of the overestimation of the gamma dose rate from a plume of finite extent, as with W-63 (MacDonnell, 2004), particularly in the near-field case. Furthermore, the Berger formulation of the build-up factor holds well where the sources are less than a few mean free photon paths from the receptor point (Raza and Avila, 2005). It is apparent that in the near-field, as in the case under consideration, a gamma-ray estimation based upon measured, or otherwise calculated, field concentration values is essential for an accurate determination of the gamma-ray dose-rate from the plume.

Fig.6 shows the gamma-ray dose build-up factor (0.511MeV gamma-rays, $a=1.748$, $b=0.1014$). For these energy photons in air the function is linear to 400-500m, after which there is an increasing gradient with distance. It has been reported that the Berger formulation (Raza and Avila, 2005) of the build-up equation holds well for sources nearer to the receptor point of less than a few mean free path lengths.

Results of an application of static and moving hemisphere models are presented in the first paper Gallacher *et al* (2016a) for the near-field ($R=75\text{m}$,) and with $R=175\text{m}$ to encompass a point at the site edge. As a model of limited physical applicability these results show the overestimation inherent in this approach. The case for which they would best approximate would be very still wind conditions and reflection under a low height atmospheric inversion layer, perhaps with low plume buoyancy in relation to surrounding warmer air. The dose values from these models, and the same release term, are some orders of magnitude greater than other more sophisticated models that take account of wind direction probability and wind speed, such as WT and ADMS models.

3.3 Building Wake

Building-wake model results are presented in Gallacher *et al* (2016a) for the same release term as the other models. The wind direction is assumed to be the primary direction over the roof for this study. Given that the wind direction probability was not taken into account there is an inherent overestimation due to this factor. The difference between the roof-top circulation concentrations and the concentration in the main building wake zone is given by equation [39] and for $H_r=3\text{m}$ and $H=53\text{m}$ the RTS zone concentration can be seen to be significantly greater than that calculated by the conventional approach, with correspondingly larger radiation doses from inhalation.

3.4 ADMS Computer Simulation Model of Site

Fig.7 shows the gamma dose response factor with varying receptor height normalised to a building height of $H=53\text{m}$. The effective value of the plume height above the ground plane, $\eta=60\text{m}$, is plausible given the stack height of 53m and plume rise due to the release efflux momentum. ADMS gamma dose rates for intermediate height receptor points are corrected by the response factor, on the assumption that the greatest contribution to dose rate occurs when the plume is in the same approximate sector and therefore can approximate to the case where it

is nearly overhead. Results for the radiation dose at the different receptor points at the site in question are presented in the first paper in comparison with the other models.

3.5 Wind Tunnel Simulation of Top of East Wing

Fig.8 shows the vertical dispersion coefficient for the unclad case vs downstream distance from the release point. Dimensions are in model units. For comparison, plume dispersion for neutral stability from R-91(Clarke *et al*, 1979) is shown for different ground roughness lengths of $z_0=1.0\text{m}$ and $z_0=0.1\text{m}$. Building generated turbulence clearly influences the dispersion from the shorter stacks, where the plume is closer to the roof surface, and this is especially the case for the release height closest to the building of $Z_{RH}=245\text{mm}$ where the building height is $H=240\text{mm}$ near the release point. From data on the boundary layer (Barlow *et al*, 2011) and given the height of the building under consideration, reflections from the boundary layer edge are not a significant source of error.

Fig.9 for the clad building case shows the vertical dispersion coefficients presented in a similar way to the unclad case. A different picture emerges for the closest release height to the top of the building ($Z_{RH}=245\text{mm}$) showing dispersion close to the R-91 curve equivalent to dispersion with $z_0=1.0\text{m}$. The different shape and size of the building in this case may be creating greater building generated turbulence, and this effect may predominate where the release is closer to the building roof. For $X=160\text{mm}$ ($Z_{RH}=255\text{mm}$) the presence of a RTS (the upstream raised section of glass canopy) may be contributing to a plume broadening effect in that location and recirculation: this measurement plane was proximal to the EW building air intakes, and thus of particular interest. Results indicate that local building effects have a significant role in determining plume dispersion in the near-field.

Fig.10 shows a plot of the dispersion coefficient values at one downstream distance corresponding to the plume concentration maximum position on the roof of the building at $X=58\text{mm}$. R-91 values for the two roughness lengths are once again shown for ease of comparison. It is interesting to note that the clad dispersion coefficients are lower than both the $z_0=0.1\text{m}$ R-91 value and the unclad cases for release heights of $Z_{RH}=260\text{mm}$ and above. The converse applies at the two lowest release heights. This may again be a local building effect of the flow field for the clad building resulting in flow being brought out of the recirculation zone and suffering less building generated turbulence. The coefficients obtained from the vertical dispersion analysis were used in the subsequent calculation of the plume vertical activity and in the gamma ray dose rate contribution.

4. Discussion

For the wind conditions used for the five year period studied, the value of using inverse-weighted wind velocities according to the marginal probability for each direction to obtain a weighted mean value of $1/U$ should reduce errors compared to the underestimation of dose contribution from lower wind velocities when using a simple mean, or even conventionally weighted mean. The probability distribution of the wind direction must also be taken into account as the wind direction associated with the plume blowing over the building is a significant factor for the dose, particularly from the inhalation and immersion terms, but also to some extent from the gamma-ray dose component. In such cases the orientation of the release point in relation to the building is a local factor that must be considered.

Applicability of the hemisphere model is limited, except perhaps in cases of very low wind speeds, but it is nevertheless an interesting model that would be expected to set an upper bound on the expected doses (Gallacher *et al*, 2016a). The moving hemisphere is a little more

physically realistic. The gamma-ray factor (Fig.6) indicates the error associated with using the semi-infinite uniform concentration approximation used in W-63 simple models which would be particularly apparent in the near-field with small plume extent.

The two building-wake models, one the standard model and the other derived to estimate the effects of RTS, applied in this case provide pessimistic estimates of the radiation dose given the assumption that the receptor point is always downwind of the release point. They could be improved by weighting the releases by a wind direction probability factor and neglecting contributions from other sectors. They are conventionally applied with the semi-infinite uniform concentration approximation which would over-estimate the gamma-ray dose component.

The ADMS building module allows for only one single building and uses analytic building wake concentration functions (Robins *et al*, 1997, Robins and MacDonald, 2001), but has the advantage of allowing for plume rise from the release stack, full meteorology, ground roughness length and calculates output using hourly wind data which takes into account direction and speed. ADMS has a specific disadvantage that the gamma-ray dose can only be calculated at the ground plane, and not at an elevated plane such as the building roof. A method of correcting the ADMS gamma-ray dose to different heights has been presented. Gamma dose rate was estimated at the roof level by using a raised ground plane approximation: in these conditions close to the release point, the line-source approximation used by ADMS4 would not come into operation (CERC, 2012b) as it would for an elevated source above the ground plane.

A method has been presented to convert measured wind tunnel concentration values into actual concentrations in the vicinity, and in particular above, a building. Limitations on measurement run time meant in this case that the concentrations were sampled just above the roof of the two building cases studied in a horizontal grid pattern. Vertical dispersion was also measured and the two sets of data used to estimate an effective total concentration per unit area across the sample grid. The method presented calculates the gamma ray dose from the plume in accordance with the measured local concentration field values. Dose results were presented in the accompanying paper at the plume concentration maximum in the roof zone using the local concentration for inhalation and immersion dose components. ADMS4 and wind tunnel dose estimates were compared at a further distal point at 175m from the stack release point to check the convergence of these two more sophisticated dose modelling approaches.

The limitations implicit in the ADMS and wind tunnel approaches could be improved, in the first case, by modifying the code to give dose output at any chosen location and, in the second, by more detailed concentration data throughout a larger sampling volume of interest but at the expense of greater wind tunnel running time.

5. Conclusion

Various methods of calculating radiation dose from inhalation, immersion and plume gamma shine have been detailed for the near-field region to a radioactive gas release on the roof of a building. The most sophisticated models presented are the wind tunnel and ADMS models, but simpler analytic models such as conventional building wake and hemispherical uniform mixing models are also presented for completeness. The results from applying the modelling approaches to a particular site for a given uniform release rate have been presented elsewhere (Gallacher *et al*, 2016). A novel method of modifying the standard building wake model to allow for RTS has been formulated.

References

- ASHRAE 2011, Building Air Intake and Exhaust Design, Chapter 45, *ASHRAE Applications Handbook*, Atlanta: American Society of Heating, Refrigeration and Air-Conditioning Engineers, Inc. Atlanta, GA.
- Barlow, JF, Dunbar, TM, Nemitz, EG, Wood, CR, Gallagher, MW, Davies, F, O'Connor, E, Harrison, RM, 2011, Boundary layer dynamics over London, UK, as observed using Doppler lidar during REPARTEE-II, *Atmos.Chem.Phys.*, 11(2011) 2111-2125
- Burt, A., Robins, A.G., Hayden, P., 2012, 'Flow and Dispersion of Radioactive Tracers at St.Thomas' Hospital', MEng Thesis, Faculty of Engineering and Physical Sciences, University of Surrey
- Cambridge Environmental Research Consultants (CERC), 2012a, 'Dispersion Modelling of radioactive emissions at St.Thomas' Hospital', CERC, Cambridge
- CERC, 2012b, P20/01M/12, http://www.cerc.co.uk/environmental-software/assets/data/doc_techspec/CERC_ADMS5_P20_01.pdf, last accessed 10/07/2014
- Chavez, M, Hajra, B., Stathopoulos, T., Bahloul, A., 2011, Near-field pollutant dispersion in the build environment by CFD and wind tunnel simulations, *Journal of Wind Engineering and Industrial Aerodynamics* 99, 330-339
- Clarke, R.H., et al, A Model for Short and Medium Range Dispersion of Radionuclides Released to the Atmosphere, 1979, NRPB R-91, Chilton, UK
- Contini, D, Cesari, D, Donateo, A, Robins, AG, 2009, Effects of Reynolds number on stack plume trajectories simulated with small scale models in a wind tunnel, *Journal of Wind Engineering and Industrial Aerodynamics*, 97, 468-474
- Decay Data Evaluation Project (DDEP), Laboratoire National Henri Becquerel, http://www.nucleide.org/DDEP_WG/DDEPdata.htm, last accessed 10/07/2014
- EnFlo, 2016, Meteorological Wind Tunnel, www.surrey.ac.uk/mes/research/fluids/enflo
- Gallacher, D.J., Robins, A.G., Burt, A., Chadwick, S, Hayden, P., Williams, M, 2016, Dispersion of positron emitting radioactive gases in a complex urban building array: a comparison of dose modelling approaches, In Preparation, *Journal of Radiological Protection*
- Hajra, B., Stathopoulos, T., Bahloul, A., 2010, Assessment of pollutant dispersion from rooftop stacks: ASHRAE, ADMS and wind tunnel simulation, *Building and Environment* 45(2010) 2768-2777
- Hajra, B., Stathopoulos, T., 2012, A wind tunnel study on the effects of downstream buildings on near-field pollutant dispersion, *Building and Environment* 52(2012): 19-31
- Hajra, B., Stathopoulos, T., Bahloul, A., 2013, A wind tunnel study on the effects of adjacent buildings on near-field pollutant dispersion from rooftop emissions in an urban environment, *Journal of Wind Engineering and Industrial Aerodynamics* 119(2013) 133-145

Hajra, B., Stathopoulos, T., Bahloul, A., 2014, Performance of ASHRAE models in assessing pollutant dispersion from rooftop emissions, *HVAC&R Research* (2014) 20, 72-79

Hort, MC, Robins, AG, 2002, The dispersion of fugitive emissions from storage tanks, *Journal of Wind Engineering and Industrial Aerodynamics* 90, 1321-1348

ICRP, 1994, Publication 68, Dose coefficients for intakes of Radionuclides by Workers, *Annals of the ICRP Vol.24/4*, Elsevier

ICRP, 1996, Publication 72, Age-dependent doses to the members of the public from intake of radionuclides: Part 5, compilation of ingestion and inhalation coefficients, *Annals of the ICRP Vol.26/1*, Elsevier

ICRP, 2007, Publication 103, The 2007 recommendations of the International Commission on Radiological Protection, 2007, *Annals of the ICRP Vol.37, Nos.2-4*, Elsevier

ICRU, 1998, Conversion coefficients for use in radiological protection against external radiation, *ICRU Report 57*, Bethesda, Maryland, US

Imai, K, Iijima, T, 1970, Assessment of gamma-exposure due to a radioactive cloud released from a point source, *Health Physics*, 18, 207-216

Jones, JA, 1980, ESCLOUD: A Computer Program to Calculate the Air Concentration, Deposition Rate and External Dose Rate from a Continuous Discharge of Radioactive Material to Atmosphere, *NRPB Report R-101*, Harwell, Didcot, Oxon

Jones HA, 1983, Models to Allow for the Effects of Coastal Sites, Plume Rise and Buildings on Dispersion of Radionuclides and Guidance on the Value of Deposition Velocity and Washout Coefficients, *NRP Report R-157*, Chilton, Didcot, Oxon

Lahti, GP, Hubner, RS, Golden, JC, 1981, Assessment of gamma-ray exposures due to finite plumes, *Health Physics* 41(August), 319-340

MacDonnell, C., 2004, Radiological Assessments for small users, *NRPB W-63*, Chilton, UK

Overcamp, TJ, Fjeld, RA, 1983, An exact solution of the Gaussian cloud approximation for gamma absorbed dose due to a ground-level release, *Health Physics* 44(4), 367-372

Overcamp, TJ, Fjeld, RA, 1987, A simple approximation for estimating centreline gamma absorbed dose rates due to a continuous Gaussian plume, *Health Physics* 53(2), 143-146

Overcamp, TJ, 1991, Modelling gamma absorbed dose due to meandering plumes, *Health Physics* 61(1), 111-115

Overcamp, TJ, 2007, Solutions to the Gaussian cloud approximation for gamma absorbed dose, *Health Physics* 92(1), 78-81

Pasquill, F, Atmospheric Diffusion: The Dispersion of Windborne Material from Industrial and other Sources, 2nd Ed., 1974, William Clowes and Sons, London

Pilkingsrud, HV, Gels, GL, 1985, An evaluation of the external radiation exposure dosimetry and calculation of maximum permissible concentration values for airborne materials containing ^{18}F , ^{15}O , ^{13}N , ^{11}C and ^{133}Xe , *Health Physics* 49(5), 805-824

Raza, S, Avila, R, 2005, Calculation of immersion doses from external exposure to a plume of radioactive material, *Health Physics*, 89(3): 247-254

Robins, AG, Carruthers, D, McHugh, C, 1997, The ADMS building effects module, *Int.J.Environment and Pollution*, Vol.8, Nos.3-6, 705-717

Robins, AG, Castro, IP, 1977a, A wind tunnel investigation of plume dispersion in the vicinity of a surface mounted cube – I. The flow field, *Atmospheric Environment* Vol.11, 291-297

Robins, AG, Castro, IP, 1977b, A wind tunnel investigation of plume dispersion in the vicinity of a surface mounted cube – II. The concentration field, *Atmospheric Environment* Vol.11, 299-311

Robins, A.G, MacDonald, R., 2001, Review of Flow and Dispersion in the Vicinity of Groups of Buildings, Annexe B, Atmospheric Dispersion Modelling Liaison Committee, Annual Report 1998/99, NRPB R-322, Chilton

Robins, AG, McHugh, C, 2001, Development and Evaluation of the ADMS Building Effects Module. *Int. J. Environment and Pollution*, 16, 1-6, 161-174

Smith, JG, Simmonds, JR, 2009, The methodology for assessing the radiological consequences of routine releases of radionuclides to the environment used in PC-CREAM 08, HPA-RPD-058, Chilton, UK

Thompson, JM, Poston, JW, 1999, Absorbed Dose from Traversing Spherically Symmetric, Gaussian Radioactive Clouds, *Health Physics*, 76(6): 639-643

Wood, CR, Lacser, A, Barlow, JF, Padhra, A, Belcher, SE, Nemitz, E, Helfter, C, Famulari, D, Grimmond, CSB, 2010, Turbulent flow at 190m height above London during 2006-2008: a climatology and the applicability of similarity theory, *Boundary Layer Meteorology*, 137:77-96

Figure 1. Recirculation Zones: Main and Roof Top Structure (RTS)

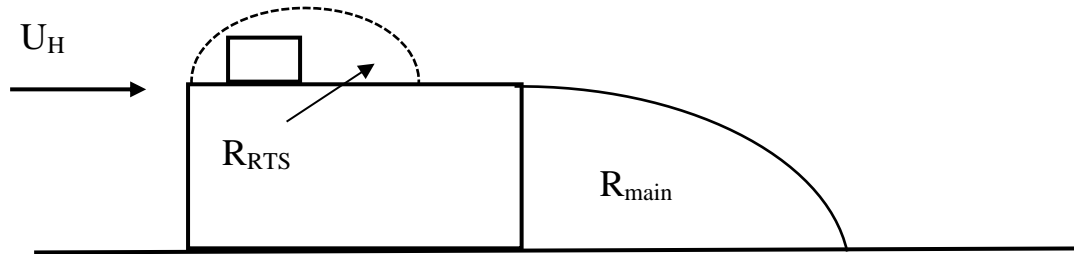


Figure 2. Co-ordinate axis and plume geometry

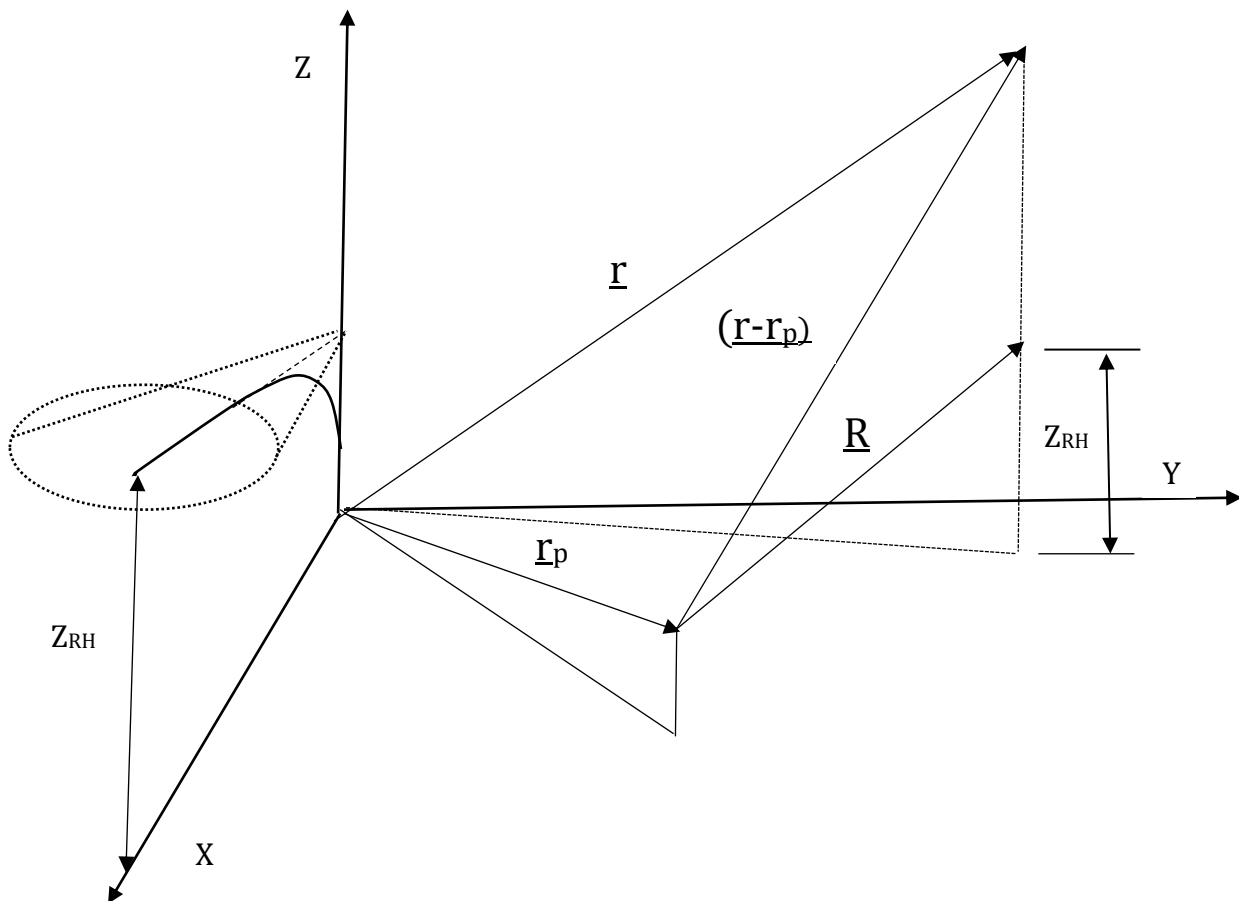


Figure 3. Five year mean reciprocal weighted wind velocity

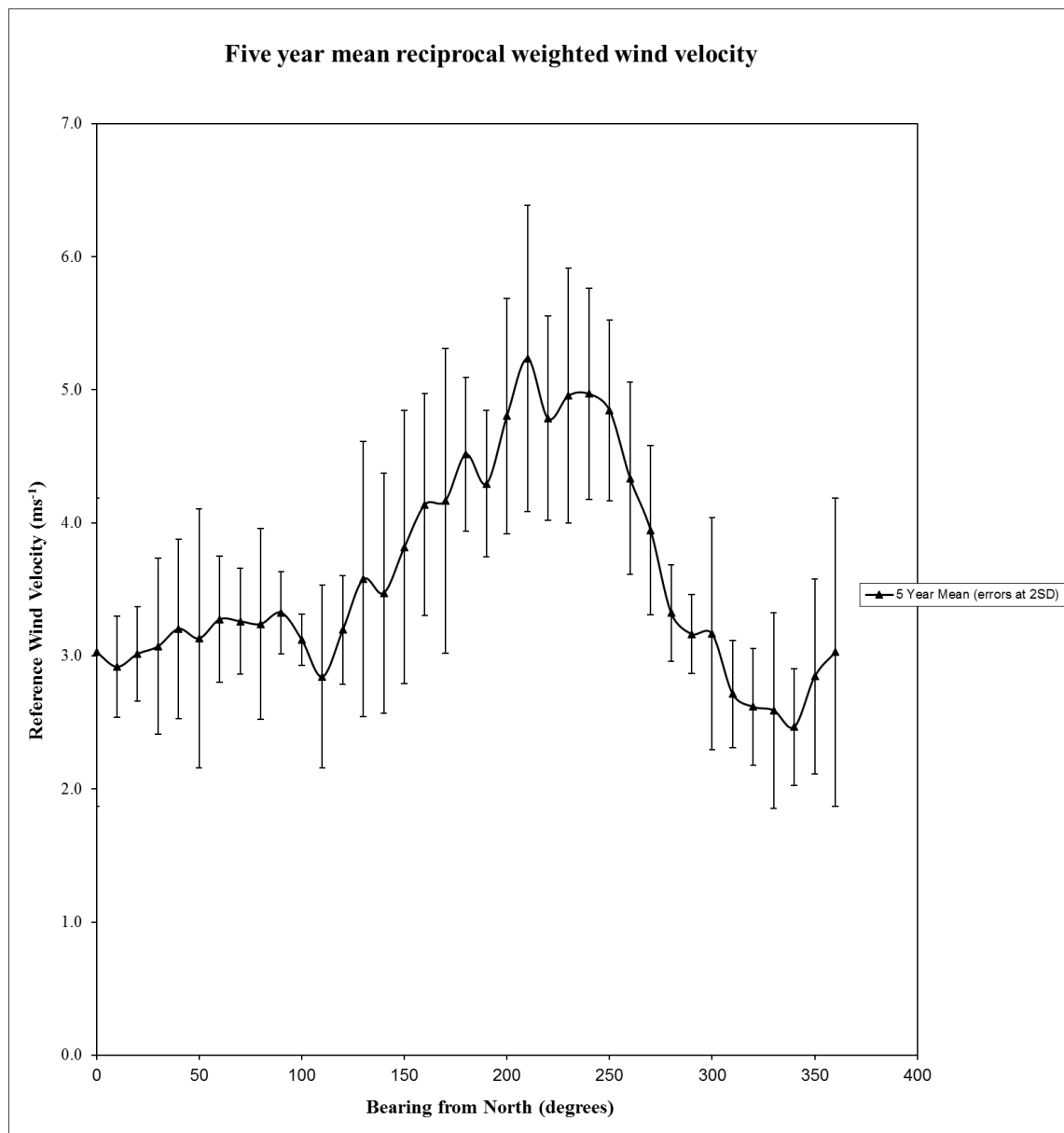


Figure 4. Wind direction probability density function with bearing from North

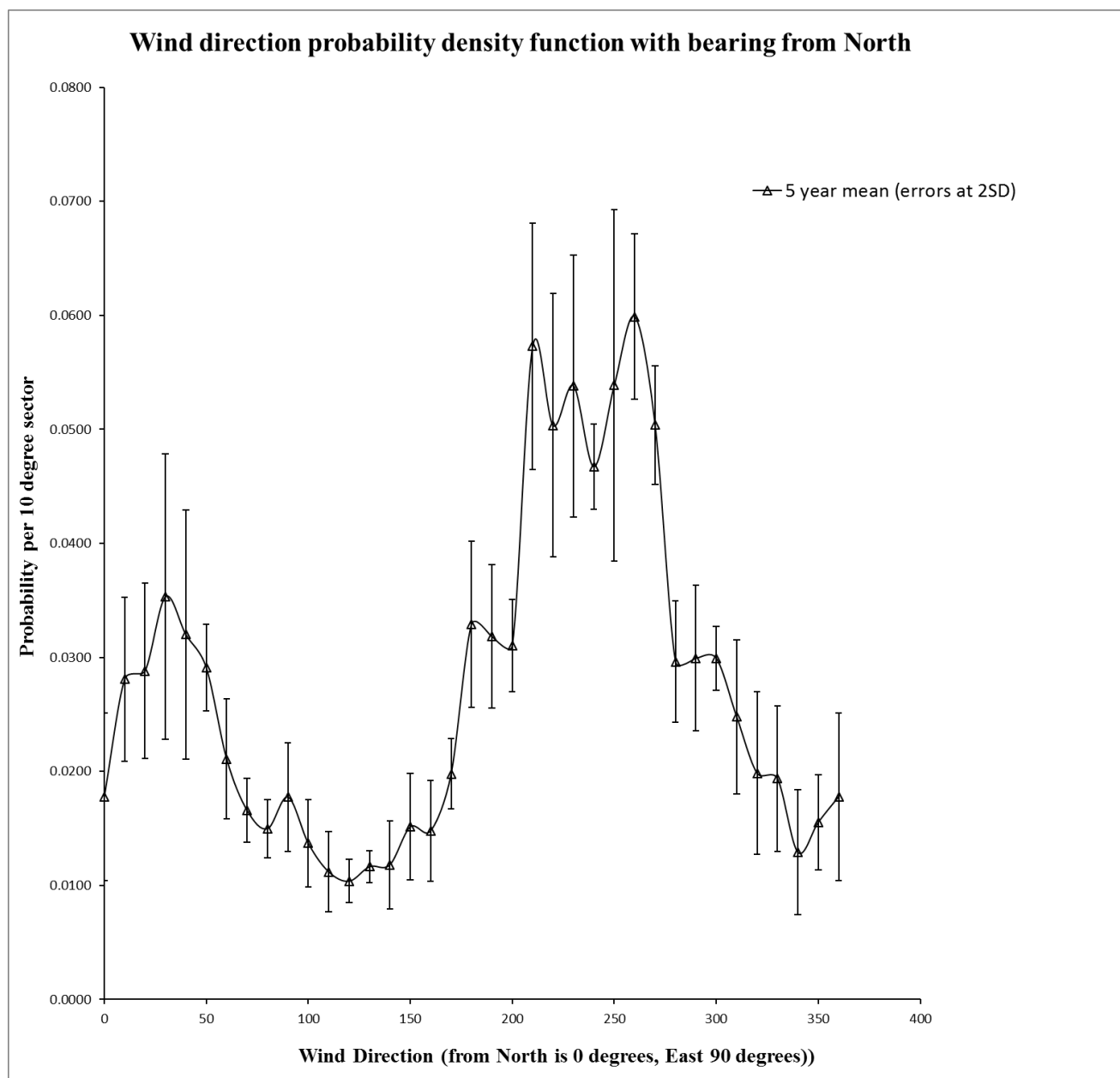


Figure 5. Gamma dose factor with distance from hemisphere centre for uniform concentration normalised to the asymptotic limit at large distances

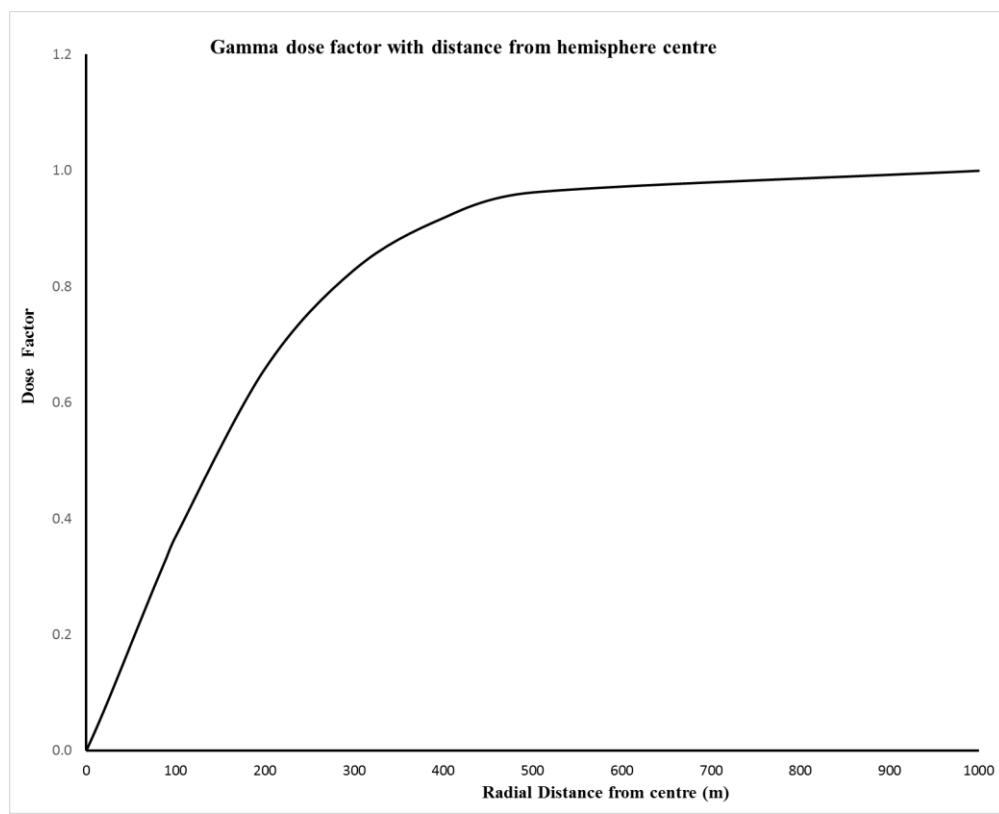


Figure 6. Gamma buildup $B(\mu r)$ with distance from hemisphere centre

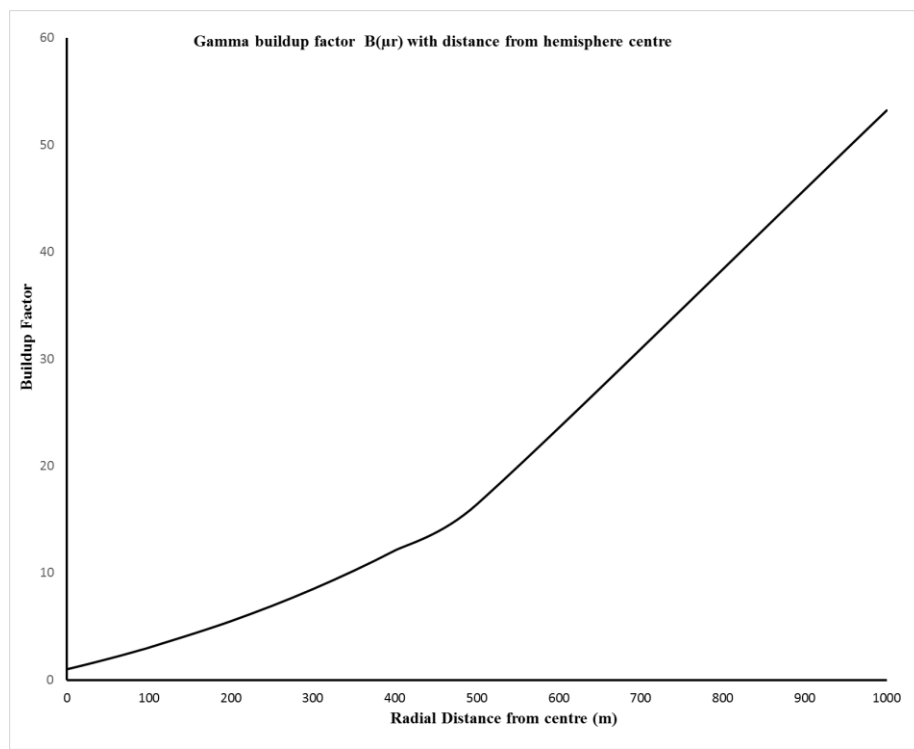


Figure 7. ADMS gamma dose rate correction factor with receptor height

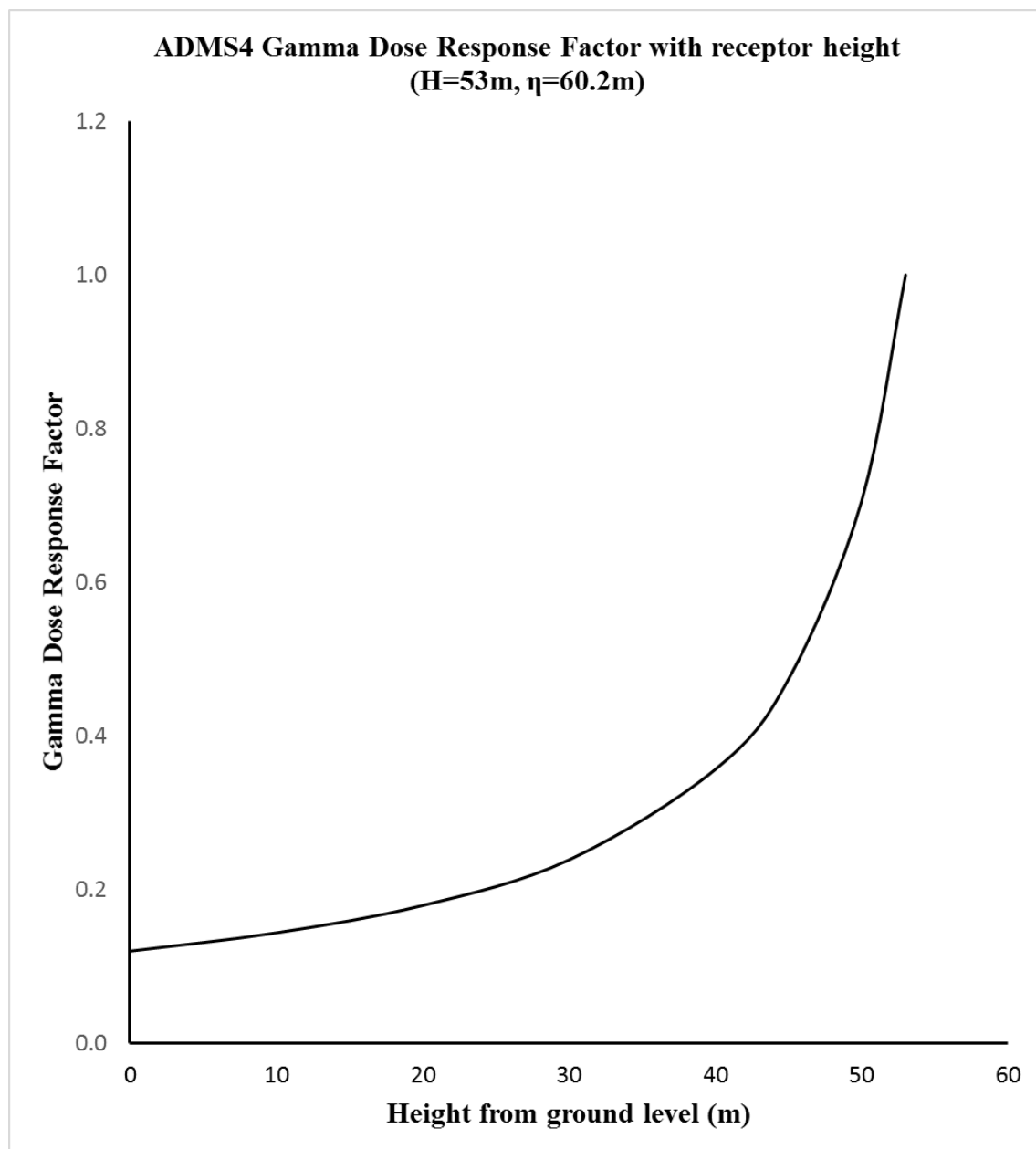


Figure 8. Unclad cases vertical dispersion coefficient

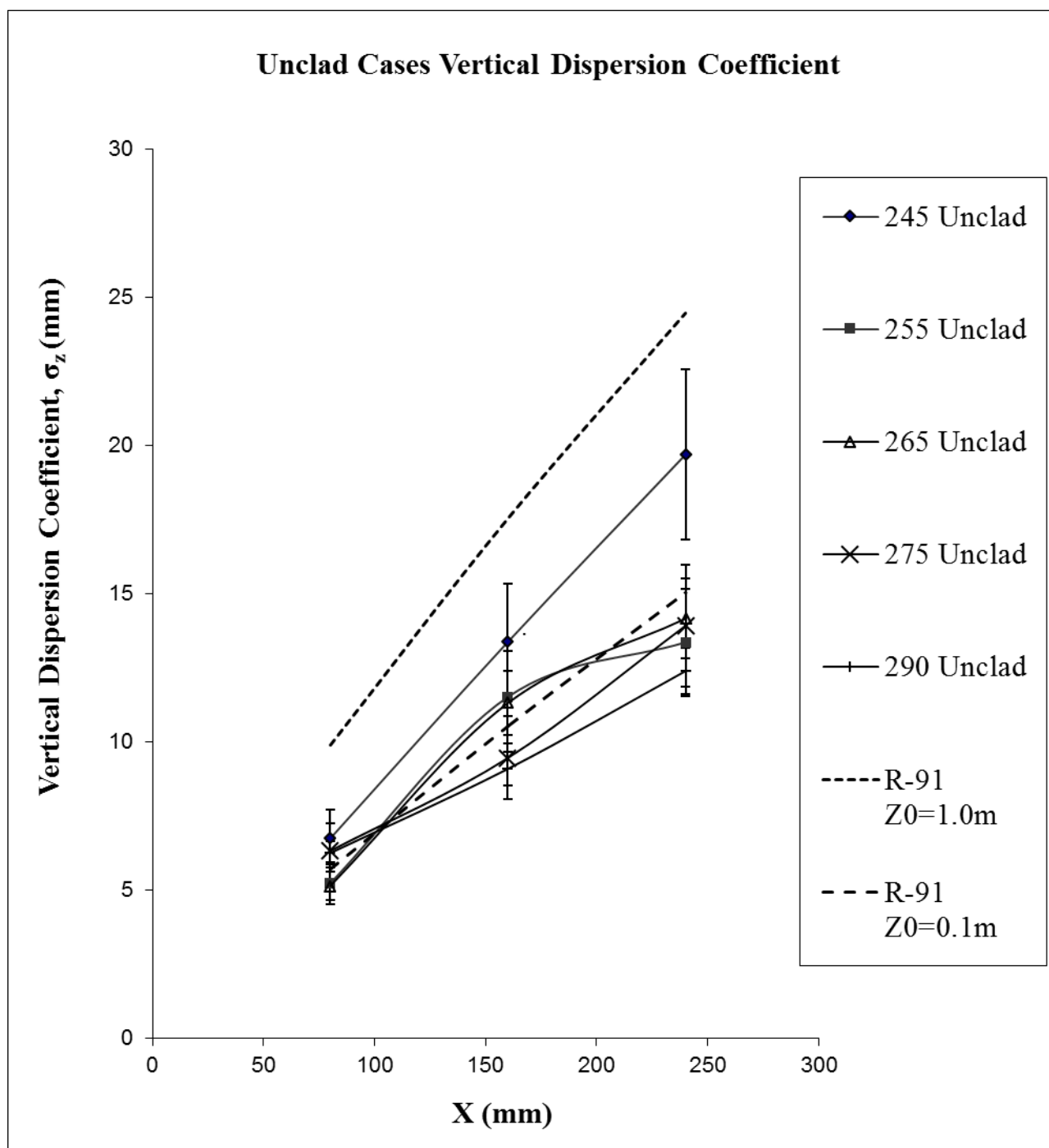


Figure 9. Clad cases vertical dispersion coefficient

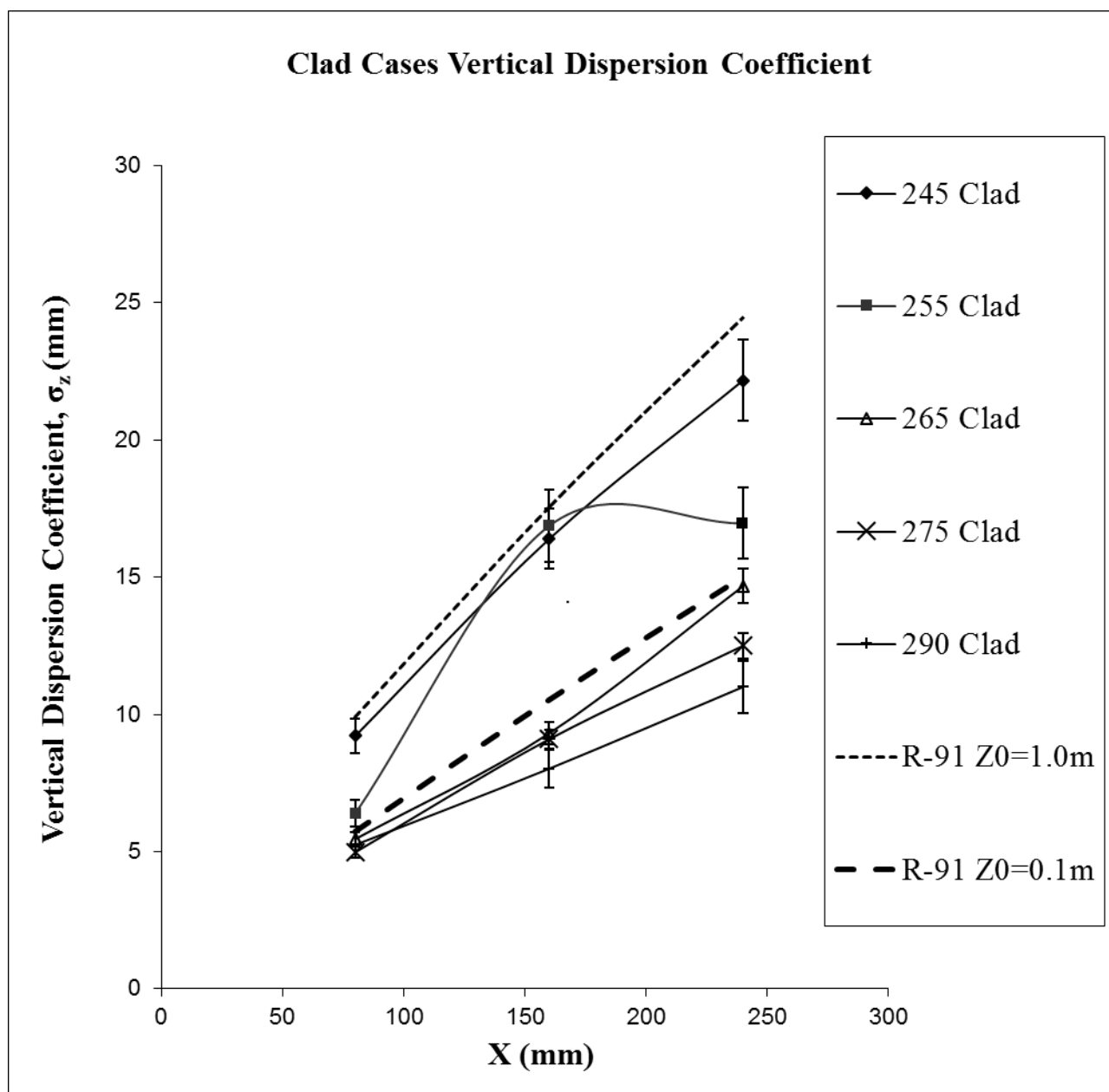


Figure 10. Vertical plume dispersion at downstream maximum concentration point

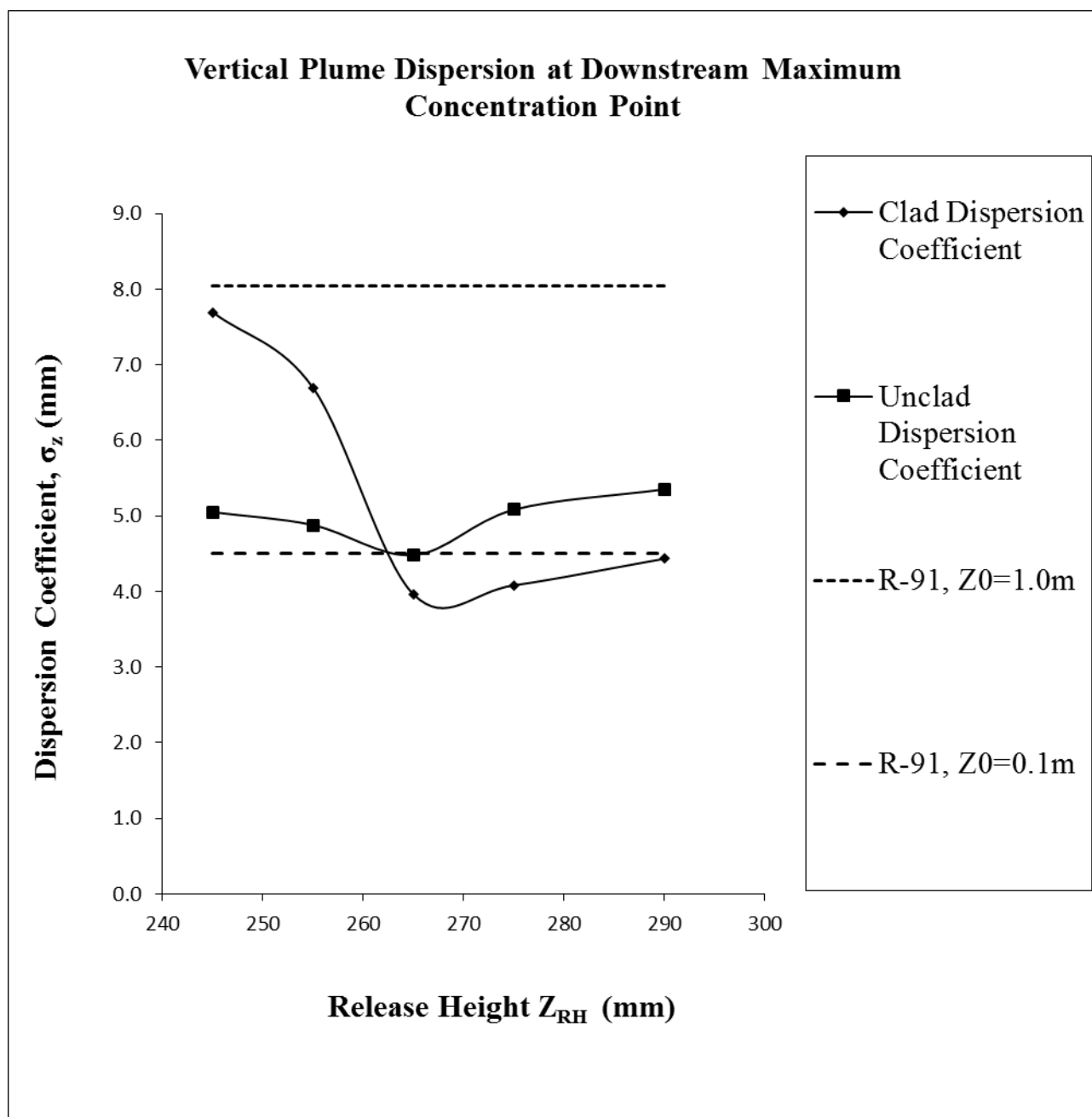


Table I. Weighted reciprocal velocities in 10 degree sectors over 5 years: all velocities in metres per second

Angle	2007	2008	2009	2010	2011	Mean (ms ⁻¹)	2SD (k=2)
0	3.989	2.974	2.581	3.041	2.562	3.029	1.159
10	3.006	2.860	2.698	2.833	3.195	2.919	0.378
20	2.906	3.063	2.769	3.210	3.129	3.015	0.354
30	2.816	2.836	3.119	3.622	2.968	3.072	0.660
40	2.932	2.997	3.275	3.762	3.053	3.204	0.675
50	3.133	3.011	2.974	3.930	2.614	3.132	0.972
60	3.585	3.377	3.336	2.988	3.092	3.275	0.475
70	3.061	3.574	3.292	3.249	3.125	3.260	0.397
80	3.220	3.670	3.143	3.451	2.718	3.241	0.715
90	3.296	3.392	3.478	3.074	3.388	3.326	0.310
100	3.058	3.110	3.128	3.034	3.281	3.122	0.193
110	2.280	3.127	3.085	2.946	2.780	2.844	0.686
120	3.520	3.063	3.238	3.156	2.999	3.195	0.406
130	3.200	4.423	3.641	3.133	3.488	3.577	1.033
140	3.513	4.090	3.652	2.898	3.211	3.473	0.902
150	4.625	3.576	3.974	3.289	3.624	3.817	1.025
160	3.457	4.478	4.274	4.434	4.042	4.137	0.833
170	4.506	4.812	4.389	3.610	3.517	4.167	1.146
180	4.583	4.815	4.750	4.236	4.189	4.515	0.578
190	4.509	4.567	4.229	4.291	3.873	4.294	0.550
200	5.218	5.240	4.768	4.191	4.595	4.803	0.885
210	5.800	5.454	4.792	4.473	5.655	5.235	1.149
220	5.169	4.818	4.839	4.145	4.953	4.785	0.767
230	4.901	5.114	5.278	4.154	5.332	4.956	0.957
240	5.043	5.303	4.724	4.417	5.357	4.969	0.795
250	4.584	4.961	5.059	4.403	5.220	4.845	0.680
260	4.251	4.721	4.464	3.761	4.476	4.335	0.722
270	3.639	4.313	3.932	3.623	4.217	3.945	0.638
280	3.239	3.565	3.152	3.195	3.462	3.323	0.361
290	3.039	3.119	3.392	3.228	3.043	3.164	0.297
300	3.019	2.970	2.876	3.024	3.939	3.166	0.873
310	2.562	2.934	2.547	2.592	2.935	2.714	0.404
320	2.581	2.945	2.327	2.602	2.635	2.618	0.440
330	2.514	2.854	2.521	3.010	2.057	2.591	0.735
340	2.701	2.665	2.318	2.460	2.191	2.467	0.438
350	2.615	3.322	2.380	3.047	2.870	2.847	0.733
360	3.989	2.974	2.581	3.041	2.562	3.029	1.159
Mean (weighted)	3.595	3.898	3.672	3.485	3.780	3.687	0.322

Note: all velocities are expressed at 10metres from ground level at the data site (Heathrow)

Table II. Wind direction probabilities at the reference data site

Angle	2007	2008	2009	2010	2011	Mean	2SD
0	0.026	0.013	0.012	0.026	0.012	0.0178	0.01468
10	0.037	0.027	0.019	0.033	0.023	0.0281	0.01437
20	0.029	0.019	0.031	0.040	0.025	0.0288	0.01541
30	0.042	0.025	0.032	0.054	0.024	0.0353	0.02506
40	0.031	0.023	0.027	0.051	0.027	0.0320	0.02191
50	0.028	0.032	0.029	0.033	0.024	0.0291	0.00756
60	0.024	0.025	0.013	0.025	0.019	0.0211	0.01050
70	0.014	0.018	0.016	0.015	0.021	0.0166	0.00563
80	0.011	0.016	0.015	0.015	0.018	0.0150	0.00510
90	0.015	0.025	0.018	0.013	0.018	0.0178	0.00950
100	0.009	0.011	0.017	0.014	0.017	0.0137	0.00762
110	0.007	0.010	0.014	0.010	0.016	0.0112	0.00701
120	0.008	0.010	0.011	0.010	0.013	0.0104	0.00379
130	0.010	0.012	0.013	0.012	0.011	0.0116	0.00279
140	0.006	0.011	0.014	0.011	0.016	0.0118	0.00771
150	0.010	0.011	0.020	0.017	0.018	0.0151	0.00937
160	0.010	0.011	0.014	0.020	0.018	0.0148	0.00884
170	0.016	0.018	0.022	0.024	0.019	0.0198	0.00618
180	0.024	0.033	0.041	0.027	0.038	0.0329	0.01455
190	0.032	0.032	0.041	0.023	0.032	0.0318	0.01254
200	0.033	0.034	0.035	0.026	0.028	0.0310	0.00811
210	0.053	0.070	0.065	0.042	0.057	0.0573	0.02162
220	0.044	0.054	0.049	0.037	0.067	0.0503	0.02310
230	0.055	0.060	0.047	0.038	0.068	0.0538	0.02298
240	0.044	0.050	0.044	0.045	0.051	0.0467	0.00745
250	0.057	0.073	0.046	0.033	0.060	0.0539	0.03079
260	0.063	0.052	0.065	0.053	0.068	0.0599	0.01456
270	0.048	0.043	0.056	0.053	0.051	0.0504	0.01041
280	0.025	0.029	0.038	0.032	0.025	0.0296	0.01060
290	0.035	0.036	0.030	0.029	0.020	0.0299	0.01274
300	0.030	0.028	0.029	0.035	0.028	0.0299	0.00557
310	0.033	0.031	0.023	0.019	0.018	0.0248	0.01353
320	0.031	0.014	0.018	0.022	0.013	0.0198	0.01430
330	0.029	0.016	0.018	0.021	0.012	0.0194	0.01279
340	0.015	0.012	0.009	0.021	0.007	0.0129	0.01096
350	0.017	0.015	0.010	0.021	0.015	0.0155	0.00835
360	0.026	0.013	0.012	0.026	0.012	0.0178	0.01468
Sum	1.000	1.000	1.000	1.000	1.000	1.000	0.0122*

*-mean value of 2SD values shown

Appendix A: Building Recirculation Zones

A model for a well-mixed region, as found in the wake immediately behind a building or over its roof is presented, following which a model for the recirculation zone around the roof top structure (RTS) is developed. The aim is to determine the relationship between the dimensionless concentration in the main recirculation zone to that in the region of the RTS.

(A.1) Well mixed wake zones: classical theory

Terminology

Main recirculation region: main well mixed zone, main wake zone

Roof top structure recirculation region: roof well mixed zone, roof zone

Note: the term ‘main wake’ is often used to define the wake downstream of the recirculation region.

We define the following quantities in the analysis.

A	building area
C	mean concentration in wake zone
H	wake region height scale (taken as the building height)
L	wake region length scale
Q	source strength
S	surface area of wake region
T	residence or wake time scale
U_H	mean wind speed (at roof level)
V	volume of wake region
W	lateral extent of building and wake region
w_E	entrainment speed

The balance equation for the well mixed zone is:

$$\frac{d(VC)}{dt} = Q - \alpha S U_H C$$

where α is a constant, and the mixing time scale follows by setting $Q=0$;

$$\frac{dC}{dt} = -\frac{\alpha S U_H C}{V}$$

We set $C(0)$ the well-mixed uniform concentration at a time $t=0$, with T as the residence time, so that:

$$C(t) = C(0)e^{-\frac{t}{T}}$$

Where:

$$T = \frac{V}{\alpha S U_H}$$

In the steady state:

$$Q = \alpha S U_H C \Rightarrow \frac{C U_H A}{Q} = \frac{A}{\alpha S}$$

The final result is written in terms of the measurable quantities, the wake time scale, T , and the length of the well-mixed region, L .

$$\frac{CU_H A}{Q} = \frac{A}{\alpha S} = \frac{U_H T}{H} \frac{AH}{V}$$

then with $V = AL/\beta$ and β an order one constant:

$$\frac{CU_H A}{Q} = \beta \frac{U_H T}{H} \frac{H}{L}$$

In dimensionless variables this is written in terms of the dimensionless concentration, χ , the dimensionless time, τ , and the dimensionless wake length, λ .

$$\chi = \beta \frac{\tau}{\lambda}$$

(A.2) *Analysis based on entrainment*

The balance equation becomes:

$$\frac{d(VC)}{dt} = Q - w_E SC$$

and again the steady state concentration and the time scale follow:

$$C = \frac{Q}{Sw_E}$$

$$T = \frac{V}{Sw_E}$$

and in dimensionless terms:

$$\tau = \frac{U_H T}{H} = \frac{V}{SH} \frac{U_H}{w_E}$$

So that:

$$\frac{w_E}{U_H} = \frac{V}{SH} \frac{1}{\tau}$$

and:

$$\chi = \frac{CU_H A}{Q} = \frac{A}{S} \frac{U_H}{w_E}$$

For the concentration, and once again using $V = AL/\beta$:

$$\chi = \frac{CU_H A}{Q} = \frac{A}{S} \frac{U_H}{w_E} = \frac{A}{S} \frac{SH}{V} \tau$$

$$\chi = \frac{AH}{V} \tau = \beta \frac{\tau}{\lambda}$$

As before. In terms of the dimensionless variables for which there are empirical functional forms, the entrainment speed is:

$$\frac{w_E}{U_H} = \frac{V}{SH} \frac{1}{\tau} = \frac{1}{\beta} \frac{A}{S} \frac{\lambda}{\tau} = \frac{1}{\beta} \frac{H}{s} \frac{\lambda}{\tau}$$

Where $A=WH$, $S=Ws$, and H/s is a shape parameter.

(A.3) The roof well mixed zone

The model for the roof zone is expressed in terms of the entrainment speed as:

$$\frac{d(VC)_r}{dt} = Q - w_E S_r C_r$$

and again a steady state concentration and time scale follow:

$$C_r = \frac{Q}{S_r w_E}$$

$$T_r = \frac{V_r}{S_r w_E}$$

And in dimensionless terms:

$$\tau_r = \frac{U_H T_r}{H} = \frac{V_r}{S_r H_r} \frac{H_r}{H} \frac{U_H}{w_E}$$

$$\chi_r = \frac{C_r U_H A}{Q} = \frac{A}{S_r} \frac{U_H}{w_E} = \frac{H}{s_r} \frac{U_H}{w_E}$$

Where $S_r = W S_r$

If the entrainment speed is taken to be the same as for the main wake:

$$\chi_r = \frac{C_r U_H A}{Q} = \frac{H}{s_r} \frac{U_H}{w_E} = \beta \frac{H_r}{s_r} \frac{s}{H} \frac{H}{H_r} \frac{\tau}{\lambda} = \beta \delta \frac{H}{H_r} \frac{\tau}{\lambda}$$

Where $\delta = \frac{H_r}{s_r} \frac{s}{H}$ is another shape factor. Taking $\delta=0.5$ leads to:

$$\chi_r = \frac{1}{2} \frac{H}{H_r} \beta \frac{\tau}{\lambda} = \frac{1}{2} \frac{H}{H_r} \chi$$

In the circumstances where the length of the RTS were sufficiently great in relation to the obstacle width the value of $\delta=1$ would be more appropriate.

Appendix B: Wind Tunnel Gamma Dose Formulation

The plume gamma shine dose expressed as an integral in (x,y,z) co-ordinates as follows in equation [B1]:

$$\dot{D}_\gamma = K Y E_\gamma \left(\frac{\mu_a}{\rho} \right) \iint dx dy \int_{z=H}^{z=\infty} dz C(x, y, z_{RH}) e^{-\left\{ \frac{(z-z_{RH})^2}{2\sigma_z^2} \right\}} B(\mu | \underline{r} - \underline{r}_p |) \frac{e^{-\mu | \underline{r} - \underline{r}_p |}}{4\pi | \underline{r} - \underline{r}_p |^2}$$

The term $C(x, y, z_{RH})$ expresses the concentration along the plume centreline of fixed height with neutral buoyancy, and this term is a function of downwind distance x and crosswind distance y , only. When considering the dose arising from the plume in the vicinity of the roof of a building height H we integrate the profile along a vertical axis from H . Close to the source, reflections from the atmospheric boundary layer edge are neglected in terms of their effect on the vertical profile. Secondly, we choose the receptor co-ordinate \underline{r}_p so that $z_p \neq z_m$, where z_m is the height of the measurement co-ordinate plane above the roof. This removes a singularity in the equation during numerical integration over the summation of sample points. Since we measured concentration values at an array of points (x_i, y_i, z_m) , where z_m was a fixed height above the roof, we may define an effective height of the concentration H_{vol} above the receptor height location. Unit area at this point of height H_{vol} and multiplied by the measured concentration $C(x, y, z = z_m)$ will therefore contain the same amount of radioactive gas (in Bq) as that of the integrated plume profile. H_{vol} enables the full activity of the plume to be accounted in the plume gamma shine dose rate calculation and may be expressed in [B2].

$$H_{vol} C(x_p, y_p, z_m) = \int_{z=H}^{z=\infty} C(x_p, y_p, z_{RH}) e^{-\left\{ \frac{(z-z_{RH})^2}{2\sigma_z^2} \right\}} dz \quad [B2]$$

We now integrate over z in equation by defining a function $J(x,y)$:

$$J(x, y) = \int_{z=H}^{z=\infty} C(x, y, z_{RH}) e^{-\left\{ \frac{(z-z_{RH})^2}{2\sigma_z^2} \right\}} B(\mu | \underline{r} - \underline{r}_p |) \frac{e^{-\mu | \underline{r} - \underline{r}_p |}}{4\pi | \underline{r} - \underline{r}_p |^2} dz \quad [B3]$$

The dose rate equation can therefore be rewritten:

$$\dot{D}_\gamma = K Y E_\gamma \left(\frac{\mu_a}{\rho} \right) \iint J(x, y) dx dy \quad [B4]$$

By inspection of equation [B2] we see that H_{vol} depends on the co-ordinate (x_p, y_p) . We now define the receptor point of interest as being the one closest to the measured plume concentration maximum in the (x,y) plane. Furthermore, we make the approximation in the near-field region of the receptor point that equation [B2] holds over the near-field array used for the dose estimation. This means we treat the lateral and vertical dispersion coefficients σ_y and σ_z as slowly-varying functions of the downstream distance x in the near-field region. Then equation [B2] applies generally over the concentration field measurement and is expressed as equation [B5].

$$H_{vol} C(x, y, z_m) = \int_{z=H}^{z=\infty} C(x, y, z_{RH}) e^{-\left\{ \frac{(z-z_{RH})^2}{2\sigma_z^2} \right\}} dz \quad [B5]$$

From [B3] and [B5] we see that a weighted mean function over the inverse-square fall off, build-up and air path attenuation factors can be defined as follows:

$$\frac{J(x,y)}{H_{vol}C(x,y,z_m)} = \frac{\int_{z=H}^{z=\infty} C(x,y,z_{RH}) e^{-\left\{\frac{(z-z_{RH})^2}{2\sigma_z^2}\right\}} B(\mu|\underline{r}-\underline{r}_p|) \frac{e^{-\mu|\underline{r}-\underline{r}_p|}}{4\pi|\underline{r}-\underline{r}_p|^2} dz}{\int_{z=H}^{z=\infty} C(x,y,z_{RH}) e^{-\left\{\frac{(z-z_{RH})^2}{2\sigma_z^2}\right\}} dz} \quad [B6]$$

It is necessary to exclude a volume around the receptor point where $|\underline{r} - \underline{r}_p| < \delta$, which is physically realisable in the form of a receptor volume in which the dose is measured. In practice this condition is satisfied during the numerical integration by the condition that for the numerical integration $z_p \neq z_{RH}$. We make one further approximation by treating the magnitude of vector $(\underline{r} - \underline{r}_p)$ as equal to the length of R_p as defined in equation [B7].

$$R_p^2 = (x - x_p)^2 + (y - y_p)^2 + (z_{RH} - z_p)^2 \quad [B7]$$

This treats the weighted values of the build-up, attenuation and inverse-square fall-off functions as equal to their values calculated for a value of R_p the distance to the plume centreline above the measurement point to the receptor point. Since R_p is a function of (x,y) , and the fixed co-ordinates z_p and z_{RH} , equation [B6] becomes [B8]:

$$J(x,y) = H_{vol}C(x,y,z_m)B(\mu R_p) \frac{e^{-\mu R_p}}{4\pi R_p^2} \quad [B8]$$

Following substitution into equation [B4]:

$$\dot{D}_\gamma = K Y E_\gamma \left(\frac{\mu_a}{\rho} \right) \iint H_{vol}C(x,y,z_m)B(\mu R_p) \frac{e^{-\mu R_p}}{4\pi R_p^2} dx dy \quad [B9]$$

From the sampled values of the concentration field this integral can be evaluated numerically by the following summation.

$$\dot{D}_\gamma = K Y E_\gamma \left(\frac{\mu_a}{\rho} \right) \sum_{i=1}^N H_{vol} \Delta_i C(x_i, y_i, z_i = z_m) B(\mu R_{p_i}) \frac{e^{-\mu R_{p_i}}}{4\pi R_{p_i}^2} \quad [B10]$$

Where Δ_i is the area element associated with the sample point $(x_i, y_i, z_i = z_m)$. Since the values of the area elements are equal due to a uniform sampling grid adopted in the experiment we write that $\Delta_i = \Delta$, a constant.